Mineralogy and mineral processing to optimise recovery of synchysite-(Ce) and apatite from carbonatite at Songwe Hill, Malawi

Submitted by
Safaa Hussein Ali Al-Ali
To the University of Exeter as a thesis for the degree of
Doctor of Philosophy in Mining and Minerals Engineering
In October 2016

I certify that all material in this thesis which is not my own work has been identified and that no material has previously been submitted and approved for the award of a degree by this or any other University.

Signature ……

Abstract

Rare earth elements (REE) are considered as critical and non-substitutable metals for electronics and green technology. A greater diversity of supply is needed and the REE occur in a wide range of REE- and REE-bearing minerals within different ore deposit types. The beneficiation processes for REE ores can vary widely based on their mineralogy and texture. It is, therefore, essential to understand the mineralogical characteristics when designing processing routes. Little research was carried out on this topic until the last few years, apart from bastnäsite, monazite, and xenotime, and most REE minerals in deposits currently under exploration are poorly understood in terms of processing characteristics.

This geometallurgical study brings together the results of process mineralogy and minerals processing to recover synchysite-(Ce) and apatite from the carbonatite at Songwe Hill, Malawi. This deposit is unusual because it is a potential carbonatite source of both LREE and HREE. Results from previous flowsheet development studies on this deposit suggest that flotation is the most promising processing route and therefore this study concentrated on testing this hypothesis. It sought to understand the mineralogy better in order to predict processing response and carried out a series of flotation experiments to improve the processing efficiency. It also investigated the fundamental magnetic properties of the rare earth fluorcarbonate minerals (including synchysite) and established for the first time that there is a systematic variation in their properties that can be applied to minerals processing.

Eight samples of REE carbonatite drill core, crushed to 1700 µm, and a composite sample ground to 53 µm and 38 µm were used throughout this research. Automated mineralogy (QEMSCAN®) was applied to determine the mineralogical characteristics of the ore deposit. This utilised a novel species identification protocol (SIP) for REE minerals in carbonatites, which was validated by electron microscopy (SEM-EDS), and electron probe microanalysis (EPMA).

The principal REE minerals at Songwe are the REE fluorcarbonates, synchysite-(Ce) and also parisite-(Ce). These are challenging minerals for automated mineralogical techniques owing to their chemical similarity and common occurrence either as bladed (needle-like) crystals, which is the main textural type at Songwe Hill, or as

syntaxial intergrowths. However, using the SIP developed in this study, the QEMSCAN® can distinguish between these minerals based on the Ca content and can also recognise syntaxial intergrowths on a scale of about > 20 µm.

The Songwe Hill carbonatite hosts about 6 wt% to 10 wt% of REE- and REE-bearing minerals. Apatite hosts the more valuable HREE in addition to P_2O_5, followed by synchysite-(Ce)/parisite-(Ce) (mainly synchysite-(Ce)), and minor florencite-(Ce), which host the LREE. These minerals are commonly associated with the predominant gangue minerals, ankerite and calcite, and, to a lesser extent Fe-Ox/CO_3 and K-feldspar, strontianite and baryte.

Fundamental magnetic properties of pure REE fluorcarbonate single crystal minerals using a vibrating sample magnetometer (VSM) were determined. The magnetic susceptibility is highly dependent on the mineral composition. It is positive (paramagnetic) for bastnäsite-(Ce) and gradually decreases as the amount of Ca increases in parisite-(Ce), becoming negative (diamagnetic) for the Ca-rich member of the series, röntgenite. Synchysite-(Ce) in this deposit was experimentally determined by magnetic separation and behaved as a diamagnetic mineral. This can be explained by the layered structure common to the REE fluorcarbonate series minerals.

Selected laboratory scale mineral processing experiments including magnetic separation and froth flotation were performed. Pre-concentration tests by magnetic separation showed a recovery of 84% for P_2O_5, 80% for Y_2O_3, and 76% for Ce_2O_3 in the non-magnetic product, with gangue minerals rejection of about 49% for ankerite and 48% for Fe-Ox/CO_3 to the magnetic product. Apatite and synchysite-(Ce) loss to the magnetic product is mainly the result of their association with the paramagnetic minerals i.e. ankerite and Fe-Ox/CO_3 as indicated by automated mineralogy.

A spectrophotometer was utilised to measure the solubility of the organic chemical reagents including fatty acids and lignin sulphonate in different alkaline solutions and to determine the appropriate operating parameters for bench flotation tests. The results indicated that the solubility of fatty acids increased with increasing the pH value from 8.5 to 10.5, while the opposite was observed for lignin sulphonate.

35 bench-scale froth flotation tests under a wide range of chemical and operating conditions including pH modifiers and dosages, soluble and insoluble collectors,

depressants, temperature, and conditioning time were performed. The results demonstrated that fatty acids and lignin sulphonate are sensitive to changes in pH, conditioning time, and temperature. These factors significantly affected flotation efficiency. A recovery of 86% for P_2O_5 and 74% for both of Y_2O_3 and Ce_2O_3 with TREO upgrading from 1.6 wt% to 3.8 wt% at a mass pull of 31% were achieved under a constant pulp pH of 9.5, elevated temperature, and long conditioning time.

This study suggests that combining magnetic separation and froth flotation techniques to pre-concentrate and upgrade the REE- and REE-bearing minerals, should be considered further to minimise the cost of the chemical reagents used in froth flotation and gangue leaching.

Acknowledgements

I am indebted to my supervisors Frances Wall and Richard Pascoe for all of their guidance throughout this research project. My great thanks go to the Higher Education Committee in Iraq for providing the funding for this PhD research. I would also like to thank Will Dawes and Aoife Brady of Mkango Resources Ltd., and Nthapo Sehlotho of Mintek for providing the drill core samples with their elemental analyses for this PhD project, and sharing and discussing the outputs of the mineral processing tests.

I am grateful to the staff members at Camborne School of Mines, especially Gavyn Rollinson for the training about QEMSCAN® Software, setting up the Species Identification Protocol, and discussing my results, along with Robert Fitzpatrick for the assistance in the minerals processing lab and discussing the results. My thanks also go to Sharon Uren for help with ICP-MS, Joe Pickles for support using EPMA, Malcolm Spence for analysing the samples by XRF, and Steve Pendray for kindly preparing the polished blocks. My thanks also go to Sam Broom-Fendley for scientific discussions and Ed Loye for helping to obtain some of the mineral samples. I also would like to thank all my colleagues in the PhD room in particular Luke Palmer, James Barnet, Ricardo Celestino, Keziah Blake-Mizen, Robert Pell, and Bethany Colgan. I greatly appreciate the support from Christopher Bryan and Rachel Bransgrove when using the Spectrophotometer instrument at the Environment and Sustainability Institute, University of Exeter.

I am also grateful to Richard Sheridan at the School of Metallurgy and Materials, University of Birmingham, for training me in the use of the VSM equipment and kindly measuring the pure REE fluorcarbonate minerals.

Special thanks to my entire family for their support and encouragement over the last four years of my PhD studies.

Contents

List of Figures

List of Tables

List of Acronyms

µm	Micrometre
Ank	Ankerite
apfu	Atoms per formula unit
Apt	Apatite
Brt	Baryte
BSE	Backscattered electron
Cal	Calcite
CAP	Chilwa Alkaline Province
CSM	Camborne School of Mines
EDS	Energy-dispersive spectrometry
EPMA	Electron probe microanalysis
Feld	K-feldspar
Florn	Florencite
Goth	Goethite
Hmt	Hematite
HREE	Heavy rare earth elements
ICP-MS	Inductively coupled plasma mass spectrometry
ICP-OES	Inductively coupled plasma optical emission spectrometry
km	Kilometre
kV	Kilovolt
LREE	Light rare earth elements
m	Meter
mm	Millimetre
MREE	Mid rare earth elements
Mt	Million metric tonnes
nA	Nanoampere
NHM	Natural History Museum
Pcl	Pyrochlore
Prst	Parisite
pXRF	Portable X-ray fluorescence
Pyt	Pyrite
QEMSCAN®	Quantitative evaluation of minerals by scanning electron microscopy
REE	Rare earth elements
REO	Rare earth oxides
SEM	Scanning electron microscopy
Sid	Siderite
SIP	Species identification protocol
Strn	Strontianite
Syn	Synchysite
T	Tesla
TREO	Total rare earth oxides
VSM	Vibrating sample magnetometer
WDS	Wavelength-dispersive spectrometry
WHIMS	Wet high intensity magnetic separator
XRD	X-ray diffraction
XRF	X-ray fluorescence

Chapter 1

Introduction and literature review

1.1 Introduction

This chapter introduces the aims of the study and its specific objectives. It then reviews the rare earth elements and their minerals, deposits, and applications. A detailed description of the REE fluorcarbonate and apatite is presented. An overview of processing REE- and REE-bearing minerals, particularly synchysite and apatite is given, together with definitions and background on the mechanisms of the main processing techniques used for these minerals, including gravity concentration, magnetic separation, and froth flotation.

1.2 Project rationale

The rare earth elements (REE) have unique physical and chemical properties, which make them essential in many high-tech products and advanced materials. REE occur in a wide variety of minerals, including silicates, oxides, carbonates, phosphates, and halides distributed in many rock types of the Earth's crust. Although there are a large number of rare earth minerals, only bastnäsite, monazite, and xenotime in addition to ion adsorption clays are the principal resources for about 95% of all the world REE (Krishnamurthy and Gupta, 2016). Other REE- and REE-bearing minerals that are also considered potential sources of REE are synchysite, parisite, gadolinite, fergusonite, apatite, eudialyte, euxenite, allanite and florencite.

In recent years there has been an increasing demand for the REE (particularly the heavy rare earth elements (HREE) for so many applications such as permanent magnets, batteries, wind turbine, hybrid cars, catalysts, polishing powders, ceramics and more (Long et al., 2010; British Geological Survey, 2011). It is important to note that China is home of the largest rare earth deposits in the world, providing approximately 86% of the world's total supply originated from its several mining districts (USGS, 2016a).

To meet the growing demand of REE and to reduce the import level of REE from China, a number of new rare earth deposits were discovered outside of China and

several are now under development and/or into production. Examples of these rare earth deposits are: Mt. Weld and Nolans Bore in Australia, Nechalacho and Hoidas Lake in Canada, Kvanefjeld in Greenland, Mrima Hill in Kenya, Kutessay in Kazakhstan, Songwe Hill in Malawi, Lofdal in Namibia, Norra Kärr in Sweden, Ngualla in Tanzania, Bear Lodge and Bokan Mountain in USA, and many more (Chakhmouradian and Wall, 2012; Mariano and Mariano, 2012; Krishnamurthy and Gupta, 2016).

Songwe Hill carbonatite deposit, the area of this study, which located in Malawi (see Chapter 2) is one of the advanced rare earth projects. The principal REE- and REE-bearing minerals in this ore deposit are apatite, synchysite, and florencite. Apatite is anomalously enriched in the HREE compared to apatites in most carbonatite deposits (Broom-Fendley, 2015). Synchysite is a member of the REE fluorcarbonate series minerals and mainly enriched in the LREE.

One of the main challenges in developing new rare earth deposits is the lack of knowledge about the rare earth minerals themselves. Fundamental properties relevant to mineral processing have not been determined for some of the most important rare earth minerals. An example of this is synchysite, the target REE mineral of this study, and one of the most common REE minerals in many deposits associated with alkaline rocks and carbonatites.

1.3 Aims of the study

The aims of this study are to characterise the mineralogy of valuable and gangue minerals at the Songwe Hill carbonatite complex, Malawi, and to determine the REE and P concentration in the minerals of interest. A further aim of this study is to utilise the mineralogical characterisation to optimise separation of fine-grained apatite and synchysite from their gangue matrices.

1.3.1 Specific objectives

1. Perform elemental analyses to identify the major, minor, and rare earth elements in eight crushed drill core samples.
2. Identify and quantify the valuable and gangue minerals of the Songwe Hill carbonatite deposit, and their characteristics in terms of mineral abundance, liberation, and association using X-ray Diffraction (XRD), Scanning Electron

Microscopy (SEM-EDS) and Quantitative Evaluation of Minerals by Scanning Electron Microscopy (QEMSCSAN®).

3. Determine the chemical composition of the valuable minerals using Electron Probe Microanalysis (EPMA).
4. Measure the magnetic properties of the REE fluorcarbonate minerals using Vibrating Sample Magnetometer (VSM).
5. Undertake selected laboratory scale mineral processing experiments using magnetic separation and bench-scale froth flotation to separate and optimise the grade and recovery of the valuable minerals.

1.3.2 Approaches

This geometallurgical research project brings together the results of process mineralogy (i.e. mineralogy and texture) and mineral processing (i.e. grade and recovery) to recover synchysite-(Ce) and apatite from a carbonatite deposit at Songwe Hill, Malawi. The crushed drill core samples from Songwe Hill were provided by Mkango Resources Ltd. via Mintek in South Africa

The mineralogy aspect was initially performed by following and combining the recent work on the mineralogy, petrology, and geochemistry of the Songwe Hill, mainly focused on the HREE mineralisation in apatite, achieved by Broom-Fendley (2015). Extensive automated mineralogy (QEMSCAN®) was applied to determine the mineralogical characteristics of the ore deposit. This was carried out by developing a novel species identification protocol (SIP) for REE minerals, which was validated by SEM-EDS and EPMA.

The mineral processing aspect was conducted by looking at the mineral processing techniques of direct interest to Mkango Resources Ltd., particularly froth flotation. Also, work was performed to measure the fundamental magnetic properties of pure single crystals of REE fluorcarbonate minerals along with conducting magnetic separation testwork on the Songwe Hill carbonatite deposit.

1.4 Rare earth elements, minerals, deposits, and their applications

1.4.1 Rare earth elements family and its properties

Rare Earth Elements (REE) are a group of elements with a very similar chemical behaviour. This group comprises 15 lanthanides (lanthanoids) plus scandium and yttrium, as defined by the International Union of Pure and Applied Chemistry (IUPAC). These REE include scandium (Sc, Z = 21), yttrium (Y, Z = 39), lanthanum (La, Z = 57) and the 15 elements following lanthanum in the Periodic Table of elements, i.e. from cerium (Ce, Z = 58) to lutetium (Lu, Z = 71) (Wall, 2014).

All lanthanides are found in nature, except promethium (a radioactive element), which has no long-lived or stable isotopes (British Geological Survey, 2011). Furthermore, earth scientists commonly do not consider Sc as a REE owing to its small ionic radius leading it to behave differently in nature (Chakhmouradian and Wall, 2012). This leaves a grouping of 14 lanthanides plus Y into the REE family, which is sometimes abbreviated as REY (rare earths and yttrium; Wall, 2014). Note the term REE used in this study refers to all rare earth elements (excluding scandium and promethium).

The REE are generally classified into light rare earth elements (LREE), with lower atomic numbers (La, Ce, Pr, Nd, Pm, Sm and Eu), and heavy rare earth elements (HREE), with higher atomic numbers (Gd, Tb, Dy, Ho, Er, Tm, Yb and Lu). Owing to its similar behaviour, ionic radius, and charge, Y is grouped with the HREE. In addition, the term mid '(M)REE' is sometimes used to refer to elements between Sm and Gd (British Geological Survey, 2011; Chakhmouradian and Wall, 2012; Hatch, 2012).

The estimated abundance of some of the REE in the Earth's crust is very low, but not lower than some economic elements, which are not considered rare elements (Henderson, 1996). For example, the abundances of Gd (3.8 ppm), Dy (3.5 ppm), and Er (2.3 ppm) in earth's crust are higher than the abundance of Au (0.004 ppm), Indium (0.05 ppm) and tungsten (1 ppm) (Taylor and McLennan, 1985; Brown and Pitfield, 2014; Schwarz-Schampera, 2014). The relative abundance of REE in the continental crust is significantly varied for two reasons: firstly, the LREE have larger ionic radii and thus are more abundant in the Earth's crust than the HREE, which have smaller ionic radii, and secondly, the elements with an even atomic number are

more concentrated than their neighbours with an odd atomic number (Oddo-Harkins effect; Figure 1.1; British Geological Survey, 2011).

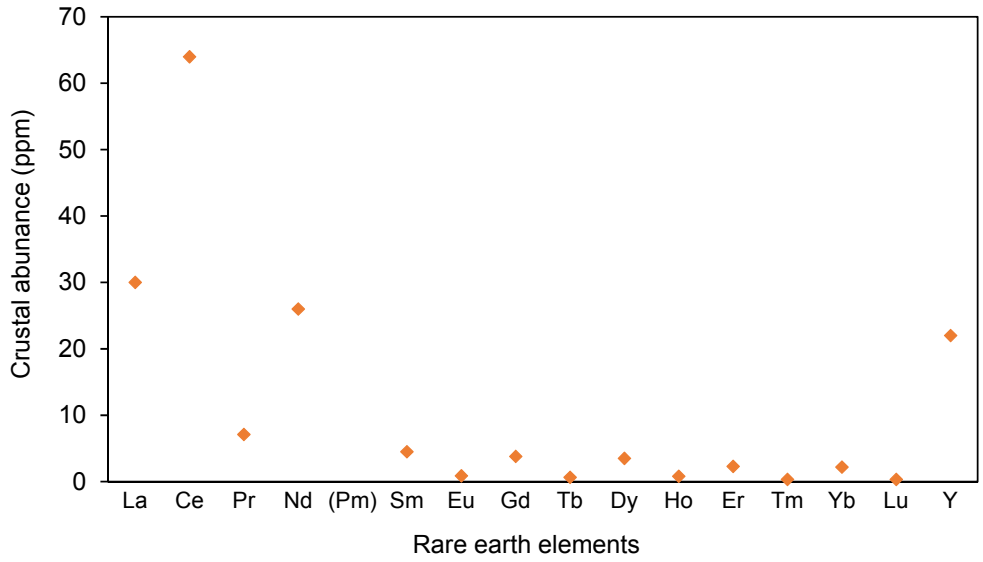

Figure 1.1: Abundance of REE in the Earth's crust, after Taylor and McClennan (1985)

The term 'rare' earth elements arises from the historical challenge of separating REE minerals and obtaining individual pure elements rather than from their natural abundance. These challenges come from the similar chemical and physical properties of the REE, and their natural occurrence together in minerals and tendency to act as a single chemical entity (Gupta and Krishnamurthy, 2005).

1.4.2 Rare earth minerals

Rare earth elements do not occur as metallic elements but are found in different types of minerals including silicates, carbonates, oxides, phosphates, and halides (British Geological Survey, 2011). There are about 200 different REE minerals that have been discovered to date and have had their chemical formula approved by the International Mineralogical Association (2016). Five or six new REE minerals are typically discovered every year (Chakhmouradian and Wall, 2012). Examples of common light and heavy REE minerals are included in Table 1.1.

Table 1.1: Common rare earth minerals and corresponding approximate REO contents, adapted from British Geological Survey (2011).

Mineral name	Mineral formula	Approximate REO wt%
Aeschynite-(Ce)	$(Ce,Ca,Fe,Th)(Ti,Nb)_2(O,OH)_6$	32
Allanite-(Ce)	$(Ce,Ca,Y)_2(Al,Fe)_3(SiO4)_3(OH)$	38
Apatite	$Ca_5(PO_4)_3(F,Cl,OH)$	19
Bastnäsite-(Ce)	$(Ce,La)(CO_3)F$	75
Brannerite	$(U,Ca,Y,Ce)(Ti,Fe)_2O_6$	9
Britholite-(Ce)	$(Ce,Ca)_5(SiO_4,PO_4)_3(OH,F)$	32
Cebaite-(Ce)	$Ba_3Ce_2(CO_3)_5F_2$	32
Eudialyte	$Na_4(Ca,Ce)_2(Fe,Mn,Y)ZrSi_8O_{22}(OH,Cl)_2$	9
Euxenite-(Y)	$(Y,Ca,Ce,U,Th)(Nb,Ta,Ti)_2O_6$	24
Fergusonite-(Ce)	$(Ce,La,Nd)NbO_4$	53
Florencite-(Ce)	$CeAl_3(PO_4)_2(OH)_6$	32
Gadolinite-(Ce)	$(Ce,La,NdY)_2FeBe_2Si_2O_{10}$	60
Huanghoite-(Ce)	$BaCe(CO_3)_2F$	39
Kainosite(Y)	$Ca_2(Y,Ce)_2Si_4O_{12}CO_3.H_2O$	38
Loparite	$(Ce,La,Na,Ca,Sr)(Ti,Nb)O_3$	30
Monazite-(Ce)	$(Ce,La,Nd,Th)(PO_4)$	65
Parisite-(Ce)	$Ca(Ce,La)_2(CO_3)_3F_2$	61
Samarskite(Y)	$(Y,Ce,U,Fe)_3(Nb,Ta,Ti)_5O_{16}$	24
Synchysite-(Ce)	$Ca(Ce,La)(CO_3)_2F$	51
Xenotime	YPO_4	61
Yttrocerite	$(Ca,Ce,Y,La)F_3.nH_2O$	53

REE minerals are defined as minerals with the REE as an essential structural and chemical component, e.g.: bastnäsite-(Ce), monazite-(Ce), and xenotime-(Y). However, other minerals can commonly contain minor or trace amounts of REE as a result of substitution into other cation sites during geological processes, e.g.: apatite, zircon, and fluorite (Levinson, 1966; Chakhmouradian and Wall, 2012). According to the International Mineralogical Association (IMA) guidelines on mineral nomenclature and classification, all determined REE mineral species must have a chemical symbol suffix by appending the predominant REE to the mineral group name (Bayliss and Levinson, 1988). For example, bastnäsite-(Ce), indicating cerium is the predominant REE within the bastnäsite crystal structure. However, most REE minerals contain significant other REE as a result of extensive substitution among these elements.

As mentioned above, although there are about 200 REE minerals, most of them are rare. Only bastnäsite, monazite, and xenotime are common REE minerals and, with ion-adsorption clay deposits (a unique deposit type), are considered principal ore mineral for about 95% of all the world rare earth element (Krishnamurthy and Gupta, 2016).

Bastnäsite is the most common and important REE mineral, which hosts approximately 75% rare earth oxides (REO), mainly dominated by LREE. Thorium contents are typically low. Bastnäsite occurs in different deposit types including carbonatites and peralkaline granites and syenites. It is currently and recently mined as a primary REE mineral at Bayan Obo and Maoniuping in China, Mountain Pass mine in California, and Mt Weld in Australia (Mariano, 1989; Mariano and Mariano, 2012; Krishnamurthy and Gupta, 2016).

Monazite is one of the most common REE minerals after bastnäsite. It contains about 70 wt% REO and is commonly enriched in LREE in addition to other components including thorium, calcium, and silicon (Wall, 2014; Krishnamurthy and Gupta, 2016). It occurs as an accessory mineral in granite and some metamorphic rocks such as gneiss, as well as in sedimentary rocks and beach sand placer deposits due to its resistance to chemical weathering (Mariano and Mariano, 2012; Wall, 2014).

The most common HREE mineral is xenotime. Xenotime is a Y-bearing phosphate and contains approximately 67 wt% REO mainly dominated by HREE (Krishnamurthy and Gupta, 2016). It occurs in some igneous rocks such as granite as an accessory mineral in addition to placer deposits such as beach sands (Mariano and Mariano, 2012).

Other REE- and REE-bearing minerals that are also considered potential (and active) economic sources for REE are synchysite, parisite, gadolinite, loparite, fergusonite, apatite, eudialyte, euxenite, allanite and florencite.

1.4.3 Rare earth deposits

REE minerals occur in a wide range of ore deposits. These deposits can be divided into carbonatite-associated deposits, including weathered carbonatite; alkaline igneous rocks, including alkaline granites; other hydrothermal deposits; ion adsorption deposits; placer deposits and seafloor deposits. REE are also produced

as by-products of other minerals and can be recovered from waste (Wall, 2014). The global distribution of REE deposits of the different categories is illustrated in Figure 1.2.

Carbonatites are igneous rocks that contain more than 50% carbonate minerals. They are thought to originate from carbon dioxide-rich and silica-poor magmas from the upper mantle (British Geological Survey, 2011). Carbonatite is considered the most dominant source for the REE (Jackson and Christiansen, 1993). However, the REE in carbonatites almost exclusively comprise the LREE, occurring in bastnäsite, allanite, and apatite. Monazite, when present, usually contains high REE contents and low Ca and Th concentrations (Gupta and Krishnamurthy, 2005). The two most well-known REE-rich carbonatites/carbonatite-related rocks are at Mountain Pass, USA, and Bayan Obo, China.

Weathering of carbonatite or alteration by hydrothermal fluids can lead to the dissolution of carbonate and concentration of the less-soluble REE. A good example of a weathered carbonatite where this has occurred is the monazite deposit at Mt Weld, Australia (Lottermoser, 1990).

Alkaline igneous rocks form from magma so enriched in alkalis that they precipitate Na- and K-oversaturated minerals, such as feldspathoids. These rocks contain characteristic mineral suites, including complex Na, Ti, and Zr silicates. Some of these minerals, such as eudialyte, can host significant REE quantities. Alkaline rock deposits are generally larger but relatively lower grade than carbonatites. These deposits typically contain higher proportions of HREE, and Zr can be an attractive co-product (Castor and Hedrick, 2006; British Geological Survey, 2011).

Ion-adsorption type deposits form from the intense chemical weathering of granites. Leached REE, from the weathering process, adsorb onto the surface of clay minerals in the weathering horizon, as well as forming secondary REE minerals. This deposit type is easy to mine and process, as well as being relatively rich in the HREE. A key example is the clay deposits of Southern China (Sanematsu and Watanabe, 2016).

1.4.4 Applications of REE

REE have unique physical and chemical properties, which make them essential in many high-tech products and advanced materials such as permanent magnets, phosphors, catalysts, batteries, polishing powders, and many more (Table 1.2).

It is important to note that the entire REE family, especially the HREE, are considered 'critical metals' (European commission, 2014). This is due to their economic importance and high supply-risk to reliance on a small number of sources dominated by China (~86% of the world's supply) (USGS, 2016a). There is a sufficient supply of the LREE, but there is a growing demand and shortage of supply of the HREE, which causes considerable price volatility.

Table 1.2: Major uses of REE in clean energy technologies and other components (Bauer et al., 2010; Lynas Corporation, 2010; Krishnamurthy and Gupta, 2016).

REE	Wind turbines	Vehicles		Lighting	Fluid catalytic cracking	Polishing powders	Auto catalysts	Ceramics
	Magnets	Magnets	Batteries	Phosphors				
La			●	●	●	●	●	●
Ce			●	●	●	●	●	●
Pr	●	●	●		●			●
Nd	●	●	●		●	●	●	●
Sm	●	●						
Eu				●				
Tb				●				
Dy	●	●						
Y				●				●

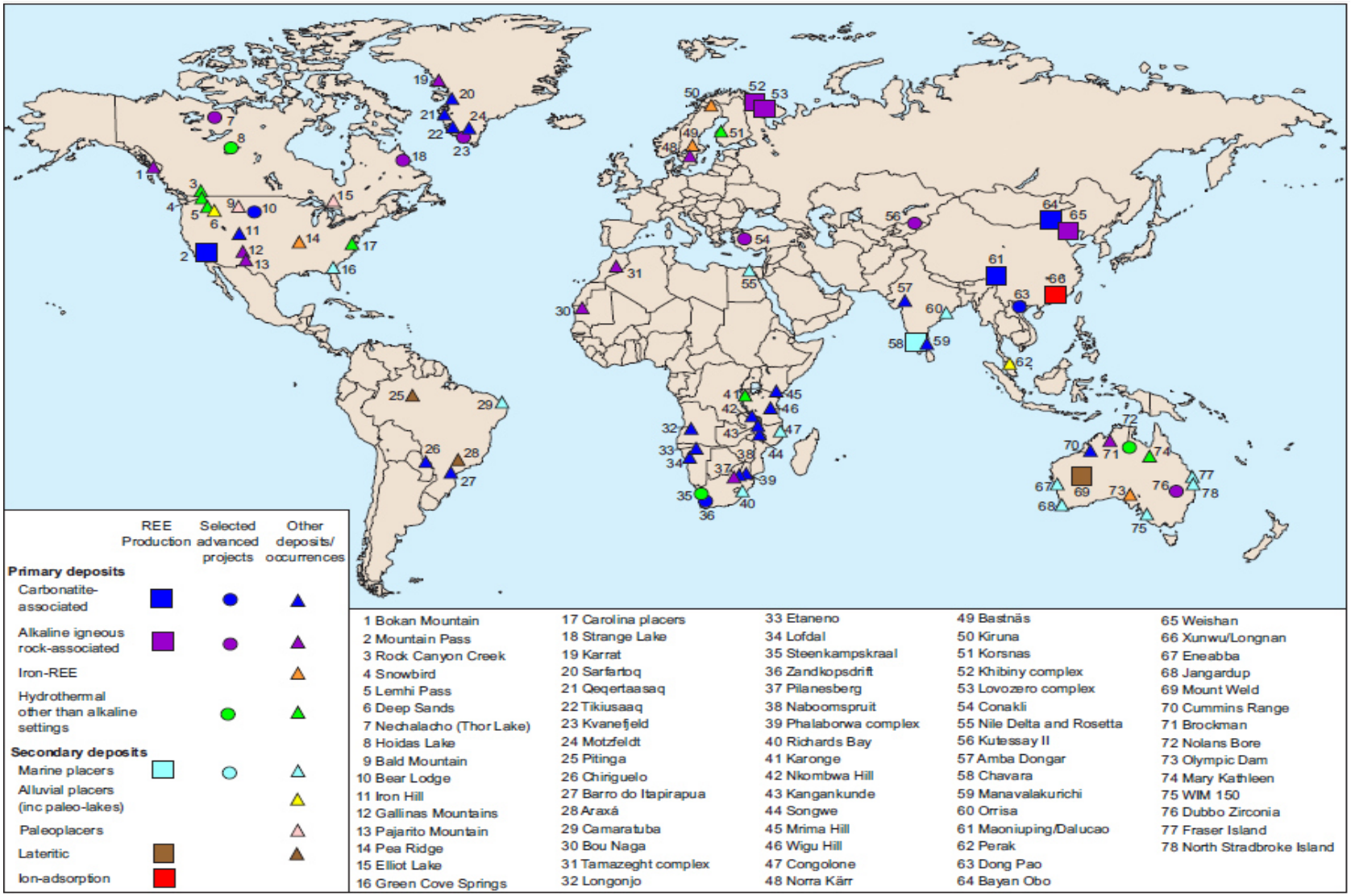

Figure 1.2: Global distribution of primary and secondary REE deposits (British Geological Survey, 2011).

1.5 REE fluorcarbonate minerals

The REE fluorcarbonate group comprises four mineral species, including bastnäsite $REE(CO_3)F$, parisite $CaREE_2(CO_3)_3F_2$, röntgenite $Ca_2REE_3(CO_3)_5F_3$, and synchysite $CaREE(CO_3)_2F$.

These minerals have a layered structure and can be assembled by the ordered stacking of layers along the c crystallographic axis. The layer characteristics of these minerals have been documented on the basis of X-ray Diffraction (XRD) data and/or Transmission Electron Microscopy (TEM) images (Oftdel, 1931; Donnay and Donnay, 1953; Donnay, 1953; Van Landuyt and Amelinckx, 1975; Ni et al., 1993; Wang et al., 1994; Ni et al., 2000). These authors described the structure of these minerals by stacking at least two of three layers (CeF), (CO_3), and (Ca) parallel to the {0001} crystallographic plane (Figure 1.3). It is important to note that the geometry of the (CO_3) layer is much more variable when present between two (CeF) layers, as in bastnäsite, than between (Ca) and (CeF) layers as in synchysite, which is considered by some authors as two different layers (Van Landuyt and Amelinckx, 1975; Meng et al., 2001).

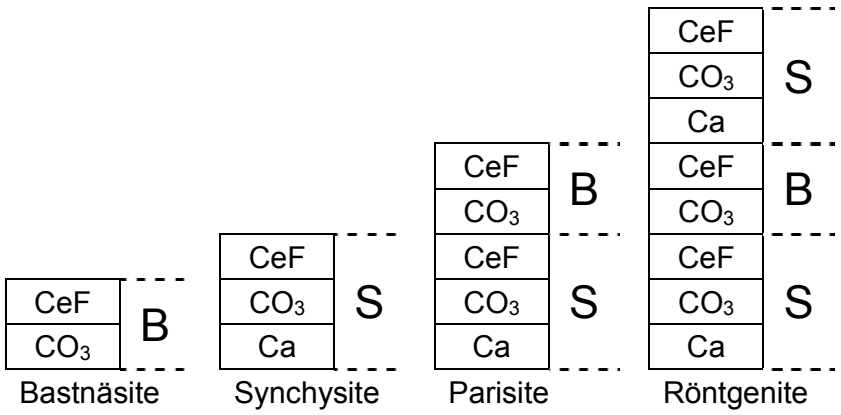

Figure 1.3: Schematic representation of the REE fluorcarbonate crystal structures illustrating the stacking mode along the c-axis including bastnäsite (B); synchysite (S); parisite (BS); and röntgenite (BS2) (Donnay and Donnay, 1953; Van Landuyt and Amelinckx, 1975; Manfredi et al., 2013).

1.5.1 Bastnäsite

Bastnäsite is an end member of the REE fluorcarbonate series with the simplest crystal structure and the highest REE content compared to other members within this group. In terms of the atomic arrangement, it is composed of layers of CeF intervening with CO_3 layers and yields Ca-absent species (Donnay and Donnay, 1953; Ni et al., 1993).

Bastnäsite is well documented in the literature because it is the most abundant member and yields more than half of the world's supply of REE. It has been exploited over the past 40 years from major deposits such as Bayan Obo, Inner Mongolia, China (750 Mt, 4.1% TREO), and Mountain Pass, California, USA (40 Mt, 8-9% TREO) (Ruberti et al, 2008; Singer 1998; Castor, 2008; Mariano and Mariano, 2012).

Four discrete species of bastnäsite are known: bastnäsite-(Ce), bastnäsite-(La), bastnäsite-(Nd), and bastnäsite-(Y). Bastnäsite-(Ce) is the most widespread species of the bastnäsite family.

In addition to the bastnäsite fluorcarbonate, hydroxyl-bastnäsite-(Ce), -(La), and -(Nd) also occur as rare species of this family (Kirillov, 1964; Pantó, 1985; Hawthorne et al., 1986; Yang et al., 2008).

1.5.2 Synchysite

Synchysite is an end member of the REE fluorcarbonate series and is the most Ca-enriched. The crystal structure of synchysite is built by stacking layers of (Ca) and (CeF) separated by layers of (CO_3) to yield a REE:Ca ratio of 1:1 (Ni et al., 1993). Although these layers possess hexagonal or trigonal symmetry, they yield a monoclinic crystal with a pronounced pseudohexagonal symmetry due to the shift of the hexagonal stacking as a result of the insertion of a Ca layer (Wang et al., 1994).

Synchysite was first discovered by Flink (1901) in syenitic pegmatites from Narssârssuk, Greenland. The name "synchysite" came from the Greek word for "synks" which means "confusion" due to a confusion concerning identity (Donnay and Donnay, 1953; Werner, 1993).

Synchysite is a principal mineral for the REE and the second most reported mineral of the REE fluorcarbonate group (Wang et al., 1994). Synchysite is reported in

several deposits as a major REE mineral, for example: in carbonatite at Songwe Hill and Kangankunde, Malawi; Barra do Itapirapuã, Brazil; and Lugiin Gol, Southern Mongolia; and in alkaline granite at Kutessay II, Kyrgyzstan, and Springer Lavergne Ontario, Canada (Chakhmouradian and Wall, 2012; Mariano and Mariano, 2012; Krishnamurthy and Gupta, 2016).

Three discrete synchysite species are known: synchysite-(Ce), synchysite-(Y), and synchysite-(Nd). Synchysite-(Ce) is the most dominant of these species, while synchysite-(Nd) is the rarest (Förster, 2001).

1.5.3 Parisite

Parisite can be regarded as a middle member of the REE fluorcarbonate group. The crystal structure of parisite, described by Ni et al. (2000), is formed through stacking the unit layers of bastnäsite and synchysite along the c-axis (BS; Figure 1.3). Thus, parisite also consists of layers of (CeF), (Ca), and (CO_3). The latter lies between the basic layers of CeF-CeF and Ca-CeF. The REE:Ca ratio for parisite, based on the ideal chemical formula, is 2:1 and its crystal structure based on the 3D X-ray diffraction data is monoclinic (Ni et al., 2000).

Parisite is an important REE mineral and occurs in several deposits, for example, as a major REE mineral in the hydrothermal ore deposit at Snowbird Mine, Montana, USA. It also occurs as an accessory REE mineral associated with britholite and synchysite in syenite in Mt. Prindle, Alaska, with emerald at Muzo, Colombia, with bastnäsite at Mountain Pass, USA and with bastnäsite and monazite at Bayan Obo, China (Mariano and Mariano, 2012).

Parisite-(Ce) is the only discrete species of this family; parisite-(Nd) was reported in the Bayan Obo iron-niobium-rare earth deposit, China and named by Zhang and Tao (1986) in Jambor et al. (1988).

1.5.4 Röntgenite

Röntgenite can also be considered a middle member of the REE fluorcarbonate group in addition to parisite. The crystal structure consists of layers of (CeF), (Ca), and (CO_3) alternating in various proportions. It can be described as stacking one portion of bastnäsite and two portions of synchysite along the c crystallographic axis to form (BS_2) to yield a REE:Ca ratio of 3:2 (Figure 1.3; Donnay, 1953; Van Landuyt and Amelinckx, 1975).

Röntgenite-(Ce) was first documented by Donnay (1953) as a new species of the REE fluorcarbonate group based on X-ray data from a single crystal obtained from Narssârssuk, Greenland. It is not reported in any other geological deposits, possibly due to its rarity but also possibly because it has a similar chemical composition to synchysite and parisite, making it difficult to distinguish between them.

1.5.5 Other mixed-layer compounds

In addition to the REE fluorcarbonate minerals described above, other mixed-layer compounds were also discovered based on transmission electron microscopy including B_2S, B_3S_2, B_3S_4, and BS_4 (Van Landuyt and Amelinckx, 1975; Meng et al., 2001). These minerals form by the ordered stacking of the main two structural unit layers ("building blocks") of bastnäsite (B layer) and synchysite (S layer) along the {0001} crystallographic plane.

1.5.6 Syntaxial intergrowths

The minerals of the REE fluorcarbonate group are often affected by stacking faults, disorder of chemical composition, polytypism, and syntaxial intergrowths (Donnay and Donnay, 1953; Meng et al., 2001). This context focuses only on syntaxial intergrowths as it is related to the subject under investigation.

Syntaxial intergrowths are significant and quite common features among the REE fluorcarbonate minerals owing to the similarity of their layered structures. These layered structures have an identical surface which is amenable to growth of any of the phases as the ore fluid composition changes (Donnay and Donnay, 1953; Ni et al., 1993).

Syntaxial intergrowth between two or more phases forms when a crystal precipitates until the conditions in the ore fluid change sufficiently for the next phase to separate out. Thus, the new phase crystallises on the original crystal. The two species alternate with each other when the solution changes periodically (Donnay and Donnay, 1953). However, Meng et al. (2001) attributed formation of the syntaxial intergrowth among different REE fluorcarbonate members due to a disordered stacking structure as a result of stacking faults of the unit layers along the c-axis.

However, REE fluorcarbonates occur as a signal crystal, syntaxial intergrowths or "polycrystals" as proposed by Donnay and Donnay (1953), and are also common

between two or even three species of the group. Mariano (1989), based on the analysis of bastnäsite and parisite from Mountain Pass and other localities, indicated from BSE images that syntaxial intergrowths are not pervasive in these minerals. However, Donnay and Donnay (1953) reported syntaxial intergrowths along the c-axis between all pairs of REE fluorcarbonate minerals (bastnäsite, parisite, röntgenite, and synchysite), except for the bastnäsite-synchysite species. The boundary surface between two syntaxial intergrown species can be planer, irregular, or both.

It is important to note that the term syntaxy, which was first introduced by Ungemach (1935), should be differentiated from the term epitaxy that was previously introduced by Royer (1928). Syntaxy describes the oriented intergrowth of two chemically identical substances alternating with each other, but having crystalising simultaneously, while epitaxy describes an oriented overgrowth of one substance crystallising on another (Donnay and Donnay, 1953).

Syntaxial intergrowths are normally distinguishable at the microscale, however it is not possible to recognise microsyntaxial intergrowth in polycrystals on a vastly smaller scale (e.g. angstrom or even nanometre scale) using conventional SEM (Van Landuyt and Amelinckx, 1975).

1.6 Phosphate rock and common phosphate minerals

Phosphate rock is a term describing any naturally occurring geological material, which comprises one or more phosphate minerals suitable for commercial use. It covers natural unprocessed phosphate ore and processed phosphate products (Notholt and Highley, 1986). It is interesting to note that the European Commission (2014) included phosphate rock as a critical and non-substitutable raw material.

Phosphate resources are generally classified into five major categories based on their origin (Van Straaten, 2002; Zapata and Roy, 2004):

1. Marine phosphate deposits (75%)
2. Igneous phosphate deposits (15–20% igneous, metamorphic, and weathered)
3. Metamorphic phosphate deposits
4. Phosphate deposits as a result of weathering
5. Biogenic deposits (2–3%)

Igneous phosphate resources are typically classified into three categories: carbonatite, nepheline-syenite, and pyroxenite. Significant igneous occurrences are found in Brazil, Finland, Russia, and South Africa. The largest deposit of igneous phosphate mined is in the Kola Peninsula, Russia, producing 12.5 Mt of apatite concentrate per year containing approximately 39% P_2O_5 (Guimarães et al., 2005; Abouzeid, 2008; USGS, 2016b).

The locations of major phosphate rock deposits worldwide, including those already in production and those yet to be mined are shown in Figure 1.4.

Figure 1.4: Worldwide distribution of the different types of phosphate rocks, after www.ifdc.org

The different types of phosphate rocks have widely different mineralogical, chemical, and textural characteristics. There are about 400 known phosphate minerals, but relatively few are abundant in natural systems. The apatite group $Ca_5(PO_4)_3(F,OH,Cl)$ is the most abundant phosphate mineral in primary environments (sedimentary, igneous, and metamorphic) as well as occurring in weathering environments. Other important phosphate minerals such as monazite, xenotime and rhabdophane widely occur as microcrystals in igneous and sedimentary rocks. Other phosphate minerals, such as the crandallite group $XAl_3(PO_4)_2(OH)_6$, variscite $AlPO_4(H_2O)$ and strengite $FePO_4.2H_2O$, are mostly found in secondary weathering environments (Huminicki and Hawthorne, 2002; Van

Straaten, 2002; Oelkers and Valsami-Jones, 2008). Some selected phosphate minerals and their chemical formula are presented in Table 1.3.

Table 1.3: Selected common phosphate minerals (Huminicki and Hawthorne, 2002).

Mineral	Chemical formula
Autunite	$Ca(UO_2)_2(PO_4)_2.10\text{-}12H_2O$
Chlorapatite	$Ca_5(PO_4)_3Cl$
Fluorapatite	$Ca_5(PO_4)_3F$
Hydroxylapatite	$Ca_5(PO_4)_3OH$
Monazite	$(REE)PO_4$
Rhabdophane	$(REE)PO_4.H_2O$
Strengite	$FePO_4.2H_2O$
Turquoise	$CuAl_6(PO_4)_4(OH)_8.4H_2O$
Variscite	$AlPO_4.2H_2O$
Vivianite	$Fe_3(PO_4)_{2.8}H_2O$
Xenotime	$(Y,REE)PO_4$

Apatite is a calcium fluor-chlor-hydroxyl phosphate mineral group, which includes fluorapatite, hydroxylapatite and chlorapatite. Of these, fluorapatite is the most common. Hydroxylapatite $Ca_5(PO_4)_3OH_2$ and chlorapatite $Ca_5(PO_4)_3Cl_2$ are much less common in nature.

Fluorapatite $Ca_5(PO_4)_3F$ most commonly occurs as well-formed crystals in igneous phosphate deposits, for example, carbonatites and mica-pyroxenites. Hydroxylapatite occurs in igneous and metamorphic deposits as well as in biogenic deposits. It makes up to 65–70% of mammal bones, the remainder being mostly organic compounds. Chlorapatite mainly occurs on islands and in caves (McClellan, 1980; Van Straaten 2002; Turek and Buckwatler, 1994).

There is also a very rare strontium-rich member of apatite $(Sr,Ca)_5(PO_4)_3(OH,F)$, with calcium partially replaced by strontium (Chakhmouradian et al., 2002).

Francolite is a carbonate-rich apatite mineral, found predominantly in sedimentary phosphate deposits, and to a much smaller extent in weathered deposits. Examples of the largest sedimentary phosphate deposits are occurred in Northern Africa, China, the Middle East, and the United States (USGS, 2016b). McClellan (1980) described a systematic series of anion and cation substitutions into fluorapatite, resulting in an empirical chemical formula for francolite of $Ca_{5-x-y}Na_xMg_y(PO_4)_{3-z}(CO_3)_zF_{0.4z}F_2$.

1.7 Mineral processing

This section reviews the mineral processing techniques used in the separation of REE- and REE-bearing minerals, particularly synchysite and apatite.

1.7.1 Processing of rare earth minerals

The separation of REE minerals from their associated matrices may be as difficult as the separation of individual REE. These challenges are due to the similarity in the chemical composition, magnetic behaviour, specific gravity, and electrostatic response between the valuable and gangue minerals in most REE deposits.

Bastnäsite, monazite, and xenotime are the only REE minerals that have been beneficiated on a commercial scale. These minerals may be beneficiated through a combination of gravity, magnetic, electrostatic and froth flotation separation techniques (Zhang and Edwards, 2012; Jordens et al., 2013). Table 1.4 shows the various possible routes that applied in the beneficiation of some REE deposits.

The only REE fluorcarbonate mineral that is well documented in the literature is bastnäsite owing to its occurrence as a principal REE mineral in the world largest REE deposits. In addition to bastnäsite, these REE deposits also contain other REE fluorcarbonates as accessory minerals including parisite and synchysite (Kynicky et al., 2012; Mariano and Mariano, 2012). Synchysite (the target REE mineral in this study) has been recently investigated as a primary REE mineral by Deng and Hill (2014) and as a secondary mineral in addition to bastnäsite by Jordens et al. (2016).

Deng and Hill (2014) determined the effect of various collectors, depressants, and dispersants on the flotation recovery of synchysite in a groundmass of ankerite/dolomite and silicates. These experiments were undertaken on deslimed and undeslimed feed samples, ground to 53 μm and 106 μm. A combination of phosphate esters and sulphosuccinamate collectors and sodium silicate, carboxymethyl cellulose, and caustic starch as depressants and/or dispersants indicated effective selectivity and a high amount of mass pull. Flotation results with salicyl-hydroxmate as a collector and sodium silicate as a depressant showed a significant improvement in the selectivity of synchysite against carbonate gangue minerals, but significantly decreased the TREO recovery. Adding sulphosuccinamate and phosphate ester as co-collectors with hydroxamate improved the TREO recovery, but large amounts of carbonate gangues were recovered to the rougher concentrate.

Table 1.4: Various mineral processing routes applied in the beneficiation of some worldwide REE ore deposits.

REE deposit	Lithology	REE minerals	Beneficiation unit operations	Reference
Bayan Obo, China	Carbonatite	Bastnäsite, parisite, and monazite	(a) Magnetic separation, froth flotation, and gravity concentration (b) Froth flotation and gravity concentration (c) Froth flotation	Kynicky et al. (2012); Krishnamurthy and Gupta (2016)
Congolone, Mozambique	Heavy mineral sand	Monazite and zircon	Gravity concentration, magnetic separation, and electrostatic separation	Krishnamurthy and Gupta (2016)
Manavalakurichi, India	Beach sand	Monazite	Gravity concentration and magnetic separation	Krishnamurthy and Gupta (2016)
Maoniuping, China	Carbonatite–syenite intrusions.	Bastnäsite and monazite	A combination of gravity concentration, magnetic separation, and froth flotation processes	Kynicky et al. (2012); Zhang and Edwards (2012)
Mianning, China	Carbonatite	Bastnäsite	(a) Gravity concentration and froth flotation (b) Froth flotation	Zhang and Edwards (2012)
Mountain Pass, CA, USA	Calcite and dolomite carbonatite	Bastnäsite, parisite, synchysite	Froth flotation	Wall and Mariano (1996); Pradip and Fuerstenau (2013); Krishnamurthy and Gupta (2016)
Mt. Weld, Australia	Weathered volcanic carbonatite	Monazite, cheralite, cerianite, rhabdophane, florencite, and bastnäsite	(a) Gravity concentration, froth flotation, and magnetic separation (b) Froth flotation	Zhang and Edwards (2012)
Weishan, China	Carbonatite	Bastnäsite and parisite	Froth flotation	Kynicky et al. (2012); Zhang and Edwards (2012)

The experimental investigation by Jordens et al. (2016) focused on understanding the effect of staged addition of benzohydroxamic acid as a collector, coupled with addition of lead ions as an activator, on bastnäsite and synchysite and other REE minerals associated with silicate and iron oxide gangue minerals in a pre-concentrated deposit. The results showed that the benzohydroxamic acid collector is much more selective towards the minerals with relatively high degrees of solubility and high REE content. This means the collector is more effective towards bastnäsite and less effective for synchysite. Also, the addition of lead ions as an activator does not affect the recovery of bastnäsite and synchysite.

As indicated from the descriptions of the REE fluorcarbonates (see Section 1.5), these minerals commonly occur together as polycrystals and they are only varied in their contents of Ca and REE. Furthermore, the literature indicated that the accessory parisite and synchysite were recovered along with bastnäsite. Thus, it may be possible to recover synchysite and parisite in the same manner as processing bastnäsite.

1.7.2 Processing of igneous phosphate

The mining and beneficiation of igneous phosphates make up approximately 15% to 20% of the world's phosphate production (Guimarães et al., 2005; Abouzeid, 2008; USGS, 2016b).

Phosphate ore deposits cannot be used directly because of their poor quality and gangue minerals content. A number of processing techniques can be applied for upgrading phosphate ores and extracting apatite. The choice of one or more of these techniques depends on the type of deposit and the gangue minerals present. Igneous phosphate can have significantly different minerals than those of sedimentary origin, including the associated gangue minerals. The most common igneous phosphate minerals extracted on a commercial scale are apatite, monazite, and xenotime. Monazite and xenotime are rare earth minerals with REE content of approximately 70%. Apatite is not a REE mineral, rather REE can substitute for Ca, and it could therefore be a potential source of REE. This is more attractive than monazite and xenotime as it is the predominant phosphate mineral in igneous deposits and the only economically feasible source of phosphorus for phosphate fertilizers and chemicals (UNIDO and IFDC, 1998; Abouzeid, 2008; Oliveira et al., 2011; Kawatra and Carlson, 2014; Krishnamurthy and Gupta, 2016).

Flowsheets for the separation of apatite from non-phosphate minerals in phosphate rocks can range from relatively simple to substantially more complex, depending on the type of impurities and the ore grade. The flowsheets include crushing, grinding, and flotation combined with other steps such as magnetic and/or gravity separation, which are proven to be successful in upgrading igneous phosphate ores (Kawatra and Carlson, 2014; Wingate and Kohmuench, 2016).

Froth flotation has been the most widely employed technique for the beneficiation of igneous phosphates due to the well-crystallised nature and inherent low porosity of apatite (Kawatra and Carlson, 2014). More than half of the marketable phosphate production of the world is upgraded using this technique (Sis and Chander, 2003).

1.8 Gravity separation

1.8.1 Basics of gravity separation

Gravity concentration, or density-based separation is one of the oldest methods for separating minerals based on differences in density, and its principles have been well known for over two thousand years (Falconer, 2003; Burt, 1984). It is widely used for treating different types of ore deposits due to its low capital and operating costs, the absence of chemical reagents, and the lack of excessive heating requirements means it is generally environmentally friendly (Falconer, 2003).

Gravity separation techniques separate minerals of different specific gravity by their relative movement in response to gravity and one or more other forces, the latter often being the resistance to motion offered by a viscous fluid, such as water or air (Burt, 1984; Wills and Finch, 2016).

For an efficient separation, a significant density difference between the valuable and gangue minerals is required. A useful test to check whether the separation possible can be gained from the concentration criterion, $\Delta\rho$:

$$\Delta\rho = \frac{\rho_h - \rho_f}{\rho_l - \rho_f} \dots\dots\dots (1)$$

Where ρ_h is the density of the heavy mineral, ρ_l is the density of the light mineral, and ρ_f is the density of the fluid medium.

A guideline for separability by gravity based on this concentration criterion is given in Table 1.5.

Table 1.5: Concentration criterion guide for gravity separation, after Gupta and Yan (2016).

Concentration criterion	Suitability to gravity separation
$\Delta\rho > 2.5$	easy down to 0.075 mm
$1.75 < \Delta\rho < 2.5$	possible down to 0.15 mm
$1.5 < \Delta\rho < 1.75$	possible down to 1.7 mm
$1.25 < \Delta\rho < 1.5$	possible down to 6.35 mm
$\Delta\rho < 1.25$	impossible at any size

Many machines have been designed, including spiral, jigs, sluices, shaking table, multi-gravity separators (MGS), Falcon, and Knelson concentrators. These devices can be used as a primary concentrator or in a combination with other mineral processing techniques such as flotation for concentrate clean-up (Burt, 1984).

1.8.2 Spiral separators

Spiral technology has gradually developed over the past 70 years and is now widely used for the treatment of iron and chromite ores, the heavy minerals in sand deposits such as ilmenite, rutile, zircon, and monazite, and recently in the recovery of fine coal (Wills and Finch, 2016).

The spiral is principally an inclined chute with a complex cross section wrapped around a central column (Figure 1.5). The feed pulp of between 15% - 45% solids and in the size ranging between 3 mm to 0.075 mm is pumped at the top of the spiral.

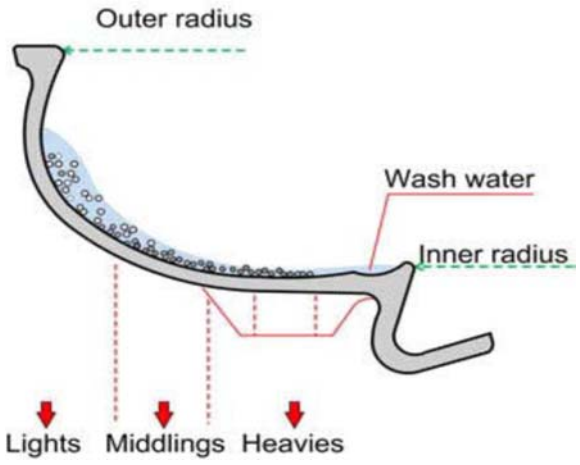

Figure 1.5: Cross section of a spiral in operation showing ideal material movement, after Wills and Finch (2016).

The mineral particles flow spirally downward and segregate into lights and heavies under the effect of a combination of gravitational and centrifugal forces. The result of this action is that the light minerals progressively move away from the centre while the heavy minerals move toward the centre.

Although different trough designs have led to many models, spirals can be classified into two broad types; namely washwater and washwaterless. The former is normally used only on cleaning stages, while the latter can be used on rougher, scavenger and cleaner stages (Falconer, 2003).

For an optimal and consistent performance, different variables have various effect should be considered when using this form of separation, including particle size and shape, feed grade and loading, pulp density, and wash water flow (Burt, 1984).

1.8.3 Centrifugal gravity separators

More recently developed gravity devices such as Kelsey centrifugal jig (KCJ), Falcon, and Knelson concentrators employ the centrifugal force as a new source of energy for the efficient recovery of fine particles. These fines have historically been a serious problem in the beneficiation of valuable mineral (Wills and Finch, 2016).

Knelson concentrator

The Knelson concentrator, one of the most common enhanced gravity separators (EGS) has been noted for its highly efficient processing of fine particles down to 10 µm. This is due to its ability to provide a centrifugal force greater than 60 times the natural gravitational force (Knelson and Jones, 1994). The standard Knelson unit consists mainly of a spinning ribbed cone (bowl) and retention zones between the ribs where dense particles are retained (Figure 1.6).

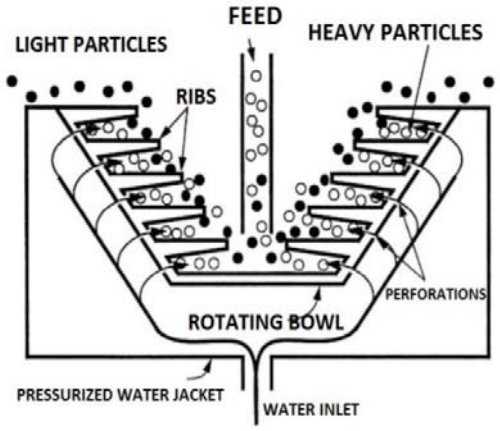

Figure 1.6: Schematic illustration of a Knelson concentrator, after Kawatra and Eisele (2001)

Feed slurry is introduced through a central feed tube to the base of the rotating bowl and is dispersed outwards under the effect of centrifugal force. Fluidisation water is pumped to the unit through perforations located in the retention zones. This creates a fluidised bed consisting of heavier particles. The particles with high specific gravity are trapped and retained in the retention zone between the ribs, while the low specific gravity particles are washed away upward into the tailings.

Falcon concentrator

Another enhanced gravity separator, which has been in operation for more than 60 years in the mining industry, is the Falcon concentrator. It is designed to treat very fine particles of a variety of minerals such as gold, platinum, silver, tin, titanium, and ultra-fine coal (Wills and Finch, 2016).

The feed is introduced from the top of the unit through a central feed tube to the spinning cone-shaped bowl. As the centrifugal force is acting more upon the heavier particles than the lighter ones, the heavier particles move to the fluidised concentrate bed while the lighter particles tend to move to the top with water. The dense particles bed is rinsed regularly to remove any remaining lights and is then flushed out through a series of ports (Falconer, 2003; Wills and Finch, 2016).

1.9 Magnetic separation

1.9.1 Magnetism and magnetic field inside materials

Magnetic fields are produced when electrical charges are in motion, which can be due to an electrical current passing through a conductor such as copper coil, or due to the orbital motion and spin of electrons within a given material (Jiles, 1998).

The magnetism of materials originates from the electrons of atoms. Each electron in an atom has two types of motion: the *orbital motion of electrons* around the atomic nucleus and the electron *spinning* around its own axis each of which has a magnetic moment within each atom (Figure 1.7). The orbital motion is similar to an electrical current passing through a loop of wire in that both are equivalent to a circulation of charge (Cullity and Graham, 2009).

The net magnetic moment of an atom is entirely due to the electrons of that atom. Although the nucleus has a small magnetic moment, it is insignificant compared to the magnetic moment generated by the electron motion and does not affect the total

magnetic moment. The magnetic moment generated from the orbital or spin motions of a single electron is called the Bohr magneton and is the smallest unit of magnetic moment of the atom (Cullity and Graham, 2009).

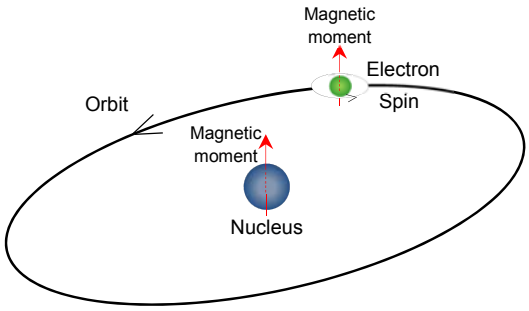

Figure 1.7: Magnetic moments associated with orbiting and spinning electron, adapted from Petty (2007).

The atoms that have completely-filled electronic shells (the electrons are paired up with each other) do not contribute to the magnetic moments as one of each pair of electrons is spinning-up while the other is spinning-down thus cancelling each other out, leading to zero atomic net spin moment. This includes the inert gases (He, Ne, Ar, etc.) and some ionic materials. In comparison, the atoms with partially-filled electronic shells are capable of generating a magnetic moment as some electrons are left unpaired, resulting in a net spin moment within each atom Examples include Fe, Mn, and Co in addition to REE. The net spin magnetic moment for an atom represents the sum of the magnetic moments of each of the constituent electrons, including both the spin and orbital magnetic moments. Thus, the total of these magnetic moments that generates from each atom will form the magnetic field of the material that consists of these atoms. Generally, the spin magnetic moment is more important than the orbital moment in the rock-forming minerals (Lowrie, 2007).

The net magnetic moment of a material depends on the presence of atoms with unpaired electrons, the degree of alignment of the individual atomic magnetic moments, and the lattice symmetry of the media. Thus, a material may contain atoms with unpaired electrons that produce magnetic moments, but still be a non-magnetic material because the random orientation of the atoms cancels the magnetic moment. In contrast, the systematic distribution of atoms with unpaired electrons means that the magnetic moments are aligned resulting in a magnetic field inside the material (Lowrie, 2007).

1.9.2 The magnetic properties of materials

When a material is placed in a magnetic field strength H (A m^{-1}), a magnetisation (magnetic moment per unit) M (A m^{-1}) is induced in the material that related to the magnetic field strength and the volume magnetic susceptibility χ (dimensionless) (Lide, 2000).

$$M = \chi H \ldots\ldots\ldots (2)$$

All materials demonstrate different magnetic behaviours when exposed to an external magnetic field, although very sensitive instrument such as Vibrating Sample Magnetometer (VSM) may be used to directly measure the magnetic moment in these materials (Wills and Finch, 2016).

All materials can be classified based on their magnetic susceptibility into one of five categories: diamagnetism, paramagnetism, ferromagnetism, antiferromagnetism and ferrimagnetism as shown in Table 1.6.

Table 1.6: Summary of different types of magnetic behaviour and the relationship between magnetism and applied magnetic field, adapted from Petty (2007)

Diamagnetism	**Paramagnetism**	**Ferromagnetism**	**Antiferromagnetism**	**Ferrimagnetism**
Atoms have no magnetic moment	Atoms have randomly oriented magnetic moments	Atoms have parallel aligned magnetic moments	Atoms have antiparallel aligned magnetic moments	Atoms have mixed parallel and antiparallel aligned magnetic moments
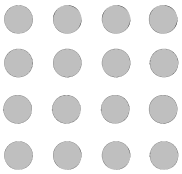	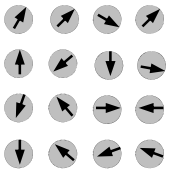	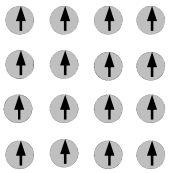	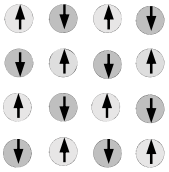	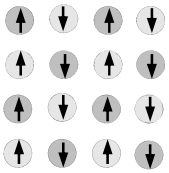
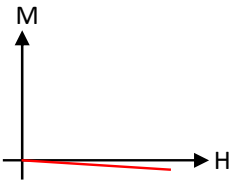	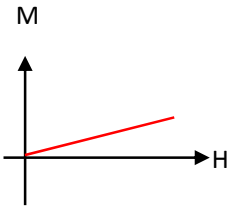	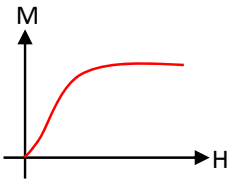	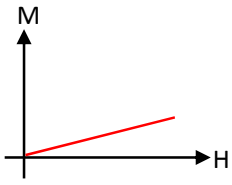	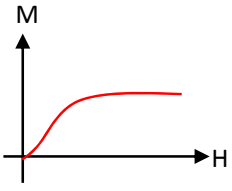
Small and negative susceptibility	Small and positive susceptibility	Large and positive susceptibility	Small and positive susceptibility	Large and positive susceptibility

Note: M= magnetisation, H= magnetic field strength.

For minerals processing purposes, materials are classified into three groups based on their behaviour when exposed to an external magnetic field. These are referred to as diamagnetic, paramagnetic, and ferromagnetic minerals. The most common

categories of magnetism at a room temperature of 20°C are diamagnetism and paramagnetism, and these account for the majority of the Periodic Table of elements. Ferromagnetism is observed in only three elements Fe, Co, and Ni and other compounds such as ferrites. Below a brief description for each category:

Diamagnetism

The atoms in a diamagnetic material have no magnetic moment unless there is an externally applied magnetic field. When a material is subject to an external magnetic field, the electron orbital motion and spinning induce and produce very weak magnetisation (M) in the opposite direction to the applied magnetic field (King, 2001; Waters et al., 2007).

Diamagnetic minerals in a magnetic separator will repel along the lines of the magnetic field to a point where the field strength is smaller (Wills and Finch, 2016).

Paramagnetism

Atoms have a magnetic moment as a result of the presence of unpaired electrons. When no external magnetic field exists, the moments are randomly oriented within the material and cancel each other out to produce a zero net magnetic field. With an external magnetic field, the moments are aligned along the direction of the applied magnetic field leading to weak magnetisation.

Paramagnetic minerals in a magnetic separator will attract along the lines of the magnetic field to a point of greater field intensity (Wills and Finch, 2016).

Ferromagnetism

It is a particular case of paramagnetism in which the magnetic moments of atoms align in parallel to each other due to magnetic domains in the material created by the strong exchange interaction between neighbouring moments. Such minerals or materials behave ferromagnetically as a result of the presence of Fe, Co, or Ni.

Ferromagnetic minerals have very high susceptibility, and the alignment of magnetic dipoles remain parallel even after the removal of the magnetic field and will require a low-intensity magnetic field to separate the ferromagnetics (Petty, 2007; Wills and Finch, 2016).

1.9.3 Low intensity magnetic separators

Low intensity magnetic separators are used to concentrate ferromagnetic materials and some highly paramagnetic minerals, and also can be used to remove iron tramps and ferromagnetic impurities (Chen and Xiong, 2015; Wills and Finch, 2016). Minerals with high magnetic susceptibility at low applied magnetic field strengths can be recovered in low intensity (<~0.3 T) magnetic separators (Wills and Finch, 2016).

Several types of low intensity magnetic separation equipment have been used in the mineral processing field. Wet drum magnetic separators are the most common type (Kelly and Spottiswood, 1982). These separators initially employed electromagnets, but with the advent and applications of ferrite or rare earth permanent magnets, permanent magnet-based separators have mostly replaced the electromagnet-based ones to retain their magnetic field intensity for an unlimited period (Norrgran and Marin, 1994; Svoboda and Fugita, 2003).

In a wet drum magnetic separator like that shown in Figure 1.8, the drum is partially submerged in a round tank and the feed pulp is introduced at the top of a rotating drum. The magnetic particles will be attracted to the rotating drum surface by the magnetic forces produced by stationary magnets within the drum. These magnetic particles are conveyed out of the magnetic field with the rotation of drum and are flushed down with water as a magnetic concentrate. The nonmagnetic particles that are not picked up by the drum surface will be discharged the separator tank as tailings (Oberteuffer, 1874; Chen and Xiong, 2015).

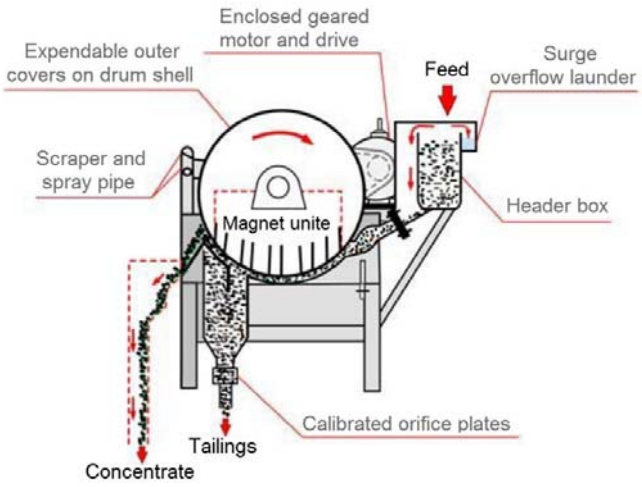

Figure 1.8: Diagram of a typical drum magnetic separator, after Wills and Finch (2016).

1.9.4 High intensity magnetic separators

High intensity magnetic separators are used for beneficiation of paramagnetic or weakly magnetic minerals that require higher magnetic field intensity than that in low intensity magnetic separators (Chen and Xiong, 2015). These separators can be carried out under either wet or dry processing conditions. For the treatment of fine weakly magnetic particles, wet high intensity magnetic separator (WHIMS) is required for efficient magnetic separation. A conventional example of WHIMS is shown in Figure 1.9. In this equipment, a ferromagnetic matrix on which paramagnetic particles are collected is used rather than fixed or moving magnetic poles. The ferromagnetic matrix can be in the form of grooved plates, steel balls, steel wool, or sheets of expanded metal. The introduction of a matrix into the applied magnetic field provides a high concentration of points of high field intensity and can effectively capture very fine (<100 μm) magnetic particles (Oberteuffer, 1874; King, 2001; Svoboda and Fugita, 2003).

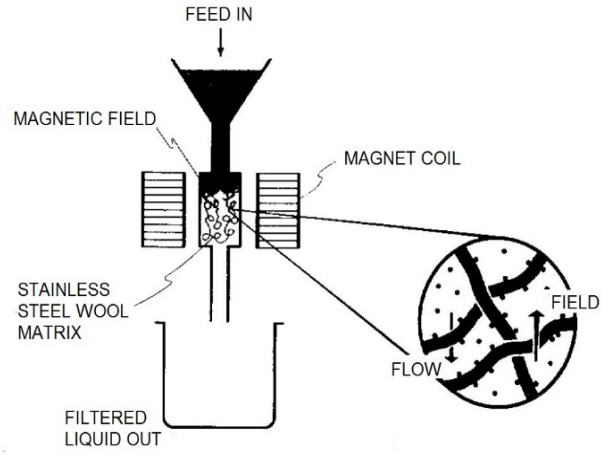

Figure 1.9: Schematic representation of a wet high intensity magnetic separator, adapted from Oberteuffer (1974).

There are two basic designs of WHIMS equipment, one that employs an electromagnet to produce a magnetic field strength, the other that uses rare earth permanent magnets. The magnetic field strength in the former can be easily varied to the required field strength by varying the electric current and thus process a wide range of weak and strong magnetic minerals. In the latter, the weaker magnetic field strength generated by permanent magnets may be not strong enough to recover some weakly paramagnetic minerals (Wills and Finch, 2016).

In WHIMS, when the feed pulp is passed down through the canister, the magnetic particles will attract and retain attached to the magnetised matrix, while nonmagnetic particle slurry passes through the matrix and is collected in a launder. The trapped magnetic particles are washed out using high-pressure water spray when the applied magnetic field is reduced to zero.

1.10 Froth flotation

Froth flotation is an efficient, and extensively utilised, physicochemical separation process for mineral separation. Flotation has found prominence as it is a selective process and can achieve specific separation of chemically similar minerals, complex and low-grade ore bodies as well as fine-grained ore deposits where the average particle size for liberation is too small for the efficient physical separation techniques using equipment such as gravity concentrator (Kelly and Spottiswood, 1982; Santana et al., 2008; Wills and Finch, 2016).

Froth flotation relies on the differences in the surface properties of the mineral particles, whether the surface is hydrophobic (water repellent), or hydrophilic (water attracting). Mineral particles become hydrophobic when chemicals known as “collectors” are adsorbed onto their surfaces and become hydrophilic when other chemicals known as “depressants” are adsorbed onto their surfaces (Kawatra, 2011; Wills and Finch, 2016).

Overall, the underlying principles of the flotation process are well established, but it can be very complex and consists of many interrelated variables, making it difficult to develop quantitative predictive models that can be utilised to simulate the operation of flotation cells in typical industrial circuits. The reason behind this difficulty is the complex interactions among three phases (solids, water, and air bubbles) and the physical and chemical factors of many micro-processes that combine to produce the overall results (King, 2001). Thus, Klimpel (1998) has explained the flotation system in a schematically represented triangle of three major categories as shown in Figure 1.10. (1) *Chemical components* include the interfacial chemistry of solid, liquid, and gas together with the flotation reagents such as collectors, depressants, frothers, activators, pH controller, dispersants, flocculants, water chemistry, and mineral chemistry. (2) *Equipment components* comprise type of flotation device, flotation cell design, flotation circuit configuration, agitation, air flow rate, and other parameters related to specific flotation machines. (3) *Operational components* include feed rate,

mineralogy of the feed ore, particle size, pulp density, and temperature. Therefore, with these interrelated components, any change in the settings of one element will automatically produce changes in other components of the system and can generate unexpected and undesirable results.

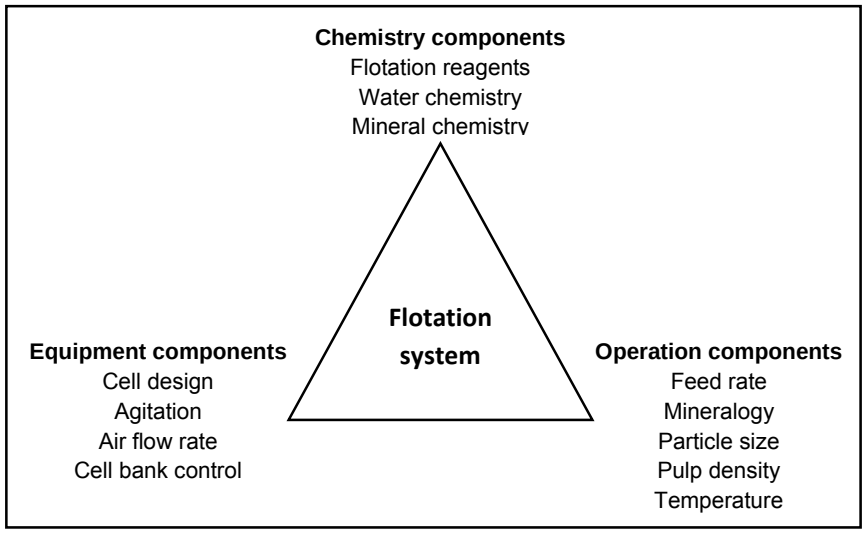

Figure 1.10: A flotation system with three interrelated components, after Klimpel (1998).

1.11 Flotation equipment

Although there are a wide variety of flotation machines currently being manufactured, with many more developed and discarded in the past, they can be divided into three distinct groups. The distinction is due to the method of introducing the air into the cell and are referred to as mechanical, column, and reactor/separator machines (Wills and Finch, 2016).

1.11.1 Mechanical flotation cells

These types of cells consist of a highly turbulent region produced by a mechanically driven impeller. This is done to provide the necessary agitation to keep the particles in suspension, disperse the air bubbles, and ensure maximum opportunity for particle-bubble contact (Gupta and Yan, 2016).

In this type of flotation cell, a feed of ground mineral particles, typically 10 μm to 100 μm in diameter, is mixed in water and agitated by an impeller. Reagents are added and air bubbles injected into the pulp at the base of a flotation cell. Hydrophobic particles are selectively attached and remain on the surface of air bubbles, rising through a pulp to form a froth layer, and are thus collected as concentrate, while the

hydrophilic particles remain in the pulp. An illustration of the principles of froth flotation concepts in a mechanical flotation cell is shown in Figure 1.11.

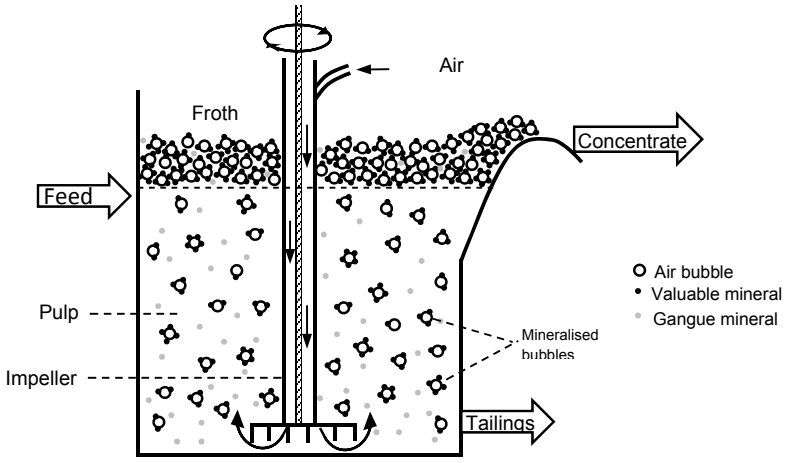

Figure 1.11: Mechanical flotation cell.

1.11.2 Flotation column

The flotation column was first invented in the early 1960s and became widely used in the 1980s after its successful performance in molybdenum concentrating plants. This technology is widely applied for processing of iron ores, phosphate, and coal, and for final stage of cleaning of copper, zinc, lead, and molybdenum sulphides. This type of technique employs the countercurrent flow of slurry and air bubbles to improve separation by reducing entrapment of mineral particles (Finch and Dobby, 1990). A general schematic of a conventional flotation column cell is shown in Figure 1.12.

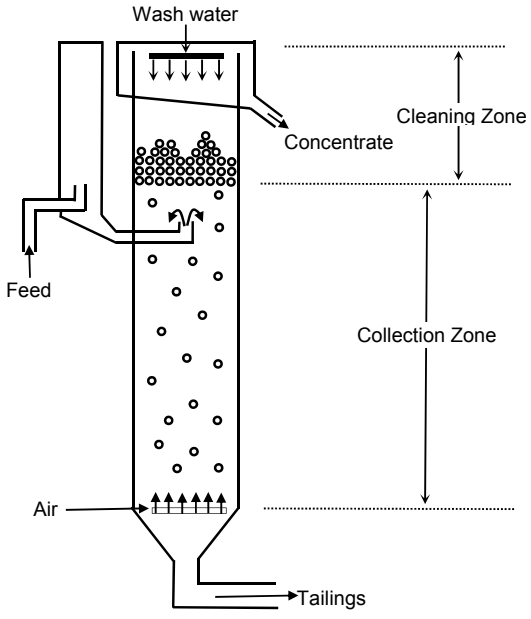

Figure 1.12: Schematic of a conventional flotation column, after Kawatra and Carlson (2014).

The significant operating difference from mechanical flotation cells is the absence of an impeller, or any agitation mechanism, which reduces energy and maintenance costs. Also, a key component in a flotation column is its utilisation of wash water, which significantly reduces the entrained gangue minerals and produces high-grade concentrates (Finch and Dobby 1990; Crozier, 1992).

The feed pulp is introduced into the column cell via a distributor located about a third of the way down from the top of the column, and descends downward through the column. The tailings are removed from the bottom whilst concentrate overflows at the top. Air bubbles generated by either internal or external porous spargers enter at the column base and rise upward, countercurrent to the solids. The design of the sparger is critical to efficient operation as the plugging of the pores for the bubble generating device can cause a significant maintenance problem. As the feed slurry works its way downward through the “collection” zone, hydrophobic particles attach to the rising bubbles and are carried upward to the “cleaning” zone (also referred to as froth zone) to flow over the lip of the column into the concentrate launder. The wash water is added by sprays at the top of the column to minimise the recovery of “entrained” hydrophilic particles into the concentrate (Crozier, 1992; Kawatra and Carlson 2014).

1.12 Hydrophobicity and hydrophilicity and kinetics of mineralised bubbles

From a practical point of view, the hydrophobicity and bubble mineralisation are considered the most important parameters in the flotation process as they control the system kinetics and selectivity of flotation process (Bulatovic, 2007).

1.12.1 Hydrophobicity and hydrophilicity

Most mineral particle surfaces have affinity for water (hydrophilic) in their natural state, thus they require a chemical reagent (collector) to be added to render the surface chemistry of the mineral to be a hydrophobic. The collector will selectively adsorb onto the surface of the desired mineral forming a thin film of non-polar oil. In contrast, hydrophobic minerals have naturally occurring non-polar surfaces, which do not readily attach to the water dipoles. Examples of these minerals are graphite, sulphur, molybdenite, diamond, coal, and talc (Kawatra, 2011; Wills and Finch, 2016).

1.12.2 Kinetics of mineralised bubbles

A flotation cell consists of two distinct zones: a pulp zone and a froth zone and within these zones, there are four sub-processes, which are considered kinetic approaches in terms of mineral particle transfer: (1) hydrophobic (selective) particles transfer from the pulp to the froth zone by attaching to bubbles, (2) hydrophilic (non-selective) particles transfer from the pulp to the froth zone by entrainment in the water films and plateau borders, (3) detachment of particles from the froth to pulp zone due to bubble coalescence and bursting, and (4) particles transfer from the froth zone to the concentrate (Laplante et al., 1989).

Sub-process 1 and part of 3 and 4 lead to transfer of hydrophobic particles from the pulp to the froth and then to the concentrate known as “recovery by true flotation”. Sub-process 2 and part of 3 and 4 lead to the transfer of hydrophilic particles from the pulp to the froth and then to the concentrate, known as “recovery by entrainment” (Laplante et al., 1989).

Transfer of the hydrophobic particles (selective) from the pulp phase into the froth phase depends on (1) the interaction of the mineral particles with the collector (2) the success of the collision and attachment of a particle and a bubble (3) the probability of the particle continuing attached to the bubble during the flotation process and (4) action of separating forces (Bulatovic, 2007).

Large numbers of physical, mechanical, and chemical factors affect the mechanism of bubble mineralisation and the transfer to the froth phase. The essential prerequisite is the hydrophobicity of the desired mineral, which means the target mineral must be rendered hydrophobic to create a condition for attachment to air bubbles.

The most widely considered theory on bubble mineralisation is the collision of hydrophobic particles with air bubbles wherein the particle is attached to the bubble. A second theory, which is under development, is “dissolved air flotation” (DAF). It includes the formation of small air bubbles on the mineral particle surfaces as a result of precipitation of dissolved air in the water (Bulatovic, 2007).

1.13 Chemical reagents

Different reagent schemes are employed in each flotation cell according to the mineralogical features of the ore. Based on their function, they can be classified into

three categories: collectors, frothers and modifiers. The most common collectors and depressants for the valuable and gangues minerals of the ore deposit under investigation are reviewed below:

1.13.1 Collectors

Collectors are relatively a large group of organic compounds that vary in their chemical composition. The basic function of collectors is to selectively adsorb onto the particle surfaces and form a hydrophobic layer causing attachment to air bubbles. They are typically heteropolar, and their molecule structure consists of a polar and a non-polar part. The polar part of the collector is inorganic and can react with water and adsorb onto the mineral surface during the adsorption process. In contrast, the non-polar part of the collector is a hydrocarbon chain, which does not react with water and so renders the mineral surface to be hydrophobic. Chemicals that are without a heteropolar structure (apolar hydrocarbon compounds) and that do not dissociate in water are also used as collectors by covering the mineral surface with a thin film (Bulatovic, 2007; Wills and Finch, 2016).

Collectors can either chemically adsorb at metal ion sites on the mineral surface known as “chemisorption” or they can be physically held on the surface, known as “physisorption”. In chemisorption, ions or molecules from the solution react with the particle surfaces thus changing their nature. This allows collectors to adsorb at particular atoms forming highly selective chemical bonds. In physisorption, ions or molecules from the solution tend to react with the particle surface as a result of electrostatic attraction, or van der Waals bonding. Physisorption is a less selective mechanism as the adsorption of the collector can take place at any point, which possesses the correct electrical charge or hydrophobic nature. Physisorbed collectors can be desorbed from the particle surface if the pH or the composition of the solution changes (Kawatra, 2001).

Different types and structures of collectors are used in the flotation of apatite and REE minerals. Fatty acids have long been proven on laboratory- and industrial-scales as efficient anionic collectors for the flotation of apatite under alkaline conditions (Lu et al., 1999; Kawatra and Carlson, 2014). They have also been used in froth flotation of REE minerals such as bastnäsite in carbonatite deposits (Fuerstenau et al., 1992; Krishnamurthy and Gupta, 2016).

Fatty acids that are used as collectors are mainly a mixture of oleic, linoleic, linolenic, palmitic, and stearic acids. Commercially, these fatty acids are known as tall oil fatty acids (TOFA), which is typically a mixture of oleic acid followed to a lesser extent by linoleic acid (Guimarães et al., 2005; Kawatra and Carlson, 2014). The ratio of fatty acids in the mixed collectors plays an important role in the phosphate flotation. A mixed collector of 54% oleic acid, 36% linoleic acid, and 10% linolenic acid at a pH of 9.5 on a bench-scale froth flotation showed a significant improvement of the P_2O_5 recovery (Cao et al., 2015).

Despite the advantages listed above, the selectivity of fatty acids towards the gangue minerals is low. Its solubility and selectivity largely depend on the pulp preparation method, pH condition, and the use of depressants. Also, unsaturated fatty acids e.g. oleic acid are more selective than saturated fatty acids e.g. stearic acid (Bulatovic, 2007).

Under alkaline conditions (pH~10) the fatty acid is ionised creating a negatively charged carboxylate ion. This negative ion then interacts with calcium at the solid-liquid interface region to form calcium carboxylate as shown in Figure 1.13. The chemisorption interaction is the primary mechanism leading to fatty acid adsorption onto the mineral surface at alkaline pH (Hu et al., 1986; Pavez et al., 1996; Maltesh et al. 1996; Lu et al., 1999; Guan 2009 cited in Kawatra and Carlson, 2014).

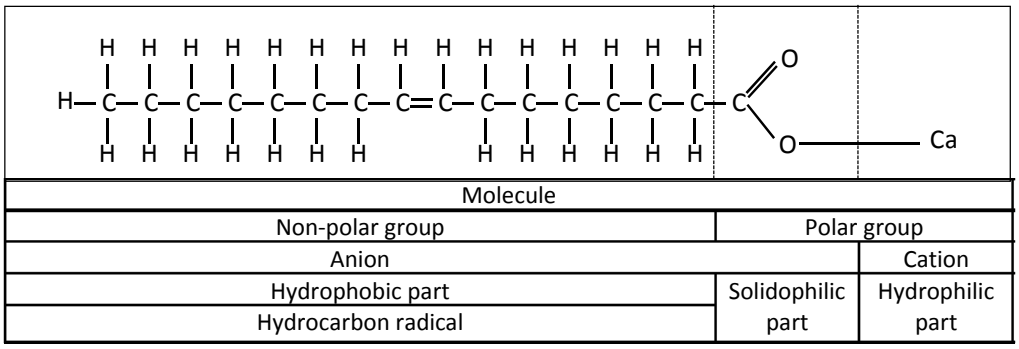

Figure 1.13: Molecular structure of calcium oleate, adapted from Bulatovic (2007).

In addition to fatty acids, other common chemistries have been widely used for recovering REE minerals e.g. bastnäsite as well as apatite are various of hydroxamates, dicarboxylic acids, and organic phosphoric acid esters (Pradip and Fuerstenau, 1991; Bulatovic, 2010).

Hydroxamate is an anionic collector and behaves in a similar way to fatty acids in solutions by forming metal cation-hydroxamate and carboxylate, respectively (Fuerstenau and Pradip, 2005; Bulatovic, 2007). Hydroxamates are ideal collectors for floating bastnäsite (REE fluorcarbonate), while they are not suitable for floating allanite (REE calcium aluminosilicate) collectors (Jordens, 2016).

Although, the selectivity of hydroxamic acids as better collectors than fatty acids was proved on a laboratory scale, the results on a commercial scale using Russian and Chinese hydroxamates showed limitations of using this collector. It has shown that the performance of hydroxamates is mainly affected by the carbon-chain length and the slime content of the feed pulp. A mixture of hydroxamates with a carbon-chain length between C7 and C9 gave better flotation efficiency compared to higher carbon-chain length hydroxamates of C9 (Bulatovic, 2007).

Furthermore, the selectivity of hydroxamate surfactants depends on the solubility of the minerals and the stability of the formed cation-hydroxamate complex (Assis et al., 1996). As the metal cation content increases the selectivity of hydroxamates increases (Jordens, 2016).

Rice bran and soybean bran oils are successfully utilised as apatite collectors and replaced the more expensive tall oil fatty acid collector in the processing of Brazilian igneous phosphates (Guimarães et al., 2005). Rice bran and soybean bran oils contain a slightly lower content of oleic and linoleic acids, which make it a desirable alternative to tall oil (Guimarães et al., 2005; Kawatra and Carlson, 2014).

1.13.2 Frothers

Frothers are usually organic hetero-polar surface-active reagents. The prime functions of frothers are (1) enhance the formation and preservation of small bubbles in the pulp zone, which leads to an increase in the number of bubbles and their collision with particles and hence improves flotation kinetics, (2) reduce the bubble rise velocity to the surface, which highly increases the residence time of bubbles and the probability of bubble-particle contact, which in turn increases kinetics, and (3) form a more stable froth layer at the top of the flotation cell to make concentrate removal easier (Klimpel and Isherwood, 1991; Klimpel, 1998; Melo and Laskowski, 2006; Cappuccitti and Nesset, 2009; Wills and Finch, 2016; Zhou et al., 2016).

It is generally accepted that adding a frother to water reduces the surface tension of the solution. This is the result of the hetero-polar nature of the frother molecules that tend to adsorb at the air-water interface, with the polar (hydrophilic) portion oriented towards the water phase and the nonpolar (hydrophobic) portion towards the air phase (Klimpel and Isherwood, 1991; Klimpel, 1998)

A wide range of frothers are used, depending on mineral type, operating conditions, cost, and availability. The alcohols group are commonly used as frothers, such as methyl isobutyl carbinol (MIBC) and polyglycols group such as polypropylene glycols and PPG alkyl ethers (Klimpel, 1998; Wills and Finch, 2016).

Frother types exhibit different hydrodynamic characteristics and thus are described as either ‘strong’ or ‘weak’. A strong frother such as Flottec F150 (a polypropylene glycol) is categorised as producing a stable froth, having a higher water carrying rate, smaller bubble size, and a high gas holdup (the latter refers to the bubble size and rise velocity in the pulp zone), while a weak frother such as MIBC that does the opposite (Melo and Laskowski, 2006; Cappuccitti and Nesset, 2009; Tan et al., 2013; Zhou et al., 2016). Thus, a strong frother will carry more water into the froth ‘wet froth’ and hence is less selective, owing to an increase in entrained particles, while using a weak frother leads to increase water drainage in the froth ‘dry froth’ and reduces the entrained particles and hence giving it improved selectivity (Klimpel and Isherwood, 1991; Cappuccitti and Nesset, 2009).

It is important to note that the frother concentration also has an influence on the gas holdup. As a frother concentration is increased, gas holdup increases as a result of decreasing the bubble size, which subsequently increases the flotation kinetics (Cappuccitti and Nesset, 2009; Tan et al., 2013).

1.13.3 Modifiers

This class of reagents cover a wide variety of chemicals that are used to make the flotation process more selective, and they can be divided into five categories: depressants, activators, pH regulators, dispersants, and flocculants.

The purpose of ***depressant*** is to inhibit the collector molecule from adsorbing onto the mineral particle surface by making it a hydrophilic and thereby prevent undesired minerals from floating. A wide range of mechanisms are employed to depress particular components. The most common approach is: *deactivation*, which leads to

removal or alteration a situation that principally leads to undesired activation of specific minerals. The second mechanism is *surface blocking*, this approach enables the reagent to first adsorb on a particular mineral, subsequently blocking a collector to adsorb onto the same mineral. The final approach called *oxidation*, uses a reagent to oxidise the mineral surface and so prevents a collector from being attached (Klimpel, 1998).

The ***pH regulator*** has a significant influence in the flotation environment, and plays a role in obtaining optimum performance for certain reagents and minerals. The charge of the surface chemistry of most minerals is influenced by the pH, and generally it can be positive under acidic conditions or negative under alkaline conditions. In a complex ore, the pH influence can be more complicated as it leads to a change in many variables at the same time. It can modify the potential-determining ions by changing the solubility of the minerals involved in the pulp. Furthermore, it controls the ionisation of certain collectors, which enhances the adsorption of the collector on the selected mineral and reduces its adsorption on the undesirable mineral (Klimpel, 1998; Kawatra, 2011).

Other modifying reagents that can be used in particular cases are dispersants and flocculants. The basic role of these chemicals is to change the fluidity of the flotation pulp by modifying the particle-particle interaction. In a pulp with high content of slime fine particles, e.g. particles below 10 μm, these fines tend to coagulate or coat each other, causing an adverse effect on the separation process. Therefore, ***dispersants*** are used to keep these fine particles separated and dispersed in a pulp to ensure the ore surface mineral is free and the collector can adsorb onto its surface. The most widely used dispersants are low molecular weight polyacrylates, sodium silicates and lignin sulphonates (Klimpel, 1998; Wills and Finch, 2016).

Corn starches and modified starches are excellent gangue depressants in the flotation of igneous phosphate ores. Corn starch is employed to depress carbonate and iron oxides at alkaline conditions because it is soluble in water and has a higher affinity to calcite than apatite (Filho et al., 2000; Guimarães et al., 2005). Other depressants such as guar gum, tannins, ethyl cellulose, and carboxy methyl cellulose were also extensively examined, but the performance of corn starch was consistently superior to that of those reagents (Filho et al., 2000).

Sodium silicate is utilised in both igneous and sedimentary phosphate flotation. It improves the depression of calcium cations by precipitating them as calcium silicate, and enhances the selectivity of fatty acid collector towards apatite (Dho and Iwasaki, 1990).

Lignin sulphonate $C_{20}H_{26}O_{10}S_2$ is a water-soluble anionic reagent that has been used as a depressant for calcite and baryte in the flotation of bastnäsite ore with fatty acid collector (Fuerstenau et al., 1982; Pradip and Fuerstenau, 2013).

The investigation by Sadowski (1992) has shown that adding sodium lignin sulphonate causes a decrease in the sorption of the anionic collector sodium dodecyl sulphate on the surface of calcite and baryte, however no effect was observed on the surface of dolomite and magnesite. Also, the results showed that the adsorption of sodium lignin sulphonate at the cationic sites e.g. Ca^{2+} and Ba^{2+} increased the negative charge created on the surface of calcite and baryte, respectively. Thus, the adsorption of the anionic sodium dodecyl sulphate collector on these minerals surfaces was reduced (Sadowski, 1992).

The laboratory experimental work by Anderson (2015) on Mountain Pass ore deposit showed that the temperature and the concentration of lignin sulphonate may play a role on its selectivity towards the gangue minerals, particularly baryte, and hence the REO grade and recovery. The flotation experimental results at a temperature of 25°C showed that as the lignin sulphonate concentration was increased the REO recovery decreased, while the grade remains constant. Conversely, at a temperature of 80°C, as the lignin sulphonate concentration was increased the REO recovery slightly changed while the grade significantly increased, indicating enhanced selectivity of the depressant. Furthermore, it is important to point out that in addition to act lignin sulphonate as a depressant, it also acts as a dispersant agent (Sadowski, 1992; Bulatovic, 2007; Bouffard et al., 2009).

1.14 Mineral processing testwork at Mintek

Various mineral processing testwork have been conducted at Mintek, South Africa including:

(1) The bench scale comminution tests performed on Songwe Hill ore deposit showed the following results (Mintek, 2014):

- The SAG mill comminution (SMC) test results and based on the A*b value of 31.7 indicated that this deposit can be characterised as a hard ore with high resistance to impact breakage.
- The Bond abrasion index (AI) test results with an AI value of 0.0573 showed that this ore deposit possesses low abrasiveness characteristics.
- The Bond rod work index (BRWI) test results with a BRWI value of 15.32 kWh t^{-1} indicated that the Songwe Hill carbonatite would respond as a hard ore when ground using conventional rod mill at standard closing screen size of 1.18 mm.
- The Bond ball work index (BBWI) test results with a BBWI value of 10.26 kWh t^{-1} for both closing screen sizes of 75 µm and 106 µm indicated that the Songwe Hill carbonatite could be classified as being of medium hardness.

(2) In order to determine the possibility of separating heavier apatite and REE-minerals from the lighter gangue minerals, several shaking table tests were conducted on two size fraction samples of P_{80} 300 µm and 150 µm using a Wilfley 8-product shaking table. The results for all ore type samples at a coarser and finer grind showed about 3% to 6% of mass pull with an average REE recovery of 6% were achieved. Thus, it was concluded that process this deposit at coarse and fine grinding using shaking table was not efficient (Mintek, 2013).

(3) Extensive forth flotation tests have been conducted at Mintek, South Africa using various reagent suites. The main approaches and findings are:

- Flotation tests at various grind levels P_{80} of 300 µm, 150 µm (undeslimed), and 150 µm (deslimed) feed samples using caustic starch, sodium silicate and sarcosine as chemical reagents were performed. The results showed high mass pull of 25%, 46%, and 49%, along with REE recovery of 41%, 69%, and 71%, respectively were obtained (Mintek, 2013).

- A number of flotation tests were conducted on composite samples ground to P_{80} of 53 µm, 38 µm, and 25 µm to see the effect of fine grinding on the liberation of the valuable minerals and hence their recovery. Sarcosine as a collector, sodium silicate as a depressant, and soda ash as a pH modifier under different dosages were used. However, the outputs showed a high mass pull was generated over the tests, the best results at a mass pull of 26% and REE recovery of about 58% were obtained by processing the feed P_{80} of 53 µm with a low dosage of sarcosine.
- Additional froth flotation tests using a range of collectors such as fatty acids, succinamates, amines, and hydroxamic acids along with a range of depressants/dispersants such as caustic starch, sodium silicate, gum arabic, and lignin sulphonate were conducted. The best results were achieved by adapting the modified Mountain Pass recipe that utilises fatty acids as a collector, sodium fluorosilicate and lignin sulphonate as depressants, and soda ash as a pH modifier at long conditioning time and elevated temperature (Pradip and Fuerstenau, 1991; Pradip and Fuerstenau, 2013; Bulatovic, 2010). Under these operating conditions a mass pull of 25% and REE recoveries of 66% were achieved (Mintek, 2014).
- Further work was focussed on reducing operating costs by conducting tests to minimise the chemical reagent dosages. Different dosages of sodium fluorosilicate including 0 g/t, 250 g/t, 500 g/t, and 1000 g/t were investigated. The highest REE recovery was achieved at the dosage of 250 g/t. Also, various dosages of sodium carbonate of 0, 1, 2, 3, 4, 5, 6,7, and 8 kg/t were tested. (Mintek, 2014).

Chapter 2

Materials and experimental methods

2.1 Introduction

This chapter describes all of the rock samples and pure single minerals used throughout this research, together with details of the analytical techniques and experimental procedures used to analyse and process these rock and mineral samples.

2.2 Materials

2.1.1 Crushed core samples

The drill core samples used in this study were obtained from Mkango Resources Ltd. Eight crushed samples P_{100} 1.7 mm representing eight drill holes from Songwe Hill, Malawi, were selected for chemical and mineralogical analyses, as well as mineral processing tests. These samples were delivered to Camborne School of Mines from Mintek, South Africa. Descriptions of each drill hole, depth, sample weight, and lithology as received from Mkango Resources Ltd. are given in Table 2.1.

Table 2.1: Details of the crushed drill core samples from Songwe Hill, Malawi, used in this study. Source: Mkango Resources Ltd.

Drill hole no.	Depth (m)		Quantity (kg)	Drill core description
	From	To		
PX05+15	2	201	2+2	Relatively homogenous calcite carbonatite - similar to and beside PX12
PX09	0	116	10	More weathered carbonatite
PX12	0	182	4	Relatively homogenous calcite carbonatite
PX13	6	137	4	Best equivalent to PX03 (black carbonatite)
PX21	3	211	4	Relatively homogenous calcite carbonatite - similar to and beside PX05
PX22b	3	348	4	Relatively homogenous calcite carbonatite - similar to and beside PX12
PX33	4	153	4	More fenite + calcite carbonatite mix
PX35	0	149	4	Ankerite-carbonatite

2.1.2 Pure single minerals

Synchysite crystals at Songwe Hill are too small, with an average size of about 30 μm (see Chapter 4, Section 4.4.5), and therefore not suitable for the magnetic properties study undertaken as part of this research. A great effort was made to acquire alternative synchysite-(Ce) and also other REE fluorcarbonate mineral samples with crystals of a sufficient size, free from impurities and matrix, and without the common feature of syntaxial intergrowth between REE fluorcarbonate minerals.

Small natural crystals without a matrix of bastnäsite-(Ce), parisite-(Ce) and röntgenite-(Ce) from several different localities were purchased and used in for measurement of their magnetic properties. These samples included: a crystal of bastnäsite-(Ce) from Zagi Mountain, Pakistan, a crystal of parisite-(Ce) from Snowbird mine, Mineral County, Montana, USA, and a couple of very small crystals of röntgenite-(Ce) from the Narssârssuk, nepheline syenite pegmatite in Greenland.

Small pieces from the large crystals i.e. bastnäsite-(Ce) and parisite-(Ce), as well as the whole small crystals of röntgenite-(Ce), were checked first by the SEM-EDS (see Section 2.5) and then measured by VSM (see Section 2.8). After measurement, these crystals were picked out, made into polished mounts and analysed by EPMA (see Section 2.6).

2.3 Whole rock analysis

2.3.1 ICP-MS and ICP-OES (South Africa and Australia)

The crushed drill core samples that formed the head sample for the mineral processing tests were analysed for REE, Na, Mg, Al, Si, P, S, K, Ca, Mn, Fe, Sr, Ba, Zr, Nb, Th, and U. All the sample preparation and analytical work were carried out by Intertek-Genalysis Laboratory Services Pty Ltd. in Johannesburg, South Africa, and Perth, Australia. All samples were milled and pulverised to P_{80} 75 μm. The samples were analysed using digestion method PF6. This method involves using a sodium peroxide fusion to ensure complete dissolution of the sample, including the refractory component. Once the digestion was completed, the sample was diluted and analysed with an ICP-MS for the REE and other trace elements. Analysis by ICP-OES was used for the major elements (Croll et al., 2014).

Internal quality assurance and quality control procedures, including the insertion of duplicate and blank samples in every batch, were applied. The results indicated that

there was no contamination nor systematic analytical issue. Certified reference materials including AMIS0185 and Geostats GRE-04 were also used (Croll et al., 2014).

2.3.2 ICP-MS (CSM)

The REE, Th, and U were analysed in all the composite samples, the magnetic separation products (Chapter 5) and the froth flotation products (Chapter 6) using an ICP-MS Agilent 7700 Series at Camborne School of Mines, University of Exeter.

All powdered samples were digested using the four-acid digestion method (a mixture of concentrated hydrofluoric (HF), hydrochloric (HCl), nitric (HNO_3), and perchloric ($HClO_4$) acids), then diluted with deionised water prior to analysis by ICP-MS.

For quality control and determination of analytical accuracy, a certified reference material including carbonatite USGS-COQ-1 was used and analysed in every batch of 20 samples. Additional analyses of this standard were made at ALS Laboratories Ltd, Spain (See Section 2.3.4). The analyses of the reference sample were within the acceptable range of results (see Appendix A-1). Also, two reagent blanks were included alongside the samples during every acid digestion batch to assess any potential elemental contamination. The results indicated that there is no contamination. Additionally, two duplicate samples were also inserted into the sample stream batch.

2.3.3 X-ray fluorescence (XRF)

The elemental compositions of all the composite samples and their magnetic separation products were analysed using a Bruker-AXS S4 Pioneer X-ray fluorescence spectrometer at Camborne School of Mines, University of Exeter.

The powdered sample was mixed with a binder solution (20% Elvacite 2013 in acetone) until the powder was dry, and then pressed in a steel die at 20 tonnes. The sample was then analysed on the XRF using the Bruker's semi-quantitative analysis package. Loss on ignition was determined by heating a portion of the sample to 1000°C for over 8 hours. The semi-quantitative software package requires this information to enable it to accurately normalise the values to 100 wt%.

2.3.4 Portable X-ray fluorescence (pXRF)

The major elements including P_2O_5, SiO_2, CaO, Fe_2O_3, and SrO in all froth flotation products (Chapter 6) were analysed using an Olympus Delta Premium DP-6000-C Portable X-ray Fluorescence at Camborne School of Mines, University of Exeter. The powders were spread out onto clean paper. Three measurements were made on different areas of each sample and their average was used to represent the elemental composition.

It is important to note that the concentrate and tailings samples of the froth flotation tests that gave the best optimised results (Appendix K, T15 and T16) were sent for the whole elemental analysis to ALS Laboratories Ltd, Spain. These samples were analysed by XRF and ICP-MS using the lithium borate fusion method. Certified reference materials including AMIS0104, SARM-5, GRE-04, and NCSDC86318 were used to check the analytical accuracy. Blank and duplicate samples were also used. All analysed element concentrations were within the lower and upper bounds (see Appendix A-2).

The analytical results for the major elements within these flotation products were compared to the pXRF results in order to identify any disparities between the pXRF and ALS results. The analytical results for P_2O_5, SiO_2, CaO, and Fe_2O_3 by pXRF versus the ALS Laboratories are presented in Figure 2.1.

It can be seen from Figure 2.1 that the analysed elemental oxides at ALS Laboratories, particularly P_2O_5, CaO, and Fe_2O_3, are relatively close to those values measured by pXRF. Interestingly, the values of P_2O_5 and CaO in the tailings products measured by pXRF are very comparable to values measured at ALS Laboratories. Note that the tailings are considered the most important product when determining the separation process.

The concentrations of SiO_2 measured by pXRF are somewhat higher than values measured at ALS Laboratories, except for values in the tailings products which are also very comparable.

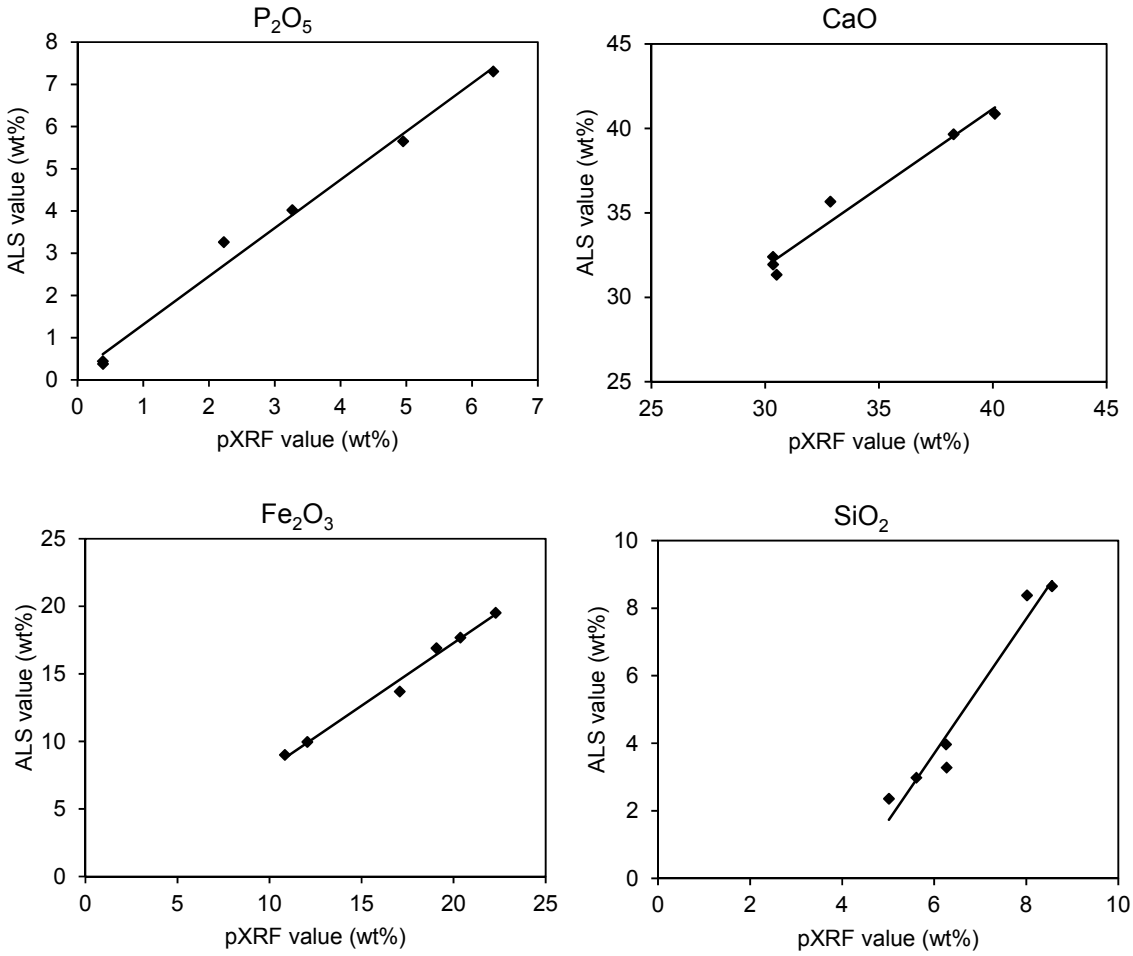

Figure 2.1: Scatter plots of the elemental analysis results for P_2O_5, CaO, Fe_2O_3, and SiO_2 in froth flotation concentrates and tailings, measured by pXRF versus ALS laboratories.

2.4 X-ray diffraction (XRD)

XRD analysis was carried out to qualitatively identify which mineralogical phases principally occur in the eight crushed drill core samples.

The samples were disaggregated with an agate mortar and pestle and then analysed using the Siemens D5000 X-ray diffractometer at Camborne School of Mines, University of Exeter. The analysis was carried out using a Cu Kα source operated with a tube voltage of 40 kV and current of 30 mA over angles of 20° to 60° 2θ, on a 0.02° step with a step time of 1 s. The profile produced by the scan has been interpreted using the JCPDS PDF-2 (2004) database and Bruker EVA software V.10.0.1.0. The software links to the International Centre for Diffraction Data (ICDD) which enables users to match the laboratory data with the data in the file.

2.5 Scanning electron microscopy with energy-dispersive X-ray microanalysis (SEM-EDS)

The SEM-EDS analyses were carried out with a JEOL JSM-5400LV Low Vacuum SEM equipped with Oxford Instruments ISIS EDS system at Camborne School of Mines, University of Exeter. Analyses were performed in high vacuum mode under an acceleration voltage of 25 kV. Backscattered electron imagery was used to distinguish the mineral phases and qualitative EDS was used for identification.

Polished Epoxy blocks of the carbonatite fractions were prepared by following the method in Pirrie et al. (2009). Each sample was mixed with approximately the same amount of graphite powder prior to resin embedding to promote particle dispersion, minimise particle agglomeration, and prevent the settling bias effect (Pascoe et al., 2007). A 30 mm diameter plastic block was prepared and the sample surface was then ground and polished to a 1 μm finish using a water-based polishing process. The quality of the polishing process was checked by examining the blocks under a reflected light microscope. The sample was finally coated with an approximately 25 nm thick layer of carbon.

REE fluorcarbonates were identified using BSE imagery in combination with the relative EDS peak-height of Ca and the REE. This was particularly effective when the fluorcarbonates formed syntaxial intergrowths. Brighter BSE images correspond to REE fluorcarbonates with higher ratios of REE to Ca, such as bastnäsite and, correspondingly, darker BSE images were interpreted as the Ca-rich REE-fluorcarbonate end-member: synchysite. Röntgenite was difficult to identify using EDS, as it is very similar chemically to both parisite and synchysite. Therefore, röntgenite was quantitatively analysed using EPMA.

2.6 Electron probe microanalysis (EPMA)

Quantitative elemental composition data was obtained using a JEOL JXA-8200 EPMA with wavelength dispersive spectrometry (WDS) at Camborne School of Mines, University of Exeter.

The elemental composition for the valuable minerals in the Songwe Hill carbonatite was carried out using operating conditions of 15 kV accelerating voltage, 20 nA beam current, and 5 μm beam diameter. The peak counting times were 10 s for La

and Ce; 20 s for Pr, Nd, Sm, Eu, Gd, Dy, Er, Y, Th, and U; and 30 s for Ca, P, and F. A variety of natural and synthetic reference materials were used.

Additional analyses for the REE fluorcarbonates (synchysite and parisite) were carried out by Aoife Brady of Mkango Resource Ltd., using a Cameca SX100 electron probe microanalysis equipped with an Oxford Instruments INCA energy dispersive X-ray microanalysis system at the Natural History Museum (NHM), London. Analyses were conducted using a 20 kV accelerating voltage, 20 nA beam current, and 5-10 μm beam diameter. The peak counting times were 20 s for Na, Mg, Al, Ca, Mn, P, La, Ce, Cl; 30 s for F, Si, Fe, Pr, Nd, Eu, Gd, S, Yb, Lu; 40 s for Sm, Dy, Er; 60 s for Y; 120 s for Th, U; and 240 s for Ba. Interference corrections were performed for La and Ce interferences on the HREE. A variety of natural and synthetic calibration materials were used.

Elemental compositions for the single crystal minerals were also obtained using the electron microprobe instrument at Camborne School of Mines, University of Exeter. The analysis was carried out using operating conditions of 20 kV accelerating voltage, 20 nA beam current, and 7 μm beam diameter. The peak counting times were 20 s for Mg, Si, Al, Sr, F, Tb, Er, Yb, and Lu; 30 s for Mn, Fe, La, Ce, Pr, Nd, Sm, Eu, Gd, and Dy; and 40 s for Ca, Ba, Y, Th, and U, with an equal time off-peak for each element. Backscattered electron imagery was used to check for homogeneity of the crystals and to locate suitable areas for analysis.

The REE were calibrated against synthetic silicate glasses from the Edinburgh Ion Probe Facility, while the other elements were calibrated against a combination of natural and synthetic minerals and metals. A manual correction was applied to the REE data to correct for the overlaps, such as Ce overlapping on the Sm Lα line. Furthermore, chondrite-normalised distributions for the REE values of each measured mineral were calculated and plotted relative to the primitive mantle values of McDonough and Sun (1995), as a means of quality control.

2.7 Quantitative evaluation of minerals by scanning electron microscopy (QEMSCAN®)

2.7.1 Materials and sample preparation

In total, 15 carbonatite rock samples of different size fractions were analysed. They comprise eight crushed drill core samples with a P_{100} of 1700 µm, two composite samples with a P_{80} of 53 µm and 38 µm, and 5 size-by-size fractions of > 40 µm, 30-40 µm, 20-30 µm, 10-20 µm, and <10 µm.

The crushed samples were treated separately by splitting each whole sample (represents an individual drill core) into small fractions to produce three representative subsamples of approximately 30 g each using a Jones riffler. One of the subsamples was used to represent the individual crushed drill core, whereas the other subsamples were used to make two composite samples. The composite samples were made from combining all the subsamples from individual drill cores together and mixing them, then subjecting the prepared composite into a rod mill to produce the 53 µm and 38 µm fractions. These size fractions were filtered using a vacuum pump, dried in an oven at 60°C, and split into small fractions of representative subsamples using the Jones riffler.

The size-by-size fractions (SxS) were obtained by subjecting the remaining portion from the ground sample of 53 µm into a Warman Cyclosizer (see Section 2.9.2) to produce size fractions within the range of >40 µm and <10 µm. These fractions were filtered, dried at 60°C, and split into small fractions of a representative subsample using a riffler.

Each size fraction of the riffled subsamples described above was further reduced by a rotary micro-riffler to about 1 g, to be used as a final representative subsample for the QEMSCAN® measurements. The carbonatite size fractions were prepared as polished blocks by following the method described in Section 2.5 above.

2.7.2 QEMSCAN® instrument

The QEMSCAN® 4300 system at Camborne School of Mines, University of Exeter, was used for this study. It is based on a Zeiss EVO 50 series scanning electron microscope fitted with up to four light element Bruker Silicon Drift Droplet (SDD) Energy Dispersive X-ray Spectrometry (EDS) detectors, an electron backscatter detector, and digital pulse processor technology that result in a number of different

configurations. The instrument has detection limits of approximately 3 wt% (Rollinson et al., 2011), while the typical spectral resolution is 1 μm but can theoretically reach as low as 0.2 μm (Rollinson et al., 2011).

The analyses were carried out using standard operating conditions including a 25 kV of electron beam accelerating voltage and 5 nA beam current from a tungsten filament operating under high vacuum conditions. The X-ray collection rate is 1000 counts (unless customised) combined from four EDS Bruker SDD detectors, with an elemental mass range between carbon and uranium. Operation of the QEMSCAN® followed quality control procedures developed in-house for sample preparation, instrument calibration, operation, and data processing (Rollinson, 2016, *pers comm.*).

Further detail about the QEMSCAN® instrument and its operating modes can be found in Appendix B.

2.8 Vibrating sample magnetometer (VSM)

A LakeShore 7300 series VSM system connected to a computer interface for system operation, data acquisition and analysis at the School of Metallurgy and Materials, University of Birmingham, was used to measure the magnetic properties of REE fluorcarbonate minerals. The mineral sample was exposed to a sequence of centring operations, followed by oscillation of the sample and synchronous detection of the voltage induced in the coil set by the magnetised sample. A 50-100 mg sample of each mineral was prepared and placed in the VSM sample holder, as shown in Figure 2.2.

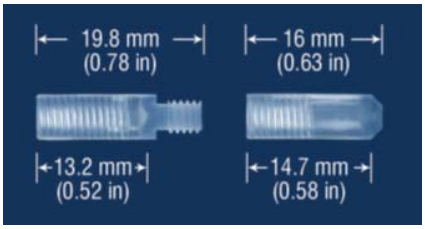

Figure 2.2: VSM sample holder, adapted from Sheridan (2014).

The sample holder was attached to an extension rod and then placed centrally in the VSM prior to measuring the magnetic properties. A schematic diagram of the vibrating sample magnetometer is shown in Figure 2.3. The sample is vibrated

sinusoidally, perpendicular to the applied magnetic field, using the vibration unit in the head. This causes an induced voltage in the pickup coils that is proportional to the magnetic moment of the sample, along with a signal received by the hall probe measuring the applied magnetic field. These signals are transferred to produce a magnetic hysteresis loop between +2 T and -2 T. The same procedure was applied to an empty sample holder prior to measuring the mineral samples, so that any magnetic effects from the sample holder could be taken into account. The magnetic moment values were converted into magnetisation using the volume of each sample, while the magnetic induction data were converted into magnetic field strengths using the constant permeability of free space 12.566 x 10^{-7} N A^{-2} (Jordens et al., 2014; Sheridan, 2014).

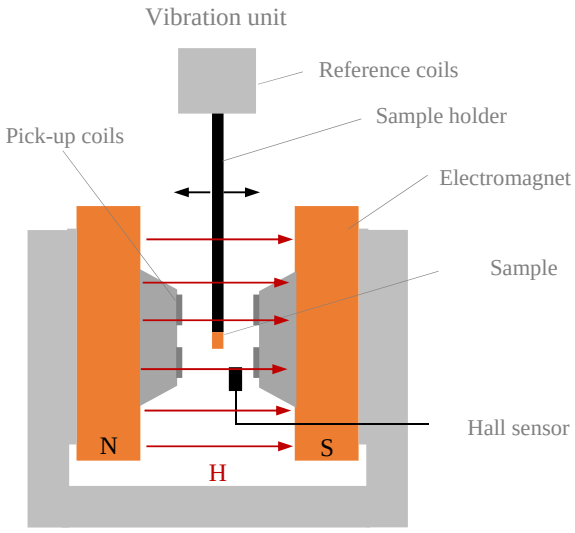

Figure 2.3: Schematic diagram of the vibrating sample magnetometer used to measure the magnetic properties of single crystal minerals as a function of magnetic field, temperature, and time, adapted from Speliotis (2005).

2.9 Particle size analyses

Particle size analyses of the composite samples after each grinding stage were determined using a Mastersizer and Warman Cyclosizer.

2.9.1 Mastersizer

A Malvern Mastersizer MAF500 laser-sizer at Camborne School of Mines, University of Exeter, was used to determine the particle size distribution of the composite samples used in this study. The ground sample was suspended in a beaker using a rotating impeller. About 10-20 g of sample was collected using a pipette and introduced into the measuring beaker connected to the Malvern Mastersizer. Duplicate measurements of the particle size distribution were collected to check for analytical consistency.

2.9.2 Warman Cyclosizer

The ground composite sample P_{80} of 53 µm was wet screened using a vibrating mechanical 45 µm sieve. The <45 µm size fraction was subjected for further classification by a Warman Cyclosizer (see Figure 2.4), to separate particles into different size fractions using the elutriation technique.

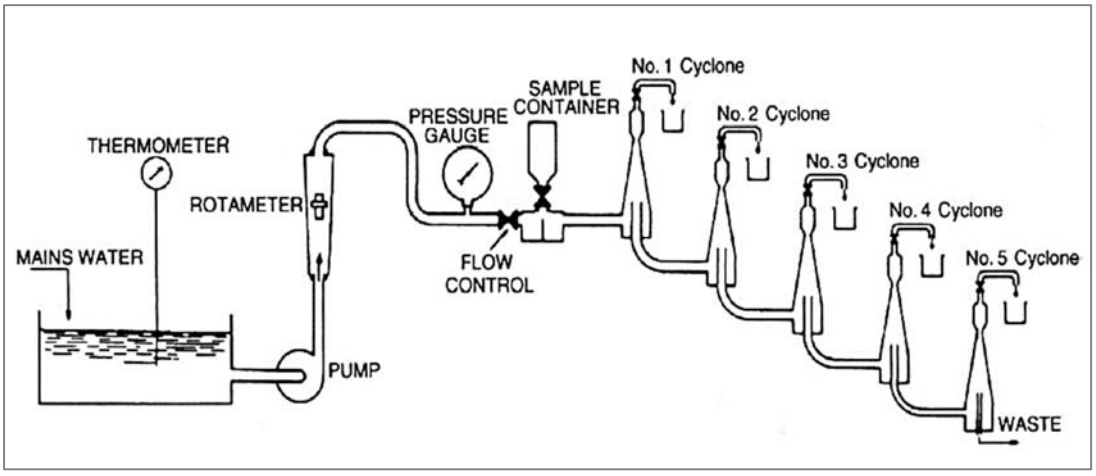

Figure 2.4: Warman Cyclosizer unit consists of five cyclones to classify sub-sieve size solid particles using the elutriation technique, after Warman (1997).

Approximately 75 g of sample was mixed with 100 mL of water, then transferred to the sample container and gently topped up with water. The sample was run on the Cyclosizer for 30 minutes at a temperature of 20°C. Each size fraction was then collected in discrete beakers using outlet tubing. Each beaker was allowed to settle,

decanted, pressure filtered, dried, and weighed. It is important to note that particles passing cyclone number 5 were also collected. A set of correction graphs was used to correct parameters including the water flow rate, temperature, time of elutriation, and fraction density. The density of each size fraction was measured using a Micromeritics AccuPyc 1330 instrument. The equivalent diameter of the five cyclones and the consequent down-stream size fractions were: 41 µm, 30 µm, 21 µm, 14 µm, 10 µm, and <10 µm.

2.10 Magnetic separation

2.10.1 Materials and sample preparation

All eight crushed drill core carbonatite samples P_{100} of 1700 µm were used for the magnetic separation experiments. A composite sample was prepared by combining similar amounts of each of sample. The composite sample was ground to different size fractions including P_{80} of 70 µm, 53 µm, and 38 µm. Furthermore, the composite sample P_{80} of 53 µm was classified into different size fractions within the range of >40 µm and <10 µm. A 50 g representative sample from each size fraction was mixed with water to achieve 25 % solids and used as a feed pulp for magnetic separation experiments.

2.10.2 Magnetic separator and experimental procedures

The wet high-intensity magnetic separator (WHIMS) manufactured by Rapid Magnetic Ltd, UK, provided with a 1 mm matrix, was used throughout this work. A two-stage separation process with different magnetic field strengths and process conditions was used to separate paramagnetic from diamagnetic minerals.

A series of magnetic separation experiments were conducted on the composite sample P_{80} of 70 µm to determine the effect of different magnetic field strengths on the separation efficiency. The water flow rate was set at 50 mL s^{-1} and processing time at 3 minutes. A flow diagram of the experimental procedure is shown in Figure 2.5.

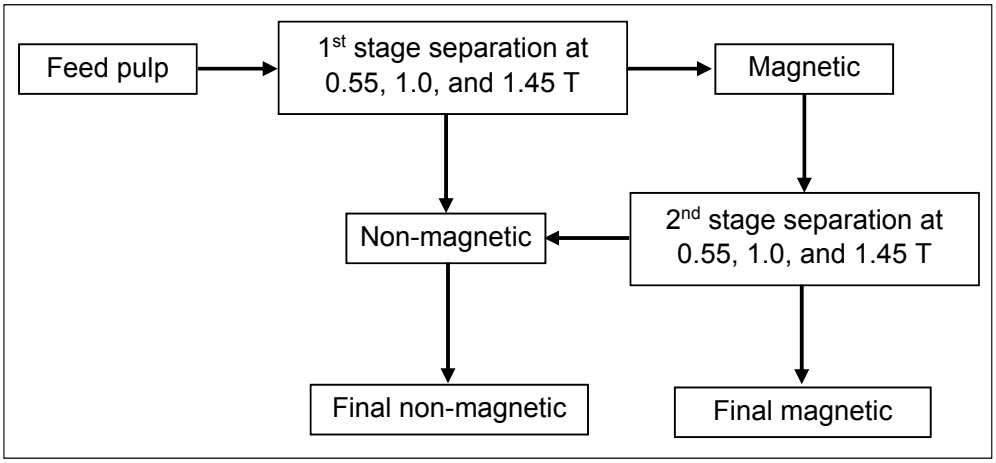

Figure 2.5: Schematic flow diagram of the two-stage magnetic separation testwork for the feed composite sample P_{80} of 70 µm to produce magnetic and non-magnetic products.

For the composite samples P_{80} of 53 µm and 38 µm, and the size-by-size fractions, a different experimental procedure was conducted. This involved applying a high magnetic field strength of 1.85 T for the first stage and subsequently subjecting the magnetic product to a lower magnetic field strength of 0.70 T, except for the 53 µm size fraction, which was subjected to an additional magnetic field strength of 1.00 T (Figure 2.6). The water flow rate was set at 25 mL s^{-1} and processing time at 3 minutes.

The magnetic separation products were collected, pressure filtered, dried, weighed, and analysed for the elemental compositions.

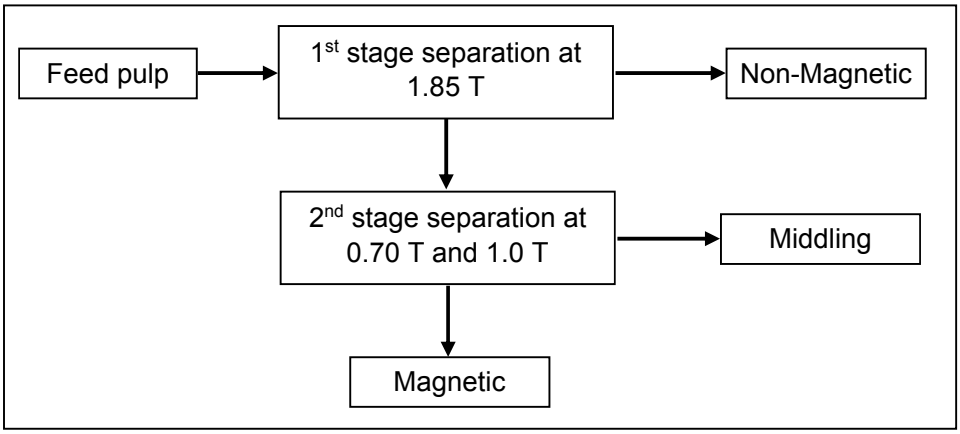

Figure 2.6: Schematic flow diagram of the two-stage magnetic separation testwork for the feed composite samples of 53 µm, 38 µm, and size-by-size fractions to produce magnetic, middling, and non-magnetic products.

2.11 Froth flotation

2.11.1 Materials and sample preparation

Seven crushed carbonatite samples P_{100} of 1700 µm including PX5+15, PX12, PX13 PX21, PX22B, PX33 and PX35 were used for the batch flotation tests. A composite sample was prepared by combining equal quantities of these crushed drill core samples, excluding drill core PX09, which contained weathering products (see Chapter 3). It is important to note that due to limited quantities of sample and in order to test different conditions and parameters, along with duplication of some experiments, the gross composite sample was split into subsamples of 300 g each using a rotary riffler.

2.11.2 Froth flotation experimental procedure

Froth flotation experiments were conducted in a laboratory scale Denver flotation machine. A 300 g composite sample was ground to P_{80} of 53 µm in a rod mill using the wet-grinding method. The ground slurry was filtered and kept wet. Froth flotation tests carried out by Mintek in South Africa have resulted that drying the feed sample after grinding reduced the REE recovery by about 5% (Mintek, 2014). Keeping the sample wet may enhance the interaction between chemical reagents and particle surfaces, thereby increasing flotation recovery (Mintek, 2014). Other possible explanations for this reduction could be due to the REE loss during transfer of the sample after the grinding, filtering, or drying steps. The water content in the filtered sample was determined from the difference in weight between the combined wet cake plus the filter paper, and the net dried feed sample. This helps determine the amount of water that should be added to reach 50% solids during the conditioning time.

A distinctive froth flotation process was applied to separate apatite and synchysite from their gangue matrices in the Songwe Hill carbonatite deposit. A simplified process flow diagram is shown in Figure 2.7. The chemical reagents used in the froth flotation experiments are described in the next section. Prior to rougher flotation, the feed sample was subjected to six conditioning treatments. The treatments were carried out using a flotation cell of 1.5 dm^3, placed in a water bath heated to a temperature of 60°C. In the first stage, after transferring the wet sample into the flotation cell, sodium carbonate and sodium fluorosilicate were added to the pulp and tap water was used to achieve a pulp density of about 50% solids. The pulp was

conditioned for 60 minutes under a constant agitation speed of 1200 rpm. During the second stage, lignin sulphonate was diluted with water, added to the pulp and conditioned for 60 minutes. During the third stage, the collector fatty acid (Betacol) was added to the pulp and conditioned for another 60 minutes. After a conditioning time of 3 hours, the pulp was then diluted to about 20% solids and compressed air was introduced to the flotation system through the agitator and controlled using an air flowmeter. The air flow rate ranged between 1.5 L min^{-1} to 5 L min^{-1} during a flotation time of 3 minutes. In the fourth stage, another dose of the collector fatty acid was added to the pulp and conditioned for 2 minutes. In the last two stages, the pulp was conditioned for 2 minutes without adding any collector or frother, to recover the remaining valuable minerals.

After completion of the flotation process, the concentrates and tailings were filtered, dried, weighed and their assay measured using a pXRF for the major elements and ICP-MS for the rare earth elements.

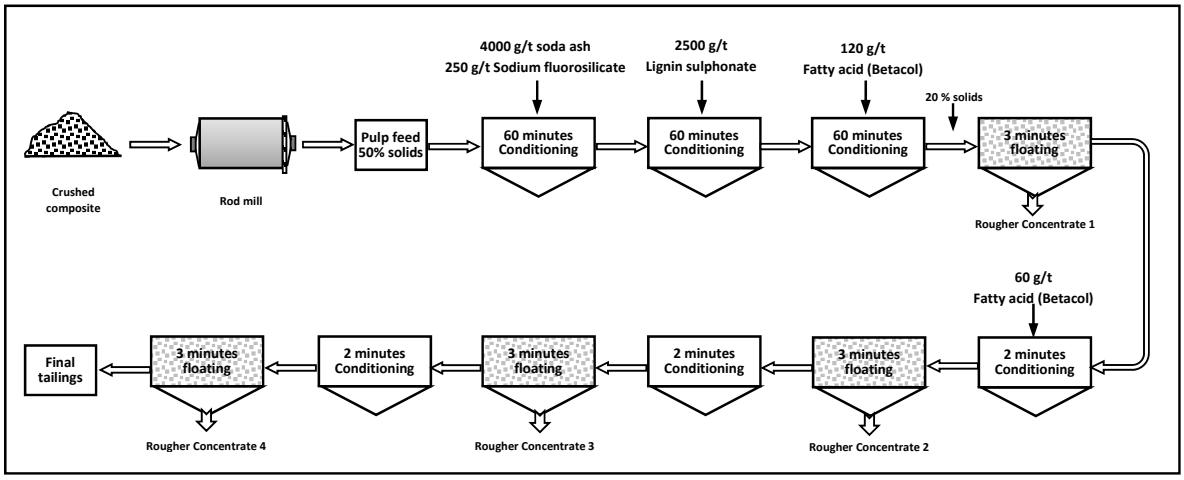

Figure 2.7: Schematic flow diagram of the froth flotation procedure used to process the Songwe Hill carbonatite deposit for its REE- and REE-bearing minerals.

2.11.3 Chemical reagents

The reagents used in the flotation tests were supplied from a variety of places. They are listed in Table 2.2 and described briefly as follows:

Sodium carbonate

Sodium carbonate (Na_2CO_3), also known as soda ash, was used as a pH controller in addition to acting as a depressant for carbonate minerals such as calcite. It is widely used in processing of the bastnäsite-rich carbonatite deposit at Mountain

pass, California (Fuerstenau et al., 1992; Pradip and Fuerstenau, 2013). Leja (1982) stated that CO_2 ions from sodium carbonate may play a significant role in reacting and precipitating Ca ions in some flotation systems.

Table 2.2: Summary of the chemical reagents, dosages, and conditioning and floating times used in batch froth flotation tests of this project.

Reagent type	Reagent name	Reagent dosage (g/t)	Conditioning time (min)	Floating time (min)
pH controller	Sodium carbonate (soda ash)	1500-20000		
	Sodium hydroxide (caustic soda)	1000-2000		
Depressants	Sodium fluorosilicate	250	10, 30, 60	
	Lignin sulphonate (Pionera 220)	2500	10, 30, 60	
Collectors	Fatty acid (Betacol CKF 30B) 1st dosage	120	10, 30, 60	3
	Fatty acid (Betacol CKF 30B) 2nd dosage	60	2	3
	Sodium oleate 1st dosage	80	10, 60	3
	Sodium oleate 2nd dosage	15	2	3

Sodium hydroxide

Sodium hydroxide NaOH was used as an alternative pH modifier to investigate its effect on the ionisation of fatty acids and sodium oleate, in addition to comparing its effect with sodium carbonate.

Sodium fluorosilicate

Sodium fluorosilicate was used as a depressant for silicate gangue minerals. It also has another function as a dispersant, therefore will disperse individual mineral particles once adsorbed onto their surfaces (Butalovic, 2007).

Lignin sulphonate

Lignin sulphonate, also called lignosulphonate or sulphonated lignin, is a by-product obtained by dissolving debarked wood sulphurous acid. The insoluble wood pulp (cellulose) is filtered off for manufacturing paper, while the filtrate (black liquor) is processed to recover fats, resins, lignins, and others (Leja, 1982).

Calcium lignin sulphonate, commercially known as Pionera F220 and supplied by Pionera, Spain, was used to conduct the froth flotation tests during this project.

Fatty acid

In these froth flotation tests, tall oil fatty acids commercially known as Betacol CKF 30B and supplied by Betachem (Pty) Ltd, South Africa, were used. Betacol is an insoluble yellow liquid emulsion obtained as a by-product of the wood pulp treatment. A list of the various chemical components form Betacol collector is shown in Appendix C.

2.11.4 Determination of the solubility of the chemical reagents

The solubility of the chemical reagents used in this work, including Betacol CKF 30B, sodium oleate, and lignin sulphonate (Pionera 220), was measured using a Jenway 7315 spectrophotometer at the Environment and Sustainability Institute, University of Exeter.

The solutions were prepared by adding 0.006 g (1 drop) of Betacol CKF 30B, 0.02 g of sodium oleate, and 0.005 g of lignin sulphonate (Pionera 220) to 30 mL of hot alkaline solution at 60°C. The pH of the solutions was adjusted to 8.5, 9.0, 9.5, 10.0, and 10.5 before and after adding the chemical reagent. Sodium carbonate and sodium hydroxide were used as pH modifiers for Betacol CKF 30B and sodium oleate, while the pH of lignin sulphonate solutions was adjusted using only sodium carbonate. All the prepared solutions were kept in a water bath at a temperature of 60°C until analysis.

The sample solutions were scanned by the spectrophotometer in a range of 320 nm to 700 nm. A wavelength of 400 nm was chosen as it gave a higher transmission percentage. A 4 mL cuvette was used and three readings for each measurement were obtained, in addition to duplication of selected sample solutions.

The spectrophotometer is based on how much light passes through the solution and the same light passes through the solvent.

Transmittance (T) is defined as the fraction of incident light which is transmitted through a solution, Equation (2.1).

$$T = (I/I_{\circ}) \times 100 \ldots\ldots\ldots (2.1)$$

Where: I represents the percentage of light that passes through the solution.

I_o represents the percentage of light that passes through the solvent.

The absorbance (A) is the amount of the light that is absorbed by the solutions, equal to the negative logarithm of the transmittance divided by 100, Equation (2.2).

$$A = -log(T/100) \dots\dots\dots (2.2)$$

Note that transmittance is usually expressed as a percentage, while absorbance is a dimensionless unit.

2.11.5 Determination of the separation performance

There are three important parameters that can be used to express the efficiency of a separation process, including the grade, recovery, and separation efficiency.

Grade

The grade or assay is the content of the valuable component in a feed, concentrate, or tailings, expressed as a weight percentage (wt%) or a part per million (ppm) of the target element(s) in the material (Leja, 1982; Wills and Finch, 2016).

Recovery

The recovery is the percentage of the total valuable component in the feed stream that is recovered in the concentrate. This can be calculated using weight and grade of the feed and concentrate as shown in the following equation:

$$R = \frac{Cc}{Ff} \times 100 \dots\dots\dots (2.3)$$

Where: C and F are the weight of the concentrate and feed, respectively.

c and *f* are the grade of the valuable mineral in the concentrate and feed, respectively.

Grade and recovery represent the most common measurements used to describe the metallurgical efficiency. Thus, it is always useful to consider the grade and recovery simultaneously using a “Grade-Recovery Curve”. Usually there is an inverse correlation between the grade and recovery of the concentrate, as an improvement in recovery often leads to a decrease in grade due to an increase in the content of gangue minerals in the concentrate, and vice versa (Wills and Finch, 2016).

Separation efficiency

This is the parameter that combines the grade and recovery of a concentrate into a single equation and was first presented by Schulz (1970), who defined the separation efficiency (SE) as follows:

$$Separation\ efficiency\ (SE) = R_m - R_g \ldots\ldots\ldots (2.4)$$

Where: R_m is the recovery of the valuable mineral in the concentrate.

R_g is the recovery of the gangue mineral in the concentrate.

By compensating the recovery and grade of valuable and gangue minerals for both of the concentrate and feed in Equation 2.3, the separation efficiency could be defined in the following form (Wills and Finch, 2016):

$$SE = \frac{Cm(c-f)}{Ff(m-f)} \times 100 \ldots\ldots\ldots (2.5)$$

Where: C and F are the weight of the concentrate and feed, respectively.

c and f are the grade of the valuable mineral in the concentrate and feed, respectively.

m is the content of the target element in the valuable mineral.

2.11.6 Flotation kinetic models

Kinetic models are often used to analyse the batch flotation results and to evaluate the effect of several parameters such as chemical reagents and operating conditions on the flotation process (Xu, 1998).

Many batch flotation tests that have been carried out in the laboratory have indicated that the classical first-order kinetic model can be utilised to evaluate and optimise the performance of the flotation process (Agar, 1987; King, 2001; Oliveira et al., 2011). The equation that describes the classical first-order kinetic model can be written as follows (Gupta and Yan, 2016):

$$R = R_\infty(1 - e^{-kt}) \ldots\ldots\ldots (2.6)$$

Where: R is the recovery of a given mineral at time t

R_∞ is the ultimate recovery after infinite flotation time t_∞

k is the flotation rate constant (min^{-1}) at time t

In practise, it is found that changing one parameter such as air flow rate or collector dosage leads to a significant change in the values of ultimate recovery and/or flotation rate constant. This can make it difficult to draw a conclusion when comparing between flotation tests under different process conditions. Xu (1998) introduced a modified rate constant K_M to overcome this situation, by combining R_∞ and K in a single equation.

$$K_M = R_\infty \times K \dots\dots\dots (2.7)$$

Also, according to Xu (1998), the modified rate constants were used to introduce another parameter, the selectivity index (SI), to measure the degree of selectivity between different minerals in a flotation system. The selectivity index can be defined as the ratio of the modified rate constants of two different minerals, Equation 2.8.

$$SI = \frac{K_M \; of \; mineral \; A}{K_M \; of \; mineral \; B} \dots\dots\dots (2.8)$$

SI is a useful tool that can be used to evaluate the separation process of a mineral over another under the given set of process variables. Changing any chemical or physical variable which results in an increase of the SI value should be considered to optimise the separation of the target mineral(s) (Natarajan and Nirdosh, 2006).

2.12 Conclusions

This chapter described all the materials, analytical techniques, and experimental procedures used throughout this research. Different standard materials were used and additional whole rock and mineral processing product analyses were sent to commercial laboratories for quality assurance and quality control. Also, the project has provided training in different analytical techniques including EPMA, QEMSCAN®, VSM, and use of a spectrophotometer.

Chapter 3

Geology, chemistry, and mineralogy of Songwe Hill

3.1 Introduction

This chapter presents the geology of the Songwe Hill carbonatite, Malawi, and characterises the crushed drill core samples used in this research. Whole-rock geochemical and mineralogical data, derived from ICP-MS, ICP-OES, XRF, XRD and SEM-EDS analyses, for the bulk core samples are outlined and discussed. The elemental composition of the valuable minerals in Songwe Hill carbonatite, obtained by EPMA is presented and discussed. The results of automated mineralogy studies by QEMSCAN® are given separately in Chapter 4.

3.2 Aims

The chapter aims to characterise the Songwe Hill carbonatite forming minerals, particularly the valuable minerals and their relationships with each other and the gangue minerals. It also aims to use the mineralogical outputs from different equipment in this chapter to be used to develop the Species Identification Protocol (SIP) and validate QEMSCAN® measurements in Chapter 4. It determines the grains shape and size to estimate the required grinding size to liberate the valuable minerals. The final focus of this chapter is to measure the chemistry of the valuable minerals, determining their elemental distribution, and identifying the identity of the REE fluorcarbonates.

3.3 Regional geology of Chilwa Alkaline Province (CAP)

The Songwe Hill carbonatite is located within the Chilwa Alkaline Province (Figure 3.1). The CAP covers approximately circular area of about 300 km to 400 km in diameter comprised mostly of intrusive alkaline rocks. These alkaline rocks are formed predominantly of two provinces: the North Nyasa Alkaline Province and the Chilwa Alkaline Province of southern Malawi (Woolley and Garson, 1970; Woolley, 2001).

The Chilwa Alkaline Province intrusions, located to the west and south of Lake Chilwa, that are of greater interest. The CAP consists of large alkaline intrusions in addition to smaller intrusions, minor plugs and dykes. It consists of a wide range of rocks including carbonatites, nephelinites, ijolites, nepheline syenites, syenites, quartz syenites, and granites (Woolley, 2001). Dixey et al. (1955) who the first described this group of alkaline intrusions and referred to them as the 'Chilwa Series', while the term 'Chilwa Alkaline Province' has used by later authors (e.g. Garson, 1966) (Woolley, 2001).

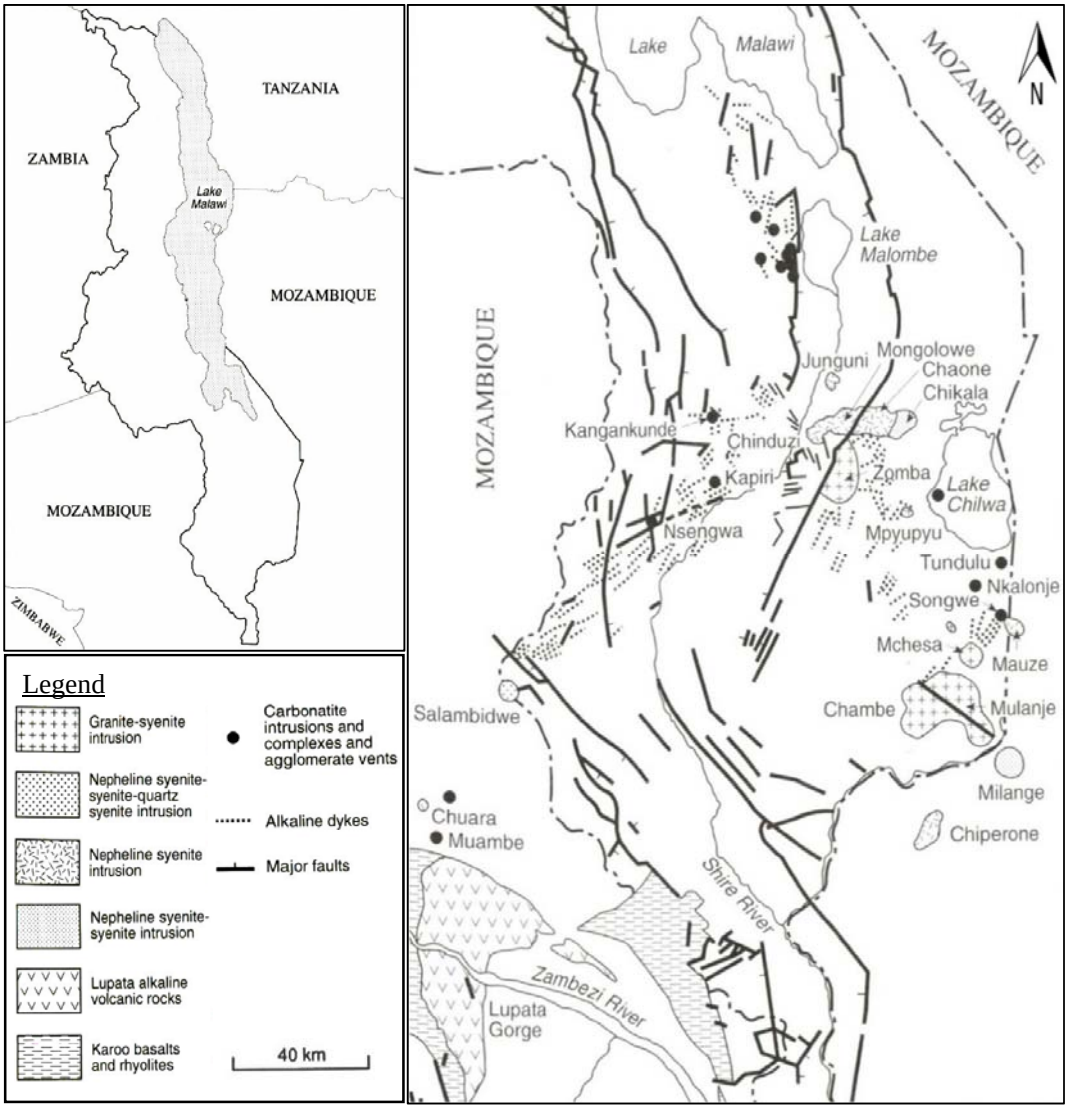

Figure 3.1: The geology of the Chilwa Province alkaline (CAP) province showing the distribution of alkaline and carbonatite intrusions in southern Malawi and Mozambique, after Woolley (2001).

Carbonatites are known to occur widely throughout the CAP, Garson (1965) documented approximately 17 carbonatite deposits located in southern Malawi and adjacent Mozambique. In addition to the large carbonatitic vent at Songwe Hill, there are three other substantial carbonatite complexes within the CAP including Chilwa Island, Kangankunde and Tundulu. Several smaller carbonatites occur throughout the CAP, which include dykes, sheets, small plugs and a volcanic vent (Swinden and Hall, 2012).

3.4 Geology of Songwe Hill area

Songwe Hill is interpreted as a circular volcanic vent approximately 800 m in diameter and expressed as a steep-sided hill above the surrounding plain with an elevation of about 230 m (See Figure 3.2; Swinden and Hall, 2012; Croll et al., 2014). Recent surface mapping and drilling, completed by Mkango Resources Ltd. in 2011, indicated that the vent complex comprises of a multi-phase intrusion characterised by various carbonatites and breccias. These lithologies exhibit a range of alteration from potassic fenitisation to low temperature hydrothermal or carbohydrothermal overprinting (Croll et al., 2014).

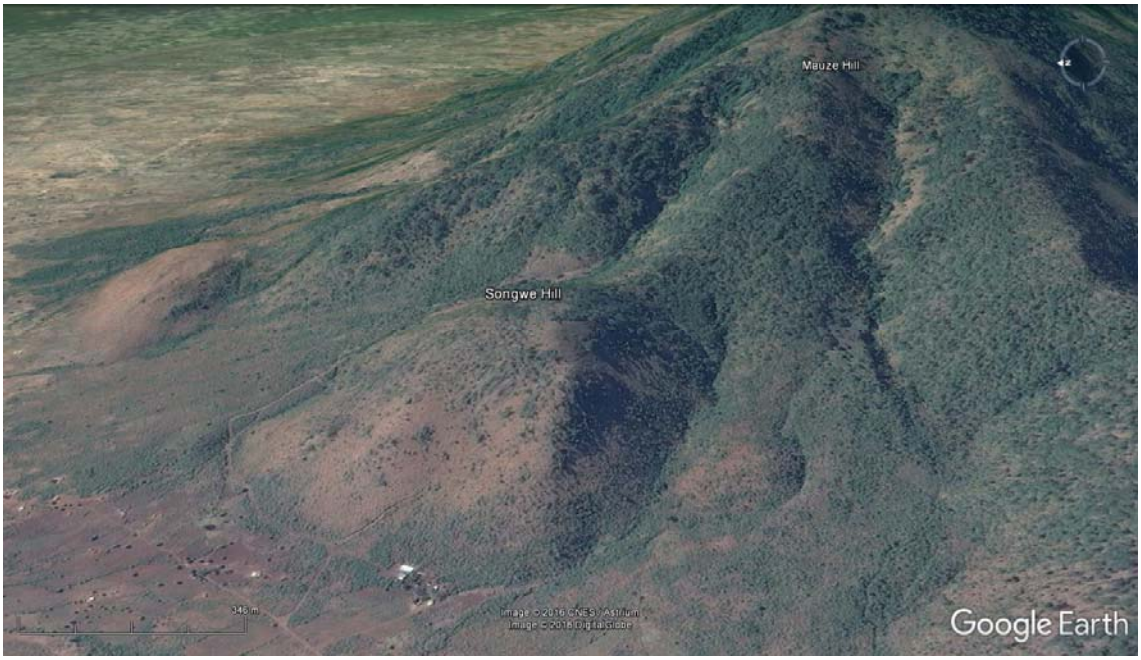

Figure 3.2: View of Songwe Hill carbonatite abuts against Mauza Hill in Malawi. Source: Google Earth.

The geology of the Songwe Hill has been more recently described by Croll et al. (2014) and by Broom-Fendley et al. (in prep), building on previous work carried out at Songwe Hill by the Geological Survey of Malawi (Garson and Walshaw, 1969). The lithological descriptions summarised in the following subsections are adapted from these contributions.

3.4.1 Carbonatite

Songwe Hill is comprised of several different stages of carbonatite intrusions (Broom-Fendley, 2015), however, there are two main carbonatite types ranging from light-grey, fine-grained, and relatively homogenous calcite-carbonatite to dark, fine-grained, and heterogenous REE-rich Fe-carbonatite (Broom-Fendley et al., 2012).

Calcite carbonatite

The calcite carbonatite comprises the largest proportion of the exposed carbonatite in Songwe Hill. It forms irregular and massive bodies that appear to have been emplaced in several phases (Croll et al., 2014).

Fe-rich carbonatite

The Fe-rich carbonatite is dominated by Fe- and Mn-rich carbonates and Fe- and Mn-oxides with apatite and minor amounts of K-feldspar (Croll et al., 2014). It is important to note that the term “Fe-rich carbonatite” is used in the field and refers to any carbonatite with a dark weathering texture and rich in Fe (Broom-Fendley, 2015).

Drill core data revealed that veining is extensive throughout the carbonatite. In general, two vein types can be distinguished: Fe-rich carbonatite veins and black Fe-Mn-rich ‘wad’ veins. The latter are porous, highly weathered, and poorly consolidated intrusions that have subjected to extreme alteration (Croll et al., 2014).

3.4.2 Fenite

Fenite forms around the carbonatite intrusion and is composed mainly of K-feldspar. Highly abraded fenite blocks and fragments also occur extensively within the intrusion, indicating some degree of movement during the emplacement history. In the upper part of Songwe Hill, fenite appears to form a roof zone on the carbonatite (Swinden and Hall, 2012).

3.4.3 Breccia

The Songwe Hill vent complex includes a considerable variety of breccias, which can be divided into two types: feldspathic-rich breccias and carbonatite-rich breccias.

The clasts range from clearly abraded pebble-sized fragments (pebble dykes) to meter-sized angular blocks. Where little rounding has occurred, Broom-Fendley et al. (in prep) interprets that the carbonatite has undergone little movement or has been gently emplaced. However, this is contrasted by the contemporaneous occurrence of extremely rounded thin dykes.

3.4.4 Silicate-rich dykes

Late-stage silicate-rich dykes have been identified in drill cores but rarely outcrop at surface. The dykes are mainly phonolitic in composition, aphanitic or porphyritic in texture and exhibit a wide degree of alteration ranging from minimal modification to extensive alteration and fenitisation. Syn-intrusion and post-intrusion faulting is apparent across Songwe Hill although displacements appear to be relatively small (Broom-Fendley, 2015).

3.5 Songwe Hill exploration

The Songwe Hill Rare Earth Project is located in southern Malawi and is owned by Mkango Resources Ltd. Since January 2010, Mkango has been exploring and evaluating the Songwe Hill deposits. It is following the previous exploration of the CAP including the Songwe Hill deposit conducted by the Japan International Cooperation Agency (JICA) and operated by the Metal Mining Agency of Japan (MMAJ) from 1886 to 1988. Mkango's exploration included litho-geochemical, soil and channel sampling, geological mapping, ground magnetic, density and radiometric surveys (Swinden and Hall, 2012).

As part of their exploration programme, Mkango conducted a two-stage diamond drilling programme: Phase 1 in 2011 and Phase 2 in 2012. In total 38 inclined and vertical drill holes (totalling 6852.28 m) were drilled to evaluate REE mineralisation in the carbonatite and related rocks of Songwe Hill deposit and to develop a resource estimation model. Based on data from the drill cores, Mkango announced in 2012 an NI 43-101 Mineral Resource Estimate prepared by MSA Group (Pty) Ltd. The total indicated mineral resource estimate for Songwe Hill was 13.2 Mt, grading 1.62 wt% TREO at a cut-off grade of 1 wt%, in addition to the inferred mineral resource estimation of 18.6 Mt grading 1.38 wt% at a cut-off grade of 1 wt% TREO. Thus, according to the tonnage and grade of the combined indicated and inferred mineral resource for Songwe Hill deposit, the deposit contains approximately 469,247 tonnes of TREO (Swinden and Hall, 2012).

3.6 Whole-rock chemistry

Carbonatites are complex ore deposits and the type of carbonatite can range between calciocarbonatite to ferrocarbonatite. These different carbonatite types principally include calcite, dolomite, and ankerite as the major rock-forming minerals as well as a wide range of accessory minerals including forsterite, aegirine, phlogopite, biotite, magnetite, apatite, and pyrochlore. Thus, its chemical composition varies based on the amount and type of the major and accessory minerals, as well as the degree of alteration. Therefore, the whole rock elemental analysis not only provides information about the overall elemental distribution and the concentration of the element(s) of interest, but can also be used together with the mineralogical data derived from SEM-EDS to validate the QEMSCAN® measurements.

The whole-rock analysis for the major, minor, some trace and all rare earth elements of the individual crushed drill core sample is presented in Table 3.1. In general, this table indicates the analysed samples are varied in terms of the concentration of elements between the samples.

The analysis results for the major elements show that the samples are dominated by CaO ranging between about 20 wt% and 37 wt% (Table 3.1), indicating that a large amount of carbonate minerals are present in the drill core samples. The highest concentration of CaO is in sample PX05+15, while PX09 has the lowest concentration. There is also an enrichment in Fe_2O_3 concentration with a range between about 9 wt% and 22 wt% throughout the analysed samples. The content of SiO_2, Al_2O_3, and K_2O ranges between approximately 3 wt% and 13 wt%, 1 wt% and 5 wt%, and 1 wt% and 3 wt%, indicating the presence of silicate minerals (e.g. K-feldspar) in the samples. Other minor elemental oxides including MgO, SrO, and BaO are present in concentrations below 2 wt% (Table 3.1). The results also demonstrate that the level of ThO_2 ranges between 284 ppm and 382 ppm, while a very trace of UO_2 of a range between 9 ppm and 15 ppm occurs throughout the samples.

Table 3.1: Whole-rock chemistry of the Songwe Hill carbonatite drill core samples used in this study as analysed by ICP-MS and ICP-OES. Data from Mkango Resources Ltd.

Oxides (wt%)	Crushed drill core samples							
	PX05+15	PX09	PX12	PX13	PX21	PX22b	PX33	PX35
Na_2O	0.07	0.05	0.07	0.08	0.06	0.05	0.11	0.07
MgO	0.89	1.6	1.43	1.57	1.39	1.61	1.27	1.45
Al_2O_3	1.74	5.01	2.12	1.98	2.76	1.24	3.22	3.26
SiO_2	5.3	12.75	6.32	5.23	7.88	3.43	9.04	9.21
P_2O_5	1.91	1.24	1.61	2.1	1.52	1.35	1.29	2.01
SO_3	0.41	0.49	0.26	0.86	0.42	0.37	0.69	0.25
K_2O	0.92	2.64	1.3	1.01	1.59	0.61	1.92	2.02
CaO	37.4	19.87	32.38	27.28	27.5	29.71	23.11	27.51
MnO	1.54	3.11	2.02	2.54	2.38	2.68	2.35	2.08
Fe_2O_3	9.69	21.27	11.21	17.32	15.89	17.43	22.44	13.98
SrO	1.08	0.61	0.92	1.51	1.28	1.25	1.04	0.81
BaO	0.77	0.93	0.49	1.64	0.8	0.69	1.31	0.47
(ppm)								
ZrO_2	290	349	358	436	241	211	287	416
Nb_2O_3	2125	1543	2588	2073	1846	1737	3165	2157
ThO_2	292	382	327	374	360	284	340	281
UO_2	15	12	13	11	11	9	11	12
La_2O_3	2971	3800	3348	5327	4153	3609	3765	3302
Ce_2O_3	4952	6784	5683	9748	7581	6469	7341	5897
Pr_2O_3	540	700	607	897	756	686	724	592
Nd_2O_3	1760	2352	2034	2875	2592	2384	2315	2137
Sm_2O_3	289	271	338	420	370	334	370	260
Eu_2O_3	78	88	95	111	121	94	101	97
Gd_2O_3	212	185	221	265	241	212	214	227
Tb_2O_3	25	17	23	28	26	25	27	29
Dy_2O_3	104	94	115	129	118	110	112	127
Ho_2O_3	17	12	17	22	16	20	18	21
Er_2O_3	47	40	41	54	47	51	43	51
Tm_2O_3	5	4	5	6	6	4	5	6
Yb_2O_3	32	28	29	39	36	35	33	41
Lu_2O_3	6	5	4	5	5	5	4	6
Y_2O_3	636	591	647	735	549	571	604	657
TREO	11674	14971	13207	20661	16617	14609	15676	13450

Note that REE were converted to their elemental oxides for ease of comparison.

The results show that the concentration of the P_2O_5 within carbonatite samples range between 1.3 wt% and 2.1 wt%. However, the concentration of P_2O_5 in igneous phosphate rocks is usually low between about 7 wt% and 15 wt% compared to the sedimentary phosphate rocks (Abouzeid, 2008), still apatite (P_2O_5) in the Songwe Hill carbonatites interesting to be considered as an economic mineral particularly in the rougher concentrate of the processed carbonatite samples (see Chapter 6).

Other potentially economic metals that occur in the samples are niobium with a concentration that ranges between 1543 ppm and 3165 ppm and zirconium with a range between 211 ppm and 436 ppm.

The results in Table 3.1 show that the samples are rich in a range of LREE and HREE with a total rare earth oxides (TREO) ranging between 1.2 wt% and 2.1 wt%. Overall, the samples are mainly dominated by Ce_2O_3 accounting for 45% of the TREO, followed by, in order of abundance, La_2O_3, 25%, Nd_2O_3 15%, Pr_2O_3 5%, Y_2O_3 4%, Sm_2O_3 2%, Gd_2O_3 2%, and other REO of about 2% (Figure 3.3).

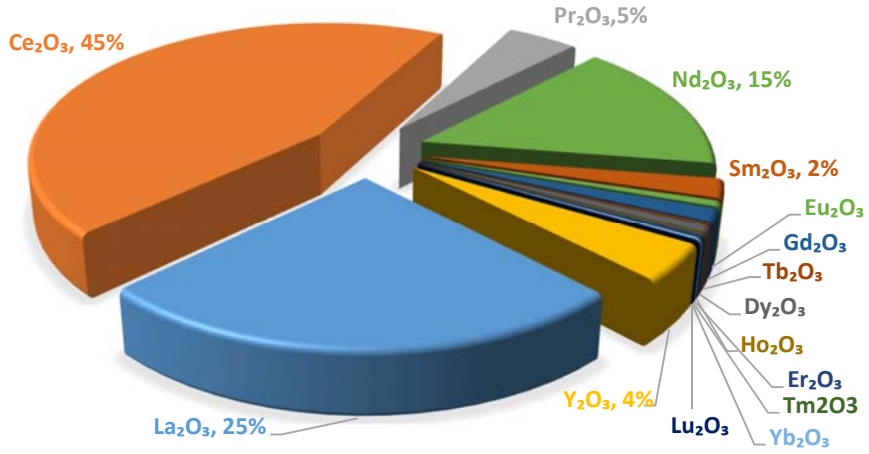

Figure 3.3: Distribution of the rare earth elements within the Songwe Hill carbonatite deposit using normalised percentages. Note the data were normalised based on the average total concentration of the REO in eight crushed drill core samples in Table 3.1.

The correlation between the concentrations of P_2O_5 and Y_2O_3 is presented in Figure 3.4. It can be seen from Figure 3.4 that there is a positive linear correlation between these two oxides. This is an interesting finding that the phosphate bearing mineral in this deposit also hosts Y_2O_3 and so the HREE. It was the first clue that apatite (the main P_2O_5 bearing mineral) hosts the HREE in the Songwe Hill carbonatite (Broom-Fendley, 2015).

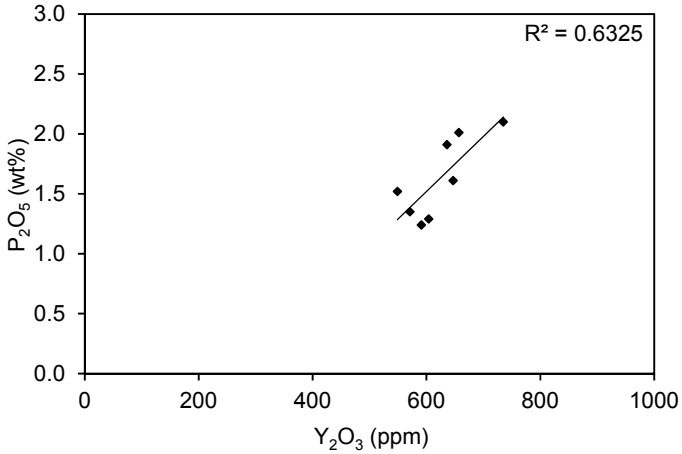

Figure 3.4: Scatter plot of the concentration of P_2O_5 versus Y_2O_3 in the Songwe Hill carbonatite samples. The relationship between these two oxides also indicates that the HREE are mainly concentrated in apatite.

Apatite is the predominant valuable component and the only REE-bearing mineral of which occurs in all the drill core samples, this will be further discussed in the SEM-EDS and EPMA sections of this chapter.

3.7 XRD

The XRD results indicate that all the drill core samples have a similar mineralogical composition, but vary slightly in their relative proportions. The main gangue minerals include calcite and ankerite; followed by K-feldspar; iron oxide/carbonate minerals; strontianite; and baryte (Figure 3.5). Iron oxide/carbonate minerals are grouped as they have weak and overlapped peaks and could include goethite, hematite, siderite, and magnetite. The principal valuable mineral, apatite, can be identified in the XRD profiles. Synchysite appears only once overlapped with the same peak of apatite and siderite. This may be due to the limitation of the XRD technique to detect minerals with an abundance of below 5 wt%.

Sample PX22b seems to be varied compare to the other samples, as it shows that ankerite is more abundant than calcite. These results are in agreement with the SEM-EDS observations (see Section 3.8).

In summary, it seems difficult to estimate the predominance of minor and trace minerals by XRD technique because most of them overlap with other minerals and do not have a good individual peak. Other potential valuable minerals such as parisite, florencite, bastnäsite, monazite and pyrochlore are not identified because of their abundances are below the detection limit of the XRD instrument of 5 wt%.

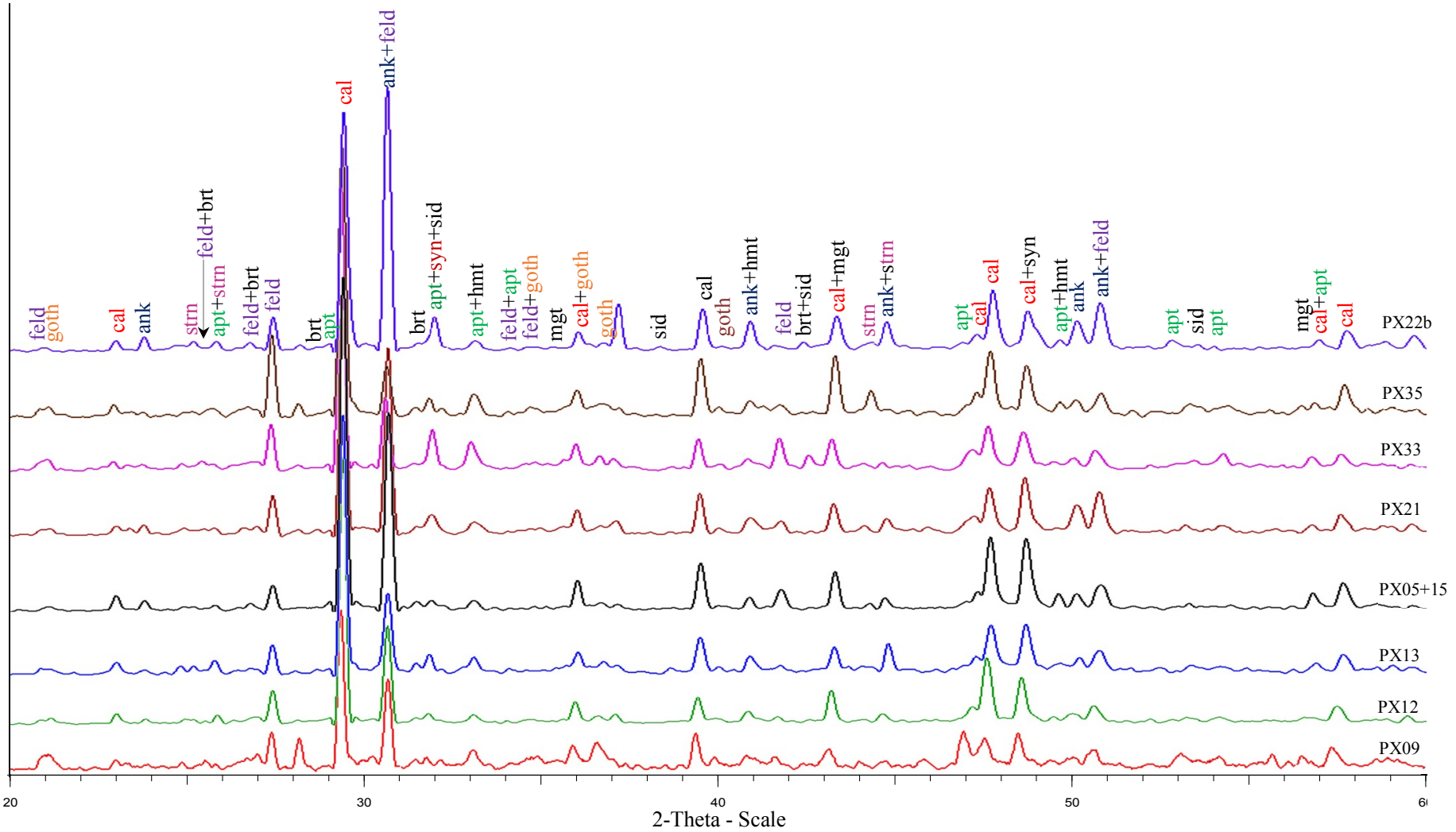

Figure 3.5: Mineralogical composition of the crushed drill core carbonatite samples of Songwe Hill used in this research as determined by XRD

Abbreviations: ank, ankerite; apt, apatite; brt, baryte; cal, calcite, feld, K-feldspar; goth, goethite; hmt, hematite; mgt, magnetite; sid, siderite; strn, strontianite; syn, synchysite.

3.8 SEM-EDS

The identification of rock-forming minerals and mineralogical characteristics (liberation, mineral association, and crystals size and shape) for all samples was carried out using a scanning electron microscope equipped with an energy dispersive X-ray spectrometry. The potential valuable and gangue minerals in the samples under investigation with their chemical formula are listed in Table 3.2.

Table 3.2: The potential valuable and gangue minerals in the Songwe Hill carbonatite deposit with their standard chemical formula.

Mineral	Chemical formula*	Mineral	Chemical formula
Ankerite	$Ca_2MgFe(CO_3)_4$	K-feldspar	$KAlSi_3O_8$
Apatite	$Ca_5(PO_4)_3(F,Cl,OH)$	Parisite-(Ce)	$CaCe_2(CO_3)_3F_2$
Baryte	$BaSO_4$	Plagioclase	$(Na,Ca)(Si,Al)_4O_8$
Bastnäsite-(Ce)	$Ce(CO_3)F$	Pyrite	FeS_2
Calcite	$CaCO_3$	Pyrochlore	$(Na,Ca)_2Nb_2O_6(OH,F)$
Dolomite	$CaMg(CO_3)_2$	Pyrophanite	$MnTiO_3$
Florencite-(Ce)	$CeAl_3(PO_4)_2(OH)_6$	Quartz	SiO_2
Fluorite	CaF_2	Rutile	TiO_2
Goethite	$FeO(OH)$	Siderite	$FeCO_3$
Hematite	Fe_2O_3	Strontianite	$SrCO_3$
Ilmenite	$FeTiO_3$	Synchysite-(Ce)	$CaCe(CO_3)_2F$

* Chemical formula from www.webmineral.com

An overall description of the crushed drill core samples in terms of their mineralogy and texture is given in the next sections and briefly summarised in Table 3.3, while a detailed description of each sample with the BSE images is given in Appendix D.

The observations obtained from the BSE images and the EDS spectra show that all the carbonatite samples contain apatite, synchysite-(Ce), and florencite-(Ce) as the predominant valuable minerals for their REE and P_2O_5 content. Ankerite, calcite, K-feldspar, iron oxides/carbonates, Fe-Mn oxides, strontianite, and baryte are the most common gangue minerals.

Table 3.3: Semiquantitave description of the valuable and gangue minerals in Songwe Hill carbonatite deposits.

Sample no.	Valuable minerals			Gangue minerals							Notes
	apatite	synchysite	Florencite	calcite	ankerite	K-feld	FeO	Fe-Mn	stront	baryte	
PX05+15	Medium	High	Low	Major_1	Major_2	Minor	Trace	Trace	Trace	Trace	Synchysite mainly granular and less acicular.
PX09	Low	High	Medium	Major_1	Major_1	Minor	Minor	Minor	Trace	Trace	Synchysite mainly appears as fibro-radial crystals and lesser as granular crystals.
PX12	High	High	Medium	Major_1	Major_1	Minor	Trace	Minor	Trace	Trace	Apatite as coarse anhedral patches. Synchysite mainly granular and lesser acicular.
PX13	High	High	Low	Major_2	Major_1	Minor	Minor	Minor	Trace	Minor	Apatite as liberated particles. Synchysite mainly appears as acicular in ankerite.
PX21	Medium	High	Medium	Major_1	Major_2	Minor	Minor	Trace	Trace	Trace	Synchysite mainly as acicular crystals. Florencite occurs in calcite groundmass.
PX22b	Medium	High	Medium	Common	Major	Minor	Trace	Minor	Trace	Trace	Synchysite granular and acicular. Apatite mainly associated and lesser liberated. Florencite stringer-like crystals.
PX33	Medium	High	medium	Minor	Major	Minor	Trace	Common	Trace	Trace	Synchysite as acicular crystals within ankerite groundmass.
PX35	High	Medium	Low	Major_2	Major_1	Minor	Minor	Trace	Trace	Trace	Apatite appears as anhedral crystals within ankerite and sometimes as liberated grains.

* the relative terms high, medium and low represent the occurrence of REE minerals compared to each other, not to all of minerals that form the whole sample. Major_1 which means calcite/ankerite is more common, while major_2 it means that mineral still major, but it less common.

Interestingly, the mineralogical composition of all samples looks similar with variation in the mineral proportions between some samples. For example, PX13 contains the highest content of REE- and REE-bearing minerals including apatite, synchysite-(Ce), and florencite-(Ce) compared to the other drill core samples, while PX09 contains the highest proportion of florencite-(Ce) and the lowest proportion of apatite with apparently similar level of synchysite-(Ce). Furthermore, PX22b and PX33 differ from the other samples as ankerite is the major gangue mineral while calcite is relatively less dominant mineral. These samples show that the valuable minerals are commonly associated with ankerite. Conversely, PX05+15 mainly predominant by calcite followed by ankerite and thus the valuable minerals are mainly associated with calcite. Samples PX35, PX21, and PX12 are similar in terms of their components and contents of valuable and gangue minerals.

The following sections illustrate a full description and discussion for the carbonatite forming minerals in the Songwe Hill deposit:

3.8.1 Valuable minerals

The minerals of interest are apatite, synchysite-(Ce), and florencite-(Ce), which occur in all carbonatite samples and are texturally very complex. These minerals are typically fine-grained, and commonly range from 50 μm to even less than 5 μm in size. They are associated with all major and minor gangue minerals, but varying in their proportions and crystal shapes, particularly synchysite-(Ce).

1. Apatite

Apatite is the predominant valuable mineral and the main host for the HREE, which occurs in all the crushed drill core samples. It commonly presents as subhedral to anhedral grains in a vein-like texture with a grain size up to 100 μm (Figure 3.6 A and B). It also occurs as well liberated coarse-grained up to 400 μm, particularly sample PX13 (Figure 3.6 C and D).

Apatite grains commonly present around the gangue mineral boundaries and are mostly associated with ankerite followed by the predominant gangue mineral calcite (except PX05+15). Furthermore, apatite is associated with K-feldspar and Fe/Mn oxides, but to a lesser extent.

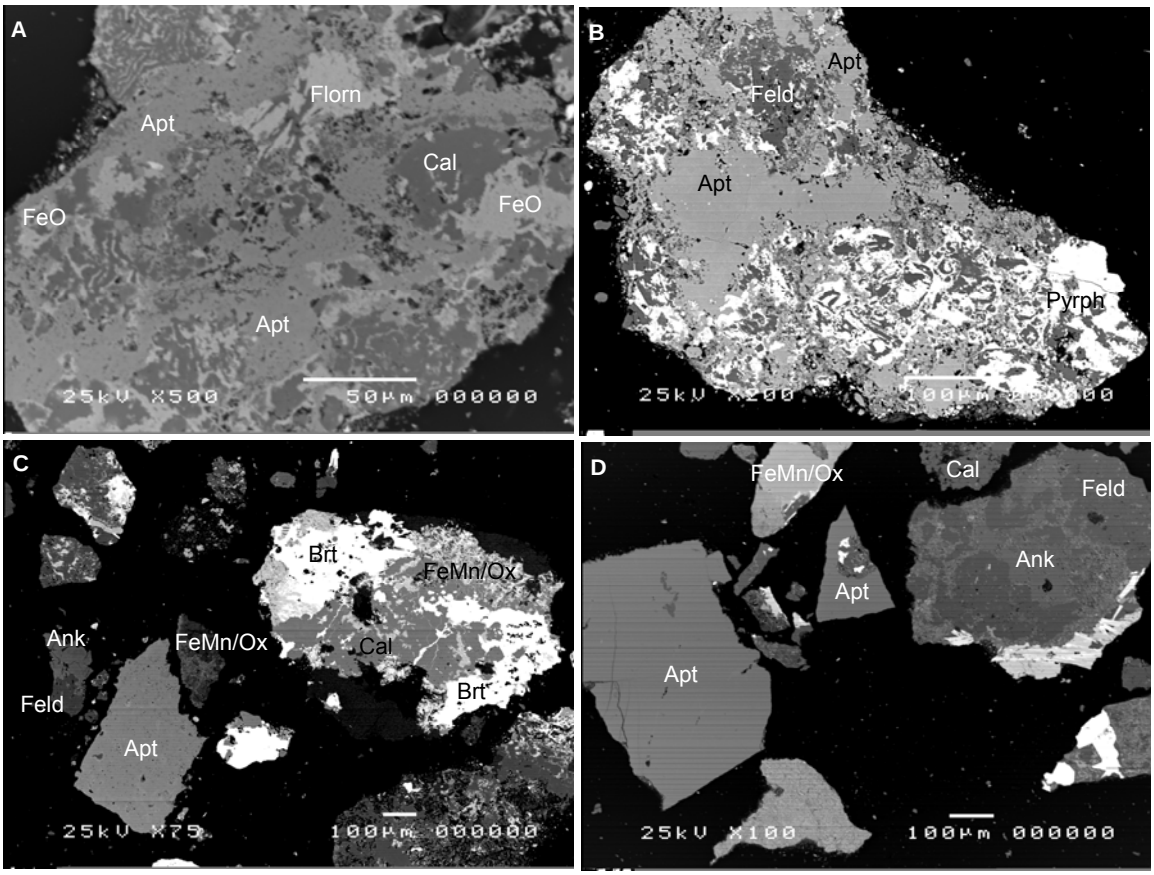

Figure 3.6: Apatite crystal shape: (A) vein-like apatite associated with calcite and iron oxides/carbonates, (B) apatite associated with pyrophanite and K-feldspar, (C) large and (D) very large liberated particles of apatite.

It is interesting to note that the large crystals of apatite are usually liberated, while the fine vein-like or patches crystals are poorly liberated and associated with other gangue minerals.

2. Synchysite-(Ce)

Synchysite-(Ce), the predominant REE mineral, occurs mainly as fine to very fine anhedral to subhedral grains. Euhedral grains also locally occur. It forms predominantly as assemblages or individuals acicular (fibro-radial) crystals (Figure 3.7 A and B). It also, to a lesser extent, occurs as granular (lath-shaped) crystals (Figure 3.7 C and D).

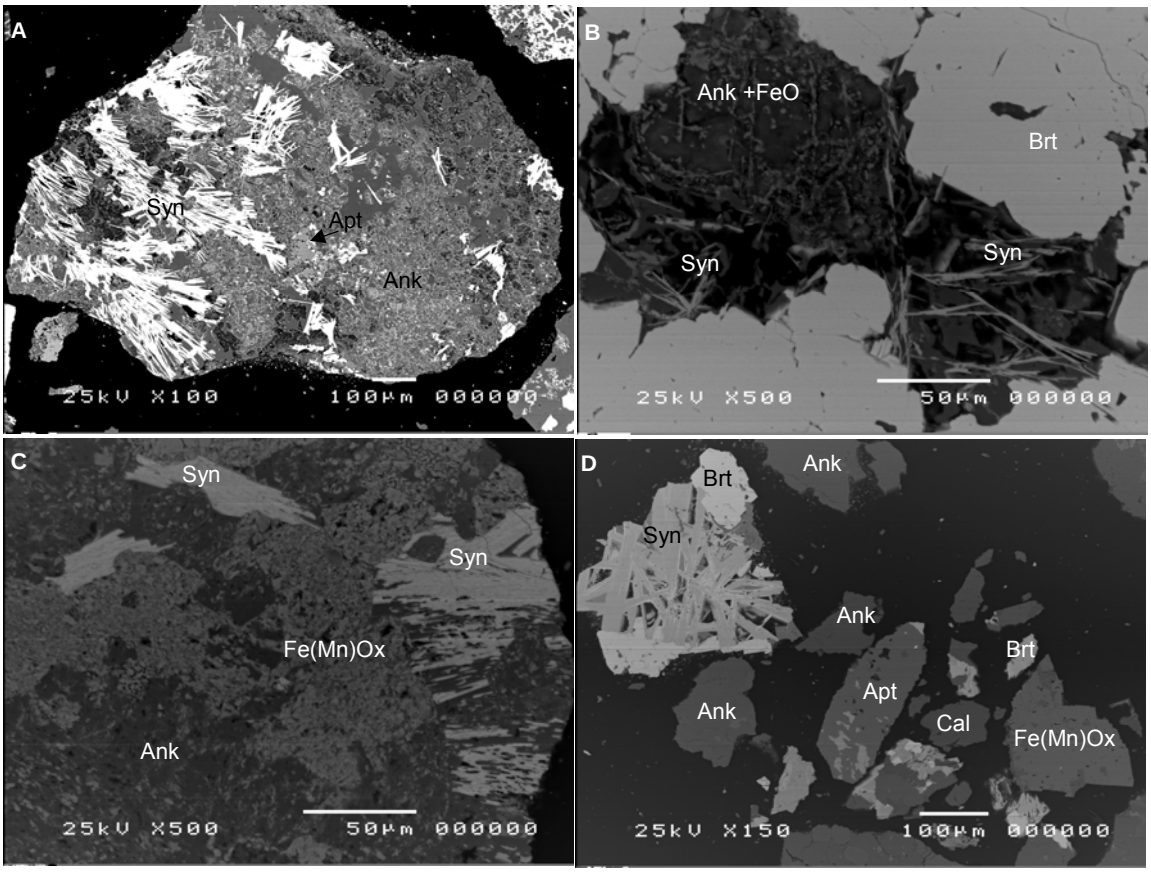

Figure 3.7: Synchysite crystal shape: (A) Assemblages of acicular (fibro-radial) crystals of synchysite associated with ankerite, (B) individual acicular crystals of synchysite in ankerite and iron oxides groundmass, (C) granular crystals of synchysite associated with Fe(Mn) oxides/carbonates and ankerite, and (D) accumulation of lath-shaped crystals of synchysite associated with baryte.

In all the samples, synchysite mainly presents as an accumulation of or as individual fibro-radial crystals except in the samples PX12 and PX05+15 in which they mostly occur as granular crystals with only a minor abundance of acicular grains. However, synchysite sometimes occurs as coarse grains to about 150 µm (particularly the granular crystals), it commonly occurs as fine to very fine grains with a size less than 25 µm. When it occurs as needle-like crystals, the grains are typically even smaller, up to about 5 µm.

Synchysite is primarily associated with the predominant gangue minerals i.e. calcite and ankerite. It is also associated with strontianite, baryte, Fe/Mn oxides, locally with K-feldspar and rarely with other valuable minerals.

Furthermore, the observations also show that synchysite crystals are mostly locked and poorly liberated in the crushed samples P_{100} 1.7 mm, particularly the needle-like

crystals, which are considered difficult to liberate. This means that to improve synchysite liberation, the target grinding size should be approximately 30 µm, however when considering grinding to this size both the grinding cost and the generation of slime should be taken into consideration. It is likely that this operation would generate large amount of slime (very fine particles of gangue minerals).

It is important to note that synchysite was the only REE fluorcarbonate mineral observed. No observations of any other REE fluorcarbonates, particularly parisite, were seen through SEM-EDS, although it is identified by EPMA (see Section 3.9).

3. Florencite-(Ce)

Florencite-(Ce) is the least common REE mineral. It occurs as anhedral vein-like grains or as individual fine patches (Figure 3.8). Florencite grains are relatively smaller than the other valuable minerals observed, with a grain size up to approximately 30 µm. This indicates a very fine grinding is required to liberate this mineral. Florencite is associated with the major gangue minerals calcite, ankerite, iron oxides/carbonates, and K-feldspar and, locally, with strontianite and baryte.

An interesting microstructure feature was observed in this deposit as indicated by the EDS spectra. In this microstructure, florencite crystals can be seen as intergrown with apatite crystals to form vein-like shape of florencite/apatite intergrowths (Figure 3.8). This microstructure will be further discussed in Chapter 4.

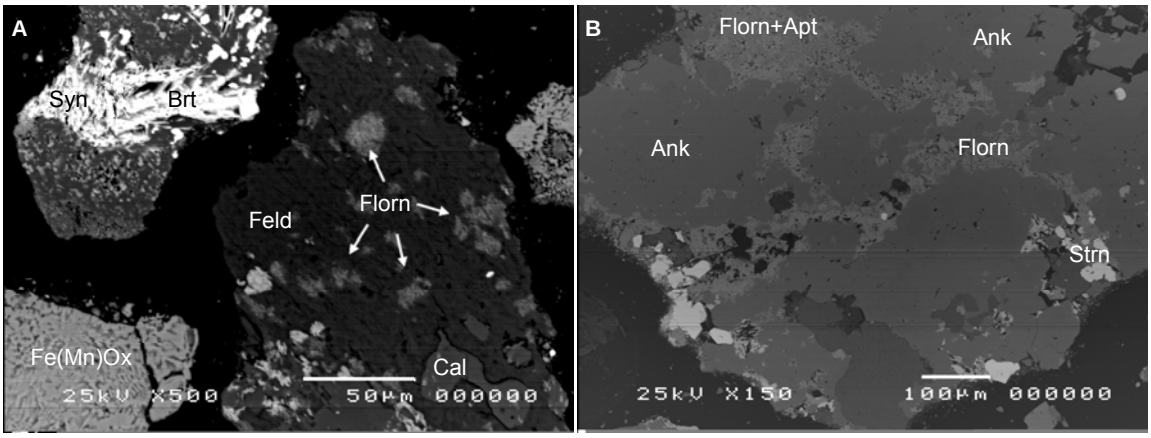

Figure 3.8: Florencite crystal shape: (A) small batches of florencite in a K-feldspar groundmass, and (B) vein-like florencite and intergrown florencite and apatite associated with ankerite.

Several sources within the literature on florencite have noted that it occurs in a variety of rock types and deposits including granitic pegmatites, carbonatites, mica

schists, hydrothermal deposits, placers, weathered zones especially in laterites (Lefebvre and Gasparrini 1980; Sawka et al. 1986; Slukin et al. 1989). In weathered rocks, florencite often appears as donut-shaped aggregates in cavities after dissolving apatite (Banfield and Eggleton 1989; Braun et al. 1993). This may explain why the amount of florencite in PX09 is higher than other samples.

3.8.2 Gangue minerals

The main gangue minerals are ankerite, calcite, minor iron oxides/carbonates and K-feldspar, trace of strontianite, baryte with very trace amounts of pyrite, Mn oxides, quartz, and plagioclase.

Ankerite and calcite are the predominant gangue minerals in all samples. The average grain size of ankerite is about 52 μm and calcite is about 61 μm.

Iron oxide/carbonate minerals occur as minor components throughout the samples. They usually occur as veins and associated with the predominant carbonate gangue minerals. They also occasionally present as Fe-Mn oxides/ carbonates.

K-feldspar is a minor gangue mineral but is the most common silicate mineral observed in all samples. In sample PX09, K-feldspar is variably altered and other weathering products such as muscovite were identified. This replacement could be due to the exposure the sample to a chemical weathering. These observations are in agreement with the description of the drill core samples (see Chapter 2, Table 2.1).

Strontianite counts as a trace gangue mineral in the Songwe Hill samples, it occurs as anhedral grains and usually infilling between synchysite and baryte. Baryte is another trace gangue mineral, which is also associated with synchysite and strontianite. As synchysite sometimes is overgrown by baryte, this may have an effect on processing coated synchysite crystals. Baryte is considered as less soluble hydrochloric acid than synchysite, thus this point should be taken in account when thinking of applying a leaching step to recover synchysite as incasing baryte may affect the solubility of synchysite within a hydrochloric acid leach.

Pyrochlore, can be considered another potential valuable mineral for its niobium content. It appears in the polished blocks as coarse-grained euhedral crystals associated with calcite and ankerite.

3.9 Mineral chemistry using EPMA

REE- and REE-bearing mineral species including apatite, synchysite-(Ce), parisite-(Ce), and florencite-(Ce) were analysed by EPMA. Also, the mineral chemistry of apatite was analysed using Laser Ablation Inductively Coupled Plasma Mass Spectrometry (LA-ICP-MS) by Broom-Fendley (2015).

The atoms per formula unit (apfu) for REE fluorcarbonates was completed by determining the amount of CO_2 and F using stoichiometry. The REE:Ca ratio was used to recognise between these minerals.

3.9.1 Apatite

The elemental composition of apatite as analysed using EPMA with the minimum, maximum, average, and standard deviation are presented in Table 3.4, while all the data are listed in Appendix E-1. It is apparent from Table 3.4 that apatite is enriched in CaO with an average of 51.1 wt% and P_2O_5 with an average of 41.4 wt%. In addition to enrich apatite in P_2O_5 as an economic element, it also shows enrichment in REE. The average TREO is approximately 1.63 wt% and it is predominant by Y_2O_3 with an average of about 0.9 wt%, followed by Nd_2O_3, Ce_2O_3, Dy_2O_3, and Gd_2O_3 with an average of 0.2 wt%, 0.2 wt%, 0.1 wt%, and 0.1 wt%, respectively.

In addition to measuring apatite using EPMA (Table 3.4), new measurements were carried out to determine the REE distribution using LA-ICP-MS by Broom-Fendley (2015). The LA-ICP-MS has lower detection limits than EPMA and so more accurate measurements. The results of selected measured points with the minimum, maximum, average, and standard deviation are listed in Table 3.5, while the complete data set is given in Appendix E-2. It can be seen from Table 3.5 that the content of TREO is between 0.16 wt% and 4.6 wt% with an average of 1.7 wt%. The average of the HREE is approximately 1.2 wt% and it is predominant by Y_2O_3 and Dy_2O_3, while the average of the LREE is approximately 0.6 wt% and it is predominant by Ce_2O_3 and Nd_2O_3.

Table 3.4: Elemental composition data (wt%) of apatite in the Songwe Hill carbonatite samples as analysed by EPMA.

Spot point	1	2	3	4	5	6	7	8	9	10	Min	Max	Avrg	σ
											(35 points)			
P_2O_5	40.89	41.75	41.67	41.77	41.81	41.71	42.50	42.12	41.13	41.93	40.49	42.50	41.44	0.46
CaO	51.30	51.30	51.23	50.28	51.22	50.90	53.73	53.09	51.00	52.91	49.03	53.73	51.16	1.11
Y_2O_3	1.21	b.d	b.d	1.22	1.05	1.03	0.31	0.44	0.82	1.22	b.d	1.99	0.86	0.45
La_2O_3	b.d	0.83	b.d	b.d	b.d	b.d	b.d	b.d	b.d	b.d	b.d	0.83	0.02	0.14
Ce_2O_3	b.d	0.89	0.93	0.65	0.47	0.45	0.338	b.d	b.d	b.d	b.d	0.93	0.22	0.30
Pr_2O_3	b.d	b.d	b.d	b.d	b.d	b.d	b.d	b.d	b.d	b.d	b.d	b.d	b.d	0.00
Nd_2O_3	0.38	0.51	0.43	0.63	0.36	0.31	b.d	b.d	0.31	0.41	b.d	0.64	0.23	0.24
Sm_2O_3	b.d	b.d	b.d	b.d	0.32	b.d	b.d	b.d	b.d	b.d	b.d	0.38	0.03	0.09
Eu_2O_3	b.d	b.d	b.d	b.d	b.d	b.d	b.d	b.d	b.d	b.d	b.d	b.d	b.d	0.00
Gd_2O_3	0.57	b.d	b.d	b.d	b.d	b.d	b.d	b.d	0.26	0.42	b.d	0.57	0.13	0.17
Dy_2O_3	0.55	b.d	b.d	b.d	0.30	b.d	b.d	b.d	b.d	0.29	b.d	0.55	0.14	0.18
Tb_2O_3	b.d	b.d	b.d	b.d	b.d	b.d	b.d	b.d	b.d	b.d	b.d	b.d	b.d	0.00
ThO_2	0.12	b.d	b.d	0.13	0.14	0.14	b.d	b.d	0.20	0.22	b.d	0.25	0.09	0.08
UO_2	b.d	b.d	b.d	b.d	b.d	b.d	b.d	b.d	b.d	b.d	b.d	b.d	b.d	0.00
F	5.32	4.82	4.48	5.41	5.44	5.30	5.56	5.17	5.44	5.54	4.48	5.75	5.19	0.30
-O=F*	2.24	2.03	1.89	2.28	2.29	2.23	2.34	2.18	2.29	2.09	1.89	2.42	2.18	0.13
Σ	98.08	98.07	96.85	97.81	98.81	97.61	100.1	98.65	96.87	96.35	95.64	98.24	96.90	0.98
apfu[a] on the basis of number of anions														
P	2.941	2.996	3.017	2.987	2.969	2.984	2.958	2.974	2.964	2.959	3.043	2.891	2.978	0.02
Ca	4.670	4.659	4.694	4.550	4.604	4.609	4.732	4.745	4.652	4.725	4.664	4.625	4.653	0.06
Y	0.055	b.d	b.d	0.055	0.047	0.046	0.014	0.020	0.037	0.008	b.d	0.085	0.039	0.02
La	b.d	0.026	b.d	b.d	b.d	b.d	b.d	b.d	b.d	b.d	b.d	0.024	0.001	0.00
Ce	b.d	0.028	0.029	0.020	0.015	0.014	0.010	b.d	b.d	0.014	b.d	0.027	0.007	0.01
Pr	b.d	b.d	b.d	b.d	b.d	b.d	b.d	b.d	b.d	b.d	b.d	b.d	b.d	0.00
Nd	0.011	0.015	0.013	0.019	0.011	0.009	b.d	b.d	0.010	b.d	b.d	0.018	0.007	0.01
Sm	b.d	b.d	b.d	b.d	0.009	b.d	b.d	b.d	b.d	b.d	b.d	0.010	0.001	0.00
Eu	b.d	b.d	b.d	b.d	b.d	b.d	b.d	b.d	b.d	b.d	b.d	b.d	b.d	0.00
Gd	0.016	b.d	b.d	b.d	b.d	b.d	b.d	b.d	0.007	b.d	b.d	0.015	0.004	0.00
Dy	0.015	b.d	b.d	b.d	0.008	b.d	b.d	b.d	b.d	b.d	b.d	0.014	0.004	0.00
Th	0.002	b.d	b.d	0.003	0.003	0.003	b.d	b.d	0.004	b.d	b.d	0.005	0.002	0.00
F	0.827	0.749	0.701	0.837	0.835	0.820	0.837	0.790	0.848	0.846	0.728	0.845	0.806	0.04
Σ	8.537	8.472	8.454	8.470	8.499	8.486	8.551	8.529	8.523	8.551	8.435	8.561	8.500	0.03

[a] Calculated by stoichiometry, and b.d is below detection limit.

Table 3.5: Distribution of REE data (wt%) of apatite in the Songwe Hill carbonatite samples as analysed by LA-ICP-MS. Data from Broom-Fendley (2015).

Spot point	1	2	3	4	5	6	7	8	9	10	Min	Max	Avrg	σ
											72 points			
La_2O_3	0.028	0.052	0.029	0.023	0.031	0.026	0.055	0.082	0.034	0.071	0.009	0.170	0.072	0.04
Ce_2O_3	0.112	0.171	0.105	0.088	0.126	0.098	0.181	0.146	0.117	0.245	0.034	0.427	0.214	0.11
Pr_2O_3	0.021	0.028	0.019	0.016	0.023	0.018	0.030	0.015	0.019	0.045	0.006	0.079	0.036	0.02
Nd_2O_3	0.123	0.151	0.103	0.092	0.138	0.106	0.196	0.060	0.106	0.246	0.034	0.468	0.201	0.10
Sm_2O_3	0.055	0.061	0.047	0.039	0.060	0.047	0.102	0.021	0.068	0.104	0.013	0.169	0.075	0.03
Eu_2O_3	0.026	0.027	0.021	0.018	0.028	0.023	0.049	0.012	0.038	0.045	0.004	0.070	0.032	0.01
Gd_2O_3	0.106	0.112	0.085	0.074	0.115	0.099	0.160	0.044	0.146	0.163	0.010	0.223	0.110	0.04
Tb_2O_3	0.022	0.023	0.018	0.017	0.024	0.023	0.032	0.009	0.034	0.030	0.001	0.040	0.021	0.01
Dy_2O_3	0.164	0.165	0.133	0.126	0.170	0.166	0.221	0.059	0.260	0.191	0.006	0.288	0.139	0.06
Ho_2O_3	0.031	0.032	0.025	0.025	0.033	0.034	0.044	0.014	0.056	0.034	0.001	0.069	0.027	0.01
Er_2O_3	0.074	0.075	0.059	0.060	0.076	0.081	0.101	0.038	0.135	0.074	0.003	0.192	0.065	0.03
Tm_2O_3	0.007	0.007	0.006	0.006	0.007	0.009	0.011	0.004	0.015	0.008	b.d	0.022	0.007	0.00
Yb_2O_3	0.031	0.031	0.027	0.030	0.032	0.038	0.049	0.021	0.063	0.030	0.001	0.097	0.034	0.01
Lu_2O_3	0.003	0.003	0.003	0.003	0.003	0.004	0.005	0.003	0.006	0.003	b.d	0.009	0.003	0.00
Y_2O_3	0.963	0.973	0.774	0.762	0.988	1.046	1.245	0.460	1.639	0.940	0.033	2.267	0.782	0.41
Σ	1.766	1.912	1.453	1.380	1.852	1.817	2.481	0.986	2.734	2.230	0.156	4.591	1.817	0.19

b.d is below detection limit.

3.9.2 Synchysite-(Ce)

The minimum, maximum, average, and standard deviation of the elemental compositions of synchysite-(Ce) analysed by EPMA at CSM and NHM are listed in Table 3.6, while the details are given in Appendices E-3 and E-4. The average TREO within synchysite is approximately 50 wt% and it is mainly LREE-enriched. The predominant REE is Ce_2O_3 followed by La_2O_3, Nd_2O_3, and Pr_2O_3. It also contains a minor to trace amounts of MREE and HREE including Sm_2O_3, Y_2O_3, and Gd_2O_3. It is interesting to note that the concentrations of Dy_2O_3 and Eu_2O_3 within synchysite analysed by EPMA at CSM were below the detection limit, while their concentrations were about 0.16 wt% and 0.14 wt%, respectively in synchysite-(Ce) analysed by EPMA at NHM. This is due to the lower detection limit of the Cameca instrument at NHM.

However 30 spot points for synchysite-(Ce) analysed at NHM were removed from the calculations due to the high content of FeO, MnO, SrO, and BaO, particularly

FeO, these elemental oxides form about 0.76 wt% of the elemental composition of synchysite-(Ce). Presence these elements is attributed to the small grain size of synchysite and its association with other Fe, Mn, Sr, and Ba bearing minerals/phases.

Table 3.6: Comparison of the elemental composition data (wt%) of synchysite-(Ce) in the Songwe Hill carbonatite samples analysed by EPMA at CSM and NHM. Note the EPMA data at NHM are from Aoife Brady (Mkango Resources Ltd).

Oxide wt%	Min	Max	Avrg	σ	Min	Max	Avrg	σ
	21 spot points (CSM)				178 spot points (NHM)			
CaO	14.00	17.83	16.70	1.10	14.33	18.11	16.36	0.73
MnO	n.a	n.a	n.a	n.a	b.d	0.09	0.01	0.02
FeO	n.a	n.a	n.a	n.a	b.d	2.29	0.36	0.55
SrO	b.d	b.d	b.d	b.d	b.d	2.52	0.35	0.30
BaO	b.d	b.d	b.d	b.d	b.d	2.74	0.05	0.22
Y_2O_3	b.d	2.06	0.61	0.68	b.d	2.70	0.56	0.47
La_2O_3	8.20	22.23	12.44	3.50	7.54	20.62	13.36	3.07
Ce_2O_3	20.18	27.75	24.21	1.98	18.76	28.62	24.47	1.40
Pr_2O_3	1.35	3.25	2.35	0.48	1.74	4.32	2.48	0.37
Nd_2O_3	3.95	12.13	7.67	1.73	4.23	12.97	8.29	1.93
Sm_2O_3	0.35	1.71	0.85	0.41	0.15	2.57	0.93	0.42
Eu_2O_3	b.d	b.d	b.d	b.d	b.d	0.53	0.14	0.10
Gd_2O_3	b.d	1.05	0.59	0.25	b.d	1.88	0.30	0.31
Dy_2O_3	b.d	b.d	b.d	b.d	b.d	0.49	0.16	0.11
ThO_2	0.19	6.73	1.29	1.35	0.02	2.82	0.80	0.51
UO_2	b.d	b.d	b.d	b.d	b.d	b.d	b.d	0.00
F[a]	5.59	6.31	5.89	0.17	5.47	6.11	5.89	0.11
CO_2 [a]	25.90	29.25	27.28	0.80	25.36	28.30	27.27	0.53
-O=F	2.35	2.66	2.48	0.07	2.31	2.57	2.48	0.05
Σ	92.61	104.38	97.40	3.14	92.18	104.22	99.55	1.95

[a] Determined by stoichiometry, b.d is below detection limit, and n.a is not analysed.

3.9.3 Parisite-(Ce)

The minimum, maximum, average, and standard deviation of the elemental composition of parisite-(Ce) analysed by EPMA are given in Table 3.7. The average of TREO within parisite-(Ce) is approximately 58 wt% and it is mainly LREE-enriched. The predominant REE is Ce_2O_3 followed by La_2O_3, Nd_2O_3, and Pr_2O_3. It also contains trace amounts of MREE and HREE including Sm_2O_3, Y_2O_3, Eu_2O_3, and Dy_2O_3 in decreasing order with a total average below 0.5 wt%.

Minor concentrations of SrO, BaO, FeO, and MnO also occur in parisite ranging between 0.4 wt% and 2.1 wt%, with an average of approximately 1.1 wt%, predominant by SrO. The concentration of ThO_2 varies between 0.08 wt% and 0.73 wt% with an average of 0.35 wt%, while UO_2 is below the detection limit in all measured samples.

In summary, synchysite-(Ce) is the predominant REE fluorcarbonate mineral identified in the Songwe Hill carbonatite samples, followed by trace amount of parisite-(Ce). These minerals are enriched in light lanthanide elements with minor to trace of MREE and HREE, especially synchysite-(Ce). The content of CaO in synchysite-(Ce) is higher than parisite-(Ce), as expected.

The REE:Ca ratios, which are determined based on the calculated apfu, the EPMA results of 185 spot points also show that synchysite-(Ce) is the predominant REE fluorcarbonate mineral in the deposit under investigation, followed by parisite-(Ce). Synchysite-(Ce) comprises about 96%, while parisite-(Ce) forms approximately 4% of the total REE fluorcarbonate minerals.

Furthermore, the correlation between CaO and TREO contents could be considered a way to distinguish between the REE fluorcarbonates although, no exact limit has been published to classify these minerals based on their content of CaO and TREO. Based on the EPMA data, the content of CaO and TREO in the REE fluorcarbonates are plotted graphically in Figure 3.9. This figure shows that there are two distinct assemblages for synchysite-(Ce) and parisite-(Ce). According to these results, synchysite-(Ce) can be identified within a range of between about 14 wt% and 18 wt% for CaO and approximately 44 wt% and 56 wt% for TREO, while parisite-(Ce) can be recognised within a range between about 9 wt% and 11 wt% for CaO and 56 wt% and 60 wt% for TREO. Note that any decrease in the percentage of CaO will be accompanied by an increase in the TREO content.

Table 3.7: Elemental composition data (wt%) of parisite-(Ce) in the Songwe Hill carbonatite samples as analysed by EPMA. Data from Aoife Brady (Mkango Resources Ltd).

Spot point	1	2	3	4	5	6	7	Min	Max	Avrg	σ
								7 points			
CaO	10.97	11.41	10.58	10.9	9.3	9.89	9.52	9.30	11.41	10.37	0.80
MnO	b.d	b.d	0.02	b.d	b.d	b.d	b.d	b.d	0.02	0.00	0.01
FeO	b.d	0.02	0.05	0.03	b.d	0.07	0.25	b.d	0.25	0.06	0.09
SrO	0.79	0.5	1.02	0.4	0.99	0.94	0.59	0.40	1.02	0.75	0.25
BaO	0.08	b.d	0.79	0.09	0.33	0.37	0.4	b.d	0.79	0.29	0.27
Y_2O_3	b.d	0.01	0.03	0.06	0.05	b.d	0.36	b.d	0.36	0.07	0.13
La_2O_3	19.75	21.56	18.03	22.12	22.14	22.87	23.45	18.03	23.45	21.42	1.89
Ce_2O_3	27.01	27.48	28.79	28.54	27.28	28.63	27.68	27.01	28.79	27.92	0.72
Pr_2O_3	2.22	2.04	2.71	2.37	2.14	2.31	2.5	2.04	2.71	2.33	0.23
Nd_2O_3	6.52	5.44	7.83	5.18	4.8	5.13	5.7	4.80	7.83	5.80	1.05
Sm_2O_3	0.52	0.28	0.54	0.23	0.24	0.24	0.35	0.23	0.54	0.34	0.13
Eu_2O_3	0.03	0.04	0.06	b.d	0.02	b.d	0.06	b.d	0.06	0.03	0.03
Gd_2O_3	b.d	b.d	b.d	b.d	b.d	b.d	b.d	b.d	b.d	b.d	0.00
Dy_2O_3	0.01	b.d	b.d	b.d	b.d	b.d	0.11	b.d	0.11	0.02	0.04
ThO_2	0.11	0.08	0.62	0.25	0.35	0.33	0.73	0.08	0.73	0.35	0.24
UO_2	b.d	b.d	b.d	b.d	b.d	b.d	b.d	b.d	b.d	b.d	0.00
F[a]	5.46	5.56	5.64	7.01	6.66	6.98	7.03	5.46	7.03	6.33	0.74
CO_2[a]	25.29	25.75	26.12	24.36	23.12	24.24	24.44	23.12	26.12	24.76	1.03
-O=F	2.30	2.34	2.37	2.95	2.80	2.94	2.96	2.30	2.96	2.67	0.31
Σ	96.47	97.83	100.45	98.59	94.62	99.06	100.21	94.76	101.07	98.39	2.17
apfu[a] on the basis of number of anions											
Ca	1.056	1.079	0.980	1.037	0.932	0.945	0.903	0.90	1.08	0.99	0.07
Mn	b.d	b.d	0.001	b.d	b.d	b.d	b.d	b.d	0.00	0.00	0.00
Fe	b.d	0.001	0.004	0.002	b.d	0.005	0.019	b.d	0.02	0.00	0.01
Sr	0.041	0.026	0.051	0.021	0.054	0.049	0.030	0.02	0.05	0.04	0.01
Ba	0.003	b.d	0.027	0.003	0.012	0.013	0.014	b.d	0.03	0.01	0.01
Σ	1.113	1.118	1.107	1.072	1.010	1.026	0.975	0.97	1.12	1.06	0.06
Y	b.d	b.d	0.001	0.003	0.002	b.d	0.017	b.d	0.02	0.00	0.01
La	0.654	0.702	0.575	0.725	0.764	0.753	0.766	0.57	0.77	0.71	0.07
Ce	0.888	0.888	0.911	0.928	0.934	0.935	0.897	0.89	0.94	0.91	0.02
Pr	0.073	0.066	0.085	0.077	0.073	0.075	0.081	0.07	0.09	0.08	0.01
Nd	0.209	0.172	0.242	0.164	0.160	0.163	0.180	0.16	0.24	0.18	0.03
Sm	0.016	0.009	0.016	0.007	0.008	0.007	0.011	0.01	0.02	0.01	0.00
Eu	0.001	0.001	0.002	b.d	0.001	b.d	0.002	0.00	0.00	0.00	0.00
Gd	b.d	b.d	b.d	b.d	b.d	b.d	b.d	b.d	b.d	b.d	0.00
Dy	b.d	b.d	b.d	b.d	b.d	b.d	0.003	b.d	0.00	0.00	0.00
Th	0.002	0.002	0.012	0.005	0.007	0.007	0.015	0.00	0.01	0.01	0.00
Σ	1.844	1.839	1.845	1.910	1.950	1.941	1.972	1.84	1.97	1.90	0.06

[a] Determined by stoichiometry, and b.d is below detection limit.

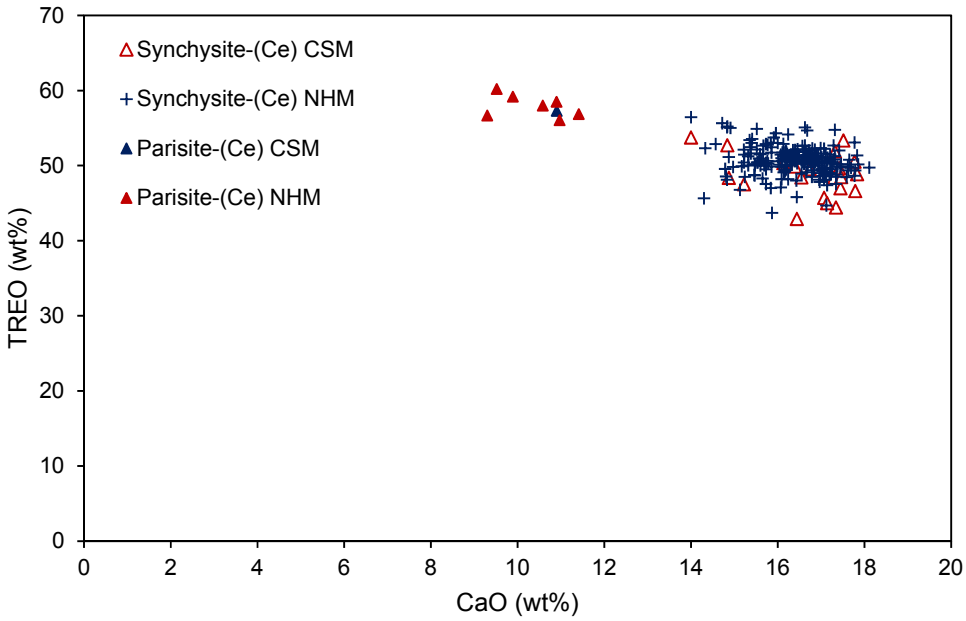

Figure 3.9: Distinction between synchysite-(Ce) and parisite-(Ce) in the Songwe Hill carbonatite samples based on the content of CaO and TREO as analysed by EPMA at CSM and NHM.

3.9.4 Florencite-(Ce)

The minimum, maximum, average, and standard deviation of the elemental composition of florencite-(Ce) analysed by EPMA are listed in Table 3.8.

The results show that the predominant non-REE are Al_2O_3 with an average of 28.5 wt% followed by P_2O_5 with an average of 24.4 wt%. This means there is a potential source for P_2O_5 and this should be considered when calculating the mass balance to track P_2O_5 bearing minerals. This will be further discussed in Chapter 4, Section 4.7.2.

Florencite-(Ce) also contains a considerable amount of LREE including Ce_2O_3, La_2O_3, Nd_2O_3, and Pr_2O_3 in order of decreasing abundance as well as a trace amount of Sm_2O_3. The TREO ranges between about 18 wt% and 27 wt% with an average of about 24 wt%.

Table 3.8: Elemental composition data (wt%) of florencite-(Ce) in the Songwe Hill carbonatite samples as analysed by EPMA. Data from Mkango Resources Ltd.

Spot point	1	2	3	4	5	6	Min	Max	Avrg	σ
							6 points			
Al_2O_3	30.22	27.17	28.71	28.22	28.07	28.77	27.17	30.22	28.53	1.01
SiO_2	0.09	0.08	0.08	0.10	0.21	0.12	0.08	0.21	0.11	0.05
P_2O_5	25.22	22.19	25.97	24.33	24.10	24.76	22.19	25.97	24.43	1.28
Na_2O	0.03	0.02	b.d	b.d	b.d	0.02	b.d	0.03	0.01	0.01
MgO	b.d	0.03	b.d	0.02	0.03	0.01	b.d	0.03	0.02	0.01
CaO	1.01	3.42	0.89	1.98	1.70	1.05	0.89	3.42	1.68	0.96
FeO	0.85	0.87	0.56	1.22	0.75	2.34	0.56	2.34	1.10	0.65
Y_2O_3	b.d	b.d	b.d	b.d	b.d	b.d	b.d	b.d	b.d	b.d
La_2O_3	8.66	6.99	8.33	8.10	9.63	10.44	6.99	10.44	8.69	1.21
Ce_2O_3	11.15	9.42	13.21	13.75	12.94	13.17	9.42	13.75	12.27	1.66
Pr_2O_3	1.17	0.88	1.86	2.02	1.11	1.07	0.88	2.02	1.35	0.47
Nd_2O_3	1.48	0.97	3.04	3.42	1.09	0.72	0.72	3.42	1.79	1.15
Sm_2O_3	b.d	0.06	0.15	0.07	b.d	b.d	b.d	0.15	0.05	0.06
Eu_2O_3	b.d	b.d	b.d	b.d	b.d	b.d	b.d	b.d	b.d	b.d
Gd_2O_3	b.d	b.d	b.d	b.d	b.d	b.d	b.d	b.d	b.d	b.d
ThO_2	b.d	b.d	b.d	b.d	b.d	b.d	b.d	b.d	b.d	b.d
UO_2	b.d	b.d	b.d	b.d	b.d	b.d	b.d	b.d	b.d	b.d
F	1.02	1.72	0.77	0.51	0.75	0.93	0.51	1.72	0.95	0.42
-O=F	0.43	0.72	0.32	0.21	0.32	0.39	0.21	0.72	0.40	0.18
Σ	80.47	74.09	83.69	83.82	80.50	*83.55	73.10	83.53	80.57	3.59
apfu[a] on the basis of number of anions										
Al	4.053	3.973	3.842	3.858	3.919	3.881	4.173	3.722	3.919	0.08
Si	0.010	0.010	0.009	0.012	0.025	0.014	0.010	0.022	0.013	0.01
P	2.430	2.331	2.496	2.389	2.417	2.399	2.448	2.298	2.411	0.05
Na	0.007	0.005	b.d	b.d	b.d	0.004	b.d	0.006	0.003	0.00
Mg	b.d	0.006	b.d	0.003	0.005	0.002	b.d	0.005	0.003	0.00
Ca	0.123	0.455	0.108	0.246	0.216	0.129	0.124	0.383	0.209	0.13
Fe	0.081	0.090	0.053	0.118	0.074	0.224	0.061	0.205	0.107	0.06
La	0.363	0.320	0.349	0.347	0.421	0.441	0.336	0.402	0.374	0.05
Ce	0.465	0.428	0.549	0.584	0.561	0.552	0.449	0.526	0.524	0.06
Pr	0.049	0.040	0.077	0.085	0.048	0.045	0.042	0.077	0.057	0.02
Nd	0.060	0.043	0.123	0.142	0.046	0.029	0.034	0.128	0.074	0.05
F	0.213	0.391	0.160	0.110	0.120	0.195	0.122	0.329	0.203	0.10
Σ	7.853	8.090	7.767	7.893	7.852	7.915	7.800	8.107	7.898	0.11

[a] Determined by stoichiometry, and b.d is below detection limit.

3.10 Conclusions

This chapter has presented the whole-rock chemistry of the carbonatite samples used in this study. The rock-forming minerals were determined by XRD and SEM-EDS, while the mineral chemistry of the valuable minerals was analysed by EPMA (this study) and used in conjunction with an additional data set analysed through LA-ICP-MS (Broom-Fendley, 2015). The following summary and conclusions can be drawn from this chapter:

- It is indicated that the deposit under investigation is enriched in a variety of LREE, MREE, and HREE.
- Based on the correlation between P_2O_5 and Y_2O_3, apatite is considered HREE bearing mineral in addition to its content of P_2O_5.
- XRD is a good technique to identify the major and common minerals with no or limited overlap, while it seems difficult to estimate the predominance of the minor and trace minerals by this technique. This is due to the overlap with other minerals and the absence of the individual peak(s).
- The SEM-EDS observations showed that the main valuable minerals are apatite, synchysite and florencite, while the main gangue minerals are ankerite, calcite, minor iron oxides/carbonates, K-feldspar, with trace amounts of strontianite, and baryte.
- Apatite commonly occurs as vein-like crystals associated with other gangue minerals and to a lesser extent as large liberated grains (up to 400 μm), while synchysite predominantly occurs as clusters or individual acicular-like crystals, and to a lesser extent as granular (lath-shaped) crystals. The granular crystals should be relatively easy to liberate and hence separate than the acicular crystals, particularly when they occur as individual needle-like crystals embedded within the gangue minerals.
- The mineral chemistry analysed by EPMA indicated that apatite hosts the more valuable HREE, while synchysite-(Ce), parisite-(Ce), and florencite-(Ce) host the LREE.
- The predominant REE fluorcarbonate mineral in the Songwe Hill carbonatite samples is synchysite-(Ce), which forms approximately 96%, followed by parisite-(Ce), which forms about 4%.

Chapter 4

Quantitative mineralogy using QEMSCAN®

4.1 Introduction

Automated mineralogy is now the technique of choice in determining the mineralogical characteristics of an ore deposit and identifying and quantifying the minerals of interest, including their liberation, association, and grain size distribution. This kind of analysis improves understanding of the ore body and provides insight into the target minerals and optimum grind size of the feed before conducting any mineral processing test. Automated mineralogy is also a vital tool for ore feed optimisation and metallurgical troubleshooting during and after the design of a mineral processing flowsheet. It is particularly useful for complex ore deposits such as the Songwe Hill carbonatite deposit under investigation.

The QEMSCAN® (Quantitative Evaluation of Minerals by Scanning Electron Microscopy) automated mineral technology is a very powerful technique used for mineral processing worldwide.

4.2 Aims

The overall aim of this chapter is to use automated mineralogy (QEMSCAN®) in conjunction with the mineralogical results in Chapter 3 to provide a comprehensive mineralogical overview of the Songwe Hill ore that will help establish a successful mineral processing strategy. This case study focuses on the characterisation and quantification of the mineralogical parameters within eight crushed drill core samples (see Chapter 2), two ground composites, and five size-by-size fractions. The parameters include: abundance of valuable and gangue minerals, average grain size, mass-size distribution, and the liberation degree of the valuable minerals and their association percentage with gangue minerals, as well as false-colour digital images of the analysed samples for the microstructural features. It also aims to discuss the potential mineral processing techniques for dressing this ore deposit based on the generated mineralogical data.

The main limitation to the QEMSCAN® system is that the technique cannot separate polymorphous minerals (same chemistry, different crystallography), such as calcite versus aragonite, as its analysis is based on X-ray spectra that only indicate the mineral chemistry. Also, minerals/phases with very similar or overlapping chemical spectra may be difficult or impossible to separate, e.g. topaz, kyanite, andalusite, and sillimanite. Very fine-grained material such as mixed clays (less than 5 μm) may also be difficult to separate chemically due to the beam excitation volume effects of a 25 kV accelerating voltage (Rollinson et al., 2011). The particular challenges identified from the mineralogical analyses in Chapter 3 were the need to accurately identify and preferably distinguish between REE fluorcarbonates, and to distinguish REE-bearing phosphate minerals, notably apatite and florencite but also potentially monazite. Detection of REE in apatite would also be very useful. Distinguishing Fe oxides is always challenging by QEMSCAN® and needs to be considered carefully. Particular studies for REE fluorcarbonates and apatite/florencite were made before interpreting the QEMSCAN® results.

4.3 Species identification protocol development and data generation

Developing the Species Identification Protocol (SIP) and generating the final data were carried out in three stages including pre-, during-, and post-measurement.

Pre-measurement

In order to optimise the SIP database, extensive chemical and mineralogical analyses were undertaken using different techniques including ICP-MS, ICP-OES, XRD, SEM-EDS, and EPMA prior to submitting the samples to QEMSCAN® analysis (see Chapter 3). This also aimed to identify the potential ore-forming minerals/phases and aided to improve understanding of the chemical and mineralogical composition of the Songwe Hill ore deposit samples, as well as for data validation and reconciliation purposes. The utilised analytical techniques (as shown in Chapter 2) included ICP-MS and ICP-OES to determine the range and distribution of major and rare earth elements; XRD to particularly identify the major and minor minerals; extensive examinations using SEM-EDS to prove the identity of the potential valuable and the present gangue minerals; and EPMA was used for determining the elemental composition of the valuable minerals and proving the identity of the REE fluorcarbonate minerals.

It is important to bear in mind that XRD and SEM techniques produced qualitative data that can be only used to compare the minerals based on their identities, rather than their quantities with the QEMSCAN® outputs. Furthermore, elemental analyses using ICP-MS and XRF were utilised for quantitatively determining the elemental distribution of the size-by-size fractions for comparison purposes of the QEMSCAN® outputs. The data generated by these analytical techniques were also utilised for quality control, calibration, and data validation and interpretation of the QEMSCAN® measurements.

During measurement

At this stage carbon-coated 30 mm diameter polished blocks were loaded into the QEMSCAN® for the mineralogical analysis. The electron beam stepping interval and the number of particles were set and defined. The accompanying software iMeasure was used for data acquisition.

At each analysis point, which represents an individual pixel in the output image, the resultant chemical X-ray spectrum is first processed by a Spectral Analysis Engine (SAE) to identify and quantify the elemental distribution at each pixel. The elemental composition at each measurement point is subsequently compared with a library of the standard spectra database of >750 known minerals or compounds in order to assign the mineral species (Haberlah et al., 2011).

Post-measurement

After the raw data and accompanying mineral data from matching X-ray spectra with a SIP database were collected, more work was carried out to amend and refine the database and mineral lists, reduce the edge effect, combine the minerals that have slight chemical variations intro groups, and also in some cases combine the groups into categories; e.g. carbonates and silicates, based on the mineralogy of the sample and the level of detail required for the study. Mineral categories and their descriptions used in this research are listed in Table 4.1.

The ideal characterisation of sample mineralogy can only be achieved by creating a mineral list to include the verified minerals based on the measurements carried out using the techniques described in Chapter 2.

Table 4.1: Mineral categories, abbreviations, and descriptions as used in this research.

Mineral Category	Mineral Description
Background	All resin related/edge effects, and others.
Calcite	Includes any phase with Ca, C, and O, may contain low Mg
Ankerite	Any phase with Fe, Ca, Mg, and O, possibly minor Mn
Dolomite	Any phase with Ca, Mg, O, and C, possibly minor Fe
Apatite	Any phase with Ca, P, and O
Florencite	Any phase with Ce, Al, P, and O
Apatite/florencite	This is a mixture of apatite & florencite: they were both intergrown and the grain size was below resolution of the scan
Synchysite/parisite	Any phase with Ce, Ca, C, F, and O
Bastnäsite	Any phase with Ce, O, F, and C
Monazite	Any phase with Ce, La, P, and O with or without Th, may contain other trace REE
Pyrochlore	Any phase with Na, Ca, Nb, O, and F
Zircon	Any phase with Zr, Si, and O, may contain trace REE and Hf
Strontianite	Any phase with Sr, C, and O
Fluorite	Any phase with Ca and F
Fe-Ox(Mn)/CO_3	Fe oxides and carbonates such as hematite, magnetite, goethite, Fe-Mn oxide and any other Fe-oxide/carbonate.
Mn Ox/CO_3	Any phase with Mn and O possibly with C and H. This may include pyrolusite, rhodochrosite, and other similar phases.
Rutile	Any phase with Ti and O. This may include rutile/anatase/brookite
Ilmenite	Any phase with Fe, Ti, and O, may include trace Ti-magnetite
Pyrophanite	Any phase with Mn, Ti, and O. Part of the ilmenite group
Quartz	Quartz and other silica minerals
K-feldspar	K-feldspars (orthoclase, sanidine, microcline): any phase with K, Al, Si, O. Mainly orthoclase and microcline
Plagioclase	Plagioclase: phases with Na, Al, Si, and O to Ca, Al, Si, and O
Biotite	Biotite, may include other micas such as zinnwaldite and phlogopite. Note Li cannot be detected using EDS.
Muscovite	Muscovite/lepidolite - any phase with K, Al, Si, and O. Note Li cannot be detected using EDS.
Chlorite	Chlorite/clinochlore - any phase with Fe, Mg, Al, Si, and O
Kaolinite	Kaolinite/halloysite/dickite and any other Al Silicates
Baryte	Any phase with Ba, S, and O
Pyrite	Includes pyrite/marcasite, trace pyrrhotite (any phase with Fe and S), and may contain jarosite (Fe, S, and O)
Sphalerite	Any phase with Zn and S, may contain minor Fe.
Galena	Any phase with Pb and S
Others	Any other mineral not included above and edge effects.

The itemised minerals in the original SIP file of the QEMSCAN® system were updated to include some new minerals such as synchysite, parisite, pyrochlore, and florencite. In addition to updating the general mineral list, the development process also included modifying the elemental ratio of some minerals within the original SIP file. This aimed to match the mineral chemistry of the SIP minerals as closely as possible to the actual samples. The new minerals were then added to a primary list and their ideal chemical formula and densities (www.webmineral.com) were inserted into the SIP. Furthermore, when possible, external minerals were used as standards such as synchysite, parisite, and pyrochlore.

The main challenges faced for SIP development of the samples under investigation were distinguishing between synchysite and parisite and between the intergrown crystals of apatite and florencite.

4.3.1 Distinction of REE fluorcarbonate minerals

More work was carried out to develop the SIP for REE fluorcarbonate minerals, particularly synchysite-(Ce) and parisite-(Ce), as they are chemically close to each other and usually crystallise next to each other as a syntaxial intergrowth, which leads to difficulty identifying the individual minerals.

Bastnäsite-(Ce) is the easiest mineral to be identified in the QEMSCAN® measurements as it has no, or sometimes very low, Ca content. While, to distinguish between synchysite-(Ce) and parisite-(Ce), a standard mineral sample containing a cluster of synchysite/parisite crystals originating from Mont Saint-Hilaire, Quebec, Canada, was used in this work (Figure 4.1).

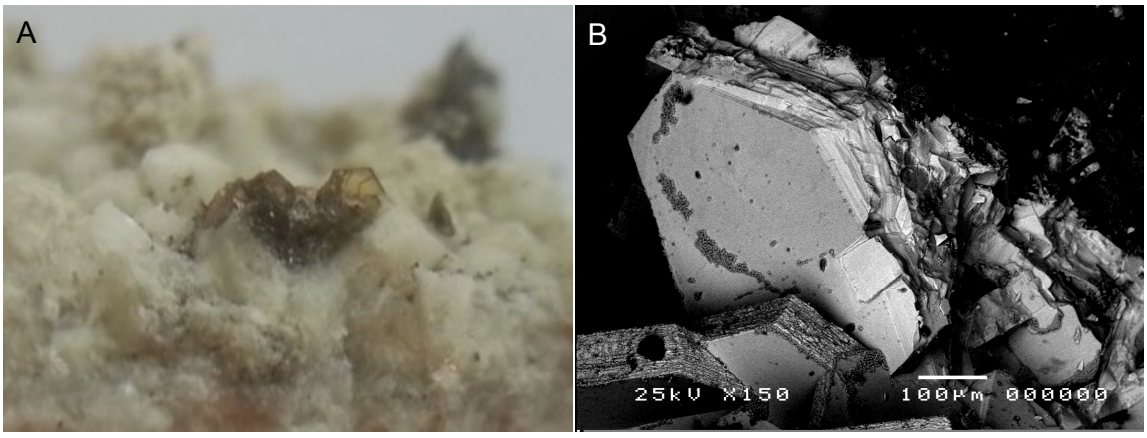

Figure 4.1: (A) A cluster of brown synchysite/parisite crystals on a white albite matrix and (B) Low-vacuum backscattered electron image showing the layer structure of the syntaxially-intergrown synchysite/parisite hexagonal crystals.

A polished mount of these crystals was prepared. The BSE image in Figure 4.2 qualitatively shows that these crystals contain syntaxial intergrowths of synchysite (grey) and parisite (light-grey). The mineral identity was proven based on the elemental composition of selected crystals analysed by EPMA. The compositional EPMA results and the REE:Ca ratios for each mineral are given in Appendix F.

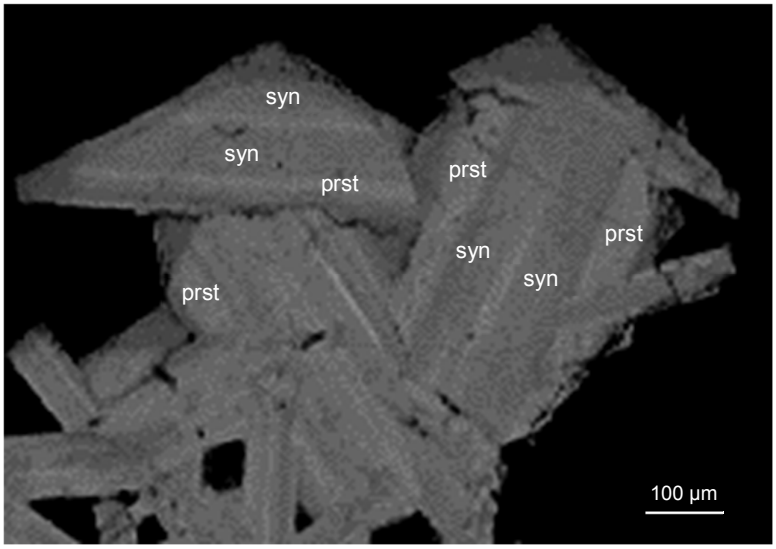

Figure 4.2: Backscattered electron image showing the syntaxial intergrowth of synchysite-(Ce) (dark grey) and parisite-(Ce) (grey) crystals in the standard mineral sample.

In order to distinguish between synchysite-(Ce) and parisite-(Ce) by QEMSCAN®, different levels for Ca of 85, 88, and 90 were applied and the best result was obtained based on the Ca level of 88, as shown in Figure 4.3.

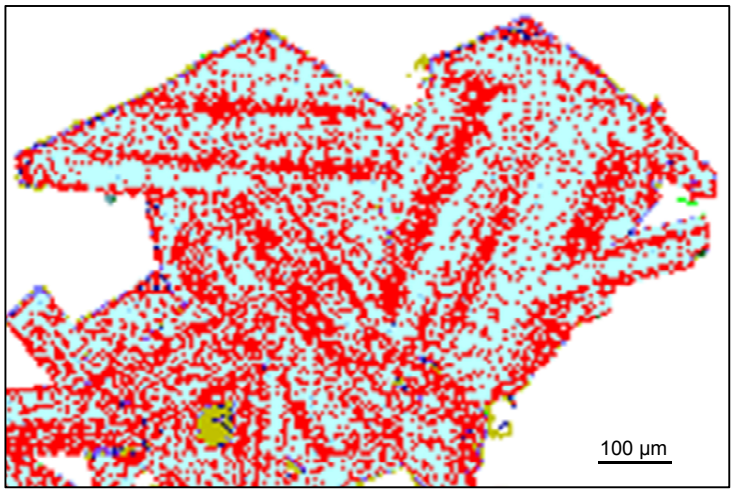

Figure 4.3: False-coloured Fieldscan image showing the syntaxial intergrowth of synchysite-(Ce) (light blue) and parisite-(Ce) (red) crystals in the standard mineral sample as determined by QEMSCAN®.

The distinction results between synchysite-(Ce) and parisite-(Ce) in the standard sample were subsequently applied to the samples under investigation to evaluate the possibility of distinguishing between synchysite and parisite. It seems there are challenges to distinguishing these minerals within the current samples based on their X-ray spectra. Therefore, they are combined into one category called "synchysite/parisite". The main challenges include:

- Synchysite and parisite are calcium REE fluorcarbonate minerals with very similar chemical compositions (see Chapter 1, Section 1.5); however, they can be distinguished by measuring the calcium and REE contents (see Chapter 3, Section 3.9). Normally, synchysite possesses a higher calcium content and lower REE content than parisite. REE here are Ce (the most predominant REE), plus La and Nd as well as minor quantities of other LREE.
- The EPMA data showed that the predominant REE fluorcarbonate mineral within the current deposit is synchysite, which comprises about 96%, followed by parisite with an abundance of approximately 4% (see Chapter 3, Section 3.9).
- Synchysite and parisite are porous and unstable minerals under an electron beam, which causes difficulties for the electron beam and excitation of X-rays. In particular, the intensity of the X-rays can be reduced, which can cause a misclassification if for example a calcium threshold is used, and this intensity moves across this threshold from one mineral to another.
- REE fluorcarbonates including bastnäsite, parisite, röntgenite, and synchysite have layered structures and are commonly syntaxially-intergrown with each other, and are also often affected by stacking faults during the crystallisation stage; furthermore, they frequently occur as sheaves of fine needle-like crystals (see the review in Chapter 1, Meng et al., 2002; Wall, 2014). All these features have made it difficult to obtain accurate data on the analysed very fine synchysite/parisite. It is indicated from the QEMSCAN® measurements (see Sections 4.4 and 4.5) that the average grain size of synchysite/parisite is 30 µm in the crushed samples of 1700 µm, and 10 µm in the ground composite sample of 53 µm.

- Characterising multiple phases that have large chemical variability in the X-ray excited area, traditionally expressed as a “boundary effect”, is another challenge to distinguish the fine and intergrown synchysite and parisite crystals.
- QEMSCAN® typically uses a lower X-ray spectrum (about 1000 counts) than the conventional scanning electron microscopy (SEM-EDS), and consequently obtains very good data about the chemistry of the analysed mineral; but requires minerals with large (>30 μm approximately, the larger the better), smooth and non-porous surfaces, and the 3 wt% per point detection issue must also be considered (Andersen et al., 2009).
- Synchysite/parisite is often associated with baryte, which may lead to overlap between cerium and barium peaks, generating another issue that affects the analysis.

However, although there is not enough of a difference to distinguish between synchysite and parisite based on the X-ray spectra in a QEMSCAN® run, it may be possible to distinguish these two minerals based on the BSE grey scale by generating a high quality BSE image coupled with image processing software, e.g. ImageJ.

4.3.2 Distinction of REE phosphate minerals

It is important to note that in some instances apatite and florencite are intimately intergrown together at a micron scale, as shown already from the SEM-EDS examination (Chapter 3) and in Figure 4.4 A and C. This intergrowth texture is observable at the spatial resolution of 10 μm and 1 μm X-ray spacing (Figure 4.4 B). The acquired EDS spectra display a combination of apatite and florencite, including P, Ca, Al, and REE as shown in Figure 4.4 D. Therefore, for clarity, the term apatite/florencite is used herein.

4.3.3 Edge effects

The edge or boundary effect is a measured point representing a combination of two or more distinct mineral phases, that often occurs between the mineral boundaries or between the mineral boundary and the surrounding resin (Pirrie et al., 2004). Therefore, the resultant X-ray spectra will include the elements that form the overlapped mineral phases, and may be assigned as an unidentified mineral grain when compared with the SIP database. The edge effect can be partially reduced

based on the degree of overlap using the tool “boundary phase processor” in the iDiscover software. However, the edge effect can be more pronounced in complex particles, particularly when they contain small grains, but can be reduced by applying high resolution measurements, e.g. down to 1 µm. It can also be reduced by high quality polishing to produce smooth and non-porous surfaces. Lastly, detailed SIP development is employed to capture the effects, which can be assigned to the correct mineral.

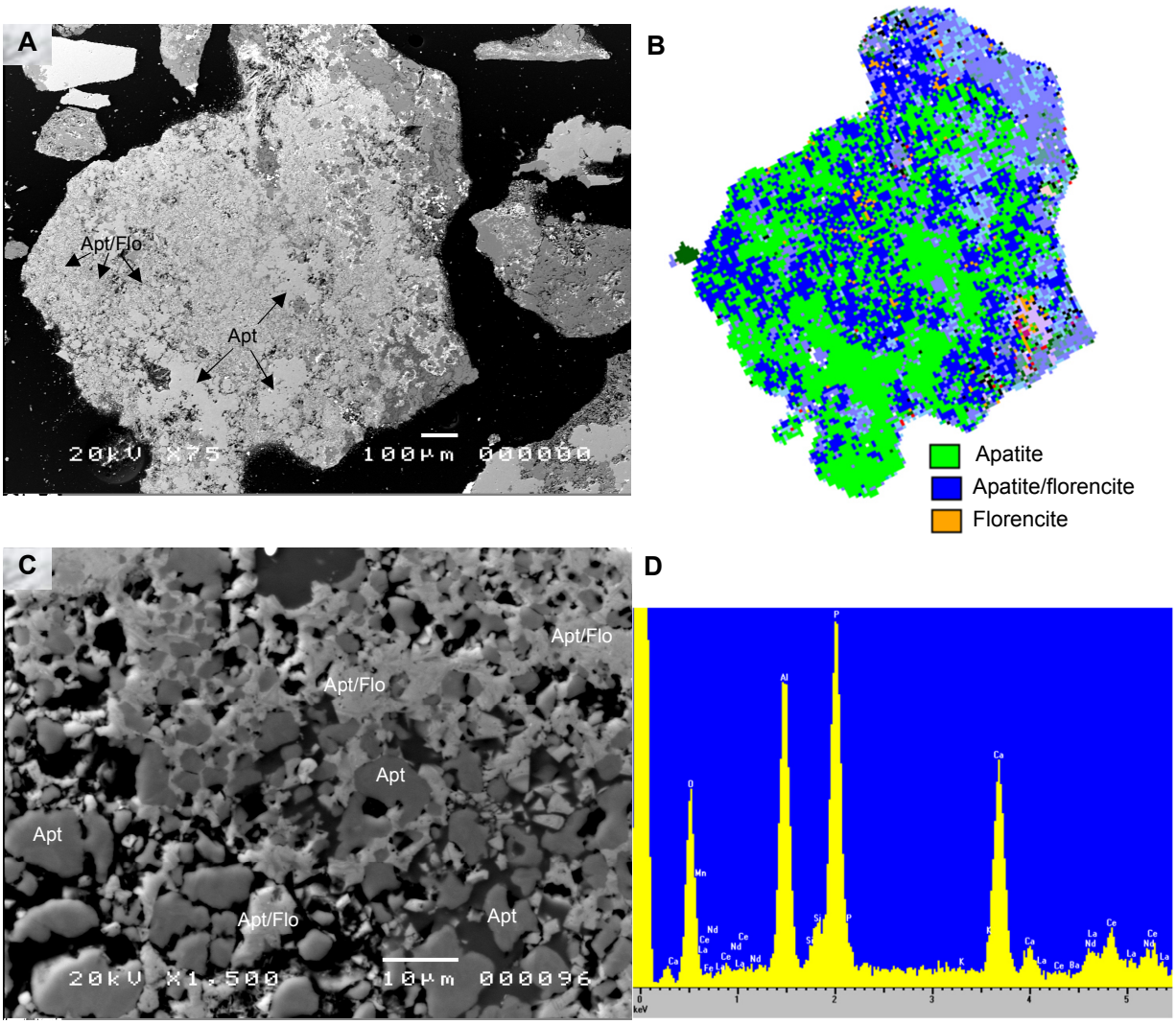

Figure 4.4: Intergrowth texture of apatite and florencite. (A) BSE image displays large composite particle contains anhedral large crystals of apatite surrounded by intergrown apatite-florencite, (B) Fieldscan image shows a large composite particle of the BSE image as a false-coloured image, (C) BSE image shows microscale individual crystals of apatite surrounded by intergrown apatite and florencite, and (D) EDS spectra of intergrown apatite and florencite crystals.

4.4 Crushed drill core samples results

4.4.1 Modal mineralogy

The mineral abundance and distribution within eight crushed drill core samples P_{100} of 1700 µm determined by QEMSCAN® are illustrated in Table 4.2 and summarised graphically in Figure 4.5, while the Fieldscan pseudo images of the measured samples are presented in Appendix G. These data are based upon analysis of several thousand particles and over two million X-ray spectra per sample, which gives a good representation for the mineralogical profile and for statistical analysis.

The samples contain several valuable minerals including REE phosphates, REE fluorcarbonates, and REE silicates. These minerals can be classified into two groups: *REE minerals* represented mainly by synchysite/parisite 1.85 wt% to 3.4 wt%, followed by florencite 0.1 wt% to 1.05 wt% with trace of bastnäsite < 0.04 wt% and monazite <0.02 wt%; and *REE-bearing minerals* represented mainly by apatite 2.34 wt% to 5.26 wt%, followed by intergrown apatite/florencite 0.14 wt% to 0.71 wt% with trace of zircon <0.03 wt% (Table 4.2 and Figure 4.5).

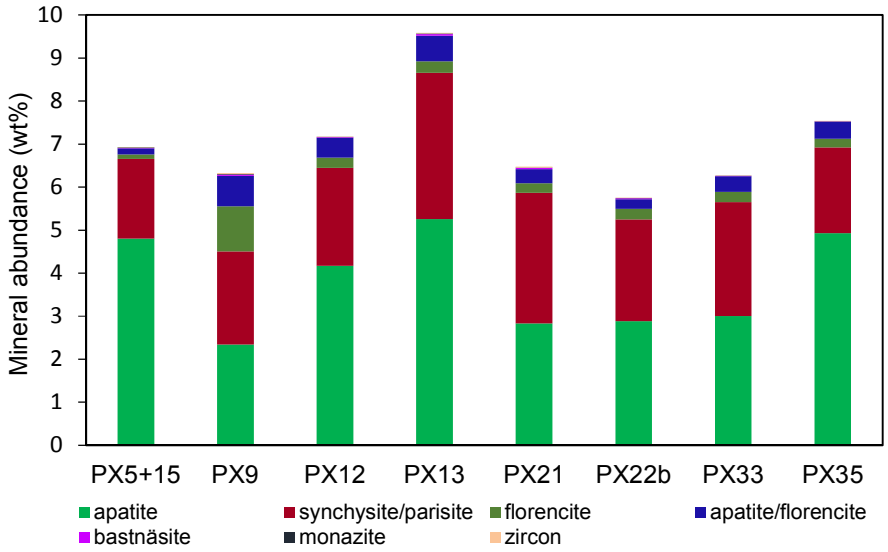

Figure 4.5: Modal mineralogy of the valuable minerals in the individual crushed drill core samples P_{100} of 1700 µm as determined by QEMSCAN®

The samples' matrices also consist of several gangue minerals from different groups including carbonates, silicates, oxides, sulphides, sulphates, and halides. It can be clearly seen from Table 4.2 that the major gangue minerals in most of the crushed samples, apart from the samples PX5+15 and PX12, are ankerite with an abundance approximately between 22 wt% and 39 wt%, followed by calcite with an abundance between 14 wt% and 50 wt%.

Table 4.2: Quantitative modal mineralogical data (wt%) of the valuable and gangue minerals in the individual crushed drill core samples P_{100} of 1700 µm as determined by QEMSCAN®

	Mineral group	Mineral name	PX05+15	PX09	PX12	PX13	PX21	PX22b	PX33	PX35
Valuable minerals	Phosphates	Apatite	4.80	2.34	4.18	5.26	2.83	2.88	3.00	4.93
		Florencite	0.10	1.05	0.24	0.27	0.23	0.25	0.24	0.21
		Apatite/florencite	0.14	0.71	0.46	0.59	0.33	0.22	0.36	0.39
		Monazite	0.01	<0.01	0.01	0.02	0.01	0.01	0.01	<0.01
	Carbonates	Synchysite/parisite	1.85	2.16	2.27	3.40	3.03	2.36	2.65	1.99
		Bastnäsite	<0.01	0.03	<0.01	0.04	0.03	0.02	<0.01	<0.01
	Silicates	Zircon	0.01	0.02	0.01	0.01	0.03	0.01	0.01	0.01
Gangue minerals	Carbonates	Calcite	50.51	14.35	36.12	26.03	29.00	29.01	22.50	26.73
		Ankerite	22.26	28.33	33.29	32.32	31.19	38.83	28.62	33.55
		Dolomite	0.01	0.03	0.07	0.76	0.03	0.03	<0.01	<0.01
		Strontianite	1.64	0.46	1.25	2.20	2.03	1.99	1.37	0.94
	Silicates	K-feldspar	7.00	15.50	8.51	5.89	10.17	4.56	11.58	12.01
		Plagioclase	0.14	0.24	0.11	0.06	0.10	0.07	0.17	0.14
		Muscovite	0.89	3.32	0.91	1.67	1.58	0.68	2.08	2.04
		Biotite	0.22	1.63	0.43	0.54	0.79	0.12	0.81	0.74
		Chlorite	0.17	1.03	0.19	0.28	0.45	0.12	0.47	0.42
		Kaolinite	0.03	0.04	0.02	0.01	0.02	0.01	0.02	0.05
		Quartz	0.20	0.19	0.16	0.39	0.13	0.09	0.12	0.11
	Oxides	Fe-Ox(Mn)/CO_3	6.30	19.47	8.32	15.00	13.87	14.26	20.24	12.36
		Mn Ox/CO_3	0.31	0.39	0.10	0.27	0.10	0.07	0.16	0.11
		Rutile	0.45	0.66	0.75	0.36	0.50	0.35	0.51	0.56
		Ilmenite	0.47	1.92	0.60	1.15	0.81	0.22	0.82	0.93
		Pyrophanite	0.17	1.04	0.25	0.24	0.18	0.05	0.27	0.34
		Pyrochlore	0.37	0.25	0.46	0.40	0.32	0.25	0.68	0.34
	Sulphides	Pyrite	0.62	0.12	0.15	0.19	0.15	1.08	0.61	0.05
		Sphalerite	0.02	<0.01	0.01	<0.01	0.02	0.04	<0.01	<0.01
		Galena	0.02	<0.01	<0.01	<0.01	<0.01	0.01	<0.01	<0.01
	Sulphates	Baryte	1.19	1.43	0.75	2.52	1.23	1.06	2.01	0.73
	Halides	Fluorite	0.09	3.24	0.38	0.09	0.85	1.32	0.65	0.30
	Mixed	Others*	0.01	0.02	0.01	0.03	0.01	0.01	0.02	0.01

* Others include trace of any other minerals not included above as well as the edge effects.

The minor gangue minerals in the Songwe Hill carbonatite complex are iron oxides/carbonates with an abundance approximately between 6 wt% and 20 wt%, followed by K-feldspar with an abundance of about 6 wt% and 16 wt%, along with trace of muscovite approximately between 1 wt% and 3 wt%, baryte 0.8 wt% - 2.5 wt%, and strontianite 0.5 wt% - 2 wt%. The deposit also consists of very trace amounts of other gangue minerals including fluorite, pyrochlore, ilmenite, rutile, pyrophanite, biotite, chlorite, plagioclase, kaolinite, quartz, pyrite, manganese oxides/carbonates, sphalerite, galena, and dolomite (Table 4.2).

In summary, while there are similarities in the overall mineralogical profiles between the different measured crushed drill core samples, the only subtle variation is the abundance of the valuable and gangue minerals throughout the samples. The QEMSCAN® results show that apatite is the predominant valuable mineral, with highest abundance occurring in sample PX13 and lowest in sample PX09, followed by synchysite/parisite with highest abundance occurring in sample PX13 and lowest in PX05+15. Florencite is relatively the least dominant valuable mineral, and occurs in approximately the same abundance in all the measured samples except sample PX09, which contains the highest proportion. The predominant gangue minerals are ankerite and calcite, minor amounts of iron oxides/carbonates and K-feldspar, trace amounts of strontianite, muscovite, and baryte, with several other very trace minerals. However, these results are widely in agreement with the observations and measurements achieved, particularly by SEM-EDS; a few valuable minerals and several gangue minerals were identified by QEMSCAN®, but were not observed by other analyses. This may be due to measuring the whole sample quantitatively, including the small grains of minerals that require a high resolution measurement to be identified, which can only be achieved by QEMSCAN®. Also, it is important to note that each instrument operates under different conditions with variable detection limits, and to some extent for a different purpose. Therefore, reconciliation will not be perfect and variations are expected.

Furthermore, based on the modal mineralogy of the measured samples, it seems that the ankerite carbonatite is the most dominant carbonatite deposit type in the Songwe Hill, followed by calcite carbonatite represented by the drill cores PX05+15 and PX12; while the lesser dominants are iron-ankerite carbonatite (drill core PX33) and weathered iron-ankerite carbonatite (drill core PX09).

4.4.2 Liberation and mineral association

Liberation and mineral association are considered the most essential parameters that need to be determined prior to any mineral processing test. When the mineral of interest, particularly fine grains in a complex ore, is encapsulated by the host particles, it requires fine grinding to achieve enough liberation for the target mineral. Increasing liberation of the valuable mineral is essential to maximise its recovery, by increasing the percentage of exposed grain surface and removing associated gangue minerals.

To avoid misinterpretation, it is important to define these two terms. *Liberation* is the area percentage of the mineral of interest compared to the area percentage of the whole host particle. *Mineral association* is related to the exposed perimeter of the mineral of interest with the background and other mineral phases (Lastra, 2002; Becker et al., 2009). The percentage of an area and perimeter of a grain is represented by the number of pixels.

However, the liberation and association of a relatively simple mineral texture of a binary particle may have similar measurements, and complex textures of ternary or quaternary particles may show differences from each other as shown in Figure 4.6. Therefore, a well liberated valuable mineral may display a poor exposure, and on the contrary a well exposed valuable mineral may be poorly liberated (Lastra, 2002; Smythe et al., 2013).

For the liberation measurements, valuable minerals are classified based on 2D mineral grain area percentage into: liberated >80%, middling 30-80%, and locked <30%.

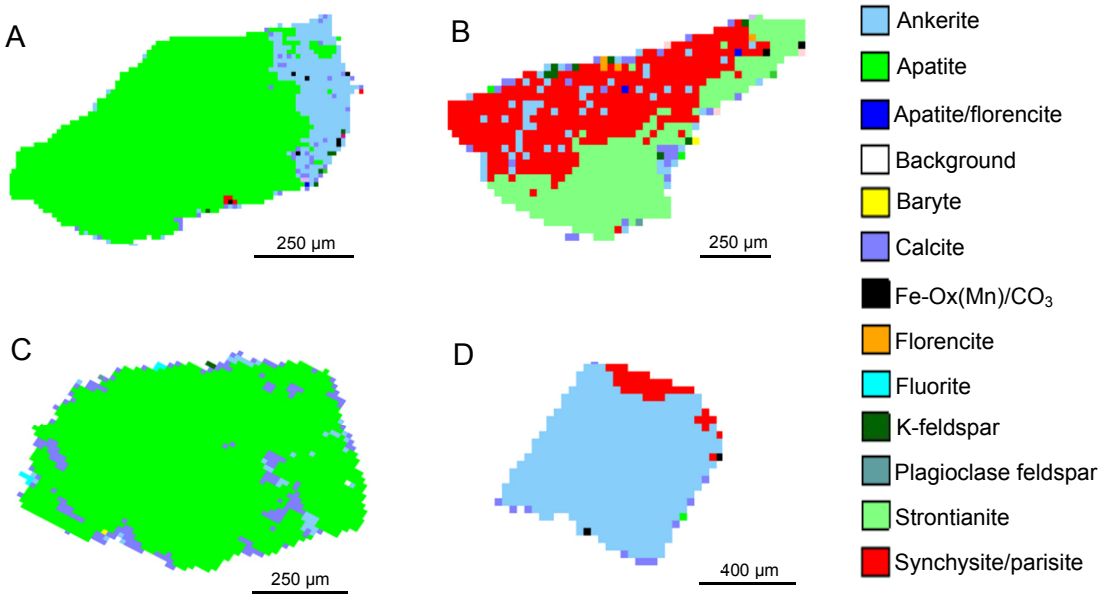

Figure 4.6: Difference between the liberation and mineral association in four composite particles containing valuable minerals (A) Apatite grain shows about 83% liberation and 58% association with gangue minerals (i.e. 42% with background), (B) Synchysite grain shows about 48% liberation and 81% association with gangue minerals (i.e. 19% with background), (C) Apatite grain shows about 90% liberation and 89% association with gangue minerals (i.e. 11% with background), and (D) Synchysite grain shows about 7% liberation and 59% association with gangue minerals (i.e. 41% with background).

4.4.3 Liberation of the valuable minerals

The results of the liberation characteristics of the valuable minerals are presented graphically in Figure 4.7.

From the data in this figure, it is apparent that apatite grains are relatively more liberated and less locked, particularly within samples PX33 and PX09, than synchysite/parisite grains, which are more locked by other minerals. However, the florencite and intergrown apatite/florencite grains are apparently poorly liberated; they are associated in about 40% with other valuable REE- and REE-bearing minerals, as will be further discussed in the next section.

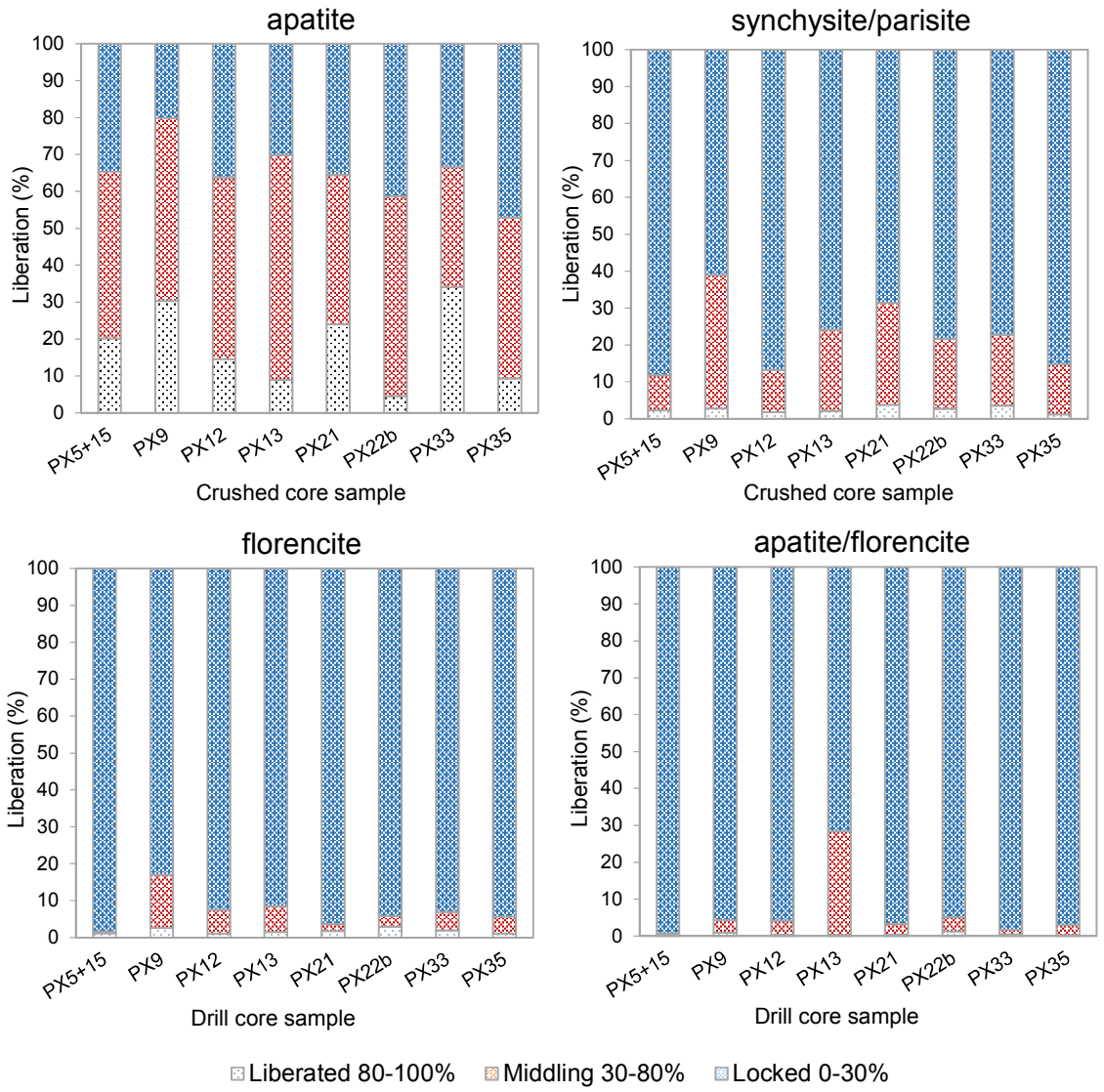

Figure 4.7: Liberation degree of apatite, synchysite/parisite, florencite, and apatite/florencite in the individual crushed drill core samples P_{100} of 1700 µm as determined by QEMSCAN®. Data were measured based on 2D area % of the whole host particle, determined by the number of pixels.

A good example of liberated and locked valuable minerals within host particles is shown in Figure 4.8. Particles A and B show large and liberated grains of apatite and synchysite/parisite, respectively, while particles C and D show very small and locked grains of apatite and synchysite/parisite, respectively. This indicates that particles A and B are fairly easy to process, whereas particles C and D are difficult to liberate and hence to process even with high fine grinding due to the small grain size.

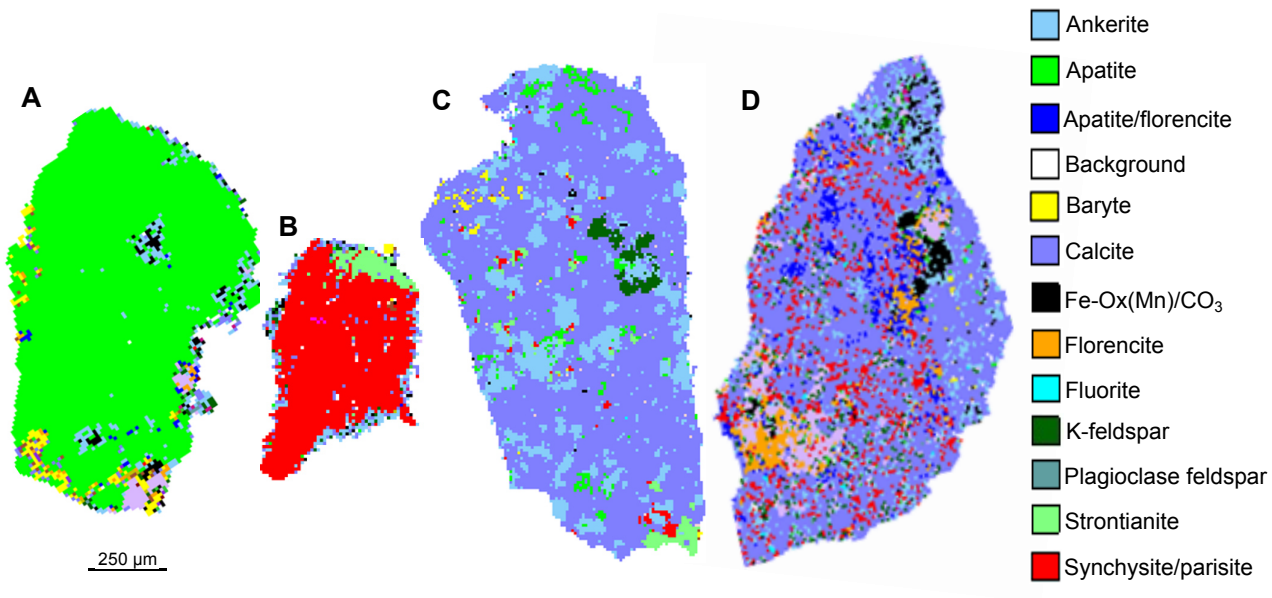

Figure 4.8: Fieldscan image (mineralogical map) illustrates liberated and locked grains of apatite and synchysite/parisite in different particles (A) large liberated apatite, (B) large liberated synchysite/parisite, (C) small locked grains of apatite and synchysite/parisite, and (D) small locked grains of synchysite/parisite and apatite/florencite.

4.4.4 Mineral association of the valuable minerals

The association percentages of the minerals of interest with other gangue minerals are illustrated in Figure 4.9. Apatite grains are mainly associated with ankerite 22% to 43%, followed by calcite 11% to 48%, and to a lesser extent with K-feldspar 2% to 19% and iron oxides/carbonates 2% to 6%. Also, apatite grains are associated with the background (resin) in approximately 11% to 20%.

Synchysite/parisite grains are mainly associated with calcite in approximately 19% to 46%, followed by ankerite 17% to 25%, and to a lesser extent with strontianite 4% to 15%, iron oxides/carbonates 3% to 9% and baryte 2% to 6%. Furthermore, synchysite/parisite grains display association with the background in approximately 10% to 14%, and with other valuable minerals in about 6% (Figure 4.9).

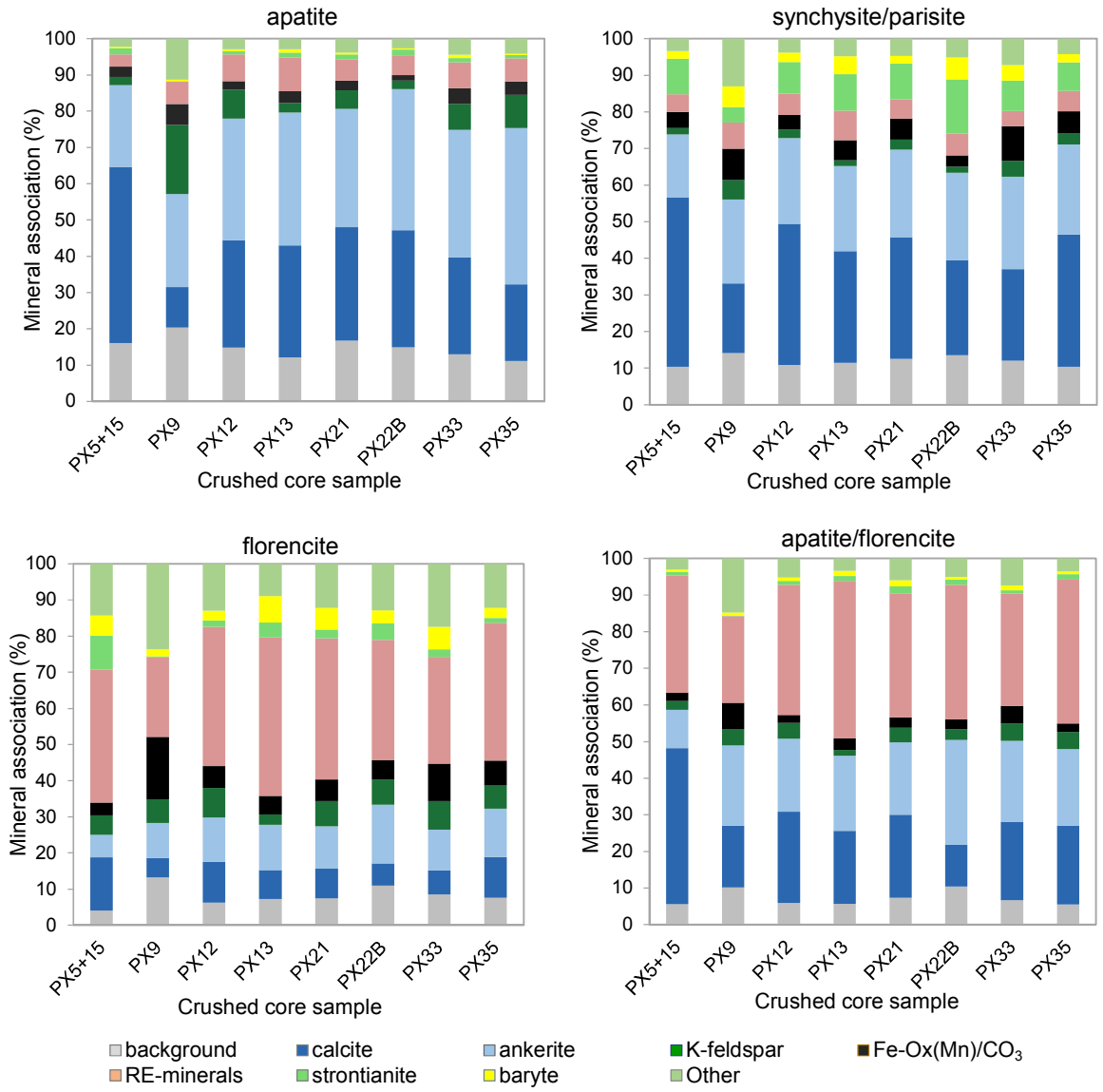

Figure 4.9: Association percentage of apatite, synchysite/parisite, florencite, and apatite/florencite valuable minerals with other gangue minerals and background within the individual crushed drill core samples P_{100} of 1700 µm as determined by QEMSCAN®. Data were measured based on the exposed perimeter % of the valuable mineral with the background (resin) and other minerals, determined by the number of pixels.

Interestingly, florencite grains appear to be mainly associated with other valuable minerals in approximately 22% to 44%, while with the background in about 4% to 13%. In terms of its association with the gangue minerals, it has approximately equal association with ankerite and calcite 6% to 16%, followed by iron oxides/carbonates 4% to 17%, and equal association with K-feldspar and muscovite 3% to 10%. The intergrown apatite/florencite grains are also mainly associated with other valuable

minerals in approximately 23% to 43%, and with the background 5% to 10%. The main gangue minerals associated with apatite/florencite are calcite 11% to 42%, followed by ankerite 10% to 28% and to a lesser extent with iron oxides/carbonates 2% to 7%.

Overall, these measurements indicate that the main valuable minerals are associated with all major, minor, and trace gangue minerals in different proportions and do not show a preferential association with one mineral due to the complex nature of the ore deposit, the average coarseness of the measured particles (1700 µm), and the fineness of the valuable minerals (50 µm for apatite and 30 µm for synchysite/parisite).

4.4.5 Average grain size of the ore-forming minerals

The average grain size of the crushed ore-forming minerals is given in Table 4.3. QEMSCAN® data indicate that the average grain size of the valuable minerals slightly varies throughout the samples. The average grain size of apatite is 50 µm, synchysite/parisite is 30 µm, florencite, apatite/florencite, bastnäsite, and zircon is 20 µm, and monazite is ≤15 µm.

It is also apparent from Table 4.3 that the average grain size of the major and minor gangue minerals slightly varies throughout the samples. The average grain size for ankerite is about 50 µm, for calcite is 60 µm, for iron oxides/carbonates is 45 µm, and for K-feldspar is 65 µm; while for other trace gangue minerals it is about <40 µm, and for very trace minerals it is approximately <20 µm.

Due to the small average grain size of the valuable minerals, it was decided to grind the crushed composite sample of P_{80} to 53 µm and 38 µm to see whether the fine grinding will significantly affect the average grain size of the minerals of interest, improve their liberation and reduce their association with the gangue minerals, and to see the percentage of fine and very fine particles generated as a result of the fine grinding.

Table 4.3: Average grain size of the ore-forming minerals in the individual crushed drill core samples P_{100} of 1700 µm as determined by QEMSCAN®.

Mineral name	PX05+15	PX09	PX12	PX13	PX21	PX22b	PX33	PX35	Average
Apatite	50.9	61.9	47.6	46.7	48.8	39.4	52.3	45.3	49.1
Florencite	20.0	25.1	20.4	19.7	21.6	24.0	19.9	21.8	21.6
Apatite/florencite	18.8	18.7	19.7	22.0	20.0	18.9	19.4	19.5	19.6
Monazite	19.3	≤15	15.2	15.7	15.4	≤15	15.9	15.5	16.1
Synchysite/parisite	27.6	32.4	27.9	31.8	34.2	30.7	30.3	28.3	30.4
Bastnäsite	19.5	18.7	≤15	19.9	25.1	17.5	≤15	≤15	20.1
Zircon	15.6	33.9	≤15	18.6	39.8	15.1	17.2	21.1	23.0
Calcite	90.9	33.2	63.1	59.4	68.3	73.7	48.2	51.3	61.0
Ankerite	47.1	40.6	51.8	53.8	56.8	76.9	41.6	48.3	52.1
Dolomite	18.4	16.6	17.3	19.9	17.1	17.4	16.5	16.0	17.4
Strontianite	43.2	54.1	37.7	48.7	54.1	48.0	45.6	40.4	46.5
K-feldspar	69.7	53.4	65.3	67.3	70.0	71.7	61.2	69.8	66.0
Plagioclase	15.9	15.9	15.7	16.4	15.9	16.1	15.8	16.2	16.0
Muscovite	32.5	35.3	31.2	61.2	35.2	32.5	32.0	36.2	37.0
Biotite	18.1	18.6	18.6	19.6	20.1	18.4	17.6	20.1	18.9
Chlorite	18.0	16.8	17.3	17.7	18.7	17.7	16.4	18.4	17.6
Kaolinite	20.7	15.4	17.1	17.9	16.0	16.2	15.2	22.0	17.6
Quartz	21.2	19.7	17.8	46.7	16.7	15.9	17.6	18.1	21.7
Fe-Ox(Mn)/CO_3	39.3	36.5	36.3	43.9	48.0	78.2	43.1	38.2	45.4
Mn Ox/CO_3	43.4	19.6	18.3	25.4	18.6	25.8	20.0	17.6	23.6
Rutile	27.4	26.7	46.7	25.0	24.1	26.4	22.6	27.6	28.3
Ilmenite	23.9	22.1	22.1	39.6	25.8	22.6	21.6	20.8	24.8
Pyrophanite	23.0	22.8	22.1	22.7	21.1	22.3	21.1	24.3	22.4
Pyrochlore	32.7	32.4	45.2	26.7	45.5	32.8	59.9	44.6	40.0
Pyrite	68.2	16.0	32.9	22.0	32.4	90.2	50.8	16.8	41.2
Sphalerite	25.9	27.5	29.1	18.3	33.7	35.4	19.1	19.5	26.1
Galena	39.1	15.9	20.1	≤15	19.0	18.3	17.7	17.1	21.0
Baryte	47.9	47.0	27.4	45.6	38.0	37.8	41.9	34.4	40.0
Fluorite	24.9	49.2	40.7	33.7	59.0	52.6	56.9	50.5	45.9
Others*	≤15	15.1	15.5	16.5	15.2	15.2	17.1	15.2	15.7

* Others include trace of any other mineral not included above as well as the edge effects.

4.4.6 Mass-size distribution of the valuable minerals

The mass-size distribution of the valuable minerals determined by QEMSCAN® is presented graphically in Figure 4.10 through 4.12. It can be seen from Figure 4.10 that approximately 50% of apatite mass occurs within the <90 µm size fraction, while about 15% to 30% of apatite mass occurs within the >250 µm size fraction in the crushed core samples of P_{100} 1700 µm. It is important to note that apatite grains seem to be coarser within PX09, while they are slightly finer within samples PX22b and PX35 compared to the other samples.

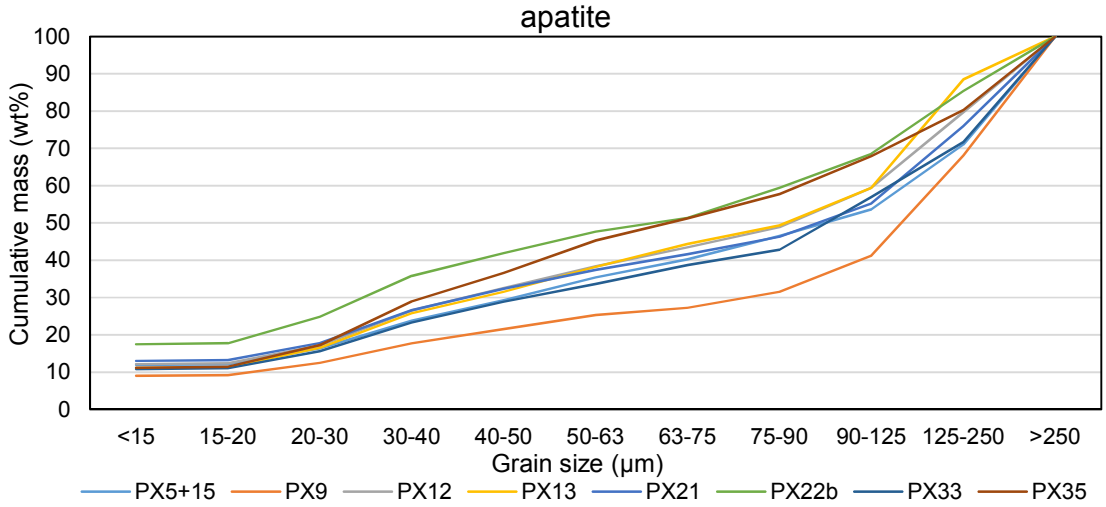

Figure 4.10: Mass-size distribution of apatite grains within the crushed drill core samples P_{100} of 1700 µm as determined by QEMSCAN®.

It can be seen from Figure 4.11 that about 50% of synchysite/parisite mass occurs within the <40 µm size fraction, while approximately 100% of its mass occurs within the <125 µm size fraction in the crushed samples P_{100} of 1700 µm. This figure also shows that synchysite/parisite grains seem to be relatively coarser within samples PX21 and PX09, as the mass percentage increases at the coarse size fractions, while they are slightly finer within samples PX05+15 and PX12, as the mass percentage increases at the finer size fractions.

Figure 4.12 shows that the mass percentage of florencite varies from one crushed drill core sample to another. The mass percentage increases as the size fraction decreases throughout samples PX33, PX05+15, PX21, PX22b, PX09, PX12, PX35, and PX13. It also indicates that approximately 100% of florencite mass occurs within the <90 µm size fraction in the crushed samples P_{100} of 1700 µm.

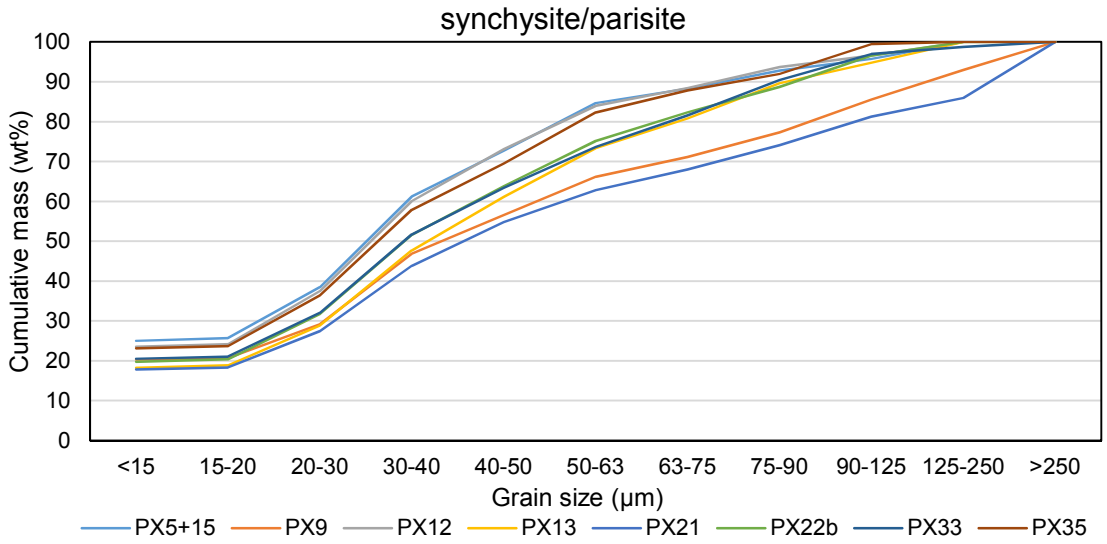

Figure 4.11: Mass-size distribution of synchysite/parisite grains within the crushed drill core samples P_{100} of 1700 µm as determined by QEMSCAN®.

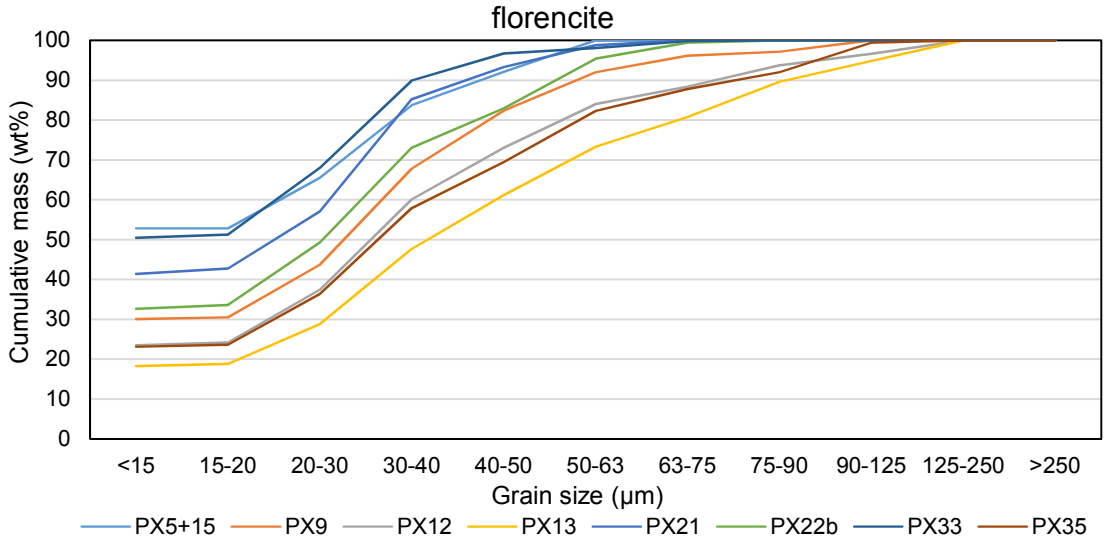

Figure 4.12: Mass-size distribution of florencite grains within the crushed drill core samples P_{100} of 1700 µm as determined by QEMSCAN®.

In summary, it can be seen from the figures above that the distribution of the valuable minerals varies between size fractions. The predominant apatite tends to be concentrated within the <250 µm size fraction, synchysite/parisite within the <75 µm size fraction, and florencite within the <50 µm size fraction. This may be attributed to the variation in the average grain size of valuable minerals within the ore deposit, as discussed in the above section.

4.5 Composite samples results

4.5.1 Modal mineralogy

The mineral abundance and distribution in the crushed composite sample P_{100} of 1700 µm (average of eight samples) and two ground composite samples P_{80} of 53 µm and 38 µm as determined by QEMSCAN®, are listed in Table 4.4.

Table 4.4 reveals that the same valuable and gangue minerals occur in the crushed and ground composite samples, with small variations in their mineral content. It is apparent from this table that the mineral content is often higher in the ground samples compared to the crushed samples, except calcite and iron oxides/carbonates, which are slightly lower. This increase in mineral content could be attributed to the measurement mode applied for these samples. The ground composite samples were measured using PMA mode with an X-ray pixel spacing of 1 µm, while the crushed samples were measured using Fieldscan image mode with a relatively higher X-ray pixel spacing of 10 µm. Therefore, PMA mode increases the measurement resolution and decreases the edge effects, which are less with smaller X-ray spacing. Furthermore, the modal mineralogy results of the crushed composite sample represent the average of the modal mineralogy of eight individual samples without measuring a new crushed composite sample.

However, the heterogeneity of carbonatite rocks creates another challenge to preparing a highly representative composite from eight coarse particle samples; variations in the modal mineralogy between the ground composite samples of 53 µm and 38 µm are very low.

It is interesting to note that very trace amounts of cassiterite, brass, Cu metal, and Cu-Fe-Mn alloy occur in the ground composite samples, and this could be attributed to contamination of the sample by the rod mill during the grinding.

Table 4.4: Quantitative modal mineralogical data (wt%) of the valuable and gangue minerals in the crushed composite sample P_{100} of 1700 µm and two ground composite samples P_{80} of 53 µm and 38 µm as determined by QEMSCAN®.

	Mineral group	Mineral name	Composite sample (µm)		
			1700	53	38
Valuable minerals	Phosphates	Apatite	3.78	5.56	5.01
		Florencite	0.32	0.60	0.64
		Apatite/florencite	0.40	0.42	0.57
		Monazite	0.01	0.01	0.02
	Carbonates	Synchysite/parisite	2.46	3.22	2.69
		Bastnäsite	0.02	0.01	0.01
	Silicates	Zircon	0.01	0.03	0.10
Gangue minerals	Carbonates	Calcite	29.28	27.04	26.61
		Ankerite	31.05	30.34	30.69
		Dolomite	0.12	0.20	0.33
		Strontianite	1.49	1.17	1.62
	Silicates	K-feldspar	9.40	9.52	9.89
		Plagioclase	0.13	0.17	0.17
		Muscovite	1.65	1.87	1.83
		Biotite	0.66	0.45	0.55
		Chlorite	0.39	0.63	0.75
		Kaolinite	0.02	0.01	0.01
		Quartz	0.17	0.14	0.16
	Oxides	Fe-Ox(Mn)/CO_3	13.73	12.69	12.16
		Mn Ox/CO_3	0.19	0.34	0.47
		Rutile	0.52	0.71	1.04
		Ilmenite	0.86	0.67	0.50
		Pyrophanite	0.32	0.33	0.44
		Pyrochlore	0.38	1.18	0.34
	Sulphides	Pyrite	0.37	0.24	0.15
		Sphalerite	0.01	<0.01	<0.01
		Galena	0.01	<0.01	<0.01
	Sulphates	Baryte	1.36	0.98	2.20
		Gypsum	0.00	0.04	0.06
	Halides	Fluorite	0.87	1.03	0.88
	Mixed	Others*	0.01	0.09	0.08

* Others include trace of spessartine and contamination: cassiterite, Zn oxide (metal galvanised), brass, Cu metal, Cu-Fe-Mn alloy, Pb-Zn-V alloy for the ground samples.

4.5.2 Liberation of the valuable minerals

The results of the liberation characteristics of the valuable minerals within the crushed composite sample P_{100} of 1700 µm and two ground composite samples P_{80} of 53 µm and 38 µm, determined by QEMSCAN®, are presented graphically in Figure 4.13. It can be clearly seen from the data in Figure 4.13 that the liberation of apatite significantly increases from 9% in the crushed composite sample of 1700 µm to 68% in the ground composite sample of 53 µm, while its liberation slightly improves to 72% in the ground composite sample of 38 µm. The percentage of middling apatite grains decreases with increasingly fine grinding. However, the percentage of locked apatite grains notably decreases from 44% to 10% as the crushed sample was ground to 53 µm; their percentage slightly increases to 13% with further fine grinding to 38 µm. This could be attributed to agglomeration of very fine gangue minerals around apatite, particularly with fine grinding, to resemble a large particle. Other possible reasons are the total number of analysed particles by QEMSCAN® and the grain size of apatite within the sample. Analysing a large number of particles increases the representation degree of the sample. It is important to note that more than 11,500 particles were measured for each sample, which is over the minimum limit for a statistically valid data set of ground samples (Pirrie and Rollinson, 2011).

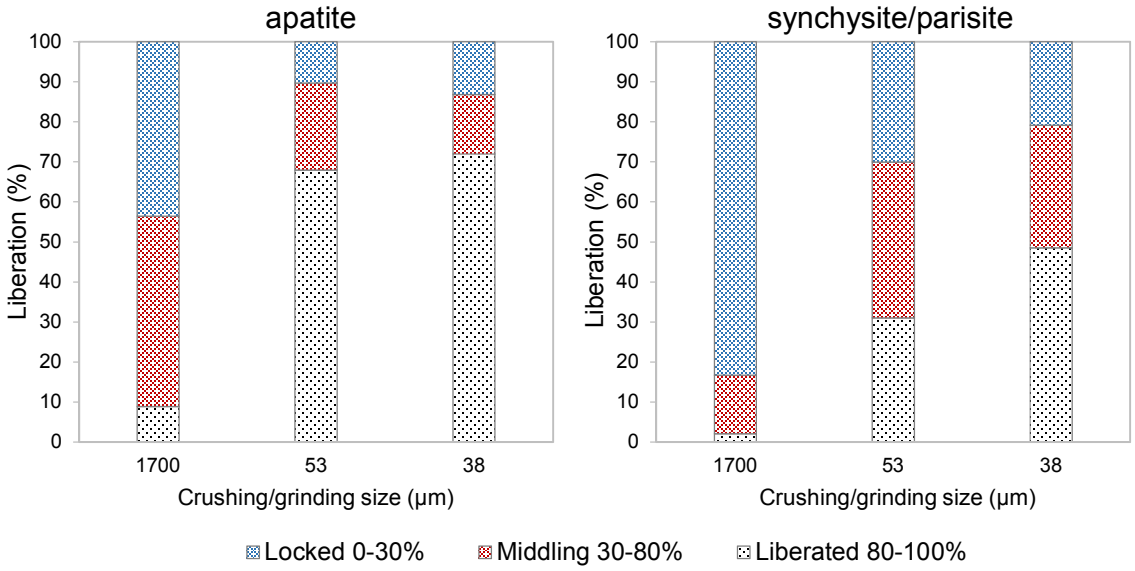

Figure 4.13: Liberation degree of apatite and synchysite/parisite in the crushed composite sample P_{100} of 1700 µm and two ground composite samples P_{80} of 53 µm and 38 µm as determined by QEMSCAN®. Data were measured based on 2D area % of the whole host particle, determined by the number of pixels.

Figure 4.13 also shows that the liberation degree of synchysite/parisite is very low in the crushed composite sample, while it increases to 31% with grinding to 53 µm and further increases to 49% with additional fine grinding to 38 µm. The middling synchysite/parisite grains decrease from 39% to 31% with increasing fine grinding from 53 µm to 38 µm. Furthermore, an improvement in the percentage of locked synchysite/parisite grains is observed. As fine grinding increases from 53 µm to 38 µm, the percentage of the locked synchysite/parisite grains decreases from 30% to 21%.

Overall, it can be inferred from the above results that there is a notable improvement in the liberation of the valuable minerals accompanied with decreasing the percentage of the middling and locked grains of these minerals, as fine grinding increases from 53 µm to 38 µm. It is also important to note that apatite grains are relatively more liberated than synchysite/parisite grains in all measured composite samples. This could be attributed to the average grain size of apatite (50 µm), which is higher than the average grain size of synchysite/parisite (30 µm), leading apatite to be more liberated than synchysite/parisite within the fine grinding samples.

4.5.3 Mineral association of the valuable minerals

The association percentages of the minerals of interest with each other and with gangue minerals within the crushed composite sample P_{100} of 1700 µm and two ground composite samples P_{80} of 53 µm and 38 µm, determined by QEMSCAN®, are illustrated in Figure 4.14. The association percentage of apatite grains with the background (resin) and valuable minerals within the crushed composite sample is 21%, while it increases to 70% and then 75% as the fine grinding increases to 53 µm and 38 µm. Apatite is also associated with the intergrown apatite/florencite in a percentage of about 5% and 10% within the composite samples of 53 µm and 38 µm, respectively. An example of apatite grains associated with intergrown apatite/florencite is illustrated in Figure 4.15. The association percentage of apatite with the predominant gangue minerals ankerite and calcite in the crushed composite is 34% and 29%, and it further decreases from 14% to 8% and from 10% to 7% within the composite samples of 53 µm and 38 µm, respectively. Also, the association of apatite with K-feldspar and iron oxides/carbonates decreases as fine grinding increases from 53 µm to 38 µm.

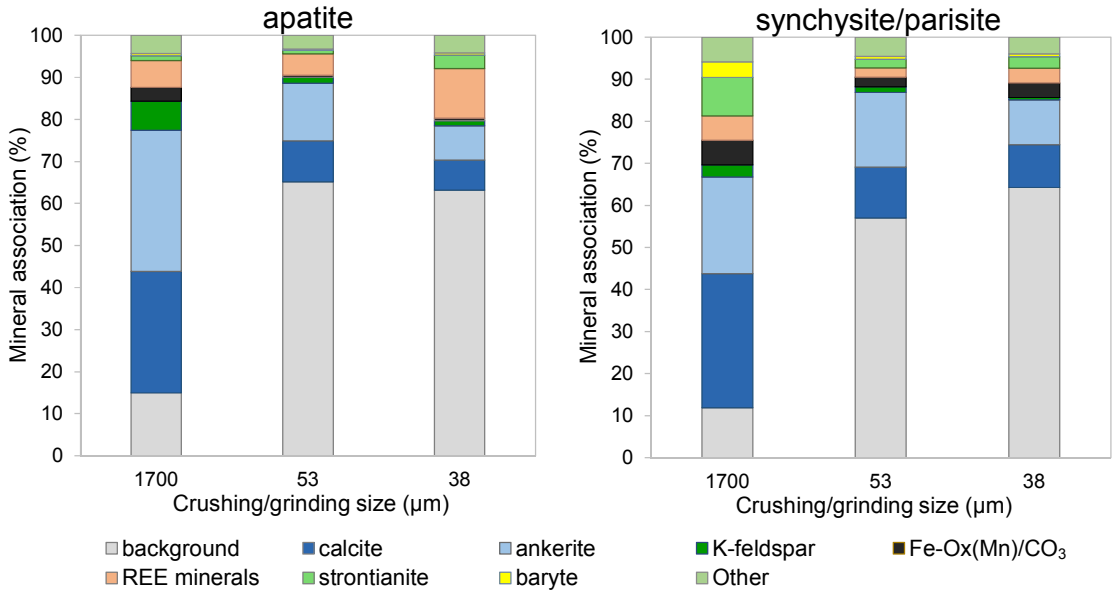

Figure 4.14: Association percentage of apatite and synchysite/parisite with other minerals and background in the crushed composite sample P_{100} of 1700 µm and two ground composite samples P_{80} of 53 µm and 38 µm as determined by QEMSCAN®. Data were measured based on the exposed perimeter % of the valuable mineral with the background (resin) and other minerals, determined by the number of pixels.

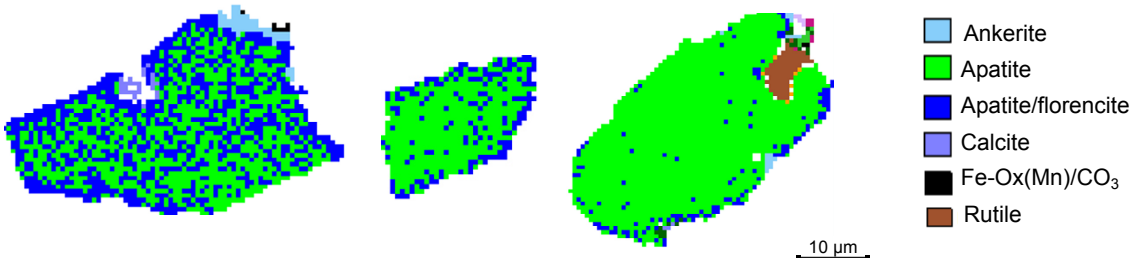

Figure 4.15: Fieldscan images illustrate the association of liberated apatite grains (green) with intergrown apatite/florencite (blue).

Figure 4.14 also shows that the association percentage of synchysite/parisite grains with the background within the crushed composite sample is 12%, while it increases to 57% and then 64% as fine grinding increases to 53 µm and 38 µm, respectively. Also, the association percentage of synchysite/parisite with the predominant gangue minerals (calcite and ankerite) in the crushed composite sample is 32% and 23%, and it decreases from 12% to 10% and from 18% to 11% within the ground composite samples of 53 µm and 38 µm, respectively. Furthermore, the association of synchysite/parisite with the minor and trace gangue minerals often decreases to some extent as fine grinding increases from 53 µm to 38 µm.

4.5.4 Average grain size of the ore-forming minerals

The average grain size of the valuable and gangue minerals in the crushed and ground composite samples is given in Table 4.5.

Table 4.5: Average grain size of the ore-forming minerals in the crushed composite sample P_{100} of 1700 µm and two ground composite samples P_{80} of 53 µm and 38 µm as determined by QEMSCAN®.

Mineral name	Composite sample (µm)		
	1700	53	38
Apatite	49.1	15.4	8.5
Florencite	21.6	8.9	5.5
Apatite/florencite	19.6	5.2	3.5
Monazite	16.1	4.4	2.9
Synchysite/parisite	30.4	9.6	5.9
Bastnäsite	20.1	4.1	2.0
Zircon	23.0	6.0	6.6
Calcite	61.0	13.0	8.3
Ankerite	52.1	11.7	8.2
Dolomite	17.4	5.8	4.7
Strontianite	46.5	10.9	10.8
K-feldspar	66.0	15.0	10.0
Plagioclase	16.0	3.3	1.9
Muscovite	37.0	7.0	3.8
Biotite	18.9	4.1	2.7
Chlorite	17.6	3.5	2.2
Kaolinite	17.6	4.3	2.2
Quartz	21.7	4.1	2.2
Fe-Ox(Mn)/CO_3	45.4	8.4	5.4
Mn Ox/CO_3	23.6	4.5	3.0
Rutile	28.3	5.8	3.6
Ilmenite	24.8	5.7	3.2
Pyrophanite	22.4	7.0	4.3
Pyrochlore	40.0	23.3	5.4
Pyrite	41.2	6.0	2.6
Sphalerite	26.1	8.7	3.0
Galena	21.0	2.9	2.5
Baryte	40.0	10.1	11.0
Gypsum	0.00	3.9	2.7
Fluorite	45.9	11.2	5.1
Others*	15.7	3.4	2.1

* Others include trace of spessartine and contamination: cassiterite, Zn oxide (metal galvanised), brass, Cu metal, Cu-Fe-Mn alloy, and Pb-Zn-V alloy.

The average grain size of the valuable minerals slightly varies throughout the crushed and ground composite samples. It can be seen from the data in Table 4.5 that the average grain size highly decreases from 49 µm to 15 µm for apatite and from 30 µm to 10 µm for synchysite/parisite with grinding the crushed composite sample to 53 µm. It is important to note, however, that fine grinding of the crushed composite sample to 53 µm and 38 µm decreases the average size of the valuable minerals, enhances the liberation degree of these minerals, and reduces their association with the gangue minerals, particularly ankerite and calcite (Figures 4.13 and 4.14). Contrary to enhancing the liberation of the valuable minerals with increasing fine grinding, it also generates an additional amount of very fine particles <10 µm. This will be further discussed in Chapter 5, Section 5.6.

4.5.5 Mass-size distribution of the valuable minerals

The mass-size distribution of the valuable minerals within the ground composite samples P_{80} of 53 µm and 38 µm, determined by QEMSCAN®, is presented graphically in Figure 4.16.

It can be seen from Figure 4.16 that the mass of valuable minerals concentrates more in the small size fractions as fine grinding increases from 53 µm to 38 µm, as expected. It is also apparent from Figure 4.16 that more than 50 wt% of apatite, synchysite/parisite, and florencite mass occurs within the <50 µm, <15 µm, and <15 µm size fractions, respectively, of the ground composite sample of 53 µm. Further grinding to 38 µm concentrates more than 80 wt% of apatite, synchysite/parisite, and florencite mass within the <40 µm, <15 µm, and <15 µm size fractions, respectively. These findings may be expected for a fine-grained deposit and suggest that increasing fine grinding concentrates the valuable minerals within very fine size fractions, and this may add more challenge to processing this complex ore deposit efficiently.

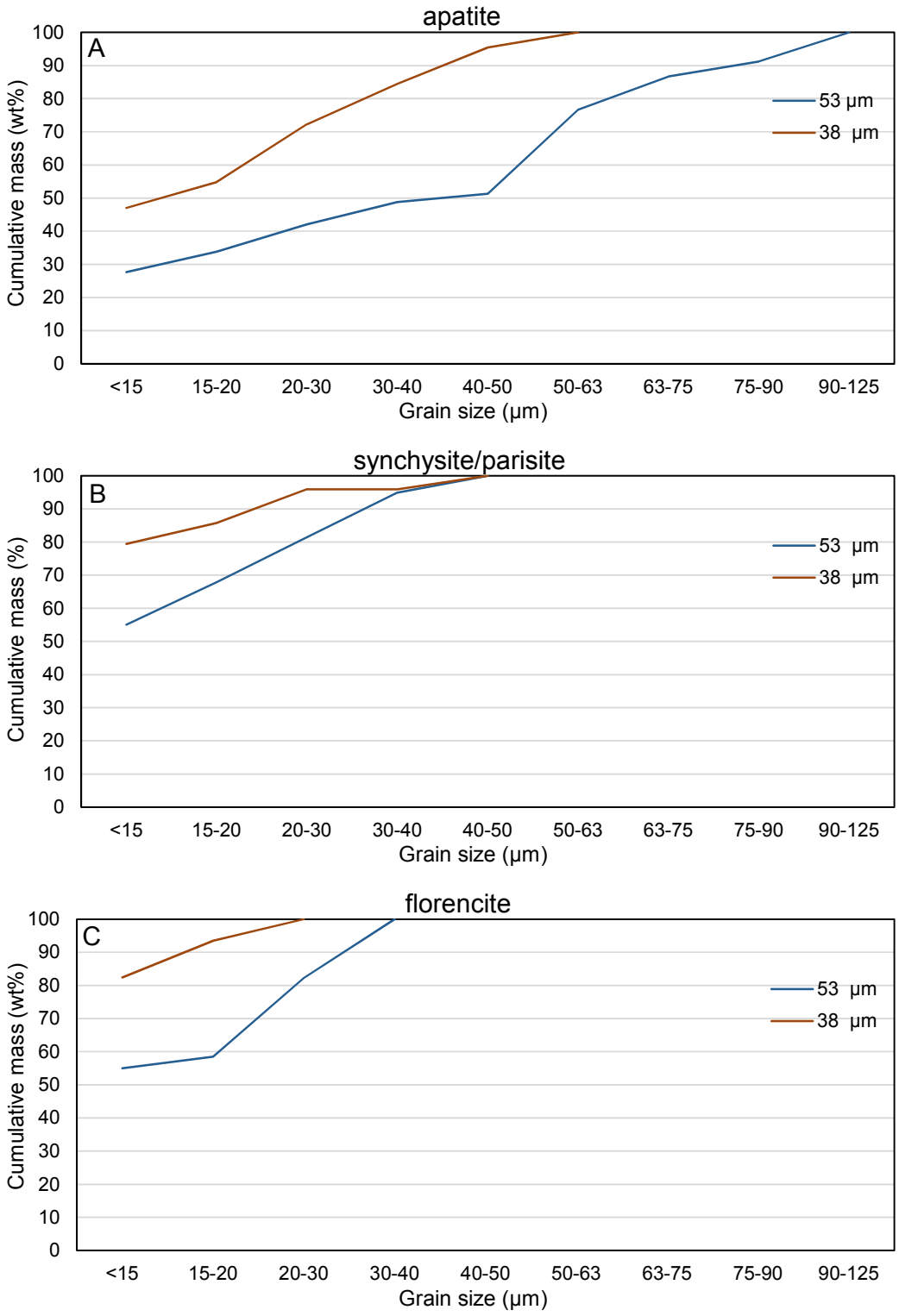

Figure 4.16: Mass-size distribution of the valuable mineral grains within the ground composite samples P_{80} of 53 µm and 38 µm. (A) apatite, (B) synchysite/parisite, and (C) florencite.

4.6 Size-by-size fractions results

4.6.1 Modal mineralogy

The mineral distribution and abundance of the size-by-size fractions of the ground composite sample P_{80} of 53 µm, including >40 µm, 30-40 µm, 20-30 µm, 10-20 µm, and <10 µm, determined by QEMSCAN®, are illustrated in Table 4.6.

This table reveals that the same valuable and gangue minerals occur in all size-by-size fraction samples, with variation and/or similarity to some extent from one size fraction to another.

Valuable minerals

The abundance of apatite in all size fractions ranges between about 2.7 wt% and 5.0 wt% (Table 4.6). It slightly decreases with decreasing the size fraction through >40 and 10-20 µm, while it increases at the <10 µm size fraction. Figure 4.17 shows that the highest abundances of normalised apatite of 24% and 23% are within the >40 µm and <10 µm size fractions, respectively.

The abundance of synchysite/parisite in all size fractions ranges between about 2.7 wt% and 3.4 wt% (Table 4.6). The highest abundance of normalised synchysite/parisite of about 26% is within the finer <10 µm fraction, while the lowest abundance of about 16% is within the coarser size >40 µm fraction; whereas it slightly varies within the middle size fractions (Figure 4.17). These variations could be due to the fine average grain size of synchysite/parisite, which is about 30 µm in the crushed samples.

Florencite is one of the least common valuable minerals in all size fractions. Its abundance ranges between about 0.3 wt% and 0.7 wt%, and it increases with decreasing the size fractions through >40 µm and >10 µm; except the size fraction of 10-20 µm, in which it slightly decreases (Table 4.6).

The abundance of apatite/florencite varies and ranges between 0.2 wt% and 0.6 wt% throughout the size fraction samples. The lowest content occurs within the >40 µm size fraction, while the highest content is within the <10 µm size fraction.

The most interesting finding is that the highest content of the valuable minerals concentrates within the finer <10 µm size fraction (Figure 4.17). This means that this deposit cannot be subjected to a desliming stage to remove very fine particles during the mineral processing tests, as this will lead to the loss of about 25% of the valuable minerals and hence the LREE and HREE.

Table 4.6: Quantitative modal mineralogical data (wt%) of the valuable and gangue minerals in the size-by-size fractions of the ground composite sample P_{80} of 53 µm as determined by QEMSCAN®.

	Mineral group	Mineral name	Size-by-size fractions (µm)				
			>40	30-40	20-30	10-20	<10
Valuable minerals	Phosphates	Apatite	4.96	4.15	3.38	3.36	4.74
		Florencite	0.28	0.42	0.61	0.49	0.70
		Apatite/florencite	0.15	0.25	0.18	0.21	0.59
		Monazite	0.01	0.02	0.01	0.01	0.01
	Carbonates	Synchysite/parisite	2.68	3.37	3.12	3.05	4.25
		Bastnäsite	0.01	0.01	0.03	0.04	0.03
	Silicates	Zircon	0.01	0.03	0.03	0.06	0.03
Gangue minerals	Carbonates	Calcite	21.99	26.16	32.97	35.79	25.62
		Ankerite	33.96	35.20	30.46	27.09	28.72
		Dolomite	0.23	0.19	0.23	0.15	0.12
		Strontianite	1.54	2.08	1.26	1.13	0.75
	Silicates	K-feldspar	9.49	5.93	10.49	9.66	8.38
		Plagioclase	0.07	0.06	0.13	0.09	0.51
		Muscovite	1.30	1.17	1.42	1.64	3.17
		Biotite	0.57	0.38	0.37	0.48	0.65
		Chlorite	0.28	0.24	0.21	0.31	1.61
		Kaolinite	0.01	0.01	0.01	0.01	0.01
		Quartz	0.18	0.20	0.25	0.24	0.43
	Oxides	Fe-Ox(Mn)/CO_3	14.77	13.29	10.03	10.91	14.56
		Mn Ox/CO_3	0.28	0.23	0.24	0.32	0.53
		Rutile	0.74	0.59	0.33	0.43	0.55
		Ilmenite	1.47	0.86	0.65	0.58	0.23
		Pyrophanite	0.86	0.67	0.42	0.44	0.29
		Pyrochlore	0.97	0.48	0.34	0.40	0.14
	Sulphides	Pyrite	0.48	0.42	0.12	0.19	0.44
		Sphalerite	0.03	0.10	0.03	0.04	0.02
		Galena	0.01	0.08	0.01	0.01	0.01
	Sulphates	Baryte	1.41	1.96	1.27	1.64	1.73
		Gypsum	0.01	0.01	0.01	0.02	0.07
	Halides	Fluorite	1.08	1.39	1.37	1.18	1.05
	Mixed	Others*	0.19	0.05	0.05	0.04	0.08

* Others include trace of spessartine and contamination: cassiterite, Zn oxide (metal galvanised), brass, Cu metal, Cu-Fe-Mn alloy, and Pb-Zn-V alloy.

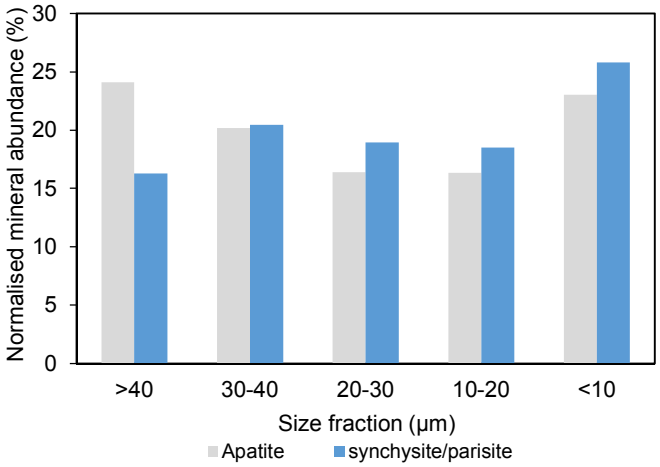

Figure 4.17: Normalised abundance of apatite and synchysite/parisite as a function of size fraction. Data were normalised based on the total content of apatite and synchysite/parisite within all size fractions.

Gangue minerals

Table 4.6 shows that the same major, minor, and trace gangue minerals occur within all size-by-size fractions as expected, with variation and/or similarity in their proportions throughout the samples.

It can be seen from Table 4.6 that the abundance of predominant gangue minerals, i.e. ankerite and calcite, varies in content from one size fraction to another. The abundance of ankerite ranges between about 27 wt% and 35 wt%, while calcite ranges between 22 wt% and 36 wt%.

Similar variations are also observed in terms of the abundance of the minor gangue minerals. Iron oxides/carbonates occur within a range between about 10 wt% and 15 wt%, K-feldspar within a range between about 6 wt% and 10 wt%, and muscovite within a range between 1 wt% and 3 wt%.

The abundance of strontianite, one of the gangue minerals preferably associated with synchysite/parisite, decreases with decreasing the size fraction of the samples; while the abundance of baryte seems slightly similar within all size fractions.

4.6.2 Liberation of the valuable minerals

The results of the liberation characteristics of the valuable minerals within the size-by-size fractions, determined by QEMSCAN®, are illustrated in Figure 4.18. The liberation of apatite gradually increases from 62% to 74% as the size fraction decreases through >40 µm and 10-20 µm, while it decreases from 74% to 62% at the <10 µm size fraction.

Also, the percentage of middling apatite decreases from 27% to 15% with decreasing the size fraction up to <10 µm. Interestingly, the locked apatite grains represent the lowest percentage compared to the liberated and middling apatite grains in all size fractions, and range between about 11% and 14%.

The decrease in the percentage of liberated apatite grains and increase in the middlings within the <10 µm size fraction could be explained due to locking or attachment to these very fine grains by gangue minerals.

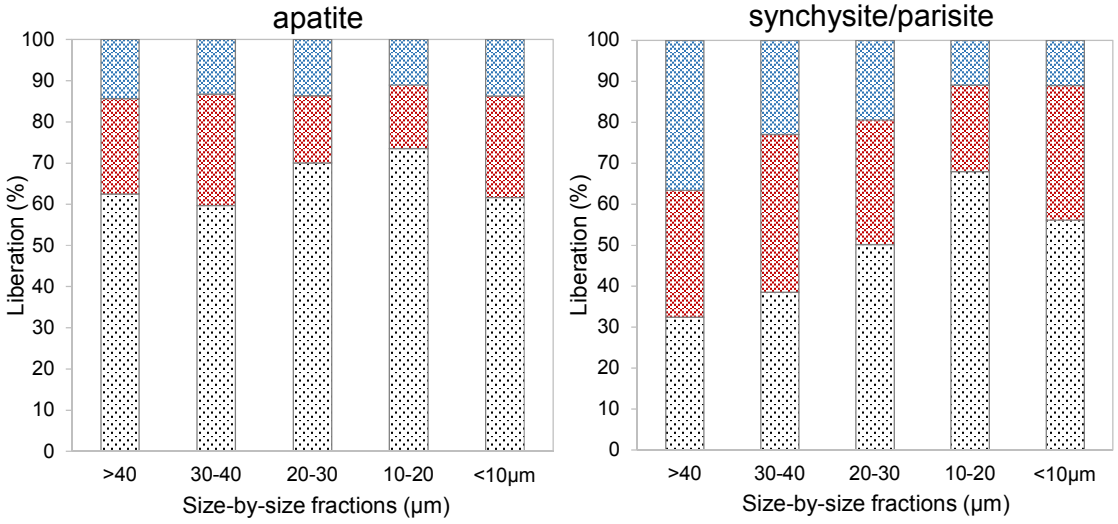

Figure 4.18: Liberation degree of apatite and synchysite/parisite in the size-by-size fractions of the ground composite sample P_{80} of 53 µm as determined by QEMSCAN®. Data were measured based on 2D area % of the whole host particle, determined by the number of pixels.

Interestingly, the liberation degree of synchysite/parisite gradually increases from 32% to 68% as the size fractions decrease through >40 and 10-20 µm, and then decreases from 68% to 56% at the <10 µm size fraction. This could be due to the same reason mentioned above about decreased apatite liberation within the same size fraction due to locking or attachment to the very fine synchysite/parisite grains by other minerals. The percentage of middling grains, except the 30-40 µm size fraction decreases with decreasing the size fractions up to <10 µm. Similarly, the locked synchysite/parisite grains decrease from 37% to 11% with decreasing the size fraction through >40 and <10 µm. The locked synchysite/parisite grains also represent, apart from the size fraction of >40 µm, the lowest percentage compared to the liberated and middling synchysite/parisite within each size fraction.

Overall, it can be inferred from the results above that there is a notable improvement in the liberation of the valuable minerals accompanied with decreasing the middling and locked grains of these minerals, as the size fractions decrease through >40 to 20 µm. On the contrary, the liberation of apatite and synchysite/parisite decreases at the <10 µm size fraction. This may be due to the agglomeration tendency of ultrafine particles within the very fine size fraction, such as <10 µm, although great effort was made to acquire dispersed particles across the polished block section by mixing the sample with graphite. Agglomeration is quite a common feature, particularly in ultrafine particles (Pascoe et al., 2007). Again, the apatite grains are relatively more liberated than synchysite/parisite grains in all size fractions. This could be due to the average size of apatite being higher than synchysite/parisite, and hence its liberation is expected to be enhanced with further grinding.

4.6.3 Mineral association of the valuable minerals

The association percentages of the valuable minerals with the gangue minerals and background within the size-by-size fractions of the ground composite sample P_{80} of 53 µm, determined by QEMSCAN®, are presented in Figure 4.19.

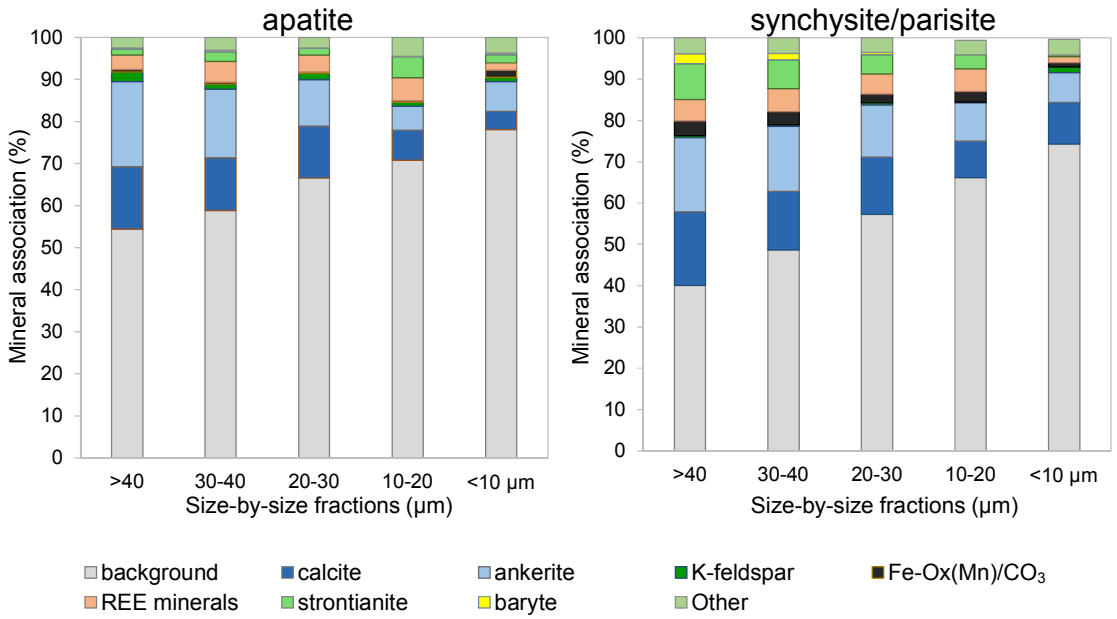

Figure 4.19: Association percentage of apatite and synchysite/parisite with other minerals and background in the size-by-size fractions of the ground composite sample P_{80} of 53 µm as determined by QEMSCAN®. Data were measured based on the exposed perimeter % of the valuable mineral with the background and other minerals, determined by the number of pixels.

Interestingly, the percentage association of apatite and synchysite/parisite grains with the background (resin) increases as the size fractions decrease through >40 µm and <10 µm. As a whole, the association of valuable minerals with the background is higher for apatite grains than synchysite/parisite grains. Also, the association of the valuable minerals with the predominant gangue minerals decreases as the size fractions decrease through >40 µm and <10 µm.

It is important to note that the association percentage of both valuable minerals, i.e. apatite and synchysite/parisite, within the size fraction of <10 µm (Figure 4.19) is higher than the liberation degree of these minerals within the same size fraction (Figure 4.18). This may be due to the association of these mineral grains with relatively large gangue minerals causing a high decrease in the liberation degree, while only having a small effect on the association percentage, as shown in Figure 4.20.

Figure 4.20: Difference between the liberation and association of the valuable minerals within the <10 µm size fraction. (A) apatite (green) and (B) synchysite/parisite (red).

4.6.4 Average grain size of the ore-forming minerals

The average grain size of the valuable and gangue minerals in the size-by-size fraction of the ground composite sample P_{80} of 53 µm is given in Table 4.7. It can be clearly seen that the average size of all minerals decreases with decreasing the size fraction, as expected. The average grain size of apatite is still higher than the average grain size of synchysite/parisite within the >40 µm, 30-40 µm, and 20-30 µm size fractions, while their averages are similar within the 10-20 µm and <10 µm size fraction (Table 4.7).

Table 4.7: Average grain size of the ore-forming minerals in the size-by-size fractions of the ground composite sample P_{80} of 53 µm as determined by QEMSCAN®.

Mineral name	Size-by-size fractions (µm)				
	>40	30-40	20-30	10-20	<10
Apatite	25.9	16.9	14.7	8.9	3.6
Florencite	9.9	9.3	10.8	6.5	3.3
Apatite/florencite	7.9	6.2	5.8	4.3	2.5
Monazite	4.6	5.0	4.3	1.6	2.9
Synchysite/parisite	16.3	13.7	12.5	8.9	3.7
Bastnäsite	5.6	3.5	4.9	2.7	2.2
Zircon	7.6	7.6	10.4	2.5	1.8
Calcite	21.8	18.2	17.0	10.9	3.9
Ankerite	22.3	17.0	14.4	9.0	3.2
Dolomite	8.4	6.3	6.9	3.3	2.3
Strontianite	22.0	17.5	15.2	8.6	4.6
K-feldspar	30.1	20.6	19.2	11.5	3.6
Plagioclase	6.7	4.1	5.7	2.2	1.7
Muscovite	13.6	10.9	9.1	5.7	2.7
Biotite	8.2	5.6	4.8	3.3	1.8
Chlorite	6.6	4.6	4.0	2.5	1.8
Kaolinite	6.8	6.3	4.4	3.5	1.7
Quartz	13.1	8.6	8.7	3.1	2.0
Fe-Ox(Mn)/CO_3	17.9	12.1	10.2	6.7	2.9
Mn Ox/CO_3	6.6	4.9	5.1	3.5	2.2
Rutile	9.0	5.9	5.6	3.1	2.3
Ilmenite	8.2	5.8	5.6	3.4	2.6
Pyrophanite	11.2	8.9	6.8	4.9	2.9
Pyrochlore	30.8	10.6	12.0	7.4	3.0
Pyrite	20.5	13.6	6.7	3.7	2.5
Sphalerite	18.4	24.9	17.4	10.9	3.6
Galena	5.5	28.6	2.9	2.5	2.4
Barite	24.6	19.1	17.3	11.0	4.5
Gypsum	5.0	3.6	3.6	2.4	1.7
Fluorite	23.1	16.4	11.6	5.3	2.5
Others*	21.2	4.7	5.2	2.8	1.6

* Others include trace of spessartine and contamination: cassiterite, Zn oxide (metal galvanised), brass, Cu metal, Cu-Fe-Mn alloy, and Pb-Zn-V alloy.

4.7 Discussion and implication of automated mineralogy in mineral processing

Characterising the quantitative modal mineralogy, liberation, mineral association, average grain size, and mass-size distribution are key parameters to improve the mineralogy understanding of the current ore deposit and identify the potential metallurgical beneficiation route to optimise recovery of the target minerals.

However, more effort was made during riffling, sample preparation, polishing, and carbon coating to ensure successful measurements and gain reliable data; the accuracy of data can be affected by other different parameters. These parameters include, for example: the heterogeneity degree of the samples and hence their representation, the agglomeration of very fine and ultrafine particles within the sample, and the total number of measured particles. For instance, there are small variations in the mineral abundance between the composite samples of 53 µm and 38 µm. Also, there is variation between the liberation and mineral association within the < 10 µm size fraction.

4.7.1 Valuable and gangue minerals

Modal mineralogy is fundamental in identifying the abundance of the valuable and gangue minerals. The QEMSCAN® measurements show that the Songwe Hill carbonatite deposit hosts about 6 wt% to 10 wt% of REE- and REE-bearing minerals, which are dominated by apatite, followed by synchysite/parisite (mainly synchysite) and minor florencite with very trace amounts of bastnäsite, monazite, and zircon. Another potential valuable mineral is pyrochlore, which comprises <0.68 wt%.

The gangue minerals in sample matrices make up between 90 wt% and 94 wt% of the modal mineralogy. They are all dominated by abundant ankerite and calcite, minor iron oxides/carbonates and K-feldspar, trace of strontianite, muscovite and baryte, and very trace amounts of fluorite, ilmenite, rutile, biotite, chlorite, pyrite, pyrophanite, Mn oxides, quartz, plagioclase, dolomite, and kaolinite.

The overall results indicate that all the analysed samples contain an economic amount of REE- and REE-bearing minerals, which are associated with the same components of gangue minerals. The only subtle variation is the degree of abundance of the valuable and gangue minerals throughout the samples.

4.7.2 REO and P_2O_5 mass balance

Based on the elemental composition of the valuable minerals determined by EPMA (see Chapter 3, Section 3.9) and their quantitative modal in the samples measured by QEMSCAN®, the REO and P_2O_5 mass balance for apatite, synchysite/parisite, and florencite can be quantitatively determined. The results of the mass balance are presented graphically in Figure 4.21.

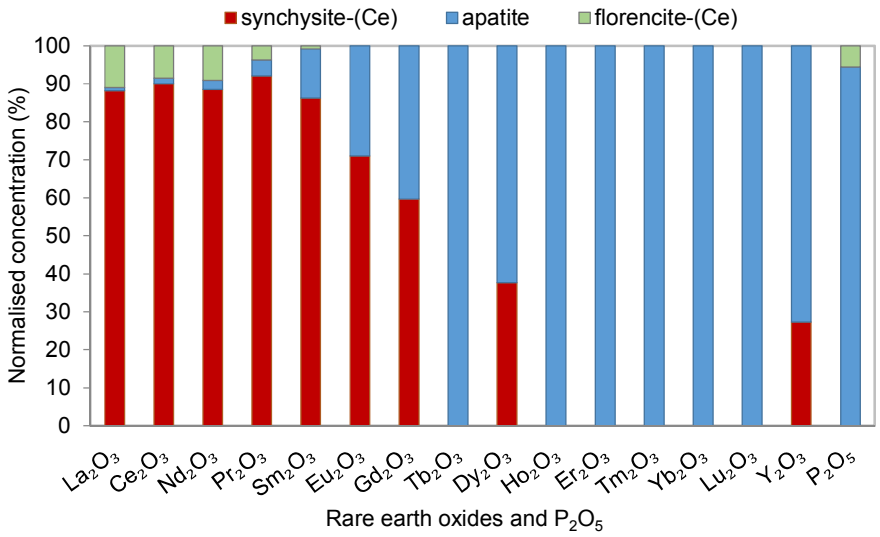

Figure 4.21: Mass balance of the REO and P_2O_5 within the valuable minerals of the Songwe Hill carbonatite samples. Data were normalised based on the total concentration of the elemental oxide within apatite, synchysite-(Ce), and florencite(Ce).

It can be seen from Figure 4.21 that P_2O_5 of 94 wt% and Y_2O_3 of 73 wt% mainly concentrate in apatite, while Ce_2O_3 of 90 wt% and La_2O_3 of 88 wt% predominantly concentrate in synchysite/parisite. Thus, P_2O_5 and Y_2O_3 can be used as proxy to track apatite and so HREE, while Ce_2O_3 and La_2O_3 can be used as proxy to track synchysite/parisite and so LREE while conducting the mineral processing tests.

4.7.3 Liberation of the valuable minerals

The liberation parameter is a key indicator for successful process separation (McIvor and Finch, 1991). The degree of liberation can be improved by grinding an ore feed sample to a finer fraction, to increase the valuable mineral liberation and decrease its association with gangue minerals, hence improving the recovery and the beneficiation process.

While the results of the crushed drill core samples reveal that all the minerals of interest are poorly liberated, the ground composite samples P_{80} of 53 µm and 38 µm

show a significant improvement in the liberation of the valuable minerals, particularly apatite. Furthermore, the size-by-size fractions of the composite sample of 53 µm show interesting results; as the size fractions decrease, the mineral liberation increases.

The QEMSCAN® measurements show that a maximum liberation degree of 50% for synchysite is achieved at the fine grinding P_{80} of 38 µm, compared to 72% of liberation degree for apatite within the same grinding size.

4.7.4 Mineral association

The mineral association results show that the valuable minerals are associated with all gangue minerals, particularly the major minerals, in different proportions and do not show a preferential association with one mineral. This is due to the complex nature of the ore deposit, the coarseness of the measured particles (1700 µm), and the fineness of the valuable minerals. Contrary to the crushed samples, the association percentage of valuable minerals with the gangues decreases with increasing fine grinding of the composite sample from 53 µm to 38 µm.

Also, the size-by-size fractions results show that the association percentage of valuable minerals with the background increases as the size fraction decreases. It also shows that the association percentage of apatite grains with the background is higher than synchysite/parisite grains.

4.7.5 Grinding

Grinding is driven by energy and grinding media consumption. Thus, it is the most energy-consuming operation in the mineral processing flowsheet, particularly for a complex and fine-grained deposit (Wills and Finch, 2016). Grinding aims to enhance the liberation of the minerals of interest and remove the associated gangue minerals.

As it can be seen from the QEMSCAN® results that the valuable minerals in the crushed drill core samples P_{100} of 1700 µm are poorly liberated. Thus, the ore deposit was first subjected to fine grinding P_{80} of 53 µm and then to P_{80} of 38 µm to see the degree of liberation within these two size fractions. While the liberation of the valuable minerals is highly enhanced with increasing the fine grinding, a substantial percentage of the valuable minerals, particularly synchysite/parisite grains, remains locked by the host gangue particles. Also, further fine grinding may be required in this case to

achieve completely liberated grains of the target minerals, which may produce extremely fine grains/particles and hence a slime problem, followed by increased cost of grinding. The slime is considered problematic in mineral processing, unless a selective grinding process is chosen to produce a relatively narrow size-range product with few oversize or ultrafine particles (Wills and Finch, 2016).

Interestingly, the results of size-by-size fractions of the ground composite P_{80} of 53 µm show a notable increase in the liberation of the valuable minerals as the size fraction decreases, particularly within the < 30 µm size fraction. These fractions of <30 µm could be processed separately, or as one product as their liberation is higher than the coarser size fractions.

4.7.6 Particle size analysis, classification and desliming

Particle size analysis, classification, and desliming of an ore deposit prior to undertaking a mineral processing test may be required to enhance the separation efficiency. The importance of particle size analysis is to determine the size range and the amount of fine, ultrafine, or even coarse particles after the grinding step. A classification step may be required to split the bulk ore sample into different products based on the particle size (e.g. fine, medium, and coarse products) or grade (e.g. high-grade and low-grade products), to be processed separately using the same or different methods. Desliming is considered a critical step because it aims to remove the ultrafine or very fine fractions from the ore sample, to increase the beneficiation process by decreasing the amount of unwanted components.

The carbonatite deposit under investigation is subjected to particle size analysis and classification using Mastersizer and Cyclosizer (see Chapter 5). The results show that proportions of the valuable minerals vary slightly from one size fraction to another, ranging between 10 wt% and 21 wt%, except the <10 µm size fraction which contains about 36 wt% of the total valuable minerals within the whole ground composite sample P_{80} of 53 µm (Figure 4.17).

Based on the automated mineralogical data for the size-by-size fractions, it can be concluded that subjecting the ore deposit to a desliming step (i.e. <10 µm) prior to conducting a processing test, will adversely affect the grade and recovery of the whole process. This can be explained as a result of losing about 23%, 26%, 28%, and 43% of apatite, synchysite/parisite, florencite, and apatite/florencite, respectively. However,

it may be possible to classify the ore deposit into different products based on the particle size, and separately process the very fine size fraction product (i.e. <10 μm).

4.7.7 Magnetic separation

Magnetic separation technique is widely used to beneficiate REE deposits, to remove the magnetic gangue minerals or concentrate the magnetic REE minerals (Krishnamurthy and Gupta, 2016).

The QEMSCAN® results showed that the current carbonatite deposit consists of a considerable amount of paramagnetic gangue minerals including ankerite (30 wt%) and iron oxides/carbonates (13 wt%). The target valuable minerals are apatite and synchysite/parisite (mainly synchysite). Apatite is a diamagnetic mineral, while there is no data available for the magnetic properties of synchysite-(Ce). Based on the magnetic properties of REE fluorcarbonate minerals, it is estimated that synchysite-(Ce) is a diamagnetic mineral (see Chapter 5). Thus, based on these results, conducting mineral processing tests using a wet high intensity magnetic separator to pre-concentrate the ore deposit is suggested for this study.

4.7.8 Froth flotation

As discussed in the literature review (see Chapter 1, Section 1.10), froth flotation has found prominence as a selective process and can achieve specific separation of chemically similar minerals, and complex and low-grade ore bodies. It also used for fine-grained ore deposits, where the average grain size to achieve high liberation is too small for efficient separation using physical processing techniques such as gravity concentration (Kelly and Spottiswood, 1982; Santana et al., 2008; Wills and Finch, 2016).

Froth flotation has been widely employed for the beneficiation of igneous phosphates due to the well-crystallised nature and inherent low porosity of apatite (Kawatra and Carlson, 2014). It is also largely applied for processing REE deposits, particularly beneficiation of bastnäsite (Krishnamurthy and Gupta, 2016). In this study, as synchysite-(Ce) is chemically similar to bastnäsite-(Ce) and both are within the same group of REE fluorcarbonates, it may be possible to process synchysite-(Ce) by froth flotation using the same chemical reagents that have been used to process bastnäsite-(Ce).

4.8 Conclusions

This chapter presented the QEMSCAN® results for the most important mineralogical parameters that need to be considered prior to conducting any mineral processing test. These quantitatively-determined mineralogical parameters included the modal mineralogy, liberation, mineral association, and average grain size based on a developed SIP for REE minerals in crushed, ground, and classified carbonatite samples. The overall results of this chapter have shown that:

- The current data highlights the importance of QEMSCAN® in determining the carbonatite ore deposit under investigation, which is a valuable tool to improve understanding of its mineralogy and the relationship between the target minerals and their matrices. Also, the generated data can be used for designing a mineral processing route and as a tool for a troubleshooting process.
- The current carbonatite deposit is considered a complex ore. This complexity is not only attributed to this deposit containing a large number of minerals, but also to the small grain size of the valuable minerals and their associations with all major, minor and even trace minerals.
- The occurrences of apatite, synchysite/parisite and florencite form about 6 wt% to 10 wt% of REE- and REE-bearing minerals in addition to the presence of very trace amounts of other economic minerals including zircon, monazite, and bastnäsite.
- P_2O_5 and Y_2O_3 can be used as proxy to track the recovery of apatite and hence the HREE, while Ce_2O_3 and La_2O_3 can be used as proxy to track the recovery of synchysite/parisite and hence the LREE during the conduction of mineral processing tests.
- While increasing the fine grinding from P_{80} 53 µm to 38 µm enhanced the liberation of the valuable minerals, these minerals are still not fully liberated. Recovering the locked grains is considered a challenge, particularly synchysite.
- Interestingly, the liberation of the size-by-size fractions gradually increased, accompanied with decreasing their association with the gangues, as the size range decreases. This could aid classification of the samples into various size ranges to be processed separately.
- Desliming the ultrafine particles of the <10 µm size fraction is not recommended as it contains about 23% of apatite and 26% of synchysite/parisite; however, it may be better to process the fine and ultrafine particles separately.

Chapter 5

Magnetic properties of REE fluorcarbonate minerals and magnetic separation experiments

5.1 Introduction

In this chapter, the results of the magnetic properties of REE fluorcarbonate minerals measured by VSM, and their elemental composition determined by EPMA are presented and discussed. The results of the particle size analysis and the magnetic separation experiments of different size fractions, experimental procedures, and process conditions are given. The possibility of pre-concentrating the valuable minerals to the non-magnetic product and rejection the paramagnetic gangue minerals to the magnetic product is discussed.

5.2 Aims

This chapter aims to:

- Investigate the use of the vibrating sample magnetometer to measure the magnetic properties and magnetic susceptibility of pure REE fluorcarbonate minerals including bastnäsite-(Ce), parisite-(Ce), and röntgenite-(Ce). It also attempts to estimate the magnetic properties of synchysite-(Ce) by comparing the elemental composition of synchysite-(Ce) in the current deposit with the measured pure minerals of the same group.
- Investigate the possibility of separating the paramagnetic gangue minerals (~43 wt%) from the diamagnetic minerals at different magnetic field strengths and size fractions P_{80} of 70 µm, 53 µm, and 38 µm in addition to the size-by-size fractions. It also focuses on experimentally determining the magnetic behaviour of synchysite within this deposit and link the QEMSCAN® measurements of the magnetic separation products to better understanding and improving the magnetic separation efficiency. Details of the methods used are given in Chapter 2.

5.3 VSM measurements

The magnetisation against applied magnetic field strength obtained from the VSM equipment for pure REE fluorcarbonate mineral samples can be seen in Figure 5.1. The slope of these correlations, which represents the magnetic susceptibility of the minerals shows that bastnäsite-(Ce), parisite-(Ce), and röntgenite-(Ce) A behave as paramagnetic minerals with a positive linear slope in decreasing order. Conversely, röntgenite-(Ce) B behaves as a diamagnetic mineral with a negative linear slope. It is important to note that the measurements of the combined röntgenite-(Ce) A and B crystals in Figure 5.2 show a negative linear slope and it seems to be in the middle between röntgenite-(Ce) A and B. This is also utilised for data validation of the VSM measurements.

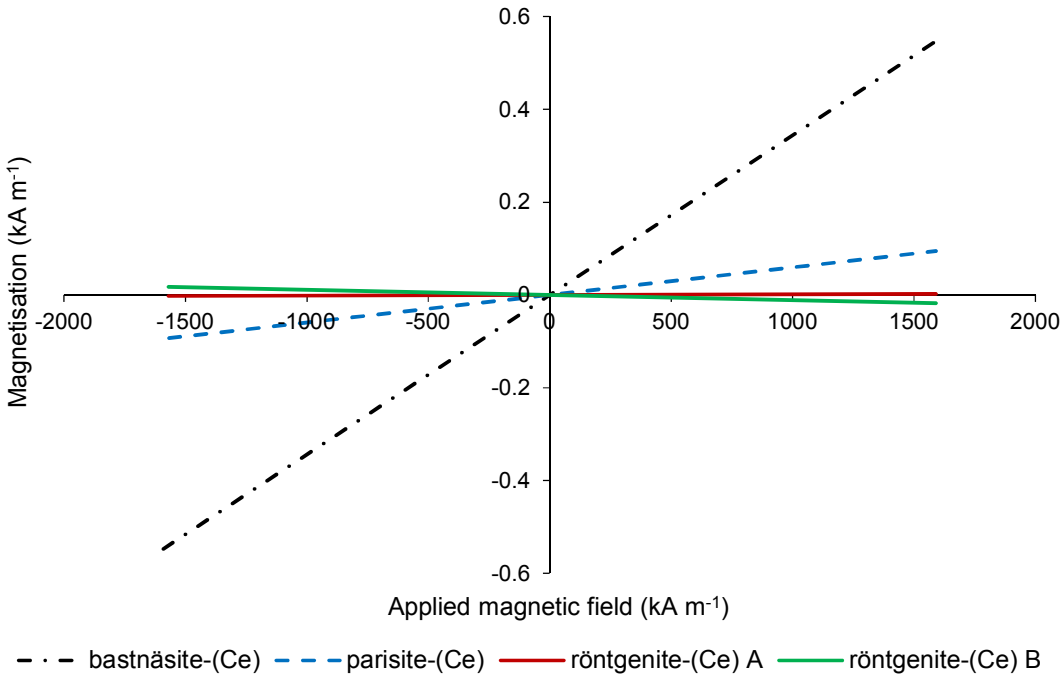

Figure 5.1: Magnetisation as a function of applied magnetic field strength showing the variations in the magnetic behaviour of pure single crystals of REE fluorcarbonate minerals including bastnäsite-(Ce), parisite-(Ce), röntgenite-(Ce) A, and röntgenite-(Ce) B as measured by VSM.

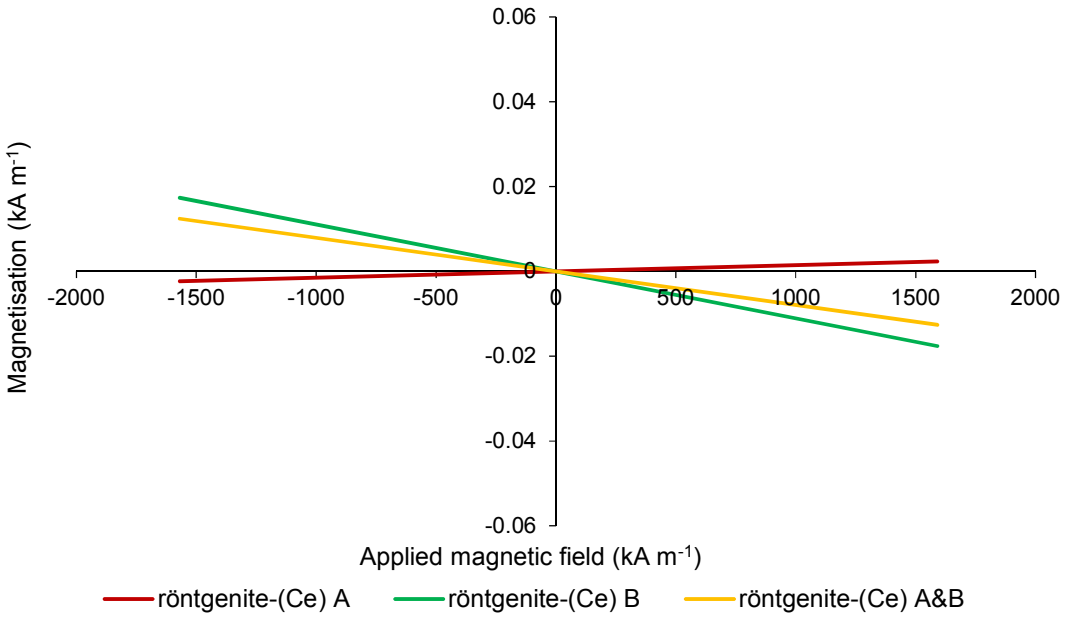

Figure 5.2: Magnetisation as a function of applied magnetic field strength showing the variations in the magnetic behaviour of röntgenite-(Ce) A and röntgenite-(Ce) B single crystals in addition to the combined crystals of röntgenite-(Ce) A & B as measured by VSM.

The dimensionless volume magnetic susceptibilities for the measured minerals by VSM are listed in Table 5.1. It is apparent that bastnäsite-(Ce) possess the highest magnetic susceptibility of 3 x 10^{-4} within the REE fluorcarbonate group. This magnetic susceptibility for bastnäsite-(Ce) is close to the reported value of 2.12 x 10^{-4} by Jordens et al. (2014). On the other hand, parisite-(Ce) possesses relatively higher magnetic susceptibility of 0.6 x 10^{-4} compared to röntgenite-(Ce) A and B. Interestingly, röntgenite-(Ce) A and B crystals exhibit positive and negative magnetic susceptibilities of 0.02 x 10^{-4} and -0.1 x 10^{-4}, respectively. It is important to note that the magnetic susceptibility of the combined röntgenite-(Ce) crystals possesses approximately an average value between röntgenite-(Ce) A and B.

Table 5.1: Summary of the VSM results showing the relative magnetitic properties and volume magnetic susceptibility of the measured REE fluorcarbonate single crystal minerals.

REE fluorcarbonate mineral	Magnetic properties [a]	Volume Magnetic susceptibility	Published data
Bastnäsite-(Ce)	Strongly paramagnetic	3.0 x 10^{-4}	2.12 x 10^{-4} [b]
Parisite-(Ce)	Moderately paramagnetic	0.6 x 10^{-4}	N/A
Röntgenite-(Ce) A	Weakly paramagnetic	0.02 x 10^{-4}	N/A
Röntgenite-(Ce) B	Diamagnetic	- 0.1 x 10^{-4}	N/A
Röntgenite-(Ce) A & B	Diamagnetic	- 0.08 x 10^{-4}	N/A

[a] The minerals are classified based on their relative magnetic susceptibilities of each other.
[b] Jordens et al. (2014).

5.4 EPMA measurements

The EPMA average results of 10 spot points each for bastnäsite-(Ce), parisite-(Ce), röntgenite-(Ce) A, and röntgenite-(Ce) B analysed by EPMA can be found in Table 5.2, while the details are given in Appendix H.

Table 5.2: Average elemental composition data (wt%) of bastnäsite-(Ce), parisite-(Ce), röntgenite-(Ce) A, and röntgenite-(Ce) B single crystal mineral as analysed by EPMA.

Oxides	Bastnäsite-(Ce)	Parisite-(Ce)	Röntgenite-(Ce) A	Röntgenite-(Ce) B
SiO_2	0.09	b.d	0.08	b.d
CaO	0.05	11.34	12.92	13.82
MnO	0.07	0.05	0.05	0.06
SrO	0.15	0.10	0.36	0.35
Y_2O_3	0.48	1.74	0.64	0.65
La_2O_3	16.19	13.83	17.20	16.76
Ce_2O_3	34.15	26.92	27.23	26.61
Pr_2O_3	4.00	3.08	2.82	2.71
Nd_2O_3	15.75	11.41	9.84	9.72
Sm_2O_3	2.13	1.86	1.32	1.39
Eu_2O_3	0.25	0.21	0.15	0.21
Gd_2O_3	1.62	1.77	1.11	1.18
Dy_2O_3	b.d	0.33	0.03	b.d
ThO_2	0.11	2.00	0.36	0.38
F meas	1.69	1.32	1.16	1.36
F calc [a]	9.08	7.40	6.01	6.03
CO_2 [a]	21.03	21.83	22.62	23.15
-O=F	3.82	3.12	2.53	2.54
Σ	101.32	100.75	100.21	100.48
TREO	74.58	61.14	60.36	59.24
CaO/TREO	0.001	0.19	0.21	0.23
CaO/Nd_2O_3	0.003	0.99	1.31	1.42
apfu on the basis of number of anions				
Si	0.003	0.000	0.011	0.000
Ca	0.002	1.113	1.955	1.946
Mn	0.002	0.004	0.005	0.006
Sr	0.003	0.005	0.029	0.026
Σ	0.011	1.123	2.001	1.978
Y	0.009	0.085	0.048	0.045
La	0.207	0.467	0.897	0.810
Ce	0.434	0.903	1.410	1.276
Pr	0.051	0.103	0.145	0.129
Nd	0.195	0.373	0.497	0.454
Sm	0.026	0.059	0.064	0.063
Eu	0.003	0.007	0.007	0.009
Gd	0.019	0.054	0.052	0.051
Dy	0.000	0.010	0.002	0.000
Th	0.001	0.042	0.011	0.012
Σ	0.944	2.101	3.134	2.849

[a] Determined by stoichiometry, b.d is below detection limit, and other analysed elements including Mg, Al, Fe, Ba, Tb, Er, Yb, Lu and U are also below detection limit.

Table 5.2 demonstrates that the measured minerals are enriched in LREE and Ce is the predominant REE. The average content of calcium oxide and TREO in bastnäsite-(Ce) is 0.05 wt% and 74.58 wt%, in parisite-(Ce) is 11.34 wt% and 61.14 wt%, in röntgenite-(Ce) A is 12.92 wt% and 60.36 wt%, and in röntgenite-(Ce) B is 13.82 wt% and 59.24 wt%, respectively. This indicates that there is a negative correlation between the average content of CaO and TREO within the measured minerals. As the CaO content increases, the TREO content decreases throughout bastnäsite-(Ce), parisite-(Ce), röntgenite-(Ce) A, and röntgenite-(Ce) B.

Also, it can be noticed from Table 5.2 that the content of MnO and FeO (which exhibits high magnetic susceptibility) is between 0.05 wt% and 0.07 wt% for MnO, while FeO content is below the detection limit of 0.069 wt% of the electron microprobe (Table 5.3) in all the measured minerals. This means that these minerals are not contaminated by the most common ferromagnetic element Fe, which would have affected the magnetisation of the measured minerals.

The concentrations of other measured elements including Mg, Al, Fe, Ba, Tb, Er, Yb, Lu, U, and in many cases Dy and Si are below detection limit of the electron microprobe (Table 5.3).

Table 5.3: The limit of detection for EPMA used in this study. The values are given in wt%.

Oxides	Detection limit	Oxides	Detection limit
F	0.090	Pr_2O_3	0.211
MgO	0.090	Nd_2O_3	0.112
Al_2O_3	0.102	Sm_2O_3	0.104
SiO_2	0.160	Eu_2O_3	0.104
CaO	0.027	Gd_2O_3	0.121
MnO	0.043	Tb_2O_3	0.138
FeO	0.069	Dy_2O_3	0.114
SrO	0.030	Er_2O_3	0.137
BaO	0.067	Yb_2O_3	0.150
Y_2O_3	0.133	Lu_2O_3	0.376
La_2O_3	0.118	ThO_2	0.064
Ce_2O_3	0.105	UO_2	0.068

There is a negative correlation between the average content of CaO and both of Nd_2O_3 and Pr_2O_3 within all the measured minerals (Figure 5.3). Also, a clear trend is seen of increasing CaO content accompanied by decreasing (Nd_2O_3 and Pr_2O_3) content throughout bastnäsite-(Ce), parisite-(Ce), röntgenite-(Ce) A, and röntgenite-(Ce) B.

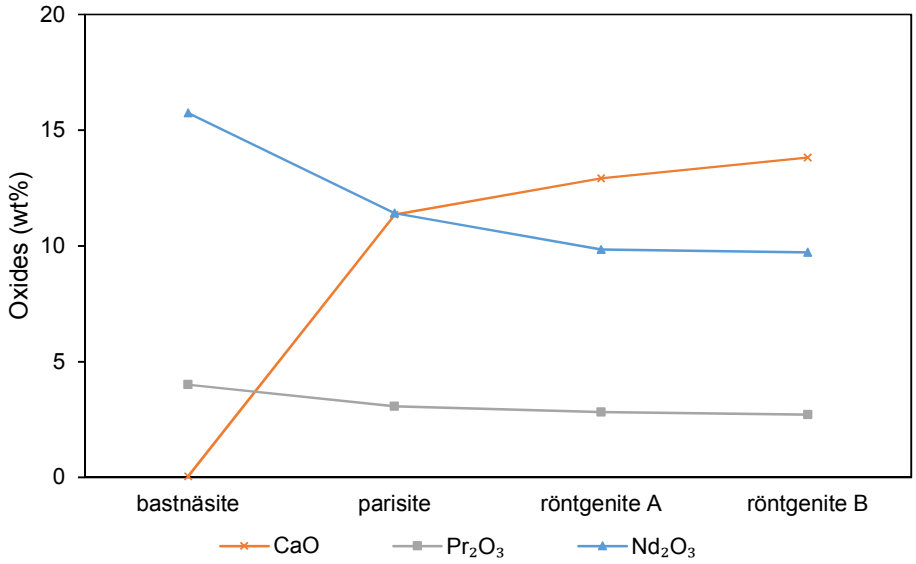

Figure 5.3: Variation in CaO, Pr_2O_3, and Nd_2O_3 contents within the measured single crystals of REE fluorcarbonate minerals. The content of the relatively higher magnetic susceptibility elements (i.e. Nd_2O_3 and Pr_2O_3) is decreased from bastnäsite through röntgenite B, while the opposite is seen for the content of the relatively lower magnetic susceptibility element (i.e. CaO).

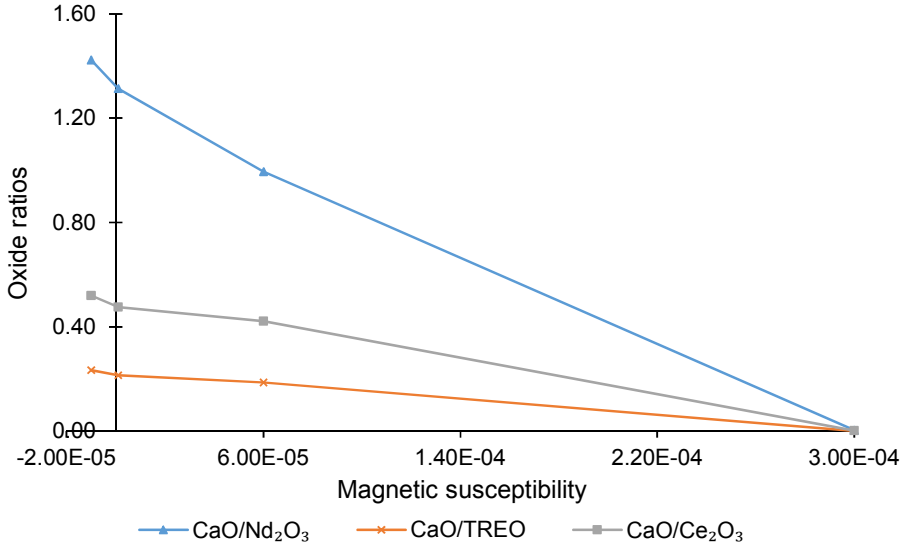

Figure 5.4: Correlation between some oxide ratios and the volume magnetic susceptibility within the measured single crystals of REE fluorcarbonate minerals. Magnetic susceptibility correlated negatively with the ratio of these oxides.

The correlation between some oxide ratios and the volume magnetic susceptibility is plotted in Figure 5.4. The magnetic susceptibility for the measured minerals decreases as the CaO/TREO, CaO/Ce_2O_3, and CaO/Nd_2O_3 ratios increase. The magnetic susceptibility being negative as the ratio of CaO/TREO, CaO/Ce_2O_3, and CaO/Nd_2O_3 increases from 0.21 to 0.23, from 0.48 to 0.52, and from 1.31 to 1.42, respectively.

Furthermore, these minerals have a layered structure and can be crystallised by the ordered stacking of at least two of three layers including (CeF), (CO_3), and (Ca) along the c-axis (Oftdel, 1931; Donnay and Donnay, 1953; Donnay, 1953; Van Landuyt and Amelinckx, 1975; Ni et al., 1993; Wang et al., 1994; Ni et al., 2000). The layer stacking feature in the REE fluorcarbonates leads to a variation in their REE:Ca ratios and crystallographic structures. Bastnäsite-(Ce) is hexagonal with no or very trace of Ca, parisite-(Ce) is monoclinic with REE:Ca of 2:1, röntgenite-(Ce) is trigonal with REE:Ca of 3:2, and synchysite-(Ce) is monoclinic with REE:Ca of 1:1 (see Chapter 1, Section 1.5). These ratios show a decrease in REE content and an increase in Ca content from bastnäsite-(Ce) through synchysite-(Ce) due to the variation in the layered structure which may have an influence on the magnetic properties of these minerals.

It is important to give an example how the variation in the elemental composition and crystallographic structure affect the magnetic behaviour of some materials. It is well-known that many iron-bearing minerals can behave as either ferromagnetic or paramagnetic materials (Rosenblum and Brownfield, 2000). For example, magnetite differs from hematite by about 3 wt% of Fe content, magnetite behaves as a ferromagnetic mineral, while hematite as a paramagnetic mineral. Also, it is reported that the minerals containing Ni, Co, Pt, REE, Mn, Co, Cr, Nb, and Ta as major components, may enhance their magnetic susceptibility (Rosenblum and Brownfield, 2000).

Another example is the magnetic behaviour of pyrrhotite. It has been reported that pyrrhotite exhibits a wide range of magnetic behaviour based on the Fe content and crystallographic structure. The hexagonal pyrrhotite Fe_9S_{10} (more Fe-rich) is antiferromagnetic mineral at the room temperature, while the monoclinic pyrrhotite Fe_7S_8 is ferrimagnetic mineral at the room temperature due to missing Fe cation in its crystal structure (Clark, 1984; Dekkers, 1989).

5.5 Magnetic properties of synchysite-(Ce)

Although the magnetic properties of synchysite (the target mineral in the deposit under study) have not measured as it was not possible to acquire a large and pure crystal, it is possible to estimate its magnetic properties by comparing the elemental composition of synchysite in this deposit with the elemental composition of the measured pure REE fluorcarbonate minerals (Table 5.4).

Table 5.4: Comparison of elemental composition data (wt%) of röntgenite-(Ce) B single crystal and synchysite-(Ce) crystals in the Songwe Hill carbonatite samples as analysed by EPMA.

Oxides	Röntgenite-(Ce) B	Synchysite-(Ce)			
	Avrg	Min	Max	Avrg	σ
CaO	13.82	14.33	18.11	16.36	0.73
MnO	0.06	b.d	0.09	0.01	0.02
FeO	b.d	b.d	2.29	0.36	0.55
SrO	0.35	b.d	2.52	0.35	0.30
BaO	b.d	b.d	2.74	0.05	0.22
Y_2O_3	0.65	b.d	2.70	0.56	0.47
La_2O_3	16.76	7.54	20.62	13.36	3.07
Ce_2O_3	26.61	18.76	28.62	24.47	1.40
Pr_2O_3	2.71	1.74	4.32	2.48	0.37
Nd_2O_3	9.72	4.23	12.97	8.29	1.93
Sm_2O_3	1.39	0.15	2.57	0.93	0.42
Eu_2O_3	0.21	b.d	0.53	0.14	0.10
Gd_2O_3	1.18	b.d	1.88	0.30	0.31
Dy_2O_3	b.d	b.d	0.49	0.16	0.11
ThO_2	0.38	0.02	2.82	0.80	0.51
UO_2	b.d	b.d	b.d	b.d	0.00
F[a]	6.03	5.47	6.11	5.89	0.11
CO_2 [a]	23.15	25.36	28.30	27.27	0.53
-O=F	2.54	2.31	2.57	2.48	0.05
Σ	100.48	92.18	104.22	99.55	1.95

[a] Determined by stoichiometry, and b.d is below detection limit.

The EPMA results in Table 5.4 show that the average Ca content in synchysite-(Ce) is higher than its average content in röntgenite-(Ce) B (diamagnetic mineral). Also, the average content of high magnetic susceptibility elements such as Ce, Pr, and Nd in synchysite-(Ce) is in general lower than their average content in röntgenite-(Ce) B. Thus, it can be estimated that synchysite-(Ce) is a diamagnetic mineral.

5.6 Particle size analysis

5.6.1 Mastersizer analysis

The results of particle size distribution determined by Malvern Mastersizer are presented in Figure 5.5. The cumulative mass percentage of the very fine particles <10 µm increases (20 wt%, 23 wt%, 32 wt% and 40 wt%) as the P_{80} decreases (100 µm, 70 µm, 53 µm and 38 µm) with fine grinding.

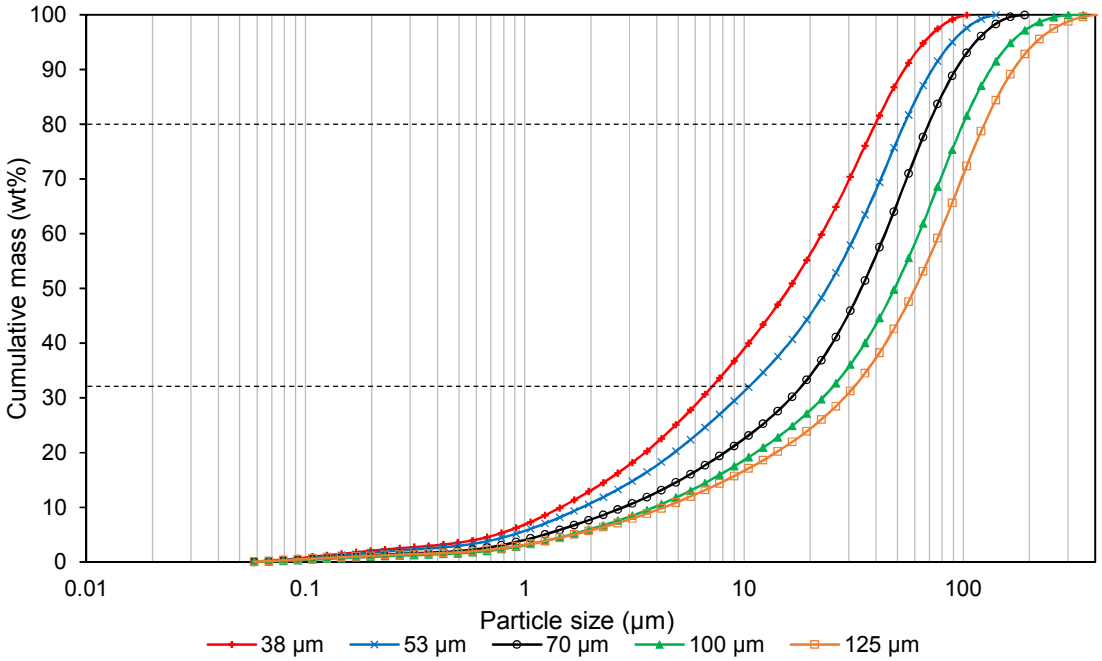

Figure 5.5: Particle size distribution of the composite sample at different grinding size as measured by Mastersizer showing the size passing fraction of P_{80} and the amount of very fine particles (<10 µm).

5.6.2 Warman Cyclosizer

The particle size distribution results of the composite sample P_{80} of 53 µm achieved by wet screening and Warman Cyclosizer are illustrated in Figure 5.6.

It is apparent from Figure 5.6 that a notable amount (~16 wt%) of the whole sample retains on the sieve 45 µm. The lowest mass percentage of about 1 wt% reports to the cyclone number 1 (41 µm) followed by cyclone number 5 with a mass percentage of 7 wt%, while the amount of materials reports to the cyclones 2, 3, and 4 is 10 wt%, 16 wt%, and 14 wt%, respectively. It is important to note that a 36 wt% of the whole sample reports to the down-stream fraction of <10 µm.

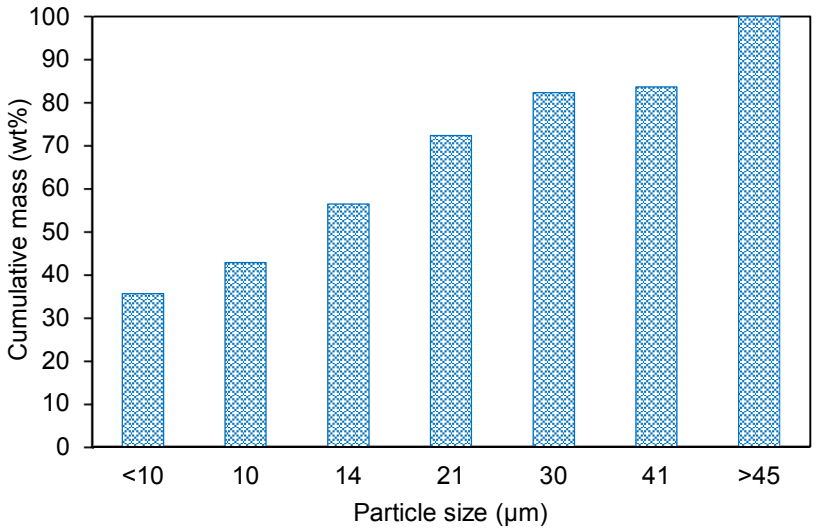

Figure 5.6: Particle size distribution of the composite sample P_{80} of 53 µm obtained by wet screening and Warman Cyclosizer. Significant amount of 36 wt% of the very fine particles (<10 µm) forms the whole composite sample.

The particle size distribution results generated by Mastersizer and Warman Cyclosizer are fairly consistent to each other and indicate that the composite sample P_{80} of 53 µm contains a high proportion of the very fine particles i.e. <10 µm.

5.7 Magnetic separation experiments of composite sample P_{80} of 70 µm

The mass recovery results of the magnetic and non-magnetic products as a function of various magnetic field strengths of the feed composite sample P_{80} of 70 µm are presented in Figure 5.7.

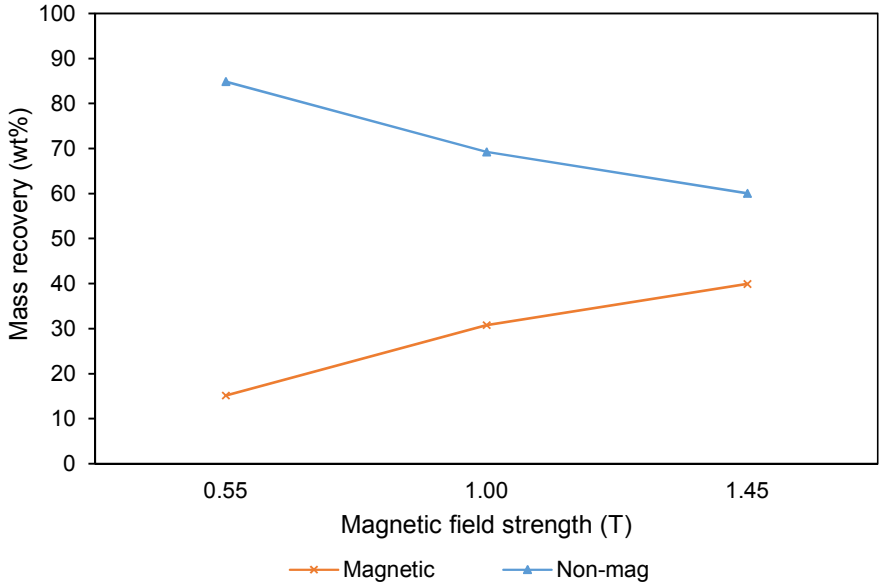

Figure 5.7: Mass recovery of the magnetic separation products as a function of magnetic field strength of the feed composite sample P_{80} of 70 µm. A gradual increase in the mass recovery of magnetic products with increasing the magnetic field strength.

It can be seen from Figure 5.7 that the mass recovery of magnetic fractions increases, while the mass recovery of non-magnetic fractions decreases, with increasing the magnetic field strength from 0.55 T through 1.45 T. This could be attributed to the presence of about 43 wt% of paramagnetic minerals, including ankerite and iron oxides/carbonates in the feed sample, in addition to the entrapment of some diamagnetic particles inside the matrix.

The efficiency of magnetic separation process as expressed by the grade and recovery of the minerals of interest in the magnetic separation products at different magnetic field strengths is shown in Table 5.5 and Figure 5.8.

Table 5.5: Grade of major and rare earth elements along with the mass recovery of the magnetic separation products of the feed composite sample P_{80} of 70 µm at different magnetic field strengths.

Sample	Mag field strength (T)	Mass (g)	Mass (%)	Grade						
				P_2O_5	SiO_2	Fe_2O_3	CaO	Y_2O_3	La_2O_3	Ce_2O_3
				(wt%)				(ppm)		
Magnetic	0.55	7.41	15.13	0.80	3.90	21.07	32.47	297	3178	3514
Non-mag	0.55	41.55	84.87	1.75	9.72	9.25	38.43	502	4562	4884
Calc. head		48.96	100.00	1.61	8.84	11.04	37.53	471	4353	4677
Magnetic	1.00	14.89	30.76	0.80	3.46	20.48	34.83	354	3788	4439
Non-mag	1.00	33.52	69.24	1.94	10.60	8.29	38.50	526	4797	5493
Calc. head		48.41	100.00	1.59	8.40	12.04	37.37	473	4487	5169
Magnetic	1.45	18.83	39.94	1.13	5.13	17.00	36.44	406	4597	4673
Non-mag	1.45	28.32	60.06	1.97	10.80	7.87	38.61	545	4820	4919
Calc. head		47.15	100.00	1.63	8.54	11.52	37.74	490	4731	4821

P_2O_5 is used as a proxy for apatite, Y_2O_3 for the HREE, Ce_2O_3 for both synchysite-(Ce) and LREE, and Fe_2O_3 for both ankerite and iron oxide/carbonate minerals.

The assay results in Table 5.5 show that the grade of P_2O_5, Y_2O_3, and Ce_2O_3 is higher in the non-magnetic fractions compared to the magnetic fractions and it gradually increases in all the products with increasing the applied magnetic field strength from 0.55 T through 1.45 T.

Conversely, the grade of Fe_2O_3, as expected, is higher in the magnetic fractions compared to the non-magnetic fractions and it gradually decreases in all the products with increasing the magnetic field strengths from 0.55 T through 1.45 T.

It can be seen from Figure 5.8 that the recovery of the target elements including P_2O_5, Y_2O_3, Ce_2O_3, and Fe_2O_3 gradually increases in the magnetic products, while it gradually decreases in the non-magnetic products with increasing the magnetic field strengths from 0.55 T through 1.45 T. The maximum rejection of 59% for Fe_2O_3 to the magnetic product is achieved at a magnetic field strength of 1.45 T. Also, at this magnetic field strength, a recovery of 72% for P_2O_5, 67% for Y_2O_3, and 61% forCe_2O_3 to the non-magnetic product is obtained.

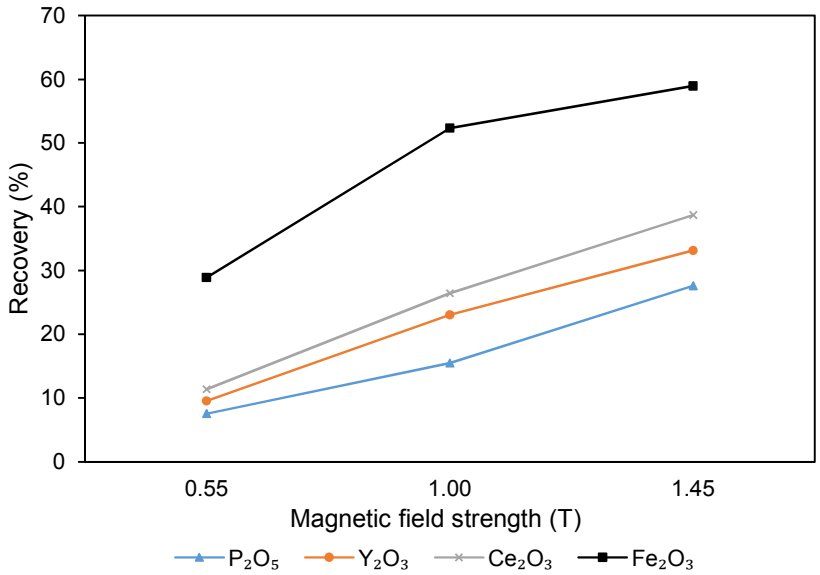

Figure 5.8: Recovery of the target components in the magnetic separation products as a function of magnetic field strengths of the feed composite sample P_{80} of 70 µm. A clear trend of increasing the recovery of all components as the magnetic field strength was increased. Note % for recovery is mass/mass.

5.8 Magnetic separation experiments of composite sample P_{80} of 53 µm

Since the previous experiments indicated that the magnetic separation was not significantly efficient with the feed sample P_{80} of 70 µm and the valuable minerals, particularly synchysite, were recovered to both the magnetic and non-magnetic products, it was important to change some parameters that could affect the magnetic separation efficiency and improve understanding of the magnetic behaviour of synchysite.

The magnetic, gravitational, and hydrodynamic drag forces are considered the most effective forces on the magnetic separation process (Oberteuffer, 1974). The effect of these forces can vary with the range of particle size in a feed sample. In the case of very large particles, the gravitational force is the most effective parameter on a

particle, while in the case of very small particles, the hydrodynamic drag force is the predominant parameter (Oberteuffer, 1974).

Three parameters were adjusted in this experiment including increasing the fine grinding to P_{80} 53 µm to improve the liberation of the valuable and gangue minerals and hence decrease the effect of the interparticles, applying high and low magnetic field strengths to determine the magnetic behaviour of synchysite, and decreasing the hydrodynamic drag force by decreasing the water flow rate from 50 mL s^{-1} to 25 mL s^{-1} in order to reduce its effect on the recovery of very fine particles.

This experiment was carried out by subjecting the feed composite sample P_{80} of 53 µm to a high magnetic field strength of 1.85 T to separate the paramagnetic minerals from diamagnetic minerals. The magnetic product was further subjected to a lower magnetic field strength of 1.0 T to investigate the possibility of recovering other diamagnetic and/or weakly paramagnetic minerals to the middling product and produce a cleaner magnetic product. Another experiment was repeated by only changing the magnetic field strength in the second stage to 0.7 T rather than 1.0 T for comparison purposes.

The mass recovery of magnetic separation products as a function of various magnetic field strengths of testwork A and B is illustrated in Figure 5.9.

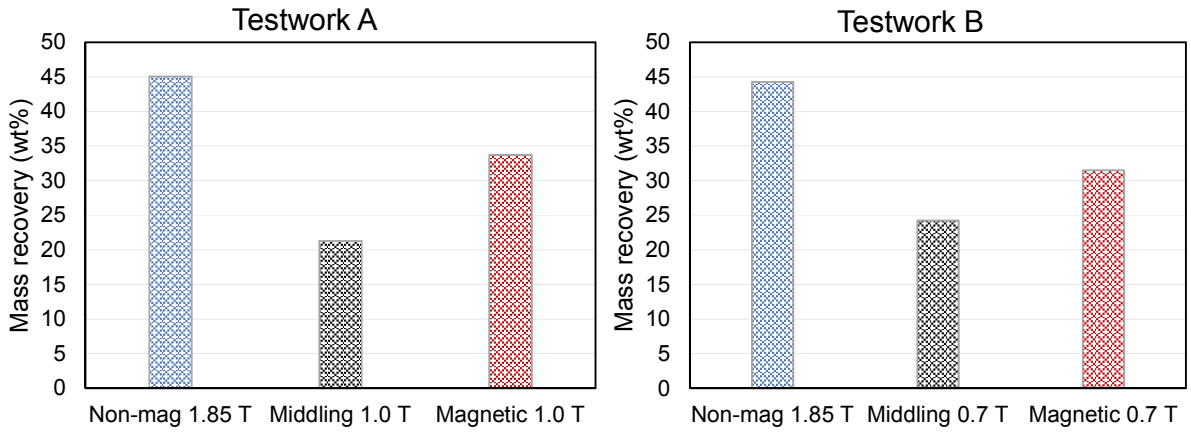

Figure 5.9: Mass recovery of the magnetic separation products of testwork A and B as a function of magnetic field strength of the feed composite sample P_{80} of 53 µm. A small variation between the different products was obtained as a result of decreasing the magnetic field strength from 1.0 T to 0.7 T.

It can be observed from Figure 5.9 that the mass recovery of non-magnetic products of 45.0 wt% and 44.2 wt% in testwork A and B, respectively is quite similar. This is due to the same initial magnetic field strength remaining constant at 1.85 T and other process conditions unchanged. The mass recovery of the magnetic fraction decreases slightly from 33.7 wt% to 31.5 wt%, while the middling fraction slightly increases from 21.2 wt% to 24.2 wt% with decreasing the applied magnetic field strength from 1.0 T to 0.7 T in testwork A and B, respectively.

The grade of the elements of interest in the magnetic separation products as a function of magnetic field strengths is shown in Table 5.6.

Table 5.6: Grade of major and rare earth elements, along with the mass recovery of magnetic separation products of the feed composite sample P_{80} of 53 µm at different magnetic field strengths.

	Sample	Mag field strength (T)	Mass (g)	Mass (%)	Grade						
					P_2O_5	SiO_2	Fe_2O_3	CaO	Y_2O_3	La_2O_3	Ce_2O_3
					(wt%)				(ppm)		
Testwork A	Non-mag	1.85	21.36	45.03	1.92	11.87	10.60	33.70	662	3681	6286
	Middling	1.0	10.09	21.27	1.68	9.07	13.12	35.16	672	4158	7440
	Magnetic	1.0	15.99	33.71	0.83	3.99	24.14	27.06	432	3102	5429
	Calc. head		47.44	100	1.50	8.62	15.70	31.77	586	3587	6242
Testwork B	Non-mag	1.85	21.13	44.25	2.00	13.24	9.63	33.86	676	3586	6246
	Middling	0.7	11.57	24.23	1.51	8.25	14.45	34.36	675	4440	8050
	Magnetic	0.7	15.05	31.52	0.76	3.77	25.33	26.78	373	2650	4736
	Calc. head		47.75	100	1.49	9.05	15.74	31.75	580	3497	6207

The elemental analysis shows expected results. The highest grade of P_2O_5 occurs in the non-magnetic products of the testwork, while it decreases in the middling products to report the least grade in the magnetic products (Table 5.6).

The grade of Ce_2O_3 is highest in the middling fractions, while its lowest grade reported in the magnetic fractions. The grade of Ce_2O_3 increases from 7440 ppm to 8050 ppm in the middling fraction of testwork A and B, respectively with decreasing the magnetic field strength from 1.0 T to 0.7 T.

The grade of Y_2O_3 is very similar in the non-magnetic and middling products of the testwork. This can be explained as Y_2O_3 is predominantly hosted by apatite and to a lesser extent by synchysite (see Chapter 4, Section 4.7.2). Table 5.6 shows that

apatite is mainly concentrated in the non-magnetic fraction, while synchysite is concentrated in the middling fractions.

Furthermore, the grade of Fe_2O_3 is higher in the magnetic products and gradually decreases in the middling and non-magnetic products as expected.

The recovery of the elements of interest in the magnetic separation products as a function of the magnetic field strengths is shown in Figure 5.10. The highest recovery of P_2O_5, Y_2O_3, and Ce_2O_3 is achieved in the non-magnetic fraction. Interestingly, the recovery of Ce_2O_3 in the middling product increases from 25% to 31% with decreasing the magnetic field strength from 1.0 T to 0.7 T of the testwork A and B, respectively. This may indicate that applying a lower magnetic field strength of 0.7 T enhances the recovery of Ce_2O_3 (synchysite) compared to a relatively higher magnetic field strength of 1.0 T in testwork A. Also, it is important to note that this change in the applied magnetic field strength leads to a small increase in the recovery of P_2O_5 from 23.8% to 24.5% in the middling products of the two testwork A and B, respectively.

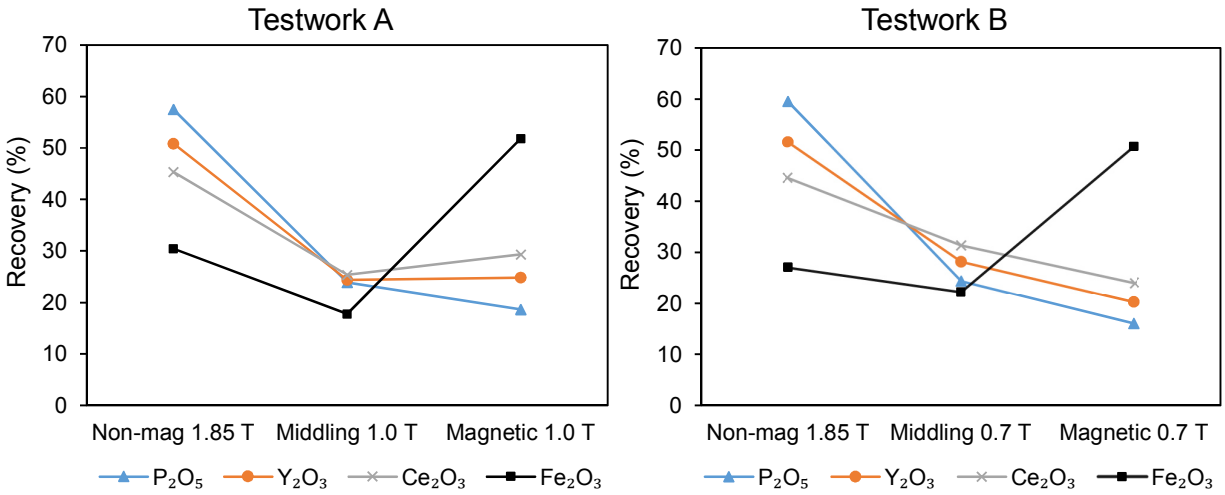

Figure 5.10: Recovery of the target components in the magnetic separation products of testwork A and B as a function of magnetic field strength of the feed composite sample P_{80} of 53 µm. The middling and magnetic products show interesting variation in the recovery of Ce_2O_3 as a result of decreasing magnetic field strength from 1.0 T to 0.7 T. Note % for recovery is mass/mass.

Overall, the best recovery for the elements of interest in the combined non-magnetic and middling products is achieved in testwork B at a lower magnetic field strength of 0.7 T with a total recovery of 84% for P_2O_5, 80% for Y_2O_3, and 76% for Ce_2O_3

compared to 81%, 75%, 70% in testwork A. Conversely, there is a similar rejection 51% of Fe_2O_3 to the magnetic fraction in both testwork A and B.

5.9 Magnetic separation experiments of composite sample P_{80} of 38 µm

It was observed in Chapter 4 that the liberation and mineral association of the valuable minerals enhanced as the fine grinding was increased from 53 µm to 38 µm. This testwork aims to determine the effect of liberation and mineral association on the separation efficiency by further grinding the composite sample to P_{80} of 38 µm and compare it with the results obtained from the ground composite sample P_{80} of 53 µm (testwork B).

The mass recovery results of processing two feed composite pulps P_{80} of 53 µm (testwork B) and 38 µm under the above separation conditions are shown in Figure 5.11. It can be observed from the graphs that the majority of the materials recovered to the non-magnetic products, followed by the magnetic products, while the lowest mass of materials recovered to the middling products. The mass recovery of non-magnetic fraction is slightly higher in the feed pulp of 38 µm compared to the feed pulp of 53 µm (testwork B), while the opposite can be seen in the magnetic fractions. The mass recovery of the middling fractions is very similar in both of the size fractions.

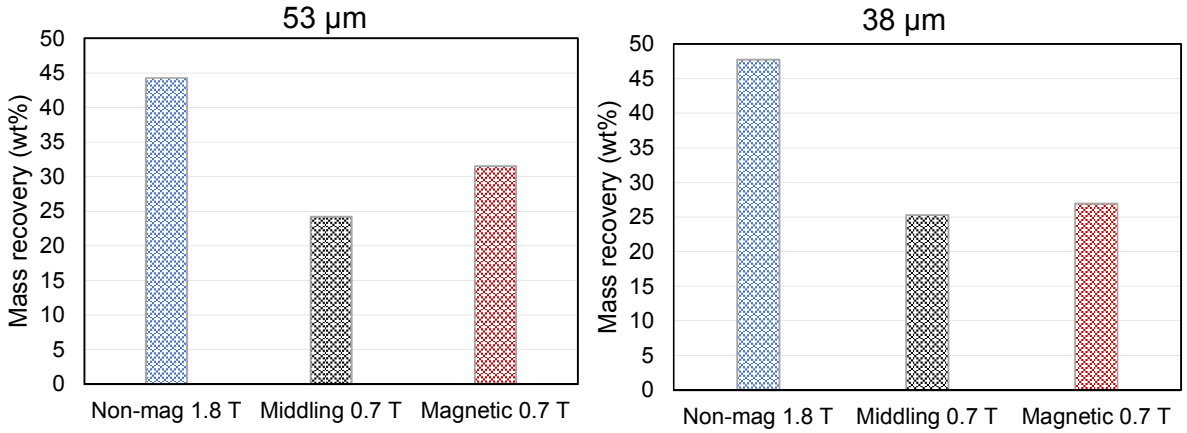

Figure 5.11: Mass recovery of the magnetic separation products as a function of magnetic field strength of different fine grinding feed composites P_{80} of 53 µm (testwork B) and 38 µm. The fine grinding to P_{80} of 38 µm did not show a significant variation between the magnetic separation products.

The grade and recovery of the elements of interest in the magnetic separation products as a function of magnetic field strengths are shown in Table 5.7 and Figure 5.12.

The head assay results of the magnetic separation products in Table 5.7 indicates that the highest grade of P_2O_5 is concentrated in the non-magnetic product and the lowest in the magnetic product. Overall, the grade of P_2O_5 is similar to the non-magnetic product of 38 µm and 53 µm (testwork B), while it is slightly lower in the middling and magnetic products of 38 µm compared to the 53 µm product (Table 5.7).

Table 5.7: Grade of major and rare earth elements along with the mass recovery of the magnetic separation products of the feed composite sample P_{80} of 38 µm.

Sample	Mag field strength (T)	Mass (g)	Mass (%)	Grade						
				P_2O_5	SiO_2	Fe_2O_3	CaO	Y_2O_3	La_2O_3	Ce_2O_3
				(wt%)				(ppm)		
Non-mag	1.8	23.16	47.76	2.04	13.57	11.02	35.64	697	4421	7520
Middling	0.7	12.26	25.28	1.34	7.94	15.24	32.39	634	4457	7660
Magnetic	0.7	13.07	26.95	0.71	3.45	26.57	24.47	347	2580	4428
Calc. head		48.49	100.00	1.51	9.42	16.28	31.81	587	3934	6722

The grade of Ce_2O_3 and La_2O_3 is higher in the middling product and slightly lower in the non-magnetic product, while the lowest grade is concentrated in the magnetic product. Interestingly, the grade of Ce_2O_3 and La_2O_3 is higher in the non-magnetic product of the feed pulp 38 µm compared to the same product in the feed pulp of 53 µm (testwork B). Conversely, the grade Ce_2O_3 and La_2O_3 is lower in the middling and magnetic products of 38 µm compared to the same products of 53 µm (Tables 5.6 and 5.7).

Also, the highest grade of Fe_2O_3 is concentrated in the magnetic product and the lowest in the non-magnetic product (Table 5.7). On the whole, the grade of Fe_2O_3 is higher in all magnetic separation products of the feed pulp 38 µm compared to those products of the feed pulp of 53 µm (testwork B). This could indicate that the fine grinding enhanced the liberation of iron oxides/carbonates and hence increased their grade in the magnetic product.

Furthermore, the highest grades for CaO and SiO_2 are concentrated in the non-magnetic product and the lowest in the magnetic product. In general, the grade of CaO and SiO_2 is slightly higher in the non-magnetic product of the 38 µm compared to the non-magnetic product of 53 µm, while they are slightly higher in the middling and magnetic products of 38 µm compared to these products of the 53 µm.

The highest recovery of the elements of interest was achieved in the non-magnetic fractions with a percentage of 65% for P_2O_5, 57% for Y_2O_3, and 53% for Ce_2O_3, while the lowest recovery was achieved in the magnetic product with a percentage of 13% for P_2O_5, 16% for Y_2O_3, and 18% for Ce_2O_3 (Figure 5.12).

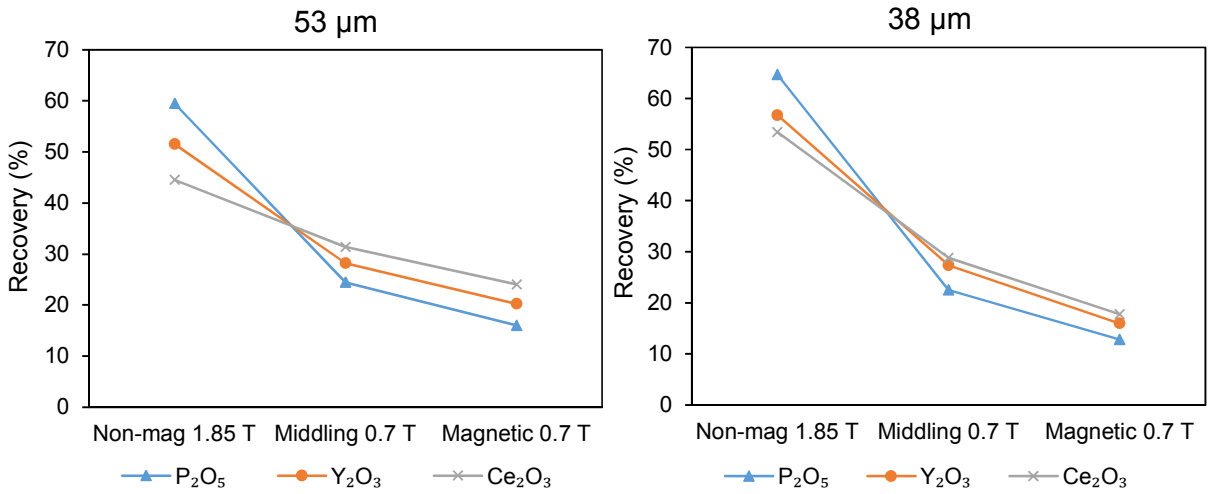

Figure 5.12: Recovery of the target components of the magnetic separation products as a function of magnetic field strength of different fine grinding feed P_{80} of 53 µm (testwork B) and 38 µm. Small variation is seen between the different products although the feed sample was ground to 38 µm. Note % for the recovery is mass/mass.

It is important to note that the recovery of these components in the non-magnetic product of the finer feed pulp of 38 µm is higher than the non-magnetic product of the feed pulp of 53 µm (testwork B), however the opposite can be seen in the middling and magnetic products. This may be due to the effect of the fine grinding on enhance the liberation degree of the valuable minerals and remove the gangue minerals, which leads to enhance the recovery of the valuable minerals.

5.10 Quantitative analysis of magnetic separation products by QEMSCAN®

5.10.1 Modal mineralogy

The distribution of the main valuable and gangue minerals of the magnetic separation products (testwork B) of the feed sample P_{80} of 53 µm as determined by QEMSCAN® is illustrated in Table 5.8. Further details are given in Appendix I.

Table 5.8: Quantitative modal mineralogical data (wt%) of the main valuable and gangue minerals in the magnetic separation products (testwork B) as determined by QEMSCAN®.

Mineral name		Feed composite sample P_{80} of 53 (µm)		
		Magnetic	Middling	Non-mag
Valuable minerals	Apatite	3.03	4.36	5.64
	Florencite	0.36	0.92	0.80
	Apatite/florencite	0.15	0.52	0.33
	Synchysite/parisite	2.78	3.33	2.96
Gangue minerals	Ankerite	47.05	26.81	20.19
	Calcite	15.80	37.12	34.15
	Fe-Ox(Mn)/CO_3	17.87	10.33	7.96
	K-feldspar	3.27	7.52	15.43

Table 5.8 reveals that there is a variation in the content of the valuable and gangue minerals throughout the magnetic separation products. The highest abundance of apatite is recovered to the non-magnetic product and it decreases in the middling product, while the least content recovered to the magnetic product. Conversely, the highest content of synchysite/parisite is recovered to the middling product and it decreases in the non-magnetic product, while the least content is recovered to the magnetic product. These results are in agreement with the results obtained from the elemental composition of the separation products of testwork B (Table 5.6).

The highest content of the predominantly paramagnetic minerals including ankerite and Iron oxide/carbonate is recovered to the magnetic product and decreases in the middling product, while the lowest content is recovered to the non-magnetic product.

Since it is difficult to track the recovery of ankerite based on the elemental composition, the calculated recovery based on the mineral content showed that about 49% of ankerite and 48% of iron oxides/carbonates are rejected to the magnetic products, in addition to approximately 17% of calcite and 11% of K-feldspar.

The fieldscan images in (Appendix I) qualitatively show that the relatively very fine particles are recovered to the non-magnetic product, the relatively small and medium particles are recovered to the middling product, and the relatively large particles are recovered to the magnetic product. Also, the images show that there are a few relatively large and liberated grains of apatite in addition to several relatively medium to small grains of synchysite/parisite are recovered to the magnetic product after a two-stage separation process. Interparticles of calcite and ankerite are commonly recovered to the middling product.

Quantitative average grain size results of the magnetic separation products are presented briefly in Table 5.9, while the details are given in Appendix I-2.

Table 5.9: Average grain size for selected valuable and gangue minerals recovered to the magnetic separation products of the feed sample P_{80} of 53 µm as determined by QEMSCAN®.

Mineral name		Feed composite sample P_{80} of 53 (µm)		
		Magnetic	Middling	Non-mag
Valuable minerals	Apatite	19.9	13.4	7.7
	Synchysite/parisite	13.3	9.7	6.0
Gangue minerals	Ankerite	19.9	10.8	5.7
	Calcite	16.0	16.5	8.2
	Fe-Ox(Mn)/CO_3	12.0	6.9	4.6
	K-feldspar	14.4	15.3	10.6

It can be seen from Table 5.9 that the relatively fine grains are recovered to the non-magnetic, medium grains to the middlings, and large grains to the magnetic product.

The recovered very fine particles to the non-magnetic product as seen in the fieldscan images (Appendix I) and the average grain size (Table 5.9) could be due to these particles being too small. An optimum size range of 5 µm to 1000 µm is considered necessary for an efficient magnetic separation (Oberteuffer, 1974). Furthermore, the modal mineralogy results showed that a notable amount of paramagnetic minerals including ankerite and iron oxide/carbonate are also recovered to the non-magnetic product although a high magnetic field strength of 1.85 T was applied. A possible explanation for this might be that these paramagnetic particles are smaller than the effective size and the hydrodynamic drag force is larger than the magnetic force, which leads these particles to pass through the matrix and fail to be trapped under the force of the slurry stream.

5.10.2 Liberation and association of valuable minerals

The results of the liberation and association percentages of the valuable minerals are presented in Figures 5.13 and 5.14, respectively.

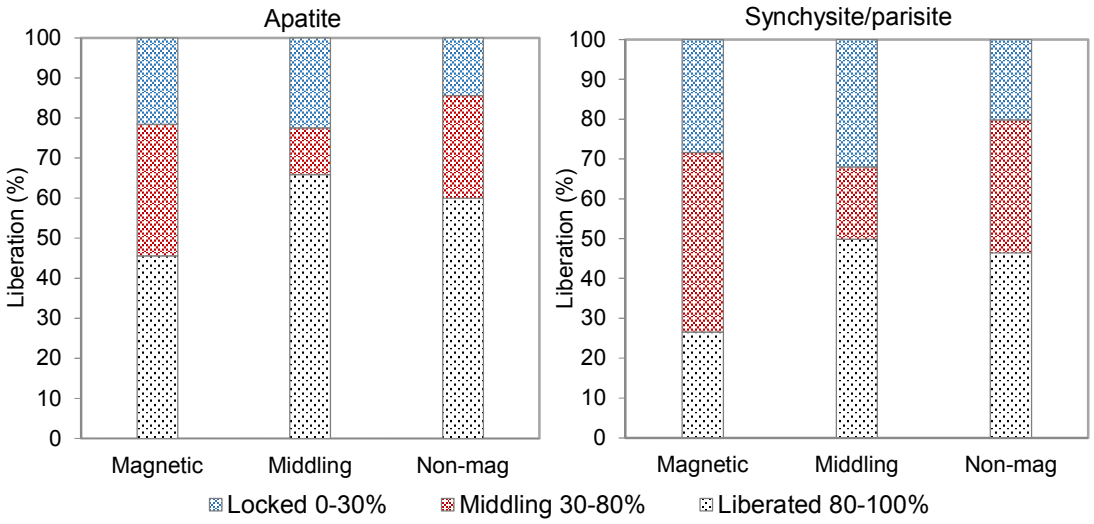

Figure 5.13: Liberation degree of apatite and synchysite/parisite in the magnetic separation products of the feed composite sample P_{80} of 53 µm as determined by QEMSCAN®. Data were measured based on 2D area % of the whole host particle, determined by the number of pixels.

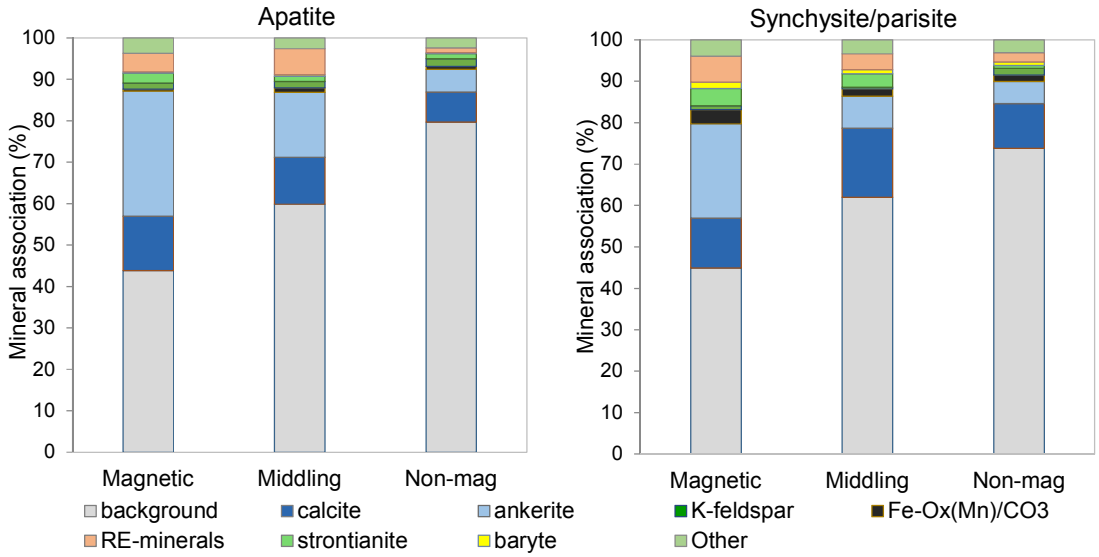

Other includes: dolomite, gypsum, pyrocholore, fluorite, Mn phases, Nb rutile, ilmenite, pyrophanite, quartz, plagioclase, biotite, muscovite, chlorite, kaolinite, pyrite, sphalarite and galena.

Figure 5.14: Association percentage of apatite and synchysite/parisite with other minerals and background in the magnetic separation products of the feed composite sample P_{80} of 53 µm as determined by QEMSCAN®. Data were measured based on the exposed perimeter % of the valuable mineral with the background (resin) and other minerals, determined by the number of pixels.

It can be seen from Figure 5.13 that the liberation degree of the valuable minerals varies between the different magnetic separation products. In general, the liberation of apatite grains is higher than synchysite/parisite grains. The highest liberated apatite of 66% and synchysite/parisite of 50% were recovered to the middling product, the slightly lower liberated grains of 60% and 46% were recovered to the non-magnetic product, and the least liberated grains of 46% and 27% were recovered to the magnetic product.

Conversely, Figure 5.14 shows that apatite grains that highly associated with the background (resin) of 80% and less with ankerite of 5% were recovered to the non-magnetic product, while apatite grains that less associated with the background of 44% and highly with ankerite of 30% were recovered to the magnetic product. In the same way, synchysite/parisite grains that highly associated with the background of 74% and less with ankerite of 5% were recovered to the non-magnetic product, while synchysite/parisite grains that less associated with the background of 45% and highly with ankerite of 23% were recovered to the magnetic.

This indicates that the least liberated apatite and synchysite/parisite grains, which are mainly associated with ankerite were recovered to the magnetic product, while the highest liberated grains and less associated with ankerite were recovered to the non-magnetic and middling products.

The separation efficiency of apatite and synchysite/parisite varies between the magnetic separation products. Apatite is mainly recovered to the non-magnetic product and to a lesser extent to the middling product. Apatite is a diamagnetic mineral, but 3.03 wt% was recovered to the magnetic product for which the following explaination is given:

Firstly, the relatively large and liberated particles of apatite in the magnetic product as shown in the fieldscan images (see Appendix I) and the liberation profile in Figure 5.13 may have trapped inside the matrix of 1 mm even though a two-stage separation process was applied. Secondly, the percentage of the non-liberated apatite grains is about 55% in the magnetic products (Figure 5.13), in addition to apatite associated with ankerite (paramagnetic mineral) with a percentage of 30% (Figure 5.14), which could lead to recover apatite to the magnetic product.

Conversly, synchysite/parisite was primarily recovered to the middling product followed by the non-magnetic product and to a lesser extent to the magnetic product. This could be attributed to the magnetic properties of synchysite, which may behave as a weakly paramagnetic to a diamagnetic mineral.

A number of other reasons could cause synchysite/parisite to be recovered to the magnetic product. Firstly, the liberation degree of synchysite/parisite is lower in the magnetic product compared to the middling and non-magnetic products (Figure 5.13). Secondly, the percentage of synchysite/parisite in association with ankerite is higher in the magnetic product compared to the middling and non-magnetic products (Figure 5.14). Thirdly, synchysite/parisite grains may have become trapped onto the other particles inside the matrix whether they are liberated or associated with other diamagnetic minerals.

5.11 Magnetic separation experiments of size-by-size fractions

The QEMSCAN® results of the size-by-size fractions (see Chapter 4, Section 4.6) showed that there is a notable increase in the liberation of the valuable minerals and decrease in their association with gangue minerals particularly the size fractions of 20-30 µm, 10-20 µm, and <10 µm. The magnetic separation experiments in this section aim to determine the effect of particle size distribution and liberation on the separation of the valuable minerals, apatite and synchysite to the non-magnetic and middling products, and the gangue minerals, ankerite and iron oxides/carbonates, to the magnetic product.

5.11.1 Mass recovery

The mass recovery of the magnetic separation products as a function of the size-by-size fraction is illustrated in Figure 5.15, while the details of the experiments can be found in Appendix J.

It can be seen from Figure 5.15 that as the size fraction decreases, the mass recovery of the magnetic products decreases from 45 wt% to 7 wt% and the non-magnetic products increases from 29 wt% to 70 wt%. The middling products remains relatively constant at between 23 wt% and 25 wt% with the exception of the 20-30 µm size fraction, which slightly increases to 30 wt%. The increase in the percentage of the materials recovered to the non-magnetic product at the size fraction of <10 µm could be due to the small size of the particles, which passed easily through the matrix even though a high magnetic field strength of 1.85 T was applied.

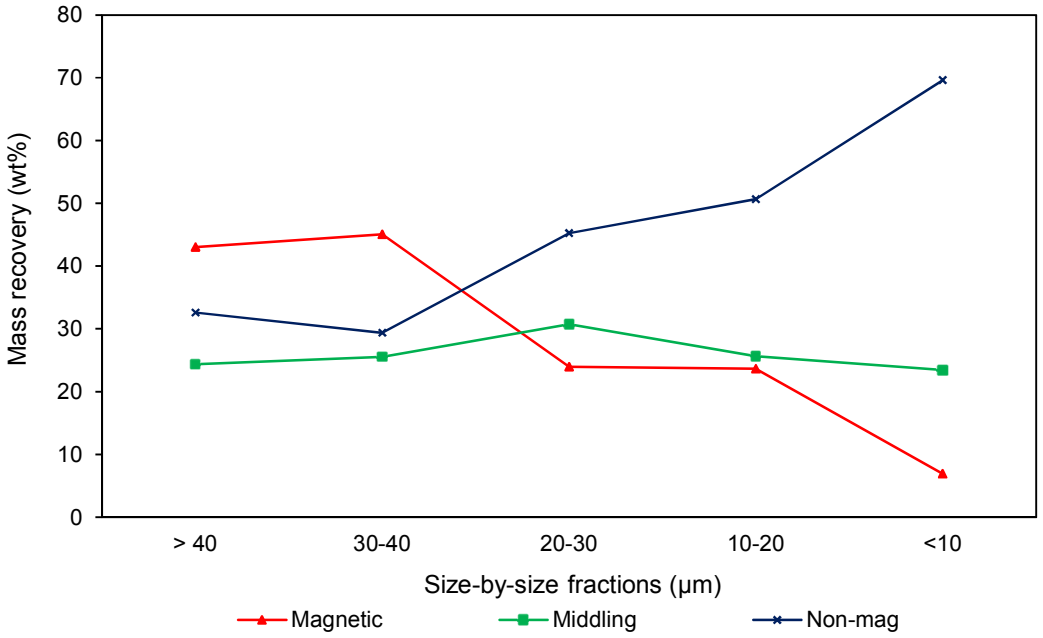

Figure 5.15: Mass recovery of the magnetic separation products as a function of size-by-size fraction. It shows an increase in the mass recovery of the non-magnetic products and a decrease in the mass recovery of the magnetic products, whilst there is a small change in the middling products.

5.11.2 Grade and recovery of P_2O_5

The grade and recovery of P_2O_5 in the magnetic separation products as a function of size-by-size fraction are shown in Figure 5.16.

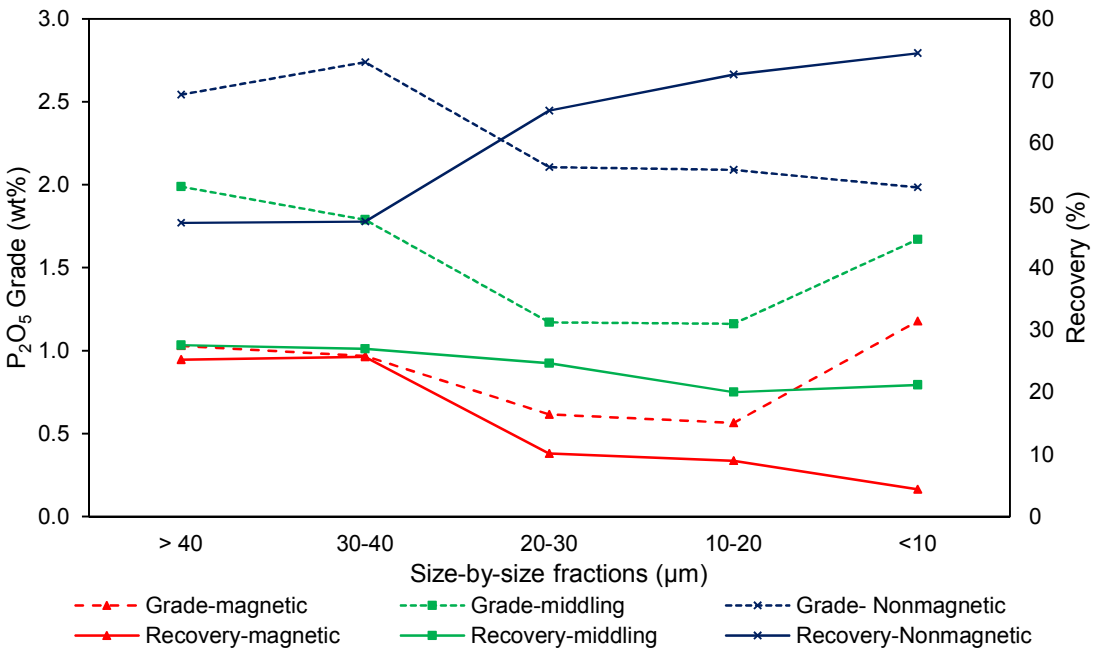

Figure 5.16: Grade and recovery of P_2O_5 in the magnetic separation products as a function of size-by-size fraction. P_2O_5 mainly recovered to the non-magnetic products, and its recovery increased as the size fraction was decreased.

It can be seen from Figure 5.16 that P_2O_5 tends to be mainly concentrated in the non-magnetic products and to a lesser extent in the middling products, while the lowest grade reported to the magnetic products. Also, the highest grade of P_2O_5 of 2.47 wt% was achieved at the size fraction of 30-40 µm providing the lowest recovery of 47% in the overall non-magnetic products.

Furthermore, the recovery of P_2O_5 gradually increases from 47% to 74% in the non-magnetic products as the size-by-size fraction decreases. Conversely, its recovery gradually decreases, particularly in the magnetic products from 25% to 4% as the size-by-size fraction decreases from >40 µm to <10 µm.

5.11.3 Grade and recovery of Ce_2O_3

The grade and recovery of Ce_2O_3 in the magnetic separation products as a function of the size-by-size fraction are shown in Figure 5.17.

The grade of Ce_2O_3 is preferentially concentrated in the middling products, while the grade is comparatively lower in the non-magnetic products (except for the size fraction of <10 µm) and to a lesser extent in the magnetic products. There is a gradual increase in the grade of Ce_2O_3 in all the products as the size range decreases from 20-30 µm to <10 µm (Figure 5.17).

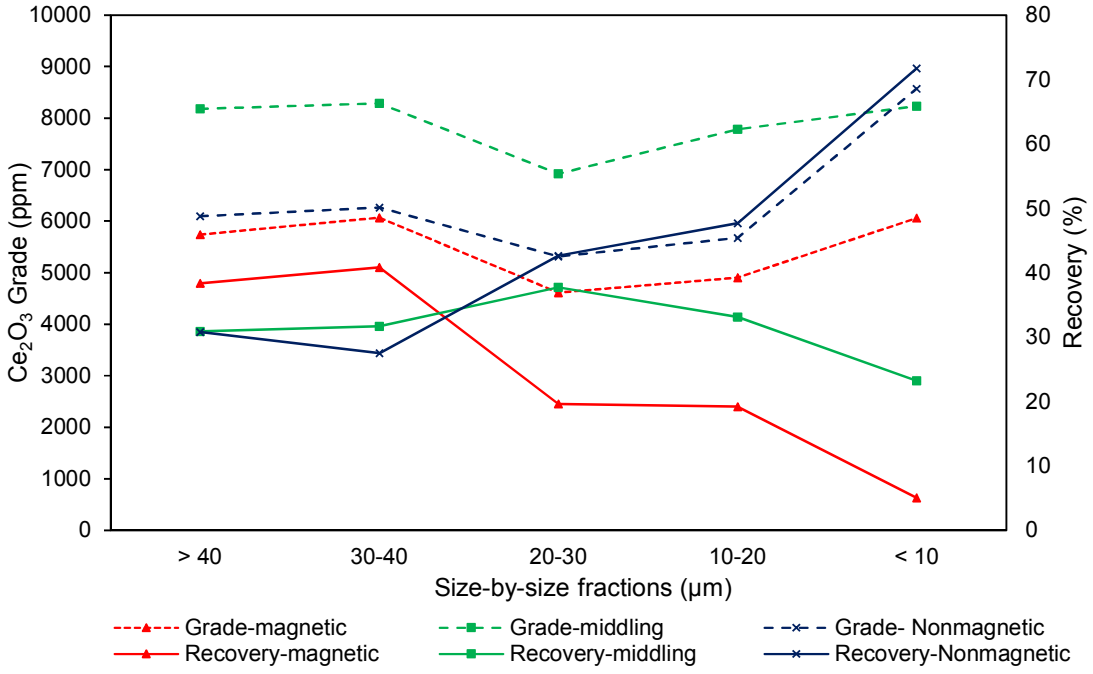

Figure 5.17: Grade and recovery of Ce_2O_3 in the magnetic separation products as a function of size-by-size fraction. A clear trend of increasing grade and recovery of Ce_2O_3 in the non-magnetic products as the size fraction was decreased from 20-30 µm to <10 µm.

Also, Figure 5.17 shows that the recovery of Ce_2O_3 is higher in the magnetic products than the non-magnetic and middling products of the size fractions >40 μm and 30-40 μm. Conversely, its recovery greatly increases from 27% to 72% in the non-magnetic products as the size fraction decreases from 20-30 μm to <10 μm, while the recovery significantly decreases from 41% to 5% in the magnetic products at the same range of size fractions. Furthermore, the recovery of Ce_2O_3 decreases from 38% to 23% in the middling product as the size fractions decreases from 20-30 μm to <10 μm.

Both of the grade and recovery of Ce_2O_3 in the non-magnetic products increase from 5315 ppm to 8573 ppm and from 43% to 72%, respectively as the size range decreases from 20-30 μm to <10 μm. Conversely, only the grade of Ce_2O_3 increases in the middling and magnetic products accompanied by decreasing the recovery within the same range of size fractions.

It is implied, based only on the grade of Ce_2O_3, that synchysite-(Ce) is a weakly paramagnetic mineral as the grade is higher in the middling products of all size fractions with the exception of the <10 μm size fraction. It can be indicated based on the grade and recovery of Ce_2O_3 at the size fractions from 20-30 μm to <10 μm that synchysite-(Ce) is a diamagnetic mineral due to the Ce_2O_3 grade and recovery increasing together.

The QEMSCAN® measurements (see Chapter 4, see Section 4.6.2) showed that at smaller size fractions (20-30 μm, 10-20 μm, and <10 μm), the liberation of synchysite-(Ce) increased (from 50%, 68%, to 56%). Also, the association of synchysite-(Ce) with the background increased (gangue minerals decreased) to 57% (20-30 μm), 66% (10-20 μm), and 74% (<10 μm). The variations between the liberation and association percentages of the size fraction of <10 μm have been discussed in Chapter 4 (see Section 4.6.3). Thus, the increase in the liberation of synchysite-(Ce) may enhance both the grade and recovery in the non-magnetic products at this range of size fractions.

Furthermore, the EPMA results (see Chapter 3, Section 3.9) indicated that the elemental composition of synchysite-(Ce) in the Songwe Hill carbonatite is highly varied throughout the measured minerals as can be seen from the minimum and maximum values. Comparison between these results and the elemental composition

of the pure minerals (see Section 5.5) indicated that synchysite-(Ce) may behave as a weakly paramagnetic to a diamagnetic mineral.

5.11.4 Grade and recovery of Fe_2O_3

The results of the grade and recovery of Fe_2O_3 in the magnetic separation products as a function of the size-by-size fraction are illustrated in Figure 5.18.

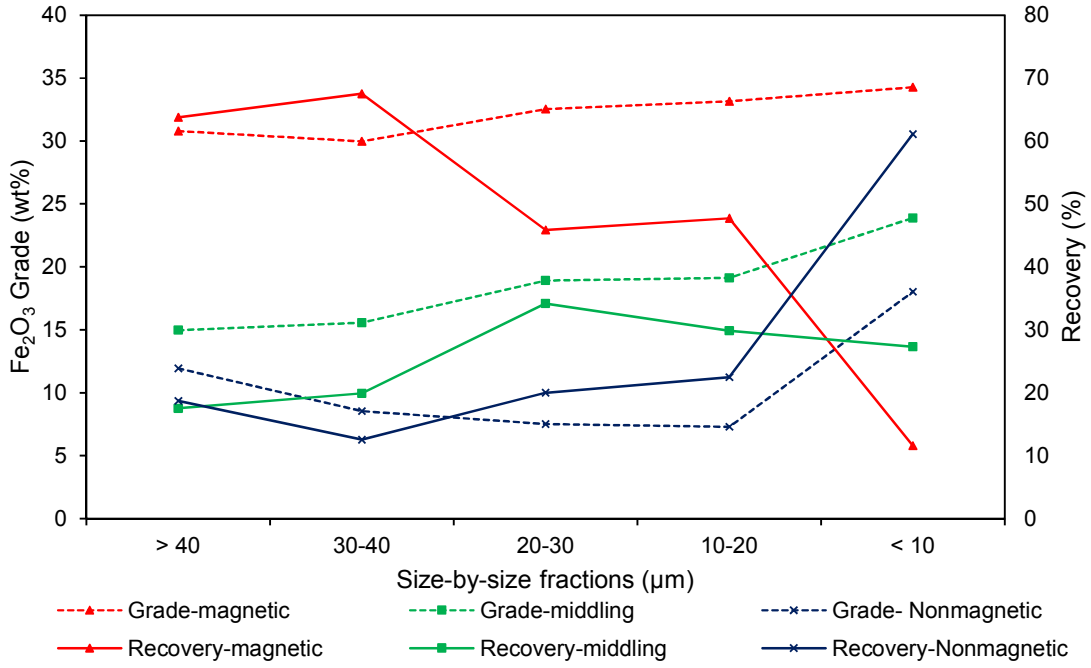

Figure 5.18: Grade and recovery of Fe_2O_3 in the magnetic separation products as a function of size-by-size fraction. Fe_2O_3 mainly concentrated in the magnetic products and its grade gradually increased as the size fraction was decreased.

It is apparent that the grade of Fe_2O_3 tends to be mainly concentrated in the magnetic products, followed by the middling products. It shows that there is a gradual increase from about 31 wt% to 34 wt% in the magnetic products, and from 15 wt% to 24 wt% in the middling products as the size fraction decreases from >40 µm to <10 µm. Conversely, the grade decreases from 12 wt% to 7 wt% in the non-magnetic products as the size fraction decreases from >40 µm to 10-20 µm with exception of <10 µm size fraction as it is significantly increases to 18 wt%. This could be due to the largest mass recovered to the non-magnetic product at this size fraction.

The increase in the grade of Fe_2O_3 in the magnetic and middling products and the decrease in the non-magnetic products as the size fraction decreases could be

attributed to the improvement in the liberation of the iron bearing minerals and decrease their association with diamagnetic minerals particularly calcite as shown by the QEMSCAN® measurements.

Also, Figure 5.18 shows that the calculated recovery of Fe_2O_3 fluctuates throughout the size-by-size fractions, particularly in the magnetic and middling products. It can be seen that the maximum rejection for Fe_2O_3 of 68% to the magnetic products achieved in the size fraction of 30-40 µm, while the minimum rejection for Fe_2O_3 of 12% to the magnetic products achieved in the size fraction of <10 µm.

5.12 Conclusions

This chapter presented the results of the magnetic properties of the REE fluorcarbonate single crystals in addition to the results of the magnetic separation experiments at different size fractions and process conditions. It is aimed to predict the magnetic behaviour of synchysite-(Ce) and determine the possibility to pre-concentrate this deposit by increasing the REE- and REE-bearing minerals recovery to non-magnetic product and rejecting the gangue minerals to a magnetic product. The following conclusions can be drawn:

1. The VSM measurements indicated that bastnäsite-(Ce) and parisite-(Ce) are paramagnetic minerals and the latter possesses a lower magnetic susceptibility. Two crystals of röntgenite-(Ce), which may be reported for the first time, exhibited a weakly paramagnetic to a diamagnetic behaviour.
2. The magnetic susceptibility of the measured minerals varies between them. Thus, these findings can be used to recover or pre-concentrate any of these minerals by applying lower or higher magnetic field strength based on the magnetic behaviour and susceptibility of the gangue minerals they are associated with.
3. It is evident experimentally and confirmed by the automated mineralogy, that the highly liberated synchysite in this deposit behaved as a diamagnetic mineral, while it was behaved as a weakly paramagnetic mineral when its degree of liberation lower and its percentage of association with paramagnetic minerals, particularly ankerite, increased.
4. The pre-concentration experiment results using magnetic separation illustrated that the fine grinding, liberation, and mineral association have influence on the

separation efficiency of the target minerals. It showed that increasing in the fine grinding from P_{80} 53 µm to 38 µm (increasing the liberation and decreasing the mineral association) led to an improvement in the recovery of apatite from 84% to 87% and synchysite from 76% to 82% in the non-magnetic product. This was accompanied by decreasing in the rejection of paramagnetic minerals (ankerite and iron oxides/carbonates) from 51% to 44%.

5. It can be concluded that recover apatite and synchysite to the magnetic product is due to:
    - Apatite and synchysite are not fully liberated and still associated with other paramagnetic minerals, particularly ankerite as indicated from the QEMSCAN® measurements, and thus could be recovered to the magnetic product.
    - Approximately 4% of REE fluorcarbonate mineral is parisite-(Ce) as shown from the EPMA measurements, which may be expected to be recovered to the magnetic product.
    - Entrapment of the relatively large diamagnetic particles inside the matrix.

Chapter 6

Froth flotation

6.1 Introduction

In this chapter, the results obtained from 35 bench-scale froth flotation tests under various conditions and parameters are presented. Potential methods to optimise the recovery of apatite and synchysite in a complex carbonatite ore deposit are discussed. The solubility of the chemical reagents used in this work was measured and their effects on the mineral selectivity in bench froth flotation experiments were tested. Furthermore, the flotation behaviour of valuable minerals was determined using the classical first-order flotation model.

6.2 Aims

This chapter considers a number of bench-scale rougher froth flotation experiments on the Songwe Hill carbonatite deposit. It aims to optimise the grade and recovery of the REE- and REE-bearing minerals, apatite and synchysite to the concentrate and reject gangue minerals, ankerite, calcite, K-feldspar, and iron oxide/carbonate to the tailings. It also aims to improve understanding the behaviour of these minerals under various conditions and parameters, and investigates potential methods to minimise energy requirements. The froth flotation experiments included investigation of both chemical and operating parameters (Figure 6.1). The effects of soda ash and caustic soda as pH modifiers, fatty acid (Betacol) and sodium oleate as collectors, lignin sulphonate and sodium fluorosilicate as depressants, conditioning time, temperature, and grinding size on the flotation efficiency are presented. The Mountain Pass recipe was used as this had given the best froth flotation results at Mintek, South Africa (see Chapter 1). Details of the methods used are given in Chapter 2.

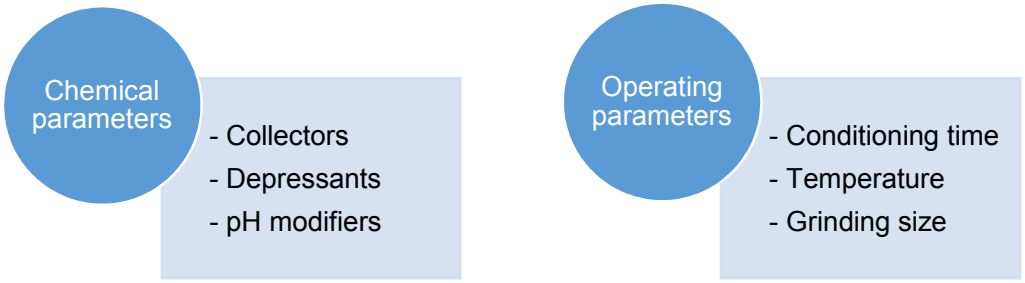

Figure 6.1: Chemical and operating parameters tested in the froth flotation experiments.

6.3 Effect of fixed soda ash dosage on flotation efficiency

Three levels of soda ash dosages of 4000, 7000 and 10000 g/t were added to the feed pulp to investigate the effect of the dosage on the apatite and synchysite grade and recovery, in addition to the mass pull rate. The experimental laboratory results are summarised graphically in Figure 6.2, while the details are given in Appendix K (T1, T2 and T3).

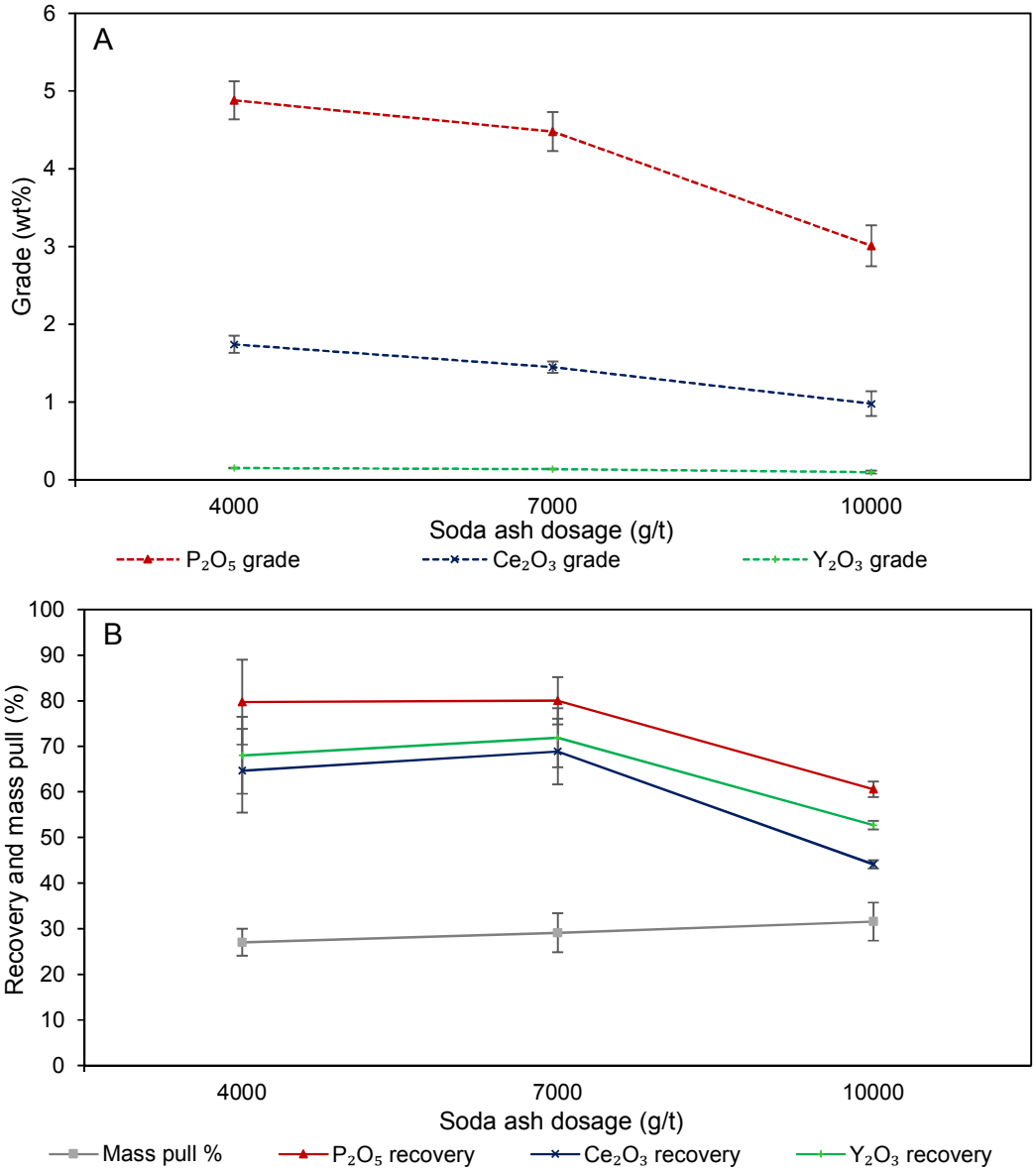

Figure 6.2: (A) Grade of the valuable minerals and (B) recovery of the valuable minerals and the mass pull as a function of soda ash dosage for three froth flotation tests of the composite sample P_{80} of 53 µm, processed under a long conditioning time of 60 minutes and high temperature of 60ºC. Highest grade obtained at soda ash dosage of 4000 g/t, highest recovery obtained at soda ash dosage of 7000 g/t, while lowest grade and recovery obtained at the dosage of 10000 g/t. Note % for both recovery and mass pull is mass/mass and error bars represent the standard deviation determined from all the experimental data.

As mentioned in Chapter 5, the concentrations of P_2O_5, Y_2O_3, and Ce_2O_3 were utilised to track the grade and recovery of apatite, HREE (predominantly hosted by apatite), and LREE (predominantly hosted by synchysite), respectively. Similarly, the concentrations of CaO, SiO_2, and Fe_2O_3 were utilised to track the grade and recovery of the carbonate, silicate, and iron oxide/carbonate gangue minerals, respectively.

The highest grades of P_2O_5, Ce_2O_3, and Y_2O_3 of 4.88 wt%, 1.7 wt%, and 1.5 wt%, respectively appears at the lowest dosage of soda ash of 4000 g/t, while the highest recovery of 80%, 69%, and 72%, respectively appears at the medium dosage of soda ash of 7000 g/t (Figure 6.2 A and 6.2 B). The increase in the amount of soda ash to 10000 g/t negatively affects both the grade and recovery of the valuable minerals.

It can also be observed from Figure 6.2 B that the mass pull rate of 27%, 29%, and 32% gradually increases as the dosage of soda ash increases in the flotation tests T1, T2 and T3, respectively. This could be explained as a result of the variation of the pH values of the feed pulp resulting from changing the soda ash dosage. Thus, this variation of the pH values might have affected the fatty acid dissociation leading to a decrease its selectivity towards the valuable minerals and a simultaneous increase the amount of gangue minerals in the rougher concentrate.

Another four flotation tests were conducted using the same experimental procedure focusing only on 4000 g/t and 7000 g/t of soda ash dosages for reproducibility purposes. The pH values during the conditioning and floating times of the flotation tests are illustrated in Figure 6.3, while further details are provided in Appendix K (T4, T5, T6 and T7).

In Figure 6.3 there is a clear trend of decreasing pulp pH value with progression of the flotation test as indicated from the stage-added reagent, decreasing from 10.35 to 9.33 at 4000 g/t soda ash dosage flotation tests, and from 10.61 to 9.74 at 7000 g/t soda ash dosage. Figure 6.3 also shows that the pulp pH value varies from one conditioning stage to another, which might affect the solubility and selectivity of the chemical reagents.

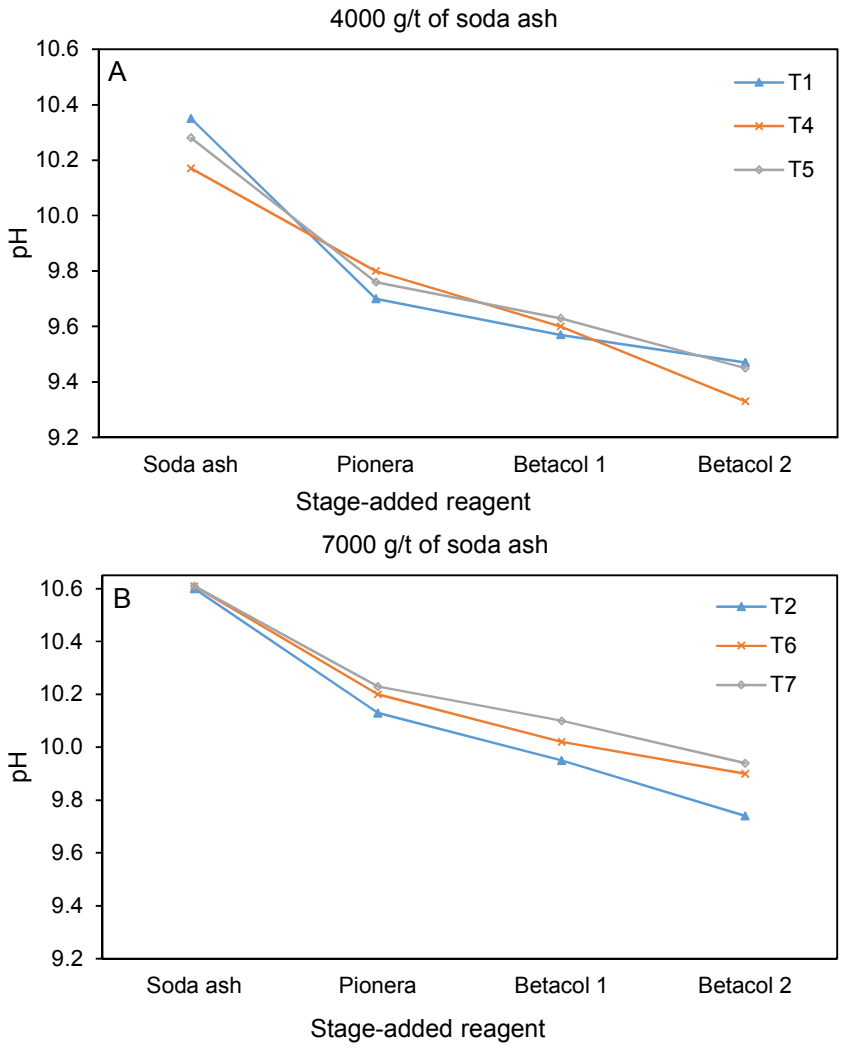

Figure 6.3: pH value at different stage-added reagent for (A) three froth flotation tests of the composite sample P_{80} of 53 µm, processed with 4000 g/t of soda ash dosage under a long conditioning time of 60 minutes and high temperature of 60ºC and (B) three froth flotation tests of the composite sample P_{80} of 53 µm, processed with 7000 g/t of soda ash dosage under a long conditioning time of 60 minutes and high temperature of 60ºC.

Overall, the results of the flotation experiments (Appendix K, T1 to T7) show that the mass pull during low soda ash dosage flotation tests is lower than at high soda ash dosage. The increase in pH value in the high soda ash dosage flotation test might have led to a change in the chemistry of the pulp and the surface charge of particles as well as the rate of dissociation and adsorption of the collector toward the valuable minerals. As pointed out in Chapter 1, the mechanism of fatty acid adsorption is predominantly chemisorption and significantly dependent on the pH of the pulp system (Hu et al., 1986; Rao et al., 1991; Pavez et al., 1996). Also, any change in pH level of the flotation system may affect the surface charge of fine particles as well

(e.g. <10 μm which form more than 30 wt% of the head sample, see Chapter 5), which could lead the fine particles aggregating so that they are recovered to the froth as entrained particles causing an increase in the mass pull. Furthermore, it can be seen from Appendix K (T1 to T7) that a high proportion of the gangue minerals, particularly the carbonates, is recovered to the concentrate during the high soda ash dosage flotation test than the low soda ash dosage flotation test. This may have been due to the selectivity of depressant (Pionera 220) being reduced at the high dosage of soda ash.

6.4 Effect of conditioning time on flotation efficiency

The initial flotation tests aimed to investigate the effect of soda ash on the flotation performance under long conditioning time of 60 minutes. A factorial experimental design was applied to determine the impact of soda ash at three levels of conditioning time, focusing on the two dosages of soda ash (4000 g/t and 7000 g/t) that gave encouraging results. Table 6.1 shows the basic experimental design for six froth flotation tests. The experimental results are summarised graphically in Figure 6.4, while the details are given in Appendix K (T1, T8, T9, T2, T10 and T11).

Table 6.1: Two variable factorial experiments to test froth flotation efficiency at two dosages of soda ash (high and low) and three levels of conditioning times (long, short, shortest).

Test no.	Variables	
	Soda ash dosage (g/t)	Conditioning time (min)
T1	4000	60
T8	4000	30
T9	4000	10
T2	7000	60
T10	7000	30
T11	7000	10

It can be seen from Figure 6.4 that the grade of P_2O_5, Ce_2O_3, and Y_2O_3 at low and high dosages of soda ash gradually increases as the conditioning time increases from 10 minutes to 60 minutes. These results indicate that the selectivity of the collector towards the valuable minerals enhances with increasing the conditioning time. Furthermore, the grade of the elements of interest is higher for flotation tests of 4000 g/t soda ash dosage compared to the flotation tests of 7000 g/t, a result consistent with the previous finding (Section 6.3).

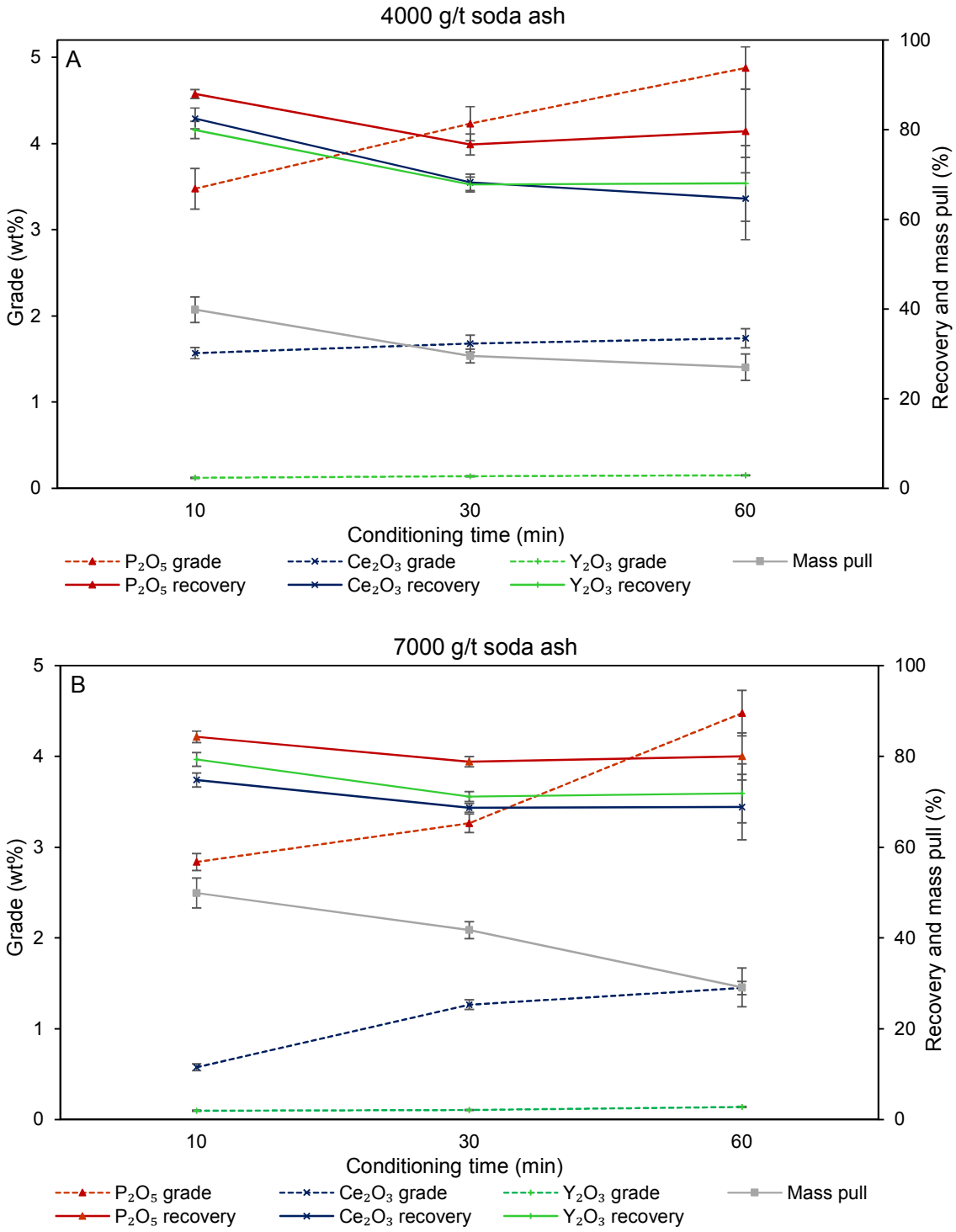

Figure 6.4: Grade and recovery of the valuable minerals in addition to the mass pull as a function of conditioning time for three froth flotation tests of the composite sample P_{80} of 53 µm, processed with (A) 4000 g/t of soda ash and (B) 7000 g/t of soda ash under a high temperature of 60ºC along with different conditioning time of 60 minutes, 30 minutes, and 10 minutes. Grade and recovery increased with increasing the conditioning time at both soda ash dosages of 4000 g/t and 7000 g/t. Note % for both recovery and mass pull is mass/mass and error bars represent the standard deviation determined from all the experimental data.

The recovery of the target elements at both low and high dosages of soda ash gradually decreases as the conditioning time increases from 10 minutes to 60 minutes, while the recovery seems inconsistent at the conditioning time of 30 minutes compared to the other flotation tests at 10 minutes and 60 minutes. This may be explained as a result of the calculated weight of the head sample being lower in the flotation tests of 60 minutes (T1 and T2) compared to the flotation tests of 30 minutes (T8 and T10).

It is also apparent from Figure 6.4 that there is a successive decrease in the mass pull rate as the conditioning time increases from 10 minutes to 60 minutes, particularly the high soda ash dosage flotation tests. These results indicate that the pH value has also an effect on the selectivity of the depressants, particularly lignin sulphonate, and therefore on the depression of the gangue minerals. The recovery of carbonate minerals increases as the conditioning time decreases, particularly during the high soda ash dosage flotation tests (Appendix K T1, T8, T9, T2, T10 and T11).

Generally, the variation in the grade, recovery, and mass pull throughout the flotation tests at different conditioning times could be explained as a result of the variation in pH values of the flotation pulp as shown in Figure 6.5.

The pH level varies throughout the flotation tests (Figure 6.5), particularly at a short conditioning time of 10 minutes. Furthermore, the value and range of pH differ in each of the conditioning stages. For example, the pH at 4000 g/t soda ash dosage flotation tests decreases from 10.3 to 9.3 and from 10.3 to 9.6 under conditioning times of 60 minutes and 10 minutes, respectively, while it decreases from 10.6 to 9.7 and from 10.6 to 10.1 under the same conditioning times, respectively of the 7000 g/t soda ash dosage flotation tests. All these variations may have influenced the dissociation and adsorption of either the collector (Betacol CKF B30) or the depressant (Pionera 200) toward the valuable and gangue minerals, respectively. The reduction in the dissociation and selectivity of the collector may influence the grade and recovery of the valuable minerals, while the reduction in the dissociation and selectivity of the depressant may cause variations in the recovery of the gangue minerals and hence the mass pull of the rougher concentrate.

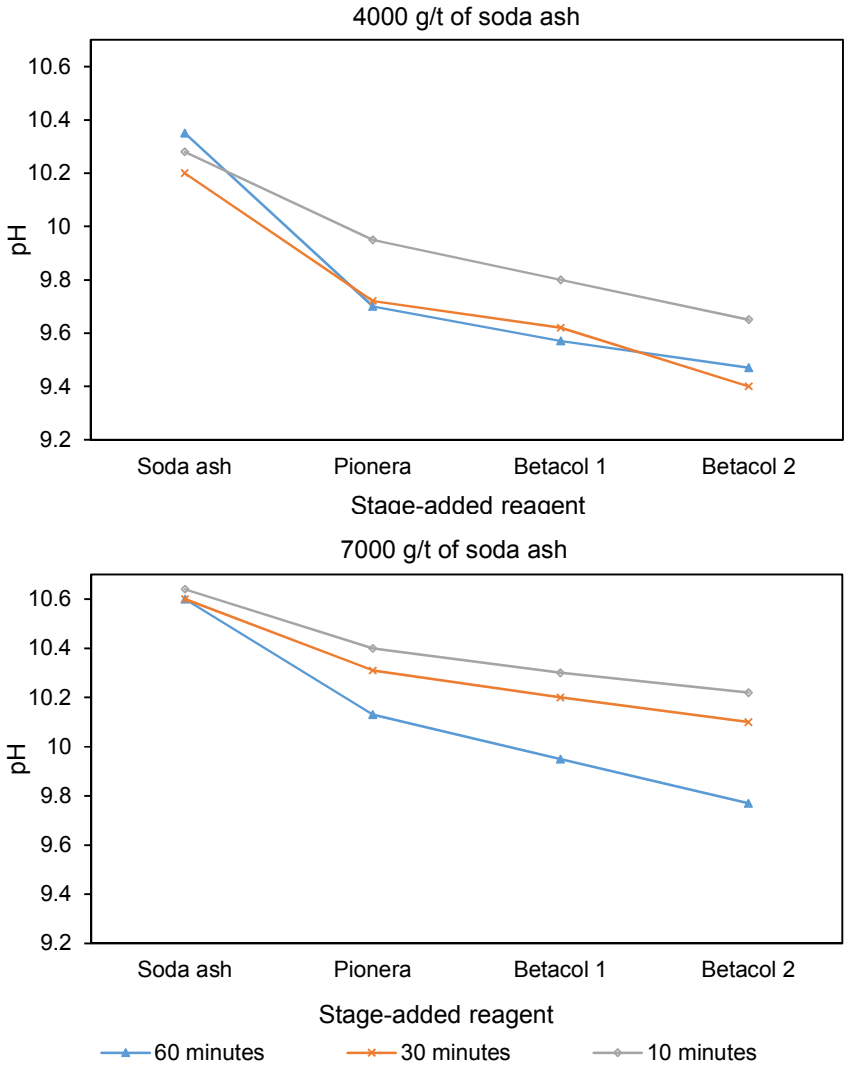

Figure 6.5: pH value at different stage-added reagent for (A) three froth flotation tests of the composite sample P_{80} of 53 µm, processed with 4000 g/t of soda ash dosage under a high temperature of 60ºC along with different conditioning time of 60 minutes, 30 minutes, and 10 minutes and (B) three froth flotation tests of the composite sample P_{80} of 53 µm, processed with 7000 g/t of soda ash dosage under a high temperature of 60ºC, along with different conditioning times of 60 minutes, 30 minutes, and 10 minutes.

The separation efficiency (SE) as a function of conditioning time for the flotation tests at 4000 g/t and 7000 g/t of soda ash is presented in Figure 6.6. The highest separation efficiency for P_2O_5 and Y_2O_3 achieves at a conditioning time of 60 minutes. Interestingly, the separation efficiency of Ce_2O_3 increases with a lower conditioning time of 10 minutes for the low dosage flotation tests, while it decreases in the high dosage flotation tests. This improvement could be attributed to the recovery of Ce_2O_3 being increased to 82.51% during conditioning time of 10 minutes

with small changes in its grade compared to other flotation tests of conditioning times of 30 minutes and 60 minutes (Appendix K T1, T8, and T9). It is evident that the separation efficiency generally increases as the conditioning time of the feed pulp increases from 10 minutes to 60 minutes.

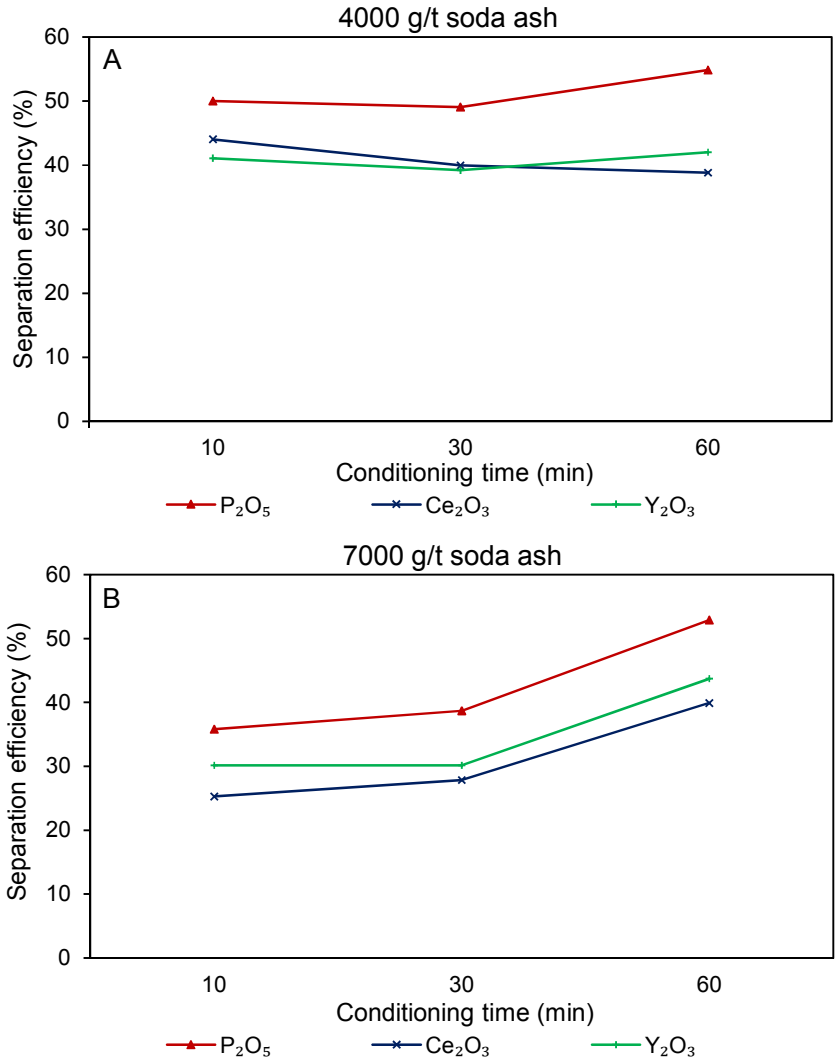

Figure 6.6: Separation efficiency of the valuable minerals as a function of conditioning time for (A) three froth flotation tests of the composite sample P_{80} of 53 µm, processed with 4000 g/t of soda ash under a high temperature of 60ºC and (B) three froth flotation tests of the composite sample P_{80} of 53 µm, processed with 7000 g/t of soda ash under a high temperature of 60ºC. Separation efficiency of apatite (P_2O_5 and Y_2O_3) increased and synchysite (Ce_2O_3) decreased with increasing the conditioning time at 4000 g/t soda ash dosage, while it increased for both minerals with increasing the conditioning time at 7000 g/t soda ash dosage. Note % for the separation efficiency is mass/mass.

In summary, it seems clear that increasing the conditioning time of the pulp prior to flotation enhanced the grade of the valuable minerals, but reduced their recoveries. It

also led to a decrease in the total mass pull of the final rougher concentrate under the same air flow rates. This could a result of increasing the interaction time of the collector and depressants with the valuable and gangue minerals, respectively and hence increase their hydrophobicity and hydrophilicity. It is experimentally verified that a water-insoluble collector requires long conditioning time to improve the probability of particle-bubble collision and attachment during the floating time (Sun et al., 1955; Runolinna et al., 1960 cited in: Parekh and Miller, 1999). This conclusion will be further discussed in Section 6.12 by using a water-soluble fatty acid salt collector.

6.5 Effect of fine grinding on flotation efficiency

In order to investigate the effect of fine grinding on the efficiency of the flotation process, another flotation test was conducted using the same operating conditions on a feed sample ground to P_{80} of 38 µm. The flotation experimental results of composite samples P_{80} 53 µm and 38 µm are summarised in Table 6.2, while the details are given in Appendix K (T1 and T12).

Table 6.2: Comparison of grade, recovery, and separation efficiency of the valuable minerals for two froth flotation tests of the composite sample P_{80} of 53 µm (T1) and 38 µm (T12), processed with 4000 g/t of soda ash under a long conditioning time of 60 minutes and high temperature of 60ºC. Note % for both recovery and separation efficiency is mass/mass.

Test no.	Grinding size (µm)	Mass pull (%)	Grade			Recovery (%)			Separation efficiency (%)		
			P_2O_5 (wt%)	Ce_2O_3 (ppm)	Y_2O_3 (ppm)	P_2O_5	Ce_2O_3	Y_2O_3	P_2O_5	Ce_2O_3	Y_2O_3
T1	53	27.01	4.88	17414	1514	79.70	64.66	68.02	54.85	38.82	42.01
T12	38	20.54	5.37	16329	1596	63.95	48.58	54.44	45.26	24.76	31.80
P-value*		0.653	0.065	0.804	0.610	0.715	0.518	0.855	0.911	0.570	0.871

**P*-value calculated based on the experimental results of T1, T4, T5, T12, and T12 (duplicate) using a two-sample *t*-test assuming unequal variances and the significance level of α=0.05 was regarded as statistically significant.

It can be seen from the data in Table 6.2 that the fine grinding of the head composite sample from P_{80} of 53 µm to 38 µm improves the grade of P_2O_5 and Y_2O_3, but reduces the grade of Ce_2O_3. This could be attributed to the effect of the variation in the alkalinity of the pulp between these two flotation tests, which could have a varied effect on the apatite and synchysite minerals.

However, the results in Table 6.2 indicate that the recovery of the valuable minerals decreases with increasing a fine grinding of the head sample. The calculated *P*-value for the valuable mineral recovery is higher than the significance level (α=0.05), which indicates that the decrease in the recovery is not statistically significant. Furthermore, the rate of mass pull decreases from about 27% to approximately 21% as the grind size of the feed decreases from a P_{80} of 53 µm to 38 µm respectively, which is again, not statistically significant as the *P*-value for the mass pull is higher than the significance level (α=0.05, Table 6.2). These results are likely to be related to an increase in the rejection of the gangue minerals to the rougher tailings in the flotation test T12 compared to the test T1 (Table 6.3). They could also be due to the presence of a high proportion of ultrafine particles as indicated from the results of the Mastersizer and Cyclosizer (see Chapter 5, Section 5.6), which may consume more reagents because of the high surface area (Schulze, 1977). Therefore, fines may be lost to the tailings because of their lower hydrophobicity (Grano et al., 2004). In practise, very fine particles need a higher collector dosage to be hydrophobic enough, and more flotation time to increase their collision efficiency with bubbles (Pease et al., 2006). Also, at very small particle sizes, hydrodynamic forces are dominant and particle-bubble attachment decreases, so flotation rates of the fines would be slower (Derjaguin and Dukhin, 1961; McIvor and Finch, 1991; Shi and Fornasiero, 2009).

Table 6.3: Comparison of grade and recovery of the gangue minerals for two froth flotation tests of the composite sample P_{80} of 53 µm (T1) and 38 µm (T12), processed with 4000 g/t of soda ash under a long conditioning time of 60 minutes and high temperature of 60ºC. Note % for the recovery is mass/mass.

Test no.	Grinding size (µm)	Mass pull (%)	Grade (wt%)			Recovery (%)		
			CaO	Fe_2O_3	SiO_2	CaO	Fe_2O_3	SiO_2
T1	53	27.01	34.75	15.98	3.10	28.50	23.75	11.46
T12	38	20.54	34.04	15.47	3.04	21.84	17.31	8.78
P-value*		0.658	0.618	0.366	0.396	0.741	0.344	0.583

**P*-value calculated based on the experimental results of T1, T4, T5, T12, and T12 (duplicate) using a two-sample *t*-test assuming unequal variances and the significance level of α=0.05 was regarded as statistically significant.

Additionally, the behaviour of the valuable and gangue minerals in the flotation experiments T1 and T12 could be affected by the correlation between the degree of

mineral liberation (surface exposure) and the response to the chemical reagents. It is evident from the QEMSCAN® measurements (see Chapter 4, Section 4.5.2) that the liberation of apatite improved from 68% to 72% and synchysite from 31% to 49% with the fine grinding from P_{80} of 53 µm to 38 µm. This may cause fatty acid to be more selective towards apatite than synchysite, taking the variation of the pH values in account. Furthermore, the texture of the particles (i.e. liberation and association) has another effect on the grade-recovery curve. It seems increasing the degree of fine grinding can improve the grade of the target minerals, but negatively decreases their recoveries (Figure 6.7).

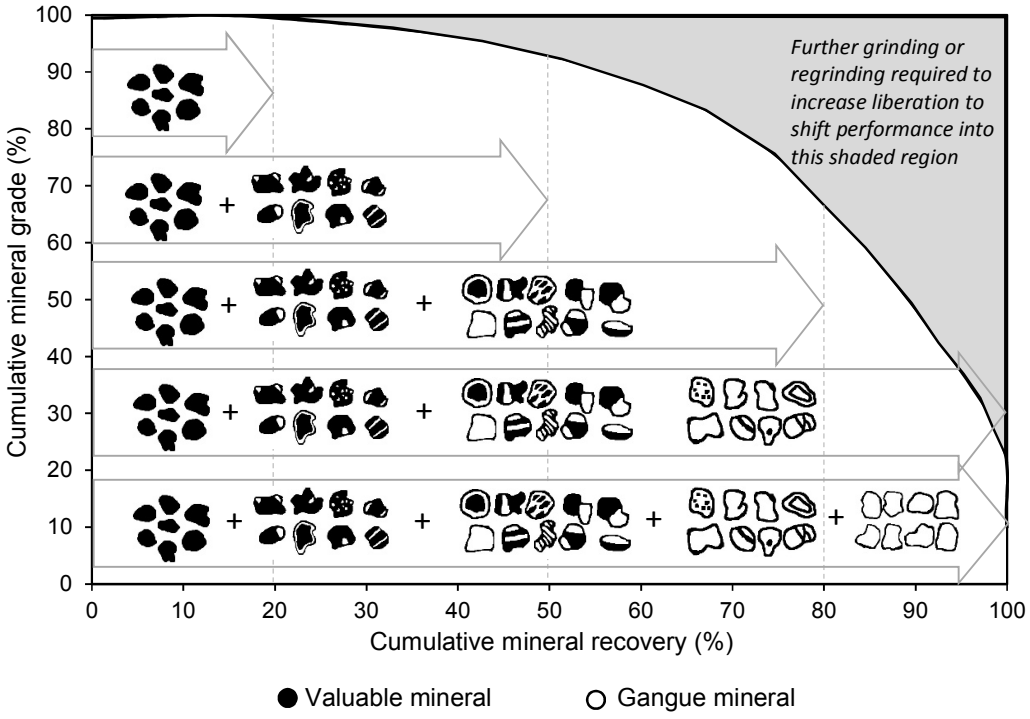

Figure 6.7: Theoretical mineralogically limited grade-recovery curve showing the effect of particle texture (liberation and mineral association) on the grade and recovery of a valuable mineral, adapted from McIvor and Finch (1991); Becker et al. (2016).

6.6 Effect of a constant pulp pH value on flotation efficiency

The previous flotation tests, conducted by conditioning the feed sample under fixed dosages of soda ash, produced ambiguous results regarding the correlation between fixed dosage and flotation efficiency. Thus, a small number of flotation tests were conducted at constant pH during the conditioning and floating times. Five flotation tests were carried out at constant pH of 8.5, 9.0, 9.5, 10.0 and 10.5. The experimental flotation results are presented graphically in Figures 6.8 and 6.9, while the experimental results can be found in Appendix K, T13 to T17.

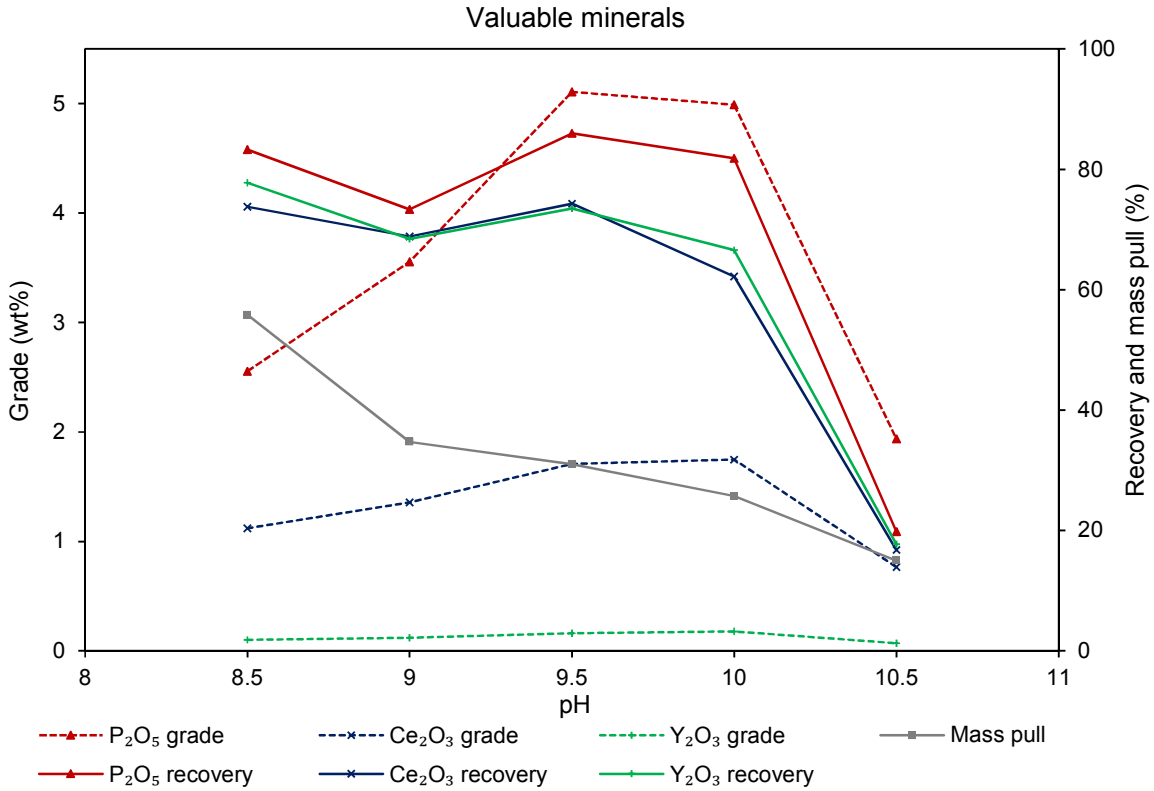

Figure 6.8: Grade and recovery of the valuable minerals along with the mass pull as a function of pH for five froth flotation tests of the composite sample P_{80} of 53 µm, processed under a constant level of pH, long conditioning time of 60 minutes, and high temperature of 60ºC. Optimum grade and recovery were achieved at a constant pH of 9.5 and 10.0. Note % for both recovery and mass pull is mass/mass.

Figure 6.8 shows there is a clear trend of increasing grade of P_2O_5 from 2.56 wt% to 5.11 wt% as the pulp pH value increases from 8.5 to 9.5, while it slightly decreases to 4.99 wt% at a pH of 10.0 and relatively highly decreases to 1.94 wt% at a pH of 10.5. The grade of Ce_2O_3 and Y_2O_3 gradually increases from 11194 ppm to 17477 ppm and from 1004 ppm to 1768 ppm, respectively as the pulp pH value increases

from 8.5 to 10.0 and then decreases to 7647 ppm and 689 ppm, respectively at a pH of 10.5. It is interesting to note that although P_2O_5 and Y_2O_3 are mainly hosted by apatite, the results show that the grade of Y_2O_3 increases and P_2O_5 reduces at a pH value of 10.0. This inconsistency might be due to the increase in the grade of synchysite, as indicated from the grade of Ce_2O_3, which also hosts about 27% of the total Y_2O_3 in the feed sample (see Chapter 4, Section 4.7.2).

Figure 6.8 also shows that the recovery of P_2O_5, Ce_2O_3, and Y_2O_3 improves from about 73% to 86%, from 69% to 74%, and from 68% to 74%, respectively as the pH value increases from 9.0 to 9.5. In contrast, their recoveries reduce to 82%, 62%, and 67%, respectively at a pH of 10.0 and then records a reduction to 20%, 17%, and 18%, respectively at a pH of 10.5.

Another interesting finding is the decrease in the mass pull rate from approximately 56% to 15% as the alkalinity of the pulp increases from 8.5 to 10.5. These results indicate that the pH value of the pulp has an impact on the selectivity of the chemical reagents toward the valuable and gangue minerals.

The improvement in the grade and recovery of apatite and synchysite in the flotation system at a pH range of 9.5 - 10.0 could be attributed to enhanced adsorption of fatty acid towards the target minerals. At a pH ~10 a negatively charged carboxylate ion can be readily adsorbed on positively charged apatite (Kawatra and Carlson, 2014).

It can be observed from Figure 6.9 that the grade of carbonate gangue minerals, as indicated by CaO content, generally decreases, while the grade of silicate and iron oxide/carbonate gangue minerals, as indicated by SiO_2, and Fe_2O_3 contents respectively, slightly increases as the pH value increases from 8.5 to 10.5. Furthermore, the recovery of carbonates, silicates and iron oxides/carbonates decreases and rejects to the tailings from about 72% to 15%, from 24% to 13%, and from 40% to 14%, respectively with increasing the pH from 8.5 to 10.5.

Therefore, the results of this experimental investigation show that the pH value did not just affect the grade and recovery of the valuable minerals, but it also affected the grade and recovery of the gangue minerals. Therefore, it may be concluded that the pH value has an effect on the selectivity of both the collector and the

depressants, particularly lignin sulphonate toward the valuable and gangue minerals, respectively. This will be further discussed in Section 6.8.

At alkaline solution, the chemical interaction between the dissociated ions of fatty acids ($RCOO^-$) with the surface Ca^{2+} leads to the formation of insoluble salts at the surface of apatite (Sis and Chander, 2003; Young and Miller, 2000; Nunes et al., 2011). This may have occurred as a result of an increase in the negative value of zeta potential onto the apatite surface (Mishra, 1982; Kawatra and Carlson, 2014; Zhou et al., 2015). In terms of synchysite, it may be possible to compare it with bastnäsite, a chemically similar mineral (see Chapter 1, Section 1.5). Work by Pavez et al. (1996) showed that the floatability of bastnäsite in the presence of sodium oleate gradually increased, when pH was increased from 4.0 to reach an optimum at pH of 9.0. Further increase in the pH led to a decrease in the bastnäsite floatability. These results were explained by the chemical interaction between oleate and REE (particularly Ce^{3+} and La^{3+}) onto the bastnäsite surface, where the zeta potential of bastnäsite is negative (Pavez et al., 1996).

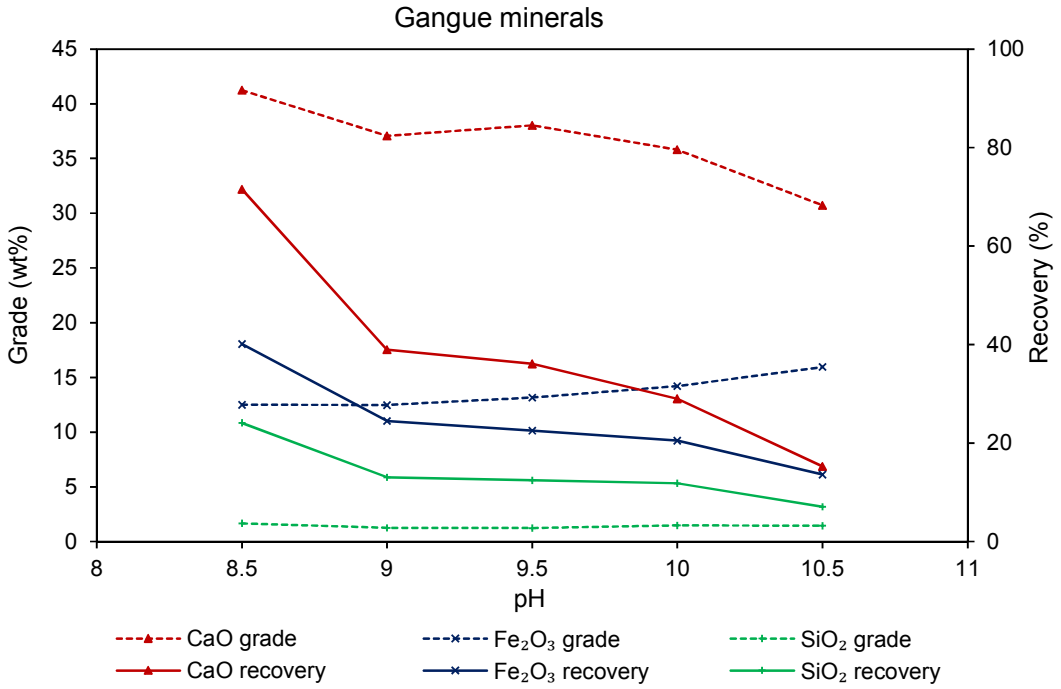

Figure 6.9: Grade and recovery of the gangue minerals as a function of pH value for five froth flotation tests of the composite sample P_{80} of 53 µm, processed under a constant level of pH, long conditioning time of 60 minutes, and high temperature of 60ºC. The recovery of the gangue minerals decreased with increasing pulp pH value. Note % for the recovery is mass/mass.

The results of the calculated separation efficiency of P_2O_5, Ce_2O_3, and Y_2O_3 are presented graphically in Figure 6.10. The separation efficiency of P_2O_5 gradually increases from about 29% to 58% as the pH increases from 8.5 to 10.0 and then sharply drops to 5% at a pH of 10.5. On the other hand, the separation efficiency of Ce_2O_3 and Y_2O_3 gradually increases from approximately 19% to 45% and from 23% to 44% as the pH value increases from 8.5 to 9.5, and decreases to 38% and 42% at a pH value of 10.0, and then declines sharply to about 2% and 3%, respectively at a pH of 10.5.

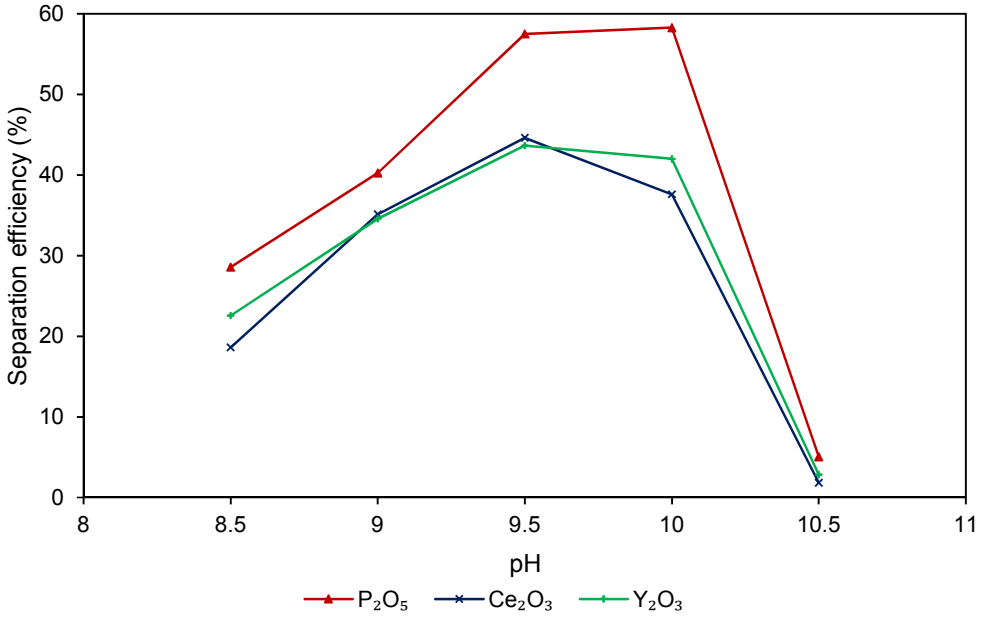

Figure 6.10: Separation efficiency of the valuable minerals as a function of pH for five froth flotation tests of the composite sample P_{80} of 53 µm, processed under constant pH, long conditioning time of 60 minutes, and high temperature of 60ºC. The highest SE for apatite (P_2O_5 and Y_2O_3) achieved at pH 10.0, while the highest SE for synchysite (Ce_2O_3) achieved at pH 9.5. Note % for the separation efficiency is mass/mass.

Since a highest grade, recovery and separation efficiency for P_2O_5, Ce_2O_3 and Y_2O_3 achieved by processing the pulp at a pH value of 9.5, all further flotation tests in this project were processed by applying this experimental condition. It is important to note that a duplicate flotation test at a pH of 9.5 was conducted and similar results to the flotation test (T15) achieved. The results are provided in Appendix K (T15 and T15 Duplicate).

In summary, keeping the feed pulp at a constant level of pH during the conditioning and floating times of the test has a crucial effect on the flotation separation

efficiency. It led to a systematic increase in the grade and recovery of the valuable minerals. The pH value may have affected the dissociation of fatty acid and its adsorption selectivity on the surface of the valuable minerals, leading to enhanced grade and recovery of the flotation process particularly at pH values of 9.5 and 10.0. Also, it is important to note that soda ash is typically utilised to control the pulp pH, which can affect the zeta potential of the minerals in addition to acting as a depressant for calcite and baryte gangue minerals (Fuerstenau et al., 1992). This probably explains why the amount of carbonate gangue minerals continuously decreases as the pH value of the pulp increases.

Furthermore, changing the pH of the pulp using sodium carbonate changes the chemistry of the aqueous phase and so the surface chemistry of particles, control the solubility of minerals, forming a new surface compound on other minerals, and modify the adsorption rate of the collector on the minerals. Therefore, understanding all the interactions between the chemical reagents and valuable and gangue minerals in a complex ore like a carbonatite deposit is a challenge that requires measurement of the different parameters individually. Determination of the zeta potential for synchysite for example, is important but it is outside the scope of this research project.

6.7 Effect of temperature on floatability of apatite and synchysite

The suggested froth flotation procedure requires conditioning the feed pulp at an elevated temperature of 60°C for 3 hours (one hour per stage) prior to flotation. It is important to note here that the average monthly temperature (daytime) for the mine site studied is within a range of 22°C and 24°C in winter, while it is within a range of 24°C and 28°C in summer (Croll et al., 2014). This consistently high temperature makes heating of the flotation cells easier to control than in more temperate climes. Heat could be obtained an on-site sulphuric acid plant, which means the costs of heating the slurry should be relatively low (Croll et al., 2014).

In order to determine the effect of different temperatures on the selectivity of the chemical reagents towards the valuable and even gangue minerals and also to see if it is possible to minimise the energy consumption, four separate flotation tests were performed by conditioning the feed pulp at 20°C, 40°C, 60°C, and 80°C and fixed pH of 9.5 using soda ash. The experimental results are presented in Figure 6.11, while the details can be found in Appendix K (T18 to T20).

It can be seen form Figure 6.11 that there has been a gradual increase in the grade of P_2O_5, Ce_2O_3, and Y_2O_3 from 3.47 wt% to 5.11 wt%, from 14939 ppm to 17088 ppm, and from 1119 ppm to 1590 ppm, respectively with increasing the temperature from 20°C through 60°C. The increase in conditioning temperature of the pulp to 80°C leads to reduce the grade P_2O_5, Ce_2O_3, and Y_2O_3 to 4.11 wt%, 16579 ppm, and 1380 ppm, respectively.

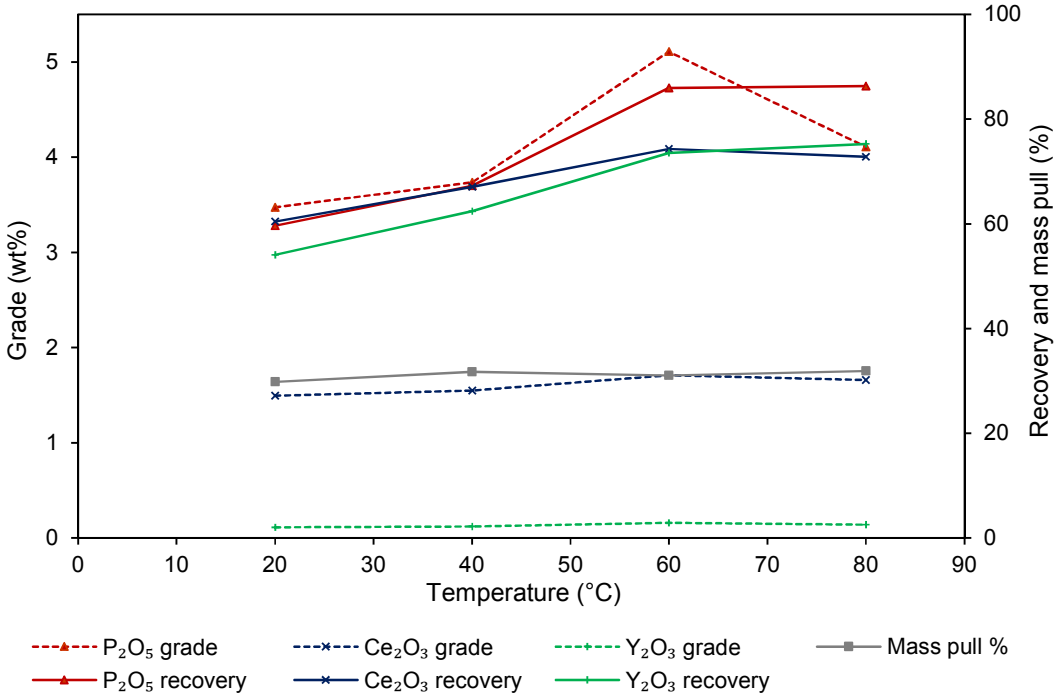

Figure 6.11: Grade and recovery of the valuable minerals and the mass pull as a function of temperature for four froth flotation tests of the composite sample P_{80} of 53 µm, processed under a constant pH of 9.5 and long conditioning time of 60 minutes, together with different conditioning temperatures of 20ºC, 40ºC, 60ºC, and 80ºC. The highest grade and recovery for apatite (P_2O_5 and Y_2O_3) and synchysite (Ce_2O_3) achieved at 60ºC. Note % for both recovery and mass pull is mass/mass.

It is important to note that a duplicate flotation test was conducted at 80°C and different results were obtained as illustrated in Appendix K, T20 Duplicate. The results show that the grade of P_2O_5 and Y_2O_3 relatively highly improves to 6.18 wt% and 1909 ppm, while their recoveries decrease to 71.19% and 53.14%. This could be as a result of decreasing mass pull from about 32% to 17%. It was noticed during the flotation experiment that after adding Betacol collector to the feed pulp, the amount of the froth formed was very low and this may be related to a lack of collector

dissociation, the reason for which is unknown. The findings by Pradip (1981), on the effect of elevated temperature on bastnäsite flotation using a fatty acid collector, showed that the grade of bastnäsite decreased while the recovery remained constant, as the temperature was increased above 75°C. A suggested explanation for these results is the adsorption of a considerable amount of fatty acid onto the surface of gangue minerals (Pradip,1981).

It is also apparent from Figure 6.11 that the recovery of P_2O_5 and Y_2O_3 gradually increases from about 60% to 86% and from 54% to 75%, respectively with increasing conditioning temperature. The grade of Ce_2O_3 increases from about 60% to 74% with increasing the temperature from 20°C to 60°C, while it slightly reduces to 73% at a temperature of 80°C.

The increase in the grade and recovery of P_2O_5, Ce_2O_3, and Y_2O_3 with increasing temperature of the pulp could be either due to the solubility of fatty acid being improved, due to its adsorption being enhanced and hence to be more selective towards the valuable minerals, or due to the solubility of the target minerals being increased. It has been reported that the use of fatty acids and their soaps to process phosphate deposits requires high temperature (Sis and Chander, 2003). The grade and recovery of bastnäsite in carbonatite were greatly improved by a using fatty acid collector at elevated temperature (Bulatovic, 2010). In chemisorbing collector systems such as fatty acids, high temperature enhances the reagent adsorption via specific chemical interaction onto mineral surfaces (Pradip and Fuerstenau, 1991). Based on the flotation results on Mountain Pass ore, Pradip (1981) suggested that increasing the feed pulp temperature led to an increase in the solubility of both fatty acid and cations onto the mineral surface, which enhanced the adsorption of fatty acid towards bastnäsite over calcite and baryte.

Interestingly, the mass pull rate of the flotation tests at different temperature remains constant at about 31 wt%, except the duplicate flotation test which had a much lower mass pull of 17.4 wt%.

The results of the calculated separation efficiency of the flotation tests at different conditioning temperatures are shown in Figure 6.12.

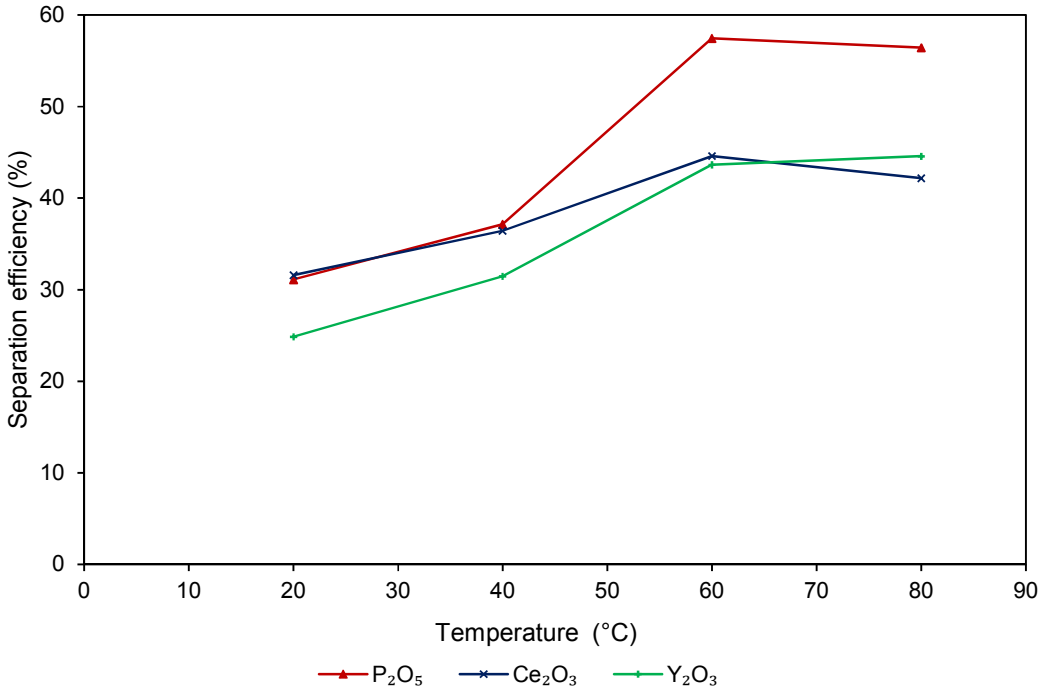

Figure 6.12: Separation efficiency of the valuable minerals as a function of temperature for four froth flotation tests of the composite sample P_{80} of 53 µm, processed under a constant pH of 9.5 and long conditioning time of 60 minutes, along with different conditioning temperatures of 20ºC, 40ºC, 60ºC, and 80ºC. The highest separation efficiency for apatite (P_2O_5 and Y_2O_3) and synchysite (Ce_2O_3) achieved at 60ºC. Note % for the separation efficiency is mass/mass.

Figure 6.12 shows that as the conditioning temperature increases from 20°C to 60°C, the separation efficiency of P_2O_5, Ce_2O_3, and Y_2O_3 increases from 31% to 57%, from 32% to 45%, and from 25% to 44% respectively. However, the separation efficiency of P_2O_5 and Ce_2O_3 slightly decreases to 56% and 42% at a temperature of 80°C, the separation efficiency of Y_2O_3 slightly increases to 45% which could be due to increase its recovery at a temperature of 80°C compared to 60°C (Figure 6.11).

6.8 Measurement of the solubility of the chemical reagents

In order to determine the degree of solubility of the chemical reagents and to identify the optimum pH value that maximised solubility, which might improve the flotation separation efficiency, a spectrophotometer was utilised to measure the solubility of the chemical reagents, including fatty acid (Betacol), sodium oleate, and lignin sulphonate (Pionera 220) in different alkaline solutions. It is important to note that soda ash and caustic soda were utilised as pH modifiers during preparation of the Betacol and sodium oleate solutions, while only soda ash was used as a pH modifier during preparation of the lignin sulphonate solutions.

The percent light transmittance values at a wavelength of 400 nm for Betacol, sodium oleate, and lignin sulphonate solutions as a function of pH values are shown in Figure 6.13.

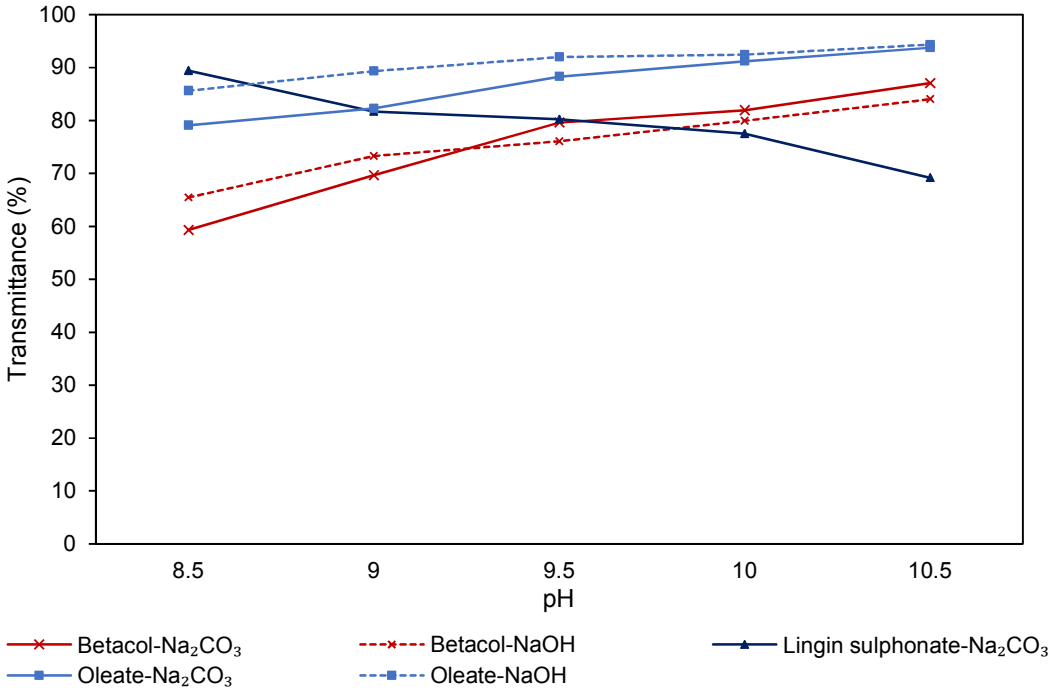

Figure 6.13: Percent light transmittance values of Betacol and sodium oleate collector, and lignin sulphonate depressant solutions as a function of pH value. The solubility of the collectors was increased with increasing pH value, while the opposite was observed for the depressant. Note the pH value of the collector solutions was adjusted using two pH modifiers including soda ash and caustic soda at a temperature of 60ºC, while the pH value of the lignin sulphonate solution was adjusted using soda ash at 60ºC.

It can be seen from Figure 6.13 that the percent light transmittance values of both Betacol and sodium oleate solutions gradually increase as the pH value increases.

These results indicate that the dissociation degree of Betacol and sodium oleate is affected by the alkalinity of the solutions, it increases with increasing the pH. Figure 6.13 also shows that the light transmittance values of Betacol solutions with soda ash are slightly lower than those with caustic soda at pH 8.5 and 9.0, while they become slightly higher at pH values of 9.5 to 10.5. Conversely, the percent light transmittance of all sodium oleate solutions with soda ash is slightly lower than those with caustic soda.

Also, the data in Figure 6.13 show a reverse linear relationship between the percent light transmittance value of lignin sulphonate solutions and the pH values. They exhibit as pH value increases from 8.5 to 10.5, the percent light transmittance of lignin sulphonate solutions decreases from approximately 89% to 69%. A photograph of lignin sulphonate solutions at different pH values is shown in Figure 6.14. These interesting findings indicate that the dissociation degree of lignin sulphonate may have improved in weak alkaline solutions. Thus, conditioning lignin sulphonate at a low alkaline degree may increase its selectivity towards the carbonate and iron oxide/carbonate gangue minerals.

Furthermore, the transmittance measurements did not show a 100% solubility of any of the measured chemical reagents, which can be attributed to incomplete dissociation of these reagents. Also, the solubility varied from one chemical reagent to another due to the variation in their concentration (see Chapter 2, Section 2.11.4).

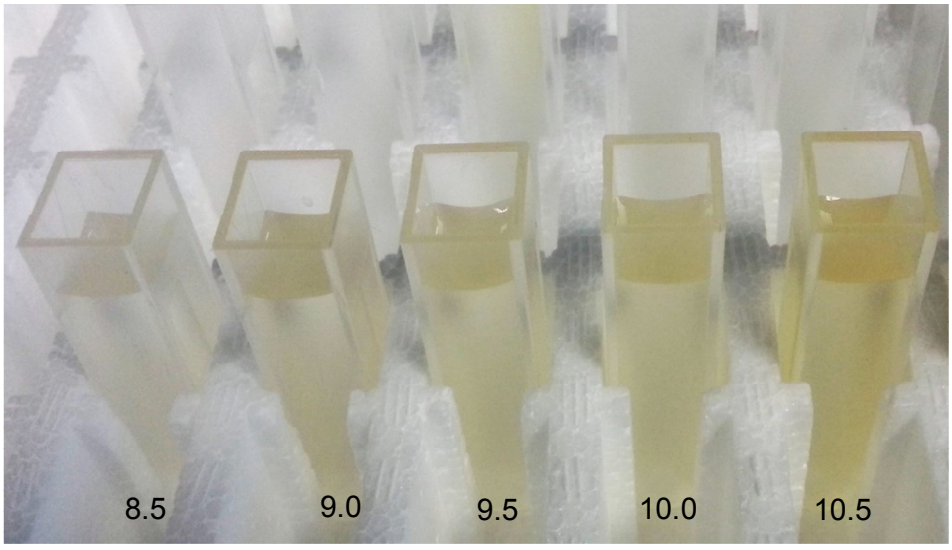

Figure 6.14: Photograph of the lignin sulphonate solutions at different pH values showing an increase in the solubility of lignin sulphonate, as indicated by the colour change with decreasing the pH value.

6.9 Effect of pH on the selectivity of lignin sulphonate

Based on the results of lignin sulphonate solubility measured by spectrophotometer, three pH values of 8.5, 9.5, and 10.5 were chosen to determine the effect of pH on the selectivity of lignin sulphonate towards the carbonate and iron oxide/carbonate gangue minerals. During conditioning of the Betacol collector, the pH was kept at 9.5 in all the flotation tests.

The experimental results of the recovery and mass pull for the gangue minerals in the rougher concentrates are shown in Figure 6.15, while the details of flotation test products are illustrated in Appendix K, T15, T21, and T22.

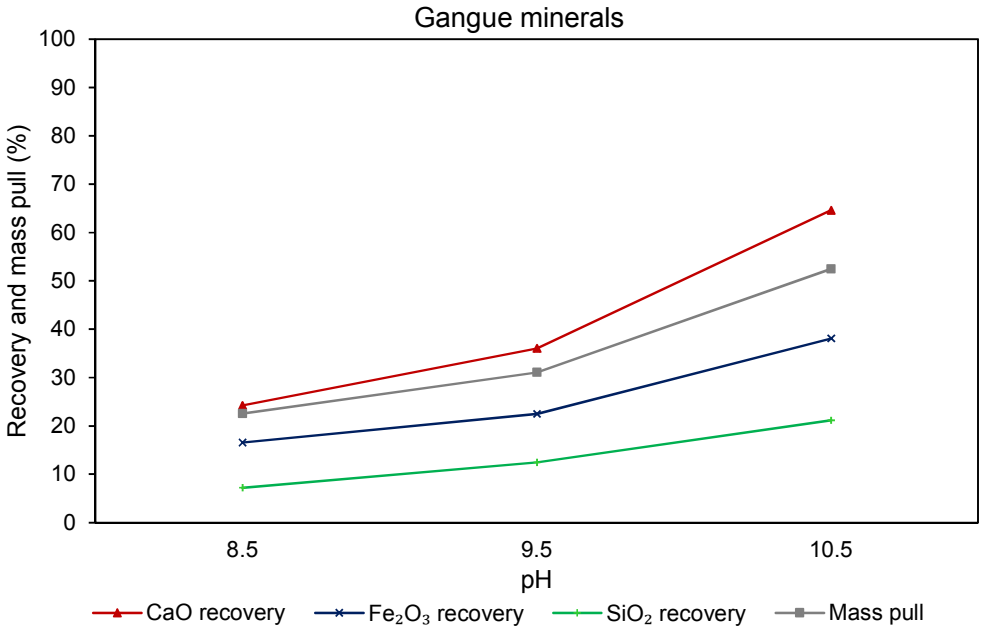

Figure 6.15: Gangue mineral recovery along with mass pull as a function of pH for three froth flotation tests of the composite sample P_{80} of 53 µm, processed under a long conditioning time of 60 minutes and high temperature of 60ºC. Note % for both recovery and mass pull is mass/mass.

Figure 6.15 illustrates that as the pH value increases from 8.5 to 10.5, the recovery of the gangue minerals increases. For example, the recovery of CaO increases from approximately 24% at pH 8.5, to 65% at pH 10.5. Also, the mass pull recovered to the rougher concentrate increases from 23% at pH 8.5, to 52% at pH 10.5. Furthermore, it can be seen from Appendix K (T15, T21, and T22) that the grade degree of CaO increases from approximately 37 wt% to 41 wt% as pH increases from 8.5 to 10.5. These relationships may be explained as a result of the decrease in the solubility of lignin sulphonate and hence its selectivity and adsorption toward the

gangue minerals as the alkaline degree of the flotation pulp increases from 8.5 to 10.5.

On the other hand, Figure 6.16 shows the effect of changing the pH value during the conditioning of depressants on the grade and recovery of the valuable minerals, maintaining the pH at 9.5 during conditioning of the Betacol collector. The grade of P_2O_5, Ce_2O_3, and Y_2O_3 increases as the pH value increases from 8.5 to 9.5 during the conditioning of depressants, while it decreases at pH 10.5 (Figure 6.16).

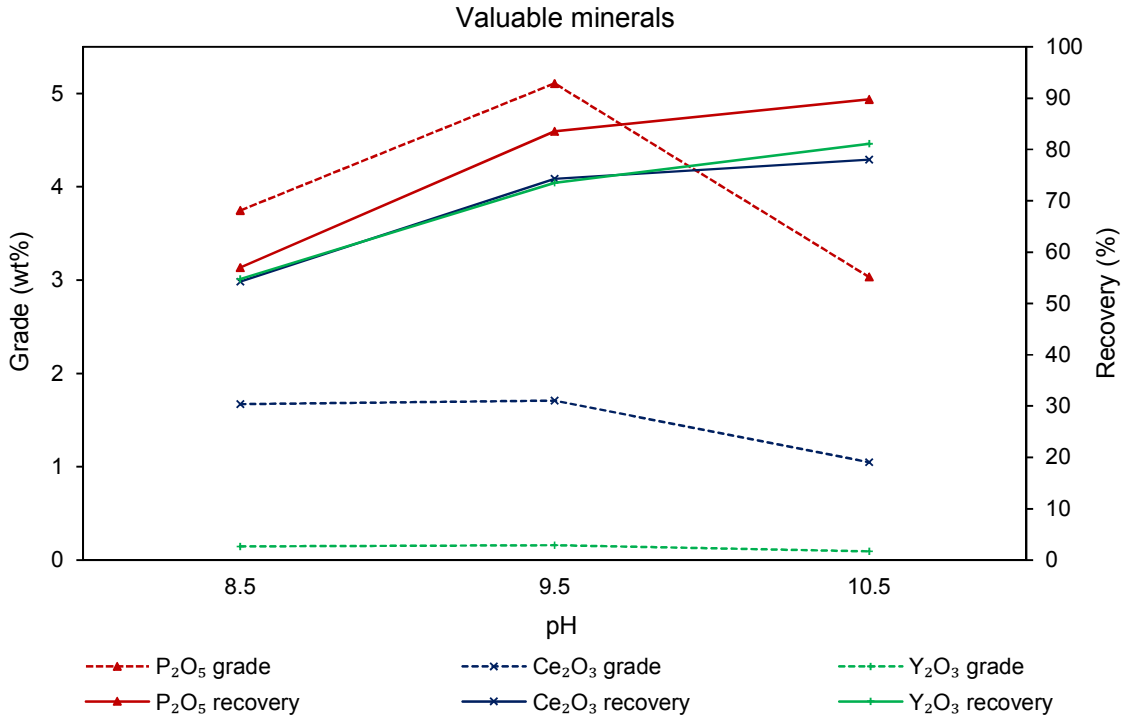

Figure 6.16: Grade and recovery of the valuable minerals as a function of pH for three froth flotation tests of the composite sample P_{80} of 53 µm, processed under a long conditioning time of 60 minutes and high temperature of 60ºC. Highest grade of valuable minerals obtained at pH 9.5, while highest recovery achieved at the pH 10.5. Note % for the recovery is mass/mass.

The increase and decrease in the grade of the P_2O_5, Ce_2O_3, and Y_2O_3 could be related to the variation in the selectivity degree of the depressants, particularly lignin sulphonate, which might have affected the amount of gangue minerals in the rougher concentrate. Therefore, it leads to decrease and increase the grade of the valuable minerals.

It is interesting to note that although the fine grinding to P_{80} of 53 µm enhanced the liberation of the valuable minerals and decreased the association with gangue minerals, they were not fully liberated. The QEMSCAN® measurements (see Chapter 4) showed that the total percentage of locked and middling apatite and synchysite are 32% and 69%, respectively and they are associated with calcite and ankerite (23% and 30%). Therefore, the increase in the selectivity of lignin sulphonate towards the carbonate gangue minerals may depress the apatite and synchysite grains that are associated with these gangues to the tailings, and hence decrease the recovery of the valuable minerals to the concentrate.

Also, Figure 6.16 shows that the recovery of P_2O_5, Ce_2O_3, and Y_2O_3 gradually increases from about 57% to 90%, from 54% to 78%, and from 55% to 81%, respectively as the pH value increases from 8.5 to 10.5 during conditioning of the depressants, with a pH of 9.5 during conditioning of the Betacol collector. This could be attributed to the decrease in the selectivity of the depressants and hence increasing the recovery of the gangue minerals to the rougher concentrate and so the mass pull. This can be seen clearly in Figure 6.17 which correlates the recovery of valuable minerals the versus mass pull.

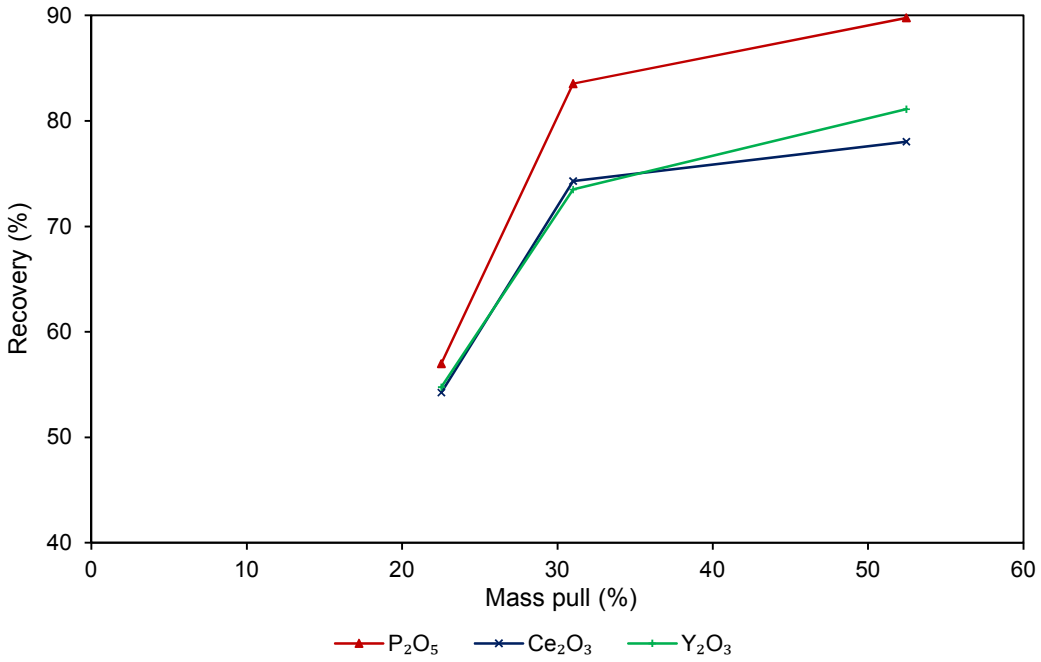

Figure 6.17: Valuable mineral recovery versus mass pull for three froth flotation tests of the composite sample P_{80} of 53 µm, processed under a long conditioning time of 60 minutes and a high temperature of 60ºC. Recovery of valuable minerals increased with increasing the mass pull. Note % for both recovery and mass pull is mass/mass.

The results of the calculated separation efficiency of the flotation tests at different pH values are shown in Figure 6.18. The separation efficiency of P_2O_5, Ce_2O_3, and Y_2O_3 varies in each of the flotation test as the pH value of the pulp changes from 8.5 to 10.5. The highest separation efficiency for P_2O_5, Ce_2O_3, and Y_2O_3 of approximately 57%, 45%, and 44%, respectively achieves at pH 9.5 corresponding with the highest grade and recovery of the valuable minerals. Conversely, the lowest separation efficiency for P_2O_5, Ce_2O_3, and Y_2O_3 of about 39%, 26%, and 29%, respectively obtains at pH 10.5 corresponding with the lowest grade, but highest recovery and mass pull.

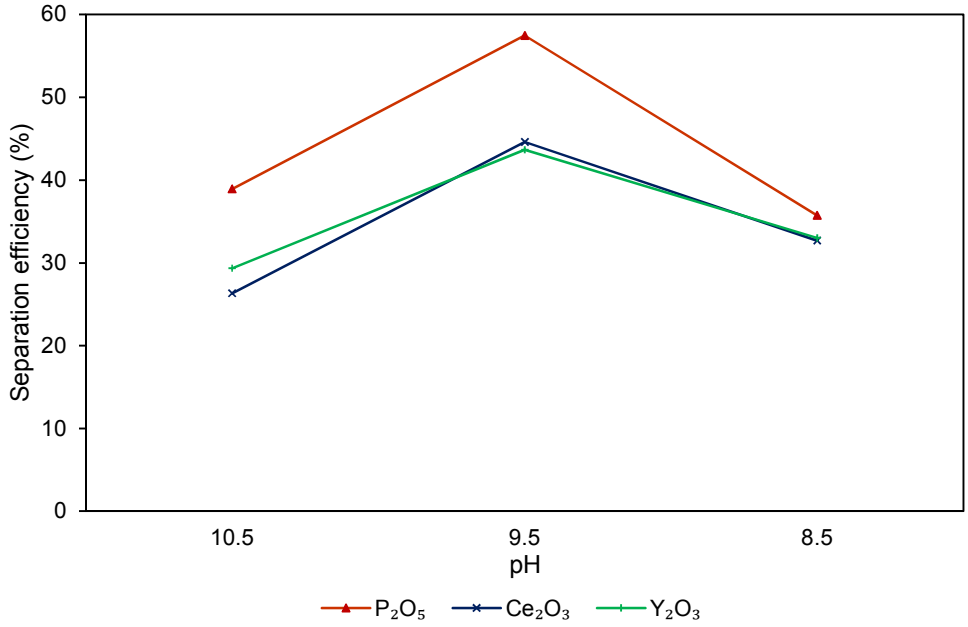

Figure 6.18: Separation efficiency of the valuable minerals as a function of pH for three froth flotation tests of the composite sample P_{80} of 53 µm, processed under a long conditioning time of 60 minutes and high temperature of 60ºC. The highest SE for apatite (P_2O_5 and Y_2O_3) and synchysite (Ce_2O_3) achieved at a pH of 9.5. Note % for the separation efficiency is mass/mass.

Overall, it can be concluded from the results above that at pH 8.5, the solubility and selectivity of lignin sulphonate toward the gangue minerals are improved and led to decrease the rate of mass pull. Also, changing the pH value during conditioning the depressants did not just affect the grade and recovery of the gangue minerals, but it also affected the grade and recovery of the valuable minerals. This could be attributed to the association of the valuable minerals with other gangue minerals particularly carbonates, the predominant gangue minerals in this deposit. It is interesting to note that the highest grade and recovery of valuable minerals is achieved at an overall pH value of 9.5 with a mass pull of 31%.

6.10 Effect of conditioning time on the selectivity of the depressants

The effect of short conditioning time of 10 minutes rather than 60 minutes on the depressants selectivity including sodium fluorosilicate and lignin sulphonate was investigated. Also, the dosage of Betacol was decreased from 120 g/t to 90 g/t during the first stage to determine its effect on the flotation efficiency.

The experimental results of the grade and recovery of CaO, Fe_2O_3, and SiO_2 at short (10 minutes) and long (60 minutes) conditioning times are shown in Table 6.4, while the details are presented in Appendix K (T15 and T23).

Table 6.4: Comparison of grade and recovery of the gangue minerals for two froth flotation tests of the composite sample P_{80} of 53 µm, processed under constant pH 9.5 and a high temperature of 60ºC with a long conditioning time of 60 minutes (T15) and a short conditioning time of 10 minutes (T23). Note % for the recovery is mass/mass.

Test no.	Conditioning time (min)	Mass pull (%)	Grade (wt%)			Recovery (%)		
			CaO	Fe_2O_3	SiO_2	CaO	Fe_2O_3	SiO_2
T15	60	31.02	38.96	11.15	2.19	35.43	22.10	12.43
T23	10	30.11	35.94	14.11	2.81	32.06	24.16	11.21

The recovered mass pull was similar in both of the flotation tests (Table 6.4), which makes the results comparable. Both the grade and recovery of CaO decrease as the conditioning time of the depressant decreases from 60 minutes to 10 minutes. Conversely, the grade and recovery of Fe_2O_3 slightly increase as the conditioning time of the depressants decreases from 60 minutes to 10 minutes.

The results of the grade, recovery, and separation efficiency of the valuable minerals are illustrated in Table 6.5. The grade, recovery, and separation efficiency of P_2O_5, Ce_2O_3, and Y_2O_3 decrease as the Betacol collector dosage decreases from 120 g/t to 90 g/t. A possible explanation for this might be that Betacol dosage affected the mass pull rate and hence the recovery of the valuable minerals. As pointed out in the literature review (see Chapter 1, Section 1.13.1), that fatty acid (Betacol) acts as a collector and a frother. Thus, decreasing Betacol dosage might have decreased its selectivity towards the valuable minerals and/or the amount of mass pull recovered to the rougher concentrate. Another possible explanation for this is the recovery of carbonate minerals decreases from 35% to 32%, which might be affected the recovery of the valuable minerals associated with (Table 6.4).

Table 6.5: Comparison of grade, recovery, and separation efficiency of the valuable minerals for two froth flotation tests of the composite sample P_{80} of 53 µm, processed under a constant pH level of 9.5 and high temperature of 60ºC with a long conditioning time of 60 minutes (T15) and a short conditioning time of 10 minutes (T24). Note % for both recovery and separation efficiency is mass/mass.

Test no.	Conditioning time (min)	Grade			Recovery (%)			Separation efficiency (%)		
		P_2O_5 (wt%)	Ce_2O_3 (ppm)	Y_2O_3 (ppm)	P_2O_5	Ce_2O_3	Y_2O_3	P_2O_5	Ce_2O_3	Y_2O_3
T15	60	5.11	17088	1590	85.97	74.30	73.51	57.47	44.60	43.66
T23	10	4.39	15616	1458	79.15	66.96	70.05	51.07	38.02	40.96

Overall, these results indicate that the increase in the conditioning time of the depressants may have no effect on their selectivity towards the gangue minerals. Also, these results lead to a question: is there a correlation between the Betacol dosage and mass pull rate in addition to the recovery of valuable minerals?

An interesting flotation test was conducted at a higher temperature of 80°C with a short conditioning time of 10 minutes for the depressants, but the Betacol collector was kept at the standard dosages of 120 g/t and 60 g/t for the first and second stage, respectively. The results are given in Appendix K, T24. The results show that the mass pull increases from 30.11% to 40.78% in the flotation tests T23 and T24, respectively. Also, the recovery of the valuable and gangue minerals increases as temperature increases from 60°C to 80°C and Betacol dosage increases from 90 g/t to 120 g/t of the flotation tests T23 and T24, respectively, Appendix K, T23 and T24.

It is interesting to note that in test T24 a too much froth formed after the first addition of Betacol requiring a decrease in air flow rate. However, when the air flow rate was decreased from 1.5 L min^{-1} to 0.5 L min^{-1} in tests T23 and T24 respectively, a high amount of mass pull of 27% formed in rougher concentrate 1 of the test T24 compared to 20% of mass pull in rougher concentrate 1 of the test T23.

6.11 Effect of NaOH versus Na_2CO_3 on the selectivity of the Betacol collector

As the spectrophotometer measurements showed that the solubility of Betacol in a 9.5 pH solution slightly varied from 80% to 76% when soda ash and caustic soda, respectively were used as pH modifiers, it was important to conduct a flotation test to determine the effect of these pH modifiers on Betacol collector in a feed pulp and see its selectivity degree towards the valuable minerals.

The experimental results of the grade, recovery, and separation efficiency of P_2O_5, Ce_2O_3, and Y_2O_3 using soda ash (sodium carbonate) versus caustic soda (sodium hydroxide) as pH modifiers under the same operating conditions are shown in Table 6.6, while the details are given in Appendix K (T15 and T25).

Table 6.6: Comparison of the grade and recovery of the valuable minerals for two froth flotation tests of the composite sample P_{80} of 53 µm, processed with different pH modifiers of Na_2CO_3 (T15) and NaOH (T25) under a constant pH level of 9.5, high temperature of 60ºC, and long conditioning time of 60 minutes. Note % for the mass pull, recovery, and separation efficiency is mass/mass.

Test no.	pH modifier	Mass pull (%)	Grade			Recovery (%)			Separation efficiency (%)		
			P_2O_5 (wt%)	Ce_2O_3 (ppm)	Y_2O_3 (ppm)	P_2O_5	Ce_2O_3	Y_2O_3	P_2O_5	Ce_2O_3	Y_2O_3
T15	Na_2CO_3	31.02	5.11	17088	1590	85.97	74.30	73.51	57.47	44.60	43.66
T25	NaOH	30.78	3.44	15268	1268	68.96	64.67	62.30	39.64	34.96	32.34
P-value*		0.476	0.206	0.065	0.053	0.027	0.038	0.020	0.006	0.033	0.038

* *P*-value calculated based on the experimental results of T15, T15 (duplicate), T25, and T25 (duplicate) using a two-sample *t*-test assuming unequal variances and the significance level of α=0.05 was regarded as statistically significant.

The table 6.6 shows that the grade, recovery, and separation efficiency of P_2O_5, Ce_2O_3, and Y_2O_3 decrease in flotation test T25 with caustic soda compared to those obtained from test T15 with soda ash under the same operating conditions. However, the results in Table 6.6 show that the grade highly decreases from T15 to T25 due to change the pH modifier from soda ash to caustic soda, the calculated *P*-value for the valuable minerals grade is higher than the significance level (α=0.05), which indicates that the decrease in the grade is not statistically significant. On the other hand, Table 6.6 also shows a notable decrease in the recovery and separation efficiency of the valuable minerals, the calculated *P*-value is lower than the significance level (α=0.05), which indicates the difference is statistically significant.

Therefore, conditioning feed pulp using soda ash rather than caustic soda would also be suggested to have an important influence on the recovery and separation efficiency of the valuable minerals.

It is interesting to note that the grade and recovery of CaO, Fe_2O_3, and SiO_2 slightly varies between the test T15 and T25. This indicates that the pH modifier did not affect the solubility and selectivity of the depressants, however it is apparent from the spectrophotometer measurements they affected slightly the solubility of the collector (Betacol). Leja (1982) stated that the ions of a pH modifier may have a side effect and play a very significant role in some flotation systems.

6.12 Sodium oleate as a collector under different conditioning time

In this flotation test, a soluble fatty acid salt 'sodium oleate' was used as a collector to determine if its selectivity towards the valuable minerals could be varied under different conditioning times of 60 minutes and 10 minutes. Multiple flotation tests were conducted to set the required dosage of sodium oleate that produce a mass pull of about 30% for the comparison purposes under the same operating conditions. Sodium oleate dosages of 80 g/t for the first stage and 15 g/t for the second stage were selected during conducting the flotation test.

The experimental results performed from two flotation tests in addition to the duplicated tests at long (60 minutes) and short (10 minutes) conditioning times are summarised in Table 6.7 and the details are given in Appendix K (T26, T26 Duplicate, T27, and T27 Duplicate).

Table 6.7: Comparison of grade, recovery, and separation efficiency of the valuable minerals for two froth flotation tests of the composite sample P_{80} of 53 µm, processed with sodium oleate collector at a constant pH level of 9.5, high temperature of 60ºC, and long conditioning time of 60 minutes (T26) and a short condition time of 10 minutes (T27). Note % for the mass pull, recovery, and separation efficiency is mass/mass.

Test no.	Conditioning time (min)	Mass pull (%)	Grade			Recovery (%)			Separation efficiency (%)		
			P_2O_5 (wt%)	Ce_2O_3 (ppm)	Y_2O_3 (ppm)	P_2O_5	Ce_2O_3	Y_2O_3	P_2O_5	Ce_2O_3	Y_2O_3
T26	60	31.63	3.52	14242	1266	74.92	66.11	67.52	44.88	35.49	36.77
T27	10	55.04	2.44	9500	853	79.00	72.76	76.02	24.97	18.26	21.51
P-value*		0.032	0.026	0.008	0.016	0.024	0.038	0.032	0.035	0.030	0.033

* *P*-value calculated based on the experimental results of T26, T26 (duplicate), T27, and T27 (duplicate) using a two-sample *t*-test assuming unequal variances and the significance level of α=0.05 was regarded as statistically significant.

It can be seen from Table 6.7 that the grade of P_2O_5, Ce_2O_3, and Y_2O_3 decreases as the conditioning time decreases from 60 minutes to 10 minutes, while the recovery, as expected, increases as the conditioning time decreases from 60 minutes to 10 minutes. The decrease and increase in the grade and recovery respectively as the decrease in conditioning time may be due to the reduction in the selectivity and adsorption of the collector toward the valuable minerals and to increase the amount of gangue minerals to the rougher concentrate, respectively. The results also show that the separation efficiency of the valuable minerals decreases as the conditioning time decreases. This may be due to the decrease in the grade degree of the valuable minerals and the increase in the mass pull from 31% to 55%, Table 6.7.

The statistical analysis using *t*-test showed that the calculated *P*-value for the grade, recovery, and separation efficiency of the valuable mineral as well as the mass pull is lower than the significance level (α=0.05), which indicates the difference is statistically significant. Thus, process feed pulp at long conditioning time of 60 minutes might have a significant effect on the increase in the grade and separation efficiency, it also may lead to significant decrease in the recovery of the target minerals.

Prior to this work, as discussed in Section 6.4, it was verified that water-insoluble collectors such as Betacol require a long conditioning time to improve the probability of particle-bubble collision and attachment (Sun et al., 1955; Runolinna et al., 1960 cited in Parekh and Miller, 1999), while this work shows the opposite. The experimental results present that long conditioning time is required to improve the selectivity/adsorption and hence the recovery whether the collector is a water-soluble or not.

6.13 Effect of NaOH versus Na_2CO_3 on the selectivity of the sodium oleate

This flotation test aims to determine the effect of caustic soda and soda ash on the selectivity of sodium oleate under the same operating conditions.

The experimental results of the grade, recovery, and separation efficiency of P_2O_5, Ce_2O_3, and Y_2O_3 using caustic soda versus soda ash as pH modifiers with a similar rate of mass pull are illustrated in Table 6.8, while the details are given in Appendix K (T26 and T28).

Table 6.8: Comparison of grade, recovery, and separation efficiency of the valuable minerals for two froth flotation tests of the composite sample P_{80} of 53 µm, processed with sodium oleate collector using different pH modifiers of NaOH (T26) and Na_2CO_3 (T28) under a constant pH level of 9.5, high temperature of 60ºC, and long conditioning time of 60 minutes. Note % for the mass pull, recovery, and separation efficiency is mass/mass.

Test no.	pH modifier	Mass pull (%)	Grade			Recovery (%)			Separation efficiency (%)		
			P_2O_5 (wt%)	Ce_2O_3 (ppm)	Y_2O_3 (ppm)	P_2O_5	Ce_2O_3	Y_2O_3	P_2O_5	Ce_2O_3	Y_2O_3
T26	NaOH	31.63	3.52	14242	1266	74.92	66.11	67.52	44.88	35.49	36.77
T28	Na_2CO_3	30.66	3.68	14804	1352	72.73	63.86	65.18	43.69	34.22	35.42

An interesting observation in these data is that the grade, recovery, and separation efficiency of P_2O_5, Ce_2O_3, and Y_2O_3 remain relatively similar under different types of pH modifiers. The slightly increase in the grade and decrease in the recovery of P_2O_5, Ce_2O_3, and Y_2O_3 with change the pH modifier from caustic soda to soda ash are attributed to the slightly decrease in the rate of mass pull from 31.63% to 30.66%, respectively.

Overall, this may have indicated that both pH modifiers have a similar effect on the solubility of sodium oleate collector as shown from the spectrophotometer measurements and hence on the selectivity and adsorption toward the valuable minerals.

6.14 Flotation kinetics

Since the main purpose of the flotation kinetics is to understand the effect of several parameters on the flotation process, four froth flotation tests were selected including (T1, T2, T15, and T16) to determine the effect of flotation pulp pH on the recovery of the valuable and gangue minerals. The experimental recovery data as a function of flotation time were fitted to the classical first-order model using equation 2.6 (see Chapter 2, Section 2.11.6). MATLAB® 2016a software was used to fit the data in non-linear regression profiles and to obtain the kinetic parameters including the ultimate recovery (R_∞), flotation rate constant (K), and modified flotation rate constant (K_M). The results are shown in Figure 6.19 and Table 6.9.

It is apparent from the results (Figure 6.19) that apatite shows the highest flotation kinetic behaviour, followed by synchysite. Also, there is a clear trend of decreasing flotation rate of carbonate, iron oxide/carbonate, and silicate gangue minerals. However, this indicates that the collector and depressants show efficient influence towards the valuable and gangue minerals, respectively, still interesting amount of valuable minerals, especially synchysite was reported to the tailings and gangue minerals, particularly carbonates (calcite and ankerite) were recovered to the concentrate. A likely explanation for these results is the degree of mineral liberation. It is indicated from the QEMSCAN® measurements that apatite is more liberated than synchysite. Furthermore, Figure 6.19 shows that the estimated recovery for apatite and synchysite over the first minute is about half their recoveries over 3 minutes. This indicates that the proportion of floatable minerals increases with increasing flotation time, however the recovery slightly increases after 6 minutes of the flotation time.

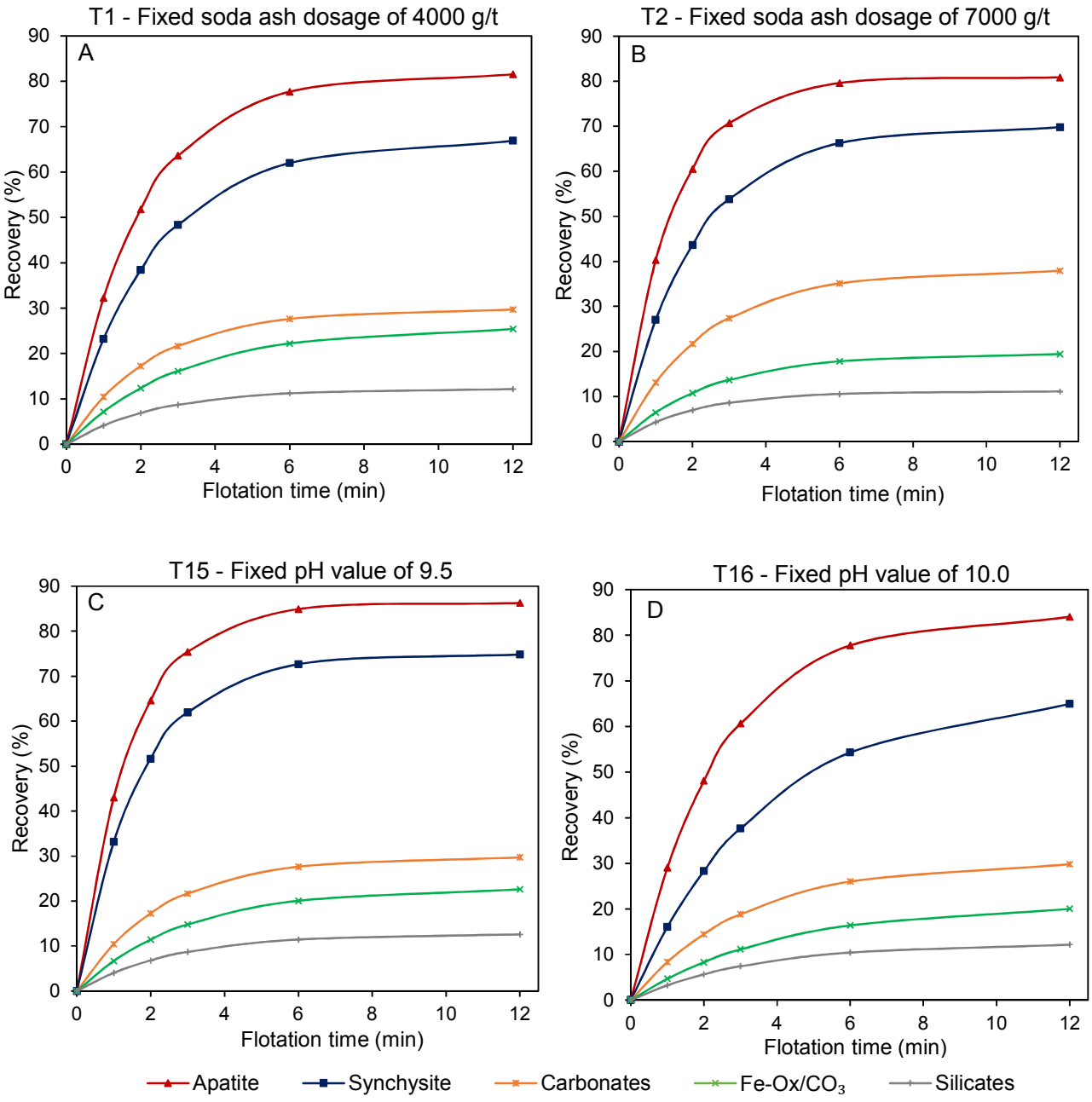

Figure 6.19: Fitting to classical first-order flotation kinetic model for the valuable and gangue minerals of two flotation tests of the composite sa mple P_{80} of 53 µm, processed under a long conditioning time of 60 minutes and high temperature of 60ºC: (A) T1 - fixed soda ash dosage of 4000 g/t, (B) T2 - fixed soda ash dosage of 7000 g/t, (C) T15 - fixed pH value of 9.5, and (D) T16 - fixed pH value of 10.0. Note P_2O_5, Ce_2O_3, CaO, Fe_2O_3, and SiO_2 were utilised as proxies for apatite, synchysite, carbonates (calcite and ankerite), iron oxides/carbonate, and silicates, respectively.

Table 6.9 presents the kinetic model parameters derived from the fitting non-linear regression profiles for the valuable and gangue minerals. For valuable minerals, the highest ultimate recovery R_∞ and rate constant K for apatite of 86.28% and 0.69 min^{-1}, respectively and for synchysite of 74.90% and 0.58 min^{-1} respectively are obtained by processing the feed pulp at a fixed pH value of 9.5, flotation test (T15). The lowest R_∞ for apatite of 80.88% is obtained at the high soda ash dosage flotation test (T2), while R_∞ for synchysite is obtained at the low soda ash dosage flotation test (T1), whereas the lowest K parameter for both apatite and synchysite of 0.42 min^{-1} and 0.27 min^{-1}, respectively is obtained by processing the feed pulp at a fixed pH value of 10.0, flotation test (T16).

In terms of the calculated modified rate constant K_M, Table 6.9 shows that the highest and lowest value of K_M for all valuable and gangue minerals achieved by processing the feed pulp at a fixed pH value of 9.5 (T15) and 10.0 (T16), respectively.

Table 6.9: Estimated kinetic parameters for the valuable and gangue minerals fitting to classical first-order flotation kinetic model for four flotation tests of composite sample P_{80} of 53 µm, processed under a long conditioning time of 60 minutes and high temperature of 60ºC: T1 - fixed soda ash dosage of 4000 g/t, T2 - fixed soda ash dosage of 7000 g/t, T15 - fixed pH of 9.5, and T16 - fixed pH of 10.0.

Test no.	Apatite			Synchysite			Carbonates			Fe-Ox/CO_3			Silicates		
	R_∞ %	K min^{-1}	K_M	R_∞ %	K min^{-1}	K_M	R_∞ %	K min^{-1}	K_M	R_∞ %	K min^{-1}	K_M	R_∞ %	K min^{-1}	K_M
T1	81.74	0.50	41.02	67.30	0.42	28.45	29.90	0.43	12.86	25.94	0.32	8.41	12.26	0.41	5.07
T2	80.88	0.69	55.83	69.99	0.49	34.19	38.16	0.42	16.09	19.60	0.40	7.83	11.18	0.49	5.47
T15	86.28	0.69	59.53	74.90	0.58	43.80	35.53	0.59	20.91	22.98	0.34	7.91	12.73	0.38	4.87
T16	84.56	0.42	35.53	67.56	0.27	18.31	30.41	0.32	9.78	21.04	0.25	5.28	12.48	0.30	3.76

Additionally, another useful parameter to evaluate the effect of different conditions on the flotation performance is the selectivity index (SI), which is the ratio of the modified flotation rate constants (K_M) of the valuable minerals (i.e. apatite and synchysite) over the gangue minerals (i.e. carbonates, iron oxides/carbonates, and silicates). The results of selectivity index for four flotation tests under different pulp pH values are shown in Figure 6.20.

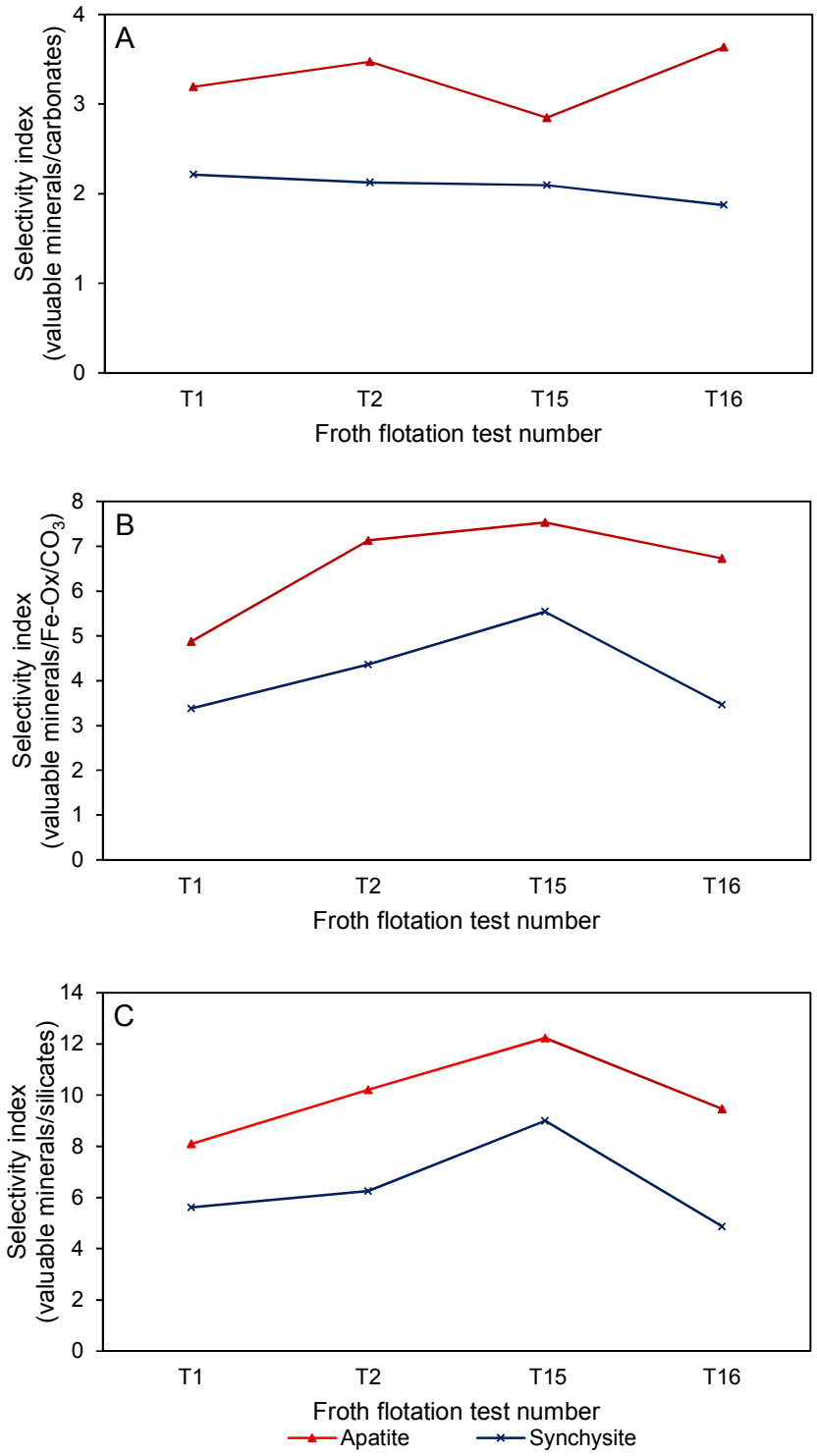

Figure 6.20: Comparison of selectivity index of the valuable minerals i.e. apatite and synchysite relative to (A) carbonates, (B) Fe-Ox/CO_3, and (C) silicates for four flotation tests of composite sample P_{80} of 53 µm, processed under a long conditioning time of 60 minutes and high temperature of 60ºC: T1 – fixed soda ash dosage of 4000 g/t, T2 – fixed soda ash dosage of 7000 g/t, T15 – fixed pH of 9.5, and T16 – fixed pH of 10.0.

Figure 6.20 A shows that the highest selectivity in flotation of apatite relative to carbonate gangue minerals occurs in the flotation test (T16) at a fixed pH value of 10.0, followed by the flotation test (T2) at a high dosage of soda ash of 7000 g/t where the conditioning of fatty acid collector performed within a pH value of about 9.8 (see Appendix K, T2), while the lowest selectivity for apatite relative to carbonates appears in the flotation test (T15) at a fixed pH value of 9.5.

The increase in apatite selectivity over carbonate gangue minerals could be due to the variation in the solubility of these minerals. It is experimentally indicated that at a pH below 8.9, the solubility of apatite is highly reduced, while it is enhanced at a pH above 8.9, however, opposite effects are observed for calcite (Amankonah et al., 1985). Therefore, this could explain that at higher alkaline pH values, the solubility of apatite increases and calcite decreases, which in turns improves the adsorption of fatty acid collector to Ca^{2+} sites on apatite than Ca^{2+} sites on calcite and hence increases its selectivity towards apatite.

In terms of selectivity of synchysite, Figure 6.20 A indicates that there is a small variation in the selectivity of synchysite relative to carbonate gangue minerals within a range of (1.87 to 2.21) under different pulp pH values of the selected froth flotation tests.

Figures 6.20 B and 6.20 C show that the selectivity in flotation of apatite and synchysite relative to iron oxide/carbonate and silicate gangue minerals has a similar trend. The highest selectivity for both apatite and synchysite relative to iron oxides/carbonates and silicates achieves in the flotation test (T15) at a fixed pH value of 9.5. The lowest selectivity for both apatite and synchysite relative to iron oxides/carbonates occurs in the flotation test (T1) at a low dosage of soda ash of 4000 g/t, while the lowest selectivity for apatite relative to silicate minerals appears also in the flotation test (T1) at a low dosage of soda ash of 4000 g/t, whereas the selectivity for synchysite relative silicate minerals occurs in the flotation test (T16) at a fixed pH value of 10.0.

Overall, based on the results in Figure 6.20, it seems likely that conditioning a fatty acid collector at a fixed pH value of 10.0 during the first stage to optimise the valuable minerals selectivity relative to carbonate gangue minerals, while conditioning fatty acid collector at a fixed pH value of 9.5 during the second stage to

optimise the valuable minerals selectivity relative to iron oxide/carbonate and silicate gangue minerals.

6.15 Conclusions

35 bench-scale rougher froth flotation tests were performed on the Songwe Hill carbonatite deposit to optimise the REE and P_2O_5 grade and recovery by gaining a thorough improved understanding the behaviour of different chemical reagents and the effect of various operating conditions. Based on the experimental results, the following key conclusions can be drawn:

- The highest recovery of apatite of 86% and synchysite of 74% at a mass pull of 31% was achieved by processing the feed pulp sample under a constant pH of 9.5 and a long conditioning time of 60 minutes. The REE recovery was improved from 66% to 74% with no reproducibility issues encountered under these processing conditions.
- The findings of this investigation showed that the recovery of apatite was always higher than the recovery of synchysite in all froth flotation tests. This may be due to the coarse-grained nature of apatite compared to synchysite, which results in a higher degree of liberation of 68% for apatite compared to 31% for synchysite.
- The grade of valuable minerals decreased while their recoveries and mass pull increased as the added fixed dosage of soda ash at the beginning of the flotation tests was increased from 4000 g/t to 7000 g/t. Further increase to 10000 g/t dropped the grade and recovery of valuable minerals and increased the mass pull rate.
- Replicating fixed soda ash dosage flotation tests to achieve similar results was a challenge due to the variations in the grade, recovery, and mass pull throughout the tests. This could be explained as a result of the heterogeneous nature of carbonatite deposit as indicated from the variation in the calculated feed grades, or the chemistry of the feed water, which led to the variation in the pH levels from one conditioning stage to another and hence affected the solubility and selectivity of the chemical reagents.
- The bench flotation tests at a constant level of pH demonstrated interesting findings. They showed a systematic improvement in the grade of the valuable miner-

als with gradual reduction in the mass pull as the pH value was increased from 8.5 up to 10 achieving a highest recovery at a pH value of 9.5. These findings indicated that the pH level has a significant influence on the solubility, selectivity and adsorption of the chemical reagents, particularly Betacol toward the valuable minerals.

- Betacol and sodium oleate reagents act as efficient collectors, particularly Betacol for both valuable minerals i.e. apatite and synchysite, in addition to their action as efficient frothers.
- This investigation has shown that the selectivity of water-soluble and insoluble collectors i.e. sodium oleate and Betacol, respectively is significantly improved as the conditioning time increases from 10 minutes to 60 minutes. This is indicated from the increase in grade of valuable minerals and reduction of the mass pull.
- The spectrophotometer measurements improved understanding behaviour of the dissociable organic chemical reagents including Betacol, sodium oleate and lignin sulphonate by measuring their solubility in different alkaline solutions. These measurements have shown that the used chemical reagents are significantly dependent on the pH level. The results showed a linear relationship between the solubility of both Betacol and sodium oleate collectors with increasing the pH value from 8.5 to 10.5. Conversely, the solubility of lignin sulphonate decreased as the pH value was increased from 8.5 to 10.5.
- The experimental flotation tests indicated, and the spectrophotometer measurements confirmed, that Betacol, sodium oleate, and lignin sulphonate are very sensitive to pH. It seems that pH controls their ionisation at certain values, therefore, enhances their selectivity towards the valuable/gangue minerals and hence the flotation efficiency.
- Lignin sulphonate is an efficient depressant for the carbonate gangue minerals, particularly at a pH of 8.5. It also controls the rate of mass pull by depressing the carbonates, calcite and ankerite, which form about 57 wt% of the carbonatite rock-forming minerals.
- The selectivity of lignin sulphonate towards the gangue minerals highly improved and hence their rejection percentage to the tailings increased as the pH level was

decreased from 10.5 to 8.5. These bench flotation tests are in agreement with the solubility of lignin sulphonate results measured by spectrophotometer.

- Processing the deposit by conditioning the depressants for 10 minutes each and the collector for 60 minutes did not show a notable effect on the selectivity of depressants towards the gangue minerals. It showed that the grade and recovery, particularly the carbonate gangue minerals are slightly decreased compared to the long conditioning time flotation tests. It also showed a similar grade of the valuable minerals and mass pull were achieved, while the recovery of apatite decreased from 86% to 79%, and synchysite from 74% to 67%.
- The mass pull rate can be reduced by enhancing the ionisation of lignin sulphonate and/or decreasing the collector dosage, however this may lead to a reduction in the recovery of valuable minerals as a result of depressing the carbonate gangue minerals that host synchysite and apatite, as indicated from the QEMSCAN® measurements.
- Increasing temperature of the feed pulp from 20°C through 60°C notably improved the selectivity of the collector towards the valuable minerals, particularly apatite. This is in agreement with published studies. Conversely, there is no effect observed from increase the temperature on the selectivity of lignin sulphonate as the recovery of carbonate gangue minerals was similar in the rougher concentrates.
- A first-order kinetic model can be used to analyse the experimental flotation data and understand better the effect of chemical, physical, and operating parameters on the flotation process. It can be used to estimate apatite and synchysite recovery over the first 60 seconds. Furthermore, the modified flotation rate constant (K_M) and hence the selectivity index are useful tools for comparative evaluation of different variables affecting flotation performance.

Chapter 7

Discussion

7.1 Introduction

This chapter discusses how the mineralogy and the texture of the ore deposit studied can affect the design of the mineral processing flowsheet and how it can aid interpretation of the results for the whole process. A recommended beneficiation flowsheet is presented and discussed. Examples of processing other synchysite-rich deposits are demonstrated and discussed.

7.2 Role of automated mineralogy in mineral processing

Characterisation of the mineralogical texture of an ore body is a powerful and integrated tool for designing processing routes and improving separation performance (Gottlieb et al., 2000; Lotter et al., 2002; Evans et al., 2011). However, a successful separation process mainly depends on differences in physical and chemical properties (such as specific gravity, magnetic and electrostatic response) and surface chemistry between the valuable and gangue minerals. Identification and quantification of the key mineralogical parameters i.e. mineral identity and content, liberation, association, and grain size distribution can also play a significant role in predicting the possible flowsheet options for processing an ore deposit. They are also a vital tool for metallurgical troubleshooting and data interpretation during and after the design of a mineral processing flowsheet.

The modal mineralogy of the Songwe Hill carbonatite, as determined by automated mineralogy, and the specific gravity and magnetic properties of the major minerals are given in Table 7.1. The consideration of these mineralogical and physical characteristics has important implications for choosing the best mineral processing technique to separate the minerals of interest from their gangue matrices. It is apparent from Table 7.1 that there is a small difference in terms of specific gravity between apatite (major valuable mineral) and ankerite and calcite (major gangue minerals). Also, the specific gravity of synchysite is higher than the major gangue minerals, but the small grain size of synchysite and its association with other gangue

minerals should also be considered for gravity separation. The QEMSCAN® data (see Chapter 4) showed that synchysite has a small average grain size of 30 µm in the crushed drill core samples P_{100} of 1700 µm and about 10 µm in the ground composite sample P_{80} of 53 µm. This, as well as its association of about 43% with other gangue minerals, primarily ankerite and calcite could add another challenge to pre-concentration of this deposit using gravity separation. Thus, gravity separation was not applied to the Songwe Hill ore deposit due to the small differences in specific gravity between the valuable and gangue minerals, small size of mineral particles, and association of the valuable minerals with other gangue minerals. It is important to note here that the motion of particles in a fluid will be affected not only by the specific gravity, but also the particle size. The gravity separation efficiency increases with increasing the particle size and the difference in specific gravity between the valuable and gangue minerals (Gupta and Yan, 2016; Wills and Finch, 2016).

Table 7.1: Mineralogical composition of the major and minor valuable and gangue minerals of the Songwe Hill carbonatite deposit along with some of their physical characteristics (Tickell, 2011; Jordens et al., 2013; Krishnamurthy and Gupta, 2016; Wills and Finch, 2016).

	Mineral name	Mineral abundance (wt%)	Specific gravity[a]	Magnetic response		
				Ferromagnetic	Paramagnetic	Diamagnetic
Valuable	Apatite	5.56	3.2			x
Valuable	Florencite-(Ce)	0.60	3.6		N/A	
Valuable	Synchysite-(Ce)	3.22	4.0			x[b]
Gangue	Ankerite	30.34	3.1		x	
Gangue	Baryte	0.98	4.48			x
Gangue	Calcite	27.04	2.7			x
Gangue	Fe-Ox/CO_3[c]	12.69	3.8-5.3		◄---- x	
Gangue	K-feldspar	9.52	2.6			x
Gangue	Muscovite	1.87	2.8			x
Gangue	Strontianite	1.17	3.8			x

[a] Data from www.webmineral.com

[b] Based on the results of this study.

[c] Including goethite, hematite, siderite (paramagnetic), and/or magnetite (ferromagnetic).

N/A not available.

Table 7.1 shows that there is an interesting difference in the magnetic properties of the valuable apatite versus a couple of gangue minerals i.e. ankerite and Fe-Ox/CO_3

which form about 43 wt% of Songwe Hill deposit. However, in reviewing the literature, no data were found on the magnetic properties of synchysite. The VSM measurements of pure single crystals of REE fluorcarbonate minerals, in addition to the magnetic separation tests that were conducted during this study indicated that there is a variation in the magnetic properties of this group of minerals and showed that the liberated synchysite behaved as a diamagnetic mineral. Thus, owing to the behaviour of the major valuable minerals as diamagnetic and the presence of interesting amounts of paramagnetic gangue minerals, a wet high intensity magnetic separator was used to pre-concentrate Songwe Hill deposit and reject a high proportion of gangue minerals.

It is interesting to note that a good recovery for both valuable apatite and synchysite was achieved to the non-magnetic product accompanied by rejecting about 50% of the gangue minerals. The magnetic stream still contains some valuable minerals even though a two-stage separation process was applied. The quantitative automated mineralogical measurements of the magnetic separation products showed that the poorly liberated valuable minerals and the associated paramagnetic minerals were recovered to the magnetic product.

Other separation techniques considered to process the Songwe Hill deposit was froth flotation. This technique can achieve a specific separation of chemically similar minerals such as apatite and calcite and is also an efficient technique to process fine-grained ore bodies where the average particle size for liberation is too small for physical separation techniques such as gravity (Kelly and Spottiswood, 1982; Santana et al., 2008; Wills and Finch, 2016). Also, froth flotation has been the most widely employed technique for the beneficiation of igneous apatite owing to the well-crystallised nature and inherent low porosity of apatite compared to the apatite in sedimentary phosphates (Kawatra and Carlson, 2014). It was decided to conduct froth flotation experiments on the Songwe Hill deposit under different chemical and operating parameters in order to optimise the grade and recovery of the valuable minerals.

In terms of grinding the ore deposit under study, the QEMSCAN® measurements showed that the valuable minerals are poorly liberated and associated with all major and minor gangue minerals in the crushed drill core samples P_{100} of 1700 µm. Grinding the composite sample to P_{80} of 53 µm enhanced the liberation of the

minerals of interest, especially apatite, and decreased their associations with other gangue minerals. However, even though further grinding to P_{80} of 38 µm increased the liberation of apatite and synchysite, these minerals are still not fully liberated and remain associated with some major gangue minerals. Also, this fine grinding to P_{80} of 38 µm generated an additional amount of very fine particles i.e. <10 µm which always have been a serious problem in the beneficiation of valuable mineral (Pease et al., 2006; Wills and Finch, 2016). Thus, all mineral processing tests were conducted using ground composite samples P_{80} of 53 µm.

It is also important to note that according to the automated mineralogical data for the size-by-size fractions, it is concluded that a desliming step, i.e. removal of the <10 µm fraction, prior to conduct a processing test will adversely affect the grade and recovery of the whole process. This can be explained as a result of losing about 23% and 26% of the total apatite and synchysite, respectively.

Finally, the combination of EPMA and QEMSCAN® measurements provided a good tool to determine the mineral processing efficiency by tracking the minerals of interests based on their elemental proxies (see Chapter 4, Section 4.7.2) rather examine the separation products using the expensive QEMSCAN®.

7.3 Songwe Carbonatite flowsheet development

The mineralogical results (Chapters 3 and 4) indicated that the complexity of the Songwe Hill deposit is not only attributed to the number of minerals but also to the small grain size of the valuable minerals and their associations with all the major, minor, and even trace minerals. The magnetic properties of REE fluorcarbonates and the mineral processing experimental results (Chapters 5 and 6) showed pre-concentration and upgrade can be achieved using magnetic separation and froth flotation.

Thus, based on the overall mineralogy and mineral processing results conducted on Songwe Hill carbonatite deposit, it is possible to suggest development of the beneficiation part of the mineral processing flowsheet.

The proposed processing flowsheet from the prefeasibility study comprises comminution, froth flotation, and hydrometallurgy circuits. It includes crushing and grinding of the composite sample to P_{80} of 53 µm, processing the head ground sample by froth flotation, and then subjecting the rougher concentrate to hydrochloric

acid leaching to remove the carbonate gangue minerals including calcite and ankerite (Croll et al., 2014; Figure 7.1).

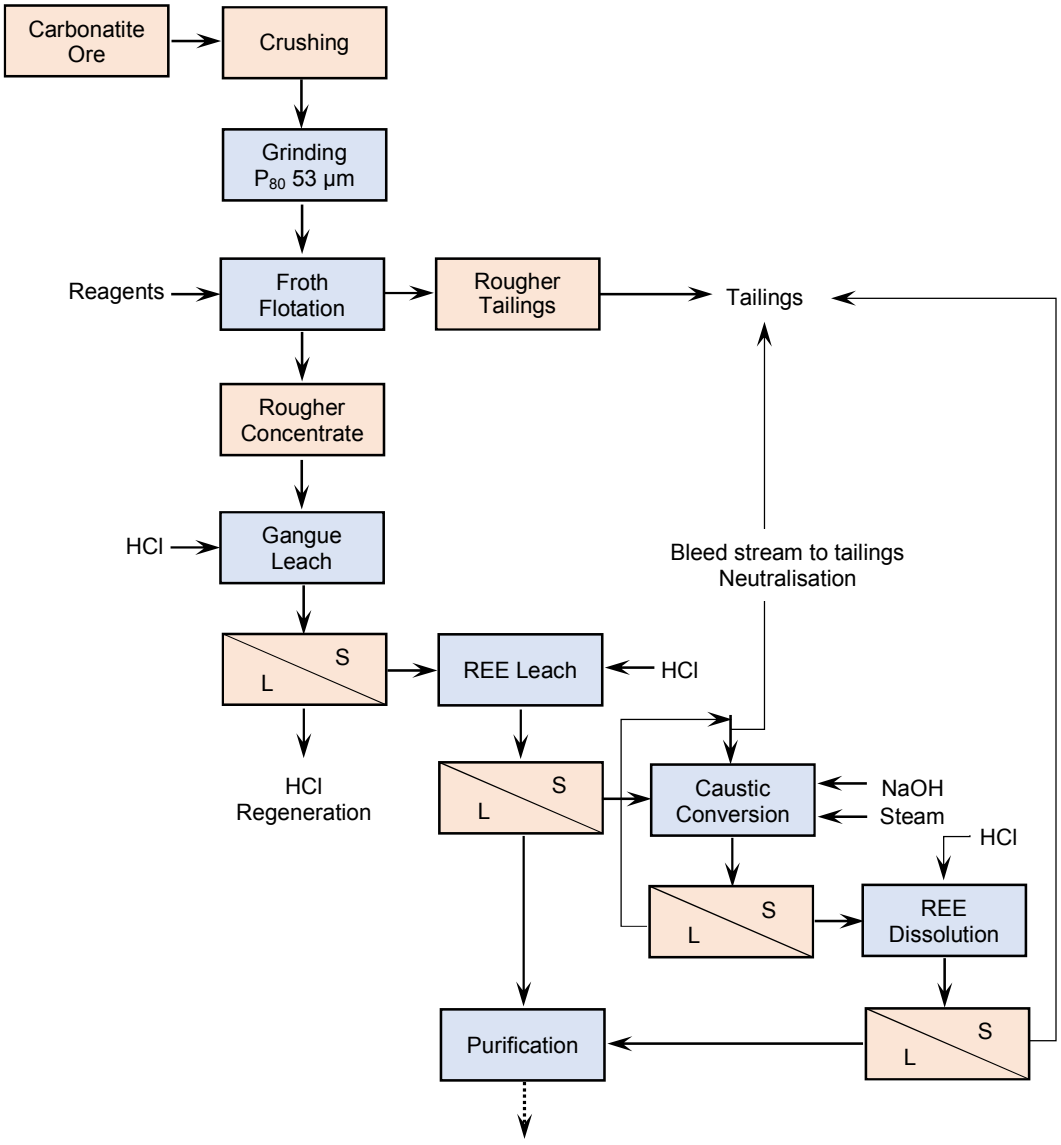

Figure 7.1: The processing flowsheet for beneficiation of Songwe Carbonatite deposit. After Croll et al. (2014).

Based on the magnetic and flotation experimental results of this study, the suggested beneficiation part for the mineral processing flowsheet includes adding a wet screening unit using a sieve of 45 µm to split the oversize particles of the ground composite sample P_{80} of 53 µm. The oversize will be further subjected to a finer grinding to improve the liberation of the locked valuable grains and avoid the large

particles to be entrapped inside the matrix for the next processing step. The sample then will be processed using a wet high intensity magnetic separator. The non-magnetic product will be used as a head sample for the flotation process, while the magnetic product will be transferred as a waste to the tailings storage facility (see Figure 7.2).

Froth flotation tests were not conducted on the non-magnetic product from the magnetic separation tests for the following reasons: firstly, more work was needed to set the required reagent dosages due to change the content of the mineral components of the new feed sample (i.e. non-magnetic product); secondly, due to the limitation of sample quantities which already have been used to conduct the magnetic separation and froth flotation tests, it was a challenge to obtain enough amount of concentrate may be several kilos to run a number of flotation tests; and thirdly, Mkango Resources Ltd. was mainly focusing on optimising the deposit under investigation using froth flotation due to the small grain size of the valuable minerals (see Chapter 4, Section 4.5.4), a small difference between the valuable and gangue minerals in terms of the specific gravity as discussed above (see Table 7.1), and it was estimated that synchysite-(Ce) would behave in the same way like bastnäsite-(Ce) as a paramagnetic mineral and will be lost with other paramagnetic minerals, while the diamagnetic apatite (hosts HREE) will be recovered to non-magnetic product.

The purpose of adding a pre-concentration step using magnetic separation prior to flotation process is to reduce the percentage of the gangue minerals. This helps to minimise the chemical reagent consumption for the flotation process and the acid consumption during the gangue leach of the rougher concentrate.

It is evident from the magnetic separation results and confirmed by the automated mineralogical measurements that about 49% of ankerite and 48% of iron oxides/carbonates were rejected to the magnetic product, in addition to rejection 17% of calcite and 11% of K-feldspar. This rejection will help to minimise the amount of the chemical reagents and hence their costs for the next processes i.e. froth flotation and leaching. The pre-feasibility study results indicated that the total cost of the chemical reagents comprises more than 70% of the total operating cost estimated for the Songwe Hill project processing plants (Croll et al., 2014).

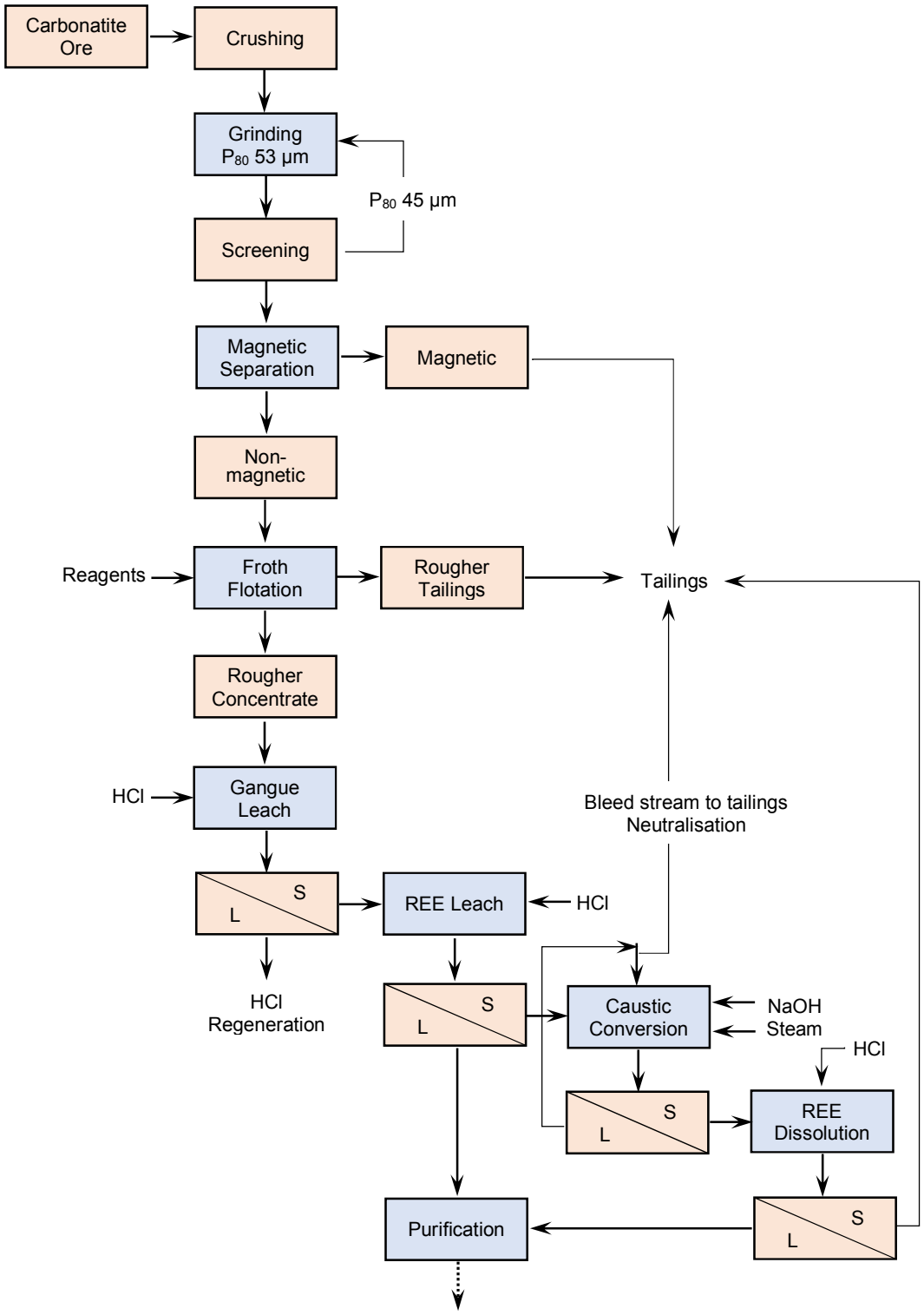

Figure 7.2: A suggested processing flowsheet for beneficiation of Songwe Carbonatite deposit based on the mineralogy and mineral processing results of this study. Modified after Croll et al. (2014).

It is important to note that about 16% of apatite and 24% of synchysite were lost to the magnetic product at the grinding size P_{80} of 53 µm owing to their association with paramagnetic minerals, particularly ankerite. This amount was decreased to 13% for apatite and 18% for synchysite with a further grinding to P_{80} of 38 µm as a result of enhancing the liberation degree of the valuable minerals.

A full economic assessment is beyond the scope of this thesis, it would be necessary to balance the losses of REE in the magnetic product against the reduction in reagents consumption in flotation and leaching processes.

It can be summarised the main contributions of this work to the flowsheet development:

- Extensive automated mineralogy on Songwe Hill deposit was carried out to determine the key mineralogical parameters including modal mineralogy, mineral liberation and association, and grain size distribution that play a role in selecting the mineral processing technique(s) to process this ore deposit. Also, the mineralogical data were used to interpret the mineral processing test results.
- Fundamental magnetic properties of REE fluorcarbonate minerals, which may be reported for the first time for some of these minerals, were measured to see the possibility to separate synchysite and apatite from their gangues. These measurements showed that the magnetic susceptibility is 3.0×10^{-4} (paramagnetic) for bastnäsite-(Ce) and gradually decreases as the amount of Ca increases in parisite-(Ce) 0.6×10^{-4}, becoming -0.1×10^{-4} (diamagnetic) for the Ca-rich member of the series, röntgenite. Synchysite-(Ce) in this deposit was experimentally determined by magnetic separation and behaved as a diamagnetic mineral.
- Magnetic separation testwork under different size fractions, experimental procedures, and process conditions were conducted. These showed that it is possible to pre-concentrate the valuable minerals along with rejection of a significant amount of gangue. It is important to note that Mkango Resources Ltd and Mintek avoided magnetic separation owing to assumption that synchysite-(Ce) would behave as a paramagnetic mineral in the same way as bastnäsite-(Ce).

- A spectrophotometer was utilised to measure the solubility of the organic chemical reagents including fatty acids and lignin sulphonate in different alkaline solutions to determine the appropriate operating parameters for bench flotation tests. The results indicated that the solubility of fatty acids increased with increasing the pH value from 8.5 to 10.5, while the opposite was observed for lignin sulphonate.
- Bench froth flotation tests under a wide range of chemical and operating conditions, including pH modifiers and dosages, water-soluble and insoluble collectors, depressants, temperature, conditioning time, and grinding size, were used to investigate possible reductions in the operating costs and improve the flotation efficiency. The flotation tests indicated that decreasing the pulp temperature from 60ºC to 20ºC led to a decrease in the flotation efficiency. Keeping the pulp pH at a constant level rather than a constant dosage improved the REE recovery from 66% to 74% with no reproducibility issue. It is important to note that these conditions and parameters were not tested in Mintek or elsewhere apart from conducting the constant dosage of 4000 g/t and 7000 g/t flotation tests.

7.4 Processing synchysite in other REE deposits

Synchysite is one of the principal valuable minerals for REE and the second most reported mineral of the REE fluorcarbonate group (Wang et al., 1994). Table 7.2 illustrates the most common deposits that contain synchysite as a major mineral and also other deposits in which synchysite is considered as a mineral of economic interest, even if it is less abundant than the principal REE minerals such as bastnäsite or parisite.

In terms of processing synchysite in REE ore deposits, the three aspects of mineral chemistry, crystal shape and size, and mineral association should be considered.

Table 7.2: Examples of some REE ore deposits contain synchysite as a principal or secondary REE mineral.

REE deposit	Lithology	REE minerals	Grade	Reference
Springer Lavergne, ON, Canada	Carbonatite	Synchysite-(Ce)	16.9 Mt at ~1.16 % REO	Mariano and Mariano (2012); Daigle (2012)
Adiounedj, Mali	Carbonatite	Synchysite-(Ce)	No data	Wall and Mariano (1990); Verplanck et al. (2015)
Lugiin Gol, Mongolia	Nepheline syenite	Synchysite-(Ce)	0.023 Mt at 3.2% REO	Haumdas et al. (1995); Krishnamurthy and Gupta (2016)
Kutessay, Kyrgyzstan	Granite	Synchysite-(Y)	16.28 Mt at 0.264% REO	Chakhmouradian and Wall (2012); Hyland and Ulrich (2014)
Barra do Itapirapuã, Brazil	Carbonatite	Parisite, synchysite, and rare bastnäsite	No data	Ruberti et al. (2008); Chakhmouradian and Wall (2012)
Gatineau, Quebec, Canada	Carbonatite	Parisite-(Ce), synchysite-(Ce), monazite	No data	Hogarth et al. (1985)
Miaoya, China	Carbonatite	Bastnäsite, synchysite, monazite	1.72%	Kynicky et al. (2012)
Huanglongpu, China	Carbonatite	Bastnäsite, synchysite, monazite, xenotime	No data	
Huayangchuan, China	Carbonatite	Bastnäsite, synchysite, xenotime, allanite	No data	
Mt. Prindle, AK, USA	Hydrothermal mineralisation in syenite	Britholite, parisite, synchysite	No data	Mariano and Mariano (2012)
Rock Canyon Creek, BC, Canada	Carbonatite	Monazite, synchysite, bastnäsite, gorceixite	No data	
Mountain Pass, CA, USA	Calcite and dolomite carbonatite	Bastnäsite, parisite, synchysite	20-47 Mt at 8.9% REO	Wall and Mariano (1996); Krishnamurthy and Gupta (2016)
Thor Lake (blachford Lake), Canada	Magmatic peralkaline syenite, gabbro, granite	Xenotime, gadolinite, Y-fluorite, bastnäsite, parisite, synchysite, monazite, columbite, zircon	No data	Krishnamurthy and Gupta (2016)
Khaldzan-Buregtey, Western Mongolia	Peralkaline granite, gabbro, basalt, pantellerite dikes, syenite	Fergusonite, allanite, bastnäsite, synchysite, britholite, monazite, chevkinitev	>1.2 Mt at 0.3% REE	
Wigu Hill, Tanzania	Weathered dolomitic carbonatite	Bastnäsite, monazite, Ce–goyazite, synchysite, parisite	As much as 20% REO	
Wet Mountains, Co, USA	Magmatic Alkaline rocks, arbonatite Dikes Thorite, xenotime, baryte, hematite, quartz	Apatite, bastnäsite, synchysite, xenotime, monazite	13.96 Mt at 1.0% REO	
Khibina (Khibiny) Kola Peninsula, Russia	Foyaite, nepheline syenite, ijolite, rischorrite, urtite, pegmatites, carbonatite	Apatite, eudialyte, burbankite, ancylite, synchysite, parisite, carbocernaite, cordylite, astrophyllite, loparite, mosandrite, lovchorrite, rinkite	9 Mt REO	Nivin et al. (2005); Krishnamurthy and Gupta (2016)

7.4.1 Mineral chemistry

It is important to determine the elemental composition of synchysite to see which species of synchysite is occurred in the host deposit in addition to determine the content of the elements that possess a high magnetic susceptibility such as Nd, Pr, and Ce.

However, there is currently no available data for the magnetic properties of other synchysite species, such as synchysite-(Y) and synchysite-(Nd), it may be possible to estimate their behaviour based on their elemental composition. Table 7.3 presents the elemental composition of synchysite-(Y) and synchysite-(Nd). In nature, other REE would be present in the crystal structures, especially other mid and heavy REE in synchysite-(Y) and La and Ce in synchysite-(Nd). However, it can be seen from this table that synchysite-(Y) is Y and Ca dominant, while synchysite-(Nd) is Nd and Ca dominant. However, the volume magnetic susceptibility of 0.2978 x 10^{-3} for Y is positive, it is much lower than the volume magnetic susceptibility of 3.3648 x 10^{-3} for Nd, and even lower than Ce which is 1.4716 x 10^{-3}. By comparing the elemental composition of these minerals in Table 7.3 with the measured pure REE fluorcarbonates (see Chapter 5), it may be predicted that synchysite-(Y) could behave as a diamagnetic mineral, while synchysite-(Nd) as a paramagnetic mineral.

Table 7.3: The theoretical elemental composition of synchysite-(Y) and synchysite-(Nd).

Oxides	Synchysite-(Y)*	Synchysite-(Nd)*
CaO	20.92	17.34
Y_2O_3	42.13	-
Nd_2O_3	-	52.03
F	7.09	5.88
CO_2	32.84	27.22
-O=F	2.98	2.47
Total	100.00	100.00

* Weight % data from www.webmineral.com

7.4.2 Crystal shape and size

Crystal shape and size need to be considered owing to their effect on the degree of liberation, the most important parameter for processing an ore deposit. As discussed in Chapter 3, synchysite often occurs as thin plates (needle-like) crystals in 2D, or granular (lath-shaped) crystals. The needle-like crystals could be occurred as

clusters or individual crystals embedded within the gangue minerals. It may be easier to unlock the granular type synchysite and the cluster of needle-like crystals than those individual needles of synchysite.

Individual small crystals of synchysite would not be expected to be unlocked and in this case synchysite behaviour will be mainly affected by the host mineral. For example, processing a synchysite-rich deposit using magnetic separation may lead to recovery of the synchysite to the non-magnetic or magnetic product depending on whether it is hosted by a diamagnetic or paramagnetic mineral, respectively. A similar situation would be expected when processing an ore deposit contains needle-like crystals of synchysite by froth flotation. Conversely, granular large crystals of synchysite would be easier to liberate and subsequently recover. Also, the agglomeration of needle-like crystals of synchysite would behave as a large particle and it should be easier to recover.

7.4.3 Mineral association

It is important to determine the association percentage of synchysite with other gangue or even valuable minerals within a crushed ore sample prior to conduct any mineral processing experiment. For example, when synchysite occurs as very small needle-like crystals and mainly associated with paramagnetic minerals, in this case a coarse grinding would be recommended prior to undertake a magnetic separation experiment to pre-concentrate the ore deposit. This will keep synchysite inside the host paramagnetic particles and remove other diamagnetic gangue minerals to the non-magnetic product. Furthermore, as mentioned in Chapter 1, syntaxial intergrowth is a common feature among REE fluorcarbonate minerals. Thus, when synchysite is syntaxially intergrown with parisite and/or bastnäsite, it may be predicted to behave as a paramagnetic particle.

An example of synchysite associated with paramagnetic minerals is the Springer Lavergne carbonatite deposit in Ontario, Canada. Synchysite is the only REE mineral in this deposit and it mostly occurs as fine-grained clusters intimately associated with iron oxides and ankerite. Other gangue minerals are K-feldspar, pyroxene/amphibole, pyrite and quartz (Mariano and Mariano, 2012 in Daigle, 2012 and Deng and Hill, 2014). However, a magnetic separation and gravity concentration were conducted on this deposit to separate synchysite from its gangue minerals,

detailed results are not published apart from qualitative photographs for the magnetic and gravity concentrates.

As mentioned above and based on the QEMSCAN® results of this study, the associated synchysite-(Ce) crystals with ankerite and iron oxides/carbonates were reported to the magnetic products. Synchysite-(Ce) crystals in the Springer Lavergne deposit are mainly associated with iron oxides and ankerite. Thus, conduct a coarse grinding followed by a magnetic separation will recover the poorly liberated synchysite with the host paramagnetic particles to magnetic product. This process aims to pre-concentrate the deposit from diamagnetic gangue minerals such as K-feldspar and quartz.

7.5 Conclusions

This chapter discussed the role of automated mineralogy in mineral processing, linked together the overall mineralogy and mineral processing results to develop the processing flowsheet, and presented the main mineralogical parameters to process other synchysite ore deposits. Key conclusions from this discussion include:

- A successful separation process not only depends on the differences in the physical and chemical properties between the valuable and gangue minerals, but also on the mineralogical parameters such as mineral identity and content, liberation, association, and grain size distribution.
- Combining magnetic separation with froth flotation process will help to reduce the cost of chemical reagents required for the flotation and hydrometallurgical processes by rejecting a significant amount of the acid consumable component, such as ankerite.
- Pre-concentration of synchysite-(Ce), synchysite-(Y) or synchysite-(Nd) rich deposits can be achieved once the mineral chemistry, grain shape and size, and the association are determined for an efficient process. Host minerals are important when the, typically fine-grained blades of synchysite are poorly liberated. The host mineral might be used as the target for recovery by physical separation or froth flotation techniques, although this has not proved possible at Songwe Hill.

Chapter 8

Conclusions and recommendations

8.1 Conclusions

In this investigation, the aim was to determine the mineralogical characteristics of a fine-grained REE carbonatite deposit at Songwe Hill, Malawi using XRD, SEM-EDS, EPMA, and QEMSCAN®. It also aimed to link these mineralogical outputs together with the magnetic properties of pure REE fluorcarbonates to optimise the recovery of synchysite-(Ce) and apatite for their LREE, HREE, and P_2O_5 and to develop the process flowsheet by conducting a selected magnetic separation and froth flotation experiments. Thus, based on the mineralogy and mineral processing results, the following conclusions can be drawn:

1. Mineralogically, the ore deposit under investigation consists of about 6 wt% to 10 wt% of REE- and REE-bearing minerals, predominantly apatite and synchysite-(Ce)/parisite-(Ce), minor florencite-(Ce) along with very trace amounts of zircon, monazite, and bastnäsite-(Ce). Apatite with an average grain size of 50 µm, hosts the more valuable HREE in addition to P_2O_5. Synchysite-(Ce)/parisite-(Ce) (mainly synchysite-(Ce)), and florencite-(Ce), with an average grain size of 30 µm and 20 µm respectively, host the LREE. It is evident that apatite is easier to liberate and hence to separate than the needle-like crystals of synchysite, however both minerals are commonly associated with the predominant gangue minerals, ankerite and calcite, and, to a lesser extent, iron oxides/carbonates, K-feldspar, strontianite, and baryte. Florencite-(Ce) is commonly associated with apatite.
2. The findings of the VSM measurements linked with the EPMA data showed variations in the magnetic behaviour of the pure REE fluorcarbonate minerals and it is highly dependent on the mineral chemistry. It is apparent that as Ca content increases from bastnäsite, parisite, and röntgenite in order, accompanied by decreasing the TREO content, the magnetic susceptibility decreases from 3×10^{-4}, 0.6×10^{-4}, and -0.1×10^{-4}, respectively. It is also evident experimentally by the magnetic separation and confirmed mineralogically by the QEMSCAN®

measurements that the highly liberated synchysite crystals in this deposit behaved as diamagnetic minerals as they recovered to the non-magnetic product.

3. The pre-concentration experimental results using a wet high intensity magnetic separator showed that the optimum recovery achieved at a fine grind size P_{80} of 53 µm. At this condition, recoveries of 84% for apatite and 76% for synchysite were achieved into the non-magnetic product, accompanied by rejection about 51% of ankerite and 49% of iron oxides/carbonates into the magnetic product. Apatite and synchysite-(Ce) lost to the magnetic product is mainly the result of their association with the paramagnetic minerals (ankerite and iron oxides/carbonates) as indicated by automated mineralogy results, and also to entrapment of the large diamagnetic particles inside the matrix.
4. The bench-scale froth flotation tests showed that adding a fixed dosage of soda ash at the beginning of the experiment did not produce similar results for the duplicated tests. This is due to the heterogeneous nature of the deposit from one sample another as indicated from the calculated feed grades, or change in the chemistry of the feed water, which led to the variations in the pH level and hence affected the action of the chemical reagents. Conversely, keeping the pulp at a constant level of pH demonstrated interesting findings. The increase in the pH level from 8.5 to 10.0 improved the grade of the valuable minerals and reduced the mass pull with achieving highest recovery at a pH of 9.5. These findings indicated that the pulp pH has a significant influence on the solubility, selectivity, and adsorption of the chemical reagents towards the valuable and gangue minerals. An improved REE recovery from 66% to 74% with no reproducibility issue was achieved.
5. Combining magnetic separation and froth flotation to pre-concentrate and upgrade the REE- and REE-bearing minerals would also help to reduce the cost of chemical reagents, which account currently for more than 70% of the total estimated operating cost to process this deposit, by rejecting about a half amount of the acid consuming mineral “ankerite” and in addition rejecting a similar amount of iron oxide/carbonate gangue minerals.

8.2 Future work and recommendations

Additional investigation work on the Songwe Hill deposit to enhance the grade and recovery of the valuable minerals and reduce the mass pull rate is recommended. The key suggestions for further work are:

1. It would be interesting to perform a selective grinding at different size fractions to avoid producing too large and too fine particles by setting up a closed circuit grinding machine. This step also requires use of QEMSCAN® to determine the valuable minerals liberation and association.
2. It is strongly recommended to determine the liberation and mineral association of the flotation products, particularly the tailings using QEMSCAN® to confirm if the liberation is the main issue in maximising the grade and recovery of the valuable minerals.
3. It has been determined that the liberation of the valuable minerals increased as the size-by-size fraction decreased. Thus, perform size-by-size flotation experiments is recommended.
4. Further flotation tests regarding the role of different collector such as hydroxamic acid need to be investigated. Several published studies indicated that hydroxamic acid is more selective to the REE minerals e.g. bastnäsite than fatty acid.
5. The grade and recovery of apatite increased as the pH value increases from 9.5 to 10.0, while the opposite occurred to synchysite. Thus, additional flotation tests might need to be conducted at a constant level of pH within the range of 9.5 to 10.0 to determine whether a small change in pH would enhance the grade and recovery of synchysite.
6. Further experiments could also be conducted to determine the effect of finer grinding down to P_{80} of 38 µm on flotation efficiency by conditioning the feed pulp with lignin sulphonate at a pH of 8.5 and with Betacol at a pH of 9.5.
7. Measurement of the solubility of lignin sulphonate at pH values below 8.5 and temperature below 60°C is recommended.
8. Further work needs to be done in order to determine the effect of ammonium lignin sulphonate as a depressant for carbonate gangue minerals rather than calcium lignin sulphonate that used in this study.
9. Setting up different collector and depressant dosages on a large batch sample would be worthwhile.
10. Further experimental investigation should also focus to determine the effect of agitation speed and pulp density on the flotation efficiency.

Bibliography

Abouzeid, A.Z.M. 2008. Physical and thermal treatment of phosphate ores - An overview. *International Journal of Mineral Processing*. 85(4):59–84.

Agar, G.E. 1987. Simulation in mineral processing *In*: B. Yarar & Z. Dogan, (eds.), *Mineral processing design*. Springer Netherlands, pp. 268–287.

Amankonah, J.O., Somasundaran,P. & Ananthapadmabhan, K.P.1985. Effects of dissolved mineral species on the electrokinetic behavior of calcite and apatite. *Colloids and Surfaces*. 15:295–307.

Andersen, J.C.Ø., Rollinson, G.K., Snook, B., Herrington, R. & Fairhurst, R.J. 2009. Use of QEMSCAN® for the characterization of Ni-rich and Ni-poor goethite in laterite ores. *Minerals Engineering*. 22(13):1119–1129.

Andersen, J.C.Ø., Stickland, R.J., Rollinson, G.K. & Shail, R.K. 2016. Indium mineralisation in SW England: Host parageneses and mineralogical relations. *Ore Geology Reviews*. 78:213–238.

Anderson, C.D. 2015. *Improved understanding of rare earth surface chemistry and its application to froth flotation*. PhD thesis. Metallurgical and Materials Engineering, Colorado School of Mines.

Anderson, K.F.E., Wall, F., Rollinson, G.K. & Moon, C.J. 2014. Quantitative mineralogical and chemical assessment of the Nkout iron ore deposit, Southern Cameroon. *Ore Geology Reviews*. 62:25–39.

Assis, S.M., Montenegro, L.C.M. & Peres, A.E.C. 1996. Utilisation of hydroxamates in minerals froth flotation. *Minerals Engineering*. 9(1):103–114.Banfield, J.F. & Eggleton, R.A. 1989. Apatite Replacement and Rare Earth Mobilization, Fractionation, and Fixation During Weathering. *Clays and Clay Minerals*. 37(2):113–127.

Bauer, D., Diamond, D., Li, J., Sandalow, D., Telleen, P. & Wanner, B. 2010, *Critical materials strategy*. U.S. Department of Energ. 1-170.

Bayliss, P. & Levinson, A.A. 1988. A system of nomenclature for rare-earth mineral species: Revision and extension. *American Mineralogist*. 73:93–99.

Becker, M., Harris, P.J., Wiese, J.G. & Bradshaw, D.J. 2009. Mineralogical characterisation of naturally floatable gangue in Merensky Reef ore flotation. *International Journal of Mineral*

Processing. 93(3–4):246–255.

Becker, M., Wightman, E.M. & Evans, C.L. 2016. *Process mineralogy*. Julius Kruttschnitt Mineral Research Centre. (Vol. 6).

Benedictus, A., Berendsen, P. & Hagni, A.M. 2008. Quantitative characterisation of processed phlogopite ore from Silver City Dome District, Kansas, USA, by automated mineralogy. *Minerals Engineering*. 21(15):1083–1093.

Boni, M., Rollinson, G., Mondillo, N., Balassone, G. & Santoro, L. 2013. Quantitative mineralogical characterization of karst bauxite deposits in the southern apennines, Italy. *Economic Geology*. 108(4):813–833.

Bouffard, S.C., Tshilombo, A. & West-Sells, P.G. 2009. Use of lignosulfonate for elemental sulfur biooxidation and copper leaching. *Minerals Engineering*. 22(1):100–103.

Braun, J.J., Pagel, M., Herbillon, A. & Rosin, C. 1993. Mobilization and redistribution of REEs and thorium in a syenitic lateritic profile: A mass balance study. *Geochimica et Cosmochimica Acta*. 57(18):4419–4434.

British Geological Survey. 2011. *Rare earth elements*. British Geological Survey, Nottingham, UK, 54 p.

Broom-Fendley, S. 2015. *Targeting heavy rare earth elements in carbonatite complexes*. PhD thesis. Camborne School of Mines.

Broom-Fendley, S., Wall, F., Gunn, A.G. & Dowman, E. 2012. Targeting heavy rare earth elements in carbonatite complexes *In*: *EGU General Assembly Conference Abstracts*., p. 8541.

Brown, T. & Pitfield, P. 2014. Tungsten *In*: G. Gunn (ed.), *Critical metals handbook*. John Wiley & Sons, pp. 385–413.

Bulatovic, S.M. 2007. *Handbook of flotation reagents: chemistry, theory and practice - flotation of sulfide ores*. Elsevier Science.

Bulatovic, S.M. 2010. *Handbook of flotation reagents: Chemistry, theory and practice - flotation of gold, PGM and oxide minerals*. Elsevier Science.

Burt, R.O. 1984. *Gravity concentration technology*. Development in mineral processing series, volume 5. Elsevier Science Pub. Co., Inc., Amsterdam.

Butcher, A.R., Helms, T.A., Gottlieb, P., Bateman, R., Ellis, S. & Johnson, N.W. 2000. Advances in the quantification of gold deportment by QemSCAN *In*: *Proceedings of the 7th Mill Operators Conference*. Kalgoorlie, WA. AusIMM, pp. 267–271.

Camm, G.S., Butcher, A.R., Pirrie, D., Hughes, P.K. & Glass, H.J. 2003. Secondary mineral phases associated with a historic arsenic calciner identified using automated scanning electron microscopy; a pilot study from Cornwall, UK. *Minerals Engineering*. 16(11):1269–1277.

Cao, Q., Cheng, J., Wen, S., Li, C., Bai, S. & Liu, D. 2015. A mixed collector system for phosphate flotation. *Minerals Engineering*. 78:114–121.

Cappuccitti, F. & Nesset, J.E. 2009. Frother and collector effects on flotation cell hydrodynamics and their implication on circuit performance *In*: *Proceedings of 7th UBC-McGill-UA International Symposium on Fundamentals of Mineral Processing*. The Canadian Institute of Mining, Metallurgy and Petroleum, pp. 169–182.

Castor, S.B. 2008. The Mountain Pass rare-earth carbonatite and associated ultrapotassic rocks, California. *The Canadian Mineralogist*. 46(4):779–806.

Castor, S.B. & Hedrick, J.B. 2006. Rare earth elements *In*: J.E. Kogel, N.C. Trivedi, J.M. Barker & S.T. Krukowski (eds.), *Industrial minerals and rocks*. Society for Mining, Metallurgy and Exploration, pp. 769–792.

Chakhmouradian, A.R., Reguir, E.P. & Mitchell, R.H. 2002. Strontium-apatite: New occurrences, and the extent of Sr-for-Ca substitution in apatite-group minerals. *The Canadian Mineralogist*. 40(1):121–136.

Chakhmouradian, A.R. & Wall, F. 2012. Rare earth elements: Minerals, mines, magnets (and more). *Elements*. 8(5):333–340.

Chen, L. & Xiong, D. 2015. Magnetic techniques for mineral processing *In*: S. Tarleton (ed.), *progress in filtration and separation*. Academic Press, pp. 287–324.

Clark, D.A. 1984. Hysteresis properties of sized dispersed monoclinic pyrrhotite grains. *Geophysical Research Letters*. 11(3):173–176.

Croll, R., Swinden, S., Hall, M., Brown, C., Beer, G., Scheepers, J., Redellinghuys, T., & Wild, G. 2014. Mkango Resources Limited: Technical report on the pre-feasibility of the Songwe REE project, Republic of Malawi. NI 43-101 report. MSA Group (Pty) Ltd.

Crozier, R.D. 1992. *Flotation: Theory, reagents, and ore testing*. Pergamon Press, Oxford, UK

Cullity, B.D. & Graham, C.D. 2009. *Introduction to magnetic materials*. John Wiley & Sons.

Daigle, P. 2012. Rare Earth Metals Inc.: Technical report on the resources estimation of the Lavergne-Springer REE project, Ontario, Canada. NI 43-101 report. Tetra Tech Wardrop.

Dekkers, M.J. 1989. Magnetic properties of natural pyrrhotite. II. High- and low-temperature

behavior of Jrs and TRM as a function of grain size. *Physics of the Earth and Planetary Interiors*. 57(3–4):266–283.

Deng, T. & Hill, G. 2014. Flotation of REE bearing minerals from silicate and carbonate host deposits *In*: *Proceeding of the 53rd Annual Conference of Metallurgists*. The Canadian Institute of Mining, Metallurgy and Petroleum.

Derjaguin, B.V. & Dukhin, S.S. 1993. Theory of flotation of small and medium-size particles. *Progress in Surface Science*. 43(1–4):241–266.

Dho, H. & Iwasaki, I. 1990. Role of sodium silicate in phosphate flotation. *Minerals & Metallurgical Processing*. 7(4):215–221.

Dillinger, A., Huddlestone-Holmes, C.R., Zwingmann, H., Ricard, L.P. & Esteban, L. 2014. Impacts of diagenesis on reservoir quality in a sedimentary geothermal play. In *39th Stanford Geothermal Workshop on Geothermal REservoir Engineering. Stanford University, California*. 1–6.

Dixey, F., Bisset, C., & Smith, W. 1955. The Chilwa Series of Southern Nyasaland: A group of alkaline and other intrusive and extrusive rocks and assoiated limestones. *Bulletin of the Geological Survey of Malawi 5.*

Donnay, G. 1953. Roentgenite, $3CeFCO_3.2CaCO_3$, A new mineral from Greenland. *American Mineralogist*. 38(9–10):868–870.

Donnay, G. & Donnay, J.D.H. 1953. The crystallography of bastnaesite, parisite, roentgenite, and synchysite. *American Mineralogist*. 38:932–963.

European Commission. 2014. *Critical raw materials for the EU.* Report of the Ad hoc working group on defining critical raw materials. Brussels.

Evans, C.L., Wightman, E.M., Manlapig, E.V. & Coulter, B.L. 2011. Application of process mineralogy as a tool in sustainable processing. *Minerals Engineering*. 24(12):1242–1248.

Falconer, A. 2003. Gravity separation: old technique/new methods. *Physical Separation in Science and Engineering*. 12(1):31–48.

Filho, L.S.L., Seidl, P.R., Correia, J.C.G. & Cerqueira, L.C.K. 2000. Molecular modelling of reagents for flotation processes. *Minerals Engineering*. 13(14-15):1495–1503.

Finch, J.A. & Dobby, G.S. 1990. *Column Flotation*. Pergamon Press, Oxford, UK.

Förster, H.J. 2001. Synchysite-(Y)-synchysite-(Ce) solid solutions from Markersbach, Erzgebirge, Germany: REE and Th mobility during high-T alteration of highly fractionated aluminous A-type granites. *Mineralogy and Petrology*. 72:259–280.

Fröhlich, S., Redfern, J., Petitpierre, L., Marshall, J.D., Power, M. & Grech, P. V. 2010. Diagenetic evolution of incised channel sandstones: Implications for reservoir characterisation of the lower carboniferous Marar formation, Ghadames basin, western Libya. *Journal of Petroleum Geology*. 33(1):3–18.

Fuerstenau, D.W. & Pradip. 2005. Zeta potentials in the flotation of oxide and silicate minerals. *Advances in Colloid and Interface Science*. 114–115:9–26.

Fuerstenau, D.W., Pradip & Herrera-Urbina, R. 1992. The surface chemistry of bastnaesite, barite and calcite in aqueous carbonate solutions. *Colloids and Surfaces*. 68(1–2):95–102.

Fuerstenau, D.W., Pradip, Khan, L.A. & Raghavan, S. 1982. An alternative reagent scheme for the flotation of Mountain Pass rare-earth ore *In*: *Proceedings of the XIV International Mineral Processing Congress*. The Canadian Institute of Mining, Metallurgy and Petroleum, pp. 1–12.

Garson, M. 1965. *Carbonatites in southern Malawi.* Bulletin of the Geological Survey of Malawi 15.

Garson, M. & Walshaw, R. 1969. *The geology of the Mlanje area.* Bulletin of the Geological Survey of Malawi 21.

Goodall, W.R. & Butcher, A.R. 2012. The use of QEMSCAN in practical gold deportment studies. *Mineral Processing and Extractive Metallurgy*. 121(4):199–204.

Goodall, W.R. & Scales, P.J. 2007. An overview of the advantages and disadvantages of the determination of gold mineralogy by automated mineralogy. *Minerals Engineering*. 20(5):506–517.

Goodall, W.R., Scales, P.J. & Butcher, A.R. 2005. The use of QEMSCAN and diagnostic leaching in the characterisation of visible gold in complex ores. *Minerals Engineering*. 18(8):877–886.

Gottlieb, P., Wilkie, G., Sutherland, D., Ho-Tun, E., Suthers, S., Perera, K., Jenkins, B., Spencer, S., Butcher, A. & Rayner, J. 2000. Using quantitative electron microscopy for process mineralogy applications. *JOM*. 52(4):24–25.

Grammatikopoulos, T., Mercer, W. & Gunning, C. 2013. Mineralogical characterisation using QEMSCAN of the Nechalacho heavy rare earth metal deposit, Northwest Territories, Canada. *Canadian Metallurgical Quarterly*. 52(3):265–277.

Grano, S., Weedon, D., Akroyd, T. & Wiseman, D. 2004. Application of a property-based

flotation model in circuit simulations *In*: *Proceedings Metallurgical Plant Design and Operating Strategies*. The Australasian Institute of Mining and Metallurgy: Melbourne, pp. 299–318.

Guimarães, R.C., Araujo, A.C. & Peres, A.E.C. 2005. Reagents in igneous phosphate ores flotation. *Minerals Engineering*. 18(2):199–204.

Gupta, A. & Yan, D. 2016. *Mineral processing design and operation: an introduction*. Elsevier B.V.

Gupta, C.K. & Krishnamurthy, N. 2005. *Extractive metallurgy of rare earths*. CRC Press.

Haberlah, D., Strong, C., Pirrie, D., Rollinson, G.K., Gottlieb, P., Botha, P.P. & Butcher, A.R. 2011. Automated petrography applications in Quaternary Science. *Quaternary Australasia*. 28(2):3–12.

Hardy, A. & Rollinson, G. 2009. Green eye cosmetics of antiquity. *Pharmaceutical Historian*. 39(1):2–7.

Hardy, A., Walton, R., Vaishnay, R., Myers, K. & Pirrie, D. 2006. Egyptian eye cosmetics ("Kohls"): Past and present. *Physical techniques in the study of art, archaeology and cultural heritage*. 1:173–203.

Hatch, G.P. 2012. Dynamics in the global market for rare earths. *Elements*. 8(5):341–346.

Haumdas, A., Burmaa, G., Bayar, G., Myagmarjav, B. & Rakaev, B. 1995. Synchysite – new resources of the rare earths *In*: *Proceedings of the 3rd International Conference on Rare Earth Development and Applications*. Baotou, Metallurgical Industry Press, pp. 718–727.

Hawthorne, F., Fleischer, M., Grew, E., Grice, J., Jambor, J., Puziewicz, J., Roberts, A., Vanko, D. & Ailczer, J. 1986. New mineral names. *American Mineralogist*. 71:1277–1282.

Henderson, P. 1996. The rare earth elements: introduction and review *In*: A.P. Jones, F. Wall & C.T. Williams (eds.), *Rare earth minerals: Chemistry, origin and ore deposits*. volume 6 of Minerlaogical Society Series. Chapman & Hall, pp. 1–19.

Hogarth, D.D., Hartree, R., Loop, J. & Solberg, T.N. 1985. Rare-earth element minerals in four carbonatites near Gatineau, Quebec. *American Mineralogist*. 70(11–12):1135–1142.

http://webmineral.com Accessed 2012 – 2016

Hu, J.S., Misra, M. & Miller, J.D. 1986. Characterization of adsorbed oleate species at the fluorite surface by FTIR spectroscopy. *International Journal of Mineral Processing*. 18(1–2):73–84.

Huminicki, D.M.C. & Hawthorne, F.C. 2002. The crystal structure of the phosphate minerals. *Reviews in Mineralogy and Geochemistry*. 48(5):123–253.

Hyland, S. & Ulrich, S. 2014. Technical report on the Kyzyl ompul licence, Kyrgyz Republic for Powertech Uranium Corp., Azarga Resources Limited, and UrAsia in Kyrgyzstan LLC. NI 43-101 report. Ravensgate.

International Mineralogical Association. 2016. *IMA list of minerals*. Available at: http://nrmima.nrm.se//IMA_Master_List_%282016-07%29.pdf [Accessed September 1, 2009].

Jackson, W.D. & Christiansen, G. 1993. *International strategic minerals inventory summary report - Rare earth oxides*. Circular 930-N. USGS.

Jambor, J., Burke, E., Ercit, T. & Grice, J. 1988. New mineral names. *American Mineralogist*. 73:1492–1499.

Jiles, D. 1998. *Introduction to magnetism and magnetic materials*. Chapman & Hall.

Jordens, A. 2016. *The beneficiation of rare earth element-bearing minerals*. PhD thesis. Mining and Materials Engineering, McGill University.

Jordens, A., Cheng, Y.P. & Waters, K.E. 2013. A review of the beneficiation of rare earth element bearing minerals. *Minerals Engineering*. 41:97–114.

Jordens, A., Marion, C., Grammatikopoulos, T., Hart, B. & Waters, K.E. 2016. Beneficiation of the Nechalacho rare earth deposit: Flotation response using benzohydroxamic acid. *Minerals Engineering*. 99:158–169.

Jordens, A., Sheridan, R.S., Rowson, N.A. & Waters, K.E. 2014. Processing a rare earth mineral deposit using gravity and magnetic separation. *Minerals Engineering*. 62:9–18.

Kawatra, S.K. 2011. Fundamental principles of froth flotation *In*: P. Darling (ed.), *SME mining engineering handbook*. Society for Mining, Metallurgy and Exploration, INC, pp. 1517–1531.

Kawatra, S.K. & Carlson, J.T. 2014. *Beneficiation of phosphate ore*. Society for Mining, Metallurgy and Exploration.

Kawatra, S.K. & Eisele, T.C. 2001. *Coal desulfurization: high-efficiency preparation methods*. Taylor & Francis.

Kelly, E.G. & Spottiswood, D.J. 1982. *Introduction to mineral processing*. Wiley, New York.

King, R. 2001. *Modelling and simulation of mineral processing systems*. Society for Mining,

Metallurgy and Exploration, Inc.

Kirillov, A.S. 1964. Hydroxyl bästnasite, a new variety of bästnasite. *Doklady Akademii Nauk SSSR*. 159:93–95.

Klimpel, R.R. 1998. *Introduction to solid-solid separation of fine particles by froth flotation*. NSF Engineering Resource Centre for Particle Science & Technology, University of Florida.

Klimpel, R.R. & Isherwood, S. 1991. Some industrial implications of changing frother chemical structure. *International Journal of Mineral Processing*. 33(1–4):369–381.

Knappett, C., Pirrie, D., Power, M.R., Nikolakopoulou, I., Hilditch, J. & Rollinson, G.K. 2011. Mineralogical analysis and provenancing of ancient ceramics using automated SEM-EDS analysis (QEMSCAN®): A pilot study on LB I pottery from Akrotiri, Thera. *Journal of Archaeological Science*. 38(2):219–232.

Knelson, B. & Jones, R. 1994. “A new generation of Knelson concentrators” a totally secure system goes on line. *Minerals Engineering*. 7(2–3):201–207.

Krishnamurthy, N. & Gupta, C.K. 2016. *Extractive metallurgy of rare earths*. CRC Press.

Kynicky, J., Smith, M.P. & Xu, C. 2012. Diversity of rare earth deposits: The key example of China. *Elements*. 8(5):361–367.

Laplante, A.R., Kaya, M. & Smith, H.W. 1989. The effect of froth on flotation kinetics - a mass transfer approach. *Mineral Processing and Extractive Metallurgy Review*. 5(1–4):147–168.

Lastra, R. 2002. A comparison of liberation determinations by particle area percentage and exposed particle perimeter percentage in a flotation concentrator. *Journal of Minerals and Materials Characterization and Engineering*. 1(1):31–37.

Lefebvre, J.J. & Gasparrini, C. 1980. Florencite, an occurence in the Zairian Copperbelt. *Canadian Mineralogist*. 18:301–311.

Leja, J. 1982. *Surface chemistry of froth flotation*. Springer, USA.

Levinson, A.A. 1966. A system of nomenclature for rare-earth minerals. *American Mineralogist*. 51:152–158.

Lide, D.R. 2000. Magnetic susceptibility of the elements and inorganic compounds *In*: *CRC handbook of chemistry and physics*. CRC Press, Boca Raton, pp. 130–135.

Long, K.R., Van Gosen, B.S., Foley, N.K., & Cordier, D. 2010. *The principal rare earth*

elements deposits of the United States - A summary of domestic deposits and a global perspective. U.S. Geological Survey Scientific Investigations Report 2010–5220, 96 p. Available at: http://pubs.usgs.gov/sir/2010/5220/.

Lotter, N.O., Kormos, L.J., Oliveira, J., Fragomeni, D. & Whiteman, E. 2011. Modern process mineralogy: Two case studies. *Minerals Engineering*. 24(7):638–650.

Lotter, N.O., Whittaker, P.J., Kormos, L., Stickling, J.S. & Wilkie, G.J. 2002. The development of process mineralogy at Falconbridge Limited, and application to the Raglan mill. *CIM bulletin*. 95(1066):85–92.

Lottermoser, B.G. 1990. Rare-earth element mineralisation within the Mt. Weld carbonatite laterite, Western Australia. *Lithos*. 24(2):151–167.

Lowrie, W. 2007. *fundamentals of geophysics*. Cambridge University Press.

Lu, Y., Liu, N., Wang, X. & Miller, J.D. 1999. Improved phosphate flotation with nonionic polymers *In*: P. Zhang, H.E. El-Shall & R. Wiegel (eds.), *Beneficiation of phosphates: Advances in research and practice*. Society for Mining, Metallurgy and Exploration, pp. 3–19.

Lynas Corporation Ltd. 2010. Will there be sufficient rare earths to meet demand from clean energy technology?. Presentation at International Minor Metals Conference, London, April 2010 Available at: www.lynascorp.com/Shared Documents/ Investors and media/Reporting Centre/Presentations/2010/MMTA_APRIL_2010.pdf [Accessed July 1, 2016].

Manfredi, T.R., Bastos Neto, A.C., Pereira, V.P., Barbanson, L. & Schuck, C. 2013. The parisite-(Ce) mineralization associated with the Fazenda Varela carbonatite (Correia Pinto, SC). *Pesquisas em Geociencias*. 40(3):295–307.

Mariano, A. & Mariano, A. 2012. Rare earth mining and exploration in North America. *Elements*. 8:369–376.

Mariano, A.N. 1989. Economic geology of rare earth elements. *Reviews in Mineralogy and Geochemistry*. 21:309–337.

Martin, R.S., Mather, T.A., Pyle, D.M., Power, M., Allen, A.G., Aiuppa, A., Horwell, C.J. & Ward, E.P.W. 2008. Composition-resolved size distributions of volcanic aerosols in the Mt. Etna plumes. *Journal of Geophysical Research Atmospheres*. 113(D17211).

McClellan, G.H. 1980. Mineralogy of carbonate fluorapatites. *Journal of the Geological Society*. 137(6):675–681.

McDonough, W.F. & Sun, S.S. 1995. The composition of the Earth. *Chemical Geology*. 120(3–4):223–253.

McIvor, R.E. & Finch, J.A. 1991. A guide to interfacing of plant grinding and flotation operations. *Minerals Engineering*. 4(1):9–23.

Melo, F. & Laskowski, J.S. 2006. Fundamental properties of flotation frothers and their effect on flotation. *Minerals Engineering*. 19(6):766-773.

Meng, D., Wu, X., Mou, T. & Li, D. 2001. Microstructural investigation of new polytypes of parisite-(Ce) by high-resolution transmission electron microscopy. *The Canadian Mineralogist*. 39(6):1713–1724.

Mintek. 2013. *Scoping metallurgical work on the Songwe rare earth project from Malawi*. External Report 6601. Mintek, South Africa.

Mintek. 2014. *Further flotation test work on the Songwe rare earth project from Malawi*. External Report 6884. Mintek, South Africa.

Mishra, S.K. 1982. Electrokinetic properties and flotation behaviour of apatite and calcite in the presence of sodium oleate and sodium metasilicate. *International Journal of Mineral Processing*. 9(1):59–73.

Mondillo, N., Balassone, G., Boni, M. & Rollinson, G. 2011. Karst bauxites in the Campania Apennines (southern Italy): A new approach. *Periodico di Mineralogia*. 80(3):407–432.

Natarajan, R. and Nirdosh, I. 2006. A comparative study of kinetics of flotation of a copper-nickel ore by N-hydrocinnamoyl-N-phenylhydroxylamine (HCNPHA) vis-a-vis potassium amyl xanthate (PAX) *In*: *Proceedings of the International Seminar on Mineral Processing Technology*. Chennai, India, pp. 236–242.

Ni, Y., Hughes, J.M. & Mariano, A.N. 1993. The atomic arrangement of bastnäsite-(Ce), $Ce(CO_3)F$, and structural elements of synchysite-(Ce), röntgenite-(Ce), and parisite-(Ce). *American Mineralogist*. 78(3–4):415–418.

Ni, Y., Post, J.E. & Hughes, J.M. 2000. The crystal structure of parisite-(Ce), $Ce_2CaF_2(CO_3)_3$. *American Mineralogist*. 85(1):251–258.

Nivin, V.A., Treloar, P.J., Konopleva, N.G. & Ikorsky, S. V. 2005. A review of the occurrence, form and origin of C-bearing species in the Khibiny Alkaline Igneous Complex, Kola Peninsula, NW Russia. *Lithos*. 85(1–4):93–112.

NIDO & IFDC 1998. *Fertilizer manual*. United Nations Industrial Development Organization (UNIDO) and International Fertilizer Development Center (IFDC). Kluwer Academic

Publishers, The Netherlands.

Norrgran, D.A. & Marin, J.A. 1994. Rare earth permanent magnet separators and their applications in mineral processing. *Minerals and Metallurgical Processing*. 11(1):41–45.

Notholt, A.J.G. & Highley, D.E. 1986. World phosphate resources, with particular reference to potential low-grade ores. *Transactions of the Institutions of Mining and Metallurgy Section B: Applied Earth Science*. 95:125–132.

Nunes, A.P.L., Peres, A.E.C., De Araujo, A.C. & Valadão, G.E.S. 2011. Electrokinetic properties of wavellite and its floatability with cationic and anionic collectors. *Journal of Colloid and Interface Science*. 361(2):632–638.

Oberteuffer, J. 1974. Magnetic separation: A review of principles, devices, and applications. *IEEE Transactions on Magnetics*. 10(2):223–238.

Oelkers, E.H. & Valsami-Jones, E. 2008. Phosphate mineral reactivity and global sustainability. *Elements*. 4(2):83–87.

Oftedal, I. 1931. Zur kristallstruktur von Bastnäsit, (Ce, La--)FCO_3. *Zeitschrift für Kristallographie*. 78(1–6):462–469.

Oliveira, M.S., Santana, R.C., Ataíde, C.H. & Barrozo, M.A.S. 2011. Recovery of apatite from flotation tailings. *Separation and Purification Technology*. 79(1):79–84.

Panto, G. 1985. Hydroxyl-bastnaesite-(Nd), a new mineral from Montenegro, Yugoslavia. *Mineralogical Magazine*. 49:717–720.

Parekh, B.K. & Miller, J.D. 1999. *Advances in flotation technology*. Society for Mining, Metallurgy and Exploration, Inc.

Pascoe, R.D., Power, M.R. & Simpson, B. 2007. QEMSCAN analysis as a tool for improved understanding of gravity separator performance. *Minerals Engineering*. 20(5):487–495.

Pavez, O., Brandao, P.R.G. & Peres, A.E.C. 1996. Adsorption of oleate and octyl-hydroxamate on to rare-earths minerals. *Minerals Engineering*. 9(3):357–366.

Pease, J.D., Curry, D.C. & Young, M.F. 2006. Designing flotation circuits for high fines recovery. *Minerals Engineering*. 19(6):831–840.

Petty, M.C. 2007. *Molecular electronics: From principles to practice*. John Wiley & Sons, Ltd.

Pirrie, D. & Rollinson, G.K. 2011. Unlocking the applications of automated mineral analysis. *Geology Today*. 27(6):226–235.

Pirrie, D., Butcher, A.R., Power, M.R., Gottlieb, P. & Miller, G.L. 2004. Rapid quantitative

mineral and phase analysis using automated scanning electron microscopy (QemSCAN); potential applications in forensic geoscience. *Geological Society, London, Special Publications*. 232(1):123–136.

Pirrie, D., Power, M.R., Rollinson, G., Camm, G.S., Hughes, S.H., Butcher, A.R. & Hughes, P. 2003. The spatial distribution and source of arsenic, copper, tin and zinc within the surface sediments of the Fal Estuary, Cornwall, UK. *Sedimentology*. 50(3):579–595.

Pirrie, D., Power, M.R., Rollinson, G.K., Wiltshire, P.E.J., Newberry, J. & Campbell, H.E. 2009. Automated SEM-EDS (QEMSCAN®) mineral analysis in forensic soil investigations: Testing instrumental reproducibility *In*: K. Ritz, L. Dawson & D. Miller (eds.), *Criminal and environmental soil forensics*. Springer, Netherlands, pp. 411–430.

Pradip & Fuerstenau, D.W. 1991. The role of inorganic and organic reagents in the flotation separation of rare-earth ores. *International Journal of Mineral Processing*. 32(1–2):1–22.

Pradip & Fuerstenau, D.W. 2013. Design and development of novel flotation reagents for the beneficiation of Mountain Pass rare-earth ore. *Minerals and Metallurgical Processing*. 30(1):1–9.

Pradip. 1981. *The surface properties and flotation of rare-earth minerals*. PhD thesis. Materials Science and Mineral Engineering, University of California.

Rao, K.H., Cases, J.M., Donato, P.D. & Forssberg, K.S.E. 1991. Mechanism of oleate adsorption on salt-type minerals: IV. Adsorption, electrokinetic, and diffuse reflectance FT-IR studies of natural fluorite in the presence of sodium oleate. *Journal of Colloid and Interface Science*. 145(2):314–329.

Rollinson, G.K., Andersen, J.C.Ø., Stickland, R.J., Boni, M. & Fairhurst, R. 2011. Characterisation of non-sulphide zinc deposits using QEMSCAN®. *Minerals Engineering*. 24(8):778–787.

Rosenblum, S. & Brownfield, I.K. 2000, *Magnetic susceptibilities of minerals - Report for US Geological Survey*. 1-37.

Ruberti, E., Enrich, G.E.R., Gomes, C.B. & Comin-Chiaramonti, P. 2008. Hydrothermal REE fluorocarbonate mineralization at Barra do Itapirapua, a multiple stockwork carbonate, southern Brazil. *The Canadian Mineralogist*. 46(4):901–914.

Rule, C. & Schouwstra, R.P. 2011. Process mineralogy delivering significant value at Anglo Platinum concentrator operations *In*: *Proceedings of the 10th International Congress for Applied Mineralogy*. Springer Berlin Heidelberg, pp. 613–621.

Sadowski, Z. 1992. The influence of sodium lignin sulfonate on the adsorption on sodium dodecyl sulfate on salt-type mineral surfaces. *Minerals Engineering*. 5(3–5):421–428.

Sanematsu, K. & Watanabe, Y. 2016. Characteristics and genesis of ion adsorption-type rare Earth element deposits *In*: P.L. Verplanck & M.W. Hitzman (eds.), *Reviews in economic geology: Rare earth and critical elements in ore deposits*. Society of Economic Geologists, Inc, pp. 55–79.

Santana, R.C., Farnese, A.C.C., Fortes, M.C.B., Ataíde, C.H. & Barrozo, M.A.S. 2008. Influence of particle size and reagent dosage on the performance of apatite flotation. *Separation and Purification Technology*. 64(1):8–15.

Santoro, L., Boni, M., Rollinson, G.K., Mondillo, N., Balassone, P. & Clegg, A.M. 2014. Mineralogical characterization of the Hakkari nonsulfide Zn(Pb) deposit (Turkey): The benefits of QEMSCAN®. *Minerals Engineering*. 69:29–39.

Sawka, W.N., Banfield, J.F. & Chappell, B.W. 1986. A weathering-related origin of widespread monazite in S-type granites. *Geochimica et Cosmochimica Acta*. 50(1):171–175.

Schulze, H.J. 1977. New theoretical and experimental investigations on stability of bubble/particle aggregates in flotation: a theory on the upper particle size of floatability. *International Journal of Mineral Processing*. 4(3):241–259.

Schwarz-Schampera, U. 2014. Indium *In*: G. Gunn (ed.), *Critical metals handbook*. John Wiley & Sons, pp. 204–229.

Sheridan, R.S. 2014. *Optimisation of HDDR processing parameters of sintered NDFEB magnets*. PhD thesis. School of Metallurgy and Materials, University of Birmingham.

Shi, Y. & Fornasiero, D. 2009. Effects of particle size and density, and turbulence on flotation recovery *In*: *Engineering our future: Are we up to the challenge?: 27 - 30 September 2009, Burswood Entertainment Complex*, pp. 528–536.

Singer, D.A. 1998. *Revised grade and tonnage model of carbonatite deposits*. Open-File Report 98-235. USGS.

Sis, H. & Chander, S. 2003. Reagents used in the flotation of phosphate ores: A critical review. *Minerals Engineering*. 16(7):577–585.

Slukin, A.D., Arapova, G.A., Zvezdinskaya, L.V. Tsvetkova, M.V. & Lapin, A.V. 1989. Mineralogy and geochemistry of laterized carbonatites of the USSR *In*: A. Barto-Kyriakidis (ed.), *Weathering: its products and deposits*. Theophrastus Publishing & Proprietary Co., S.A. (Ltd.), Athens, pp. 171–189.

Smythe, D.M., Lombard, A. & Coetzee, L.L. 2013. Rare Earth Element deportment studies utilising QEMSCAN technology. *Minerals Engineering*. 52:52–61.

Speirs, J.C., McGowan, H.A. & Neil, D.T. 2008. Polar eolian sand transport: grain characteristics determined by an automated Scanning Electron Microscope (QEMSCAN®). *Arctic, Antarctic, and Alpine Research*. 40(4):731–743.

Speliotis, D. 2005. *Getting the most from your vibrating sample magnetometer*. ADE Technologies, Inc., Newton, MA, USA.

Svoboda, J. & Fujita, T. 2003. Recent developments in magnetic methods of material separation. *Minerals Engineering*. 16(9):785–792.

Swinden, S. and Hall, M. 2012. Mineral resource estimate for the Songwe Hill rare earth element (REE) project, Phalombe District, Republic of Malawi. NI 43-101 report. MSA Group (Pty) Ltd.

Tan, Y.H., Rafiei, A.A., Elmahdy, A. & Finch, J.A. 2013. Bubble size, gas holdup and bubble velocity profile of some alcohols and commercial frothers. *International Journal of Mineral Processing*. 119:1–5.

Taylor, S.R. & McLennan, S.M. 1985. *The continental crust: its composition and evolution*. Blackwell Scientific Pub., Palo Alto, CA.

Tickell, F.G. 2011. *The techniques of sedimentary mineralogy*. Elsevier (Vol. 4).

Turek, S.L. & Buckwatler, J.A. 1994. *Orthopaedics: Principles and Applications*. Lippincott Williams & Wilkins.

USGS. 2016a. Mineral commodity summaries: Rare earths. Available at: https://minerals.usgs.gov/minerals/pubs/commodity/rare_earths/mcs-2016-raree.pdf.

USGS. 2016b. Mineral commodity summaries: Phosphate rock. Available at: https://minerals.usgs.gov/minerals/pubs/commodity/phosphate_rock/mcs-2016-phosp.pdf.

Van Landuyt, J. & Amelinckx, S. 1975. Multiple beam direct lattice imaging of new mixed-layer compounds of the bastnaesite-synchisite series. *American Mineralogist*. 60:351.

Van Straaten, P. 2002. *Rocks for crops: Agrominerals of sub-Saharan Africa*. ICRAF, Nairobi, Kenya.

Verplanck, P.L., Farmer, G.L. & Mariano, A.N. 2015. Nd and Sr isotopic composition of rare earth element mineralized carbonatites *In*: G.J. Simandl & M. Neetz (eds.), *Symposium on strategic and critical materials proceedings*. British Columbia Ministry of Energy and

Mines, British Columbia Geological Survey, pp. 65–68.

Wall, F. & Mariano, A. 1996. Rare earth minerals in carbonatites: A discussion centred on the Kangankunde Carbonatite, Malawi *In*: A. Jones, F. Wall & C.T. Williams (eds.), *Rare earth minerals: Chemistry, origin and ore deposits*. volume 6 of Minerlaogical Society Series. Chapman & Hall, pp. 193–225.

Wall, F. 2014. Rare earth elements *In*: G. Gunn (ed.), *Critical metals handbook*. John Wiley & Sons, pp. 312–339.

Walters, A., Lusty, P. & Hill, A. 2011. *Rare earth elements*. British Geological Survey.

Wang, L., Ni, Y., Hughes, J.M., Bayliss, P. & Drexler, J.W. 1994. The atomic arrangement of synchysite-(Ce), $CeCaF(CO_3)_2$. *The Canadian Mineralogist*. 32:865–871.

Warman. 1997. *Cyclosizer instruction manual: Particle size analysis in the sub-sieve range*. Bulletin WCS/2. Warman International Ltd., Australia.

Waters, K.E., Rowson, N.A., Greenwood, R.W. & Williams, A.J. 2007. Characterising the effect of microwave radiation on the magnetic properties of pyrite. *Separation and Purification Technology*. 56(1):9–17.

Werner, R. 1993. Synchysite from Norway. *The Norwegian rock and mineral guide (English version)*. 4:221–226.

Williamson, B.J., Rollinson, G. & Pirrie, D. 2013. Automated mineralogical analysis of PM10: New parameters for assessing PM toxicity. *Environmental Science and Technology*. 47(11):5570–5577.

Wills, B.A. & Finch, J.A. 2016. *Wills' Mineral Processing Technology*. Elsevier Ltd.

Wingate, E. & Kohmuench, J. 2016. An optimized approach to phosphate recovery *In*: P. Zhang, J. Miller, E. Wingate & L.L. Filho (eds.), *Beneficiation of phosphates: Comprehensive extraction, technology innovations, advanced reagents*. Society for Mining, Metallurgy and Exploration, pp. 43–54.

Woolley, A. 2001. *Alkaline rocks and carbonatites of the World.* Part 3: Africa. The Geological Society.

Woolley, A.R. & Garson, M.S. 1970. Petrochemical and tectonic relationship of the Malawi carbonatite-alkaline province and the Lupata-Lebombo volcanics *In*: T.N. Clifford & I.G. Gass (eds.), *African magmatism and tectonics*. Oliver & Boyd, Edinburgh, pp. 237–262.

www.ifdc.org [Accessed February 12, 2014]

www.periodictable.com [Accessed April 7, 2016].

Xu, M. 1998. Modified flotation rate constant and selectivity index. *Minerals Engineering*. 11(3):271–278.

Yang, H., Dembowski, R.F., Conrad, P.G. & Downs, R.T. 2008. Crystal structure and Raman spectrum of hydroxyl-bästnasite-(Ce), $CeCO_3(OH)$. *American Mineralogist*. 93(4):698–701.

Young, C.A. & Miller, J.D. 2000. Effect of temperature on oleate adsorption at a calcite surface: an FT-NIR/IRS study and review. *International Journal of Mineral Processing*. 58(1):331–350.

Zapata, F. & Roy, R. 2004. *Use of phosphate rocks for sustainable agriculture*. FAO Fertilizer and Plant Nutrition Bulletin 13.

Zhang, J. & Edwards, C. 2012. Review of rare earth mineral processing technology *In*: *Proceedings of the 44th Annual Meeting of the Canadian Mineral Processors*. CIM, Ottawa, pp. 79–102.

Zhou, F., Wang, L., Xu, Z., Liu, Q. & Chi, R. 2015. Reactive oily bubble technology for flotation of apatite, dolomite and quartz. *International Journal of Mineral Processing*. 134:74–81.

Zhou, X., Jordens, A., Cappuccitti, F., Finch, J.A. & Waters, K.E. 2016. Gas dispersion properties of collector/frother blends. *Minerals Engineering*. 96–97:20–25.

Appendix A- Certified reference materials

Table A-1: The results of REE for the carbonatite certified reference material USGS COQ-1 analysed at CSM and ALS Laboratories Ltd that used to check the accuracy and precision of the analytical data.

Oxides	CRM value	ALS value*	Batch-1	Batch-2	Batch-3	Batch-4
Ce	1700	1818.33	1673.25	1812.56	1689.01	1769.67
Dy	18	17.91	15.50	16.39	16.46	16.35
Er	7	7.70	6.86	7.22	7.66	7.00
Eu	15	15.58	12.51	13.42	13.56	13.33
Gd	50	29.50	27.29	29.80	28.47	29.65
Ho	3	3.41	2.65	2.85	3.21	2.82
La	750	926.33	825.61	884.16	847.47	862.59
Lu	-	0.86	0.77	0.81	1.23	0.81
Nd	480	493.66	416.68	449.24	419.39	435.85
Pr	150	160.00	140.48	152.43	143.46	149.99
Sm	56	55.63	47.15	51.16	48.04	48.17
Tb	4	3.90	2.35	3.31	2.82	3.23
Tm	-	1.08	0.86	0.92	1.36	0.90
Yb	6	6.35	5.10	5.50	5.82	5.47
Y	81	91.57	80.11	86.00	83.93	83.00

* Average of three analyses.

Table A-2: The results of major, minor, trace, and rare earth elements of the certified reference materials along with blank and duplicate samples that used to check the accuracy and precision of the analytical data, analysed at ALS Laboratories Ltd, Spain.

Standards	AMISO104			SARM-5			Blanks			Duplicates			
Elements (%)	Measured	Lower bound	Upper bound	Measured	Lower bound	Upper bound	Measured	Lower bound	Upper bound	Conc 2 T16	Measured	Lower bound	Upper bound
Al	1.132	1.088	1.240	2.141	2.093	2.332	<0.005	<0.005	0.022	0.690	0.693	0.669	0.714
Ba	2.866	2.712	3.008	<0.009	<0.009	0.023	<0.009	<0.009	0.018	0.654	0.659	0.631	0.682
Ca	1.015	0.889	1.026	1.963	1.792	2.010	<0.007	<0.007	0.022	25.49	25.59	24.89	26.19
Cr	0.018	<0.007	0.037	2.398	2.272	2.530	<0.007	<0.007	0.014	0.009	0.009	<0.007	0.014
Fe	14.475	14.055	15.010	8.903	8.550	9.215	<0.007	<0.007	0.014	9.573	9.552	9.316	9.809
K	0.218	0.188	0.244	0.070	0.053	0.096	<0.008	<0.008	0.035	0.128	0.100	0.103	0.125
LOI	4.24	<0.01	0.02	<0.01	<0.01	0.01	0.02	-	-	28.60	28.50	27.83	29.27
Mg	0.213	0.185	0.237	15.195	14.780	15.770	<0.006	<0.006	0.012	0.553	0.553	0.533	0.573
Mn	35.27	34.38	36.23	0.168	0.146	0.195	<0.008	<0.008	0.016	1.493	1.492	1.447	1.538
Na	0.083	0.055	0.093	0.258	0.244	0.305	<0.007	<0.007	0.014	0.184	0.137	0.149	0.172
P	0.0215	0.0155	0.0229	0.0051	0.0067	0.0112	<0.0004	<0.0004	0.0014	1.7545	1.7783	1.7218	1.8110
Si	8.414	8.233	8.875	23.80	23.20	24.57	<0.005	<0.005	0.010	1.395	1.416	1.365	1.446
Sr	0.034	0.012	0.050	<0.008	<0.008	0.020	<0.008	<0.008	0.016	1.842	1.846	1.790	1.898
Ti	0.159	0.140	0.184	0.111	0.101	0.139	<0.006	<0.006	0.012	0.399	0.398	0.383	0.414

Standards	GRE-04			NCSDC86318			Blanks			Duplicates			
Elements (ppm)	Measured	Lower bound	Upper bound	Measured	Lower bound	Upper bound	Measured	Lower bound	Upper bound	Conc 3 T16	Measured	Lower bound	Upper bound
Ce	6050	5700	6560	443	397	463	<3	<3	6	9310	9120	8890	9540
Dy	95.4	89.5	103.5	3200	2990	3450	<0.3	<0.3	0.6	181.5	177.0	182.5	186.0
Er	27.2	26.4	30.8	1755	1625	1875	<0.2	<0.2	0.4	70.5	69.9	67.5	72.9
Eu	99.2	93.3	108.0	19.4	17.4	20.4	<0.2	<0.2	0.4	128.0	127.0	123.0	132.0
Gd	218	216	249	2300	2020	2320	<0.3	<0.3	0.6	293	289	281	301
Hf	23	18	23	7	7	12	1	<1	2	2	2	<1	3
Ho	12.90	12.50	14.50	588	520	598	<0.05	<0.05	0.10	28.7	27.8	27.2	29.3
La	2750	2540	2930	1850	1820	2100	<3	<3	6	5050	4840	4770	5120
Lu	1.88	1.59	1.93	265	245	283	<0.05	<0.05	0.10	6.70	6.71	6.42	6.99
Nb	3610	3300	3800	71	64	76	1	<1	2	1270	1250	1215	1305
Nd	2810	2510	2890	3300	3190	3670	<0.5	<0.5	1.0	3360	3270	3200	3430
Pr	726	670	772	721	685	789	<0.2	<0.2	0.4	941	918	897	962
Rb	1	<1	2	377	342	396	<1	<1	2	31	31	29	33
Sm	409	363	418	1685	1600	1840	<0.2	<0.2	0.4	490	469	463	496
Sn	73	59	81	9	<5	10	<5	<5	10	7	10	<5	10
Ta	131.0	113.0	131.0	4.4	4.3	6.5	<0.5	<0.5	1.0	5.9	2.9	5.2	6.6
Tb	22.8	22.7	26.2	494	437	503	<0.05	<0.05	0.10	35.9	35.5	34.4	37.0
Th	136.5	123.5	142.5	66.7	62.0	72.0	<0.3	<0.3	0.6	482	477	462	497
Tm	3.04	2.75	3.27	271	251	289	0.07	<0.05	0.10	8.68	8.80	8.38	9.10
U	128.0	116.0	134.0	11.4	10.2	12.3	<0.3	<0.3	0.6	12.9	12.8	12.1	13.6
W	<5	<5	10	8	<5	22	<5	<5	10	21	22	16	27
Y	314	294	345	17300	15800	18200	<3	<3	6	784	768	746	806
Yb	15.0	13.8	16.3	1860	1710	1970	<0.2	<0.2	0.4	50.2	49.1	47.7	51.6
Zr	1000	870	1020	200	200	250	<10	<10	20	70	70	60	80

Appendix B: QEMSCAN® applications, instrument, and operating modes

1. Introduction

QEMSCAN®, previously known as QEM*SEM, was one of the earliest automated quantitative mineralogical techniques, first developed by the division of Mineral and Process Engineering of the Commonwealth Scientific and Industrial Research Organisation (CSIRO) in Australia from 1974 onwards. It was originally designed to support the mining industry in rapidly quantifying the mineralogy of ore deposits and determining the liberation characteristics of valuable minerals for mineral processing applications (Butcher et al. 2000; Pirrie et al., 2004; Goodall and Scales, 2007).

QEMSCAN® has been used to characterise a wide range of ore deposit types including zinc-lead deposits (Rollinson et al., 2011; Santoro et al., 2014), gold deposits (Goodall and Scales, 2007, Goodall and Butcher, 2012), nickle–iron laterite deposits (Andersen et al., 2009; Anderson et al., 2014), bauxites (Boni et al., 2013), rare earth deposits (Grammatikopoulos et al., 2013; Smythe et al., 2013), indium deposits (Andersen et al, 2016), and oil and gas reservoirs (Fröhlich et al., 2010; Dillinger et al., 2014). Furthermore, several case studies utilised QEMSCAN® to develop an understanding of ore deposits and optimise mineral processing (Goodall et al., 2005; Pascoe et al., 2007; Benedictus et al., 2008; Becker et al., 2009; Lotter et al, 2011; Rule and Schouwstra, 2011).

Along with using the technology in mining, mineral processing, and oil and gas industries, QEMSCAN® is also being used in other areas such as: environmental processes and paleoclimate (Camm et al., 2003; Pirrie et al., 2003; Martin et al., 2008; Speirs et al., 2008; Haberlah et al., 2011; Mondillo et al., 2011; Williamson et al., 2013), forensic geoscience (Pirrie et al., 2004; Pirrie et al., 2009), and archaeology (Hardy et al., 2006; Hardy and Rollinson, 2009; Knappett et al., 2011).

2. QEMSCAN® instrument

QEMSCAN® is an automated mineral/phase analysis system based on a Scanning Electron Microscope (SEM) that provides rapid determination and quantification of the mineralogy of an ore. It is able to identify trace minerals/phases and the textural features of particles including grain/particle size distribution, liberation, and mineral association through a predefined X-ray pixel spacing and number of particles.

Sample analysis by QEMSCAN® utilises a combination of backscattered electrons (BSE) and energy dispersive X-rays (EDS) to examine a sample. An electron beam is rastered across the sample surface producing a BSE to create a digital particle map. Particles are differentiated from the resin mounting medium by BSE brightness and contrast and set the BSE threshold of particles above the resin. As the mounting media are excluded and reported as background, the X-ray acquisition will be specifically limited to the mineral particles leading to more efficient and less time-consuming process. Energy dispersive X-ray analysis at a pre-defined space is utilised to identify minerals/phases. At each analysis point the X-ray elemental spectrum is compared with a database of >750 known minerals or compounds and assigned to the most appropriate mineral/phase. It takes approximately 10 milliseconds for each analysis, taking stage movements into account, allows >100,000 point determinations to be made every hour (Pirrie et al., 2004; Goodall et al., 2005). The whole process is computer controlled using iExplorer software package v. 4.3 that includes iMeasure for data acquisition and iDiscover for the spectral interpretation and data processing and reporting. Processing data involves checking the mineral/phase assignments are correct, developing the database as required and creating the report templates to allow specific data outputs. Once complete, data outputs may include modal mineralogy parameters (mineral volume/mass, average grain size), mineralogical characteristics (mineral liberation and association data), mass size distribution, theoretical grade-recovery curve, image-grid liberation, and false colour sample/particle images.

3. QEMSCAN® operating modes

Several modes of operation can be carried out using QEMSCAN®, with each measurement mode designed to cover a particular mineralogical or metallurgical aspect. The main measurement modes available include: bulk mineralogical analysis (BMA), particle mineralogical analysis (PMA), specific/trace mineral search (S/TMS), and FieldScan images (FSI) (Gottlieb, 2000; Pirrie et al., 2004; Goodall and Scales, 2007, Pirrie and Rollinson, 2011).

The BMA mode can be applied to very rapidly determine within 30 minutes to 90 minutes to provide abundant data for the bulk mineralogy, mineral grain and particle size distribution, and mineral association. It is performed using linear scans in which the electron beam is rastered at pre-specified point spacing to collect 40,000-100,000 points and covering the entire polished section (Gottlieb et al., 2000).

The FieldScan image or Field stitch mode is used for modal and textural mineralogy measurements. It provides immediate quantitative mineralogical data including from fine grain minerals which can be used to compare with other samples and other data generated by other techniques such as XRF, XRD or SEM. The sample field view is divided into pre-set number of pixels and each pixel represents a chemical spectrum. The pixels within each field of view are then stitched together and processed offline to produce a pseudo-map of the measured sample.

The PMA mode is used to obtain detailed mineralogical mapping of individual particles, particularly liberation and locking characteristics (Pirrie et al., 2004). It is the optimal mode for characterising metallurgical products for both valuable and gangue minerals by mapping a pre-defined number of particles at a pre-selected point spacing. This process generates a grid of pixels for each particle and can resolve mineral textures and associations.

The specific/trace mineral search is a mode of measurement would be selected to map the mineralogy of low grade deposit searching for a specific or trace mineral(s) that containing high level of metal and can be located by thresholding of the backscattered electron intensity (BSI). It is important to note that the results obtained from this mode will present only the target mineral(s).

The measurement modes of QEMSCAN® analysis applied for this study were FieldScan image (FSI) and particle mineral analysis (PMA). FSI mode was applied for the crushed core samples at a 10 µm of beam stepping interval (X-ray pixel spacing) to scan the entire polished surface and acquire information including modal mineralogy, average grain size, liberation, and mineral association. PMA mode was used for the ground composite samples and size-by-size fractions at a beam spacing of 1 µm to achieve high spatial mineralogical analytical resolution to generate detailed data on mineral abundance, mineral liberation and association, and particle/grain size distribution. Also, to characterise the fine grained minerals within the scanned particles and to reduce the boundary effect that may result from low spatial resolution.

Appendix C – The chemical components of Betacol collector

Section 3. COMPOSITION / INFORMATION ON INGREDIENTS

3.1 Chemical Characterization

Synonyms: -

Component	CAS EINECS REACH	Amount %	Regulation (EU) 67/548/E	Regulation (EU) No. 1272/2008 Hazard Statements
Oleic Acid	112-80-1 204-007-1 -			H315 H319 H335
Tall Oil Fatty Acids	61790-12-3 263-107-3 -		R38	H317
Linoleic Acid	60-33-3 200-470-9 -			H315
Hexan-1-ol	111-27-3 203-852-3 603-059-00-6		Xn R22 S2,24,25	H226 H302 H312 H319
1-pentanol	71-41-0 200-752-1 603-200-00-1		Xn R10, R20 Xi R37/38 S1/2,36/37, 46	H226 H315 H332 H335
Cyclohexanol	108-93-0 203-630-6 603-009-00-3		Xn R20/22 Xi R37/38 S2,24/25	H302 H315 H332 H335
2-methylcyclohexanol, mixed isomers	583-59-5 209-512-0 603-010-00-9		Xn R20 S2,24/25	H302 H332 H319
Isononylphenol, ethoxylated	37205-87-1 - -		Xi R36/38 N R51/53	H302 H315 H318 H411/2
4-nonylphenol branched, ethoxylated	127087-87-0 - -			H302 H315 H318/9 H411/2
Dinonylphenyl polyoxyethylene	9014-93-1 - -			H319
Polyethylene glycol	25322-68-3 500-038-2- -			H319 H335
Lauryl ether carboxylic acid / Alkyl ether carboxylic acid	27306-90-7 - -			H315 H318

Note 1: Confidential information on composition has been omitted. The supplied product may not necessarily contain all of the components listed above.
Note 2: For full text of Hazard Statements and R-phrases refer to Section 16.1.

Section 4. FIRST AID MEASURES

4.1 Description of First Aid Measures

General Advice Never give fluids or induce vomiting if a patient is unconscious or is having convulsions.

Appendix D- A full description of the samples used in this study

PX05+15: The most common valuable minerals are synchysite-(Ce) and apatite with a trace of florencite-(Ce). The dominant gangue mineral is calcite followed by ankerite, minor particles of K-feldspar and traces of iron oxides, Fe-Mn oxides, strontianite, baryte, and pyrochlore.

Synchysite mainly occurs as individual granular crystals associated with strontianite or baryte within a calcite/ankerite background (Figures 1, 2, and 3). It also occurs as acicular crystals associated with strontianite, (Figure 3). The granular grains commonly form larger crystals (up to about 150 μm) than the acicular ones which usually form about 5 μm. Apatite occurs as large liberated grains (Figure 2) and as fine crystals in calcite groundmass. Florencite-(Ce) is irregular-shaped and forms fined grained crystals associated with calcite.

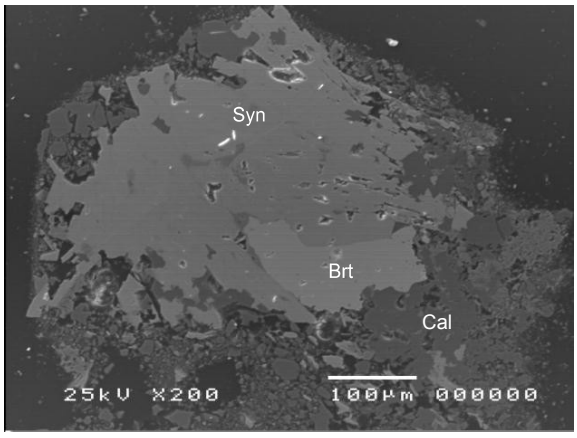

Figure 1: A large granular synchysite-(Ce) crystal associated with baryte within calcite particle.

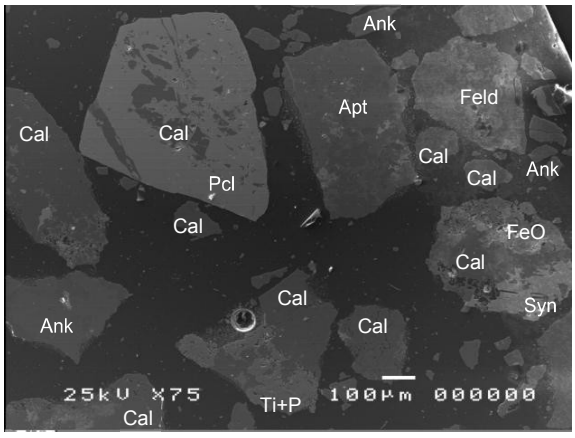

Figure 2: A large liberated particle of apatite. Large particle of pyrochlore intergrown with calcite.

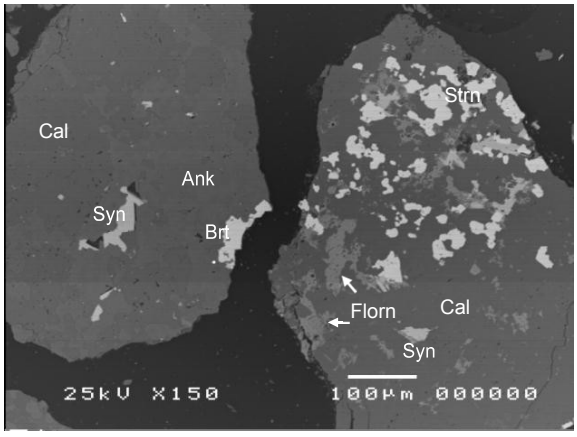

Figure 3: Anhedral crystals of florencite and synchysite with irregular crystals of strontianite in background of calcite.

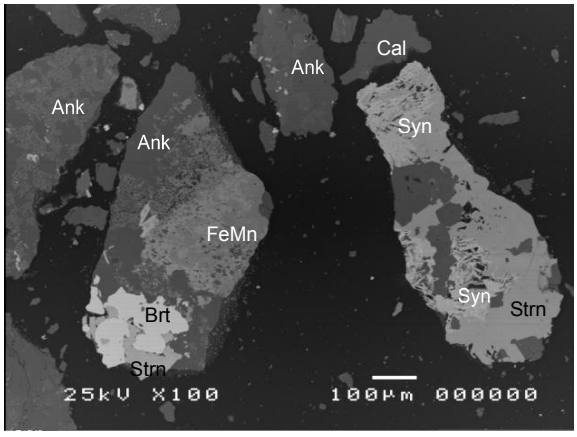

Figure 4: Needle crystals of synchysite intergrown with strontianite and calcite.

Abbreviations: Ank, ankerite; Apt, apatite; brt, baryte; Cal, calcite, Feld, K-feldspar; FeMn, Fe(Mn) oxides/ carbonates; FeO, iron oxide/carbonate; Pcl, pyrochlore; Strn, strontianite; Syn, synchysite; Ti, titanium

PX09: The common rare earth minerals are synchysite-(Ce), florencite-(Ce), and apatite as a REE- and REE-bearing minerals. The major gangue minerals are calcite and ankerite, minor quantities of K-feldspar, iron oxides and Mn-Fe oxides with trace of baryte and strontianite.

Synchysite-(Ce) mainly occurs as a single fibro-radial crystal (less than 5 μm) or as an aggregate of fibro-radial crystals (~25 μm) (Figures 5 and 6), Locally, granular crystals, between 25-50 μm, occur in calcite and sometimes in ankerite groundmass (Figure 7). Florencite-(Ce) occurs as irregular patches mainly surrounded by calcite and scarcely by K-feldspar and ankerite (< ~30 μm), (Figures 6 and 7). Apatite appeared once as a large liberated particle (~200 μm), (Figure 8).

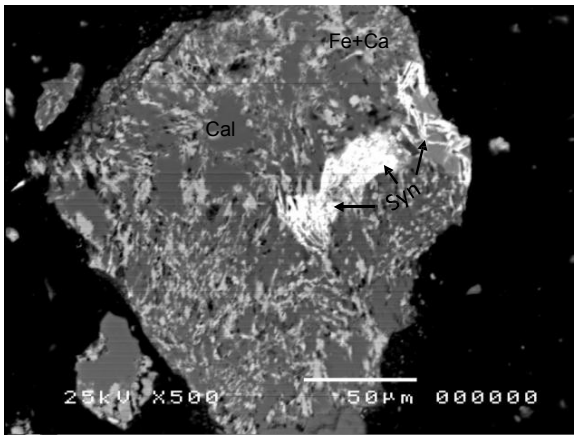

Figure 5: Fibro-radial aggregate of synchysite crystals intergrown with groundmass of calcite.

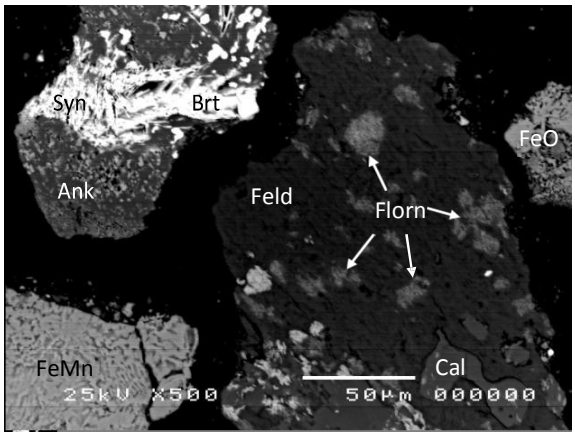

Figure 6: Fibro-radial synchysite associated with baryte within ankerite. Bands of florencite crystals intergrown with K-feldspar.

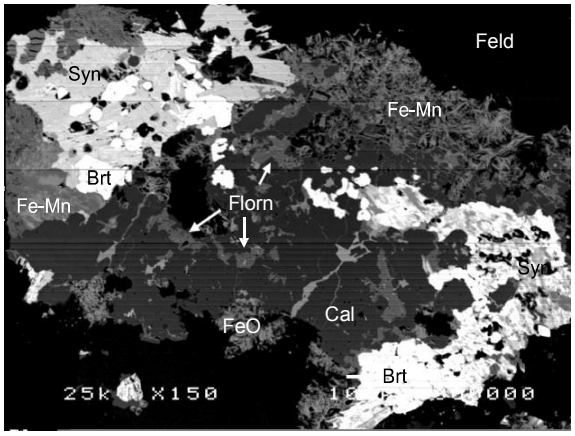

Figure 7: Granular and needle crystals of synchysite associated with baryte within Fe-Mn oxides or calcite groundmass. Anhedral crystals of florencite within calcite.

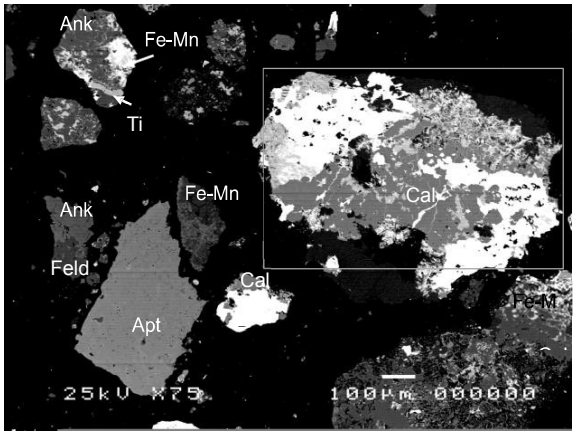

Figure 8: Large subhedral particle of apatite and veins of Fe-Mn oxides in calcite and ankerite.

PX012: Apatite, synchysite-(Ce), and florencite-(Ce) are the common valuable minerals in this sample, while calcite and ankerite are the major gangue minerals with minor K-feldspar and Fe-Mn oxides and trace baryte, strontianite and pyrite.

Apatite occurs as coarse anhedral grains up to about 100 µm mostly associated with calcite and lesser with K-feldspar (Figures 9, 10, and 11) and sometimes appears as liberated particles, (Figure 12). Synchysite-(Ce) commonly occurs as granular, subhedral to anhedral crystals up to about 50 µm (Figures 10, 11, and 12) and locally as acicular crystals which display epitaxial lateral overgrowths. Florencite occurs as both coarse (~100 µm) and fine (<30 µm) patches within calcite and ankerite groundmass.

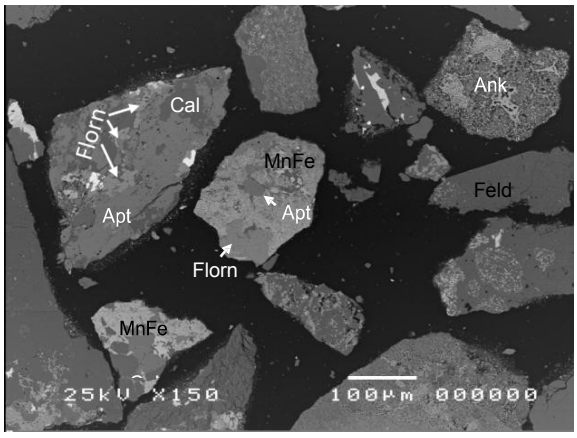

Figure 9: Individual bands of florencite associated with coarse anhedral apatite crystal within calcite.

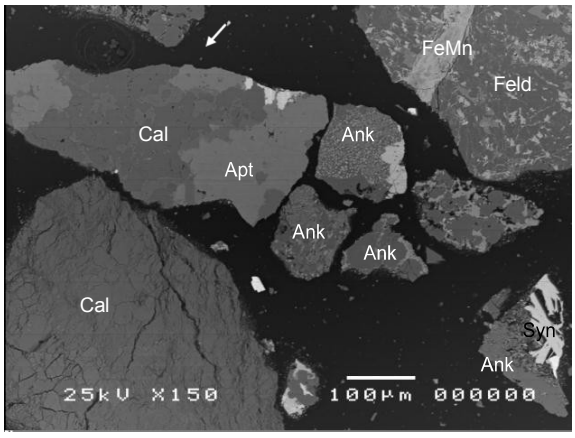

Figure 10: Anhedral crystals of apatite associated with calcite and angular fine crystals of synchysite within ankerite.

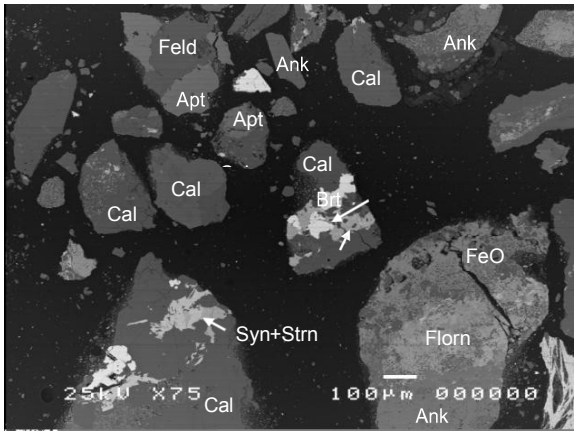

Figure 11: Coarse tabular crystals of synchysite associated with strontianite within calcite. Anhedral patch of florencite intergrown with ankerite.

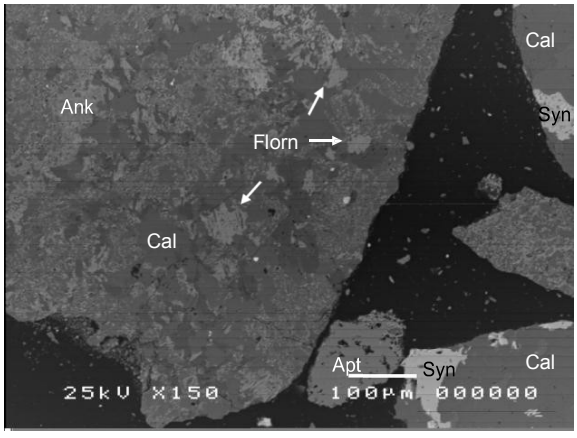

Figure 12: A large particle of liberated apatite, patches crystals of florencite and granular synchysite within calcite background.

PX13: The common valuable minerals are apatite and synchysite-(Ce) with trace of florencite-(Ce). The dominant gangue minerals are ankerite followed by calcite, minor K-feldspar, iron oxides, Fe-Mn oxides and baryte with trace of strontianite.

Apatite commonly occurs as well liberated large particles (up to ~400 µm), (Figures 13 and 14) and locally as fine patches (up to ~100 µm) within an ankerite groundmass (Figure 15). Synchysite mostly forms acicular crystals (up to ~25 µm) with epitaxial lateral overgrowths in an ankerite groundmass (Figure 16), and less commonly as granular crystals within ankerite (Figure 15). Florencite occurs as fine (< ~10 µm) anhedral crystals associated with synchysite in a groundmass of ankerite.

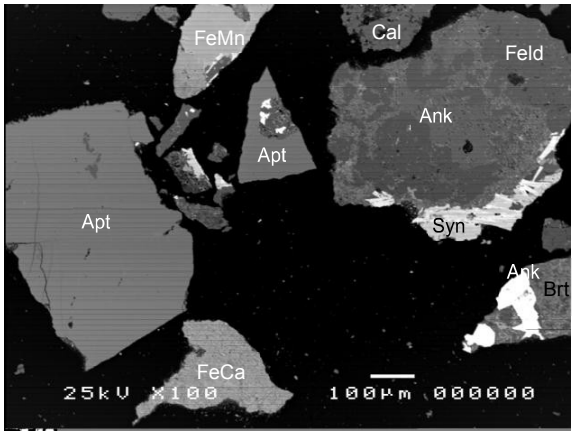

Figure 13: Two large liberated particles of apatite, angular synchysite along the edge of K-feldspar and an ankerite particle.

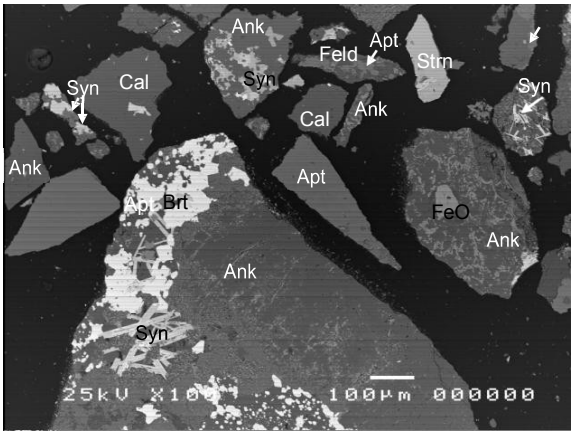

Figure 14: Two liberated apatite particles and one associated with K-feldspar. Longitudinal crystals of synchysite associated with baryte within ankerite.

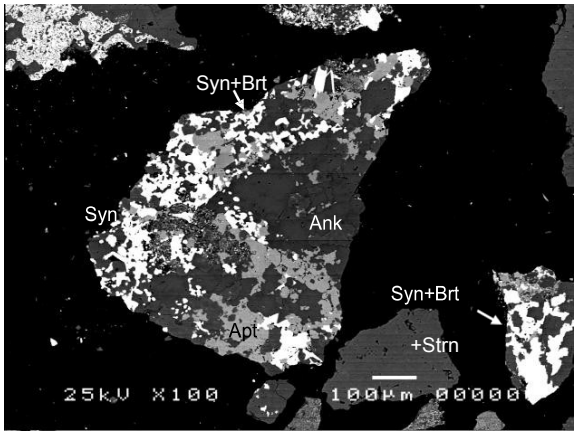

Figure 15: Large veins-like aggregates of apatite and fine crystals of synchysite associated with baryte in ankerite groundmass.

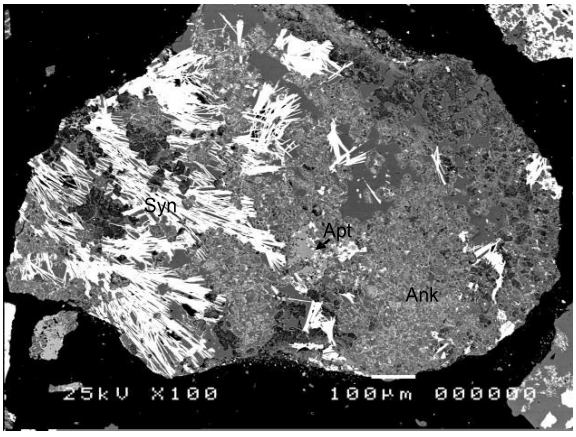

Figure 16: Fibro-radial aggregate of synchysite with bands of apatite in ankerite groundmass.

PX021: The common REE- and REE-bearing minerals are synchysite-(Ce), followed by apatite and florencite-(Ce). The major gangue minerals are calcite and ankerite, minor amounts of iron oxides and K-feldspar, trace of strontianite and baryte.

Synchysite appears as irregular clusters of fibro-radial crystals (< ~20 µm) to form nest microstructure, (Figure 17) and as anhedral granular crystals (< ~30 µm) within calcite and ankerite (Figure 18). Apatite occurs as anhedral, non-liberated crystals (vein-like or patches) up to about 50 µm associated with calcite and ankerite (Figures 19 and 20). Florencite occurs as anhedral bands within calcite groundmass (less than about 40 µm) (Figures 19 and 20).

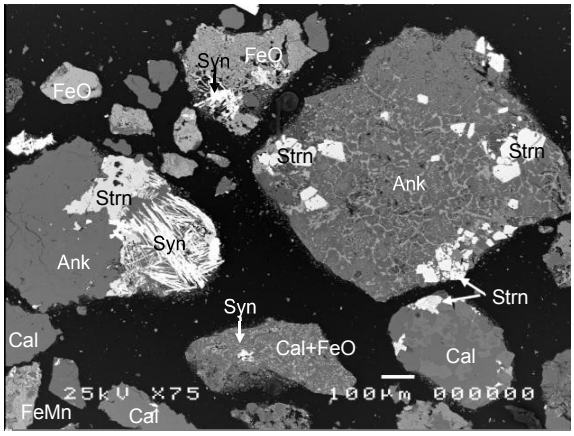

Figure 17: Aggregate of fibro-radial synchysite crystals associated with strontianite and ankerite.

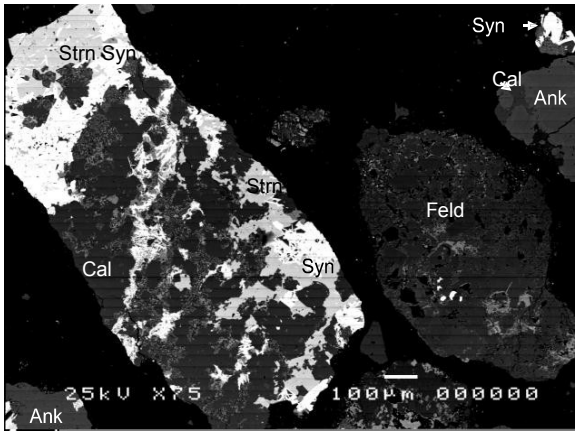

Figure 18: Accumulation of fine acicular crystals of synchysite associated with strontianite within calcite. A large particle of K-feldspar.

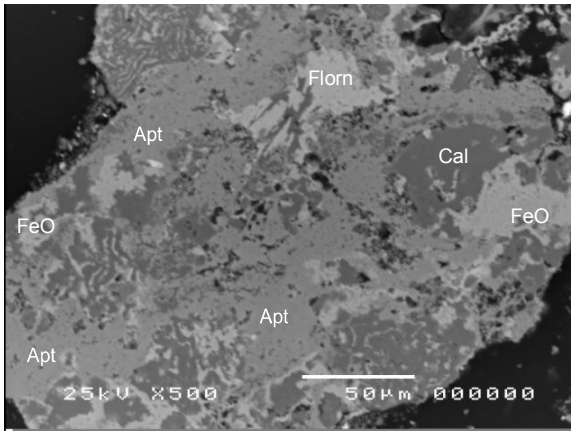

Figure 19: Anhedral large vein-like apatite crystals and patches of florencite and iron oxides within calcite.

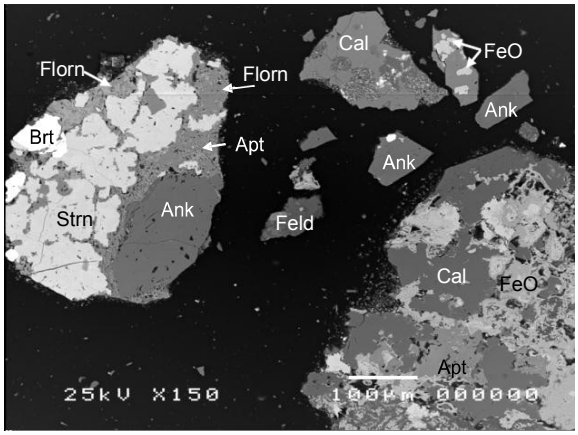

Figure 20: Anhedral bands of florencite and apatite associated with strontianite and ankerite.

PX22b: The most abundant valuable minerals are synchysite-(Ce), apatite and florencite-(Ce). The most dominant gangue mineral is ankerite followed by calcite, minor K-feldspar and Fe-Mn oxides with trace of iron oxides, baryte and strontianite.

Synchysite appears as fine to very fine grained (usually < ~30 µm and scarcely up to ~50 µm) in both crystal habits: granular and acicular are mostly associated with ankerite (Figures 21 and 22). It also appears as irregular aggregates of syntaxial intergrowth with parisite surrounded by baryte (Figure 23). Apatite occurs as anhedral crystals (up to ~ 50 µm) associated with ankerite groundmass (Figure 21) and to a lesser extent appears as a liberated particle (Figure 23). Florencite-(Ce) occurs as a vein-like aggregate of crystals in association with apatite in ankerite groundmass or with synchysite in calcite groundmass (Figure 24). This figure also shows that apatite intergrown with florencite to form irregular vein-like shape.

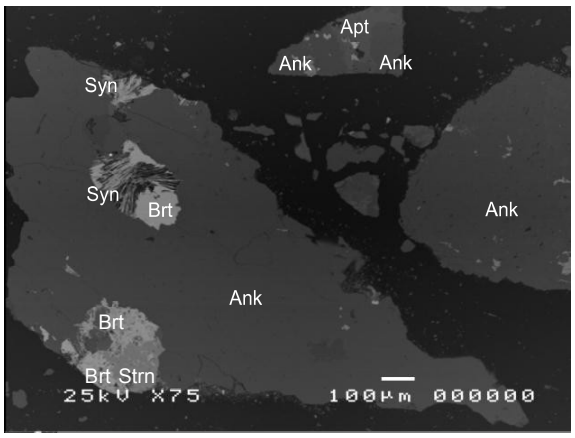

Figure 21: Fibro-radial aggregate of synchysite associated with baryte and strontianite at different places of ankerite particle.

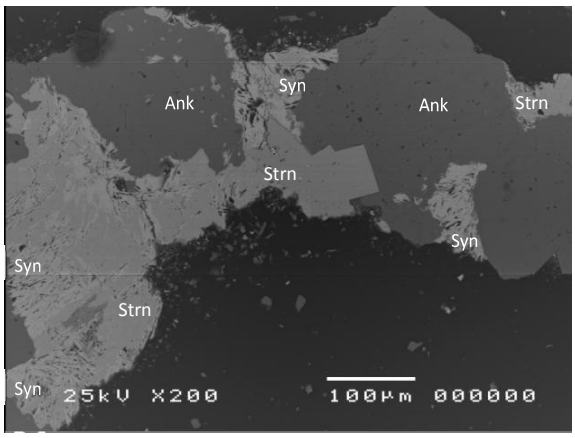

Figure 22: Fibro-radial aggregate of synchysite with strontianite at the edges of ankerite particles.

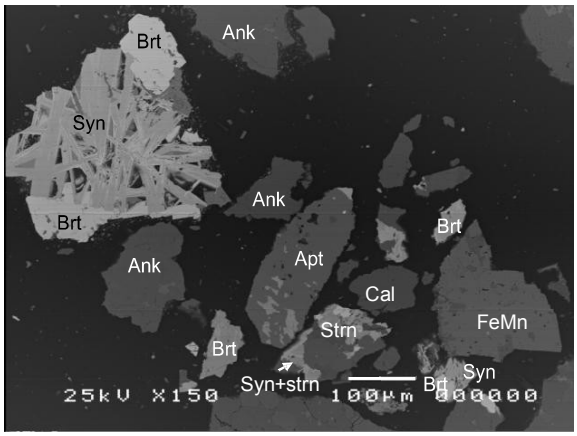

Figure 23: Accumulation of lath-shaped synchysite crystals associated with baryte. A large particle of apatite.

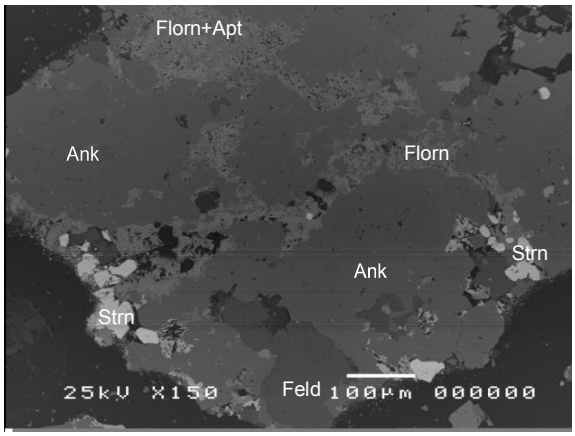

Figure 24: Fine vein-like aggregate crystals of florencite associated with apatite in ankerite background.

PX033: The most common valuable minerals are synchysite-(Ce) followed by apatite and florencite-(Ce). The dominant gangue mineral is ankerite followed by Fe-Mn oxides, minor K-feldspar, calcite and iron oxides with traces of baryte and strontianite.

Synchysite commonly appears as fine to very fine acicular crystals (up to ~5 µm) (Figures 25 and 26) to form regular and irregular epitaxial overgrowths microstructures and to a lesser extent as granular/lath-shaped crystals (< ~30 µm), commonly associated with ankerite (Figure 27). Apatite occurs as anhedral fine to coarse grains (up to 100 µm) within K-feldspar and ankerite groundmass (Figure 28). Florencite occurs as irregular vein-like shape (up to 30 µm) associated with strontianite and Iron-manganese oxides and as individual fine to very fine patches associated with K-feldspar and ankerite (Figure 26).

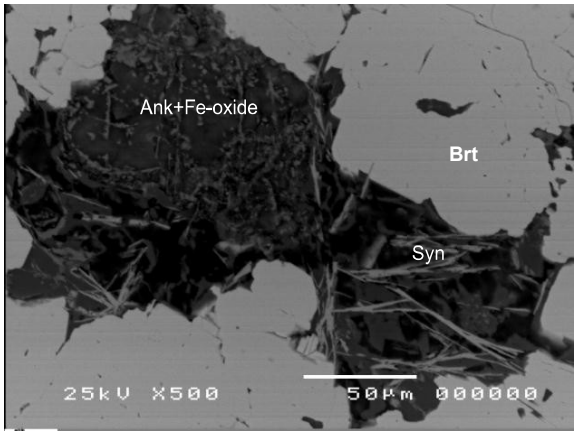

Figure 25: Fine needle crystals of synchysite in ankerite and iron oxide background.

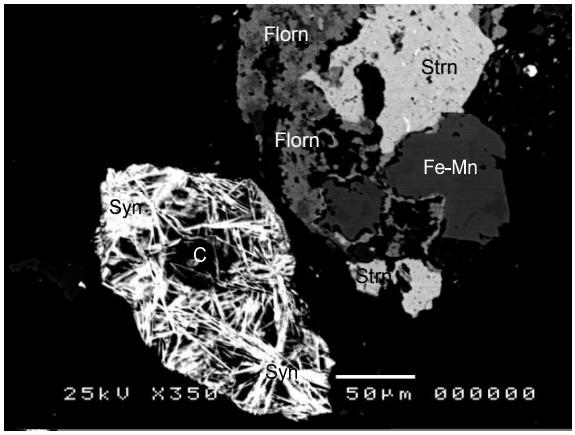

Figure 26: BSI illustrates assemblage of fibro-radial crystals of synchysite. Anhedral florencite crystal associated with strontianite.

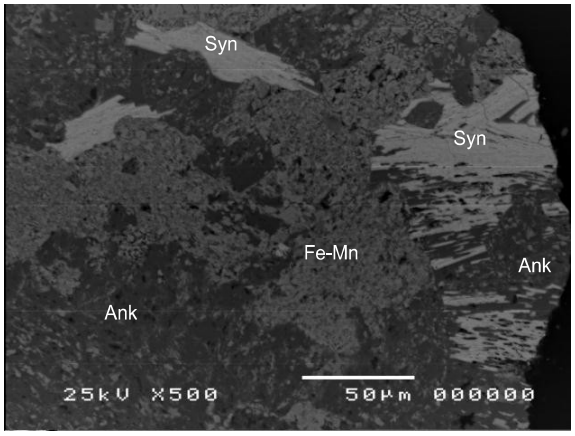

Figure 27: Tabular-lath-shaped synchysite crystals associated with Fe-Mn oxides in ankerite groundmass.

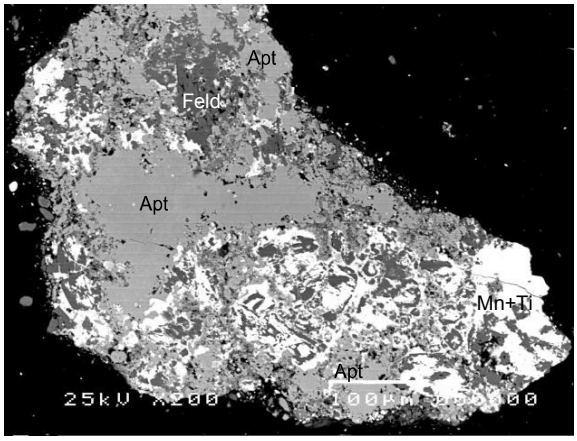

Figure 28: Anhedral large crystal of apatite associated with Mn-Ti oxides and K-feldspar groundmass.

PX035: The common valuable mineral is apatite, followed by synchysite-(Ce) with accessory of florencite-(Ce). The major gangue minerals are ankerite and calcite, minor of K-feldspar and iron oxides with trace patches of Mn-Fe oxides, baryte and strontianite.

Apatite appears as fine to coarse anhedral vein-like crystals usually less than about ~50 µm and sometimes reaches up to 250 µm associated mainly with ankerite, secondarily with K-feldspar, and scarcely with calcite groundmass (Figures 29 through 32). Synchysite occurs commonly as irregular cluster of fibro-radial crystals less than 5 µm (Figures 30 and 31) and to a lesser extent as fine anhedral lath-shaped crystals up to 30 µm. Florencite occurs as anhedral fine patches associated with ankerite and calcite background.

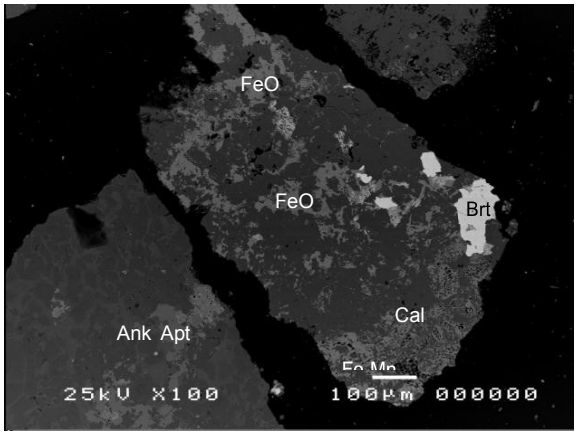

Figure 29: Anhedral vein-like apatite within large particle of ankerite. Veins of iron oxides in large particle of calcite.

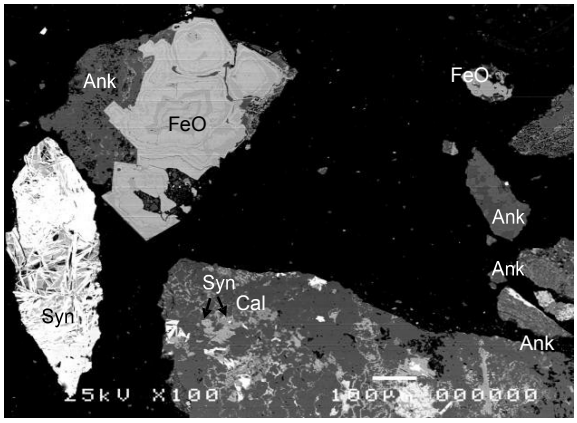

Figure 30: Large fibro-radial aggregate of synchysite and fine lath-shaped synchysite within calcite.

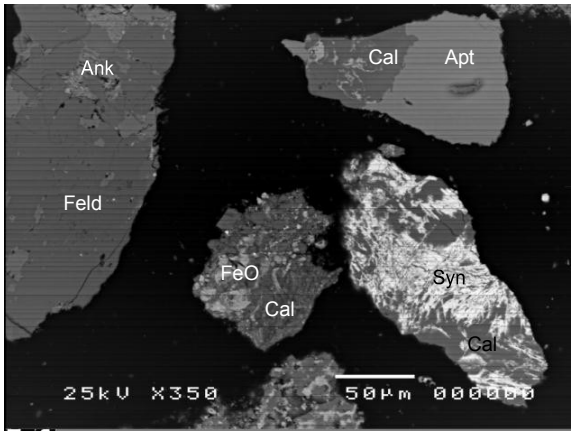

Figure 31: Euhedral crystal of apatite associate with calcite. Fibro-radial aggregate of synchysite within calcite.

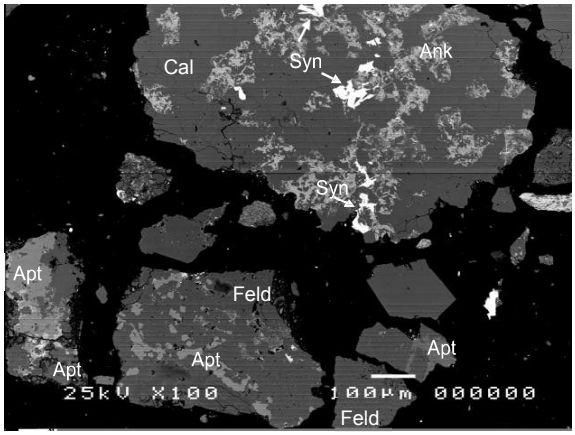

Figure 32: A large grain of apatite associated with calcite. Vein-like apatite associated with K-feldspar. Fine tabular crystals of synchysite within calcite.

Appendix E – EPMA data of apatite and synchysite-(Ce)

Table E-1: The elemental composition data (wt%) of apatite in Songwe Hill carbonatite samples, analysed by EPMA.

Spot	1	2	3	4	5	6	7	8	9	10	11	12
P_2O_5	41.42	41.85	41.68	41.73	41.36	41.88	41.42	42.02	41.05	40.66	40.83	41.58
CaO	52.42	51.93	51.86	51.18	52.20	52.60	50.34	51.57	50.20	50.26	50.28	49.77
Y_2O_3	0.55	0.96	0.83	1.05	0.50	0.43	0.84	0.93	0.79	1.22	1.44	1.41
La_2O_3	0.00	0.00	0.00	0.00	0.00	0.00	0.00	0.00	0.00	b.d	b.d	b.d
Ce_2O_3	b.d	b.d	b.d	b.d	0.37	b.d	b.d	b.d	0.34	b.d	b.d	b.d
Pr_2O_3	b.d	b.d	b.d	b.d	b.d	b.d	b.d	b.d	b.d	b.d	b.d	b.d
Nd_2O_3	b.d	b.d	b.d	0.45	b.d	b.d	b.d	b.d	0.51	0.41	b.d	b.d
Sm_2O_3	b.d	b.d	b.d	b.d	b.d	b.d	b.d	b.d	0.40	b.d	b.d	0.272
Eu_2O_3	b.d	b.d	b.d	b.d	b.d	b.d	b.d	b.d	b.d	b.d	b.d	b.d
Gd_2O_3	b.d	b.d	b.d	b.d	b.d	b.d	b.d	b.d	b.d	0.42	0.42	0.26
Dy_2O_3	b.d	b.d	b.d	b.d	b.d	0.25	0.29	0.30	b.d	0.29	b.d	0.42
ThO_2	b.d	0.108	b.d	0.15	b.d	b.d	b.d	0.09	0.16	0.22	0.24	0.17
UO_2	b.d	b.d	b.d	b.d	b.d	b.d	b.d	b.d	b.d	b.d	b.d	b.d
F	5.29	5.56	5.30	5.18	4.68	5.02	5.17	5.53	4.82	4.97	5.45	4.88
-O=F[a]	2.23	2.34	2.23	2.18	1.97	2.11	2.18	2.33	2.03	2.09	2.29	2.05
Σ	97.45	98.07	97.44	97.56	97.13	98.06	95.88	98.11	96.23	96.35	96.35	96.69
apfu[a] on the basis of number of anions												
P	2.961	2.967	2.976	2.986	2.983	2.981	3.001	2.979	2.995	2.971	2.962	3.012
Ca	4.743	4.660	4.686	4.635	4.763	4.738	4.617	4.627	4.635	4.647	4.616	4.563
Y	0.025	0.043	0.037	0.047	0.023	0.019	0.038	0.041	0.036	0.056	0.066	0.064
La	b.d	b.d	b.d	b.d	b.d	b.d	b.d	b.d	b.d	b.d	b.d	b.d
Ce	b.d	b.d	b.d	b.d	0.011	b.d	b.d	b.d	0.011	b.d	b.d	b.d
Pr	b.d	b.d	b.d	b.d	b.d	b.d	b.d	b.d	b.d	b.d	b.d	b.d
Nd	b.d	b.d	b.d	0.014	b.d	b.d	b.d	b.d	0.016	0.013	b.d	b.d
Sm	b.d	b.d	b.d	b.d	b.d	b.d	b.d	b.d	0.011	b.d	b.d	0.008
Eu	b.d	b.d	b.d	b.d	b.d	b.d	b.d	b.d	b.d	b.d	b.d	b.d
Gd	b.d	b.d	b.d	b.d	b.d	b.d	b.d	b.d	b.d	0.012	0.012	0.007
Dy	b.d	b.d	b.d	b.d	b.d	0.007	0.008	0.008	b.d	0.008	b.d	0.011
Th	b.d	0.002	b.d	0.003	b.d	b.d	b.d	0.002	0.003	0.004	0.005	0.003
F	0.818	0.853	0.819	0.802	0.729	0.772	0.811	0.847	0.760	0.785	0.854	0.764
Σ	8.546	8.525	8.518	8.487	8.509	8.516	8.475	8.505	8.467	8.496	8.514	8.433

[a] Calculated by stoichiometry and b.d. is below detection limit.

Table E-1: (Continued)

Spot	13	14	15	16	17	18	19	20	21	22	23	24	25
P_2O_5	41.46	40.86	41.54	41.27	40.62	41.35	41.41	40.78	41.29	41.74	41.40	40.49	41.38
CaO	51.80	51.08	51.15	50.77	49.82	49.03	52.41	49.81	51.58	51.86	50.52	49.39	49.79
Y_2O_3	0.79	0.81	0.72	0.63	0.90	1.99	0.31	1.49	0.69	0.68	1.06	1.52	1.44
La_2O_3	0.00	b.d	b.d	b.d	b.d	b.d	b.d	b.d	b.d	b.d	b.d	b.d	b.d
Ce_2O_3	b.d	b.d	b.d	0.76	0.79	b.d	b.d	b.d	b.d	b.d	0.40	0.43	0.37
Pr_2O_3	b.d	b.d	b.d	b.d	b.d	b.d	b.d	b.d	b.d	b.d	b.d	b.d	b.d
Nd_2O_3	b.d	b.d	b.d	0.64	0.60	0.46	b.d	0.37	0.31	b.d	0.51	0.47	0.41
Sm_2O_3	b.d	b.d	b.d	b.d	b.d	b.d	b.d	b.d	b.d	b.d	b.d	b.d	b.d
Eu_2O_3	b.d	b.d	b.d	b.d	b.d	b.d	b.d	b.d	b.d	b.d	b.d	b.d	b.d
Gd_2O_3	b.d	b.d	0.30	0.29	0.37	0.35	b.d	0.34	0.24	0.26	0.31	b.d	b.d
Dy_2O_3	b.d	b.d	0.27	0.30	b.d	0.41	b.d	0.29	b.d	0.38	b.d	0.34	0.38
ThO_2	0.11	b.d	0.10	0.18	0.25	0.13	b.d	0.10	0.08	b.d	0.16	0.10	0.13
UO_2	b.d	b.d	b.d	b.d	b.d	b.d	b.d	b.d	b.d	b.d	b.d	b.d	b.d
F	5.20	5.30	5.73	4.94	4.94	4.96	5.09	5.21	4.84	5.75	5.32	5.02	4.89
-O=F[a]	2.19	2.23	2.41	2.08	2.08	2.09	2.14	2.19	2.04	2.42	2.24	2.11	2.06
Σ	97.18	95.82	97.39	97.70	96.20	96.59	97.08	96.18	96.99	98.24	97.44	95.64	96.74
apfu[a] on the basis of number of anions													
P	2.973	2.967	2.967	2.980	2.977	3.006	2.972	2.973	2.982	2.958	2.977	2.976	3.002
Ca	4.702	4.694	4.623	4.639	4.621	4.511	4.760	4.596	4.715	4.652	4.598	4.595	4.571
Y	0.036	0.037	0.032	0.029	0.041	0.091	0.014	0.068	0.031	0.030	0.048	0.070	0.066
La	b.d	b.d	b.d	b.d	b.d	b.d	b.d	b.d	b.d	b.d	b.d	b.d	b.d
Ce	b.d	b.d	b.d	0.024	0.025	b.d	b.d	b.d	b.d	b.d	0.013	0.014	0.012
Pr	b.d	b.d	b.d	b.d	b.d	b.d	b.d	b.d	b.d	b.d	b.d	b.d	b.d
Nd	b.d	b.d	b.d	0.020	0.018	0.014	b.d	0.011	0.010	b.d	0.016	0.014	0.013
Sm	b.d	b.d	b.d	b.d	b.d	b.d	b.d	b.d	b.d	b.d	b.d	b.d	b.d
Eu	b.d	b.d	b.d	b.d	b.d	b.d	b.d	b.d	b.d	b.d	b.d	b.d	b.d
Gd	b.d	b.d	0.008	0.008	0.011	0.010	b.d	0.010	0.007	0.007	0.009	b.d	b.d
Dy	b.d	b.d	0.007	0.008	b.d	0.011	b.d	0.008	b.d	0.010	b.d	0.010	0.010
Th	0.002	b.d	0.002	0.003	0.005	0.003	b.d	0.002	0.002	b.d	0.003	0.002	0.003
F	0.807	0.833	0.885	0.772	0.783	0.780	0.790	0.821	0.756	0.881	0.827	0.798	0.768
Σ	8.520	8.531	8.524	8.482	8.482	8.426	8.536	8.489	8.502	8.539	8.489	8.479	8.444

[a] Calculated by stoichiometry, and b.d. is below detection limit.

Table E-2: Distribution of REE in apatite in Songwe Hill carbonatite samples, analysed by LA-ICP-MS. Data from Broom-Fendley (2015).

Spot	1	2	3	4	5	6	7	8	9	10	11	12	13	14	15
La_2O_3	0.016	0.009	0.016	0.020	0.029	0.017	0.082	0.051	0.043	0.040	0.050	0.059	0.117	0.045	0.029
Ce_2O_3	0.059	0.034	0.066	0.076	0.115	0.058	0.146	0.156	0.144	0.140	0.143	0.161	0.233	0.160	0.105
Pr_2O_3	0.011	0.006	0.013	0.014	0.021	0.009	0.015	0.027	0.022	0.022	0.021	0.026	0.030	0.031	0.020
Nd_2O_3	0.060	0.034	0.073	0.079	0.121	0.052	0.061	0.184	0.132	0.131	0.117	0.134	0.131	0.190	0.122
Sm_2O_3	0.028	0.017	0.033	0.036	0.053	0.033	0.021	0.091	0.076	0.074	0.063	0.056	0.042	0.089	0.056
Eu_2O_3	0.014	0.009	0.016	0.018	0.026	0.022	0.013	0.042	0.041	0.042	0.035	0.026	0.019	0.041	0.025
Gd_2O_3	0.059	0.039	0.067	0.078	0.113	0.086	0.045	0.138	0.159	0.152	0.137	0.099	0.067	0.151	0.094
Tb_2O_3	0.014	0.009	0.016	0.017	0.025	0.020	0.009	0.026	0.035	0.037	0.033	0.020	0.014	0.029	0.018
Dy_2O_3	0.110	0.072	0.117	0.127	0.188	0.169	0.060	0.182	0.277	0.287	0.288	0.139	0.097	0.194	0.122
Ho_2O_3	0.022	0.015	0.024	0.025	0.037	0.042	0.014	0.036	0.060	0.065	0.069	0.027	0.019	0.037	0.023
Er_2O_3	0.056	0.035	0.060	0.061	0.089	0.111	0.039	0.085	0.155	0.171	0.192	0.064	0.046	0.087	0.055
Tm_2O_3	0.006	0.004	0.007	0.006	0.009	0.012	0.005	0.010	0.017	0.018	0.022	0.007	0.005	0.009	0.006
Yb_2O_3	0.027	0.019	0.032	0.030	0.039	0.055	0.021	0.045	0.068	0.078	0.097	0.031	0.023	0.039	0.025
Lu_2O_3	0.003	0.002	0.003	0.003	0.003	0.007	0.003	0.005	0.006	0.007	0.009	0.003	0.002	0.004	0.002
Y_2O_3	0.680	0.437	0.732	0.766	1.114	1.284	0.460	1.045	1.813	1.973	2.267	0.781	0.527	1.087	0.714
Σ	1.165	0.740	1.275	1.358	1.979	1.976	0.991	2.122	3.049	3.237	3.544	1.632	1.372	2.191	1.418

Table E-2: (Continued)

Spot	16	17	18	19	20	21	22	23	24	25	26	27	28	29	30
La_2O_3	0.041	0.042	0.050	0.045	0.048	0.042	0.039	0.035	0.028	0.093	0.065	0.085	0.069	0.029	0.124
Ce_2O_3	0.152	0.138	0.171	0.146	0.104	0.142	0.140	0.123	0.105	0.225	0.323	0.340	0.294	0.129	0.360
Pr_2O_3	0.029	0.027	0.033	0.028	0.017	0.028	0.028	0.024	0.020	0.037	0.065	0.056	0.059	0.026	0.057
Nd_2O_3	0.171	0.157	0.198	0.173	0.095	0.174	0.169	0.148	0.117	0.190	0.421	0.327	0.366	0.161	0.319
Sm_2O_3	0.081	0.075	0.092	0.082	0.043	0.081	0.077	0.068	0.056	0.077	0.122	0.106	0.117	0.067	0.112
Eu_2O_3	0.036	0.033	0.040	0.037	0.019	0.037	0.036	0.031	0.026	0.034	0.046	0.042	0.046	0.029	0.044
Gd_2O_3	0.135	0.125	0.156	0.148	0.075	0.146	0.142	0.124	0.099	0.138	0.125	0.119	0.132	0.089	0.125
Tb_2O_3	0.024	0.024	0.029	0.029	0.014	0.029	0.029	0.024	0.019	0.028	0.021	0.021	0.024	0.017	0.020
Dy_2O_3	0.171	0.164	0.203	0.199	0.105	0.203	0.199	0.171	0.139	0.197	0.132	0.134	0.151	0.114	0.123
Ho_2O_3	0.031	0.030	0.038	0.038	0.019	0.038	0.038	0.033	0.026	0.038	0.025	0.027	0.030	0.024	0.025
Er_2O_3	0.075	0.072	0.090	0.090	0.046	0.091	0.091	0.078	0.061	0.088	0.060	0.066	0.075	0.057	0.057
Tm_2O_3	0.008	0.008	0.010	0.010	0.005	0.009	0.009	0.008	0.007	0.009	0.007	0.008	0.009	0.007	0.006
Yb_2O_3	0.037	0.035	0.042	0.041	0.021	0.039	0.040	0.035	0.030	0.039	0.034	0.039	0.044	0.034	0.031
Lu_2O_3	0.004	0.003	0.004	0.004	0.002	0.004	0.004	0.003	0.003	0.004	0.004	0.004	0.005	0.003	0.003
Y_2O_3	1.013	0.936	1.107	1.148	0.575	1.139	1.115	0.976	0.807	1.083	0.766	0.796	0.895	0.672	0.723
Σ	2.008	1.868	2.264	2.217	1.189	2.200	2.156	1.880	1.543	2.280	2.215	2.169	2.316	1.457	2.130

Table E-2: (Continued)

Spot	31	32	33	34	35	36	37	38	39	40	41	42	43	44	45	46
La_2O_3	0.111	0.116	0.109	0.082	0.087	0.075	0.076	0.170	0.139	0.116	0.108	0.135	0.143	0.136	0.078	0.136
Ce_2O_3	0.408	0.419	0.317	0.247	0.244	0.215	0.225	0.354	0.417	0.332	0.304	0.408	0.425	0.395	0.224	0.427
Pr_2O_3	0.079	0.076	0.053	0.047	0.043	0.044	0.038	0.044	0.065	0.054	0.047	0.068	0.071	0.063	0.035	0.068
Nd_2O_3	0.468	0.433	0.298	0.323	0.270	0.297	0.230	0.200	0.344	0.269	0.239	0.372	0.384	0.331	0.184	0.363
Sm_2O_3	0.169	0.162	0.108	0.160	0.134	0.135	0.074	0.055	0.100	0.078	0.069	0.111	0.115	0.098	0.055	0.105
Eu_2O_3	0.069	0.065	0.045	0.070	0.062	0.062	0.031	0.024	0.036	0.030	0.025	0.039	0.040	0.033	0.020	0.037
Gd_2O_3	0.210	0.202	0.149	0.223	0.205	0.204	0.098	0.081	0.115	0.094	0.082	0.128	0.134	0.109	0.064	0.118
Tb_2O_3	0.040	0.040	0.028	0.037	0.038	0.036	0.017	0.016	0.019	0.016	0.013	0.021	0.021	0.018	0.011	0.019
Dy_2O_3	0.249	0.252	0.158	0.196	0.202	0.196	0.094	0.094	0.116	0.100	0.084	0.128	0.129	0.113	0.069	0.122
Ho_2O_3	0.046	0.047	0.030	0.033	0.035	0.034	0.017	0.018	0.020	0.018	0.015	0.022	0.022	0.020	0.012	0.022
Er_2O_3	0.104	0.107	0.061	0.064	0.068	0.065	0.037	0.041	0.051	0.046	0.039	0.055	0.055	0.050	0.032	0.054
Tm_2O_3	0.011	0.011	0.007	0.007	0.007	0.007	0.004	0.005	0.007	0.006	0.005	0.007	0.007	0.007	0.004	0.007
Yb_2O_3	0.049	0.051	0.028	0.029	0.027	0.026	0.021	0.023	0.035	0.032	0.026	0.037	0.037	0.035	0.024	0.037
Lu_2O_3	0.006	0.006	0.003	0.003	0.003	0.003	0.002	0.003	0.004	0.004	0.003	0.004	0.004	0.004	0.003	0.004
Y_2O_3	1.269	1.278	0.747	0.805	0.850	0.832	0.444	0.469	0.564	0.501	0.421	0.619	0.616	0.567	0.373	0.592
Σ	3.286	3.264	2.142	2.326	2.273	2.230	1.410	1.599	2.033	1.696	1.480	2.153	2.205	1.978	1.189	2.113

Table E-2: (Continued)

Spot	47	48	49	50	51	52	53	54	55	56	57	58	59	60	61	62
La_2O_3	0.105	0.142	0.123	0.107	0.135	0.111	0.135	0.111	0.030	0.041	0.043	0.034	0.028	0.048	0.148	0.163
Ce_2O_3	0.299	0.378	0.373	0.289	0.387	0.322	0.387	0.322	0.112	0.132	0.129	0.138	0.110	0.134	0.243	0.280
Pr_2O_3	0.046	0.058	0.061	0.044	0.059	0.051	0.059	0.051	0.025	0.020	0.020	0.027	0.022	0.021	0.022	0.026
Nd_2O_3	0.244	0.295	0.323	0.235	0.313	0.270	0.313	0.270	0.160	0.102	0.105	0.201	0.152	0.105	0.082	0.092
Sm_2O_3	0.073	0.088	0.099	0.073	0.094	0.086	0.094	0.086	0.063	0.032	0.032	0.073	0.058	0.032	0.013	0.017
Eu_2O_3	0.027	0.032	0.034	0.027	0.033	0.030	0.033	0.030	0.025	0.012	0.013	0.028	0.024	0.013	0.004	0.006
Gd_2O_3	0.087	0.103	0.111	0.083	0.107	0.099	0.107	0.099	0.073	0.035	0.036	0.080	0.067	0.036	0.010	0.018
Tb_2O_3	0.015	0.017	0.018	0.014	0.018	0.016	0.018	0.016	0.011	0.006	0.006	0.011	0.010	0.006	0.001	0.002
Dy_2O_3	0.096	0.106	0.112	0.085	0.115	0.105	0.115	0.105	0.058	0.034	0.037	0.060	0.057	0.037	0.006	0.014
Ho_2O_3	0.018	0.019	0.019	0.015	0.021	0.019	0.021	0.019	0.010	0.007	0.007	0.011	0.010	0.007	0.001	0.003
Er_2O_3	0.045	0.047	0.048	0.038	0.052	0.048	0.052	0.048	0.024	0.017	0.019	0.026	0.026	0.019	0.003	0.009
Tm_2O_3	0.006	0.006	0.006	0.005	0.007	0.006	0.007	0.006	0.003	0.002	0.003	0.003	0.003	0.003	b.d	0.001
Yb_2O_3	0.032	0.032	0.032	0.027	0.037	0.034	0.037	0.034	0.017	0.012	0.014	0.016	0.016	0.014	0.001	0.007
Lu_2O_3	0.004	0.004	0.004	0.003	0.004	0.004	0.004	0.004	0.002	0.001	0.002	0.002	0.002	0.002	b.d	0.001
Y_2O_3	0.500	0.522	0.538	0.408	0.585	0.545	0.585	0.545	0.312	0.207	0.230	0.320	0.317	0.224	0.033	0.103
Σ	1.597	1.848	1.900	1.453	1.968	1.747	1.968	1.747	0.924	0.661	0.697	1.030	0.903	0.700	0.568	0.743

Table E-3: The elemental composition data (wt%) of synchysite-(Ce) in Songwe Hill carbonatite samples, analysed by EPMA at CSM.

Spot	1	2	3	4	5	6	7	8	9	10	11	12
CaO	17.45	17.07	15.22	17.35	17.32	17.83	17.42	17.30	16.13	17.46	16.44	16.55
SrO	b.d	b.d	b.d	b.d	b.d	b.d	b.d	b.d	b.d	b.d	b.d	b.d
BaO	b.d	b.d	b.d	b.d	b.d	b.d	b.d	b.d	b.d	b.d	b.d	b.d
Y_2O_3	1.88	1.16	1.76	b.d	2.06	b.d	0.49	b.d	0.94	b.d	0.57	1.80
La_2O_3	9.37	10.36	10.48	10.16	9.71	12.95	11.29	12.09	9.27	8.20	11.75	8.89
Ce_2O_3	19.20	23.07	21.76	24.61	20.42	27.75	25.31	26.56	23.51	24.61	24.62	20.18
Pr_2O_3	1.93	1.89	2.13	3.09	2.52	2.87	2.74	2.53	2.76	3.25	1.35	2.64
Nd_2O_3	7.56	8.26	7.89	8.73	7.29	7.67	7.77	7.17	9.89	12.13	9.03	6.85
Sm_2O_3	1.01	1.32	0.98	0.91	1.71	0.43	0.68	0.70	0.96	1.23	0.62	1.65
Eu_2O_3	b.d	b.d	b.d	b.d	b.d	b.d	b.d	b.d	b.d	b.d	b.d	b.d
Gd_2O_3	0.64	0.94	0.70	b.d	0.72	0.21	0.57	0.58	1.05	0.91	0.54	0.91
Dy_2O_3	b.d	b.d	b.d	b.d	b.d	b.d	b.d	b.d	b.d	b.d	b.d	b.d
ThO_2	1.13	0.51	0.19	0.97	1.29	0.63	0.21	0.49	0.85	0.59	1.53	6.73
UO_2	b.d	b.d	b.d	b.d	b.d	b.d	b.d	b.d	b.d	b.d	b.d	b.d
F[a]	5.51	5.86	5.69	5.59	5.76	6.16	5.98	5.97	5.91	5.85	5.93	5.82
CO_2 [a]	25.54	27.13	26.35	25.90	26.66	28.53	27.71	27.68	27.40	27.10	27.48	26.94
-O=F	2.32	2.47	2.40	2.35	2.42	2.59	2.52	2.52	2.49	2.46	2.50	2.45
Σ	88.58	95.47	92.61	92.83	93.06	101.92	98.06	98.68	97.34	97.55	98.40	96.39
apfu[a] on the basis of number of anions												
Ca	1.054	1.009	1.015	0.923	1.022	0.952	1.008	0.986	0.989	0.933	0.993	0.958
Sr	b.d	b.d	b.d	b.d	b.d	b.d	b.d	b.d	b.d	b.d	b.d	b.d
Ba	b.d	b.d	b.d	b.d	b.d	b.d	b.d	b.d	b.d	b.d	b.d	b.d
Σ	1.05	1.01	1.01	0.92	1.02	0.95	1.01	0.99	0.99	0.93	0.99	0.96
Y	0.057	0.033	0.052	b.d	0.060	b.d	0.014	b.d	0.027	b.d	0.016	0.052
La	0.199	0.206	0.214	0.212	0.197	0.245	0.220	0.236	0.182	0.163	0.230	0.178
Ce	0.404	0.456	0.442	0.510	0.411	0.521	0.489	0.514	0.459	0.486	0.478	0.402
Pr	0.040	0.037	0.043	0.064	0.050	0.054	0.053	0.049	0.054	0.064	0.026	0.052
Nd	0.155	0.159	0.156	0.177	0.143	0.141	0.146	0.135	0.188	0.234	0.171	0.133
Sm	0.020	0.025	0.019	0.018	0.032	0.008	0.012	0.013	0.018	0.023	0.011	0.031
Eu	b.d	b.d	b.d	b.d	b.d	b.d	b.d	b.d	b.d	b.d	b.d	b.d
Gd	0.012	0.017	0.013	b.d	0.013	0.004	0.010	0.010	0.019	0.016	0.009	0.016
Dy	b.d	b.d	b.d	b.d	b.d	b.d	b.d	b.d	b.d	b.d	b.d	b.d
Th	0.015	0.006	0.002	0.012	0.016	0.007	0.002	0.006	0.010	0.007	0.018	0.083
Σ	0.90	0.94	0.94	0.99	0.92	0.98	0.95	0.96	0.96	0.99	0.96	0.95

[a] Determined by stoichiometry, and b.d is below detection limit.

Table E-3: (Continued)

Spot	13	14	15	16	17	18	19	20	21
CaO	14.84	16.40	17.77	17.79	17.14	14.00	16.74	17.52	14.87
SrO	b.d	b.d	b.d	b.d	b.d	b.d	b.d	b.d	b.d
BaO	b.d	b.d	b.d	b.d	b.d	b.d	b.d	b.d	b.d
Y_2O_3	b.d	b.d	b.d	b.d	1.29	b.d	0.92	0.76	0.60
La_2O_3	17.31	17.11	16.80	12.49	8.52	22.23	12.92	13.89	13.73
Ce_2O_3	25.41	24.78	25.44	24.29	21.36	24.64	25.40	26.89	23.86
Pr_2O_3	2.30	1.57	2.00	1.76	2.43	2.21	2.13	2.50	2.19
Nd_2O_3	6.52	5.42	5.42	7.20	9.38	3.95	6.82	8.23	6.88
Sm_2O_3	0.60	0.42	0.45	0.37	1.34	0.35	0.68	0.64	0.73
Eu_2O_3	b.d	b.d	b.d	b.d	b.d	b.d	b.d	b.d	b.d
Gd_2O_3	0.57	0.58	0.41	0.50	0.68	0.37	0.64	0.45	0.40
Dy_2O_3	b.d	b.d	b.d	b.d	b.d	b.d	b.d	b.d	b.d
ThO_2	1.01	1.52	1.51	1.08	1.57	0.64	1.52	0.62	1.44
UO_2	b.d	b.d	b.d	b.d	b.d	b.d	b.d	b.d	b.d
F[a]	5.88	5.91	6.16	5.87	5.71	5.84	5.95	6.31	5.64
CO_2 [a]	27.24	27.37	28.54	27.21	26.45	27.05	27.55	29.25	26.14
-O=F	2.48	2.49	2.59	2.47	2.40	2.46	2.50	2.66	2.38
Σ	99.21	98.59	101.91	96.08	93.47	98.82	98.76	104.38	94.10
apfu[a] on the basis of number of anions									
Ca	0.854	0.938	0.975	1.026	1.015	0.812	0.951	0.939	0.893
Sr	b.d	b.d	b.d	b.d	b.d	b.d	b.d	b.d	b.d
Ba	b.d	b.d	b.d	b.d	b.d	b.d	b.d	b.d	b.d
Σ	0.85	0.94	0.98	1.03	1.02	0.81	0.95	0.94	0.89
Y	b.d	b.d	b.d	b.d	0.038	b.d	0.026	0.020	0.018
La	0.343	0.337	0.317	0.248	0.174	0.444	0.253	0.256	0.284
Ce	0.499	0.484	0.477	0.479	0.432	0.488	0.493	0.493	0.489
Pr	0.045	0.030	0.037	0.034	0.049	0.044	0.041	0.046	0.045
Nd	0.125	0.103	0.099	0.138	0.185	0.076	0.129	0.147	0.138
Sm	0.011	0.008	0.008	0.007	0.026	0.007	0.012	0.011	0.014
Eu	b.d	b.d	b.d	b.d	b.d	b.d	b.d	b.d	b.d
Gd	0.010	0.010	0.007	0.009	0.012	0.007	0.011	0.007	0.007
Dy	b.d	b.d	b.d	b.d	b.d	b.d	b.d	b.d	b.d
Th	0.012	0.018	0.018	0.013	0.020	0.008	0.018	0.007	0.018
Σ	0.90	0.94	0.94	0.99	0.92	0.98	0.95	0.96	0.96

[a] Determined by stoichiometry, and b.d is below detection limit.

Table E-4: The elemental composition data (wt%) of synchysite-(Ce) in Songwe Hill carbonatite samples analysed by EPMA at NHM. Data from Aoife Brady (Mkango Resources Ltd.)

Spot	1	2	3	4	5	6	7	8	9	10	11	12	13	14	15	16	17	18
CaO	17.26	17.86	17.59	17.69	16.19	17.21	17.04	16.93	16.20	16.87	15.47	17.21	17.04	16.98	16.84	15.41	16.28	17.01
MnO	0.01	b.d	b.d	b.d	0.02	0.03	b.d	b.d	0.03	0.02	b.d	0.02	0.01	0.01	b.d	0.04	0.01	b.d
FeO	0.04	0.01	0.02	b.d	0.04	0.07	0.01	0.01	0.06	0.03	0.05	0.07	0.07	0.07	0.02	0.41	0.33	0.04
SrO	0.52	0.52	0.67	0.80	0.18	0.23	0.38	0.15	0.42	0.50	0.53	0.35	0.73	0.36	0.67	b.d	0.08	b.d
BaO	b.d	b.d	b.d	b.d	b.d	0.01	b.d	b.d	b.d	b.d	b.d	b.d	b.d	b.d	0.01	b.d	0.14	b.d
Y_2O_3	0.96	0.47	0.57	0.43	0.35	1.30	1.12	0.83	0.66	0.11	0.15	0.24	2.70	1.54	0.10	1.07	1.15	1.25
La_2O_3	8.66	10.96	10.78	11.65	12.42	10.71	11.46	10.72	10.99	9.50	9.47	9.21	9.63	9.24	10.65	12.28	11.48	12.03
Ce_2O_3	20.45	21.32	21.20	22.99	24.46	24.38	24.05	24.04	25.00	24.49	24.39	24.47	22.96	23.70	24.97	26.13	24.04	24.78
Pr_2O_3	2.80	2.68	2.43	2.73	2.90	2.84	2.80	2.74	2.98	2.99	2.96	2.99	2.52	2.73	2.76	2.67	2.53	2.57
Nd_2O_3	12.50	11.24	10.34	9.81	9.91	10.19	9.56	9.92	10.33	11.55	11.58	11.64	9.19	10.29	10.33	9.76	9.43	8.95
Sm_2O_3	2.57	1.96	1.78	1.33	1.25	1.28	1.08	1.14	1.25	1.36	1.25	1.37	0.90	1.05	1.10	1.04	1.12	0.90
Eu_2O_3	0.53	0.38	0.30	0.22	0.18	0.22	0.13	0.16	0.20	0.14	0.08	0.18	0.10	0.09	0.13	0.18	0.22	0.12
Gd_2O_3	1.39	0.82	0.75	0.35	0.26	0.24	0.16	0.17	0.24	0.29	0.23	0.35	0.20	0.18	0.15	0.17	0.39	0.21
Dy_2O_3	0.49	0.33	0.31	0.21	0.15	0.33	0.25	0.25	0.17	0.07	0.08	0.13	0.43	0.19	0.08	0.25	0.30	0.30
ThO_2	0.75	0.70	0.59	0.49	0.29	1.41	0.85	1.27	0.44	0.60	0.61	0.42	2.80	1.42	0.39	0.47	0.46	0.37
UO_2	b.d	b.d	b.d	b.d	b.d	b.d	b.d	b.d	b.d	b.d	b.d	b.d	b.d	b.d	b.d	b.d	b.d	b.d
F[a]	5.93	6.00	5.85	5.96	5.85	6.08	5.95	5.88	5.88	5.87	5.67	5.92	6.02	5.87	5.85	5.94	5.83	5.92
CO_2 [a]	27.49	27.78	27.09	27.61	27.10	28.17	27.56	27.26	27.25	27.21	26.28	27.41	27.88	27.18	27.11	27.54	27.03	27.44
-O=F	2.50	2.53	2.46	2.51	2.46	2.56	2.50	2.48	2.48	2.47	2.39	2.49	2.53	2.47	2.46	2.50	2.46	2.49
Σ	99.97	100.65	97.91	99.93	99.23	102.36	100.07	99.13	99.79	99.26	96.60	99.62	100.88	98.55	98.84	101.41	98.53	99.51
apfu[a] on the basis of number of anions																		
Ca	0.974	0.997	1.008	0.994	0.927	0.948	0.959	0.964	0.922	0.962	0.913	0.974	0.950	0.969	0.963	0.866	0.934	0.962
Mn	b.d	b.d	b.d	b.d	0.001	0.001	b.d	b.d	0.001	0.001	b.d	0.001	b.d	b.d	b.d	0.002	b.d	b.d
Fe	0.002	b.d	0.001	b.d	0.002	0.003	b.d	b.d	0.003	0.001	0.002	0.003	0.003	0.003	0.001	0.018	0.015	0.002
Sr	0.016	0.016	0.021	0.024	0.006	0.007	0.012	0.005	0.013	0.015	0.017	0.011	0.022	0.011	0.021	b.d	0.002	b.d
Ba	b.d	b.d	b.d	b.d	b.d	b.d	b.d	b.d	b.d	b.d	b.d	b.d	b.d	b.d	b.d	b.d	0.003	b.d
Σ	1.00	1.02	1.04	1.03	0.94	0.97	0.98	0.98	0.95	0.99	0.94	1.00	0.99	0.99	0.99	0.92	0.96	0.97
Y	0.027	0.013	0.016	0.012	0.010	0.036	0.031	0.023	0.019	0.003	0.004	0.007	0.075	0.044	0.003	0.030	0.033	0.035
La	0.168	0.211	0.213	0.225	0.245	0.203	0.222	0.210	0.215	0.187	0.192	0.180	0.185	0.182	0.210	0.237	0.227	0.234
Ce	0.394	0.407	0.415	0.441	0.478	0.459	0.462	0.468	0.486	0.477	0.492	0.473	0.437	0.462	0.488	0.501	0.471	0.479
Pr	0.054	0.051	0.047	0.052	0.056	0.053	0.054	0.053	0.058	0.058	0.059	0.058	0.048	0.053	0.054	0.051	0.049	0.049
Nd	0.235	0.209	0.197	0.184	0.189	0.187	0.179	0.188	0.196	0.220	0.228	0.220	0.171	0.196	0.197	0.183	0.180	0.169
Sm	0.047	0.035	0.033	0.024	0.023	0.023	0.020	0.021	0.023	0.025	0.024	0.025	0.016	0.019	0.020	0.019	0.021	0.016
Eu	0.010	0.007	0.005	0.004	0.003	0.004	0.002	0.003	0.004	0.003	0.002	0.003	0.002	0.002	0.002	0.003	0.004	0.002
Gd	0.024	0.014	0.013	0.006	0.005	0.004	0.003	0.003	0.004	0.005	0.004	0.006	0.003	0.003	0.003	0.003	0.007	0.004
Dy	0.008	0.006	0.005	0.004	0.003	0.005	0.004	0.004	0.003	0.001	0.001	0.002	0.007	0.003	0.001	0.004	0.005	0.005
Th	0.009	0.008	0.007	0.006	0.004	0.016	0.010	0.015	0.005	0.007	0.008	0.005	0.033	0.017	0.005	0.006	0.006	0.004
Σ	0.98	0.96	0.95	0.96	1.02	0.99	0.99	0.99	1.01	0.99	1.01	0.98	0.98	0.98	0.98	1.04	1.00	1.00

[a] Determined by stoichiometry, and b.d is below detection limit.

Table E-4: (Continued)

Spot	19	20	21	22	23	24	25	26	27	28	29	30	31	32	33	34	35	36
CaO	17.10	17.26	17.23	16.96	17.62	16.63	18.11	16.96	16.14	17.63	16.32	17.20	17.45	16.66	16.18	17.25	16.77	17.36
MnO	0.01	0.01	0.01	b.d	0.01	b.d	b.d	b.d	b.d	b.d	b.d	b.d	b.d	0.02	b.d	b.d	b.d	b.d
FeO	0.05	0.01	0.09	0.05	0.07	0.72	0.03	0.69	1.42	0.14	1.92	0.43	0.09	0.16	0.44	0.14	0.02	0.03
SrO	0.15	0.19	0.04	0.06	0.22	0.22	0.57	0.72	0.61	0.76	0.44	0.66	0.90	0.64	0.45	0.24	0.61	0.78
BaO	b.d	b.d	b.d	b.d	b.d	b.d	0.01	0.03	b.d	0.01	b.d	b.d	b.d	b.d	0.01	b.d	b.d	0.02
Y_2O_3	1.22	1.03	1.78	2.05	1.33	0.67	0.84	0.50	0.76	0.55	0.60	0.54	0.34	0.32	0.39	0.36	0.67	0.57
La_2O_3	9.80	11.02	10.07	7.54	9.32	14.34	13.57	15.60	14.11	15.25	14.60	14.95	15.43	14.72	15.33	14.48	13.81	13.77
Ce_2O_3	22.74	23.63	23.21	18.76	24.45	23.64	22.84	23.45	22.31	22.51	22.93	22.69	23.43	24.04	24.36	23.53	24.34	23.84
Pr_2O_3	2.73	2.66	2.65	2.60	2.92	2.22	2.09	2.02	2.12	1.92	2.11	1.97	2.00	2.17	2.28	2.18	2.20	2.16
Nd_2O_3	10.07	9.39	9.18	12.97	10.45	7.79	7.78	6.80	7.45	6.76	7.58	6.93	6.75	7.63	7.42	7.63	7.53	6.64
Sm_2O_3	1.32	1.11	1.04	2.34	1.06	1.04	1.22	0.88	1.12	1.03	1.12	0.93	0.86	1.02	1.07	1.09	0.91	0.79
Eu_2O_3	0.20	0.15	0.12	0.36	0.08	0.17	0.30	0.21	0.25	0.33	0.27	0.21	0.25	0.20	0.22	0.29	0.13	0.19
Gd_2O_3	0.45	0.27	0.40	1.06	0.09	0.57	0.83	0.64	0.71	0.78	0.66	0.61	0.51	0.59	0.64	0.68	0.41	0.33
Dy_2O_3	0.35	0.25	0.36	0.43	0.19	0.31	0.26	0.18	0.26	0.24	0.25	0.18	0.16	0.13	0.22	0.21	0.21	0.22
ThO_2	1.46	1.13	1.18	1.36	0.46	0.97	1.08	1.22	1.36	1.46	1.25	1.29	0.82	0.79	1.01	1.01	1.15	1.27
UO_2	b.d	b.d	b.d	b.d	b.d	b.d	b.d	b.d	b.d	b.d	b.d	b.d	b.d	b.d	b.d	b.d	b.d	b.d
F[a]	5.85	5.89	5.86	5.79	5.95	5.95	6.04	6.01	5.90	5.98	6.04	5.92	5.96	5.91	5.96	5.94	5.89	5.87
CO_2 [a]	27.08	27.28	27.15	26.80	27.55	27.56	27.98	27.83	27.33	27.72	27.98	27.40	27.62	27.40	27.62	27.53	27.31	27.19
-O=F	2.46	2.48	2.47	2.44	2.50	2.50	2.54	2.53	2.48	2.52	2.54	2.49	2.51	2.49	2.51	2.50	2.48	2.47
Σ	98.21	98.89	98.03	96.86	99.38	100.41	101.2	101.4	99.49	100.63	101.82	99.49	100.18	100.01	101.2	100.2	99.54	98.65
apfu[a] on the basis of number of anions																		
Ca	0.980	0.982	0.984	0.982	0.992	0.936	1.004	0.945	0.916	0.987	0.904	0.974	0.980	0.944	0.909	0.972	0.953	0.990
Mn	b.d	b.d	b.d	b.d	b.d	b.d	b.d	b.d	b.d	b.d	b.d	b.d	b.d	0.001	b.d	b.d	b.d	b.d
Fe	0.002	b.d	0.004	0.002	0.003	0.032	0.001	0.030	0.063	0.006	0.083	0.019	0.004	0.007	0.019	0.006	0.001	0.001
Sr	0.005	0.006	0.001	0.002	0.007	0.007	0.017	0.022	0.019	0.023	0.013	0.020	0.027	0.020	0.014	0.007	0.019	0.024
Ba	b.d	b.d	b.d	b.d	b.d	b.d	b.d	0.001	b.d	b.d	b.d	b.d	b.d	b.d	b.d	b.d	b.d	b.d
Σ	0.99	0.99	1.00	1.00	1.01	0.98	1.03	1.00	1.00	1.02	1.01	1.02	1.02	0.98	0.95	0.99	0.98	1.02
Y	0.035	0.029	0.050	0.059	0.037	0.019	0.023	0.014	0.021	0.015	0.017	0.015	0.009	0.009	0.011	0.010	0.019	0.016
La	0.193	0.216	0.198	0.150	0.181	0.278	0.259	0.299	0.276	0.294	0.278	0.291	0.298	0.287	0.297	0.281	0.270	0.270
Ce	0.445	0.459	0.453	0.371	0.470	0.455	0.432	0.446	0.433	0.430	0.434	0.439	0.450	0.465	0.468	0.453	0.473	0.465
Pr	0.053	0.051	0.051	0.051	0.056	0.042	0.039	0.038	0.041	0.037	0.040	0.038	0.038	0.042	0.044	0.042	0.043	0.042
Nd	0.192	0.178	0.175	0.250	0.196	0.146	0.144	0.126	0.141	0.126	0.140	0.131	0.126	0.144	0.139	0.143	0.143	0.126
Sm	0.024	0.020	0.019	0.044	0.019	0.019	0.022	0.016	0.020	0.019	0.020	0.017	0.016	0.019	0.019	0.020	0.017	0.014
Eu	0.004	0.003	0.002	0.007	0.001	0.003	0.005	0.004	0.005	0.006	0.005	0.004	0.004	0.004	0.004	0.005	0.002	0.003
Gd	0.008	0.005	0.007	0.019	0.002	0.010	0.014	0.011	0.012	0.014	0.011	0.011	0.009	0.010	0.011	0.012	0.007	0.006
Dy	0.006	0.004	0.006	0.007	0.003	0.005	0.004	0.003	0.004	0.004	0.004	0.003	0.003	0.002	0.004	0.004	0.004	0.004
Th	0.018	0.014	0.014	0.017	0.006	0.012	0.013	0.014	0.016	0.017	0.015	0.016	0.010	0.010	0.012	0.012	0.014	0.015
Σ	0.98	0.98	0.98	0.98	0.97	0.99	0.96	0.97	0.97	0.96	0.96	0.96	0.96	0.99	1.01	0.98	0.99	0.96

[a] Determined by stoichiometry, and b.d is below detection limit.

Table E-4: (Continued)

Spot	37	38	39	40	41	42	43	44	45	46	47	48	49	50	51	52	53	54
CaO	17.13	17.65	15.87	16.43	16.61	15.63	17.77	16.38	16.01	17.01	16.89	16.83	14.83	15.73	16.14	16.17	16.09	16.59
MnO	b.d	0.01	b.d	0.01	0.01	b.d	b.d	0.02	b.d	b.d	b.d	0.02	b.d	b.d	b.d	b.d	b.d	0.01
FeO	0.06	0.03	0.45	0.14	0.18	0.92	0.06	0.26	0.09	0.08	0.11	0.03	0.22	2.20	0.12	2.14	1.41	0.15
SrO	0.73	0.23	b.d	0.37	0.40	0.37	1.29	0.45	0.47	0.57	0.74	0.47	0.29	0.01	0.04	b.d	b.d	b.d
BaO	b.d	0.02	0.02	b.d	b.d	b.d	0.10	b.d	b.d	b.d	b.d	0.04	b.d	b.d	0.04	b.d	b.d	0.03
Y_2O_3	0.43	0.24	0.91	0.42	0.62	0.53	0.76	0.34	0.54	0.96	0.21	0.49	1.04	1.18	1.13	0.68	0.71	0.37
La_2O_3	13.78	12.74	12.08	14.81	14.86	14.57	14.80	14.84	14.35	14.50	16.14	14.28	13.56	9.71	11.11	10.62	10.47	10.50
Ce_2O_3	22.84	24.27	19.54	23.79	23.72	23.39	22.64	23.86	23.08	22.34	24.95	22.59	21.94	22.88	24.04	22.65	22.84	24.88
Pr_2O_3	2.22	2.61	1.84	2.23	2.22	2.20	1.91	2.28	2.27	2.05	2.05	2.18	2.12	2.84	2.67	2.56	2.70	2.95
Nd_2O_3	8.11	8.87	6.93	7.74	7.42	7.85	6.55	7.75	8.03	7.15	6.41	7.61	7.19	10.32	9.91	10.50	10.70	10.99
Sm_2O_3	1.14	1.19	1.13	1.15	1.04	1.08	0.93	1.08	1.22	1.04	0.71	1.06	1.04	1.40	1.30	1.38	1.40	1.41
Eu_2O_3	0.29	0.28	0.28	0.27	0.30	0.29	0.26	0.26	0.26	0.27	0.12	0.30	0.23	0.21	0.23	0.26	0.18	0.19
Gd_2O_3	0.69	0.48	0.71	0.68	0.63	0.56	0.53	0.60	0.61	0.66	0.21	0.65	0.69	0.56	0.54	0.49	0.53	0.33
Dy_2O_3	0.20	0.11	0.29	0.16	0.27	0.18	0.27	0.14	0.22	0.34	0.09	0.21	0.30	0.39	0.34	0.20	0.30	0.18
ThO_2	1.45	0.57	1.18	1.04	1.53	1.25	1.37	1.01	1.44	1.55	0.67	1.53	1.99	0.87	0.65	0.72	0.68	0.64
UO_2	b.d	b.d	b.d	b.d	b.d	b.d	b.d	b.d	b.d	b.d	b.d	b.d	b.d	b.d	b.d	b.d	b.d	b.d
F[a]	5.93	5.98	6.08	5.99	5.96	5.86	6.00	5.91	5.83	5.89	5.94	5.85	5.58	5.92	5.85	5.92	5.87	5.92
CO_2 [a]	27.48	27.69	28.15	27.74	27.60	27.16	27.79	27.37	26.99	27.28	27.50	27.10	25.84	27.41	27.09	27.44	27.20	27.40
-O=F	2.50	2.52	2.56	2.52	2.51	2.47	2.53	2.49	2.45	2.48	2.50	2.46	2.35	2.49	2.46	2.49	2.47	2.49
Σ	100.09	100.58	96.68	100.98	101.05	99.51	100.6	100.22	99.05	99.29	100.34	98.92	95.86	99.42	98.88	99.47	98.85	100.22
apfu[a] on the basis of number of anions																		
Ca	0.967	0.988	0.866	0.918	0.933	0.893	0.992	0.928	0.920	0.967	0.952	0.962	0.877	0.890	0.925	0.914	0.917	0.939
Mn	b.d	b.d	b.d	b.d	b.d	b.d	b.d	0.001	b.d	b.d	b.d	0.001	b.d	b.d	b.d	b.d	b.d	b.d
Fe	0.003	0.001	0.019	0.006	0.008	0.041	0.003	0.012	0.004	0.004	0.005	0.001	0.010	0.097	0.005	0.094	0.063	0.007
Sr	0.022	0.007	b.d	0.011	0.012	0.011	0.039	0.014	0.015	0.018	0.023	0.015	0.009	b.d	0.001	b.d	b.d	b.d
Ba	b.d	b.d	b.d	b.d	b.d	b.d	0.002	b.d	b.d	b.d	b.d	0.001	b.d	b.d	0.001	b.d	b.d	0.001
Σ	1.00	1.00	1.08	0.96	0.96	0.95	1.04	0.96	0.94	0.99	0.98	0.99	0.97	1.00	0.94	1.02	0.99	0.95
Y	0.012	0.007	0.025	0.012	0.017	0.015	0.021	0.010	0.015	0.027	0.006	0.014	0.031	0.033	0.032	0.019	0.020	0.010
La	0.268	0.246	0.227	0.285	0.287	0.287	0.284	0.289	0.284	0.284	0.313	0.281	0.276	0.189	0.219	0.207	0.205	0.205
Ce	0.441	0.464	0.364	0.454	0.455	0.457	0.432	0.462	0.453	0.434	0.481	0.441	0.443	0.442	0.471	0.437	0.445	0.481
Pr	0.043	0.050	0.034	0.042	0.042	0.043	0.036	0.044	0.044	0.040	0.039	0.042	0.043	0.055	0.052	0.049	0.052	0.057
Nd	0.153	0.166	0.126	0.144	0.139	0.150	0.122	0.146	0.154	0.135	0.120	0.145	0.142	0.195	0.189	0.198	0.203	0.207
Sm	0.021	0.021	0.020	0.021	0.019	0.020	0.017	0.020	0.023	0.019	0.013	0.019	0.020	0.025	0.024	0.025	0.026	0.026
Eu	0.005	0.005	0.005	0.005	0.005	0.005	0.005	0.005	0.005	0.005	0.002	0.005	0.004	0.004	0.004	0.005	0.003	0.003
Gd	0.012	0.008	0.012	0.012	0.011	0.010	0.009	0.011	0.011	0.012	0.004	0.011	0.013	0.010	0.010	0.009	0.009	0.006
Dy	0.003	0.002	0.005	0.003	0.005	0.003	0.005	0.002	0.004	0.006	0.002	0.004	0.005	0.007	0.006	0.003	0.005	0.003
Th	0.017	0.007	0.014	0.012	0.018	0.015	0.016	0.012	0.018	0.019	0.008	0.019	0.025	0.010	0.008	0.009	0.008	0.008
Σ	0.97	0.98	0.83	0.99	1.00	1.00	0.95	1.00	1.01	0.98	0.99	0.98	1.00	0.97	1.01	0.96	0.98	1.01

[a] Determined by stoichiometry, and b.d is below detection limit.

Table E-4: (Continued)

Spot	55	56	57	58	59	60	61	62	63	64	65	66	67	68	69	70	71	72
CaO	16.99	16.57	15.65	16.79	16.78	17.35	16.97	15.73	16.20	16.46	17.11	15.57	16.68	16.63	17.12	16.32	16.17	16.61
MnO	b.d	b.d	b.d	b.d	0.01	b.d	b.d	b.d	0.06	b.d	b.d	b.d	b.d	b.d	b.d	b.d	b.d	b.d
FeO	0.08	0.26	0.01	0.01	0.29	0.02	0.16	0.02	0.31	0.03	0.03	0.04	b.d	b.d	b.d	b.d	b.d	b.d
SrO	b.d	b.d	0.90	0.40	0.06	0.64	0.60	0.15	b.d	b.d	0.74	0.23	0.42	0.42	0.32	0.43	0.41	0.60
BaO	b.d	0.10	2.74	b.d	b.d	b.d	b.d	b.d	b.d	b.d	b.d	0.02	0.02	0.01	0.03	b.d	b.d	0.03
Y_2O_3	0.34	0.64	0.06	0.16	0.18	b.d	0.01	b.d	0.08	0.14	0.05	0.05	0.07	0.06	0.05	0.09	0.04	0.04
La_2O_3	10.86	10.34	10.46	10.31	10.84	11.20	11.98	11.04	10.66	11.30	10.81	11.49	17.99	17.60	17.66	17.79	17.17	18.44
Ce_2O_3	25.16	24.92	24.74	23.34	24.63	23.89	23.24	24.94	24.33	25.50	24.49	25.99	24.11	24.44	23.38	24.67	24.55	23.86
Pr_2O_3	3.00	2.96	2.71	2.75	2.84	2.61	2.43	2.78	2.81	2.77	2.75	2.80	4.24	4.32	1.87	2.04	2.21	1.97
Nd_2O_3	10.98	11.48	9.27	10.27	10.36	9.81	8.98	10.35	10.15	10.11	9.99	9.62	5.32	5.74	5.16	5.25	6.41	5.53
Sm_2O_3	1.37	1.44	0.89	1.17	1.15	1.05	0.94	1.01	1.08	1.00	0.98	0.88	0.59	0.56	0.43	0.27	0.44	0.37
Eu_2O_3	0.19	0.18	0.07	0.15	0.12	0.09	0.09	0.11	0.09	0.07	0.07	0.04	0.49	0.49	0.05	0.01	0.02	0.03
Gd_2O_3	0.29	0.46	0.06	0.23	0.22	0.09	0.11	0.07	0.21	0.08	b.d	b.d	1.88	1.87	b.d	b.d	b.d	b.d
Dy_2O_3	0.16	0.21	0.03	0.11	0.08	0.05	0.06	0.08	0.07	0.07	0.05	0.07	b.d	b.d	b.d	b.d	0.03	b.d
ThO_2	0.62	0.55	0.53	1.27	0.76	0.73	0.70	0.55	0.47	0.45	0.53	0.25	0.07	0.08	0.12	0.03	0.12	0.11
UO_2	b.d	b.d	b.d	b.d	b.d	b.d	b.d	b.d	b.d	b.d	b.d	b.d	b.d	b.d	b.d	b.d	b.d	b.d
F[a]	6.00	6.00	5.75	5.76	5.87	5.84	5.73	5.69	5.75	5.82	5.85	5.70	6.09	6.11	5.74	5.74	5.77	5.81
CO_2 [a]	27.79	27.79	26.66	26.68	27.20	27.06	26.53	26.37	26.62	26.95	27.08	26.42	28.23	28.30	26.60	26.58	26.73	26.90
-O=F	2.53	2.53	2.42	2.42	2.47	2.46	2.41	2.40	2.42	2.45	2.46	2.40	2.57	2.57	2.42	2.42	2.43	2.44
Σ	101.45	101.59	98.56	97.12	99.14	98.11	96.22	96.74	97.01	98.40	98.31	96.95	103.84	104.22	97.35	96.88	97.80	97.98
apfu[a] on the basis of number of anions																		
Ca	0.948	0.925	0.912	0.976	0.957	0.995	0.992	0.924	0.940	0.948	0.979	0.914	0.915	0.910	0.980	0.952	0.937	0.957
Mn	b.d	b.d	b.d	b.d	b.d	b.d	b.d	b.d	0.003	b.d	b.d	b.d	b.d	b.d	b.d	b.d	b.d	b.d
Fe	0.003	0.011	b.d	b.d	0.013	0.001	0.007	0.001	0.014	0.001	0.001	0.002	b.d	b.d	b.d	b.d	b.d	b.d
Sr	b.d	b.d	0.028	0.013	0.002	0.020	0.019	0.005	b.d	b.d	0.023	0.007	0.012	0.012	0.010	0.014	0.013	0.019
Ba	b.d	0.002	0.058	b.d	b.d	b.d	b.d	b.d	b.d	b.d	b.d	b.d	b.d	b.d	0.001	b.d	b.d	0.001
Σ	0.96	0.95	1.03	1.00	0.98	1.02	1.02	0.94	0.98	0.95	1.02	0.93	0.94	0.93	1.05	0.97	0.96	0.98
Y	0.009	0.018	0.002	0.005	0.005	b.d	b.d	b.d	0.002	0.004	0.001	0.001	0.002	0.002	0.001	0.003	0.001	0.001
La	0.209	0.199	0.210	0.206	0.213	0.221	0.241	0.223	0.213	0.224	0.213	0.232	0.340	0.332	0.348	0.357	0.343	0.366
Ce	0.480	0.475	0.492	0.464	0.480	0.468	0.464	0.501	0.483	0.502	0.479	0.521	0.452	0.457	0.457	0.492	0.486	0.470
Pr	0.057	0.056	0.054	0.054	0.055	0.051	0.048	0.056	0.055	0.054	0.054	0.056	0.079	0.080	0.036	0.040	0.044	0.039
Nd	0.204	0.214	0.180	0.199	0.197	0.187	0.175	0.203	0.196	0.194	0.191	0.188	0.097	0.105	0.098	0.102	0.124	0.106
Sm	0.025	0.026	0.017	0.022	0.021	0.019	0.018	0.019	0.020	0.019	0.018	0.017	0.010	0.010	0.008	0.005	0.008	0.007
Eu	0.003	0.003	0.001	0.003	0.002	0.002	0.002	0.002	0.002	0.001	0.001	0.001	0.009	0.009	0.001	b.d	b.d	0.001
Gd	0.005	0.008	0.001	0.004	0.004	0.002	0.002	0.001	0.004	0.001	b.d	b.d	0.032	0.032	b.d	b.d	b.d	b.d
Dy	0.003	0.004	0.001	0.002	0.001	0.001	0.001	0.001	0.001	0.001	0.001	0.001	b.d	b.d	b.d	b.d	0.001	b.d
Th	0.007	0.007	0.007	0.016	0.009	0.009	0.009	0.007	0.006	0.006	0.006	0.003	0.001	0.001	0.001	b.d	0.001	0.001
Σ	1.00	1.01	0.96	0.97	0.99	0.96	0.96	1.01	0.98	1.01	0.96	1.02	1.02	1.03	0.95	1.00	1.01	0.99

[a] Determined by stoichiometry, and b.d is below detection limit.

Table E-4: (Continued)

Spot	73	74	75	76	77	78	79	80	81	82	83	84	85	86	87	88	89	90
CaO	16.32	16.42	16.57	16.31	16.39	15.84	16.45	16.69	14.33	16.04	15.32	15.69	15.53	15.86	15.23	15.46	14.81	14.79
MnO	b.d	b.d	b.d	b.d	b.d	b.d	b.d	b.d	b.d	b.d	b.d	b.d	b.d	b.d	b.d	0.01	b.d	0.01
FeO	0.02	b.d	b.d	0.03	0.02	0.09	b.d	0.01	0.03	b.d	0.50	0.20	0.10	0.50	0.14	0.76	0.90	0.33
SrO	0.54	0.58	0.61	0.57	0.56	0.56	0.52	0.50	0.35	0.61	0.17	0.21	0.18	0.17	0.19	0.12	0.18	0.18
BaO	b.d	b.d	b.d	0.02	b.d	b.d	0.02	b.d	0.04	b.d	0.06	b.d	0.02	b.d	b.d	b.d	0.01	0.18
Y_2O_3	b.d	b.d	b.d	0.04	0.01	b.d	0.16	0.37	0.12	b.d	0.17	0.20	0.26	0.30	0.24	0.24	0.27	0.25
La_2O_3	17.48	18.19	18.23	18.89	18.36	17.30	17.56	17.50	18.18	17.34	16.74	16.66	16.43	16.37	14.30	12.64	12.72	13.79
Ce_2O_3	25.42	25.01	25.11	24.28	24.84	22.34	24.56	24.06	25.76	24.86	24.01	23.89	24.05	23.72	25.36	24.24	24.30	24.47
Pr_2O_3	2.12	2.07	1.75	1.91	1.94	1.79	2.10	1.90	2.00	1.93	1.99	1.99	2.17	2.05	2.44	2.46	2.31	2.20
Nd_2O_3	5.69	5.18	5.12	5.11	5.13	5.27	5.62	5.53	5.96	5.64	6.31	6.44	6.71	6.54	7.98	8.06	7.85	7.66
Sm_2O_3	0.21	0.17	0.22	0.27	0.27	0.30	0.30	0.35	0.31	0.34	0.57	0.62	0.59	0.60	0.81	0.80	0.76	0.83
Eu_2O_3	b.d	b.d	0.04	0.03	0.06	0.01	b.d	0.04	b.d	b.d	0.16	0.15	0.06	0.12	0.07	0.06	0.09	0.15
Gd_2O_3	b.d	b.d	b.d	b.d	b.d	b.d	b.d	b.d	b.d	b.d	b.d	b.d	0.05	0.04	0.16	0.19	0.17	0.12
Dy_2O_3	b.d	b.d	b.d	0.02	b.d	b.d	0.02	0.04	b.d	b.d	0.08	0.09	0.09	0.11	0.10	0.07	0.08	0.09
ThO_2	0.03	0.06	0.05	0.09	0.04	0.07	0.05	0.11	0.07	0.02	0.42	0.49	0.27	0.29	0.45	0.83	0.92	0.72
UO_2	b.d	b.d	b.d	b.d	b.d	b.d	b.d	b.d	b.d	b.d	b.d	b.d	b.d	b.d	b.d	b.d	b.d	b.d
F[a]	5.81	5.80	5.81	5.78	5.79	5.47	5.78	5.79	5.64	5.71	5.67	5.69	5.67	5.72	5.72	5.65	5.57	5.58
CO_2 [a]	26.90	26.87	26.91	26.78	26.83	25.36	26.78	26.80	26.11	26.45	26.28	26.36	26.27	26.49	26.49	26.16	25.80	25.86
-O=F	2.45	2.44	2.45	2.43	2.44	2.31	2.43	2.44	2.37	2.40	2.39	2.40	2.39	2.41	2.41	2.38	2.35	2.35
Σ	98.24	98.03	98.09	97.78	97.93	92.18	97.60	97.38	96.70	96.65	96.23	96.52	96.18	96.62	97.42	95.62	94.65	95.25
apfu[a] on the basis of number of anions																		
Ca	0.941	0.947	0.955	0.945	0.947	0.969	0.952	0.965	0.851	0.940	0.904	0.922	0.917	0.928	0.892	0.916	0.889	0.885
Mn	b.d	b.d	b.d	b.d	b.d	b.d	b.d	b.d	b.d	b.d	b.d	b.d	b.d	b.d	b.d	b.d	b.d	b.d
Fe	0.001	b.d	b.d	0.001	0.001	0.004	b.d	b.d	0.001	b.d	0.023	0.009	0.005	0.023	0.006	0.035	0.042	0.015
Sr	0.017	0.018	0.019	0.018	0.018	0.019	0.016	0.016	0.011	0.019	0.005	0.007	0.006	0.005	0.006	0.004	0.006	0.006
Ba	b.d	b.d	b.d	b.d	b.d	b.d	b.d	b.d	0.001	b.d	0.001	b.d	b.d	b.d	b.d	b.d	b.d	0.004
Σ	0.97	0.97	0.98	0.97	0.97	1.00	0.97	0.99	0.87	0.97	0.94	0.95	0.93	0.96	0.91	0.97	0.95	0.93
Y	b.d	b.d	b.d	0.001	b.d	b.d	0.005	0.011	0.004	b.d	0.005	0.006	0.008	0.009	0.007	0.007	0.008	0.007
La	0.347	0.361	0.362	0.377	0.365	0.364	0.350	0.348	0.372	0.350	0.340	0.337	0.334	0.330	0.288	0.258	0.263	0.284
Ce	0.501	0.493	0.494	0.481	0.490	0.467	0.486	0.476	0.523	0.498	0.484	0.480	0.485	0.474	0.507	0.491	0.499	0.500
Pr	0.042	0.041	0.034	0.038	0.038	0.037	0.041	0.037	0.040	0.038	0.040	0.040	0.044	0.041	0.049	0.050	0.047	0.045
Nd	0.109	0.100	0.098	0.099	0.099	0.107	0.108	0.107	0.118	0.110	0.124	0.126	0.132	0.128	0.156	0.159	0.157	0.153
Sm	0.004	0.003	0.004	0.005	0.005	0.006	0.006	0.007	0.006	0.006	0.011	0.012	0.011	0.011	0.015	0.015	0.015	0.016
Eu	b.d	b.d	0.001	0.001	0.001	b.d	b.d	0.001	b.d	b.d	0.003	0.003	0.001	0.002	0.001	0.001	0.002	0.003
Gd	b.d	b.d	b.d	b.d	b.d	b.d	b.d	b.d	b.d	b.d	b.d	b.d	0.001	0.001	0.003	0.003	0.003	0.002
Dy	b.d	b.d	b.d	b.d	b.d	b.d	b.d	0.001	b.d	b.d	0.001	0.002	0.002	0.002	0.002	0.001	0.001	0.002
Th	b.d	0.001	0.001	0.001	b.d	0.001	0.001	0.001	0.001	b.d	0.005	0.006	0.003	0.004	0.006	0.010	0.012	0.009
Σ	1.00	1.00	0.99	1.00	1.00	0.98	1.00	0.99	1.06	1.00	1.01	1.01	1.02	1.00	1.03	1.00	1.01	1.02

[a] Determined by stoichiometry, and b.d is below detection limit.

Table E-4: (Continued)

Spot	91	92	93	94	95	96	97	98	99	100	101	102	103	104	105	106	107	108
CaO	16.30	16.35	16.11	15.67	16.75	16.72	14.72	16.46	16.63	14.91	15.40	15.77	16.41	15.84	15.22	15.91	15.52	16.20
MnO	0.02	0.05	0.04	0.03	0.05	b.d	b.d	b.d	b.d	b.d	b.d	b.d	0.01	0.02	b.d	b.d	0.04	0.04
FeO	0.14	0.09	0.17	0.37	0.61	b.d	b.d	b.d	0.01	0.11	0.04	0.02	0.02	0.20	1.00	0.08	0.34	0.54
SrO	0.23	0.34	0.37	0.12	0.69	0.57	0.39	0.54	0.26	0.01	0.14	0.42	0.21	0.38	0.52	0.74	0.31	0.51
BaO	0.01	0.11	0.07	0.01	0.03	b.d	b.d	0.05	0.06	b.d	0.06	0.08	b.d	0.11	b.d	0.08	0.12	0.02
Y_2O_3	0.14	0.20	b.d	0.26	0.01	0.43	0.41	0.11	0.40	0.28	0.24	0.20	0.54	0.17	0.31	0.14	0.24	0.21
La_2O_3	12.51	12.74	13.90	12.70	14.52	19.29	19.54	17.77	15.70	16.00	15.84	12.85	14.86	15.56	16.21	17.39	14.57	16.04
Ce_2O_3	25.52	25.75	25.79	25.07	25.53	25.59	27.59	25.25	23.97	27.30	26.52	28.05	25.69	28.62	25.89	26.70	24.95	24.48
Pr_2O_3	2.75	2.61	2.61	2.82	2.34	1.96	2.21	2.19	2.38	2.78	2.34	2.60	2.47	2.03	2.39	2.29	2.57	2.27
Nd_2O_3	9.32	9.45	8.53	10.00	7.74	4.51	5.49	6.36	7.85	7.99	7.45	8.28	7.55	6.12	6.71	6.64	8.82	7.10
Sm_2O_3	1.01	0.94	0.81	1.16	0.69	0.17	0.31	0.43	0.70	0.60	0.53	0.70	0.63	0.44	0.49	0.51	0.79	0.58
Eu_2O_3	0.07	0.14	0.04	0.15	0.12	b.d	0.04	0.05	0.08	b.d	0.04	0.01	0.10	0.04	0.06	0.03	0.09	0.04
Gd_2O_3	0.08	0.19	0.05	0.36	0.02	b.d	b.d	b.d	b.d	b.d	b.d	0.05	b.d	b.d	b.d	b.d	0.07	b.d
Dy_2O_3	0.08	0.04	0.01	0.15	0.01	0.08	0.07	0.03	0.17	0.08	0.06	0.04	0.11	0.07	0.07	0.04	0.04	0.05
ThO_2	0.72	0.70	0.40	0.62	0.27	0.22	0.42	0.30	1.55	0.68	0.70	1.60	1.01	0.92	0.57	0.95	1.42	1.72
UO_2	b.d	b.d	b.d	b.d	b.d	b.d	b.d	b.d	b.d	b.d	b.d	b.d	b.d	b.d	b.d	b.d	b.d	b.d
F[a]	5.86	5.93	5.87	5.89	5.96	5.96	5.95	5.93	5.94	5.92	5.85	6.00	5.94	5.99	5.88	6.03	5.91	5.94
CO_2 [a]	27.16	27.47	27.19	27.28	27.59	27.60	27.56	27.48	27.53	27.42	27.11	27.80	27.51	27.73	27.26	27.94	27.38	27.53
-O=F	2.47	2.50	2.47	2.48	2.51	2.51	2.51	2.50	2.50	2.49	2.46	2.53	2.50	2.52	2.48	2.54	2.49	2.50
Σ	99.59	100.80	99.66	100.41	100.54	100.67	102.40	100.56	100.87	101.77	100.15	102.45	100.75	102.05	100.29	103.13	101.01	100.95
apfu[a] on the basis of number of anions																		
Ca	0.930	0.922	0.919	0.890	0.941	0.940	0.828	0.929	0.936	0.843	0.879	0.877	0.925	0.884	0.865	0.883	0.878	0.912
Mn	0.001	0.002	0.002	0.001	0.002	b.d	b.d	b.d	b.d	b.d	b.d	b.d	b.d	0.001	b.d	b.d	0.002	0.002
Fe	0.006	0.004	0.008	0.016	0.027	b.d	b.d	b.d	b.d	0.005	0.002	0.001	0.001	0.009	0.044	0.003	0.015	0.024
Sr	0.007	0.010	0.011	0.004	0.021	0.017	0.012	0.016	0.008	b.d	0.004	0.013	0.006	0.011	0.016	0.022	0.009	0.016
Ba	b.d	0.002	0.001	b.d	0.001	b.d	b.d	0.001	0.001	b.d	0.001	0.002	b.d	0.002	b.d	0.002	0.002	b.d
Σ	0.95	0.95	0.95	0.92	1.00	0.96	0.85	0.95	0.95	0.86	0.90	0.92	0.94	0.92	0.94	0.92	0.92	0.96
Y	0.004	0.006	b.d	0.007	b.d	0.012	0.011	0.003	0.011	0.008	0.007	0.006	0.015	0.005	0.009	0.004	0.007	0.006
La	0.246	0.247	0.273	0.248	0.281	0.373	0.378	0.345	0.304	0.311	0.311	0.246	0.288	0.299	0.317	0.332	0.284	0.311
Ce	0.498	0.496	0.503	0.487	0.490	0.491	0.530	0.487	0.461	0.527	0.517	0.533	0.495	0.546	0.503	0.506	0.482	0.471
Pr	0.053	0.050	0.051	0.054	0.045	0.037	0.042	0.042	0.046	0.053	0.045	0.049	0.047	0.039	0.046	0.043	0.049	0.043
Nd	0.177	0.178	0.162	0.189	0.145	0.084	0.103	0.120	0.147	0.151	0.142	0.154	0.142	0.114	0.127	0.123	0.166	0.133
Sm	0.019	0.017	0.015	0.021	0.012	0.003	0.006	0.008	0.013	0.011	0.010	0.013	0.011	0.008	0.009	0.009	0.014	0.011
Eu	0.001	0.003	0.001	0.003	0.002	b.d	0.001	0.001	0.001	b.d	0.001	b.d	0.002	0.001	0.001	0.001	0.002	0.001
Gd	0.001	0.003	0.001	0.006	b.d	b.d	b.d	b.d	b.d	b.d	b.d	0.001	b.d	b.d	b.d	b.d	0.001	b.d
Dy	0.001	0.001	b.d	0.003	b.d	0.001	0.001	0.001	0.003	0.001	0.001	0.001	0.002	0.001	0.001	0.001	0.001	0.001
Th	0.009	0.008	0.005	0.007	0.003	0.003	0.005	0.004	0.019	0.008	0.008	0.019	0.012	0.011	0.007	0.011	0.017	0.021
Σ	1.01	1.01	1.01	1.03	0.98	1.01	1.08	1.01	1.01	1.07	1.04	1.02	1.01	1.02	1.02	1.03	1.02	1.00

[a] Determined by stoichiometry, and b.d is below detection limit.

Table E-4: (Continued)

Spot	109	110	111	112	113	114	115	116	117	118	119	120	121	122	123	124	125	126
CaO	16.14	16.16	16.29	14.57	15.17	16.09	15.54	16.43	17.20	15.78	16.22	16.93	16.00	15.73	14.83	15.52	16.63	15.96
MnO	b.d	b.d	b.d	b.d	b.d	b.d	b.d	0.01	0.06	0.02	0.01	b.d	b.d	b.d	b.d	b.d	b.d	b.d
FeO	0.01	1.31	0.04	0.10	0.53	1.13	1.91	1.88	1.60	2.26	2.29	b.d	0.01	b.d	0.04	0.03	b.d	b.d
SrO	0.80	0.44	0.51	0.85	2.52	0.26	0.21	0.06	0.07	0.05	0.04	0.38	0.43	0.43	0.33	0.40	0.39	0.40
BaO	b.d	0.03	0.02	b.d	b.d	0.01	b.d	b.d	b.d	0.01	0.03	0.08	0.08	0.77	0.04	0.04	b.d	0.02
Y_2O_3	1.44	0.59	0.54	0.56	1.34	0.75	0.77	1.09	1.08	0.98	1.00	b.d	0.03	0.03	0.04	0.02	0.58	0.69
La_2O_3	11.96	10.76	11.66	11.34	11.45	10.83	11.38	10.11	10.55	11.05	10.76	20.18	20.62	19.78	20.56	20.37	20.02	20.62
Ce_2O_3	25.71	24.75	26.08	27.52	23.60	26.15	25.66	24.04	24.47	25.25	25.03	24.97	25.57	25.89	27.02	26.95	24.68	25.40
Pr_2O_3	2.73	2.75	2.60	2.85	2.52	2.90	2.73	2.61	2.60	2.59	2.72	1.74	1.90	2.11	2.05	2.17	2.15	2.11
Nd_2O_3	8.57	8.95	8.40	9.41	8.60	9.43	8.75	8.66	8.68	8.93	8.99	4.23	4.64	4.90	5.13	5.09	4.87	5.03
Sm_2O_3	0.81	0.87	0.77	0.92	1.30	0.74	0.76	0.90	0.91	0.88	0.90	0.16	0.26	0.15	0.24	0.23	0.28	0.28
Eu_2O_3	0.10	0.19	0.13	0.07	0.23	0.02	0.10	0.10	0.13	0.13	0.09	0.03	b.d	b.d	0.06	0.02	0.02	0.06
Gd_2O_3	0.13	0.14	0.15	0.08	0.54	0.06	0.13	0.26	0.29	0.26	0.25	b.d	b.d	b.d	b.d	b.d	b.d	b.d
Dy_2O_3	0.29	0.15	0.13	0.11	0.33	0.12	0.16	0.24	0.18	0.22	0.24	0.05	b.d	b.d	b.d	0.03	0.08	0.11
ThO_2	2.02	1.64	1.62	2.03	2.82	1.08	1.20	1.11	1.13	1.06	1.10	0.47	0.47	0.33	0.65	0.26	0.26	0.37
UO_2	b.d	b.d	b.d	b.d	b.d	b.d	b.d	b.d	b.d	b.d	b.d	b.d	b.d	b.d	b.d	b.d	b.d	b.d
F[a]	6.01	5.91	5.87	5.87	5.98	5.97	5.95	5.88	6.03	5.99	6.04	5.93	5.93	5.90	5.91	5.98	5.98	6.01
CO_2 [a]	27.84	27.36	27.17	27.18	27.69	27.67	27.57	27.25	27.91	27.76	27.97	27.46	27.47	27.35	27.40	27.68	27.72	27.84
-O=F	2.53	2.49	2.47	2.47	2.52	2.51	2.51	2.48	2.54	2.52	2.54	2.50	2.50	2.49	2.49	2.52	2.52	2.53
Σ	102.16	99.73	99.68	101.16	102.27	101.04	100.53	98.37	100.58	100.90	101.39	100.18	101.10	100.98	101.93	102.40	101.25	102.40
apfu[a] on the basis of number of anions																		
Ca	0.899	0.916	0.929	0.831	0.850	0.901	0.874	0.935	0.955	0.882	0.899	0.956	0.902	0.892	0.839	0.869	0.930	0.890
Mn	b.d	b.d	b.d	b.d	b.d	b.d	b.d	b.d	0.003	0.001	b.d	b.d	b.d	b.d	b.d	b.d	b.d	b.d
Fe	b.d	0.058	0.002	0.004	0.023	0.049	0.084	0.084	0.069	0.099	0.099	b.d	b.d	b.d	0.002	0.001	b.d	b.d
Sr	0.024	0.013	0.016	0.026	0.076	0.008	0.006	0.002	0.002	0.002	0.001	0.012	0.013	0.013	0.010	0.012	0.012	0.012
Ba	b.d	0.001	b.d	b.d	b.d	b.d	b.d	b.d	b.d	b.d	0.001	0.002	0.002	0.016	0.001	0.001	b.d	b.d
Σ	0.93	1.00	0.95	0.87	0.96	0.97	0.98	1.03	1.04	0.99	1.01	0.97	0.93	0.93	0.86	0.89	0.95	0.90
Y	0.040	0.017	0.015	0.016	0.037	0.021	0.022	0.031	0.030	0.027	0.028	b.d	0.001	0.001	0.001	0.001	0.016	0.019
La	0.229	0.210	0.229	0.223	0.221	0.209	0.220	0.198	0.202	0.213	0.205	0.392	0.400	0.386	0.400	0.393	0.386	0.396
Ce	0.490	0.479	0.508	0.537	0.452	0.500	0.493	0.467	0.464	0.482	0.474	0.482	0.493	0.502	0.522	0.516	0.472	0.484
Pr	0.052	0.053	0.050	0.055	0.048	0.055	0.052	0.051	0.049	0.049	0.051	0.033	0.036	0.041	0.039	0.041	0.041	0.040
Nd	0.159	0.169	0.160	0.179	0.161	0.176	0.164	0.164	0.161	0.166	0.166	0.080	0.087	0.093	0.097	0.095	0.091	0.093
Sm	0.015	0.016	0.014	0.017	0.023	0.013	0.014	0.016	0.016	0.016	0.016	0.003	0.005	0.003	0.004	0.004	0.005	0.005
Eu	0.002	0.003	0.002	0.001	0.004	b.d	0.002	0.002	0.002	0.002	0.002	0.001	b.d	b.d	0.001	b.d	b.d	0.001
Gd	0.002	0.002	0.003	0.001	0.009	0.001	0.002	0.005	0.005	0.004	0.004	b.d	b.d	b.d	b.d	b.d	b.d	b.d
Dy	0.005	0.003	0.002	0.002	0.006	0.002	0.003	0.004	0.003	0.004	0.004	0.001	b.d	b.d	b.d	0.001	0.001	0.002
Th	0.024	0.020	0.020	0.025	0.034	0.013	0.014	0.013	0.013	0.013	0.013	0.006	0.006	0.004	0.008	0.003	0.003	0.004
Σ	1.02	0.97	1.00	1.06	0.99	0.99	0.99	0.95	0.95	0.98	0.96	1.00	1.03	1.03	1.07	1.05	1.02	1.04

[a] Determined by stoichiometry, and b.d is below detection limit.

Table E-4: (Continued)

Spot	127	128	129	130	131	132	133	134	135	136	137	138	139	140	141	142	143	144
CaO	16.80	16.22	16.66	16.90	17.29	16.24	16.55	16.81	17.07	16.61	17.15	16.49	16.35	16.85	16.74	17.01	16.84	17.38
MnO	b.d	b.d	0.02	0.01	0.01	b.d	0.02	b.d	b.d	b.d	0.01	0.01	b.d	0.01	b.d	0.02	b.d	0.01
FeO	0.01	0.13	0.35	0.12	0.04	0.01	0.05	0.01	0.07	0.62	0.01	0.21	0.11	0.07	0.05	0.03	0.27	0.10
SrO	0.57	0.13	0.09	0.12	0.29	0.14	0.34	0.58	0.15	0.13	b.d	0.15	0.37	0.05	0.64	0.53	0.51	0.68
BaO	0.33	0.05	b.d	0.04	0.02	0.17	0.07	0.03	0.25	b.d	b.d	b.d	b.d	b.d	b.d	0.02	b.d	b.d
Y_2O_3	0.24	1.71	1.81	1.91	0.38	0.54	0.70	0.05	0.56	0.46	0.34	0.50	0.60	0.37	0.11	1.28	0.28	0.83
La_2O_3	19.52	11.83	10.95	11.75	11.35	14.11	12.94	14.79	14.15	11.74	11.75	12.11	12.42	11.95	11.80	10.03	11.42	10.52
Ce_2O_3	25.33	25.89	23.99	25.30	24.02	26.88	24.57	25.63	25.97	24.45	24.70	25.05	25.25	26.04	26.32	23.20	25.74	24.15
Pr_2O_3	2.01	2.58	2.45	2.53	3.03	2.68	2.23	2.31	2.47	2.73	2.76	2.65	2.75	2.75	2.73	2.72	2.79	2.53
Nd_2O_3	4.86	8.07	8.00	8.19	12.02	8.87	7.58	7.62	8.08	9.42	9.54	9.43	8.99	8.80	8.87	10.28	9.90	9.47
Sm_2O_3	0.22	0.70	0.87	0.80	1.38	0.73	0.62	0.58	0.75	1.15	1.23	1.08	0.95	0.86	0.75	1.35	0.93	1.29
Eu_2O_3	0.04	0.11	0.13	0.06	0.10	0.04	0.06	0.04	0.11	0.08	0.21	0.17	0.10	0.08	0.08	0.19	0.08	0.23
Gd_2O_3	b.d	0.29	0.47	0.32	0.32	0.12	0.12	b.d	b.d	0.26	0.35	0.22	0.13	b.d	b.d	0.27	0.05	0.57
Dy_2O_3	0.06	0.38	0.45	0.39	0.09	0.17	0.12	0.03	0.15	0.22	0.18	0.14	0.12	0.09	0.04	0.21	0.05	0.28
ThO_2	0.32	0.41	0.72	0.66	0.82	0.25	0.11	0.16	0.10	0.64	0.74	0.62	0.56	0.45	0.44	1.34	0.59	0.67
UO_2	b.d	b.d	b.d	b.d	b.d	b.d	b.d	b.d	b.d	b.d	b.d	b.d	b.d	b.d	b.d	b.d	b.d	b.d
F[a]	6.01	5.90	5.92	5.98	6.10	6.02	5.73	5.89	6.00	5.90	5.93	5.90	5.88	5.88	5.88	5.92	5.97	5.95
CO_2 [a]	27.83	27.32	27.41	27.71	28.26	27.89	26.54	27.28	27.80	27.32	27.46	27.35	27.24	27.23	27.23	27.42	27.64	27.55
-O=F	2.53	2.48	2.49	2.52	2.57	2.54	2.41	2.48	2.53	2.48	2.50	2.49	2.48	2.48	2.47	2.49	2.51	2.50
Σ	101.74	99.43	98.44	100.47	103.13	102.50	96.19	99.47	101.28	99.40	99.96	99.78	99.45	99.13	99.33	99.47	100.74	99.84
apfu[a] on the basis of number of anions																		
Ca	0.936	0.921	0.941	0.946	0.949	0.903	0.966	0.955	0.952	0.943	0.969	0.935	0.932	0.960	0.954	0.963	0.945	0.979
Mn	b.d	b.d	0.001	b.d	b.d	b.d	0.001	b.d	b.d	b.d	b.d	b.d	b.d	b.d	b.d	0.001	b.d	b.d
Fe	b.d	0.006	0.015	0.005	0.002	b.d	0.002	b.d	0.003	0.027	b.d	0.009	0.005	0.003	0.002	0.001	0.012	0.004
Sr	0.017	0.004	0.003	0.004	0.009	0.004	0.011	0.018	0.005	0.004	b.d	0.005	0.011	0.002	0.020	0.016	0.015	0.021
Ba	0.007	0.001	b.d	0.001	b.d	0.003	0.001	0.001	0.005	b.d	b.d	b.d	b.d	b.d	b.d	b.d	b.d	b.d
Σ	0.97	0.94	0.99	0.96	0.97	0.92	0.99	0.98	0.97	0.98	0.98	0.96	0.95	0.97	0.98	0.99	0.98	1.01
Y	0.007	0.048	0.051	0.053	0.010	0.015	0.020	0.001	0.016	0.013	0.010	0.014	0.017	0.010	0.003	0.036	0.008	0.023
La	0.374	0.231	0.213	0.226	0.214	0.270	0.260	0.289	0.272	0.229	0.229	0.236	0.244	0.234	0.231	0.195	0.221	0.204
Ce	0.482	0.502	0.463	0.484	0.451	0.511	0.490	0.498	0.495	0.474	0.477	0.485	0.492	0.507	0.512	0.449	0.493	0.465
Pr	0.038	0.050	0.047	0.048	0.057	0.051	0.044	0.045	0.047	0.053	0.053	0.051	0.053	0.053	0.053	0.052	0.053	0.048
Nd	0.090	0.153	0.151	0.153	0.220	0.164	0.147	0.144	0.150	0.178	0.180	0.178	0.171	0.167	0.168	0.194	0.185	0.178
Sm	0.004	0.013	0.016	0.014	0.024	0.013	0.012	0.011	0.013	0.021	0.022	0.020	0.017	0.016	0.014	0.025	0.017	0.023
Eu	0.001	0.002	0.002	0.001	0.002	0.001	0.001	0.001	0.002	0.001	0.004	0.003	0.002	0.001	0.001	0.003	0.001	0.004
Gd	b.d	0.005	0.008	0.006	0.005	0.002	0.002	b.d	b.d	0.005	0.006	0.004	0.002	b.d	b.d	0.005	0.001	0.010
Dy	0.001	0.006	0.008	0.007	0.001	0.003	0.002	0.001	0.003	0.004	0.003	0.002	0.002	0.002	0.001	0.004	0.001	0.005
Th	0.004	0.005	0.009	0.008	0.010	0.003	0.001	0.002	0.001	0.008	0.009	0.007	0.007	0.005	0.005	0.016	0.007	0.008
Σ	1.00	1.02	0.97	1.00	0.99	1.03	0.98	0.99	1.00	0.99	0.99	1.00	1.01	1.00	0.99	0.98	0.99	0.97

[a] Determined by stoichiometry, and b.d is below detection limit.

Table E-4: (Continued)

Spot	145	146	147	148	149	150	151	152	153	154	155	156	157	158	159	160	161	162
CaO	16.67	17.15	17.08	16.24	17.32	16.87	16.09	16.69	17.27	15.38	16.65	15.76	16.11	15.32	15.73	15.13	17.11	16.86
MnO	0.03	0.02	b.d	0.03	b.d	0.02	0.09	0.04	0.01	0.01	b.d	0.01	0.03	0.05	0.02	0.04	b.d	b.d
FeO	0.17	0.25	0.10	0.14	0.11	0.19	1.38	0.91	0.25	1.47	0.15	0.16	0.33	1.89	0.19	1.76	0.26	0.19
SrO	b.d	b.d	0.02	0.06	b.d	b.d	0.09	0.03	0.16	0.03	b.d	b.d	b.d	0.03	b.d	b.d	0.07	0.03
BaO	b.d	0.04	b.d	b.d	0.03	0.04	0.03	b.d	0.03	0.03	b.d	0.05	b.d	0.14	0.10	0.03	b.d	b.d
Y_2O_3	0.83	0.93	0.77	0.83	0.72	0.87	0.76	0.90	0.88	0.62	0.94	0.69	0.78	0.67	0.81	0.89	0.35	0.30
La_2O_3	11.39	9.22	9.64	8.73	9.97	9.84	8.92	10.02	10.73	10.54	9.37	9.40	8.98	9.52	9.39	8.06	13.76	14.36
Ce_2O_3	25.30	23.58	23.82	22.96	24.46	24.29	22.58	24.03	24.21	25.22	24.01	23.79	23.90	25.68	23.53	22.91	25.03	25.29
Pr_2O_3	2.71	2.80	2.75	2.66	2.71	2.82	2.62	2.68	2.65	2.82	2.89	2.90	2.90	2.62	2.85	2.46	2.38	2.52
Nd_2O_3	9.80	11.31	10.63	10.59	10.68	10.92	10.53	10.20	9.74	10.30	11.69	11.21	11.46	10.43	11.03	9.69	8.24	8.02
Sm_2O_3	1.01	1.70	1.70	1.52	1.62	1.68	1.57	1.40	1.32	1.40	1.78	1.61	1.63	1.42	1.57	1.49	1.12	1.04
Eu_2O_3	0.08	0.28	0.26	0.16	0.26	0.22	0.26	0.19	0.15	0.19	0.27	0.19	0.19	0.19	0.22	0.25	0.22	0.15
Gd_2O_3	0.15	0.60	0.62	0.50	0.63	0.74	0.77	0.59	0.37	0.37	0.61	0.64	0.63	0.50	0.59	0.76	0.36	0.31
Dy_2O_3	0.16	0.29	0.25	0.24	0.21	0.26	0.18	0.23	0.20	0.16	0.28	0.22	0.20	0.21	0.24	0.26	0.12	0.13
ThO_2	0.58	1.17	0.95	0.94	0.80	1.03	0.98	0.86	1.56	0.60	0.85	0.57	0.78	0.85	0.57	1.18	1.78	1.13
UO_2	b.d	b.d	b.d	b.d	b.d	b.d	b.d	b.d	b.d	b.d	b.d	b.d	b.d	b.d	b.d	b.d	b.d	b.d
F[a]	5.92	5.97	5.91	5.68	5.99	5.98	5.79	5.94	5.99	5.89	5.95	5.73	5.81	5.95	5.85	5.94	6.05	6.01
CO_2 [a]	27.42	27.67	27.39	26.32	27.75	27.71	26.81	27.53	27.73	27.29	27.55	26.53	26.90	27.55	27.10	27.53	28.05	27.84
-O=F	2.49	2.51	2.49	2.39	2.52	2.52	2.44	2.50	2.52	2.48	2.50	2.41	2.44	2.50	2.46	2.50	2.55	2.53
Σ	99.87	100.61	99.56	95.55	100.86	101.13	97.34	100.02	100.86	100.09	100.64	97.17	98.30	100.79	98.71	98.29	102.49	101.80
apfu[a] on the basis of number of anions																		
Ca	0.943	0.962	0.967	0.956	0.969	0.944	0.929	0.939	0.966	0.873	0.938	0.922	0.929	0.862	0.892	0.843	0.946	0.939
Mn	0.001	0.001	b.d	0.001	b.d	0.001	0.004	0.002	b.d	b.d	b.d	b.d	0.001	0.002	0.001	0.002	b.d	b.d
Fe	0.008	0.011	0.004	0.006	0.005	0.008	0.062	0.040	0.011	0.065	0.007	0.007	0.015	0.083	0.008	0.077	0.011	0.008
Sr	b.d	b.d	0.001	0.002	b.d	b.d	0.003	0.001	0.005	0.001	b.d	b.d	b.d	0.001	b.d	b.d	0.002	0.001
Ba	b.d	0.001	b.d	b.d	0.001	0.001	0.001	b.d	0.001	0.001	b.d	0.001	b.d	0.003	0.002	0.001	b.d	b.d
Σ	0.96	0.98	0.98	0.98	0.98	0.96	1.02	1.00	0.99	0.95	0.95	0.94	0.95	0.97	0.98	1.05	0.97	0.96
Y	0.023	0.026	0.022	0.024	0.020	0.024	0.022	0.025	0.024	0.017	0.026	0.020	0.022	0.019	0.023	0.025	0.010	0.008
La	0.222	0.178	0.188	0.177	0.192	0.190	0.177	0.194	0.207	0.206	0.182	0.189	0.178	0.184	0.183	0.155	0.262	0.275
Ce	0.489	0.452	0.461	0.462	0.467	0.465	0.446	0.462	0.463	0.489	0.462	0.475	0.471	0.494	0.456	0.436	0.473	0.481
Pr	0.052	0.053	0.053	0.053	0.052	0.054	0.051	0.051	0.050	0.054	0.055	0.058	0.057	0.050	0.055	0.047	0.045	0.048
Nd	0.185	0.211	0.201	0.208	0.199	0.204	0.203	0.191	0.182	0.195	0.219	0.219	0.220	0.196	0.209	0.180	0.152	0.149
Sm	0.018	0.031	0.031	0.029	0.029	0.030	0.029	0.025	0.024	0.026	0.032	0.030	0.030	0.026	0.029	0.027	0.020	0.019
Eu	0.001	0.005	0.005	0.003	0.005	0.004	0.005	0.003	0.003	0.003	0.005	0.004	0.003	0.003	0.004	0.004	0.004	0.003
Gd	0.003	0.010	0.011	0.009	0.011	0.013	0.014	0.010	0.006	0.007	0.011	0.012	0.011	0.009	0.010	0.013	0.006	0.005
Dy	0.003	0.005	0.004	0.004	0.004	0.004	0.003	0.004	0.003	0.003	0.005	0.004	0.003	0.004	0.004	0.004	0.002	0.002
Th	0.007	0.014	0.011	0.012	0.010	0.012	0.012	0.010	0.019	0.007	0.010	0.007	0.010	0.010	0.007	0.014	0.021	0.013
Σ	1.00	0.99	0.99	0.98	0.99	1.00	0.96	0.98	0.98	1.01	1.01	1.02	1.01	0.99	0.98	0.91	0.99	1.00

[a] Determined by stoichiometry, and b.d is below detection limit.

Table E-4: (Continued)

Spot	163	164	165	166	167	168	169	170	171	172	173	174	175	176	177	178
CaO	16.07	15.66	17.08	16.59	15.73	15.59	16.07	15.60	15.86	16.27	15.86	15.35	15.47	15.24	16.18	15.37
MnO	b.d	0.01	b.d	0.01	0.01	b.d	0.09	0.01	b.d	b.d	b.d	b.d	0.01	0.06	b.d	0.01
FeO	1.16	1.72	1.12	0.82	1.88	0.07	0.83	0.74	0.47	1.03	0.34	0.19	1.23	0.64	0.60	0.31
SrO	0.25	0.20	0.16	0.22	0.25	0.25	0.25	0.20	0.14	0.26	0.32	0.30	0.97	0.78	0.27	0.61
BaO	0.08	0.04	b.d	b.d	0.03	0.24	0.03	0.11	0.19	0.08	0.24	0.50	0.17	0.19	0.16	0.43
Y_2O_3	0.34	0.24	0.21	0.20	0.33	0.80	0.84	0.87	0.97	1.55	1.13	1.11	0.69	0.68	1.13	0.47
La_2O_3	13.77	13.72	13.61	13.82	12.82	14.33	12.60	13.62	13.65	13.11	15.45	15.93	14.71	13.99	15.20	15.55
Ce_2O_3	25.59	25.66	24.70	25.66	23.33	25.52	23.10	24.75	25.65	24.43	25.65	26.22	24.38	23.72	25.27	26.79
Pr_2O_3	2.20	2.55	2.48	2.42	2.23	2.53	2.38	2.47	2.64	2.49	2.51	2.43	2.17	2.34	2.32	2.35
Nd_2O_3	7.74	8.13	8.08	7.96	7.17	7.13	6.97	7.10	7.47	7.39	6.63	6.59	5.89	6.64	6.53	6.52
Sm_2O_3	1.03	0.92	0.95	0.88	0.92	0.67	0.71	0.73	0.78	0.80	0.62	0.65	0.54	0.63	0.63	0.55
Eu_2O_3	0.23	0.08	0.12	0.08	0.11	0.12	0.06	0.10	0.12	0.13	0.05	0.08	0.09	0.11	0.13	0.10
Gd_2O_3	0.41	0.24	0.18	0.18	0.44	0.20	0.22	0.16	0.16	0.37	0.09	0.09	0.02	0.20	0.25	b.d
Dy_2O_3	0.15	0.06	0.09	0.06	0.20	0.20	0.21	0.21	0.30	0.43	0.31	0.31	0.20	0.19	0.25	0.13
ThO_2	1.42	1.06	1.08	0.83	1.60	0.58	0.62	0.57	0.86	1.15	0.71	0.70	0.51	0.88	0.85	0.67
UO_2	b.d	b.d	b.d	b.d	b.d	b.d	b.d	b.d	b.d	b.d	b.d	b.d	b.d	b.d	b.d	b.d
F[a]	6.03	6.00	6.03	5.97	5.78	5.79	5.67	5.76	5.91	5.99	5.95	5.94	5.77	5.66	5.97	5.90
CO_2 [a]	27.92	27.81	27.96	27.66	26.78	26.83	26.29	26.69	27.36	27.73	27.56	27.51	26.75	26.21	27.64	27.32
-O=F	2.54	2.53	2.54	2.51	2.43	2.44	2.39	2.43	2.49	2.52	2.51	2.50	2.43	2.38	2.51	2.48
Σ	102.20	101.93	101.50	100.95	97.46	98.49	96.34	97.53	100.21	100.82	101.11	101.47	97.41	96.02	100.98	100.73
Ca	0.892	0.872	0.947	0.930	0.910	0.902	0.929	0.905	0.899	0.910	0.892	0.866	0.897	0.901	0.908	0.873
Mn	b.d	b.d	b.d	b.d	b.d	b.d	0.004	b.d	b.d	b.d	b.d	b.d	b.d	0.003	b.d	b.d
Fe	0.050	0.075	0.048	0.036	0.085	0.003	0.037	0.034	0.021	0.045	0.015	0.008	0.056	0.030	0.026	0.014
Sr	0.008	0.006	0.005	0.007	0.008	0.008	0.008	0.006	0.004	0.008	0.010	0.009	0.030	0.025	0.008	0.019
Ba	0.002	0.001	b.d	b.d	0.001	0.005	0.001	0.002	0.004	0.002	0.005	0.010	0.004	0.004	0.003	0.009
Σ	0.97	0.97	1.01	0.98	1.02	0.92	1.09	0.96	0.94	0.97	0.93	0.90	1.00	0.97	0.95	0.92
Y	0.009	0.007	0.006	0.006	0.009	0.023	0.024	0.025	0.027	0.043	0.032	0.031	0.020	0.020	0.031	0.013
La	0.263	0.263	0.260	0.267	0.255	0.285	0.251	0.272	0.266	0.253	0.299	0.309	0.294	0.285	0.294	0.304
Ce	0.485	0.488	0.468	0.492	0.461	0.504	0.456	0.491	0.497	0.467	0.493	0.505	0.483	0.479	0.485	0.520
Pr	0.042	0.048	0.047	0.046	0.044	0.050	0.047	0.049	0.051	0.047	0.048	0.047	0.043	0.047	0.044	0.045
Nd	0.143	0.151	0.149	0.149	0.138	0.137	0.134	0.137	0.141	0.138	0.124	0.124	0.114	0.131	0.122	0.123
Sm	0.018	0.016	0.017	0.016	0.017	0.012	0.013	0.014	0.014	0.014	0.011	0.012	0.010	0.012	0.011	0.010
Eu	0.004	0.001	0.002	0.001	0.002	0.002	0.001	0.002	0.002	0.002	0.001	0.001	0.002	0.002	0.002	0.002
Gd	0.007	0.004	0.003	0.003	0.008	0.004	0.004	0.003	0.003	0.006	0.002	0.002	b.d	0.004	0.004	b.d
Dy	0.003	0.001	0.002	0.001	0.003	0.003	0.004	0.004	0.005	0.007	0.005	0.005	0.003	0.003	0.004	0.002
Th	0.017	0.013	0.013	0.010	0.020	0.007	0.008	0.007	0.010	0.014	0.008	0.008	0.006	0.011	0.010	0.008
Σ	0.99	0.99	0.97	0.99	0.96	1.03	0.94	1.00	1.02	0.99	1.02	1.04	0.97	0.99	1.01	1.03

[a] Determined by stoichiometry, and b.d is below detection limit.

Appendix F: EPMA data (wt%) and BSE image of the syntaxial intergrowth of synchysite-(Ce) and parisite-(Ce) crystals of the standard sample.

Spot no	1	2	3	4	5	6	7	8
Mineral	Parisite	Synchysite	Synchysite	Parisite	Parisite	Synchysite	Synchysite	Parisite
SiO_2	b.d.	b.d.	b.d.	b.d.	b.d.	b.d.	b.d.	b.d.
CaO	11.89	15.04	15.01	11.25	10.88	14.95	15.28	11.02
MnO	b.d.	b.d.	b.d.	0.05	b.d.	b.d.	b.d.	0.064
SrO	0.39	0.24	0.28	0.30	0.41	0.30	0.32	0.51
Y_2O_3	0.59	0.84	0.75	0.77	0.43	0.82	0.70	0.33
La_2O_3	18.45	18.10	16.81	19.48	18.46	17.01	16.66	18.10
Ce_2O_3	29.20	26.85	27.35	28.85	29.95	27.14	24.85	30.20
Pr_2O_3	2.51	2.36	2.34	2.37	2.45	2.36	2.12	2.64
Nd_2O_3	7.33	6.96	7.05	7.05	7.23	7.08	6.78	7.57
Sm_2O_3	0.74	0.84	0.80	0.83	0.68	0.86	0.71	0.74
Eu_2O_3	0.17	0.19	0.20	0.18	0.21	0.20	0.15	0.16
Gd_2O_3	0.74	0.69	0.82	0.80	0.61	0.78	0.55	0.53
Tb_2O_3	b.d.	b.d.	b.d.	b.d.	b.d.	b.d.	b.d.	b.d.
Dy_2O_3	b.d.	b.d.	b.d.	b.d.	b.d.	0.1297	b.d.	b.d.
ThO_2	0.67	1.51	0.46	1.09	0.65	0.79	1.25	0.46
F	1.35	1.15	1.28	1.37	1.28	1.27	1.21	1.33
CO_2[a]	21.70	23.76	23.33	21.43	20.95	23.43	23.03	21.13
apfu[a] on the basis of number of anions								
Ca	1.181	0.907	0.923	1.126	1.110	0.915	0.958	1.116
Mn	b.d.	b.d.	b.d.	b.d.	b.d.	b.d.	b.d.	0.005
Sr	0.021	0.008	0.009	0.016	0.023	0.010	0.011	0.028
Σ	1.20	0.92	0.93	1.14	1.13	0.92	0.97	1.15
Y	0.029	0.025	0.023	0.038	0.022	0.025	0.022	0.016
La	0.630	0.376	0.356	0.671	0.649	0.358	0.360	0.631
Ce	0.991	0.553	0.575	0.986	1.045	0.567	0.532	1.045
Pr	0.085	0.048	0.049	0.081	0.085	0.049	0.045	0.091
Nd	0.243	0.140	0.144	0.235	0.246	0.144	0.142	0.256
Sm	0.024	0.016	0.016	0.027	0.022	0.017	0.014	0.024
Eu	0.005	0.004	0.004	0.006	0.007	0.004	0.003	0.005
Gd	0.023	0.013	0.016	0.025	0.019	0.015	0.011	0.017
Dy	b.d.	b.d.	b.d.	b.d.	b.d.	0.002	b.d.	b.d.
Th	0.014	0.019	0.006	0.023	0.014	0.010	0.017	0.010
Σ	2.04	1.20	1.19	2.09	2.11	1.19	1.15	2.10

[a] Calculated by stoichiometry, and b.d is below detection limit.

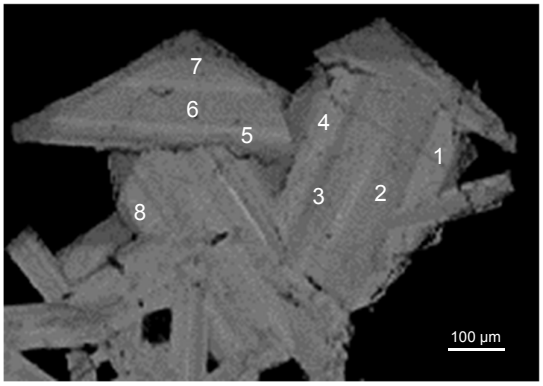

Appendix G – Fieldscan images of the crushed core samples

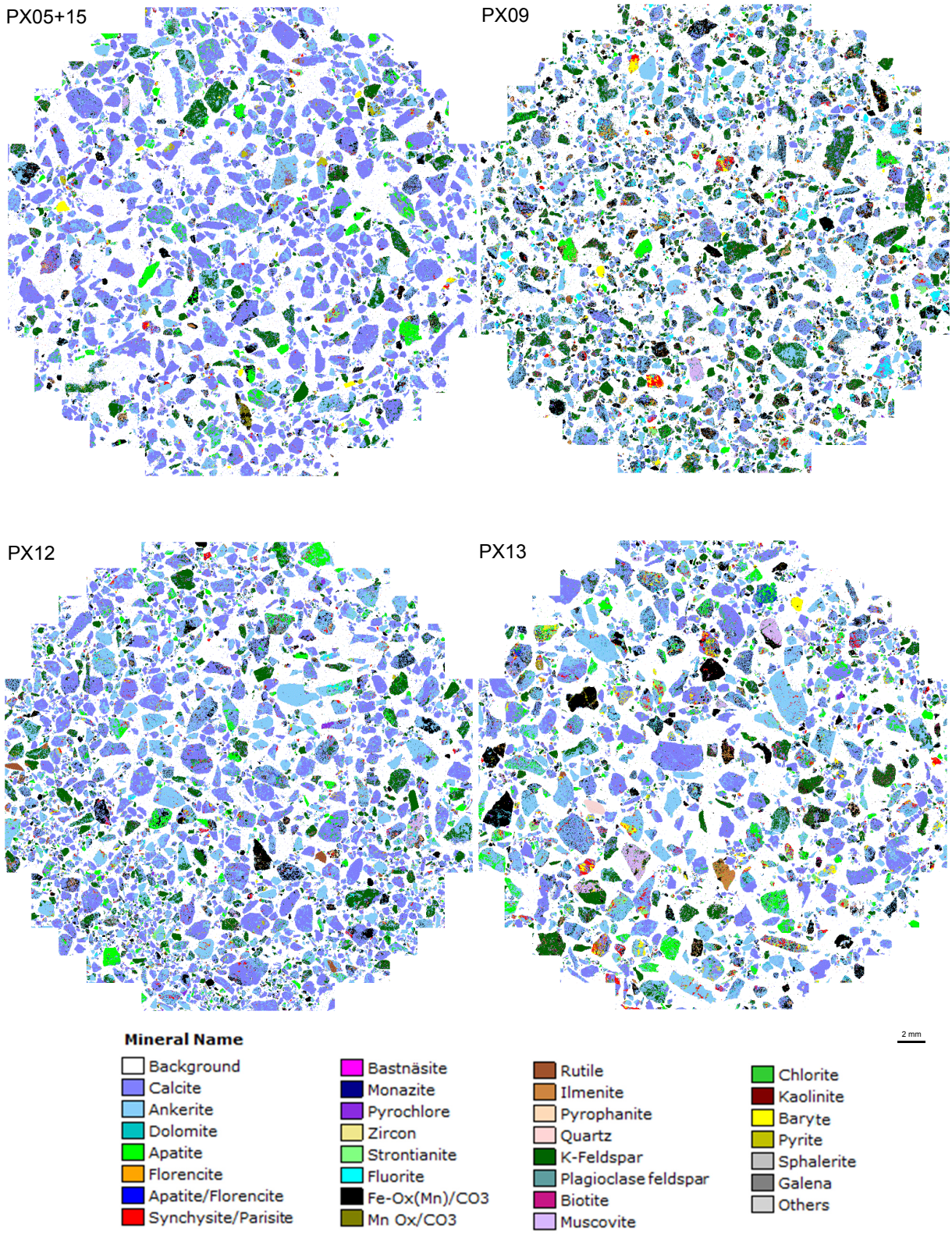

Figure G-1: Fieldscan images display psudocolored partilcs of PX05+15, PX09, PX12, and PX13 crushed core samples.

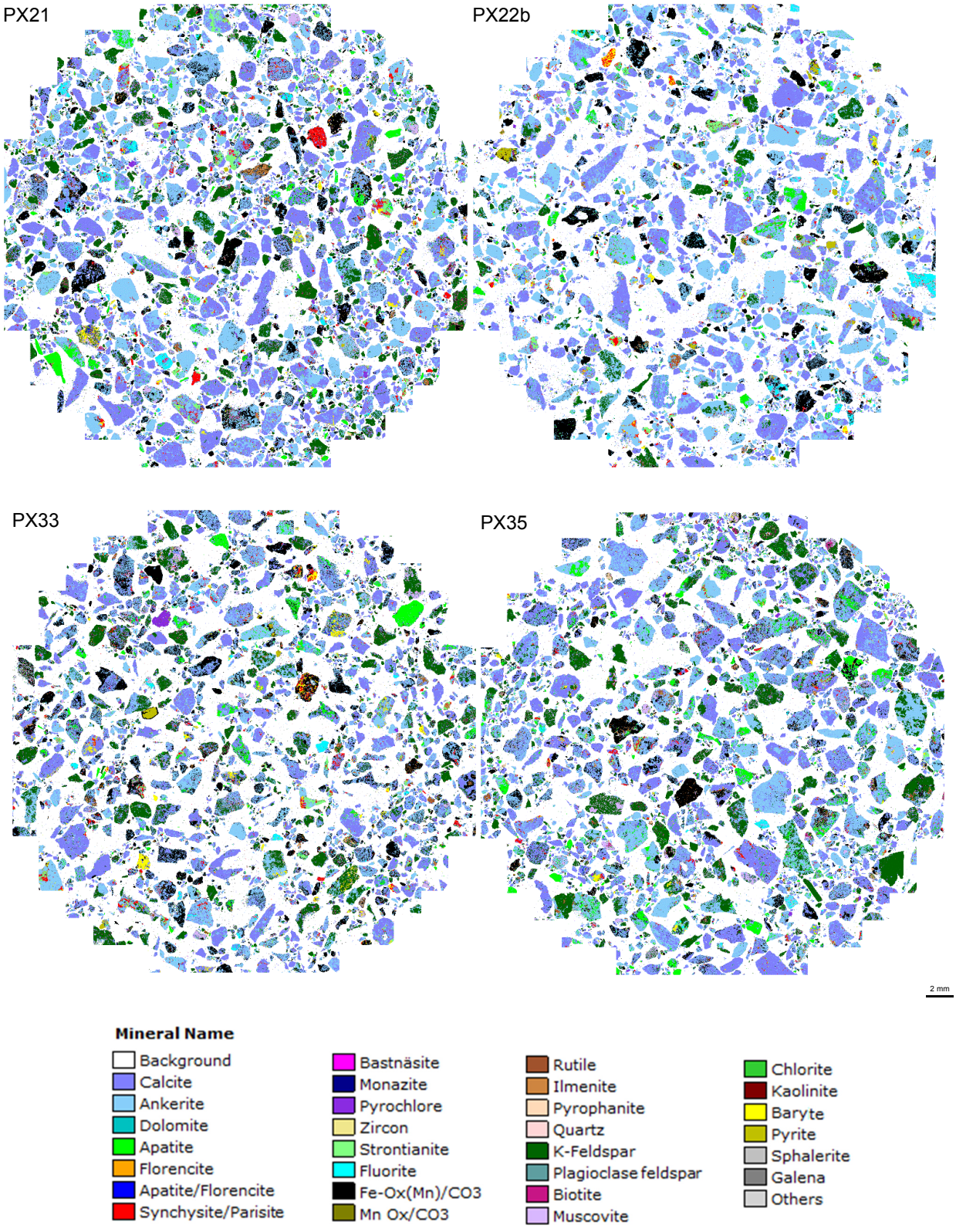

Figure G-2: Fieldscan images display psudocolored partilcs of PX21, PX22b, PX33, and PX35 crushed core samples.

Appendix H – EPMA data of the pure REE fluorcarbonat minerals

Table H-1: The elemental composition data (wt%) of bastnäsite-(Ce) single crystal mineral, analysed by EPMA.

Spot	1	2	3	4	5	6	7	8	9	10
SiO_2	0.16	b.d	0.18	0.16	b.d	b.d	0.17	b.d	0.22	b.d
CaO	0.06	0.05	0.06	0.07	b.d	0.04	0.07	0.04	0.04	0.04
MnO	0.07	0.09	0.10	b.d	0.06	0.06	0.08	0.07	0.09	0.06
SrO	0.16	0.10	0.22	0.17	0.05	0.13	0.15	0.08	0.19	0.23
Y_2O_3	0.56	0.51	0.51	0.50	0.47	0.44	0.52	0.47	0.39	0.42
La_2O_3	16.13	16.21	15.77	15.74	16.14	15.93	17.04	16.18	16.19	16.52
Ce_2O_3	34.30	34.43	34.21	34.42	34.20	34.56	32.49	34.19	34.61	34.13
Pr_2O_3	4.12	3.83	3.89	4.24	3.93	4.00	3.92	4.10	3.99	4.01
Nd_2O_3	15.83	15.80	15.81	15.90	15.62	16.03	15.75	15.61	15.63	15.50
Sm_2O_3	2.17	2.20	2.01	2.11	2.09	2.15	2.11	2.24	2.17	2.05
Eu_2O_3	0.24	0.28	0.29	0.18	0.25	0.25	0.29	0.21	0.28	0.26
Gd_2O_3	1.60	1.61	1.68	1.53	1.48	1.46	1.93	1.76	1.60	1.59
ThO_2	0.00	0.12	b.d	b.d	0.19	0.13	0.12	0.16	0.20	0.17
F meas	1.775	1.699	1.708	1.717	1.702	1.653	1.664	1.68	1.653	1.672
F calc [a]	8.75	8.66	9.10	9.24	9.10	9.17	9.16	9.12	9.30	9.17
CO_2 [a]	20.27	20.07	21.08	21.40	21.08	21.24	21.22	21.13	21.55	21.24
-O=F	3.69	3.65	3.83	3.89	3.83	3.86	3.86	3.84	3.92	3.86
Σ	100.74	100.30	101.07	101.77	100.83	101.71	101.14	101.52	102.54	101.53
TREO	74.95	74.87	74.17	74.62	74.18	74.82	74.05	74.76	74.86	74.48
CaO/TREO	0.001	0.001	0.001	0.001	b.d	0.001	0.001	0.001	0.001	0.001
CaO/Nd_2O_3	0.004	0.003	0.004	0.004	b.d	0.002	0.004	0.003	0.003	0.003
apfu[a] on the basis of number of anions										
Si	0.006	b.d	0.006	0.006	b.d	b.d	0.006	b.d	0.007	b.d
Ca	0.002	0.002	0.002	0.002	b.d	0.001	0.002	0.002	0.001	0.002
Mn	0.002	0.003	0.003	b.d	0.002	0.002	0.002	0.002	0.003	0.002
Sr	0.003	0.002	0.004	0.003	0.001	0.003	0.003	0.002	0.004	0.005
Σ	0.013	0.007	0.015	0.011	0.003	0.006	0.013	0.006	0.015	0.009
Y	0.010	0.010	0.009	0.009	0.009	0.008	0.010	0.009	0.007	0.008
La	0.211	0.214	0.202	0.199	0.207	0.203	0.217	0.207	0.203	0.210
Ce	0.445	0.451	0.434	0.432	0.436	0.437	0.411	0.434	0.431	0.432
Pr	0.053	0.050	0.049	0.053	0.050	0.050	0.049	0.052	0.049	0.051
Nd	0.200	0.202	0.196	0.195	0.194	0.198	0.194	0.193	0.190	0.191
Sm	0.027	0.027	0.024	0.025	0.025	0.026	0.025	0.027	0.025	0.024
Eu	0.003	0.003	0.003	0.002	0.003	0.003	0.003	0.002	0.003	0.003
Gd	0.019	0.019	0.019	0.017	0.017	0.017	0.022	0.020	0.018	0.018
Th	b.d	0.001	b.d	b.d	0.002	0.001	0.001	0.001	0.002	0.001
Σ	0.968	0.977	0.936	0.932	0.943	0.943	0.932	0.945	0.928	0.938

[a] Determined by stoichiometry, TREO is total rare earth oxides, b.d is below detection limit, and other analysed elements including Mg, Al, Fe, Ba, Tb, Dy, Er, Yb, Lu and U are below detection limit.

Table H-2: The elemental composition data (wt%) of parisite-(Ce) single crystal mineral, analysed by EPMA

Spot	1	2	3	4	5	6	7	8	9	10
SiO_2	b.d	b.d	b.d	b.d	b.d	b.d	b.d	b.d	b.d	b.d
CaO	11.34	11.31	11.52	11.5	11.45	10.93	11.25	11.35	11.36	11.43
MnO	0.06	0.06	0.05	0.05	0.06	0.06	0.06	b.d	0.05	0.06
SrO	0.15	0.16	0.15	0.12	0.02	0.01	0.08	0.06	0.09	0.16
Y_2O_3	1.44	1.46	1.73	1.97	1.78	1.95	1.46	1.94	1.87	1.8
La_2O_3	14.11	14.15	13.78	13.82	13.81	13.73	13.81	13.86	13.37	13.86
Ce_2O_3	27.34	27.22	26.8	26.82	26.94	26.75	27.35	26.71	26.6	26.65
Pr_2O_3	3.04	2.95	3.12	2.98	3.21	2.99	3.08	3.11	3.06	3.23
Nd_2O_3	11.4	11.25	11.33	11.59	11.46	11.49	11.3	11.27	11.43	11.57
Sm_2O_3	1.81	1.79	1.87	1.95	1.8	1.82	1.81	1.88	1.92	1.97
Eu_2O_3	0.22	0.21	0.19	0.2	0.13	0.29	0.18	0.18	0.25	0.22
Gd_2O_3	1.42	1.67	1.76	1.84	1.75	1.8	1.76	1.8	1.92	1.94
Dy_2O_3	0.3	0.27	0.31	0.35	0.34	0.33	0.31	0.35	0.4	0.3
ThO_2	1.98	2.17	2.03	2.01	1.94	1.95	2.17	1.92	1.81	2.03
F meas	1.25	1.36	1.22	1.14	1.43	1.38	1.39	1.36	1.37	1.27
F calc [a]	7.39	7.4	7.42	7.47	7.42	7.33	7.38	7.4	7.37	7.46
CO_2 [a]	21.81	21.82	21.94	22.05	21.95	21.48	21.75	21.77	21.75	22.01
-O=F	3.11	3.11	3.12	3.15	3.12	3.09	3.11	3.12	3.1	3.14
Σ	100.69	100.77	100.88	101.56	100.92	99.83	100.63	100.49	100.14	101.54
TREO	61.08	60.97	60.89	61.52	61.22	61.15	61.06	61.10	60.82	61.54
CaO/TREO	0.19	0.19	0.19	0.19	0.19	0.18	0.18	0.19	0.19	0.19
CaO/Nd_2O_3	0.99	1.01	1.02	0.99	1.00	0.95	1.00	1.01	0.99	0.99
apfu[a] on the basis of number of anions										
Si	b.d	b.d	b.d	b.d	b.d	b.d	b.d	b.d	b.d	b.d
Ca	1.114	1.111	1.127	1.118	1.119	1.087	1.108	1.116	1.12	1.113
Mn	0.005	0.005	0.004	0.004	0.005	0.005	0.005	b.d	0.004	0.004
Sr	0.008	0.009	0.008	0.006	0.001	b.d	0.004	0.003	0.005	0.008
Σ	1.127	1.125	1.139	1.128	1.125	1.092	1.117	1.119	1.129	1.125
Y	0.07	0.071	0.084	0.095	0.086	0.096	0.071	0.095	0.091	0.087
La	0.477	0.479	0.464	0.463	0.465	0.47	0.468	0.469	0.454	0.465
Ce	0.918	0.914	0.896	0.891	0.9	0.909	0.92	0.898	0.896	0.887
Pr	0.102	0.099	0.104	0.098	0.107	0.101	0.103	0.104	0.102	0.107
Nd	0.373	0.368	0.369	0.376	0.374	0.381	0.371	0.37	0.376	0.375
Sm	0.057	0.057	0.059	0.061	0.057	0.058	0.057	0.059	0.061	0.062
Eu	0.007	0.007	0.006	0.006	0.004	0.009	0.006	0.006	0.008	0.007
Gd	0.043	0.051	0.053	0.055	0.053	0.056	0.054	0.055	0.059	0.058
Dy	0.009	0.008	0.009	0.01	0.01	0.01	0.009	0.01	0.012	0.009
Th	0.041	0.045	0.042	0.041	0.04	0.041	0.045	0.04	0.038	0.042
Σ	2.097	2.099	2.086	2.096	2.096	2.131	2.104	2.106	2.097	2.099

[a] Determined by stoichiometry, TREO is total rare earth oxides, b.d is below detection limit, and other analysed elements including Mg, Al, Fe, Ba, Tb, Er, Yb, Lu and U are below detection limit.

Table H-3: The elemental composition data (wt%) of röntgenite-(Ce) A single crystal mineral, analysed by EPMA.

Spot	1	2	3	4	5	6	7	8	9	10
SiO_2	b.d	b.d	b.d	0.79	b.d	b.d	b.d	b.d	b.d	b.d
CaO	12.62	13.7	13.74	13.13	13.5	12.97	12.96	12.2	12.29	12.06
MnO	b.d	0.06	b.d	0.16	0.05	0.04	0.09	0.04	b.d	0.08
SrO	0.39	0.31	0.36	0.21	0.4	0.47	0.38	0.4	0.29	0.37
Y_2O_3	0.53	0.5	0.56	1.42	0.59	0.52	0.51	0.58	0.61	0.56
La_2O_3	17.37	16.81	17.09	16.02	17.39	17.01	17.71	17.5	17.56	17.58
Ce_2O_3	27.24	27.34	27.37	23.63	27.72	26.64	27.9	28.23	28.06	28.21
Pr_2O_3	2.91	2.74	2.83	2.69	2.9	2.82	2.86	2.83	2.88	2.79
Nd_2O_3	9.95	9.77	9.73	10.32	9.66	9.49	9.89	9.84	9.86	9.89
Sm_2O_3	1.43	1.23	1.21	1.87	1.27	1.35	1.23	1.21	1.23	1.21
Eu_2O_3	0.19	b.d	0.12	0.22	0.12	0.2	0.18	0.13	0.23	0.15
Gd_2O_3	1.12	0.98	0.98	2	0.98	1.22	0.97	0.92	1.05	0.88
Dy_2O_3	b.d	b.d	b.d	0.34	b.d	b.d	b.d	b.d	b.d	b.d
ThO_2	0.25	0.23	0.21	1.68	0.21	0.26	0.21	0.2	0.19	0.14
F meas	1.16	1.12	1.2	1.12	1.19	1.17	1.17	1.2	1.09	1.14
F calc [a]	5.97	6.01	6.06	6.17	6.08	5.92	6.05	5.95	5.97	5.92
CO_2	22.33	22.91	23.02	23.29	23.03	22.74	22.5	22.14	22.17	22.02
-O=F	2.51	2.53	2.55	2.6	2.56	2.49	2.55	2.5	2.51	2.49
Σ	99.79	100.06	100.73	101.34	101.34	99.16	100.8	99.67	99.88	99.37
TREO	60.74	59.37	59.89	58.51	60.63	59.25	61.25	61.24	61.48	61.27
CaO/TREO	0.21	0.23	0.23	0.22	0.22	0.22	0.21	0.20	0.20	0.20
CaO/Nd_2O_3	1.27	1.40	1.41	1.27	1.40	1.37	1.31	1.24	1.25	1.22
apfu[a] on the basis of number of anions										
Si	b.d	b.d	b.d	0.109	b.d	b.d	b.d	b.d	b.d	b.d
Ca	1.931	2.060	2.054	1.933	2.013	1.973	1.962	1.877	1.887	1.864
Mn	b.d	0.007	b.d	0.018	0.005	0.005	b.d	0.005	b.d	0.010
Sr	0.032	0.025	0.029	0.017	0.033	0.039	0.031	0.033	0.024	0.031
Σ	1.963	2.092	2.083	2.077	2.051	2.017	1.993	1.915	1.911	1.905
Y	0.04	0.037	0.042	0.104	0.044	0.039	0.038	0.044	0.046	0.043
La	0.915	0.87	0.879	0.811	0.893	0.891	0.923	0.927	0.928	0.935
Ce	1.424	1.405	1.398	1.188	1.413	1.385	1.443	1.484	1.472	1.49
Pr	0.151	0.14	0.144	0.134	0.147	0.146	0.147	0.148	0.15	0.146
Nd	0.508	0.49	0.485	0.506	0.48	0.481	0.499	0.505	0.505	0.51
Sm	0.07	0.059	0.058	0.088	0.061	0.066	0.060	0.06	0.061	0.06
Eu	0.009	0	0.006	0.01	0.006	0.01	0.008	0.007	0.011	0.007
Gd	0.053	0.046	0.045	0.091	0.045	0.057	0.046	0.044	0.05	0.042
Dy	b.d	b.d	b.d	0.015	b.d	b.d	b.d	b.d	b.d	b.d
Th	0.008	0.007	0.007	0.053	0.007	0.008	0.007	0.007	0.006	0.005
Σ	3.178	3.054	3.064	3.000	3.096	3.083	3.172	3.226	3.229	3.238

[a] Determined by stoichiometry, TREO is total rare earth oxides, b.d is below detection limit, and other analysed elements including Mg, Al, Fe, Ba, Tb, Er, Yb, Lu and U are below detection limit.

Table H-4: The elemental composition data (wt%) of röntgenite-(Ce) B single crystal mineral, analysed by EPMA.

Spot	1	2	3	4	5	6	7	8	9	10
SiO_2	b.d	b.d	b.d	b.d	b.d	b.d	b.d	b.d	b.d	b.d
CaO	14.2	13.08	14.13	13.8	13.9	14.04	13.72	14.09	13.92	13.33
MnO	b.d	0.07	0.05	0.09	0.06	0.07	0.06	0.05	0.07	0.05
SrO	0.32	0.22	0.37	0.27	0.29	0.38	0.49	0.39	0.32	0.4
Y_2O_3	0.6	0.99	0.5	0.61	0.62	0.6	0.55	0.69	0.67	0.66
La_2O_3	15.99	15.63	16.77	16.9	16.65	17.61	16.73	16.88	17.38	17.08
Ce_2O_3	26.61	24.55	26.3	26.63	26.39	28.59	26.87	26.69	26.46	27.05
Pr_2O_3	2.79	2.45	2.71	2.84	2.74	2.72	2.75	2.82	2.57	2.73
Nd_2O_3	9.87	9.18	9.8	9.64	9.93	10.56	9.26	9.7	9.37	9.89
Sm_2O_3	1.35	1.49	1.37	1.37	1.46	1.46	1.3	1.36	1.37	1.38
Eu_2O_3	0.24	0.22	0.21	0.17	0.17	0.27	0.22	0.17	0.23	0.22
Gd_2O_3	1.11	1.34	1.23	1.2	1.13	1.01	1.11	1.16	1.29	1.17
Dy_2O_3	b.d	b.d	b.d	b.d	b.d	b.d	b.d	b.d	b.d	b.d
ThO_2	0.26	1.00	0.32	0.37	0.30	0.27	0.34	0.30	0.34	0.30
F meas	1.31	1.34	1.41	1.51	1.48	0.86	1.40	1.44	1.52	1.37
F calc [a]	6.03	5.73	6.04	6.03	6.02	6.31	5.99	6.08	6.05	6.03
CO_2 [a]	23.11	23.11	23.18	23.02	23.01	23.91	22.91	23.28	23.11	22.84
-O=F	2.54	2.41	2.54	2.54	2.54	2.66	2.52	2.56	2.55	2.54
Σ	99.94	96.65	100.44	100.4	100.13	105.14	99.78	101.1	100.6	100.59
TREO	58.56	55.85	58.89	59.36	59.09	62.82	58.79	59.47	59.34	60.18
CaO/TREO	0.24	0.23	0.24	0.23	0.24	0.22	0.23	0.24	0.23	0.22
CaO/Nd_2O_3	1.44	1.42	1.44	1.43	1.40	1.33	1.48	1.45	1.49	1.35
apfu[a] on the basis of number of anions										
Si	b.d	b.d	b.d	b.d	b.d	b.d	b.d	b.d	b.d	b.d
Ca	2.124	2.002	2.107	2.066	2.083	2.018	2.065	2.089	2.076	0.826
Mn	b.d	0.009	0.006	0.010	0.007	0.008	0.007	0.005	0.008	0.003
Sr	0.026	0.018	0.030	0.022	0.024	0.029	0.040	0.032	0.026	0.013
Σ	2.150	2.029	2.143	2.098	2.114	2.055	2.112	2.126	2.110	0.842
Y	0.045	0.075	0.037	0.045	0.046	0.043	0.041	0.051	0.050	0.020
La	0.823	0.824	0.861	0.871	0.859	0.871	0.867	0.862	0.893	0.364
Ce	1.360	1.284	1.340	1.363	1.352	1.404	1.383	1.352	1.349	0.572
Pr	0.142	0.127	0.137	0.144	0.140	0.133	0.141	0.142	0.130	0.058
Nd	0.492	0.468	0.487	0.481	0.496	0.506	0.465	0.479	0.466	0.204
Sm	0.065	0.073	0.066	0.066	0.070	0.067	0.063	0.065	0.066	0.027
Eu	0.011	0.011	0.010	0.008	0.008	0.012	0.010	0.008	0.011	0.004
Gd	0.051	0.063	0.057	0.056	0.052	0.045	0.052	0.053	0.060	0.022
Dy	b.d	b.d	b.d	b.d	b.d	b.d	b.d	b.d	b.d	b.d
Th	0.008	0.033	0.010	0.012	0.010	0.008	0.011	0.010	0.011	0.004
Σ	2.997	2.958	3.005	3.046	3.033	3.089	3.033	3.022	3.036	1.275

[a] Determined by stoichiometry, TREO is total rare earth oxides, b.d is below detection limit, and other analysed elements including Mg, Al, Fe, Ba, Tb, Er, Yb, Lu and U are below detection limit.

Appendix I – QEMSCAN® results of the magnetic products

Table I-1: Modal mineralogical data of the magnetic separation products of the feed sample P_{80} of 53 µm determined by QEMSCAN®.

	Mineral group	Mineral name	Feed sample P_{80} 53 µm		
			Magnetic	Middling	Non-mag
Valuable minerals	Phosphates	Apatite	3.03	4.36	5.64
		Florencite	0.36	0.92	0.80
		apatite/florencite	0.15	0.52	0.33
		Monazite	0.04	0.05	0.01
	Carbonates	synchysite/parisite	2.78	3.33	2.96
		Bastnäsite	0.01	0.01	0.01
	Silicates	Zircon	0.19	0.05	0.01
Gangue minerals	Carbonates	Calcite	15.80	37.12	34.15
		Ankerite	47.05	26.81	20.19
		Dolomite	0.11	0.06	0.16
		Strontianite	0.70	1.09	1.15
	Silicates	K-feldspar	3.27	7.52	15.43
		plagioclase feldspar	0.05	0.15	0.57
		Muscovite	0.98	1.41	3.44
		biotite	0.50	0.71	0.51
		chlorite	0.62	0.54	1.01
		kaolinite	0.01	0.01	0.02
		quartz	0.15	0.21	0.33
	Oxides	Fe-Ox(Mn)/CO_3	17.87	10.33	7.96
		Mn Ox/CO_3	0.39	0.32	0.36
		rutile	0.38	1.18	0.43
		ilmenite	1.52	0.64	0.21
		pyrophanite	1.17	0.36	0.16
		pyrochlore	0.17	0.07	0.11
	Sulphides	pyrite	0.13	0.07	0.23
		sphalerite	0.01	0.01	<0.01
		galena	0.01	0.00	0.00
	Sulphates	baryte	0.69	0.65	2.16
		gypsum	0.01	0.03	0.03
	Halides	fluorite	0.28	0.47	1.41
	Mixed	Others	1.58	1.02	0.22

Others include trace of spessartine and contamination: cassiterite, Zn oxide (metal galvanised), brass, Cu metal, Cu-Fe-Mn alloy, Pb-Zn-V alloy.

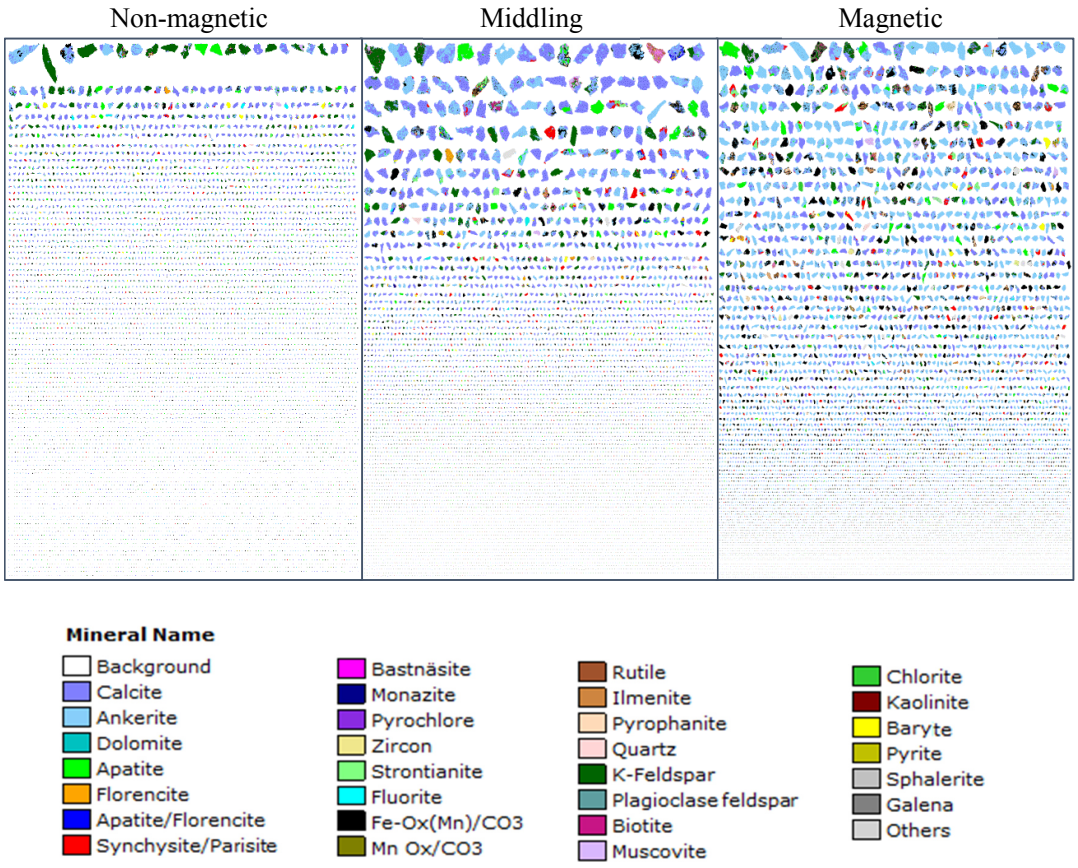

Figure I-1: The fieldscan images display psudocoloured particles of the magnetic separation products determined by QEMSCAN®.

Table I-2: Average grain size of the valuable and gangue minerals recovered to the magnetic separation products of the feed P_{80} of 53 µm determined by QEMSCAN®.

Mineral name	Feed sample P_{80} 53 µm		
	Magnetic	Middling	Non-mag
apatite	19.9	13.4	7.7
florencite	9.1	10.6	7.2
apatite/florencite	6.2	6.5	3.8
monazite	10.0	10.6	2.9
synchysite/parisite	13.3	9.7	6.0
bastnäsite	3.4	3.7	2.9
zircon	26.7	9.0	2.9
calcite	16.0	16.5	8.2
ankerite	19.9	10.8	5.7
dolomite	5.6	4.2	4.4
strontianite	13.9	13.4	8.3
K-feldspar	14.4	15.3	10.6
plagioclase feldspar	3.7	3.8	3.2
muscovite	9.4	6.4	5.2
biotite	5.3	5.3	3.5
chlorite	6.2	3.8	3.4
kaolinite	3.4	3.3	4.3
quartz	7.8	6.5	3.8
Fe-Ox(Mn)/CO_3	12.0	6.9	4.6
Mn Ox/CO_3	5.2	4.1	3.7
Rutile	5.7	6.1	3.4
ilmenite	5.9	5.3	4.1
pyrophanite	9.1	6.8	5.8
Pyrite	4.7	3.4	4.0
sphalerite	7.4	6.4	2.9
galena	2.9	0.0	0.0
Baryte	18.4	8.2	9.1
Gypsum	3.4	3.2	3.0
Fluorite	8.3	6.3	6.3
Pyrochlore	7.0	5.2	5.9
Others	19.1	24.8	5.3

Others include trace of spessartine and contamination: cassiterite, Zn oxide (metal galvanised), brass, Cu metal, Cu-Fe-Mn alloy, Pb-Zn-V alloy.

Appendix J – size-by-size magnetic separation tests

Table J-1: Data for the magnetic separation products at the size fraction of >40 µm.

Grade, recovery and mass pull																											
Products	Mass (g)	Mass (wt%)	Grade																								
			P_2O_5	SiO_2	CaO	Fe_2O_3	SrO	BaO	Y_2O_3	La_2O_3	Ce_2O_3	Pr_2O_3	Nd_2O_3	Sm_2O_3	Eu_2O_3	Gd_2O_3	Tb_2O_3	Dy_2O_3	Ho_2O_3	Er_2O_3	Tm_2O_3	Yb_2O_3	Lu_2O_3	ThO_2	UO_2	TREO
			(wt%)						(ppm)																		(wt%)
Magnetic	20.76	43.06	1.03	5.05	23.56	30.80	0.60	0.67	445	3296	5742	630	2107	306	76	209	24	104	16	37	5	27	4	310	22	1.30
Middling	11.73	24.34	1.99	9.70	31.02	14.96	1.13	0.84	768	4829	8179	886	2908	415	111	288	35	165	27	65	8	47	7	418	21	1.87
Non-magnetic	15.72	32.60	2.54	16.80	26.61	11.92	1.24	0.38	771	3570	6094	663	2207	326	93	238	31	156	27	66	8	48	7	318	15	1.43
Mid + non-mag	27.45	56.94	2.31	13.76	28.49	13.22	1.20	0.57	769	4108	6985	758	2507	364	101	259	33	160	27	66	8	47	7	360	18	1.62
Calc. head	48.21	100.00	1.76	10.01	26.37	20.79	0.94	0.61	630	3758	6450	703	2335	339	90	237	29	136	22	53	7	39	6	339	20	1.48
Meas. head	50		1.92	10.84	29.50	20.86		0.36	612	3754	6462	703	2327	330	92	227	28	135	22	54	7	39	6	339	12	1.30
Products	Mass (g)	Mass (wt%)	Recovery (%)																								
			P_2O_5	SiO_2	CaO	Fe_2O_3	SrO	BaO	Y_2O_3	La_2O_3	Ce_2O_3	Pr_2O_3	Nd_2O_3	Sm_2O_3	Eu_2O_3	Gd_2O_3	Tb_2O_3	Dy_2O_3	Ho_2O_3	Er_2O_3	Tm_2O_3	Yb_2O_3	Lu_2O_3	ThO_2	UO_2	TREO
Magnetic	20.76	43.06	25.25	21.73	38.48	63.80	27.67	46.78	30.42	37.76	38.34	38.59	38.87	38.87	36.36	37.83	35.84	32.95	30.87	29.91	29.88	30.49	31.46	39.39	48.48	37.82
Middling	11.73	24.34	27.56	23.58	28.63	17.51	29.28	33.18	29.69	31.27	30.86	30.69	30.31	29.80	29.91	29.51	29.56	29.67	29.68	29.64	29.51	29.35	29.45	30.01	26.01	30.74
Non-magnetic	15.72	32.60	47.20	54.69	32.89	18.69	43.05	20.04	39.90	30.96	30.80	30.72	30.82	31.33	33.73	32.67	34.60	37.39	39.44	40.45	40.61	40.17	39.09	30.59	25.51	31.43
Mid + non-mag	27.45	56.94	74.75	78.27	61.52	36.20	72.33	53.22	69.58	62.24	61.66	61.41	61.13	61.13	63.64	62.17	64.16	67.05	69.13	70.09	70.12	69.51	68.54	60.61	51.52	62.18
Calc. head	48.21	100.00	100	100	100	100	100	100	100	100	100	100	100	100	100	100	100	100	100	100	100	100	100	100	100	100

Table J-2: Data for the magnetic separation products at the size fraction of 30-40 µm.

Grade, recovery and mass pull																											
Products	Mass (g)	Mass (wt%)	Grade																								
			P_2O_5	SiO_2	CaO	Fe_2O_3	SrO	BaO	Y_2O_3	La_2O_3	Ce_2O_3	Pr_2O_3	Nd_2O_3	Sm_2O_3	Eu_2O_3	Gd_2O_3	Tb_2O_3	Dy_2O_3	Ho_2O_3	Er_2O_3	Tm_2O_3	Yb_2O_3	Lu_2O_3	ThO_2	UO_2	TREO
			(wt%)						(ppm)																		(wt%)
Magnetic	21.60	45.05	0.97	3.33	24.03	29.97	0.62	0.56	444	3488	6069	668	2210	315	80	208	23	103	16	36	4	26	4	329	16	1.37
Middling	12.26	25.57	1.79	6.59	32.25	15.57	1.07	0.83	705	4833	8287	900	2970	414	111	278	33	153	25	59	7	42	6	417	18	1.88
Non-magnetic	14.09	29.38	2.74	11.33	31.25	8.54	1.69	0.79	837	3620	6265	682	2258	335	96	246	32	163	28	70	9	52	7	310	23	1.47
Mid + non-mag	26.35	54.95	2.30	9.12	31.72	11.81	1.40	0.81	776	4184	7206	783	2590	372	103	261	32	158	27	65	8	47	7	359.78	20.65	1.66
Calc. head	47.95	100.00	1.70	6.51	28.26	19.99	1.05	0.70	626	3870	6693	732	2419	346	93	237	28	134	22	52	7	38	6	346	19	1.53
Meas. head	50		1.91	7.29	30.50	19.67	1.11	1.06	618	3886	6697	730	2411	340	94	227	27	131	22	52	7	37	5	335	11	1.53
Products	Mass (g)	Mass (wt%)	Recovery (%)																								
			P_2O_5	SiO_2	CaO	Fe_2O_3	SrO	BaO	Y_2O_3	La_2O_3	Ce_2O_3	Pr_2O_3	Nd_2O_3	Sm_2O_3	Eu_2O_3	Gd_2O_3	Tb_2O_3	Dy_2O_3	Ho_2O_3	Er_2O_3	Tm_2O_3	Yb_2O_3	Lu_2O_3	ThO_2	UO_2	TREO
Magnetic	21.60	45.05	25.67	23.04	38.32	67.53	26.73	36.39	31.92	40.60	40.85	41.16	41.17	40.97	38.86	39.53	37.26	34.87	32.62	31.51	30.88	31.50	32.67	42.87	39.12	40.32
Middling	12.26	25.57	26.94	25.88	29.19	19.91	26.02	30.38	28.78	31.93	31.66	31.44	31.40	30.58	30.70	29.98	29.79	29.33	29.11	28.79	28.18	28.50	28.71	30.81	25.28	31.45
Non-magnetic	14.09	29.38	47.39	51.08	32.50	12.56	47.25	33.23	39.30	27.48	27.50	27.40	27.43	28.46	30.44	30.49	32.94	35.81	38.28	39.70	40.94	40.00	38.62	26.32	35.59	28.23
Mid + non-mag	26.35	54.95	74.33	76.96	61.68	32.47	73.27	63.61	68.08	59.40	59.15	58.84	58.83	59.03	61.14	60.47	62.74	65.13	67.38	68.49	69.12	68.50	67.33	57.13	60.88	59.68
Calc. head	47.95	100.00	100	100	100	100	100	100	100	100	100	100	100	100	100	100	100	100	100	100	100	100	100	100	100	100

Table J-3: Data for the magnetic separation products at the size fraction of 20-30 µm.

Grade, recovery and mass pull																												
Products	Mass (g)	Mass (wt%)	Grade																									
			P_2O_5	SiO_2	CaO	Fe_2O_3	SrO	BaO	Y_2O_3	La_2O_3	Ce_2O_3	Pr_2O_3	Nd_2O_3	Sm_2O_3	Eu_2O_3	Gd_2O_3	Tb_2O_3	Dy_2O_3	Ho_2O_3	Er_2O_3	Tm_2O_3	Yb_2O_3	Lu_2O_3	ThO_2	UO_2	TREO
			(wt%)						(ppm)																			(wt%)
Magnetic	11.54	23.99	0.62	2.76	23.38	32.53	0.41	0.39	333	2507	4613	502	1676	245	61	163	19	80	12	27	3	21	3	254	18	1.03
Middling	14.79	30.75	1.17	5.76	32.07	18.91	0.76	0.54	532	3911	6919	754	2497	346	93	223	26	118	19	44	6	33	5	270	12	1.55
Non-magnetic	21.77	45.26	2.11	11.96	34.58	7.51	1.31	1.17	644	3032	5315	565	1880	276	76	196	25	125	22	54	7	42	6	265	14	1.23
Mid + non-mag	36.55	76.01	1.73	9.45	33.57	12.12	1.09	0.92	598	3387	5964	641	2130	305	83	207	25	122	20	50	6	39	6	266.88	13.32	1.36
Calc. head	48.09	100.00	1.46	7.85	31.12	17.02	0.93	0.79	535	3176	5640	608	2021	290	78	196	24	112	18	44	6	34	5	263.82	14.49	1.28
Meas. head	50		1.67	8.14	33.84	16.86	1.01	0.82	531	3278	5660	617	2043	288	80	193	23	111	18	45	6	34	5	284.80	8.98	1.29
Products	Mass (g)	Mass (wt%)	Recovery (%)																									
			P_2O_5	SiO_2	CaO	Fe_2O_3	SrO	BaO	Y_2O_3	La_2O_3	Ce_2O_3	Pr_2O_3	Nd_2O_3	Sm_2O_3	Eu_2O_3	Gd_2O_3	Tb_2O_3	Dy_2O_3	Ho_2O_3	Er_2O_3	Tm_2O_3	Yb_2O_3	Lu_2O_3	ThO_2	UO_2	TREO
Magnetic	11.54	23.99	10.12	8.44	18.02	45.85	10.60	11.87	14.96	18.94	19.62	19.80	19.90	20.22	18.78	19.88	18.79	17.09	15.55	14.75	14.47	14.57	15.40	23.11	30.15	19.26
Middling	14.79	30.75	24.63	22.56	31.69	34.18	25.10	20.87	30.58	37.86	37.73	38.13	38.00	36.68	36.90	35.01	33.47	32.34	31.39	30.66	29.62	29.67	30.34	31.49	25.99	37.34
Non-magnetic	21.77	45.26	65.25	69.00	50.29	19.97	64.30	67.26	54.47	43.20	42.65	42.07	42.11	43.10	44.32	45.12	47.74	50.57	53.06	54.59	55.91	55.76	54.27	45.40	43.86	43.41
Mid + non-mag	36.55	76.01	89.88	91.56	81.98	54.15	89.40	88.13	85.04	81.06	80.38	80.20	80.10	79.78	81.22	80.12	81.21	82.91	84.45	85.25	85.53	85.43	84.60	76.89	69.85	80.74
Calc. head	48.09	100.00	100	100	100	100	100	100	100	100	100	100	100	100	100	100	100	100	100	100	100	100	100	100	100	100

Table J-4: Data for the magnetic separation products at the size fraction of 10-20 µm.

Grade, recovery and mass pull																												
Products	Mass (g)	Mass (wt%)	Grade																									
			P_2O_5	SiO_2	CaO	Fe_2O_3	SrO	BaO	Y_2O_3	La_2O_3	Ce_2O_3	Pr_2O_3	Nd_2O_3	Sm_2O_3	Eu_2O_3	Gd_2O_3	Tb_2O_3	Dy_2O_3	Ho_2O_3	Er_2O_3	Tm_2O_3	Yb_2O_3	Lu_2O_3	ThO_2	UO_2	TREO
			(wt%)						(ppm)																			(wt%)
Magnetic	11.28	23.66	0.56	2.59	24.04	33.17	0.39	0.38	331	2722	4903	533	1767	251	63	163	18	78	12	27	3	21	3	257	15	1.09
Middling	12.24	25.66	1.16	5.33	32.22	19.12	0.79	0.62	545	4420	7781	835	2730	372	100	236	27	121	19	45	6	33	5	365	11	1.73
Non-magnetic	24.17	50.68	2.09	10.94	36.37	7.29	1.37	1.23	593	3283	5675	600	1962	278	77	189	23	117	20	50	7	39	6	265	11	1.29
Mid + non-mag	36.41	76.34	1.78	9.06	34.98	11.26	1.17	1.02	577	3665	6383	679	2220	310	85	205	25	118	20	48	6	37	5	298	11	1.44
Calc. head	47.69	100.00	1.49	7.53	32.39	16.44	0.99	0.87	519	3442	6033	644	2113	296	80	195	23	109	18	43	6	33	5	289	12	1.36
Meas. head	50		1.53	7.38	33.60	16.49	1.03	0.91	532	3601	6306	668	2204	306	84	199	24	112	18	44	6	35	5	299	9	1.09
Products	Mass (g)	Mass (wt%)	Recovery (%)																									
			P_2O_5	SiO_2	CaO	Fe_2O_3	SrO	BaO	Y_2O_3	La_2O_3	Ce_2O_3	Pr_2O_3	Nd_2O_3	Sm_2O_3	Eu_2O_3	Gd_2O_3	Tb_2O_3	Dy_2O_3	Ho_2O_3	Er_2O_3	Tm_2O_3	Yb_2O_3	Lu_2O_3	ThO_2	UO_2	TREO
Magnetic	11.28	23.66	8.96	8.14	17.56	47.71	9.30	10.25	15.11	18.71	19.22	19.57	19.79	20.07	18.80	19.75	18.76	17.02	15.78	14.88	14.42	14.67	14.51	21.07	29.85	19.01
Middling	12.24	25.66	20.00	18.17	25.53	29.83	20.53	18.29	26.96	32.96	33.10	33.25	33.16	32.27	32.18	31.11	30.01	28.59	27.83	26.65	25.96	25.54	25.64	32.43	23.72	32.70
Non-magnetic	24.17	50.68	71.05	73.69	56.91	22.46	70.16	71.46	57.93	48.34	47.68	47.18	47.06	47.66	49.03	49.15	51.23	54.39	56.39	58.47	59.62	59.79	59.84	46.50	46.43	48.29
Mid + non-mag	36.41	76.34	91.04	91.86	82.44	52.29	90.70	89.75	84.89	81.29	80.78	80.43	80.21	79.93	81.20	80.25	81.24	82.98	84.22	85.12	85.58	85.33	85.49	78.93	70.15	80.99
Calc. head	47.69	100.00	100	100	100	100	100	100	100	100	100	100	100	100	100	100	100	100	100	100	100	100	100	100	100	100

Table J-5: Data for the magnetic separation products at the size fraction of <10 µm.

Grade, recovery and mass pull																											
Products	Mass (g)	Mass (wt%)	Grade																								
			P_2O_5	SiO_2	CaO	Fe_2O_3	SrO	BaO	Y_2O_3	La_2O_3	Ce_2O_3	Pr_2O_3	Nd_2O_3	Sm_2O_3	Eu_2O_3	Gd_2O_3	Tb_2O_3	Dy_2O_3	Ho_2O_3	Er_2O_3	Tm_2O_3	Yb_2O_3	Lu_2O_3	ThO_2	UO_2	TREO
			(wt%)						(ppm)																		(wt%)
Magnetic	3.31	6.93	1.18	5.36	20.37	34.27	0.47	0.56	448	3275	6058	654	2193	335	74	230	26	109	16	37	4	26	4	361	38	1.35
Middling	11.23	23.46	1.67	7.92	27.55	23.89	0.81	0.78	583	4609	8232	876	2871	396	105	249	29	130	20	48	6	34	5	407	15	1.82
Non-magnetic	33.32	69.61	1.98	10.09	30.24	18.02	1.04	0.95	663	4827	8573	900	2949	409	110	260	30	142	23	54	7	39	5	413	13	1.90
Mid + non-mag	44.55	93.07	1.91	9.54	29.56	19.50	0.98	0.91	643	4772	8487	894	2929	405	109	257	30	139	22	53	7	38	5	412	13	1.88
Calc. head	47.87	100.00	1.85	9.25	28.93	20.53	0.94	0.88	629	4669	8319	877	2878	401	106	255	30	137	22	52	6	37	5	408	15	1.84
Meas. head	50		1.98	10.08	31.71	20.91	0.97	0.89	634	4583	8099	860	2836	391	106	250	29	135	22	51	6	38	6	338	12	1.80
Products	Mass (g)	Mass (wt%)	Recovery (%)																								
			P_2O_5	SiO_2	CaO	Fe_2O_3	SrO	BaO	Y_2O_3	La_2O_3	Ce_2O_3	Pr_2O_3	Nd_2O_3	Sm_2O_3	Eu_2O_3	Gd_2O_3	Tb_2O_3	Dy_2O_3	Ho_2O_3	Er_2O_3	Tm_2O_3	Yb_2O_3	Lu_2O_3	ThO_2	UO_2	TREO
Magnetic	3.31	6.93	4.40	4.01	4.88	11.56	3.45	4.36	4.93	4.86	5.04	5.16	5.28	5.80	4.82	6.24	6.12	5.51	5.07	4.90	4.74	4.87	5.13	6.13	17.22	5.07
Middling	11.23	23.46	21.14	20.07	22.34	27.31	20.24	20.76	21.75	23.16	23.22	23.41	23.40	23.16	23.28	22.90	22.77	22.27	21.87	21.70	21.47	21.47	22.66	23.41	23.17	23.17
Non-magnetic	33.32	69.61	74.46	75.91	72.78	61.13	76.30	74.88	73.32	71.98	71.74	71.43	71.32	71.04	71.89	70.86	71.11	72.22	73.07	73.41	73.79	73.66	72.21	70.46	59.60	71.76
Mid + non-mag	44.55	93.07	95.60	95.99	95.12	88.44	96.55	95.64	95.07	95.14	94.96	94.84	94.72	94.20	95.18	93.76	93.88	94.49	94.93	95.10	95.26	95.13	94.87	93.87	82.78	94.93
Calc. head	47.87	100.00	100	100	100	100	100	100	100	100	100	100	100	100	100	100	100	100	100	100	100	100	100	100	100	100

Appendix K – Froth flotation tests

Data for bench flotation test T1

1st stage	Grinding		
mill type	rod mill	**rods weight**	4109 g
charge	296.7 g	**rotational speed**	74 rpm
grind P_{80}	53 µm	**grinding time**	21 min
solids	50 wt%	**pH**	natural

2nd stage	Conditioning and floating												
Operating stage	Operating time (min)		Reagents (g/t)				Data						
	Conditioning	Floating	Na_2CO_3	Na_2SiF_6	Pionera 220	Betacol	pH	Temp (°C)	Solids (wt%)	Agitator speed (rpm)	Air flow rate (L/min)	Paddle rate	Cell volume (dm^3)
Condition1	60		4000	250			10.35	58	50	1200			1.5
Condition2	60				2500		9.7	58	50	1200			1.5
Condition3	60					120	9.57	58	50	1200			1.5
rougher conc 1		3					9.47	58	20	1200	2-5	1/15 s	1.5
rougher conc 2	2	3				60	9.34	56	20	1200	2-5	1/15 s	1.5

3rd stage		Grade, recovery and mass pull																										
Products	Mass (g)	Mass (wt%)	Grade																									
			P_2O_5	SiO_2 [a]	CaO	Fe_2O_3	SrO	BaO	Y_2O_3	La_2O_3	Ce_2O_3	Pr_2O_3	Nd_2O_3	Sm_2O_3	Eu_2O_3	Gd_2O_3	Tb_2O_3	Dy_2O_3	Ho_2O_3	Er_2O_3	Tm_2O_3	Yb_2O_3	Lu_2O_3	ThO_2	UO_2	TREO
			(wt%)						(ppm)																			(wt%)
RC1	55.54	19.14	5.42	3.28	36.55	14.38	1.98	1.05	1600	10131	17861	1698	5752	823	228	559	68	335	56	133	16	87	12	775	15	3.94
RC2	22.83	7.87	3.55	2.65	30.38	19.89	1.95	1.10	1306	9259	16329	1675	5629	786	215	511	60	283	46	106	13	68	9	758	18	3.63
Calc. RC	78.37	27.01	4.88	3.10	34.75	15.98	1.97	1.07	1515	9877	17415	1691	5716	812	224	545	66	320	53	125	15	82	11	770	16	3.85
RT	211.76	72.99	0.46	8.85	32.27	18.99	0.79	0.76	264	1951	3523	372	1255	168	46	105	12	57	9	24	3	22	3	171	9	0.78
Calc. head	290.13	100.00	1.65	7.30	32.94	18.18	1.11	0.84	601	4092	7275	729	2460	342	94	224	27	128	21	51	6	38	5	333	11	1.61
Meas. head	300		1.80	6.83	32.40	15.54	1.16	0.87	609	4028	7201	721	2438	341	93	217	25	124	20	49	6	37	5	318	11	1.59

Products	Mass (g)	Mass (wt%)	Recovery (%)																							
			P_2O_5	SiO_2	CaO	Fe_2O_3	SrO	BaO	Y_2O_3	La_2O_3	Ce_2O_3	Pr_2O_3	Nd_2O_3	Sm_2O_3	Eu_2O_3	Gd_2O_3	Tb_2O_3	Dy_2O_3	Ho_2O_3	Er_2O_3	Tm_2O_3	Yb_2O_3	Lu_2O_3	ThO_2	UO_2	TREO
RC1	55.54	19.14	62.78	8.60	21.24	15.14	34.08	23.87	50.93	47.40	47.00	44.62	44.76	46.03	46.52	47.82	49.05	50.15	50.91	49.88	47.72	44.00	40.87	44.62	27.30	46.82
RC2	22.83	7.87	16.92	2.86	7.26	8.61	13.85	10.26	17.09	17.81	17.66	18.09	18.00	18.06	18.02	17.99	17.83	17.45	16.99	16.35	15.39	14.07	13.33	17.93	13.15	17.75
calc. RC	78.37	27.01	79.70	11.46	28.50	23.75	47.94	34.13	68.02	65.21	64.66	62.71	62.77	64.09	64.54	65.81	66.88	67.59	67.90	66.24	63.11	58.07	54.21	62.55	40.45	64.56
RT	211.76	72.99	20.30	88.54	71.50	76.25	52.06	65.87	31.98	34.79	35.34	37.29	37.23	35.91	35.46	34.19	33.12	32.41	32.10	33.76	36.89	41.93	45.79	37.45	59.55	35.44
Calc. head	290.13	100.00	100	100	100	100	100	100	100	100	100	100	100	100	100	100	100	100	100	100	100	100	100	100	100	100

[a] Note that a correction factor was added to the concentration of SiO_2 in the concentrate 1, 2, and 3 based on the analysed samples at ALS Laboratories Ltd, Spain (see Chapter 2, Section 2.3.4).

Data for bench flotation test T2

1st stage	Grinding		
mill type	rod mill	**rods weight**	4109 g
charge	289.2 g	**rotational speed**	74 rpm
grind P_{80}	53 µm	**grinding time**	21 min
solids	50 wt%	**pH**	natural

2nd stage	Conditioning and floating												
Operating stage	Operating time (min)		Reagents (g/t)				Data						
	Conditioning	Floating	Na_2CO_3	Na_2SiF_6	Pionera 220	Betacol	pH	Temp (°C)	Solids (wt%)	Agitator speed (rpm)	Air flow rate (L/min)	Paddle rate	Cell volume (dm^3)
Condition1	60		7000	250			10.60	57	50	1200			1.5
Condition2	60				2500		10.13	58	50	1200			1.5
Condition3	60					120	9.95	58	50	1200			1.5
rougher conc 1		3					9.77	57	20	1200	2-5	1/15 s	1.5
rougher conc 2	2	3				60	9.74	57	20	1200	2-5	1/15 s	1.5

3rd stage		Grade, recovery and mass pull																										
Products	Mass (g)	Mass (wt%)	Grade																									
			P_2O_5	SiO_2	CaO	Fe_2O_3	SrO	BaO	Y_2O_3	La_2O_3	Ce_2O_3	Pr_2O_3	Nd_2O_3	Sm_2O_3	Eu_2O_3	Gd_2O_3	Tb_2O_3	Dy_2O_3	Ho_2O_3	Er_2O_3	Tm_2O_3	Yb_2O_3	Lu_2O_3	ThO_2	UO_2	TREO
			(wt%)						(ppm)																			(wt%)
RC1	59.85	21.42	5.37	3.16	39.28	11.73	2.77	0.71	1581	8785	15365	1576	5259	753	211	516	64	318	54	129	16	85	11	667	12	3.47
RC2	21.49	7.69	1.99	2.00	41.61	13.38	1.58	0.60	859	6667	12067	1224	4091	560	149	352	40	185	30	68	8	49	7	519	10	2.64
Calc. RC	81.34	29.11	4.48	2.86	39.89	12.17	2.46	0.68	1390	8226	14494	1483	4951	702	195	473	58	283	47	113	14	75	10	628	12	3.25
RT	198.06	70.89	0.46	9.92	28.26	21.78	0.50	0.84	224	1559	2798	304	1015	140	37	84	9	45	7	19	3	17	3	158	10	0.63
Calc. head	279.40	100.00	1.63	7.86	31.65	18.98	1.07	0.79	563	3500	6203	647	2161	304	83	197	24	115	19	46	6	34	5	295	10	1.39
Meas. head	300		1.80	6.83	32.40	15.54	1.16	0.87	609	4028	7201	721	2438	341	93	217	25	124	20	49	6	37	5	318	11	1.59

Products	Mass (g)	Mass (wt%)	Recovery (%)																							
			P_2O_5	SiO_2	CaO	Fe_2O_3	SrO	BaO	Y_2O_3	La_2O_3	Ce_2O_3	Pr_2O_3	Nd_2O_3	Sm_2O_3	Eu_2O_3	Gd_2O_3	Tb_2O_3	Dy_2O_3	Ho_2O_3	Er_2O_3	Tm_2O_3	Yb_2O_3	Lu_2O_3	ThO_2	UO_2	TREO
RC1	59.85	21.42	70.59	8.62	26.58	13.24	55.57	19.14	60.13	53.77	53.06	52.17	52.13	53.08	54.73	56.07	58.36	59.53	60.25	59.79	57.14	53.10	48.16	48.49	25.94	53.49
RC2	21.49	7.69	9.40	1.95	10.11	5.42	11.37	5.81	11.73	14.65	14.96	14.55	14.56	14.16	13.88	13.72	13.10	12.45	11.93	11.40	11.06	11.05	10.97	13.53	7.33	14.58
calc. RC	81.34	29.11	79.99	10.57	36.70	18.66	66.94	24.94	71.86	68.42	68.03	66.73	66.69	67.24	68.61	69.78	71.45	71.98	72.18	71.19	68.21	64.15	59.13	62.02	33.27	68.07
RT	198.06	70.89	20.01	89.43	63.30	81.34	33.06	75.06	28.14	31.58	31.97	33.27	33.31	32.76	31.39	30.22	28.55	28.02	27.82	28.81	31.79	35.85	40.87	37.98	66.73	31.93
Calc. head	279.40	100.00	100	100	100	100	100		100	100	100	100	100	100	100	100	100	100	100	100	100	100	100	100	100	100

Data for bench flotation test T3

1st stage	Grinding		
mill type	rod mill	**rods weight**	4109 g
charge	306.6 g	**rotational speed**	74 rpm
grind P_{80}	53 µm	**grinding time**	21 min
solids	50 wt%	**pH**	natural

2nd stage	Conditioning and floating												
Operating stage	Operating time (min)		Reagents (g/t)				Data						
	Conditioning	Floating	Na_2CO_3	Na_2SiF_6	Pionera 220	Betacol	pH	Temp (°C)	Solids (wt%)	Agitator speed (rpm)	Air flow rate (L/min)	Paddle rate	Cell volume (dm^3)
Condition1	60		10000	250			10.80	58	50	1200			1.5
Condition2	60				2500		10.44	58	50	1200			1.5
Condition3	60					120	10.31	58	50	1200			1.5
rougher conc 1		3					10.22	57	20	1200	2-5	1/15 s	1.5
rougher conc 2	2	3				60	10.19	57	20	1200	2-5	1/15 s	1.5

3rd stage		Grade, recovery and mass pull																										
Products	Mass (g)	Mass (wt%)	Grade																									
			P_2O_5	SiO_2	CaO	Fe_2O_3	SrO	BaO	Y_2O_3	La_2O_3	Ce_2O_3	Pr_2O_3	Nd_2O_3	Sm_2O_3	Eu_2O_3	Gd_2O_3	Tb_2O_3	Dy_2O_3	Ho_2O_3	Er_2O_3	Tm_2O_3	Yb_2O_3	Lu_2O_3	ThO_2	UO_2	TREO
			(wt%)						(ppm)																			(wt%)
RC1	26.88	8.86	2.75	3.69	33.47	16.23	2.03	0.86	830	4801	8582	905	3079	434	120	289	35	172	29	68	8	48	7	128	10	1.94
RC2	68.8	22.68	3.11	2.35	39.61	12.91	2.00	0.53	1053	5621	10269	1032	3470	494	137	333	42	207	35	85	11	60	8	425	9	2.29
Calc. RC	95.68	31.55	3.01	2.73	37.89	13.85	2.01	0.62	990	5391	9795	997	3360	477	132	321	40	197	33	80	10	56	8	341	9	2.19
RT	207.62	68.45	0.90	9.68	29.38	20.50	0.71	0.84	410	3073	5719	579	1937	268	72	167	19	89	14	34	4	26	3	243	10	1.24
Calc. head	303.30	100.00	1.57	7.49	32.07	18.40	1.12	0.77	593	3804	7005	710	2386	334	91	216	26	123	20	49	6	36	4	274	10	1.54
Meas. head	300		1.80	6.83	32.40	15.54	1.16	0.87	609	4028	7201	721	2438	341	93	217	25	124	20	49	6	37	5	318	11	1.59

Products	Mass (g)	Mass (wt%)	Recovery (%)																									
			P_2O_5	SiO_2	CaO	Fe_2O_3	SrO	BaO	Y_2O_3	La_2O_3	Ce_2O_3	Pr_2O_3	Nd_2O_3	Sm_2O_3	Eu_2O_3	Gd_2O_3	Tb_2O_3	Dy_2O_3	Ho_2O_3	Er_2O_3	Tm_2O_3	Yb_2O_3	Lu_2O_3	ThO_2	UO_2	TREO
RC1	55.54	19.14	15.57	4.36	9.25	7.82	16.01	9.97	12.42	11.19	10.86	11.29	11.43	11.53	11.75	11.88	12.17	12.40	12.53	12.39	12.17	11.90	13.26	4.14	9.32	11.17
RC2	22.83	7.87	45.01	7.13	28.02	15.92	40.37	15.54	40.29	33.52	33.25	32.96	32.99	33.57	34.21	35.06	36.96	38.12	39.40	39.56	39.12	37.74	42.04	35.17	19.83	33.66
calc. RC	78.37	27.01	60.58	11.50	37.27	23.73	56.38	25.51	52.70	44.71	44.11	44.25	44.42	45.09	45.96	46.94	49.13	50.51	51.93	51.95	51.29	49.64	55.30	39.32	29.15	44.83
RT	211.76	72.99	39.42	88.50	62.73	76.27	43.62	74.49	47.30	55.29	55.89	55.75	55.58	54.91	54.04	53.06	50.87	49.49	48.07	48.05	48.71	50.36	44.70	60.68	70.85	55.17
Calc. head	290.13	100.00	100	100	100	100	100	100	100	100	100	100	100	100	100	100	100	100	100	100	100	100	100	100	100	100

Data for bench flotation test T3 (Duplicate)

1st stage	**Grinding**		
mill type	rod mill	**rods weight**	4109 g
charge	303.1 g	**rotational speed**	74 rpm
grind P_{80}	53 µm	**grinding time**	21 min
solids	50 wt%	**pH**	natural

2nd stage	**Conditioning and floating**												
Operating stage	Operating time (min)		Reagents (g/t)				Data						
	Conditioning	Floating	Na_2CO_3	Na_2SiF_6	Pionera 220	Betacol	pH	Temp (°C)	Solids (wt%)	Agitator speed (rpm)	Air flow rate (L/min)	Paddle rate	Cell volume (dm^3)
Condition1	60		10000	250			10.71	58	50	1200			1.5
Condition2	60				2500		10.40	58	50	1200			1.5
Condition3	60					120	10.19	58	50	1200			1.5
rougher conc 1		3					10.10	58	20	1200	2-5	1/15 s	1.5
rougher conc 2	2	3				60	10.07	58	20	1200	2-5	1/15 s	1.5

3rd stage		**Grade, recovery and mass pull**													
products	Mass (g)	Mass (wt%)	Grade							Recovery						
			P_2O_5	SiO_2	CaO	Fe_2O_3	Y_2O_3	La_2O_3	Ce_2O_3	P_2O_5	SiO_2	CaO	Fe_2O_3	Y_2O_3	La_2O_3	Ce_2O_3
			(wt%)				(ppm)			(%)						
RC1	62.57	20.93	2.43	2.91	34.05	12.04	764	3910	8014	32.37	9.62	23.37	15.31	31.74	23.52	26.89
RC2	49.38	16.52	2.91	1.92	33.41	11.94	681	4708	6984	30.60	5.01	18.10	11.98	22.33	22.35	18.49
Calc. RC	111.95	37.45	2.64	2.47	33.77	12.00	727	4262	7560	62.97	14.63	41.46	27.28	54.06	45.86	45.38
RT	187	62.55	0.93	8.64	28.54	19.14	370	3012	5447	37.03	85.37	58.54	72.72	45.94	54.14	54.62
Calc. head	298.95	100.00	1.57	6.33	30.50	16.46	504	3480	6238	100	100	100	100	100	100	100
Meas. head	300		1.80	6.83	32.40	15.54	609	4028	7201							

Data for bench flotation test T4

1st stage	Grinding		
mill type	rod mill	**rods weight**	4109 g
charge	313.03 g	**rotational speed**	74 rpm
grind P_{80}	53 µm	**grinding time**	21 min
solids	50 wt%	**pH**	natural

2nd stage	Conditioning and floating											
operation stage	operation time (min)		Reagents (g/t)				Data					
	Conditioning	Floating	Na_2CO_3	Na_2SiF_6	Pionera 220	Betacol	pH	Temp (°C)	Solids (wt%)	Agitator speed (rpm)	Air flow rate (L/min)	Paddle rate
Condition1	60		4000	250			10.17	58	50	1200		
Condition2	60				2500		9.80	58	50	1200		
Condition3	60					120	9.60	58	50	1200		
Rougher Conc 1		3					9.36	58	20	1200	2-5	1/15 s
Rougher Conc 2	2	3				60	9.33	58	20	1200	2-5	1/15 s
Rougher Conc 3	4	6					9.31	58	20	1200	5	1/30 s

3rd stage		Grade, recovery and mass pull													
products	Mass (g)	Mass (wt%)	Grade							Recovery						
			P_2O_5	SiO_2	CaO	Fe_2O_3	Y_2O_3	La_2O_3	Ce_2O_3	P_2O_5	SiO_2	CaO	Fe_2O_3	Y_2O_3	La_2O_3	Ce_2O_3
			(wt%)				(ppm)			(%)						
RC1	44.6	14.37	5.24	3.21	34.86	12.74	1634	9210	16361	46.58	6.37	15.65	10.08	38.05	33.77	33.13
RC2	17.44	5.62	4.05	3.14	27.84	20.08	1353	8710	15540	14.09	2.43	4.89	6.22	12.32	12.49	12.31
RC3	3.51	1.13	1.52	2.96	27.29	19.50	687	3441	6024	1.06	0.46	0.96	1.21	1.26	0.99	0.96
Calc. RC	65.55	21.12	4.72	3.18	32.59	15.05	1508	8768.06	15589	61.74	9.27	21.50	17.51	51.63	47.25	46.40
RT	244.86	78.88	0.78	8.33	31.86	18.98	378	2620	4821	38.26	90.73	78.50	82.49	48.37	52.75	53.60
Calc. head	310.41	100.00	1.62	7.24	32.01	18.15	617	3918	7095	100	100	100	100	100	100	100
Meas. head	300		1.80	6.83	32.40	15.54	609	4028	7201							

Data for bench flotation test T5

1st stage	**Grinding**		
mill type	rod mill	**rods weight**	4109 g
charge	303 g	**rotational speed**	74 rpm
grind P_{80}	53 µm	**grinding time**	21 min
solids	50 wt%	**pH**	natural

2nd stage	**Conditioning and floating**											
operation stage	operation time (min)		Reagents (g/t)				Data					
	Conditioning	Floating	Na_2CO_3	Na_2SiF_6	Pionera 220	Betacol	pH	Temp (°C)	Solids (wt%)	Agitator speed (rpm)	Air flow rate (L/min)	Paddle rate
Condition1	60		4000	250			10.28	58	50	1200		
Condition2	60				2500		9.76	58	50	1200		
Condition3	60					120	9.63	58	50	1200		
Rougher Conc 1		3					9.53	58	20	1200	1.5	1/15 s
Rougher Conc 2	2	3				60	9.45	58	20	1200	1.5-2.5	1/15 s
Rougher Conc 3	4	6					9.41	58	20	1200	5	1/30 s

3rd stage		**Grade, recovery and mass pull**													
products	Mass (g)	Mass (wt%)	Grade							Recovery						
			P_2O_5	SiO_2	CaO	Fe_2O_3	Y_2O_3	La_2O_3	Ce_2O_3	P_2O_5	SiO_2	CaO	Fe_2O_3	Y_2O_3	La_2O_3	Ce_2O_3
			(wt%)				(ppm)			(%)						
RC1	50.44	16.85	4.63	3.04	35.89	13.03	1484	9127	16104	48.87	7.32	18.39	12.53	40.71	40.94	39.23
RC2	19.72	6.59	4.14	2.77	26.59	22.78	1410	8451	14651	17.05	2.61	5.33	8.57	15.12	14.82	13.95
RC3	2.01	0.67	1.16	2.50	26.98	19.06	573	3814	6524	0.49	0.24	0.55	0.73	0.63	0.68	0.63
Calc. RC	72.17	24.11	4.40	2.95	33.10	15.86	1439	8794	15440	66.41	10.17	24.27	21.83	56.45	56.44	53.82
RT	227.12	75.89	0.71	8.29	32.83	18.05	353	2157	4210	33.59	89.83	75.73	78.17	43.55	43.56	46.18
Calc. head	299.29	100.00	1.60	7.00	32.89	17.53	614	3758	6918	100	100	100	100	100	100	100
Meas. head	300		1.80	6.83	32.40	15.54	609	4028	7201							

Data for bench flotation test T6

1st stage	Grinding		
mill type	rod mill	**rods weight**	4109 g
harge	306.4 g	**rotational speed**	74 rpm
grind P_{80}	53 µm	**grinding time**	21 min
solids	50 wt%	**pH**	natural

2nd stage	Conditioning and floating											
operation stage	operation time (min)		Reagents (g/t)				Data					
	Conditioning	Floating	Na_2CO_3	Na_2SiF_6	Pionera 220	Betacol	pH	Temp (°C)	Solids (wt%)	Agitator speed (rpm)	Air flow rate (L/min)	Paddle rate
Condition1	60		7000	250			10.61	58	50	1200		
Condition2	60				2500		10.20	58	50	1200		
Condition3	60					120	10.02	58	50	1200		
Rougher Conc 1		3					9.97	58	20	1200	2-5	1/15 s
Rougher Conc 2	2	3				60	9.90	58	20	1200	2-5	1/15 s
Rougher Conc 3	4	6					9.86	58	20	1200	5	1/30 s

3rd stage	Grade, recovery and mass pull															
products	Mass (g)	Mass (wt%)	Grade							Recovery						
			P_2O_5	SiO_2	CaO	Fe_2O_3	Y_2O_3	La_2O_3	Ce_2O_3	P_2O_5	SiO_2	CaO	Fe_2O_3	Y_2O_3	La_2O_3	Ce_2O_3
			(wt%)				(ppm)			(%)						
RC1	33.43	11.00	5.32	3.42	35.67	13.30	1542	8401	15210	35.79	5.44	12.40	8.02	28.28	27.15	25.90
RC2	50.13	16.49	3.48	2.44	42.26	12.14	1156	6018	11757	35.09	5.82	22.02	10.97	31.79	29.16	30.02
RC3	1.25	0.41	2.51	2.60	24.21	13.96	974	3241	6907	0.63	0.15	0.31	0.31	0.67	0.39	0.44
calc. RC	84.81	27.90	4.19	2.83	39.40	12.63	1305	6916	13046	71.51	11.42	34.73	19.30	60.73	56.70	56.35
RT	219.12	72.10	0.65	8.49	28.66	20.43	327	2044	3911	28.49	88.58	65.27	80.70	39.27	43.30	43.65
Calc. head	303.93	100.00	1.64	6.91	31.65	18.25	600	3404	6460	100	100	100	100	100	100	100
Meas. head	300		1.80	6.83	32.40	15.54	609	4028	7201							

Data for bench flotation test T7

1st stage	Grinding		
mill type	rod mill	**rods weight**	4109 g
charge	292 g	**rotational speed**	74 rpm
grind P_{80}	53 µm	**grinding time**	21 min
solids	50 wt%	**pH**	natural

2nd stage	Conditioning and floating											
operation stage	operation time (min)		Reagents (g/t)				Data					
	Conditioning	Floating	Na_2CO_3	Na_2SiF_6	Pionera 220	Betacol	pH	Temp (°C)	Solids (wt%)	Agitator speed (rpm)	Air flow rate (L/min)	Paddle rate
Condition1	60		7000	250			10.61	58	50	1200		
Condition2	60				2500		10.23	58	50	1200		
Condition3	60					120	10.10	58	50	1200		
Rougher Conc 1		3					9.99	58	20	1200	2-5	1/15 s
Rougher Conc 2	2	3				60	9.94	58	20	1200	2-5	1/15 s
Rougher Conc 3	4	6					9.89	58	20	1200	5	1/30 s

3rd stage		Grade, recovery and mass pull													
products	Mass (g)	Mass (wt%)	Grade							Recovery						
			P_2O_5	SiO_2	CaO	Fe_2O_3	Y_2O_3	La_2O_3	Ce_2O_3	P_2O_5	SiO_2	CaO	Fe_2O_3	Y_2O_3	La_2O_3	Ce_2O_3
			(wt%)				(ppm)			(%)						
RC1	41.3	14.25	5.89	3.28	38.21	11.93	1610	8941	15467	47.62	6.64	17.17	6.64	35.88	31.70	30.36
RC2	60.91	21.01	2.72	2.19	40.46	13.34	1073	7060	13081	32.44	6.53	26.81	6.53	35.27	36.92	37.87
RC3	1.71	0.59	2.61	3.06	27.18	15.90	955	4307	7941	0.71	0.26	0.38	0.26	0.72	0.63	0.65
calc. RC	103.92	35.85	3.98	2.63	39.34	12.82	1285	7762	13944	80.93	13.43	44.48	13.43	72.03	69.25	68.88
RT	185.97	64.15	0.52	9.49	27.44	21.31	279	1926	3521	19.07	86.57	55.52	86.57	27.97	30.75	31.12
Calc. head	289.89	100.00	1.76	7.03	31.71	18.27	639	4018	7258	100	100	100	100	100	100.00	100
Meas. head	300		1.80	6.83	32.40	15.54	609	4028	7201							

Data for bench flotation test T8

1st stage	Grinding		
mill type	rod mill	**rods weight**	4109 g
charge	299.0 g	**rotational speed**	74 rpm
grind P_{80}	53 µm	**grinding time**	21 min
solids	50 wt%	**pH**	natural

2nd stage	Conditioning and floating												
Operating stage	Operating time (min)		Reagents (g/t)				Data						
	Conditioning	Floating	Na_2CO_3	Na_2SiF_6	Pionera 220	Betacol	pH	Temp (°C)	Solids (wt%)	Agitator speed (rpm)	Air flow rate (L/min)	Paddle rate	Cell volume (dm^3)
Condition1	30		4000	250			10.22	58	50	1200			1.5
Condition2	30				2500		9.72	58	50	1200			1.5
Condition3	30					120	9.62	58	50	1200			1.5
Rougher Conc1		3					9.40	58	20	1200	2-5	1/15 s	1.5
Rougher Conc2	2	3				60	9.34	58	20	1200	2-5	1/15 s	1.5
Rougher Conc3	4	6					9.30	58	20	1200	5	1/30 s	1.5

3rd stage		Grade, recovery and mass pull																										
Products	Mass (g)	Mass (wt%)	Grade																									
			P_2O_5	SiO_2	CaO	Fe_2O_3	SrO	BaO	Y_2O_3	La_2O_3	Ce_2O_3	Pr_2O_3	Nd_2O_3	Sm_2O_3	Eu_2O_3	Gd_2O_3	Tb_2O_3	Dy_2O_3	Ho_2O_3	Er_2O_3	Tm_2O_3	Yb_2O_3	Lu_2O_3	ThO_2	UO_2	TREO
			(wt%)						(ppm)																			(wt%)
RC1	62.17	20.92	4.87	2.87	38.05	13.05	2.08	1.18	1479	9693	17079	1615	5416	772	211	503	61	293	48	113	14	74	10	646	13	3.74
RC2	21.99	7.40	2.95	2.82	29.88	21.07	1.57	0.77	1290	9637	17103	1604	5411	758	204	482	57	269	43	99	12	63	9	679	18	3.70
RC3	3.58	1.20	0.99	3.23	32.04	19.25	0.87	0.63	676	4839	9790	917	3119	428	115	266	31	142	22	53	7	38	5	393	13	2.04
Calc. RC	87.74	29.53	4.23	2.87	35.76	15.31	1.90	1.05	1399	9481	16788	1584	5321	754	205	488	59	281	46	107	13	69	10	644	14	3.7
RT	209.37	70.47	0.54	8.27	31.79	19.36	0.79	0.74	279	1807	3269	348	1163	160	43	99	12	55	9	23	3	21	3	154	8	0.73
Calc. head	297.11	100.00	1.63	6.68	32.96	18.17	1.12	0.83	609	4073	7261	713	2391	335	91	214	25	122	20	48	6	35	5	298	10	1.60
Meas. head	300		1.80	6.83	32.40	15.54	1.16	0.87	609	4028	7201	721	2438	341	93	217	25	124	20	49	6	37	5	318	11	1.59

Products	Mass (g)	Mass (wt%)	Recovery (%)																									
			P_2O_5	SiO_2	CaO	Fe_2O_3	SrO	BaO	Y_2O_3	La_2O_3	Ce_2O_3	Pr_2O_3	Nd_2O_3	Sm_2O_3	Eu_2O_3	Gd_2O_3	Tb_2O_3	Dy_2O_3	Ho_2O_3	Er_2O_3	Tm_2O_3	Yb_2O_3	Lu_2O_3	ThO_2	UO_2	TREO
RC1	62.17	20.92	62.56	9.00	24.16	15.03	38.90	29.58	50.79	49.80	49.22	47.43	47.40	48.15	48.61	49.16	49.94	50.27	49.78	49.15	47.06	43.37	39.92	45.27	26.60	49.04
RC2	21.99	7.40	13.43	3.12	6.71	8.58	10.41	6.84	15.67	17.51	17.43	16.65	16.75	16.72	16.61	16.65	16.44	16.34	15.94	15.27	14.17	13.17	12.24	16.83	12.81	17.19
RC3	3.58	1.20	0.73	0.58	1.17	1.28	0.94	0.90	1.34	1.43	1.62	1.55	1.57	1.54	1.52	1.50	1.44	1.40	1.35	1.32	1.28	1.29	1.26	1.59	1.57	1.54
Calc. RC	87.74	29.53	76.72	12.71	32.04	24.89	50.25	37.32	67.79	68.74	68.27	65.63	65.72	66.41	66.74	67.31	67.82	68.01	67.07	65.74	62.51	57.83	53.41	63.68	40.98	67.77
RT	209.37	70.47	23.28	87.29	67.96	75.11	49.75	62.68	32.21	31.26	31.73	34.37	34.28	33.59	33.26	32.69	32.18	31.99	32.93	34.26	37.49	42.17	46.59	36.32	59.02	32.23
Calc. head	297.11	100.00	100	100	100	100	100	100	100	100	100	100	100	100	100	100	100	100	100	100	100	100	100	100	100	100

Data for bench flotation test T9

1st stage	Grinding		
mill type	rod mill	**rods weight**	4109 g
charge	296.5 g	**rotational speed**	74 rpm
grind P_{80}	53 µm	**grinding time**	21 min
solids	50 wt%	**pH**	natural

2nd stage	Conditioning and floating												
Operating stage	Operating time (min)		Reagents (g/t)				Data						
	Conditioning	Floating	Na_2CO_3	Na_2SiF_6	Pionera 220	Betacol	pH	Temp (°C)	Solids (wt%)	Agitator speed (rpm)	Air flow rate (L/min)	Paddle rate	Cell volume (dm^3)
Condition1	10		4000	250			10.28	58	50	1200			1.5
Condition2	10				2500		9.95	58	50	1200			1.5
Condition3	10					120	9.80	58	50	1200			1.5
Rougher Conc1		3					9.65	58	20	1200	2-5	1/15 s	1.5
Rougher Conc2	2	3				60	9.56	58	20	1200	2-5	1/15 s	1.5
Rougher Conc3	4	6					9.49	58	20	1200	5	1/30 s	1.5

3rd stage		Grade, recovery and mass pull																										
Products	Mass (g)	Mass (wt%)	Grade																									
			P_2O_5	SiO_2	CaO	Fe_2O_3	SrO	BaO	Y_2O_3	La_2O_3	Ce_2O_3	Pr_2O_3	Nd_2O_3	Sm_2O_3	Eu_2O_3	Gd_2O_3	Tb_2O_3	Dy_2O_3	Ho_2O_3	Er_2O_3	Tm_2O_3	Yb_2O_3	Lu_2O_3	ThO_2	UO_2	TREO
			(wt%)						(ppm)																			(wt%)
RC1	86.54	29.57	4.19	2.49	39.98	11.93	1.96	1.05	1367	9654	16824	1524	5095	714	195	468	56	268	44	103	12	68	9	605	11	3.64
RC2	26.09	8.91	1.51	2.60	33.50	20.30	1.46	0.70	853	6209	12953	1179	3965	544	146	339	39	178	28	65	8	44	6	497	12	2.66
RC3	4.05	1.38	0.88	2.31	31.72	18.62	1.00	0.57	583	4248	8938	825	2789	383	102	236	27	122	19	44	6	34	5	292	11	1.84
Calc. RC	116.68	39.86	3.48	2.51	38.24	14.03	1.82	0.95	1225	8696	15684	1423	4762	665	181	431	51	243	39	92	11	61	9	570	11	3.4
RT	176.02	60.14	0.31	8.85	28.24	21.38	0.60	0.72	204	1222	2204	237	794	109	29	66	8	39	7	18	3	18	3	107	9	0.50
Calc. head	292.7	100	1.58	6.32	32.23	18.45	1.09	0.81	611	4201	7578	710	2376	330	89	212	25	120	20	47	6	35	5	292	10	1.64
Meas. head	300		1.80	6.83	32.40	15.54	1.16	0.87	609	4028	7201	721	2438	341	93	217	25	124	20	49	6	37	5	318	11	1.59

Products	Mass (g)	Mass (wt%)	Recovery (%)																									
			P_2O_5	SiO_2	CaO	Fe_2O_3	SrO	BaO	Y_2O_3	La_2O_3	Ce_2O_3	Pr_2O_3	Nd_2O_3	Sm_2O_3	Eu_2O_3	Gd_2O_3	Tb_2O_3	Dy_2O_3	Ho_2O_3	Er_2O_3	Tm_2O_3	Yb_2O_3	Lu_2O_3	ThO_2	UO_2	TREO
RC1	86.54	29.57	78.69	11.66	36.67	19.11	53.37	38.24	66.18	67.94	65.64	63.49	63.40	63.94	64.52	65.34	65.88	66.02	65.87	64.16	60.95	57.20	53.35	61.33	33.58	65.76
RC2	26.09	8.91	8.53	3.67	9.26	9.81	11.94	7.67	12.46	13.17	15.24	14.81	14.87	14.69	14.56	14.27	13.84	13.24	12.60	12.15	11.58	11.15	10.81	15.19	11.43	14.46
RC3	4.05	1.38	0.77	0.50	1.36	1.40	1.27	0.97	1.32	1.40	1.63	1.61	1.62	1.60	1.58	1.54	1.48	1.41	1.34	1.30	1.32	1.32	1.33	1.38	1.51	1.55
Calc. RC	116.68	39.86	87.99	15.83	47.30	30.32	66.58	46.88	79.95	82.51	82.51	79.91	79.90	80.23	80.66	81.16	81.19	80.67	79.82	77.61	73.85	69.67	65.49	77.91	46.51	81.78
RT	176.02	60.13	12.01	84.17	52.70	69.68	33.42	53.12	20.05	17.49	17.49	20.09	20.10	19.77	19.34	18.84	18.81	19.33	20.18	22.39	26.15	30.33	34.51	22.09	53.49	18.22
Calc. head	292.7	100	100	100	100	100	100	100	100	100	100	100	100	100	100	100	100	100	100	100	100	100	100	100	100	100

Data for bench flotation test T10

1st stage	Grinding		
mill type	rod mill	**rods weight**	4109 g
charge	299.4 g	**rotational speed**	74 rpm
grind P_{80}	53 µm	**grinding time**	21 min
solids	50 wt%	**pH**	natural

2nd stage	Conditioning and floating												
Operating stage	Operating time (min)		Reagents (g/t)				Data						
	Conditioning	Floating	Na_2CO_3	Na_2SiF_6	Pionera 220	Betacol	pH	Temp (°C)	Solids (wt%)	Agitator speed (rpm)	Air flow rate (L/min)	Paddle rate	Cell volume (dm^3)
Condition1	30		7000	250			10.60	58	50	1200			1.5
Condition2	30				2500		10.31	58	50	1200			1.5
Condition3	30					120	10.20	58	50	1200			1.5
Rougher Conc1		3					10.10	58	20	1200	2-5	1/15 s	1.5
Rougher Conc2	2	3				60	10.03	58	20	1200	2-5	1/15 s	1.5
Rougher Conc3	4	6					9.98	58	20	1200	5	1/30 s	1.5

3rd stage		Grade, recovery and mass pull																										
Products	Mass (g)	Mass (wt%)	Grade																									
			P_2O_5	SiO_2	CaO	Fe_2O_3	SrO	BaO	Y_2O_3	La_2O_3	Ce_2O_3	Pr_2O_3	Nd_2O_3	Sm_2O_3	Eu_2O_3	Gd_2O_3	Tb_2O_3	Dy_2O_3	Ho_2O_3	Er_2O_3	Tm_2O_3	Yb_2O_3	Lu_2O_3	ThO_2	UO_2	TREO
			(wt%)						(ppm)																			(wt%)
RC1	55.42	18.70	4.08	2.96	37.43	12.93	2.16	0.71	1232	8212	14506	1363	4621	641	170	421	49	243	39	94	12	62	8	575	17	3.17
RC2	66.8	22.54	2.61	2.26	41.06	12.96	1.63	0.56	907	5956	11181	1093	3647	506	137	325	39	184	30	71	9	51	7	448	9	2.41
RC3	1.46	0.49	2.33	3.17	24.96	16.15	1.08	0.76	1038	5622	10525	1065	3620	520	145	349	43	209	35	83	10	57	8	228	12	2.33
Calc. RC	123.68	41.73	3.26	2.58	39.24	12.98	1.86	0.63	1054	6963	12663	1214	4083	566	152	369	43	211	34	81	10	56	8	503	13	2.8
RT	172.71	58.27	0.63	9.94	26.15	21.76	0.61	1.07	306	2318	4134	440	1475	203	53	125	14	66	10	26	3	21	3	155	10	0.92
Calc. head	296.39	100.00	1.73	6.87	31.61	18.10	1.13	0.89	618	4256	7693	763	2563	355	95	226	26	126	20	49	6	36	5	300	11	1.68
Meas. head	300		1.80	6.83	32.40	15.54	1.16	0.87	609	4028	7201	721	2438	341	93	217	25	124	20	49	6	37	5	318	11	1.59

Products	Mass (g)	Mass (wt%)	Recovery (%)																									
			P_2O_5	SiO_2	CaO	Fe_2O_3	SrO	BaO	Y_2O_3	La_2O_3	Ce_2O_3	Pr_2O_3	Nd_2O_3	Sm_2O_3	Eu_2O_3	Gd_2O_3	Tb_2O_3	Dy_2O_3	Ho_2O_3	Er_2O_3	Tm_2O_3	Yb_2O_3	Lu_2O_3	ThO_2	UO_2	TREO
RC1	55.42	18.70	44.14	8.05	22.14	13.36	35.74	14.90	37.27	36.08	35.26	33.42	33.71	33.79	33.66	34.79	34.88	36.06	36.02	35.95	36.04	32.42	29.62	35.82	28.15	35.17
RC2	66.8	22.54	34.03	7.42	29.27	16.14	32.43	14.19	33.06	31.54	32.75	32.31	32.06	32.12	32.74	32.39	33.04	32.83	33.13	32.63	31.49	32.06	32.05	33.66	17.48	32.31
RC3	1.46	0.49	0.67	0.22	0.39	0.44	0.47	0.42	0.83	0.65	0.67	0.69	0.70	0.72	0.76	0.76	0.80	0.82	0.84	0.84	0.80	0.78	0.75	0.37	0.53	0.68
Calc. RC	123.68	41.73	78.84	15.69	51.80	29.94	68.64	29.51	71.15	68.27	68.68	66.41	66.47	66.64	67.16	67.94	68.72	69.71	69.99	69.42	68.32	65.27	62.42	69.86	46.17	68.17
RT	172.71	58.27	21.16	84.31	48.20	70.06	31.36	70.49	28.85	31.73	31.32	33.59	33.53	33.36	32.84	32.06	31.28	30.29	30.01	30.58	31.68	34.73	37.58	30.14	53.83	31.83
Calc. head	292.7	100	100	100	100	100	100	100	100	100	100	100	100	100	100	100	100	100	100	100	100	100	100	100	100	100

Data for bench flotation test T11

1st stage	Grinding		
mill type	rod mill	**rods weight**	4109 g
charge	298.0 g	**rotational speed**	74 rpm
grind P_{80}	53 µm	**grinding time**	21 min
solids	50 wt%	**pH**	natural

2nd stage	Conditioning and floating												
Operating stage	Operating time (min)		Reagents (g/t)				Data						
	Conditioning	Floating	Na_2CO_3	Na_2SiF_6	Pionera 220	Betacol	pH	Temp (°C)	Solids (wt%)	Agitator speed (rpm)	Air flow rate (L/min)	Paddle rate	Cell volume (dm^3)
Condition1	10		7000	250			10.64	58	50	1200			1.5
Condition2	10				2500		10.40	58	50	1200			1.5
Condition3	10					120	10.30	58	50	1200			1.5
Rougher Conc1		3					10.22	58	20	1200	2-5	1/15 s	1.5
Rougher Conc2	2	3				60	10.14	58	20	1200	2-5	1/15 s	1.5
Rougher Conc3	4	6					10.09	58	20	1200	5	1/30 s	1.5

3rd stage		Grade, recovery and mass pull																										
Products	Mass (g)	Mass (wt%)	Grade																									
			P_2O_5	SiO_2	CaO	Fe_2O_3	SrO	BaO	Y_2O_3	La_2O_3	Ce_2O_3	Pr_2O_3	Nd_2O_3	Sm_2O_3	Eu_2O_3	Gd_2O_3	Tb_2O_3	Dy_2O_3	Ho_2O_3	Er_2O_3	Tm_2O_3	Yb_2O_3	Lu_2O_3	ThO_2	UO_2	TREO
			(wt%)						(ppm)																			(wt%)
RC1	78.25	52.54	3.74	2.76	38.29	12.18	2.03	0.73	1171	6290	12039	1171	3934	561	156	378	46	228	38	92	11	63	9	475	10	2.62
RC2	67.56	45.36	1.82	2.17	39.73	13.77	1.45	0.62	748	5179	10016	959	3201	439	118	278	32	152	24	58	7	43	6	389	8	2.13
RC3	1.33	0.89	1.17	3.57	22.36	17.02	0.76	0.88	643	4239	8220	794	2670	369	99	235	28	131	21	51	6	37	5	281	12	1.75
Calc. RC	147.14	49.92	2.84	2.50	38.81	12.96	1.75	0.68	972	5761	11076	1070	3586	504	138	331	40	193	32	76	9	54	8	434	9	2.4
RT	147.6	50.08	0.53	11.45	23.21	23.17	0.53	0.73	252	1934	3462	369	1226	168	44	100	11	54	9	21	3	18	3	139	11	0.77
Calc. head	294.74	100.00	1.68	6.98	30.99	18.07	1.14	0.71	611	3844	7263	719	2404	336	91	215	26	123	20	49	6	36	5	286	10	1.57
Meas. head	300		1.80	6.83	32.40	15.54	1.16	0.87	609	4028	7201	721	2438	341	93	217	25	124	20	49	6	37	5	318	11	1.59

Products	Mass (g)	Mass (wt%)	Recovery (%)																									
			P_2O_5	SiO_2	CaO	Fe_2O_3	SrO	BaO	Y_2O_3	La_2O_3	Ce_2O_3	Pr_2O_3	Nd_2O_3	Sm_2O_3	Eu_2O_3	Gd_2O_3	Tb_2O_3	Dy_2O_3	Ho_2O_3	Er_2O_3	Tm_2O_3	Yb_2O_3	Lu_2O_3	ThO_2	UO_2	TREO
RC1	78.25	52.54	59.16	10.51	32.80	17.90	47.28	27.50	50.83	43.43	44.01	43.22	43.44	44.43	45.44	46.59	48.06	49.22	50.30	49.99	48.99	46.50	44.31	44.07	25.66	44.14
RC2	67.56	45.36	24.85	7.13	29.38	17.47	29.19	19.99	28.04	30.88	31.61	30.56	30.52	30.01	29.81	29.63	29.01	28.36	27.59	27.50	27.23	27.45	27.71	31.16	18.22	30.95
RC3	1.33	0.89	0.31	0.23	0.33	0.42	0.30	0.56	0.47	0.50	0.51	0.50	0.50	0.50	0.49	0.49	0.49	0.48	0.48	0.47	0.47	0.46	0.45	0.44	0.53	0.50
Calc. RC	147.14	49.92	84.32	17.87	62.51	35.79	76.77	48.05	79.34	74.81	76.13	74.28	74.46	74.93	75.75	76.71	77.55	78.05	78.37	77.97	76.68	74.41	72.46	75.67	44.41	75.59
RT	147.6	50.08	15.68	82.13	37.49	64.21	23.23	51.95	20.66	25.19	23.87	25.72	25.54	25.07	24.25	23.29	22.45	21.95	21.63	22.03	23.32	25.59	27.54	24.33	55.59	24.41
Calc. head	294.74	100.00	100	100	100	100	100	100	100	100	100	100	100	100	100	100	100	100	100	100	100	100	100	100	100	100

Data for bench flotation test T12

1st stage	Grinding		
mill type	rod mill	**rods weight**	4109 g
charge	298.0 g	**rotational speed**	74 rpm
grind P_{80}	38 µm	**grinding time**	26 min
solids	50 wt%	**pH**	natural

2nd stage	Conditioning and floating												
Operating stage	Operating time (min)		Reagents (g/t)				Data						
	Conditioning	Floating	Na_2CO_3	Na_2SiF_6	Pionera 220	Betacol	pH	Temp (°C)	Solids (wt%)	Agitator speed (rpm)	Air flow rate (L/min)	Paddle rate	Cell volume (dm^3)
Condition1	60		4000	250			10.30	58	50	1200			1.5
Condition2	60				2500		10.10	58	50	1200			1.5
Condition3	60					120	9.98	58	50	1200			1.5
Rougher Conc1		3					9.87	58	20	1200	1.5	1/15 s	1.5
Rougher Conc2	2	3				60	9.77	58	20	1200	1.5-2.5	1/15 s	1.5
Rougher Conc3	4	6					9.72	58	20	1200	5	1/30 s	1.5

3rd stage		Grade, recovery and mass pull																										
Products	Mass (g)	Mass (wt%)	Grade																									
			P_2O_5	SiO_2	CaO	Fe_2O_3	SrO	BaO	Y_2O_3	La_2O_3	Ce_2O_3	Pr_2O_3	Nd_2O_3	Sm_2O_3	Eu_2O_3	Gd_2O_3	Tb_2O_3	Dy_2O_3	Ho_2O_3	Er_2O_3	Tm_2O_3	Yb_2O_3	Lu_2O_3	ThO_2	UO_2	TREO
			(wt%)						(ppm)																			(wt%)
RC1	36.17	12.61	6.09	3.18	38.46	12.42	2.32	1.89	1719	10281	17959	1791	6117	884	258	685	69	366	59	144	19	98	13	731	20	4.05
RC2	17.72	6.18	4.99	2.76	26.25	20.14	1.44	1.82	1595	8649	15219	1579	5396	778	219	537	66	330	55	131	16	84	11	566	24	3.47
RC3	5.03	1.75	1.56	3.01	29.73	20.95	0.92	1.37	711	4714	8528	887	3031	427	115	274	32	156	25	60	7	43	6	237	16	1.90
Calc. RC	58.92	20.54	5.37	3.04	34.04	15.47	1.94	1.83	1596	9315	16329	1650	5637	813	234	606	65	337	55	133	17	89	12	639	21	3.7
RT	227.87	79.46	0.78	8.17	31.50	19.11	0.99	0.78	348	2511	4470	477	1611	219	59	139	15	75	12	30	4	25	4	136	9	1.00
Calc. head	286.79	100.00	1.73	7.11	32.02	18.36	1.18	1.00	604	3908	6906	718	2438	341	95	235	25	129	21	51	7	38	6	239	12	1.55
Meas. head	300		1.80	6.83	32.40	15.54	1.16	0.87	609	4028	7201	721	2438	341	93	217	25	124	20	49	6	37	5	318	11	1.59

Products	Mass (g)	Mass (wt%)	Recovery (%)																							
			P_2O_5	SiO_2	CaO	Fe_2O_3	SrO	BaO	Y_2O_3	La_2O_3	Ce_2O_3	Pr_2O_3	Nd_2O_3	Sm_2O_3	Eu_2O_3	Gd_2O_3	Tb_2O_3	Dy_2O_3	Ho_2O_3	Er_2O_3	Tm_2O_3	Yb_2O_3	Lu_2O_3	ThO_2	UO_2	TREO
RC1	36.17	12.61	44.51	5.64	15.15	8.53	24.81	23.94	35.89	33.17	32.79	31.45	31.64	32.67	34.26	36.84	34.50	35.83	35.54	35.30	35.95	32.22	29.90	38.51	21.58	32.87
RC2	17.72	6.18	17.85	2.40	5.07	6.78	7.51	11.32	16.30	13.67	13.62	13.58	13.67	14.08	14.22	14.14	16.15	15.84	16.13	15.79	14.43	13.56	12.36	14.61	12.47	13.80
RC3	5.03	1.75	1.59	0.75	1.63	2.00	1.37	2.41	2.06	2.12	2.17	2.16	2.18	2.19	2.12	2.05	2.20	2.12	2.10	2.04	1.94	1.95	1.88	1.74	2.34	2.15
Calc. RC	58.92	20.54	63.95	8.78	21.84	17.31	33.69	37.66	54.25	48.96	48.58	47.19	47.49	48.95	50.60	53.03	52.85	53.79	53.78	53.13	52.32	47.73	44.14	54.86	36.40	48.82
RT	227.87	79.46	36.05	91.22	78.16	82.69	66.31	62.34	45.75	51.04	51.42	52.81	52.51	51.05	49.40	46.97	47.15	46.21	46.22	46.87	47.68	52.27	55.86	45.14	63.60	51.18
Calc. head	294.74	100.00	100	100	100	100	100	100	100	100	100	100	100	100	100	100	100	100	100	100	100	100	100	100	100	100

Data for bench flotation test T12 (Duplicate)

1st stage	Grinding		
mill type	rod mill	**rods weight**	4109 g
charge	304.2 g	**rotational speed**	74 rpm
grind P_{80}	38 µm	**grinding time**	26 min
solids	50 wt%	**pH**	natural

2nd stage	Conditioning and floating											
operation stage	operation time (min)		Reagents (g/t)				Data					
	Conditioning	Floating	Na_2CO_3	Na_2SiF_6	Pionera 220	Betacol	pH	Temp (°C)	Solids (wt%)	Agitator speed (rpm)	Air flow rate (L/min)	Paddle rate
Condition1	60		4000	250			10.5	58	50	1200		
Condition2	60				2500		10.3	58	50	1200		
Condition3	60					120	10.1	58	50	1200		
Rougher Conc 1		3					9.93	58	20	1200	1.5	1/15 s
Rougher Conc 2	2	3				60	9.84	58	20	1200	1.5-2.5	1/15 s
Rougher Conc 3	4	6					9.78	58	20	1200	5	1/30 s

3rd stage		Grade, recovery and mass pull													
products	Mass (g)	Mass (wt%)	Grade							Recovery						
			P_2O_5	SiO_2	CaO	Fe_2O_3	Y_2O_3	La_2O_3	Ce_2O_3	P_2O_5	SiO_2	CaO	Fe_2O_3	Y_2O_3	La_2O_3	Ce_2O_3
			(wt%)				(ppm)			(%)						
RC1	45	15.02	5.64	2.98	37.84	12.07	1610	9194	16894	48.23	6.66	18.05	10.13	41.82	36.05	35.94
RC2	21	7.01	5.01	2.85	25.76	18.73	1450	8117	15055	19.99	2.97	5.73	7.34	17.57	14.85	14.95
RC3	5.76	1.92	1.56	2.90	30.20	21.32	426	4370	7047	1.46	0.83	1.84	2.29	1.42	0.83	1.92
Calc. RC	71.76	23.95	5.11	2.94	33.69	14.76	1468	8492	15565	69.69	10.46	25.63	19.77	60.81	53.10	52.81
RT	227.87	76.05	0.70	7.91	30.79	18.87	298	2362	4380	30.31	89.54	74.37	80.23	39.19	46.90	47.19
Calc. head	299.63	100.00	1.76	6.72	31.48	17.89	578	3830	7059	100	100	100	100	100	100	100
Meas. head	300		1.80	6.83	32.40	15.54	609	4028	7201							

Data for bench flotation test T13

1st stage	Grinding		
mill type	rod mill	**rods weight**	4109 g
charge	300 g	**rotational speed**	74 rpm
grind P_{80}	53 µm	**grinding time**	21 min
solids	50 wt%	**pH**	8.5

2nd stage	Conditioning and floating												
Operating stage	Operating time (min)		Reagents (g/t)				Data						
	Conditioning	Floating	Na_2CO_3	Na_2SiF_6	Pionera 220	Betacol	pH	Temp (°C)	Solids (wt%)	Agitator speed (rpm)	Air flow rate (L/min)	Paddle rate	Cell volume (dm^3)
Condition1	60		500	250			8.5	60	50	1200			1.5
Condition2	60		667		2500		8.5	60	50	1200			1.5
Condition3	60		333			120	8.5	60	50	1200			1.5
Rougher Conc1		3					8.5	60	20	1200	1.5	1/15 s	1.5
Rougher Conc2	2	3				60	8.5	60	20	1200	1.5-2.5	1/15 s	1.5
Rougher Conc3	4	6					8.5	60	20	1200	5	1/30 s	1.5

3rd stage		Grade, recovery and mass pull																									
Products	Mass (g)	Mass (wt%)	Grade																								
			P_2O_5	SiO_2	CaO	Fe_2O_3	SrO	BaO	Y_2O_3	La_2O_3	Ce_2O_3	Pr_2O_3	Nd_2O_3	Sm_2O_3	Eu_2O_3	Gd_2O_3	Tb_2O_3	Dy_2O_3	Ho_2O_3	Er_2O_3	Tm_2O_3	Yb_2O_3	Lu_2O_3	ThO_2	UO_2	TREO
			(wt%)						(ppm)																		(wt%)
RC1	75.42	25.44	3.84	3.94	42.06	11.16	1.74	1.91	1398	8024	14936	1471	5062	718	197	483	59	291	48	116	14	82	11	654	15	3.29
RC2	61.38	20.70	1.73	3.71	39.81	13.82	1.48	1.00	748	4918	9250	913	3140	431	118	281	33	158	26	63	8	49	7	402	12	2.01
RC3	28.75	9.70	0.96	2.86	42.17	13.17	0.97	0.62	517	3114	5535	588	2036	283	77	187	22	111	18	46	7	40	7	273	10	1.26
Calc. RC	165.55	55.84	2.56	3.67	41.24	12.49	1.51	1.35	1004	6020	11195	1111	3824	536	147	357	43	211	35	85	11	62	9	495	13	2.5
RT	130.93	44.16	0.65	14.63	20.76	23.58	0.64	0.66	363	2789	5026	527	1805	247	66	153	18	82	14	32	4	26	4	257	15	1.12
Calc. head	296.48	100.00	1.71	8.51	32.20	17.39	1.12	1.04	721	4593	8470	853	2932	408	111	267	32	154	25	62	8	46	7	390	14	1.87
Meas. head	300		1.80	6.83	32.40	15.54	1.16	0.87	609	4028	7201	721	2438	341	93	217	25	124	20	49	6	37	5	318	11	1.59

Products	Mass (g)	Mass (wt%)	Recovery (%)																								
			P_2O_5	SiO_2	CaO	Fe_2O_3	SrO	BaO	Y_2O_3	La_2O_3	Ce_2O_3	Pr_2O_3	Nd_2O_3	Sm_2O_3	Eu_2O_3	Gd_2O_3	Tb_2O_3	Dy_2O_3	Ho_2O_3	Er_2O_3	Tm_2O_3	Yb_2O_3	Lu_2O_3	ThO_2	UO_2	TREO
RC1	75.42	25.44	56.99	11.79	33.23	16.33	39.38	46.62	49.34	44.44	44.85	43.87	43.91	44.71	45.16	46.01	47.11	48.17	48.11	48.11	46.52	45.06	41.88	42.70	26.80	44.79
RC2	61.38	20.70	20.85	9.03	25.60	16.45	27.23	19.74	21.48	22.17	22.61	22.17	22.17	21.84	21.98	21.83	21.30	21.31	21.11	21.30	20.80	22.00	22.14	21.36	18.34	22.31
RC3	28.75	9.70	5.43	3.26	12.70	7.34	8.39	5.76	6.95	6.58	6.34	6.69	6.73	6.73	6.72	6.78	6.87	6.97	7.10	7.32	8.01	8.48	9.64	6.79	6.70	6.53
Calc. RC	165.55	55.84	83.26	24.08	71.53	40.12	74.99	72.12	77.77	73.18	73.80	72.73	72.82	73.27	73.86	74.62	75.28	76.45	76.33	76.73	75.33	75.54	73.66	70.85	51.84	73.64
RT	130.93	44.16	16.74	75.92	28.47	59.88	25.01	27.88	22.23	26.82	26.20	27.27	27.18	26.73	26.14	25.38	24.72	23.55	23.67	23.27	24.67	24.46	26.34	29.15	48.16	26.36
Calc. head	296.48	100.00	100	100	100	100	100	100	100	100	100	100	100	100	100	100	100	100	100	100	100	100	100	100	100	100

Data for bench flotation test T14

1st stage	Grinding		
mill type	rod mill	**rods weight**	4109 g
charge	300 g	**rotational speed**	74 rpm
grind P_{80}	53 µm	**grinding time**	21 min
solids	50 wt%	**pH**	9.0

2nd stage	Conditioning and floating												
Operating stage	Operating time (min)		Reagents (g/t)				Data						
	Conditioning	Floating	Na_2CO_3	Na_2SiF_6	Pionera 220	Betacol	pH	Temp (°C)	Solids (wt%)	Agitator speed (rpm)	Air flow rate (L/min)	Paddle rate	Cell volume (dm^3)
Condition1	60		966	250			9.0	60	50	1200			1.5
Condition2	60		1066		2500		9.0	60	50	1200			1.5
Condition3	60		400			120	9.0	60	50	1200			1.5
Rougher Conc1		3					9.0	60	20	1200	1.5	1/15 s	1.5
Rougher Conc2	2	3				60	9.0	60	20	1200	1.5-2.5	1/15 s	1.5
Rougher Conc3	4	6					9.0	60	20	1200	5	1/30 s	1.5

3rd stage		Grade, recovery and mass pull																									
Products	Mass (g)	Mass (wt%)	Grade																								
			P_2O_5	SiO_2	CaO	Fe_2O_3	SrO	BaO	Y_2O_3	La_2O_3	Ce_2O_3	Pr_2O_3	Nd_2O_3	Sm_2O_3	Eu_2O_3	Gd_2O_3	Tb_2O_3	Dy_2O_3	Ho_2O_3	Er_2O_3	Tm_2O_3	Yb_2O_3	Lu_2O_3	ThO_2	UO_2	TREO
			(wt%)						(ppm)																		(wt%)
RC1	48.63	16.37	4.84	2.91	39.55	10.54	1.85	1.39	1444	10031	17588	1822	6063	844	235	549	65	314	50	122	14	78	10	781	15	3.92
RC2	47.38	15.95	2.63	2.53	35.11	13.86	1.74	1.45	1012	5980	10610	1108	3728	529	149	355	43	213	35	86	10	58	8	490	16	2.39
RC3	7.10	2.39	0.92	3.76	33.12	16.57	0.96	1.10	525	3238	5827	617	2135	298	81	194	23	113	18	46	6	38	6	296	14	1.32
Calc. RC	103.11	34.70	3.56	2.80	37.07	12.48	1.74	1.40	1182	7702	13572	1411	4719	661	185	435	52	254	41	100	11	66	9	614	15	3.0
RT	194.02	65.30	0.69	9.91	30.87	20.48	0.83	0.48	290	1816	3264	350	1180	165	45	105	12	61	10	26	3	22	3	165	8	0.74
Calc. head	297.13	100.00	1.68	7.44	33.02	17.70	1.15	0.80	600	3859	6841	718	2409	337	93	219	26	128	21	52	6	37	5	320	10	1.54
Meas. head	300		1.80	6.83	32.40	15.54	1.16	0.87	609	4028	7201	721	2438	341	93	217	25	124	20	49	6	37	5	318	11	1.59

Products	Mass (g)	Mass (wt%)	Recovery (%)																							
			P_2O_5	SiO_2	CaO	Fe_2O_3	SrO	BaO	Y_2O_3	La_2O_3	Ce_2O_3	Pr_2O_3	Nd_2O_3	Sm_2O_3	Eu_2O_3	Gd_2O_3	Tb_2O_3	Dy_2O_3	Ho_2O_3	Er_2O_3	Tm_2O_3	Yb_2O_3	Lu_2O_3	ThO_2	UO_2	TREO
RC1	48.63	16.37	47.10	6.41	19.60	9.74	26.48	28.49	39.43	42.55	42.08	41.53	41.20	40.92	41.10	40.99	40.96	40.22	40.10	38.62	37.95	33.85	33.18	39.86	23.72	41.83
RC2	47.38	15.95	24.94	5.43	16.96	12.49	24.20	28.89	26.92	24.71	24.73	24.59	24.68	24.98	25.44	25.77	26.45	26.62	26.83	26.59	26.60	24.76	24.60	24.38	25.23	24.85
RC3	7.10	2.39	1.30	1.21	2.40	2.24	1.99	3.30	2.09	2.00	2.04	2.05	2.12	2.11	2.07	2.11	2.12	2.11	2.14	2.12	2.47	2.43	2.72	2.21	3.19	2.05
Calc. RC	103.11	34.70	73.34	13.04	38.95	24.46	52.68	60.67	68.44	69.27	68.84	68.17	68.00	68.01	68.61	68.88	69.53	68.95	69.07	67.32	67.02	61.05	60.50	66.45	52.14	68.73
RT	194.02	65.30	26.66	86.96	61.05	75.54	47.32	39.33	31.56	30.73	31.16	31.83	32.00	31.99	31.39	31.12	30.47	31.05	30.93	32.68	32.98	38.95	39.50	33.55	47.86	31.27
Calc. head	296.48	100.00	100	100	100	100	100	100	100	100	100	100	100	100	100	100	100	100	100	100	100	100	100	100	100	100

Data for bench flotation test T15

1st stage	Grinding		
mill type	rod mill	**rods weight**	4109 g
charge	302 g	**rotational speed**	74 rpm
grind P_{80}	53 µm	**grinding time**	21 min
solids	50 wt%	**pH**	9.5

2nd stage	Conditioning and floating												
Operating stage	Operating time (min)		Reagents (g/t)				Data						
	Conditioning	Floating	Na_2CO_3	Na_2SiF_6	Pionera 220	Betacol	pH	Temp (°C)	Solids (wt%)	Agitator speed (rpm)	Air flow rate (L/min)	Paddle rate	Cell volume (dm^3)
Condition1	60		966	250			9.5	60	50	1200			1.5
Condition2	60		1066		2500		9.5	60	50	1200			1.5
Condition3	60		400			120	9.5	60	50	1200			1.5
Rougher Conc1		3					9.5	60	20	1200	1.5	1/15 s	1.5
Rougher Conc2	2	3				60	9.5	60	20	1200	1.5-2.5	1/15 s	1.5
Rougher Conc3	4	6					9.5	60	20	1200	5	1/30 s	1.5

3rd stage	Grade, recovery and mass pull																														
Products	Mass (g)	Mass (wt%)	Grade																												
			P_2O_5	Na_2O	MgO	Al_2O_3	SiO_2	K_2O	CaO	MnO	Fe_2O_3	SrO	BaO	Y_2O_3	La_2O_3	Ce_2O_3	Pr_2O_3	Nd_2O_3	Sm_2O_3	Eu_2O_3	Gd_2O_3	Tb_2O_3	Dy_2O_3	Ho_2O_3	Er_2O_3	Tm_2O_3	Yb_2O_3	Lu_2O_3	ThO_2	UO_2	TREO
			(wt%)											(ppm)																	(wt%)
RC1	73.57	24.56	5.65	0.11	0.74	1.08	2.36	0.10	40.87	1.42	9.00	2.38	1.00	1702	9605	17921	1662	6509	933	257	601	75	366	59	140	17	95	12	835	17	4.00
RC2	16.89	5.64	3.26	0.26	1.04	1.59	3.97	0.35	31.34	2.47	19.52	1.55	1.19	1246	7928	14876	1486	5424	801	203	460	55	264	41	99	12	66	9	721	20	3.30
RC3	2.47	0.82	1.54	0.40	1.14	2.05	5.35	0.28	34.22	2.41	18.06	0.95	0.89	636	3976	7414	757	2694	392	101	231	28	139	21	51	7	42	6	387	14	1.65
Calc. RC	92.93	31.02	5.11	0.15	0.81	1.20	2.73	0.15	38.96	1.64	11.15	2.19	1.03	1590	9151	17088	1606	6210	895	243	565	70	342	55	130	16	89	11	802	17	3.81
RT	206.62	68.98	0.38	0.07	1.72	2.87	8.65	1.99	31.94	2.51	17.68	0.73	0.82	258	1536	2659	290	1030	139	38	81	10	49	9	22	3	22	3	155	11	0.62
Calc.	299.55	100.00	1.84	0.09	1.44	2.35	6.81	1.42	34.12	2.24	15.66	1.18	0.89	671	3899	7135	698	2637	373	102	231	29	140	23	56	7	43	6	356	13	1.61
Meas.	300		1.80	0.10	1.41	2.38	6.83	1.37	32.40	2.24	15.54	1.16	0.87	609	4028	7201	721	2438	341	93	217	25	124	20	49	6	37	5	318	11	1.59

Products	Mass (g)	Mass (wt%)	Recovery (%)																												
			P_2O_5	Na_2O	MgO	Al_2O_3	SiO_2	K_2O	CaO	MnO	Fe_2O_3	SrO	BaO	Y_2O_3	La_2O_3	Ce_2O_3	Pr_2O_3	Nd_2O_3	Sm_2O_3	Eu_2O_3	Gd_2O_3	Tb_2O_3	Dy_2O_3	Ho_2O_3	Er_2O_3	Tm_2O_3	Yb_2O_3	Lu_2O_3	ThO_2	UO_2	TREO
RC1	73.57	24.56	75.30	29.31	12.70	11.32	8.50	1.79	29.42	15.58	14.12	49.41	27.72	62.26	60.51	61.69	58.44	60.62	61.42	62.00	63.86	63.69	64.34	62.28	61.91	58.65	54.53	51.24	57.63	31.27	61.14
RC2	16.89	5.64	9.98	15.65	4.10	3.82	3.28	1.37	5.18	6.22	7.03	7.37	7.59	10.46	11.47	11.75	12.00	11.60	12.10	11.22	11.23	10.76	10.65	9.90	10.00	9.55	8.68	8.63	11.42	8.60	11.58
RC3	2.47	0.82	0.69	3.54	0.65	0.72	0.65	0.17	0.83	0.89	0.95	0.66	0.82	0.78	0.84	0.86	0.89	0.84	0.87	0.82	0.82	0.81	0.82	0.75	0.76	0.79	0.80	0.85	0.90	0.91	0.85
Calc. RC	92.93	31.02	85.97	48.50	17.45	15.86	12.43	3.33	35.43	22.68	22.10	57.45	36.13	73.51	72.82	74.30	71.33	73.06	74.39	74.04	75.90	75.26	75.81	72.93	72.68	68.99	64.00	60.73	69.95	40.78	73.57
RT	206.62	68.98	14.03	51.50	82.55	84.14	87.57	96.67	64.57	77.32	77.90	42.55	63.87	26.49	27.18	25.70	28.67	26.94	25.61	25.96	24.10	24.74	24.19	27.07	27.32	31.01	36.00	39.27	30.05	59.22	26.43
Calc.	299.55	100.00	100	100	100	100	100	100	100	100	100	100	100	100	100	100	100	100	100	100	100	100	100	100	100	100	100	100	100	100	100

Data for bench flotation test T15 (Duplicate)

1st stage	Grinding		
mill type	rod mill	**rods weight**	4109 g
charge	302 g	**rotational speed**	74 rpm
grind P_{80}	53 µm	**grinding time**	21 min
solids	50 wt%	**pH**	9.5

2nd stage	Conditioning and floating												
Operating stage	Operating time (min)		Reagents (g/t)				Data						
	Conditioning	Floating	Na_2CO_3	Na_2SiF_6	Pionera 220	Betacol	pH	Temp (°C)	Solids (wt%)	Agitator speed (rpm)	Air flow rate (L/min)	Paddle rate	Cell volume (dm^3)
Condition1	60		2933	250			9.5	60	50	1200			1.5
Condition2	60		1033		2500		9.5	60	50	1200			1.5
Condition3	60		533			120	9.5	60	50	1200			1.5
Rougher Conc1		3					9.5	60	20	1200	1.5	1/15 s	1.5
Rougher Conc2	2	3	567			60	9.5	60	20	1200	1.5-2.5	1/15 s	1.5
Rougher Conc3	4	6					9.5	60	20	1200	5	1/30 s	1.5

3rd stage		Grade, recovery and mass pull																								
Products	Mass (g)	Mass (wt%)	Grade																							
			P_2O_5	SiO_2	CaO	Fe_2O_3	SrO	BaO	Y_2O_3	La_2O_3	Ce_2O_3	Pr_2O_3	Nd_2O_3	Sm_2O_3	Eu_2O_3	Gd_2O_3	Tb_2O_3	Dy_2O_3	Ho_2O_3	Er_2O_3	Tm_2O_3	Yb_2O_3	Lu_2O_3	ThO_2	UO_2	TREO
			(wt%)						(ppm)																	(wt%)
RC1	68.39	22.88	4.52	2.95	39.28	12.28	2.21	1.04	1516	10091	17659	1581	5317	754	207	496	59	290	47	113	13	74	10	684	13	3.82
RC2	20.39	6.82	3.63	2.47	34.63	19.06	2.06	1.02	1466	9609	16612	1590	5247	743	207	486	58	287	46	114	13	72	9	761	14	3.66
RC3	2.26	0.76	1.97	2.32	35.67	15.42	1.23	0.67	1024	7143	12808	1287	4385	612	166	394	45	219	35	81	10	56	8	528	13	2.83
Calc. RC	91.04	30.46	4.25	2.83	38.15	13.87	2.15	1.03	1493	9910	17304	1576	5278	748	206	491	59	288	47	112	13	73	10	698	13	3.76
RT	207.83	69.54	0.30	9.01	31.10	19.88	0.65	0.83	232	1593	2844	304	1019	142	37	85	9	46	7	20	2	18	2	151	9	0.64
Calc. head	298.87	100.00	1.50	7.13	33.24	18.05	1.10	0.89	616	4126	7249	692	2316	326	89	208	24	120	19	48	6	35	5	317	11	1.59
Meas. head	300		1.80	6.83	32.40	15.54	1.16	0.87	609	4028	7201	721	2438	341	93	217	25	124	20	49	6	37	5	318	11	1.59

Products	Mass (g)	Mass (wt%)	Recovery (%)																							
			P_2O_5	SiO_2	CaO	Fe_2O_3	SrO	BaO	Y_2O_3	La_2O_3	Ce_2O_3	Pr_2O_3	Nd_2O_3	Sm_2O_3	Eu_2O_3	Gd_2O_3	Tb_2O_3	Dy_2O_3	Ho_2O_3	Er_2O_3	Tm_2O_3	Yb_2O_3	Lu_2O_3	ThO_2	UO_2	TREO
RC1	68.39	22.88	68.73	9.47	27.04	15.56	45.78	26.68	56.35	55.96	55.75	52.33	52.53	52.87	53.56	54.43	55.60	55.42	56.28	53.99	54.99	48.49	48.98	49.33	28.12	55.09
RC2	20.39	6.82	16.47	2.37	7.11	7.20	12.70	7.83	16.25	15.89	15.63	15.68	15.45	15.52	15.97	15.91	16.31	16.33	16.35	16.17	15.63	14.06	13.55	16.37	9.28	15.71
RC3	2.26	0.76	0.99	0.24	0.81	0.65	0.84	0.57	1.26	1.31	1.34	1.41	1.43	1.42	1.41	1.43	1.41	1.38	1.36	1.28	1.32	1.21	1.25	1.26	0.89	1.35
Calc. RC	91.04	30.46	86.18	12.08	34.95	23.41	59.33	35.08	73.85	73.15	72.72	69.42	69.42	69.81	70.95	71.77	73.33	73.13	73.99	71.44	71.94	63.76	63.78	66.96	38.29	72.15
RT	207.83	69.54	13.82	87.92	65.05	76.59	40.67	64.92	26.15	26.85	27.28	30.58	30.58	30.19	29.05	28.23	26.67	26.87	26.01	28.56	28.06	36.24	36.22	33.04	61.71	27.85
Calc. head	296.48	100.00	100	100	100	100	100	100	100	100	100	100	100	100	100	100	100	100	100	100	100	100	100	100	100	100

Data for bench flotation test T16

1st stage	Grinding		
mill type	rod mill	**rods weight**	4109 g
charge	300 g	**rotational speed**	74 rpm
grind P_{80}	53 µm	**grinding time**	21 min
solids	50 wt%	**pH**	10.0

2nd stage	Conditioning and floating												
Operating stage	Operating time (min)		Reagents (g/t)				Data						
	Conditioning	Floating	Na_2CO_3	Na_2SiF_6	Pionera 220	Betacol	pH	Temp (°C)	Solids (wt%)	Agitator speed (rpm)	Air flow rate (L/min)	Paddle rate	Cell volume (dm^3)
Condition1	60		2333	250			10.0	60	50	1200			1.5
Condition2	60		2666		2500		10.0	60	50	1200			1.5
Condition3	60		667			120	10.0	60	50	1200			1.5
Rougher Conc1		3	2333				10.0	60	20	1200	1.5	1/15 s	1.5
Rougher Conc2	2	3				60	10.0	60	20	1200	1.5-2.5	1/15 s	1.5
Rougher Conc3	4	6					10.0	60	20	1200	5	1/30 s	1.5

3rd stage	Grade, recovery and mass pull																														
Products	Mass (g)	Mass (wt%)	Grade																												
			P_2O_5	Na_2O	MgO	Al_2O_3	SiO_2	K_2O	CaO	MnO	Fe_2O_3	SrO	BaO	Y_2O_3	La_2O_3	Ce_2O_3	Pr_2O_3	Nd_2O_3	Sm_2O_3	Eu_2O_3	Gd_2O_3	Tb_2O_3	Dy_2O_3	Ho_2O_3	Er_2O_3	Tm_2O_3	Yb_2O_3	Lu_2O_3	ThO_2	UO_2	TREO
			(wt%)											(ppm)																	(wt%)
RC1	44.15	14.85	7.30	0.18	0.81	1.33	3.28	0.07	39.65	1.52	9.96	2.81	0.68	1956	8538	15813	1586	5680	864	233	564	75	381	64	153	20	108	14	739	16	3.60
RC2	30.16	10.14	4.02	0.25	0.92	1.30	2.98	0.15	35.67	1.93	13.69	2.18	0.73	1549	10919	20381	1978	7010	1000	263	586	70	342	52	119	15	82	11	896	18	4.44
RC3	2.14	0.72	2.99	0.43	1.21	2.39	6.26	0.25	32.64	2.28	16.48	1.16	0.78	996	5923	10905	1101	3919	568	148	338	41	208	33	81	10	57	8	515	15	2.43
Calc. RC	76.45	25.72	5.89	0.22	0.86	1.35	3.25	0.11	37.88	1.70	11.61	2.51	0.70	1768	9404	17477	1727	6156	909	242	566	72	361	58	138	17	96	12	794	17	3.90
RT	220.84	74.28	0.44	0.08	1.63	2.82	8.38	1.80	32.40	2.43	16.90	0.72	0.93	307	2140	3678	406	1423	192	55	112	14	63	11	26	4	24	4	216	12	0.85
Calc.	297.29	100.00	1.84	0.12	1.43	2.44	7.06	1.37	33.81	2.24	15.54	1.18	0.87	683	4008	7226	746	2640	376	103	229	29	139	23	55	7	43	6	365	13	1.63
Meas.	300		1.80	0.10	1.41	2.38	6.83	1.37	32.40	2.24	15.54	1.16	0.87	609	4028	7201	721	2438	341	93	217	25	124	20	49	6	37	5	318	11	1.59

Products	Mass (g)	Mass (wt%)	Recovery (%)																												
			P_2O_5	Na_2O	MgO	Al_2O_3	SiO_2	K_2O	CaO	MnO	Fe_2O_3	SrO	BaO	Y_2O_3	La_2O_3	Ce_2O_3	Pr_2O_3	Nd_2O_3	Sm_2O_3	Eu_2O_3	Gd_2O_3	Tb_2O_3	Dy_2O_3	Ho_2O_3	Er_2O_3	Tm_2O_3	Yb_2O_3	Lu_2O_3	ThO_2	UO_2	TREO
RC1	44.15	14.85	58.90	23.82	8.39	8.07	6.90	0.80	17.42	10.07	9.51	35.29	11.52	42.52	31.63	32.50	31.58	31.95	34.09	33.56	36.60	38.18	40.61	40.79	41.35	39.94	37.57	34.72	30.08	18.77	32.81
RC2	30.16	10.14	22.15	21.86	6.49	5.42	4.29	1.15	10.70	8.72	8.94	18.71	8.51	23.01	27.64	28.61	26.91	26.94	26.94	25.89	25.98	24.32	24.90	22.66	22.11	20.76	19.50	19.05	24.92	14.12	27.60
RC3	2.14	0.72	1.17	2.71	0.61	0.71	0.64	0.13	0.69	0.73	0.76	0.71	0.65	1.05	1.06	1.09	1.06	1.07	1.09	1.04	1.06	1.02	1.08	1.02	1.06	0.98	0.97	0.94	1.02	0.84	1.07
Calc. RC	76.45	25.72	82.21	48.38	15.49	14.19	11.82	2.07	28.81	19.52	19.21	54.71	20.67	66.58	60.33	62.19	59.55	59.96	62.12	60.49	63.64	63.53	66.59	64.47	64.52	61.68	58.04	54.71	56.02	33.73	61.48
RT	220.84	74.28	17.79	51.62	84.51	85.81	88.18	97.93	71.19	80.48	80.79	45.29	79.33	33.42	39.67	37.81	40.45	40.04	37.88	39.51	36.36	36.47	33.41	35.53	35.48	38.32	41.96	45.29	43.98	66.27	38.52
Calc.	297.29	100.00	100	100	100	100	100	100	100	100	100	100	100	100	100	100	100	100	100	100	100	100	100	100	100	100	100	100	100	100	100

Data for bench flotation test T17

1st stage	Grinding		
mill type	rod mill	**rods weight**	4109 g
charge	300 g	**rotational speed**	74 rpm
grind P_{80}	53 µm	**grinding time**	21 min
solids	50 wt%	**pH**	10.5

2nd stage	Conditioning and floating												
Operating stage	Operating time (min)		Reagents (g/t)				Data						
	Conditioning	Floating	Na_2CO_3	Na_2SiF_6	Pionera 220	Betacol	pH	Temp (°C)	Solids (wt%)	Agitator speed (rpm)	Air flow rate (L/min)	Paddle rate	Cell volume (dm^3)
Condition1	60		8000	250			10.5	60	50	1200			1.5
Condition2	60		10000		2500		10.5	60	50	1200			1.5
Condition3	60		2000			120	10.5	60	50	1200			1.5
Rougher Conc1		3					10.5	60	20	1200	1.5	1/15 s	1.5
Rougher Conc2	2	3				60	10.5	60	20	1200	1.5-2.5	1/15 s	1.5
Rougher Conc3	4	6					10.5	60	20	1200	5	1/30 s	1.5

3rd stage		Grade, recovery and mass pull																									
Products	Mass (g)	Mass (wt%)	Grade																								
			P_2O_5	SiO_2	CaO	Fe_2O_3	SrO	BaO	Y_2O_3	La_2O_3	Ce_2O_3	Pr_2O_3	Nd_2O_3	Sm_2O_3	Eu_2O_3	Gd_2O_3	Tb_2O_3	Dy_2O_3	Ho_2O_3	Er_2O_3	Tm_2O_3	Yb_2O_3	Lu_2O_3	ThO_2	UO_2	TREO
			(wt%)						(ppm)																		(wt%)
RC1	21.07	7.12	1.61	3.02	27.90	16.46	1.92	0.78	637	4239	7648	792	2645	369	102	235	27	134	21	53	6	37	5	321	9	1.70
RC2	19.7	6.66	2.40	3.40	34.41	15.22	2.34	0.67	754	4244	7644	789	2633	375	104	247	30	151	25	63	7	44	6	329	8	1.71
RC3	3.49	1.18	1.35	3.64	26.99	16.95	0.95	0.92	646	4341	7672	807	2792	385	104	250	29	140	23	56	7	44	6	382	14	1.73
Calc. RC	44.26	14.96	1.94	3.24	30.73	15.95	2.03	0.74	690	4249	7648	792	2651	373	103	241	29	142	23	58	7	41	5	329	9	1.7
RT	251.58	85.04	1.38	7.49	30.06	17.83	0.95	0.88	564	3679	6690	678	2258	317	88	202	24	117	19	47	5	34	4	271	9	1.47
Calc. head	295.84	100.00	1.46	6.85	30.16	17.55	1.12	0.86	583	3764	6834	695	2317	325	90	208	24	121	19	49	5	35	5	279	9	1.51
Meas. head	300		1.80	6.83	32.40	15.54	1.16	0.87	609	4028	7201	721	2438	341	93	217	25	124	20	49	6	37	5	318	11	1.59

Products	Mass (g)	Mass (wt%)	Recovery (%)																								
			P_2O_5	SiO_2	CaO	Fe_2O_3	SrO	BaO	Y_2O_3	La_2O_3	Ce_2O_3	Pr_2O_3	Nd_2O_3	Sm_2O_3	Eu_2O_3	Gd_2O_3	Tb_2O_3	Dy_2O_3	Ho_2O_3	Er_2O_3	Tm_2O_3	Yb_2O_3	Lu_2O_3	ThO_2	UO_2	TREO
RC1	21.07	7.12	7.83	3.13	6.59	6.68	12.23	6.47	7.78	8.02	7.97	8.12	8.13	8.07	8.05	8.04	8.02	7.94	7.90	7.83	7.85	7.66	7.81	8.18	7.20	8.01
RC2	19.7	6.66	10.91	3.31	7.60	5.77	13.97	5.19	8.62	7.51	7.45	7.56	7.57	7.68	7.71	7.89	8.21	8.37	8.59	8.60	8.68	8.34	8.47	7.84	5.59	7.56
RC3	3.49	1.18	1.09	0.63	1.06	1.14	1.00	1.26	1.31	1.36	1.32	1.37	1.42	1.39	1.36	1.42	1.41	1.37	1.41	1.35	1.50	1.49	1.52	1.61	1.73	1.35
Calc. RC	44.26	14.96	19.83	7.07	15.24	13.60	27.21	12.92	17.70	16.89	16.74	17.05	17.12	17.14	17.12	17.35	17.64	17.68	17.90	17.78	18.03	17.48	17.80	17.63	14.52	16.92
RT	251.58	85.04	80.17	92.93	84.76	86.40	72.79	87.08	82.30	83.11	83.26	82.95	82.88	82.86	82.88	82.65	82.36	82.32	82.10	82.22	81.97	82.52	82.20	82.37	85.48	83.08
Calc. head	296.48	100.00	100	100	100	100	100	100	100	100	100	100	100	100	100	100	100	100	100	100	100	100	100	100	100	100

Data for bench flotation test T18

1st stage	Grinding		
mill type	rod mill	**rods weight**	4109 g
charge	295 g	**rotational speed**	74 rpm
grind P_{80}	53 µm	**grinding time**	21 min
solids	50 wt%	**pH**	9.5

2nd stage	Conditioning and floating												
Operating stage	Operating time (min)		Reagents (g/t)				Data						
	Conditioning	Floating	Na_2CO_3	Na_2SiF_6	Pionera 220	Betacol	pH	Temp (°C)	Solids (wt%)	Agitator speed (rpm)	Air flow rate (L/min)	Paddle rate	Cell volume (dm^3)
Condition1	60		1933	250			9.5	20	50	1200			1.5
Condition2	60		800		2500		9.5	20	50	1200			1.5
Condition3	60		167			120	9.5	20	50	1200			1.5
Rougher Conc1		3					9.5	20	20	1200	0.5	1/15 s	1.5
Rougher Conc2	2	3	267			60	9.5	20	20	1200	1.5	1/15 s	1.5
Rougher Conc3	4	6					9.5	20	20	1200	5	1/30 s	1.5

3rd stage		Grade, recovery and mass pull																									
Products	Mass (g)	Mass (wt%)	Grade																								
			P_2O_5	SiO_2	CaO	Fe_2O_3	SrO	BaO	Y_2O_3	La_2O_3	Ce_2O_3	Pr_2O_3	Nd_2O_3	Sm_2O_3	Eu_2O_3	Gd_2O_3	Tb_2O_3	Dy_2O_3	Ho_2O_3	Er_2O_3	Tm_2O_3	Yb_2O_3	Lu_2O_3	ThO_2	UO_2	TREO
			(wt%)						(ppm)																		(wt%)
RC1	59.91	20.50	4.62	2.70	36.54	15.12	1.76	1.38	1359	10238	17740	1639	5496	757	205	486	57	276	44	104	12	67	9	670	15	3.85
RC2	16.71	5.72	1.17	3.44	34.61	16.67	1.24	1.20	708	5563	11002	1012	3382	458	123	285	31	150	24	56	7	40	6	431	16	2.28
RC3	10.47	3.58	0.61	2.44	41.42	12.91	0.77	0.72	405	2608	5204	481	1621	221	59	139	15	79	13	33	5	30	5	202	10	1.09
Calc. RC	87.09	29.80	3.47	2.81	36.76	15.15	1.54	1.26	1119	8423	14940	1379	4624	635	172	405	47	228	37	86	10	57	8	568	14	3.2
RT	205.13	70.20	1.00	8.98	32.20	18.62	0.99	0.73	404	2324	4155	445	1500	210	57	134	15	80	13	33	4	27	4	193	8	0.94
Calc. head	292.22	100.00	1.74	7.14	33.56	17.59	1.16	0.89	617	4142	7370	723	2431	336	91	215	25	124	20	49	6	36	5	305	10	1.62
Meas. head	300		1.80	6.83	32.40	15.54	1.16	0.87	609	4028	7201	721	2438	341	93	217	25	124	20	49	6	37	5	318	11	1.59

Products	Mass (g)	Mass (wt%)	Recovery (%)																							
			P_2O_5	SiO_2	CaO	Fe_2O_3	SrO	BaO	Y_2O_3	La_2O_3	Ce_2O_3	Pr_2O_3	Nd_2O_3	Sm_2O_3	Eu_2O_3	Gd_2O_3	Tb_2O_3	Dy_2O_3	Ho_2O_3	Er_2O_3	Tm_2O_3	Yb_2O_3	Lu_2O_3	ThO_2	UO_2	TREO
RC1	59.91	20.50	54.52	7.76	22.33	17.62	31.21	31.85	45.14	50.67	49.35	46.46	46.34	46.11	46.16	46.26	47.23	45.65	45.15	43.62	41.43	38.37	35.33	45.08	30.06	48.74
RC2	16.71	5.72	3.85	2.75	5.90	5.42	6.14	7.76	6.56	7.68	8.54	8.00	7.96	7.79	7.68	7.56	7.27	6.91	6.72	6.52	6.41	6.39	6.49	8.08	8.84	8.07
RC3	10.47	3.58	1.27	1.12	4.42	2.63	2.38	2.91	2.35	2.26	2.53	2.38	2.39	2.35	2.32	2.31	2.23	2.28	2.33	2.44	2.70	3.03	3.39	2.37	3.53	2.42
Calc. RC	87.09	29.80	59.63	11.73	32.65	25.67	39.74	42.52	54.06	60.61	60.42	56.84	56.68	56.25	56.15	56.14	56.74	54.84	54.19	52.58	50.54	47.80	45.21	55.53	42.43	59.22
RT	205.13	70.20	40.37	88.27	67.35	74.33	60.26	57.48	45.94	39.39	39.58	43.16	43.32	43.75	43.85	43.86	43.26	45.16	45.81	47.42	49.46	52.20	54.79	44.47	57.57	40.78
Calc. head	292.22	100.00	100	100	100	100	100	100	100	100	100	100	100	100	100	100	100	100	100	100	100	100	100	100	100	100

Data for bench flotation test T19

1st stage	Grinding		
mill type	rod mill	**rods weight**	4109 g
charge	298 g	**rotational speed**	74 rpm
grind P_{80}	53 µm	**grinding time**	21 min
solids	50 wt%	**pH**	9.5

2nd stage	Conditioning and floating												
Operating stage	Operating time (min)		Reagents (g/t)				Data						
	Conditioning	Floating	Na_2CO_3	Na_2SiF_6	Pionera 220	Betacol	pH	Temp (°C)	Solids (wt%)	Agitator speed (rpm)	Air flow rate (L/min)	Paddle rate	Cell volume (dm^3)
Condition1	60		2133	250			9.5	40	50	1200			1.5
Condition2	60		866		2500		9.5	40	50	1200			1.5
Condition3	60		333			120	9.5	40	50	1200			1.5
Rougher Conc1		3					9.5	40	20	1200	0.5	1/15 s	1.5
Rougher Conc2	2	3	133			60	9.5	40	20	1200	1.5	1/15 s	1.5
Rougher Conc3	4	6					9.5	40	20	1200	5	1/30 s	1.5

3rd stage		Grade, recovery and mass pull																									
Products	Mass (g)	Mass (wt%)	Grade																								
			P_2O_5	SiO_2	CaO	Fe_2O_3	SrO	BaO	Y_2O_3	La_2O_3	Ce_2O_3	Pr_2O_3	Nd_2O_3	Sm_2O_3	Eu_2O_3	Gd_2O_3	Tb_2O_3	Dy_2O_3	Ho_2O_3	Er_2O_3	Tm_2O_3	Yb_2O_3	Lu_2O_3	ThO_2	UO_2	TREO
			(wt%)						(ppm)																		(wt%)
RC1	56.07	19.01	4.26	3.14	37.77	14.26	1.99	1.40	1235	9435	16707	1564	5316	741	204	498	59	281	44	109	12	70	9	522	17	3.63
RC2	30.35	10.29	3.26	2.59	30.38	19.75	1.67	1.47	1211	8235	14525	1373	4631	647	177	425	50	247	40	95	11	63	8	589	18	3.17
RC3	7.06	2.39	1.65	1.96	34.81	18.43	1.01	1.23	777	4988	9813	958	3280	462	127	294	34	163	26	62	7	43	6	221	15	2.10
Calc. RC	93.48	31.70	3.74	2.87	35.14	16.36	1.81	1.41	1192	8710	15478	1456	4940	689	190	459	54	261	42	101	12	66	9	521	17	3.4
RT	201.43	68.30	0.84	8.90	32.57	18.84	0.89	0.70	333	1976	3534	376	1276	175	48	113	13	66	11	28	4	24	4	146	8	0.80
Calc. head	294.91	100.00	1.76	6.99	33.38	18.06	1.18	0.93	606	4111	7320	718	2438	338	93	223	26	128	21	51	6	37	5	265	11	1.61
Meas. head	300		1.80	6.83	32.40	15.54	1.16	0.87	609	4028	7201	721	2438	341	93	217	25	124	20	49	6	37	5	318	11	1.59

Products	Mass (g)	Mass (wt%)	Recovery (%)																							
			P_2O_5	SiO_2	CaO	Fe_2O_3	SrO	BaO	Y_2O_3	La_2O_3	Ce_2O_3	Pr_2O_3	Nd_2O_3	Sm_2O_3	Eu_2O_3	Gd_2O_3	Tb_2O_3	Dy_2O_3	Ho_2O_3	Er_2O_3	Tm_2O_3	Yb_2O_3	Lu_2O_3	ThO_2	UO_2	TREO
RC1	56.07	19.01	45.96	8.54	21.51	15.02	32.06	28.74	38.75	43.64	43.39	41.41	41.46	41.68	41.74	42.54	43.32	41.74	40.67	40.49	38.04	35.85	32.47	37.47	28.64	42.80
RC2	30.35	10.29	19.07	3.81	9.36	11.26	14.54	16.31	20.57	20.62	20.42	19.68	19.55	19.70	19.62	19.65	20.07	19.85	19.96	19.16	18.59	17.30	16.53	22.88	16.91	20.26
RC3	7.06	2.39	2.25	0.67	2.50	2.44	2.05	3.17	3.07	2.90	3.21	3.19	3.22	3.27	3.26	3.16	3.13	3.04	3.00	2.92	2.90	2.78	2.79	1.99	3.22	3.12
Calc. RC	93.48	31.70	67.28	13.02	33.37	28.72	48.65	48.22	62.40	67.16	67.02	64.28	64.23	64.66	64.62	65.35	66.52	64.64	63.63	62.56	59.53	55.93	51.80	62.35	48.76	66.18
RT	201.43	68.30	32.72	86.98	66.63	71.28	51.35	51.78	37.60	32.84	32.98	35.72	35.77	35.34	35.38	34.65	33.48	35.36	36.37	37.44	40.47	44.07	48.20	37.65	51.24	33.82
Calc. head	294.91	100.00	100	100	100	100	100	100	100	100	100	100	100	100	100	100	100	100	100	100	100	100	100	100	100	100

Data for bench flotation test T20

1st stage	Grinding		
mill type	rod mill	**rods weight**	4109 g
charge	300 g	**rotational speed**	74 rpm
grind P_{80}	53 µm	**grinding time**	21 min
solids	50 wt%	**pH**	9.5

2nd stage	Conditioning and floating												
Operating stage	Operating time (min)		Reagents (g/t)				Data						
	Conditioning	Floating	Na_2CO_3	Na_2SiF_6	Pionera 220	Betacol	pH	Temp (°C)	Solids (wt%)	Agitator speed (rpm)	Air flow rate (L/min)	Paddle rate	Cell volume (dm^3)
Condition1	60		2500	250			9.5	80	50	1200			1.5
Condition2	60		1333		2500		9.5	80	50	1200			1.5
Condition3	60		400			120	9.5	80	50	1200			1.5
Rougher Conc1		3					9.5	80	20	1200	0.5	1/15 s	1.5
Rougher Conc2	2	3	333			60	9.5	80	20	1200	1.5	1/15 s	1.5
Rougher Conc3	4	6					9.5	80	20	1200	5	1/30 s	1.5

3rd stage		Grade, recovery and mass pull																									
Products	Mass (g)	Mass (wt%)	Grade																								
			P_2O_5	SiO_2	CaO	Fe_2O_3	SrO	BaO	Y_2O_3	La_2O_3	Ce_2O_3	Pr_2O_3	Nd_2O_3	Sm_2O_3	Eu_2O_3	Gd_2O_3	Tb_2O_3	Dy_2O_3	Ho_2O_3	Er_2O_3	Tm_2O_3	Yb_2O_3	Lu_2O_3	ThO_2	UO_2	TREO
			(wt%)						(ppm)																		(wt%)
RC1	62.95	21.22	4.57	2.95	39.21	12.06	2.11	1.27	1452	9303	17297	1722	5912	830	226	520	63	302	50	120	14	80	11	761	16	3.79
RC2	28.76	9.70	3.41	2.38	35.25	17.69	1.96	1.19	1290	9058	15751	1662	5460	765	211	498	60	280	46	107	13	69	10	718	14	3.53
RC3	2.84	0.96	1.05	2.24	32.97	16.47	1.02	0.82	707	5099	9063	964	3174	443	121	282	33	155	25	59	7	43	6	406	11	2.02
Calc. RC	94.55	31.88	4.11	2.76	37.82	13.91	2.03	1.23	1380	9102	16579	1681	5692	799	218	506	61	291	48	114	14	76	11	738	15	3.66
RT	202.05	68.12	0.31	10.67	35.47	18.72	0.76	0.85	213	1579	2901	311	1026	139	38	86	10	46	8	20	3	19	3	144	8	0.64
Calc. head	296.60	100.00	1.52	8.15	36.21	17.19	1.17	0.97	585	3977	7261	748	2514	350	95	220	26	124	20	50	6	37	6	333	10	3.79
Meas. head	300		1.80	6.83	32.40	15.54	1.16	0.87	609	4028	7201	721	2438	341	93	217	25	124	20	49	6	37	5	318	11	1.59

Products	Mass (g)	Mass (wt%)	Recovery (%)																							
			P_2O_5	SiO_2	CaO	Fe_2O_3	SrO	BaO	Y_2O_3	La_2O_3	Ce_2O_3	Pr_2O_3	Nd_2O_3	Sm_2O_3	Eu_2O_3	Gd_2O_3	Tb_2O_3	Dy_2O_3	Ho_2O_3	Er_2O_3	Tm_2O_3	Yb_2O_3	Lu_2O_3	ThO_2	UO_2	TREO
RC1	62.95	21.22	63.85	7.69	22.98	14.90	38.32	27.83	52.70	49.64	50.56	48.89	49.92	50.41	50.33	50.13	50.82	51.70	51.92	51.15	49.16	45.93	43.56	48.48	32.63	50.22
RC2	28.76	9.70	21.77	2.84	9.44	9.98	16.29	11.84	21.38	22.08	21.03	21.56	21.06	21.21	21.48	21.93	22.08	21.92	21.65	20.82	19.86	18.03	16.73	20.90	12.81	21.35
RC3	2.84	0.96	0.66	0.26	0.87	0.92	0.83	0.81	1.16	1.23	1.20	1.24	1.21	1.21	1.21	1.23	1.21	1.20	1.16	1.14	1.12	1.11	1.11	1.17	1.00	1.21
Calc. RC	94.55	31.88	86.28	10.79	33.29	25.79	55.44	40.48	75.23	72.95	72.78	71.68	72.19	72.83	73.02	73.29	74.11	74.82	74.73	73.11	70.13	65.08	61.40	70.55	46.44	72.78
RT	202.05	68.12	13.72	89.21	66.71	74.21	44.56	59.52	24.77	27.05	27.22	28.32	27.81	27.17	26.98	26.71	25.89	25.18	25.27	26.89	29.87	34.92	38.60	29.45	53.56	27.22
Calc. head	296.60	100.00	100	100	100	100	100	100	100	100	100	100	100	100	100	100	100	100	100	100	100	100	100	100	100	100

Data for bench flotation test T20 (Duplicate)

1st stage	**Grinding**		
mill type	rod mill	**rods weight**	4109 g
charge	300 g	**rotational speed**	74 rpm
grind P_{80}	53 µm	**grinding time**	21 min
solids	50 wt%	**pH**	9.5

2nd stage	**Conditioning and floating**												
Operating stage	Operating time (min)		Reagents (g/t)				Data						
	Conditioning	Floating	Na_2CO_3	Na_2SiF_6	Pionera 220	Betacol	pH	Temp (°C)	Solids (wt%)	Agitator speed (rpm)	Air flow rate (L/min)	Paddle rate	Cell volume (dm^3)
Condition1	60		2933	250			9.5	80	50	1200			1.5
Condition2	60		1200		2500		9.5	80	50	1200			1.5
Condition3	60		300			120	9.5	80	50	1200			1.5
Rougher Conc1		3					9.5	80	20	1200	1.5	1/15 s	1.5
Rougher Conc2	2	3	833			60	9.5	80	20	1200	1.5	1/15 s	1.5
Rougher Conc3	4	6					9.5	80	20	1200	5	1/30 s	1.5

3rd stage		**Grade, recovery and mass pull**							
Products	Mass (g)	Mass (wt%)	Grade						
			P_2O_5	SiO_2	CaO	Fe_2O_3	SrO	Y_2O_3	ThO_2
			(wt%)					(ppm)	
RC1	26.75	9.00	6.44	3.19	35.69	11.95	2.37	1937	910
RC2	22.9	7.71	6.28	3.02	35.43	14.09	2.41	1969	904
RC3	2.08	0.70	1.65	2.92	32.03	16.29	1.18	893	547
Calc. RC	51.73	17.41	6.18	3.10	35.43	13.07	2.34	1909.50	892.35
RT	245.41	82.59	0.53	8.55	32.56	18.72	0.88	354.94	299
Calc. head	297.14	100.00	1.51	7.60	33.06	17.73	1.14	626	402
Meas. head	300		1.80	6.83	32.40	15.54	1.16	609	318

Products	Mass (g)	Mass (wt%)	Recovery (%)						
			P_2O_5	SiO_2	CaO	Fe_2O_3	SrO	Y_2O_3	ThO_2
RC1	26.75	9.00	38.36	3.78	9.72	6.07	18.75	27.88	20.35
RC2	22.9	7.71	32.07	3.06	8.26	6.12	16.37	24.26	17.31
RC3	2.08	0.70	0.76	0.27	0.68	0.64	0.73	1.00	0.95
Calc. RC	51.73	17.41	71.19	7.10	18.66	12.83	35.85	53.14	38.62
RT	245.41	82.59	28.81	92.90	81.34	87.17	64.15	46.86	61.38
Calc. head	297.14	100.00	100	100	100	100	100	100	100

Data for bench flotation test T21

1st stage	Grinding		
mill type	rod mill	**rods weight**	4109 g
charge	300 g	**rotational speed**	74 rpm
grind P_{80}	53 µm	**grinding time**	21 min
solids	50 wt%	**pH**	9.5

2nd stage	Conditioning and floating												
Operating stage	Operating time (min)		Reagents (g/t)				Data						
	Conditioning	Floating	Na_2CO_3	Na_2SiF_6	Pionera 220	Betacol	pH	Temp (°C)	Solids (wt%)	Agitator speed (rpm)	Air flow rate (L/min)	Paddle rate	Cell volume (dm^3)
Condition1	60		500	250			8.5	60	50	1200			1.5
Condition2	60		100		2500		8.5	60	50	1200			1.5
Condition3	60		1633			120	9.5	60	50	1200			1.5
Rougher Conc1		3					9.5	60	20	1200	1.5	1/15 s	1.5
Rougher Conc2	2	3	300			60	9.5	60	20	1200	1.5	1/15 s	1.5
Rougher Conc3	4	6					9.5	60	20	1200	5	1/30 s	1.5

3rd stage		Grade, recovery and mass pull																									
Products	Mass (g)	Mass (wt%)	Grade																								
			P_2O_5	SiO_2	CaO	Fe_2O_3	SrO	BaO	Y_2O_3	La_2O_3	Ce_2O_3	Pr_2O_3	Nd_2O_3	Sm_2O_3	Eu_2O_3	Gd_2O_3	Tb_2O_3	Dy_2O_3	Ho_2O_3	Er_2O_3	Tm_2O_3	Yb_2O_3	Lu_2O_3	ThO_2	UO_2	TREO
			(wt%)						(ppm)																		(wt%)
RC1	38.8	13.05	4.33	2.37	40.64	9.63	1.84	1.38	1514	10080	17604	1715	5778	816	229	568	68	337	54	135	15	86	11	771	22	3.90
RC2	25.34	8.52	3.12	2.32	30.89	17.18	1.54	1.73	1445	9490	16294	1675	5554	782	218	525	63	316	51	126	14	82	10	693	20	3.66
RC3	2.86	0.96	1.30	2.02	33.95	14.03	1.05	0.61	663	4910	8446	863	2848	392	106	250	29	139	22	54	6	42	5	365	13	1.88
Calc. RC	67.00	22.53	3.75	2.33	36.67	12.67	1.69	1.48	1452	9636	16718	1663	5569	785	219	538	65	321	52	128	15	83	10	724	21	3.7
RT	230.37	77.47	0.82	8.74	33.35	18.57	0.987	0.69	349	2314	4100	431	1436	199	54	126	14	72	11	29	3	25	3	189	9	0.92
Calc. head	297.37	100.00	1.48	7.30	34.10	17.24	1.15	0.87	597	3964	6943	709	2367	331	91	219	26	128	20	51	6	38	5	310	12	1.55
Meas. head	300		1.80	6.83	32.40	15.54	1.16	0.87	609	4028	7201	721	2438	341	93	217	25	124	20	49	6	37	5	318	11	1.59

Products	Mass (g)	Mass (wt%)	Recovery (%)																								
			P_2O_5	SiO_2	CaO	Fe_2O_3	SrO	BaO	Y_2O_3	La_2O_3	Ce_2O_3	Pr_2O_3	Nd_2O_3	Sm_2O_3	Eu_2O_3	Gd_2O_3	Tb_2O_3	Dy_2O_3	Ho_2O_3	Er_2O_3	Tm_2O_3	Yb_2O_3	Lu_2O_3	ThO_2	UO_2	TREO
RC1	38.8	13.05	38.16	4.23	15.55	7.29	20.91	20.71	33.08	33.18	33.08	31.56	31.85	32.15	32.72	33.84	34.69	34.41	34.76	34.12	34.07	29.84	29.10	32.48	25.47	32.85
RC2	25.34	8.52	17.98	2.70	7.72	8.49	11.44	16.89	20.62	20.40	20.00	20.13	19.99	20.13	20.35	20.43	20.90	21.10	21.35	20.91	20.90	18.60	17.81	19.05	14.67	20.15
RC3	2.86	0.96	0.84	0.26	0.96	0.78	0.89	0.67	1.07	1.19	1.17	1.17	1.16	1.14	1.11	1.10	1.07	1.05	1.02	1.01	1.05	1.07	1.07	1.13	1.07	1.17
Calc. RC	67.00	22.53	56.99	7.20	24.23	16.56	33.24	38.27	54.76	54.78	54.25	52.86	53.00	53.41	54.18	55.36	56.66	56.56	57.13	56.04	56.03	49.51	47.98	52.66	41.21	54.17
RT	230.37	77.47	43.01	92.80	75.77	83.44	66.76	61.73	45.24	45.22	45.75	47.14	47.00	46.59	45.82	44.64	43.34	43.44	42.87	43.96	43.97	50.49	52.02	47.34	58.79	45.83
Calc. head	297.37	100.00	100	100	100	100	100	100	100	100	100	100	100	100	100	100	100	100	100	100	100	100	100	100	100	100

Data for bench flotation test T22

1st stage	Grinding		
mill type	rod mill	**rods weight**	4109 g
charge	302 g	**rotational speed**	74 rpm
grind P_{80}	53 µm	**grinding time**	21 min
solids	50 wt%	**pH**	9.5

2nd stage	Conditioning and floating													
Operating stage	Operating time (min)		Reagents (g/t)					Data						
	Conditioning	Floating	Na_2CO_3	HCl 4M cm^3	Na_2SiF_6	Pionera 220	Betacol	pH	Temp (°C)	Solids (wt%)	Agitator speed (rpm)	Air flow rate (L/min)	Paddle rate	Cell volume (dm^3)
Condition1	60		6000		250			10.5	60	50	1200			1.5
Condition2	60		2666			2500		10.5	60	50	1200			1.5
Condition3	60			41			120	9.5	60	50	1200			1.5
Rougher Conc1		3						9.5	60	20	1200	1.5	1/15 s	1.5
Rougher Conc2	2	3					60	9.5	60	20	1200	1.5	1/15 s	1.5
Rougher Conc3	4	6						9.5	60	20	1200	5	1/30 s	1.5

3rd stage		Grade, recovery and mass pull																									
Products	Mass (g)	Mass (wt%)	Grade																								
			P_2O_5	SiO_2	CaO	Fe_2O_3	SrO	BaO	Y_2O_3	La_2O_3	Ce_2O_3	Pr_2O_3	Nd_2O_3	Sm_2O_3	Eu_2O_3	Gd_2O_3	Tb_2O_3	Dy_2O_3	Ho_2O_3	Er_2O_3	Tm_2O_3	Yb_2O_3	Lu_2O_3	ThO_2	UO_2	TREO
			(wt%)						(ppm)																		(wt%)
RC1	70.65	23.68	4.46	3.36	39.84	11.86	2.41	0.58	1221	6847	11937	1181	3993	569	159	382	47	239	40	97	12	65	9	491	10	2.68
RC2	79.85	26.76	1.93	2.40	42.69	13.11	1.39	0.54	704	5036	9474	931	3144	427	115	270	30	147	23	56	7	42	6	390	8	2.04
RC3	6.09	2.04	0.98	5.19	24.95	20.92	0.70	0.96	488	3448	6694	653	2214	305	82	191	21	103	16	39	5	29	4	299	12	1.43
Calc. RC	156.59	52.48	3.03	2.94	40.71	12.85	1.82	0.57	929	5791	10477	1033	3491	487	133	318	37	186	31	74	9	52	7	432	9	2.3
RT	141.80	47.52	0.38	12.09	24.64	23.08	0.471	1.02	239	1807	3258	345	1168	160	42	96	10	51	8	21	3	18	3	164	12	0.72
Calc. head	298.39	100.00	1.77	7.29	33.07	17.71	1.18	0.78	601	3898	7046	706	2387	331	90	212	24	122	20	49	6	36	5	305	10	1.55
Meas. head	300		1.80	6.83	32.40	15.54	1.16	0.87	609	4028	7201	721	2438	341	93	217	25	124	20	49	6	37	5	318	11	1.59

Products	Mass (g)	Mass (wt%)	Recovery (%)																								
			P_2O_5	SiO_2	CaO	Fe_2O_3	SrO	BaO	Y_2O_3	La_2O_3	Ce_2O_3	Pr_2O_3	Nd_2O_3	Sm_2O_3	Eu_2O_3	Gd_2O_3	Tb_2O_3	Dy_2O_3	Ho_2O_3	Er_2O_3	Tm_2O_3	Yb_2O_3	Lu_2O_3	ThO_2	UO_2	TREO
RC1	70.65	23.68	59.51	10.91	28.52	15.86	48.26	17.44	48.10	41.59	40.11	39.59	39.60	40.68	41.77	42.56	45.43	46.20	47.15	47.18	45.90	43.23	40.57	38.16	23.03	40.84
RC2	79.85	26.76	29.13	8.80	34.54	19.81	31.59	18.42	31.36	34.57	35.98	35.30	35.25	34.52	34.18	34.08	33.17	32.09	31.27	30.99	30.76	31.26	31.71	34.22	21.16	35.17
RC3	6.09	2.04	1.13	1.45	1.54	2.41	1.21	2.51	1.66	1.81	1.94	1.89	1.89	1.88	1.86	1.84	1.77	1.72	1.68	1.64	1.65	1.65	1.66	2.00	2.42	1.88
Calc. RC	156.59	52.48	89.77	21.16	64.60	38.07	81.06	38.37	81.12	77.97	78.03	76.77	76.74	77.07	77.81	78.48	80.36	80.01	80.10	79.81	78.31	76.13	73.94	74.38	46.61	77.88
RT	141.80	47.52	10.23	78.84	35.40	61.93	18.94	61.63	18.88	22.03	21.97	23.23	23.26	22.93	22.19	21.52	19.64	19.99	19.90	20.19	21.69	23.87	26.06	25.62	53.39	22.12
Calc. head	298.39	100.00	100	100	100	100	100	100	100	100	100	100	100	100	100	100	100	100	100	100	100	100	100	100	100	100

Data for bench flotation test T23

1st stage	Grinding		
mill type	rod mill	**rods weight**	4109 g
charge	300 g	**rotational speed**	74 rpm
grind P_{80}	53 µm	**grinding time**	21 min
solids	50 wt%	**pH**	9.5

2nd stage	Conditioning and floating												
Operating stage	Operating time (min)		Reagents (g/t)				Data						
	Conditioning	Floating	Na_2CO_3	Na_2SiF_6	Pionera 220	Betacol	pH	Temp (°C)	Solids (wt%)	Agitator speed (rpm)	Air flow rate (L/min)	Paddle rate	Cell volume (dm^3)
Condition1	10		1000	250			9.5	60	50	1200			1.5
Condition2	10		867		2500		9.5	60	50	1200			1.5
Condition3	60		1167			90	9.5	60	50	1200			1.5
Rougher Conc1		3					9.5	60	20	1200	1.5	1/15 s	1.5
Rougher Conc2	2	3	167			60	9.5	60	20	1200	1.5	1/15 s	1.5
Rougher Conc3	4	6					9.5	60	20	1200	5	1/30 s	1.5

3rd stage		Grade, recovery and mass pull																									
Products	Mass (g)	Mass (wt%)	Grade																								
			P_2O_5	SiO_2	CaO	Fe_2O_3	SrO	BaO	Y_2O_3	La_2O_3	Ce_2O_3	Pr_2O_3	Nd_2O_3	Sm_2O_3	Eu_2O_3	Gd_2O_3	Tb_2O_3	Dy_2O_3	Ho_2O_3	Er_2O_3	Tm_2O_3	Yb_2O_3	Lu_2O_3	ThO_2	UO_2	TREO
			(wt%)						(ppm)																		(wt%)
RC1	59.84	20.21	5.11	2.94	37.75	11.91	2.07	0.88	1591	9458	16613	1507	5136	728	220	517	61	317	53	127	15	80	12	721	14	3.64
RC2	25.39	8.58	3.09	2.56	32.37	18.57	1.98	0.81	1241	7480	13899	1393	4590	680	176	432	50	241	40	95	12	64	8	591	13	3.04
RC3	3.90	1.32	1.84	2.58	31.48	18.79	1.37	0.66	801	5694	11485	1069	3583	492	132	308	36	165	26	61	8	44	6	443	10	2.39
Calc. RC	89.13	30.11	4.39	2.81	35.94	14.11	2.01	0.85	1456	8730	15616	1455	4912	704	203	484	57	288	48	115	14	74	10	672	14	3.4
RT	206.93	69.89	0.50	9.60	32.81	19.07	0.76	0.90	268	1886	3318	354	1202	171	47	108	11	55	9	23	3	20	3	147	11	0.75
Calc. head	296.06	100.00	1.67	7.55	33.75	17.58	1.14	0.89	626	3946	7020	686	2319	331	94	221	25	125	21	50	6	36	5	305	12	1.55
Meas. head	300		1.80	6.83	32.40	15.54	1.16	0.87	609	4028	7201	721	2438	341	93	217	25	124	20	49	6	37	5	318	11	1.59

Products	Mass (g)	Mass (wt%)	Recovery (%)																								
			P_2O_5	SiO_2	CaO	Fe_2O_3	SrO	BaO	Y_2O_3	La_2O_3	Ce_2O_3	Pr_2O_3	Nd_2O_3	Sm_2O_3	Eu_2O_3	Gd_2O_3	Tb_2O_3	Dy_2O_3	Ho_2O_3	Er_2O_3	Tm_2O_3	Yb_2O_3	Lu_2O_3	ThO_2	UO_2	TREO
RC1	59.84	20.21	61.85	7.85	22.60	13.69	36.72	20.02	51.37	48.45	47.83	44.41	44.77	44.44	47.32	47.23	50.12	51.15	51.25	50.97	48.14	44.82	45.51	47.77	24.10	47.47
RC2	25.39	8.58	15.85	2.90	8.23	9.06	14.91	7.85	17.00	16.26	16.98	17.42	16.98	17.61	16.06	16.74	17.35	16.52	16.63	16.12	16.43	15.16	13.06	16.61	9.82	16.81
RC3	3.90	1.32	1.45	0.45	1.23	1.41	1.59	0.98	1.69	1.90	2.15	2.05	2.04	1.96	1.85	1.84	1.90	1.74	1.64	1.61	1.59	1.59	1.65	1.91	1.15	2.03
Calc. RC	89.13	30.11	79.15	11.21	32.06	24.16	53.23	28.84	70.05	66.60	66.96	63.88	63.78	64.00	65.23	65.81	69.37	69.41	69.53	68.70	66.17	61.57	60.23	66.29	35.07	66.31
RT	206.93	69.89	20.85	88.79	67.94	75.84	46.77	71.16	29.95	33.40	33.04	36.12	36.22	36.00	34.77	34.19	30.63	30.59	30.47	31.30	33.83	38.43	39.77	33.71	64.93	33.69
Calc. head	296.06	100.00	100	100	100	100	100	100	100	100	100	100	100	100	100	100	100	100	100	100	100	100	100	100	100	100

Data for bench flotation test T24

1st stage	Grinding		
mill type	rod mill	**rods weight**	4109 g
charge	292 g	**rotational speed**	74 rpm
grind P_{80}	53 µm	**grinding time**	21 min
solids	50 wt%	**pH**	9.5

2nd stage	Conditioning and floating												
Operating stage	Operating time (min)		Reagents (g/t)				Data						
	Conditioning	Floating	Na_2CO_3	Na_2SiF_6	Pionera 220	Betacol	pH	Temp (°C)	Solids (wt%)	Agitator speed (rpm)	Air flow rate (L/min)	Paddle rate	Cell volume (dm^3)
Condition1	10		2226	250			9.5	80	50	1200			1.5
Condition2	10		1027		2500		9.5	80	50	1200			1.5
Condition3	60		1370			120	9.5	80	50	1200			1.5
Rougher Conc1		3					9.5	80	20	1200	0.5	1/15 s	1.5
Rougher Conc2	2	3	171			60	9.5	80	20	1200	1.5	1/15 s	1.5
Rougher Conc3	4	6					9.5	80	20	1200	5	1/30 s	1.5

3rd stage		Grade, recovery and mass pull							
Products	Mass (g)	Mass (wt%)	Grade						
			P_2O_5	SiO_2	CaO	Fe_2O_3	SrO	Y_2O_3	ThO_2
			(wt%)					(ppm)	
RC1	78.18	27.22	4.72	5.59	41.80	11.45	2.05	1472	891
RC2	32.86	11.44	2.18	4.94	37.35	17.37	1.91	872	726
RC3	6.08	2.12	1.09	5.10	34.75	17.54	1.08	638	478
Calc. RC	117.12	40.78	1.09	5.38	40.18	13.42	1.96	1260	823
RT	170.06	59.22	3.82	10.648	31.29	20.29	0.58	185	110
Calc. head	287.18	100	0.23	8.50	34.92	17.49	1.15	624	401
Meas. head	300		1.80	6.83	32.40	15.54	1.16	609	318

Products	Mass (g)	Mass (wt%)	Recovery (%)						
			P_2O_5	SiO_2	CaO	Fe_2O_3	SrO	Y_2O_3	ThO_2
RC1	78.18	27.22	75.79	17.89	32.59	17.82	48.77	64.26	60.56
RC2	32.86	11.44	14.69	6.65	12.24	11.37	19.06	16.01	20.72
RC3	6.08	2.12	1.36	1.27	2.11	2.12	2.00	2.17	2.53
Calc. RC	117.12	40.78	91.84	25.82	46.93	31.31	69.82	82.43	83.80
RT	170.06	59.22	8.16	74.18	53.07	68.69	30.18	17.57	16.20
Calc. head	287.18	100	100	100	100	100	100	100	100

Data for bench flotation test T25

1st stage	Grinding		
mill type	rod mill	**rods weight**	4109 g
charge	301 g	**rotational speed**	74 rpm
grind P_{80}	53 µm	**grinding time**	21 min
solids	50 wt%	**pH**	9.5

2nd stage	Conditioning and floating												
Operating stage	Operating time (min)		Reagents (g/t)				Data						
	Conditioning	Floating	NaOH	Na_2SiF_6	Pionera 220	Betacol	pH	Temp (°C)	Solids (wt%)	Agitator speed (rpm)	Air flow rate (L/min)	Paddle rate	Cell volume (dm^3)
Condition1	60		1133	250			9.5	60	50	1200			1.5
Condition2	60		467		2500		9.5	60	50	1200			1.5
Condition3	60		107			120	9.5	60	50	1200			1.5
Rougher Conc1		3					9.5	60	20	1200	1.5	1/15 s	1.5
Rougher Conc2	2	3	173			60	9.5	60	20	1200	1.5	1/15 s	1.5
Rougher Conc3	4	6					9.5	60	20	1200	5	1/30 s	1.5

3rd stage		Grade, recovery and mass pull																									
Products	Mass (g)	Mass (wt%)	Grade																								
			P_2O_5	SiO_2	CaO	Fe_2O_3	SrO	BaO	Y_2O_3	La_2O_3	Ce_2O_3	Pr_2O_3	Nd_2O_3	Sm_2O_3	Eu_2O_3	Gd_2O_3	Tb_2O_3	Dy_2O_3	Ho_2O_3	Er_2O_3	Tm_2O_3	Yb_2O_3	Lu_2O_3	ThO_2	UO_2	TREO
			(wt%)						(ppm)																		(wt%)
RC1	68.8	23.09	3.95	2.67	39.41	12.53	1.71	0.89	1405	9954	17219	1591	5264	730	198	470	54	264	41	101	11	67	8	582	12	3.74
RC2	16.47	5.53	2.21	2.16	35.25	15.40	1.82	1.15	903	5103	9944	923	3066	433	119	283	33	166	26	66	8	48	6	368	13	2.11
RC3	6.44	2.16	1.19	1.38	41.02	11.70	1.16	0.69	739	4083	8035	745	2452	348	95	226	27	133	21	55	6	43	5	293	11	1.70
Calc. RC	91.71	30.78	3.44	2.49	38.78	12.98	1.69	0.92	1268	8670	15268	1412	4672	650	176	419	49	237	37	91	10	62	8	523	12	3.3
RT	206.28	69.22	0.69	9.65	31.74	19.95	0.83	0.62	341	2097	3708	389	1284	180	48	112	13	64	10	27	3	22	3	166	8	0.83
Calc. head	297.99	100.00	1.54	7.45	33.91	17.80	1.10	0.72	626	4120	7265	704	2327	324	87	207	24	117	18	47	5	35	4	276	9	1.59
Meas. head	300		1.80	6.83	32.40	15.54	1.16	0.87	609	4028	7201	721	2438	341	93	217	25	124	20	49	6	37	5	318	11	1.59

Products	Mass (g)	Mass (wt%)	Recovery (%)																								
			P_2O_5	SiO_2	CaO	Fe_2O_3	SrO	BaO	Y_2O_3	La_2O_3	Ce_2O_3	Pr_2O_3	Nd_2O_3	Sm_2O_3	Eu_2O_3	Gd_2O_3	Tb_2O_3	Dy_2O_3	Ho_2O_3	Er_2O_3	Tm_2O_3	Yb_2O_3	Lu_2O_3	ThO_2	UO_2	TREO
RC1	68.8	23.09	59.34	8.27	26.84	16.24	36.02	28.66	51.79	55.78	54.72	52.19	52.23	51.98	52.29	52.47	52.91	52.08	52.01	50.06	49.64	44.86	43.84	48.68	30.10	54.24
RC2	16.47	5.53	7.94	1.60	5.75	4.78	9.18	8.89	7.97	6.85	7.56	7.24	7.28	7.38	7.50	7.56	7.76	7.81	7.91	7.89	7.89	7.66	7.52	7.38	7.69	7.34
RC3	6.44	2.16	1.68	0.40	2.61	1.42	2.29	2.08	2.55	2.14	2.39	2.29	2.28	2.32	2.36	2.36	2.41	2.45	2.52	2.54	2.58	2.66	2.73	2.29	2.50	2.31
Calc. RC	91.71	30.78	68.96	10.28	35.20	22.44	47.49	39.63	62.30	64.76	64.67	61.72	61.79	61.68	62.15	62.39	63.08	62.34	62.44	60.48	60.10	55.18	54.09	58.36	40.29	63.89
RT	206.28	69.22	31.04	89.72	64.80	77.56	52.51	60.37	37.70	35.24	35.33	38.28	38.21	38.32	37.85	37.61	36.92	37.66	37.56	39.52	39.90	44.82	45.91	41.64	59.71	36.11
Calc. head	297.99	100.00	100	100	100	100	100	100	100	100	100	100	100	100	100	100	100	100	100	100	100	100	100	100	100	100

Data for bench flotation test T25 (Duplicate)

1st stage	Grinding		
mill type	rod mill	**rods weight**	4109 g
charge	305.5 g	**rotational speed**	74 rpm
grind P_{80}	53 µm	**grinding time**	21 min
solids	50 wt%	**pH**	natural

2nd stage	Conditioning and floating											
operation stage	operation time (min)		Reagents (g/t)				Data					
	Conditioning	Floating	NaOH	Na_2SiF_6	Pionera 220	Betacol	pH	Temp (°C)	Solids (wt%)	Agitator speed (rpm)	Air flow rate (L/min)	Paddle rate
Condition1	60		973	250			9.5	60	50	1200		
Condition2	60		466		2500		9.5	60	50	1200		
Condition3	60		227			120	9.5	60	50	1200		
Rougher Conc 1		3					9.5	60	20	1200	1.5	1/15 s
Rougher Conc 2	2	3	80			60	9.5	60	20	1200	1.5	1/15 s
Rougher Conc 3	4	6					9.5	60	20	1200	5	1/30 s

3rd stage	Grade, recovery and mass pull														
products	Mass (g)	Mass (wt%)	Grade							Recovery						
			P_2O_5	SiO_2	CaO	Fe_2O_3	Y_2O_3	La_2O_3	Ce_2O_3	P_2O_5	SiO_2	CaO	Fe_2O_3	Y_2O_3	La_2O_3	Ce_2O_3
			(wt%)				(ppm)			(%)						
RC1	66.25	21.99	4.05	2.70	39.60	12.10	1325	9657	17120	59.03	8.12	25.74	15.07	51.06	53.58	53.25
RC2	21.68	7.20	2.01	1.85	34.81	14.90	790	4831	9412	9.59	1.82	7.40	6.07	9.96	8.77	9.58
RC3	7.01	2.33	1.23	1.25	38.29	11.42	584	5256	7245	1.89	0.40	2.63	1.50	2.38	3.09	2.38
Calc. RC	94.94	31.52	3.38	2.40	38.41	12.69	1148	8230	14630	70.50	10.34	35.77	22.65	63.40	65.43	65.22
RT	206.28	68.48	0.65	9.57	31.74	19.95	305	2001	3591	29.50	89.66	64.23	77.35	36.60	34.57	34.78
Calc. head	301.22	100.00	1.51	7.31	33.84	17.66	571	3964	7071	100	100	100	100	100	100	100
Meas. head	300		1.80	6.83	32.40	15.54	609	4028	7201							

Data for bench flotation test T26

1st stage	Grinding		
mill type	rod mill	**rods weight**	4109 g
charge	300.5 g	**rotational speed**	74 rpm
grind P_{80}	53 µm	**grinding time**	21 min
solids	50 wt%	**pH**	9.5

2nd stage	Conditioning and floating												
Operating stage	Operating time (min)		Reagents (g/t)				Data						
	Conditioning	Floating	NaOH	Na_2SiF_6	Pionera 220	Sodium oleate	pH	Temp (°C)	Solids (wt%)	Agitator speed (rpm)	Air flow rate (L/min)	Paddle rate	Cell volume (dm^3)
Condition1	60		1013	250			9.5	60	50	1200			1.5
Condition2	60		507		2500		9.5	60	50	1200			1.5
Condition3	60		240			80	9.5	60	50	1200			1.5
Rougher Conc1		3					9.5	60	20	1200	1.5	1/15 s	1.5
Rougher Conc2	2	3	93			15	9.5	60	20	1200	1.5	1/15 s	1.5
Rougher Conc3	4	6					9.5	60	20	1200	5	1/30 s	1.5

3rd stage		Grade, recovery and mass pull																									
Products	Mass (g)	Mass (wt%)	Grade																								
			P_2O_5	SiO_2	CaO	Fe_2O_3	SrO	BaO	Y_2O_3	La_2O_3	Ce_2O_3	Pr_2O_3	Nd_2O_3	Sm_2O_3	Eu_2O_3	Gd_2O_3	Tb_2O_3	Dy_2O_3	Ho_2O_3	Er_2O_3	Tm_2O_3	Yb_2O_3	Lu_2O_3	ThO_2	UO_2	TREO
			(wt%)						(ppm)																		(wt%)
RC1	66.24	22.34	4.16	2.50	36.50	14.22	1.73	1.16	1420	9197	15953	1608	5330	745	204	489	58	282	45	110	12	73	9	651	17	3.55
RC2	25.36	8.55	2.08	2.86	28.64	20.98	1.44	0.68	940	5937	10593	1068	3583	502	136	326	38	190	30	74	8	51	6	454	18	2.35
RC3	2.20	0.74	0.77	3.12	30.74	18.28	0.84	0.46	399	2781	4802	500	1656	226	60	142	16	79	13	33	4	29	4	221	9	1.07
Calc. RC	93.80	31.63	3.52	2.61	34.24	16.14	1.63	1.01	1266	8165	14242	1436	4772	667	182	436	51	252	40	98	11	66	8	588	17	3.2
RT	202.75	68.37	0.54	8.53	31.56	19.86	0.86	0.58	282	1905	3378	355	1189	161	43	100	11	56	9	23	3	21	3	153	7	0.75
Calc. head	296.55	100.00	1.49	6.66	32.41	18.68	1.10	0.72	593	3885	6814	697	2322	321	87	207	24	118	19	47	5	35	5	290	10	1.52
Meas. head	300		1.80	6.83	32.40	15.54	1.16	0.87	609	4028	7201	721	2438	341	93	217	25	124	20	49	6	37	5	318	11	1.59

Products	Mass (g)	Mass (wt%)	Recovery (%)																								
			P_2O_5	SiO_2	CaO	Fe_2O_3	SrO	BaO	Y_2O_3	La_2O_3	Ce_2O_3	Pr_2O_3	Nd_2O_3	Sm_2O_3	Eu_2O_3	Gd_2O_3	Tb_2O_3	Dy_2O_3	Ho_2O_3	Er_2O_3	Tm_2O_3	Yb_2O_3	Lu_2O_3	ThO_2	UO_2	TREO
RC1	66.24	22.34	62.58	8.40	25.16	17.00	35.07	36.00	53.47	52.88	52.29	51.54	51.27	51.82	52.25	52.80	53.94	53.40	53.95	52.04	51.56	46.01	44.30	50.13	37.24	52.29
RC2	25.36	8.55	11.95	3.67	7.56	9.60	11.20	8.04	13.55	13.07	13.29	13.11	13.19	13.35	13.34	13.47	13.72	13.72	13.69	13.39	13.20	12.24	11.95	13.37	15.03	13.23
RC3	2.20	0.74	0.38	0.35	0.70	0.73	0.56	0.48	0.50	0.53	0.52	0.53	0.53	0.52	0.51	0.51	0.49	0.50	0.50	0.52	0.54	0.60	0.60	0.56	0.68	0.52
Calc. RC	93.80	31.63	74.92	12.42	33.42	27.33	46.84	44.52	67.52	66.48	66.11	65.18	64.99	65.70	66.10	66.77	68.14	67.62	68.14	65.95	65.29	58.84	56.86	64.06	52.95	66.04
RT	202.75	68.37	25.08	87.58	66.58	72.67	53.16	55.48	32.48	33.52	33.89	34.82	35.01	34.30	33.90	33.23	31.86	32.38	31.86	34.05	34.71	41.16	43.14	35.94	47.05	33.96
Calc. head	297.99	100.00	100	100	100	100	100	100	100	100	100	100	100	100	100	100	100	100	100	100	100	100	100	100	100	100

Data for bench flotation test T26 (Duplicate)

1st stage	Grinding		
mill type	rod mill	**rods weight**	4109 g
charge	302.7 g	**rotational speed**	74 rpm
grind P_{80}	53 µm	**grinding time**	21 min
solids	50 wt%	**pH**	natural

2nd stage	Conditioning and floating											
operation stage	operation time (min)		Reagents (g/t)				Data					
	Conditioning	Floating	NaOH	Na_2SiF_6	Pionera 220	Sodium oleate	pH	Temp (°C)	Solids (wt%)	Agitator speed (rpm)	Air flow rate (L/min)	Paddle rate
Condition1	60		1039	250			9.5	60	50	1200		
Condition2	60		500		2500		9.5	60	50	1200		
Condition3	60		226			80	9.5	60	50	1200		
Rougher Conc 1		3					9.5	60	20	1200	1.5	1/15 s
Rougher Conc 2	2	3	93			15	9.5	60	20	1200	1.5	1/15 s
Rougher Conc 3	4	6					9.5	60	20	1200	5	1/30 s

3rd stage		Grade, recovery and mass pull													
products	Mass (g)	Mass (wt%)	Grade							Recovery						
			P_2O_5	SiO_2	CaO	Fe_2O_3	Y_2O_3	La_2O_3	Ce_2O_3	P_2O_5	SiO_2	CaO	Fe_2O_3	Y_2O_3	La_2O_3	Ce_2O_3
			(wt%)				(ppm)			(%)						
RC1	73.18	24.62	3.86	2.67	37.48	16.64	1414	8752	15392	63.33	9.72	28.54	22.45	56.40	54.74	54.69
RC2	20.67	6.95	2.46	2.85	26.75	19.98	987	6425	11004	11.42	2.93	5.75	7.61	11.12	11.35	11.04
RC3	2.34	0.79	0.78	3.64	28.76	19.74	388	2101	4912	0.41	0.42	0.70	0.85	0.49	0.42	0.56
Calc. RC	96.19	32.36	3.48	2.73	34.96	17.43	1297	8090	14194	75.16	13.08	35.00	30.92	68.01	66.51	66.29
RT	201.04	67.64	0.55	8.69	31.07	18.64	291.87	1949	3453	24.84	86.92	65.00	69.08	31.99	33.49	33.71
Calc. head	297.23	100.00	1.50	6.76	32.33	18.25	617	3937	6929	100	100	100	100	100	100	100
Meas. head	300		1.80	6.83	32.40	15.54	609	4028	7201							

Data for bench flotation test T27

1st stage	Grinding		
mill type	rod mill	**rods weight**	4109 g
charge	296 g	**rotational speed**	74 rpm
grind P_{80}	53 µm	**grinding time**	21 min
solids	50 wt%	**pH**	9.5

2nd stage	Conditioning and floating												
Operating stage	Operating time (min)		Reagents (g/t)				Data						
	Conditioning	Floating	NaOH	Na_2SiF_6	Pionera 220	Sodium oleate	pH	Temp (°C)	Solids (wt%)	Agitator speed (rpm)	Air flow rate (L/min)	Paddle rate	Cell volume (dm^3)
Condition1	10		627	250			9.5	60	50	1200			1.5
Condition2	10		267		2500		9.5	60	50	1200			1.5
Condition3	10		120			80	9.5	60	50	1200			1.5
Rougher Conc1		3					9.5	60	20	1200	1.5	1/15 s	1.5
Rougher Conc2	2	3	93			15	9.5	60	20	1200	1.5	1/15 s	1.5
Rougher Conc3	4	6					9.5	60	20	1200	5	1/30 s	1.5

3rd stage		Grade, recovery and mass pull																									
Products	Mass (g)	Mass (wt%)	Grade																								
			P_2O_5	SiO_2	CaO	Fe_2O_3	SrO	BaO	Y_2O_3	La_2O_3	Ce_2O_3	Pr_2O_3	Nd_2O_3	Sm_2O_3	Eu_2O_3	Gd_2O_3	Tb_2O_3	Dy_2O_3	Ho_2O_3	Er_2O_3	Tm_2O_3	Yb_2O_3	Lu_2O_3	ThO_2	UO_2	TREO
			(wt%)						(ppm)																		(wt%)
RC1	95.67	32.50	3.27	3.99	41.83	11.71	1.49	0.85	1062	6192	11617	1112	3668	515	141	339	40	198	32	79	9	56	7	420	13	2.51
RC2	61.44	20.87	1.28	4.43	36.27	17.27	1.19	0.68	561	3457	6568	632	2101	292	79	186	21	106	17	43	5	33	4	254	9	1.41
RC3	4.93	1.67	0.87	3.84	39.48	14.20	1.00	0.67	440	2883	4979	522	1714	235	62	147	17	82	13	34	4	30	4	209	7	1.12
Calc. RC	162.04	55.04	2.44	4.15	39.65	13.90	1.36	0.78	853	5054	9501	912	3015	422	115	275	32	160	25	64	7	46	6	351	11	2.0
RT	132.34	44.96	0.80	13.31	26.11	23.78	0.81	0.55	330	2494	4355	451	1493	205	54	123	13	65	10	26	3	20	3	202	8	0.96
Calc. head	294.38	100.00	1.70	8.27	33.56	18.34	1.11	0.68	618	3903	7187	705	2331	325	87	207	24	117	18	47	5	35	4	284	10	1.56
Meas. head	300		1.80	6.83	32.40	15.54	1.16	0.87	609	4028	7201	721	2438	341	93	217	25	124	20	49	6	37	5	318	11	1.59

Products	Mass (g)	Mass (wt%)	Recovery (%)																								
			P_2O_5	SiO_2	CaO	Fe_2O_3	SrO	BaO	Y_2O_3	La_2O_3	Ce_2O_3	Pr_2O_3	Nd_2O_3	Sm_2O_3	Eu_2O_3	Gd_2O_3	Tb_2O_3	Dy_2O_3	Ho_2O_3	Er_2O_3	Tm_2O_3	Yb_2O_3	Lu_2O_3	ThO_2	UO_2	TREO
RC1	95.67	32.50	62.45	15.68	40.50	20.75	43.60	40.80	55.86	51.56	52.53	51.27	51.15	51.57	52.44	53.20	54.52	55.05	55.66	55.03	55.79	52.06	51.31	48.05	43.47	52.17
RC2	61.44	20.87	15.70	11.18	22.55	19.66	22.30	21.01	18.97	18.48	19.07	18.73	18.82	18.79	18.80	18.79	18.85	18.83	18.89	19.09	19.09	20.06	20.77	18.68	18.91	18.86
RC3	4.93	1.67	0.85	0.78	1.97	1.30	1.50	1.65	1.19	1.24	1.16	1.24	1.23	1.21	1.19	1.19	1.17	1.17	1.18	1.23	1.29	1.43	1.57	1.23	1.24	1.20
Calc. RC	162.04	55.04	79.00	27.64	65.02	41.71	67.40	63.46	76.02	71.28	72.76	71.25	71.20	71.57	72.44	73.17	74.54	75.05	75.73	75.35	76.16	73.54	73.64	67.96	63.62	72.23
RT	132.34	44.96	21.00	72.36	34.98	58.29	32.60	36.54	23.98	28.72	27.24	28.75	28.80	28.43	27.56	26.83	25.46	24.95	24.27	24.65	23.84	26.46	26.36	32.04	36.38	27.77
Calc. head	294.38	100.00	100	100	100	100	100	100	100	100	100	100	100	100	100	100	100	100	100	100	100	100	100	100	100	100

Data for bench flotation test T27 (Duplicate)

1st stage	**Grinding**		
mill type	rod mill	**rods weight**	4109 g
charge	299 g	**rotational speed**	74 rpm
grind P_{80}	53 µm	**grinding time**	21 min
solids	50 wt%	**pH**	natural

2nd stage	**Conditioning and floating**											
operation stage	operation time (min)		Reagents (g/t)				Data					
	Conditioning	Floating	NaOH	Na_2SiF_6	Pionera 220	Sodium oleate	pH	Temp (°C)	Solids (wt%)	Agitator speed (rpm)	Air flow rate (L/min)	Paddle rate
Condition1	10		607	250			9.5	60	50	1200		
Condition2	10		273		2500		9.5	60	50	1200		
Condition3	10		113			80	9.5	60	50	1200		
Rougher Conc 1		3					9.5	60	20	1200	1.5	1/15 s
Rougher Conc 2	2	3	106			15	9.5	60	20	1200	1.5	1/15 s
Rougher Conc 3	4	6					9.5	60	20	1200	5	1/30 s

3rd stage		**Grade, recovery and mass pull**													
products	Mass (g)	Mass (wt%)	Grade							Recovery						
			P_2O_5	SiO_2	CaO	Fe_2O_3	Y_2O_3	La_2O_3	Ce_2O_3	P_2O_5	SiO_2	CaO	Fe_2O_3	Y_2O_3	La_2O_3	Ce_2O_3
			(wt%)				(ppm)			(%)						
RC1	74.92	25.45	3.73	3.80	40.79	11.32	1031	5901	11175	55.68	11.71	31.87	15.99	43.61	39.00	40.47
RC2	73.45	24.95	1.48	3.98	36.25	15.93	716	4701	8482	21.71	12.34	27.77	22.07	29.69	30.46	30.11
RC3	5.21	1.77	1.01	4.15	39.23	13.93	483	3068	5187	1.05	0.89	2.13	1.37	1.42	1.41	1.31
Calc. RC	153.58	52.16	2.56	3.90	38.57	13.61	861.45	5231	9684	78.44	24.94	61.77	39.43	74.72	70.87	71.88
RT	140.85	47.84	0.77	12.52	26.03	22.80	317.81	2345	4130	21.56	75.06	38.23	60.57	25.28	29.13	28.12
Calc. head	294.43	100.00	1.70	8.02	32.56	18.01	601	3850	7026	100	100	100	100	100	100	100
Meas. head	300		1.80	6.83	32.40	15.54	609	4028	7201							

Data for bench flotation test T28

1st stage	Grinding		
mill type	rod mill	**rods weight**	4109 g
charge	303.5 g	**rotational speed**	74 rpm
grind P_{80}	53 µm	**grinding time**	21 min
solids	50 wt%	**pH**	9.5

2nd stage	Conditioning and floating												
Operating stage	Operating time (min)		Reagents (g/t)				Data						
	Conditioning	Floating	Na_2CO_3	Na_2SiF_6	Pionera 220	Sodium oleate	pH	Temp (°C)	Solids (wt%)	Agitator speed (rpm)	Air flow rate (L/min)	Paddle rate	Cell volume (dm^3)
Condition1	60		2167	250			9.5	60	50	1200			1.5
Condition2	60		1133		2500		9.5	60	50	1200			1.5
Condition3	60		600			80	9.5	60	50	1200			1.5
Rougher Conc1		3					9.5	60	20	1200	1.5	1/15 s	1.5
Rougher Conc2	2	3	233			15	9.5	60	20	1200	1.5	1/15 s	1.5
Rougher Conc3	4	6					9.5	60	20	1200	5	1/30 s	1.5

3rd stage		Grade, recovery and mass pull																									
Products	Mass (g)	Mass (wt%)	Grade																								
			P_2O_5	SiO_2	CaO	Fe_2O_3	SrO	BaO	Y_2O_3	La_2O_3	Ce_2O_3	Pr_2O_3	Nd_2O_3	Sm_2O_3	Eu_2O_3	Gd_2O_3	Tb_2O_3	Dy_2O_3	Ho_2O_3	Er_2O_3	Tm_2O_3	Yb_2O_3	Lu_2O_3	ThO_2	UO_2	TREO
			(wt%)						(ppm)																		(wt%)
RC1	73.25	24.39	3.92	2.87	34.34	13.99	2.13	1.20	1408	8655	15266	1505	5037	710	196	470	56	275	44	106	12	69	8	636	21	3.38
RC2	16.46	5.48	3.06	2.85	23.83	23.52	1.31	0.90	1245	7940	14178	1407	4654	649	178	421	50	242	39	94	11	64	8	571	12	3.12
RC3	2.35	0.78	0.76	4.13	26.66	21.19	0.76	0.81	377	2762	4821	502	1663	22s6	60	140	16	76	12	30	4	25	3	221	10	1.07
Calc. RC	92.06	30.66	3.68	2.90	32.27	15.88	1.95	1.13	1352	8377	14805	1462	4882	686	190	453	54	264	42	102	12	67	8	613	19	3.3
RT	208.22	69.34	0.61	8.85	34.55	17.44	0.77	0.85	319	2091	3704	389	1288	179	48	111	12	62	10	26	3	23	3	162	8	0.83
Calc. head	300.28	100.00	1.55	7.02	33.85	16.97	1.13	0.93	636	4018	7107	718	2390	335	91	216	25	124	20	49	6	36	5	300	11	1.58
Meas. head	300		1.80	6.83	32.40	15.54	1.16	0.87	609	4028	7201	721	2438	341	93	217	25	124	20	49	6	37	5	318	11	1.59

Products	Mass (g)	Mass (wt%)	Recovery (%)																								
			P_2O_5	SiO_2	CaO	Fe_2O_3	SrO	BaO	Y_2O_3	La_2O_3	Ce_2O_3	Pr_2O_3	Nd_2O_3	Sm_2O_3	Eu_2O_3	Gd_2O_3	Tb_2O_3	Dy_2O_3	Ho_2O_3	Er_2O_3	Tm_2O_3	Yb_2O_3	Lu_2O_3	ThO_2	UO_2	TREO
RC1	73.25	24.39	61.54	9.96	24.75	20.12	45.91	31.28	53.99	52.54	52.40	51.15	51.41	51.74	52.57	53.10	54.44	54.13	54.46	52.55	52.43	46.21	44.33	51.61	45.33	52.29
RC2	16.46	5.48	10.81	2.22	3.86	7.60	6.37	5.27	10.73	10.83	10.94	10.75	10.67	10.64	10.73	10.70	10.85	10.74	10.81	10.48	10.47	9.60	9.28	10.43	6.03	10.83
RC3	2.35	0.78	0.38	0.46	0.62	0.98	0.53	0.68	0.46	0.54	0.53	0.55	0.54	0.53	0.52	0.51	0.49	0.48	0.47	0.48	0.49	0.54	0.55	0.57	0.71	0.53
Calc. RC	92.06	30.66	72.73	12.64	29.23	28.70	52.80	37.22	65.18	63.91	63.86	62.44	62.62	62.91	63.81	64.31	65.78	65.35	65.74	63.51	63.40	56.36	54.17	62.61	52.07	63.66
RT	208.22	69.34	27.27	87.36	70.77	71.30	47.20	62.78	34.82	36.09	36.14	37.56	37.38	37.09	36.19	35.69	34.22	34.65	34.26	36.49	36.60	43.64	45.83	37.39	47.93	36.34
Calc. head	300.28	100.00	100	100	100	100	100	100	100	100	100	100	100	100	100	100	100	100	100	100	100	100	100	100	100	100